INMATEH –

AGRICULTURAL ENGINEERING

MAY - AUGUST

Editorial

The National Institute of Research-Development for Machines and Installations designed to Agriculture and Food Industry - INMA Bucharest has the oldest and most prestigious research activity in the field of agricultural machinery and mechanizing technologies in Romania.

Short History

- ✓ In 1927, the first research **Center for Agricultural Machinery** in Agricultural Research Institute of Romania - ICAR (Establishing Law was published in O.D. no. 97/05.05.1927) was established;

- ✓ In 1930, was founded **The Testing Department of Agricultural Machinery and Tools** by transforming Agricultural Research Centre of ICAR - that founded the science of methodologies and experimental techniaues in the field (Decision no. 2000/1930 of ICAR Manager - GHEORGHE IONESCU ŞIŞEŞTI);

- ✓ In 1952, was established the Research Institute for Mechanization and Electrification of Agriculture - ICMA Băneasa, by transforming the Department of Agricultural Machines and Tools Testing;

- ✓ In 1979, the Research Institute of Scientific and Technological Engineering for Agricultural Machinery and Tools – ICSITMUA was founded - subordinated to Ministry of Machine Building Industry - MICM, by unifying ICMA subordinated to MAA with ICPMA subordinated to MICM;

- ✓ In 1996 the National Institute of Research-Development for Machines and Installations designed to Agriculture and Food Industry – INMA was founded – according to G.D. no.1308/25.11.1996, by reorganizing ICSITMUA, G.D no. 1308/1996 coordinated by the Ministry of Education and Research G.D. no. 823/2004;

- ✓ In 2008 INMA has been accredited to carry out research and developing activities financed from public funds under G.D. no. 551/2007, Decision of the National Authority for Scientific Research - ANCSno. 9634/2008.

As a result of widening the spectrum of communication, dissemination and implementation of scientific research results, in 2000 was founded the institute magazine, issued under the name of SCIENTIFIC PAPERS **(INMATEH)**, ISSN 1583 – 1019.

Starting with volume 30, no. 1/2010, the magazine changed its name to INMATEH - **Agricultural Engineering**, appearing both in print format (ISSN 2068 - 4215), and online (ISSN online: 2068 - 2239). The magazine is bilingual, abstract being published in native language and English, with a rhythm of three issues / year: January-April, May-August, September-December and is recognized by CNCSIS – with B^+ category. Published articles are from the field of AGRICULTURAL ENGINEERING: technologies and technical eauipment for agriculture and food industry, renewable energy, machinery testing, environment, transport in agriculture etc. and are evaluated by specialists inside the country and abroad, in mentioned domains.

Technical level and performance processes, technology and machinery for agriculture and food industry increasing, according to national reauirements and European and international regulations, as well as exploitation of renewable resources in terms of efficiency, life, health and environment protection represent referential elements for the magazine „INMATEH - **Agricultural Engineering**".

We are thankful to all readers, publishers and assessors.

Editor in chief,
Ph. D. Eng. Vladut Nicolae-Valentin

CONTENT

EXPERIMENTAL STUDY OF THE MOVEMENT CONTROLLABILITY
OF A MACHINE-AND-TRACTOR AGGREGATE OF THE MODULAR TYPE
/
MODUĻA TIPA MAŠĪNAS – TRAKTORA AGREGĀTA KUSTĪBAS VADĪBAS EKSPERIMENTĀLIE PĒTĪJUMI

Ivanovs S.[1)], Bulgakov V.[2)], Nadykto V.[3)], Ihnatiev Ye.[3)], Smolinskyi S.[1)], Kiernicki Z.[4)] [1]

[1)] Latvia University of Life Sciences and Technologies, Latvia
[2)] National University of Life and Environmental Sciences of Ukraine, Ukraine
[3)] Dmytro Motornyi Tavria State Agrotechnological University, Ukraine,
[4)] Lublin University of Technology, Poland
Correspondence: Tel.+37129403708, e-mail: semjons @apollo.lv
DOI: https://doi.org/10.35633/inmateh-61-01

Keywords: movement, tractor, controllability, turning

ABSTRACT

The paper presents an analysis of the basic principles of formation, the properties and characteristics of a new modular energy tool, consisting of the energy and the technology modules. The purpose of this study is to assess the degree of impact of the throttle in the hydraulic line, connecting the cavity of the hydraulic cylinder, upon the controllability of the modular power tool with a mounted plough during the movement of the ploughing aggregate on the headland. As a result of the conducted tests, it was proved that increasing the controllability of the movement of the aggregate on the basis of a mobile power tool is possible by throttling one of the hydraulic cylinders that limit the mutual reciprocal rotation of the modules in a horizontal plane. Installation of the throttle modular power tool on the limiting hydraulic cylinder with a drag coefficient $1.03 \times 10^6 \cdot N \cdot m \cdot s \cdot rad^{-1}$ allows one to reduce two times the delay in the reaction of the relative bearing of the energy module to a change in the angle of rotation of its driven wheels.

ABSTRAKTS

Darbā analizēti jauna moduļa tipa enerģētiska un tehnoloģiska līdzekļa vērtēšanas un raksturošanas pamatprincipi. Pētījumu mērķis – droseles ietekmes pakāpes novērtēšana hidrocilindru dobumus savienojošajā hidromaģistrālē aršanas agregāta ar uzkarināmu arklu kustības laikā pagrieziena joslā. Pētījumu rezultātā pierādījies, ka agregāta kustības vadības uzlabošanās uz mobilā enerģētiskā līdzekļa bāzes iespējama pie viena hidrocilindra droselēšanas, ierobežojot moduļu savstarpējo pagriešanos horizontālā plaknē. Ierobežojoša hidrocilindra uzstādīšana moduļa tipa enerģētiskajam līdzeklim ar droseles pretestības koeficientu $1.03 \times 10^6 \cdot N \cdot m \cdot s \cdot rad^{-1}$ ļauj divas reizes samazināt enerģētiskā moduļa virziena leņķa reakcijas nokavēšanos uz dzenošo riteņu pagriešanos.

INTRODUCTION

Agriculture is the largest user of tractor equipment used to perform field work. One of the perspective directions is the modular construction of tractors *(Pădureanu et al., 2013; Klets, 2013; Bindi et al, 2013).* In this embodiment, the tractor consists of the energy and the technological modules. Their combination in a single design of a machine-and-tractor aggregate is a modular energy tool (Fig. 1).

The controllability of tractors was investigated by many scientists *(Wong, 2008; Taran and Bondarenko, 2017, Aoki et al., 2009; Bochtis et al., 2010; Popa and Buculei, 2013).* However, the controllability of energy modular units has a number of features and their further detailed study is required.

An energy module is a tractor the energy saturation of which should ideally be more than $14 \ kW \cdot t^{-1}$. However, as practice shows, under real conditions, the efficiency of using a modular energy tool can also occur with a lower energy saturation of the energy module *(Bulgakov et al., 2015).*

The technological module of the modular energy tool is a bridge the wheels of which are driven from a synchronous power take-off shaft of the energy module *(Kutjkov, 2004; Gjachev, 1981).*

---

[1] *Ivanovs S., Dr.Eng, Bulgakov V., Prof. Ph.D. Eng; Nadykto V., Prof. Ph.D.; Ihnatiev Ye., Dr.; Smolinskyi S., Dr.; Kiernicki Z., Prof. Ph.Dr.*

In the frontal part of the technological module there is a hitch mechanism with which it is attached to the rear mounted mechanism of the energy module. Coordination of the peripheral linear speeds of the wheels of the technological module and the rear wheels of the energy module is carried out using a special gearbox, located on the frame of the technological module.

Fig. 1 - A modular energy tool

For aggregation with the agricultural implements the technological module is equipped with a hydraulic mounted system, its own power take-off shaft, a saddle device and a brake system. In a horizontal plane the energy module is connected to the technology module by means of a vertical hinge. Its presence ensures the rotation of the technological module relative to the energy module by ± 30° during the movement of the modular energy tool on the headland. In a longitudinal-vertical plane the energy module is connected to the technology module using a horizontal hinge. Due to it the modular energy tool can carry out quite satisfactory copying of the longitudinal profile of the field surface. The limited turning ability of the technological module relative to the energy module in a horizontal plane is provided by two hydraulic cylinders, connecting the frames of the energy and the technological modules. To ensure the flow of oil from the over-piston cavity of the hydraulic cylinder into the under-piston cavity, the cavities are interconnected by a hydraulic line. However, in the process of experimental research of the modular energy tool it was found that, when it moves as part of the aggregate on the headland, the technological module may have increased vibrations in a horizontal plane. As a result, a decrease in the movement speed of the modular energy tool on the field headland was required. And this, as it is known, leads to lower efficiency of this or that machine-and-tractor aggregate *(Bulgakov et al., 2018; Samorodov and Pelipenko,2016).* To eliminate this drawback, a throttle with a resistance coefficient $K_m = 1.03 \times 10^6$·H·m·s·rad^{-1} was mounted in the hydraulic hose of one of the hydraulic cylinders, connecting the energy and the technological modules (Fig. 2). The substantiation methodology of the value of this coefficient is described in detail *in (Bulgakov et al., 2019).*

The purpose of this study is to assess the impact degree of the use of the aforementioned inductor with a resistance coefficient $K_m = 1.03 \times 106$ H m s rad^{-1} upon the controllability of a modular power tool with a mounted plough during the movement of this ploughing machine-and-tractor aggregate on the headland.
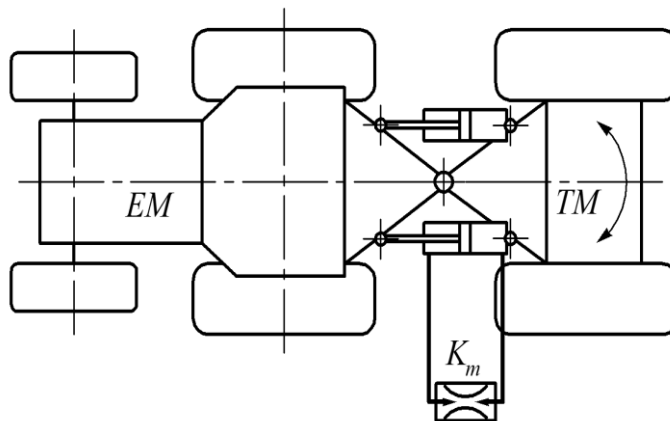
Fig. 2 - An installation scheme of a throttle in the hydraulic cylinder, connecting the energy and the technological modules of the modular energy tool

EM – the energy module; TM – the technology module; K_m – the inductor generating the resistance coefficient

MATERIALS AND METHODS

Experimental research of the ploughing aggregate based on a modular energy tool (table 1) were carried out on the field after peeling stubble of winter wheat (Fig. 3).

Table 1

Technical characteristics of a modular energy tool

Energy module	
Operating mass [kg]	3900
Engine power [kW]	77.2
Energy saturation rate [kW·t^{-1}]	19.8
Front wheels track [mm]	1500
Rear wheels track [mm]	1500
Front wheels tire size	13.6R20
Rear wheels tire size	15.5R38
Technological module	
Operating mass [kg]	2600
Wheel track [mm]	1500
Tire size	16.9R38

Fig. 3 - The ploughing aggregate, based on a modular energy tool

During experimental field research of the movement of this ploughing machine-and-tractor aggregate, based on a modular power tool on the headland, the average value of the soil moisture in the field in the 0 ... 10 cm layer was 15.3%. The soil density in the same layer did not exceed 1.24 g cm^3. The average value of the movement speed of this ploughing machine-and-tractor aggregate on the headland was 2.4 m s^{-1}. The longitudinal oscillations of the field irregularities were also recorded *(Dospehov, 2012)*.

The movement of the investigated ploughing aggregate on the headland was effected in the same gear with a throttle installed (K_m = 1.03×10^6 H m s rad^{-1}) in the hydraulic cylinder and without it (K_m = 0). The path of the movement of the aggregate was equal to 50 m. Based on this, the speed of the aggregate (V_a) was determined by the formula:

$$V_a = 50 \cdot (t)^{-1}$$

(1)

where t – the passage time of the aggregate is 50 m long.

To record the movement time of the modular power tool with a plough on the headland, an electronic stopwatch with a measurement accuracy of ± 0.1 s was used.

In the process of the movement of the modular energy tool, the turning angle of the driven wheels of the energy module (α) and its relative bearing angle (φ) were recorded.

To measure the soil moisture (W), an MG-44 electronic device (Ukraine) was applied with an accuracy of ± 1%. The measurement of the soil density (ρ_g) was carried out by a device that we have developed according to the methodology *(Nadykto and Kotov, 2015)*. The number of measurements of each of the parameters W and ρ_g was 50.

The turning angle of the energy module's driven wheels of the modular energy tool was recorded using a variable resistor SP-3A with a linear characteristic and a rating of 470 Ohm. The resistor was mounted on the rotation axis of the left frontal wheel of the energy module of the modular energy tool (Fig. 4).

Fig. 4 - Resistor SP-3A (440 Om)

Fig. 5 - The field profile meter

In order to measure the oscillations of the longitudinal field profile, a special instrument (Ukraine) was used, the recording element of which was a variable resistor SP-3A with a linear characteristic and a nominal value of 470 Ohm (Fig. 5).

The relative bearing angle (φ) of the energy module of the modular energy tool was recorded using a GY-521 gyroscope with an Arduino microcontroller (China).

The electrical signals from the gyroscope and resistors for recording the angle α, as well as the oscillations of the longitudinal profile of the field, were transmitted to an analogue-to-digital converter and then to a personal computer. The repeatability of the measurement of these parameters was 3.

Statistical characteristics, such as dispersion, as well as normalised correlation functions and spectral densities were calculated from the resulting data arrays *(Box et al., 2005).*

To analyse the movement controllability of the ploughing aggregate, based on the modular energy tool at different throttling values of the hydraulic cylinder, a normalised cross-correlation function *(Dospehov, 2012)* was applied that relates the oscillations of the turning angle of the energy module's driven wheels of the modular energy tool (α) with the oscillations of its relative bearing angle (φ).

RESULTS AND DISCUSSION

Analysis of the data, characterising the fluctuations in the irregularities of the longitudinal profile of the field surface, showed that the correlation length of the normalised correlation function of this process is 1 m (Fig. 6 a).

Knowing the movement speed of the machine-and-tractor aggregate, it's easy to determine the time of the correlation link. In this case, at the aggregate velocity of 2.4 m s^{-1}, it is equal to: 1 (2.4)$^{-1}$ = 0.42 s. In addition, it can be considered that the oscillations of the longitudinal profile of the field surface practically do not have a hidden periodic component. The information on the changes in the correlation function that take place in the graph, shown in Fig. 6a, is not enough to determine the source of their generation.

In addition, the dispersion of the oscillations of the discussed process is 0.91 cm^2. It is mainly concentrated in a rather narrow frequency range 0...2 m^{-1} (Fig. 7). Considering that the speed of the movement of this ploughing machine-and-tractor aggregate is 2.4 m s^{-1}, the range is 0...4.8 s^{-1} or 0...0.76 Hz.

The cut-off frequency of the spectral density, as can be seen from the graph, shown in Fig. 6 b, practically does not exceed 6 m^{-1} or 14.4 s^{-1}, which is equal to 2.3 Hz.

When this ploughing aggregate moved on the agrotechnical background with such characteristics of longitudinal profile oscillations, the control action in the form of the turning angle of the driven wheels of the

modular energy tool changed in a very narrow range. Thus, the main part of the dispersion of this parameter's oscillations is concentrated in the frequency range 0...2.0 s^{-1} , or 0...0.32 Hz (Fig. 8).
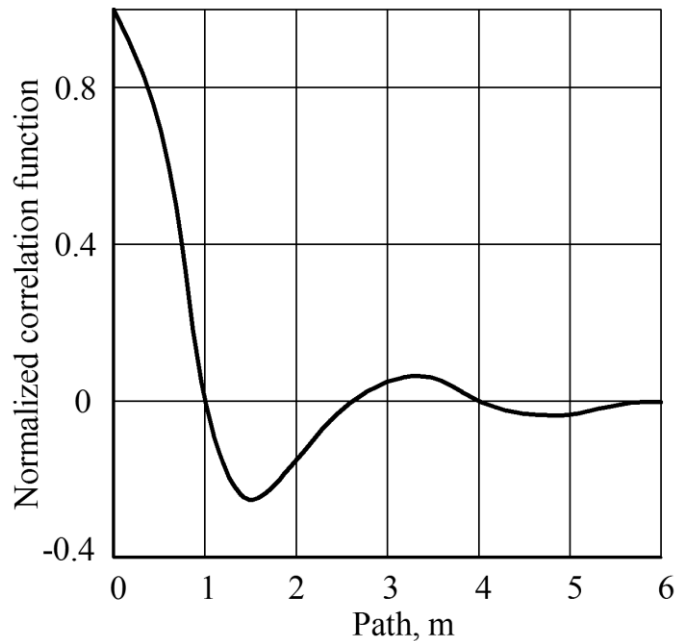
Fig. 6 - A normalised correlation function of oscillations of the field surface longitudinal profile
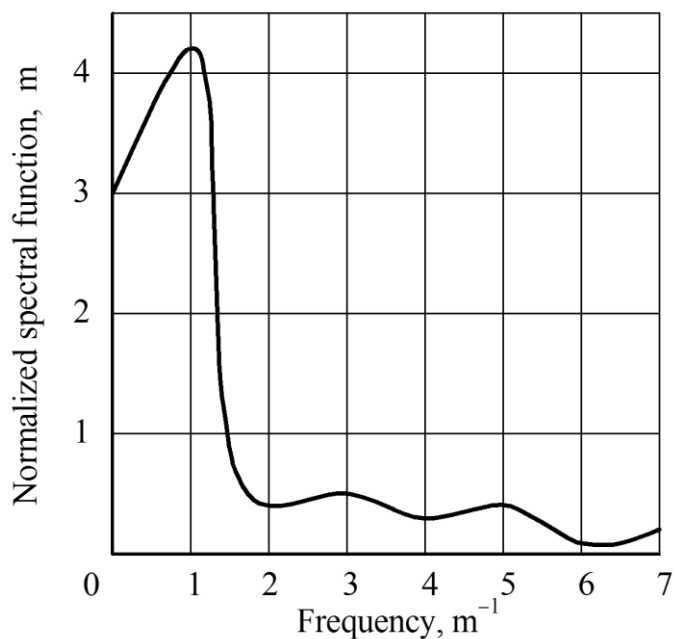
Fig. 7 - Spectral density of oscillations of the field surface longitudinal profile

The maximum value of the normalised spectral density of angle α oscillations falls on a rather narrow frequency range: 0.30 ... 0.35 s^{-1}.

As it turned out, the block-modular unit worked out the fluctuations in the input impact differently. In the absence of the hydraulic cylinder throttling of the technological module of the modular energy facility a positive correlation was found between the parameters α and φ. But, first, it is rather weak since the maximum value of the mutual correlation function does not exceed the mark (Curve 2 presented in Fig. 9).
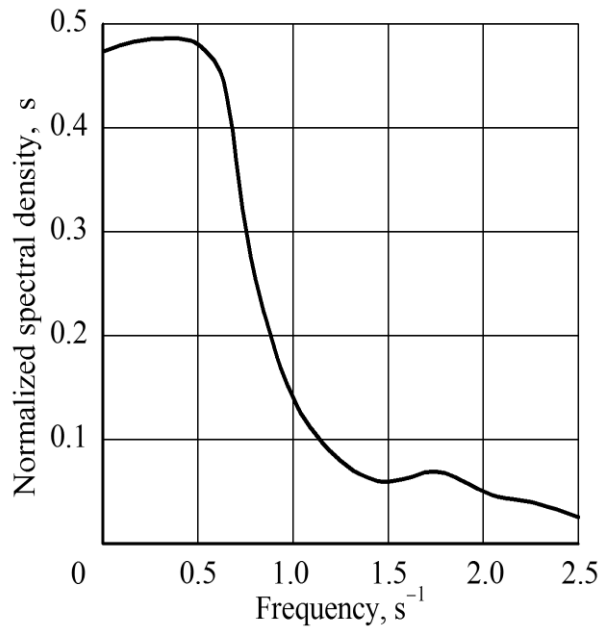
**Fig. 8 - Normalised spectral density of the turning angle oscillations
of the modular energy tool's driven wheels**
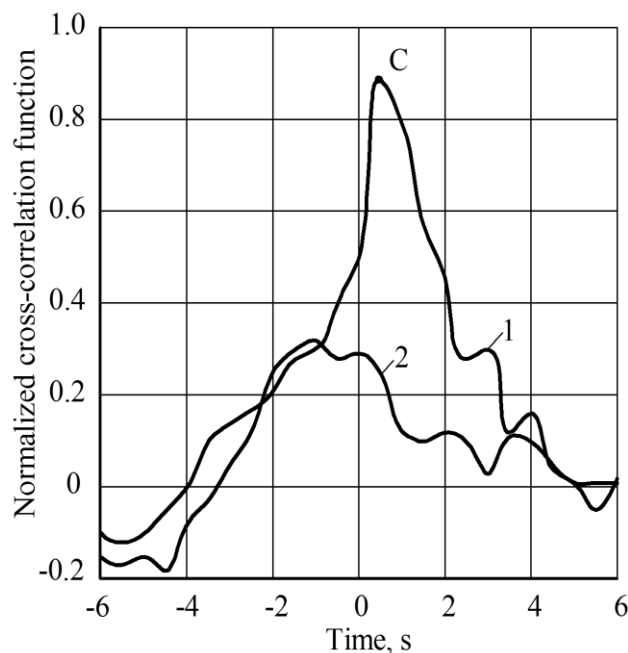
**Fig. 9 - The normalised mutual correlation functions of the relative bearing angle φ oscillations,
caused by angle α fluctuations at various throttling levels of the technological module's hydraulic cylinder**
1) $K_m = 1.03 \times 10^6$ N m s rad^{-1}; 2) $K_m = 0$

Second, the maximum value of this function is shifted to the left of the zero coordinate by about 1 s. This means that the input of this dynamic system is not the turning angle α of the driven wheels of the modular energy tool but its relative bearing angle φ. That is, the control impact is a reaction to the change in the relative bearing angle φ with a delay in time at the level of 1 s.

Besides, the cause of the change in the relative bearing angle φ of the modular energy tool may be the fluctuations in the expanding (turning out) moment, acting from the side of the technological module, or some other disturbance.

At the same time, the introduction of a hydraulic damper into the hydraulic cylinder of the technological module of the modular energy tool with a stiffness coefficient $K_m = 1.03 \times 10^6$ N m s rad^{-1} essentially changes the behaviour of the mutual correlation function $\alpha - \varphi$. The data obtained and processed by statistical methods of the experimental field investigations give reason to state the following:

First, the strength of the correlation link between the changes in the parameters $α$ and $φ$ sharply increases. Compared with the variant $K_m = 0$, the maximum of the mutual correlation function increases 2.6 times, reaching the level of 0.89.

Second, the maximum of the estimated function (Curve 1, Point C, shown in Fig. 9) is shifted to the right of the zero ordinate. And this indicates that the control impact (that is, angle $α$) is the input, and the relative bearing angle of the modular energy tool $φ$ is the output of the dynamic system under consideration.

Third, the delay in the reaction of the relative bearing angle $φ$ to a change in the control impact of the wheels of the modular energy tool is reduced almost two times. In this case it is approximately equal to 0.51 s. Such a result is desirable since the reaction of the consideration tracking dynamic system to a change in the control impact should, in the ideal, be instantaneous. That is, it proceeds with zero delay. But, since it is impossible to achieve this in practice, any structural and technological solution, aimed at reducing the response of a dynamic system to the useful input signal, is desirable. In our case, such a solution is to install a throttle in the hydraulic cylinder of the technological module of the modular energy facility

CONCLUSIONS

It is possible to increase the controllability of the aggregate movement on the basis of a modular energy tool, consisting of the energy and the technological modules, by throttling one of the hydraulic cylinders, which limit the mutual turning ability of these modules in a horizontal plane.

The equipment of the hydraulic cylinder of the modular power tool with a throttle, having a resistance coefficient 1.03×10^6 N m s rad^{-1} , makes it possible:

– to bring the maximum value of the mutual correlation function between the control impact, i.e., the turning angle of the energy module's driven wheels of the modular energy tool and its relative bearing angle to the level of 0.89;

– to shift the maximum value of this cross-correlation function to the right of the zero ordinate, thereby providing the turning angle of the energy module's driven wheels of the modular energy tool with a role of input (rather than output) impact;

– to reduce practically two times the delay in the reaction of the relative bearing angle of the energy module of the modular energy tool to a change in the turning angle of its driven wheels.

REFERENCES

[1]   Aoki, A., Marumo, Y., Kageyama, I. and Kuwahara, K., (2009), Controllability and Loading Conditions of Tractor and Semitrailer Combinations in Lane Change, *Transactions of the Japan Society of Mechanical Engineers, Series C*, Vol.75, No.749, pp. 66-73;

[2]   Bindi, I., Blackwell, P., Riethmuller, G., Davies, S., Whitlock, A. Neale, T., (2013), This Controlled Traffic Farming Technical Manual. It Updates the Tramline Farming Systems: Technical Traffic Farming Technical Manual. It Updates the Tramline Farming Systems*: Technical Manual Bulletin 4607*, p. 78. Published by the Department of Agriculture and food, Western Australia;

[3]   Box, G.E., Hunter, W.G.; Hunter, J.S. (2005), *Statistics for Experimenters: Design, Innovation, and Discovery* (2nd ed.). Wiley. 664 p;

[4]   Bulgakov, V., Kyurchev, V., Nadykto, V., Olt, J., (2015), Structure Development and Results of

[5]   Testing a Novel Modular Power Unit. *Agriculture and Agricultural Science Procedia.* Elsevier Srl, pp.40–44. https://doi.org/10.1016/j.aaspro.2015.12.028;

[6]   Bulgakov, V., Ivanovs, S., Nadykto, V., Kuvachov, V., Masalabov, V., (2018). Research on the turning ability of a two-machine aggregate. *INMATEH - Agricultural Engineering,* 54, pp.139–146;

[7]   Bulgakov, V., Parakhin, O., Mitkov, V., Chorna, T., (2019), The Coefficient Determination of a Damper Washer Hydraulic Resistance for Reducing a Technical Module Oscillation Amplitude. *Modern Development Paths of Agricultural Production*. Springer International Publishing, pp. 183–190. https://doi.org/10.1007/978-3-030-14918-5_20;

[8]   Dospehov, B., (2012), *Methodology of field experiments.* Nauka, Moscow/Russia, 352 p. (In Russian: Metodika polevogo opyta);

[9]   Gjachev L., (1981), *Stability of the movement of agricultural machines and aggregates.* Moscow/Russia, 206 p. (In Russian);

[10]   Kutjkov G., (2004), Tractors and cars. *Theory and technological properties.* Moscow/Russia, 504 p. (In Russian);

[11]   Nadykto, V., Kotov, O., (2015), *Method for determining soil bulk density* (in Ukrainian: Sposib viznachennya shchilnosti gruntu). Patent UA No 97828;

[12]   Pădureanu, V., Lupu, M.I., Canja, C.M., (2013), Theoretical research to improve traction performance of wheeled tractors by using a supplementary driven axle. *Computational Mechanics and Virtual Engineering.* Braşov/ Romania, pp. 410–415;Klets, D.M. (2013), Modelling of mobile vehicle skid in traction movement mode. *Motrol Commission of Motorization and Energetics in Agriculture*, 15 (7), Lublin/Poland, pp. 157-162;

[14]   Popa, G., Buculei, M. (2013), Experimental determination of u-650 tractor traction performances equipped with supplementary hydrostatic transmission. *INMATEH-Agricultural Engineering*, 41 (3), pp. 65-68, Bucharest / Romania;

[15]   Samorodov, V., Pelipenko, E., (2016), Analysis of the development of modern transmission wheeled tractors. *International Collection of Scientific Proceedings «European Cooperation»*, 6 (13), pp.49-57;

[16]   Taran, I., Bondarenko, A., (2017), Conceptual approach to select parameters of hydrostatic and mechanical transmissions for wheel tractors designed for agricultural operations. *Archives of Transport,* Volume 41, Issue 1, pp. 89-100;

[17]   Wong, J.Y., (2008), *Theory of Ground Vehicles*. John Wiley & Sons, ISBN 978-0-470-17038-0.

RESEARCH ON CHANGES IN BIOMASS DURING GASIFICATION
/
ДОСЛІДЖЕННЯ ЗМІНИ МАСИ РОСЛИННОЇ БІОМАСИ В ПРОЦЕСІЇ ЇЇ ГАЗИФІКАЦІЇ

Genadii Golub[1)], *Savelii* Kukharets [2)], *Jonas* Čėsna [3)], *Oleh* Skydan [2)], *Yaroslav* Yarosh[2)], *Mykolai* Kukharets [2)] [1]
[1)]National University of Life and Environmental Sciences of Ukraine / Ukraine,
[2)] Zhytomyr National Agroecological University / Ukraine,
[3)] Vytautas Magnus University Agriculture Academy / Lithuania
Tel: +380676653548, E-mail: saveliy_76@ukr.net

Keywords: gasifier, straw, burning gas, fuel, gasification rate, model.

ABSTRACT
The article suggests that the rate of plant biomass gas generation is proportional to the amount of plant biomass, which can still be gasified. To analyse the change in fuel mass during the operation of the gasifier for a certain period of time, three models can be used with the following assumptions: the change in fuel mass is inversely proportional to the fuel mass and time, the change in fuel mass is inversely proportional to the fuel mass, the change in fuel mass is inversely proportional to time. The coefficients of the fuel gasification rate are experimentally found.

АБСТРАКТ
В статті зроблено припущення, що швидкість газогенерації рослинної біомаси пропорційна кількості рослинної біомаси, що ще може бути газифікована. Для аналізу зміни маси палива в процесі роботи газогенератора упродовж певного періоду часу можна використати три моделі із наступними допущеннями: зміна маси палива обернено пропорційна масі палива і часу, зміна маси палива обернено пропорційна масі палива, зміна маси палива обернено пропорційна часу. Експериментальним шляхом знайдено коефіцієнти швидкості газифікації палива.

INTRODUCTION

When burning plant biomass there are difficulties associated with the heterogeneity of biomass, relatively high humidity, low specific energy, low melting point of ash *(Golub et al, 2018a; Golub et al, 2018b; Thiagarajan et al, 2018)*. Therefore, the use of gasifiers for biomass gasification will be appropriate for the consumer to obtain a stable energy supply *(Patra, Sheth, 2015)*. Analysis of scientific research allows us to conclude that the gasification of biomass is a complex process based on the equations of thermochemical equilibrium, kinetics, heat transfer and mass transfer *(Melgar et al, 2007; Zainal et al, 2001; De La Hoz et al, 2017)*, which are based on the rate of biomass gasification.

Taking into account the stoichiometric equilibrium of the reaction of combustible gas formation *(Fani Mostafa et al, 2018; La Villetta et al, 2017; Jia et al, 2018)* and considering the formation of resins, the equation of wood gas formation will be:

$$m_1 C_x H_y O_z N_n + m_2 H_2 0 + m_3 \left(O_2 + \lambda N_2 \right) =$$
$$= m_4 CO + m_5 H_2 + m_6 CO_2 + m_7 H_2 0 + m_8 CH_4 + \left(nm_1 + \lambda m_3 \right) N_2 + m_9 C_{xtar} H_{ytar} O_{ztar}, \tag{1}$$

where: m_1 – specific consumption of dry fuel (biomass) in the formation of combustible gas, mol/sec; m_2 – specific fuel moisture consumption, mol/sec; m_3 – specific air consumption, mol/sec; m_4 – specific content of carbon monoxide in the wood gas (output), mol/sec; m_5 – specific content of hydrogen in the wood gas (output), mol/sec; m_6 – specific content of carbon dioxide in the wood gas (output), mol/sec; m_7 – specific content of moisture in the wood gas (output), mol/sec; m_8 – specific content of methane in the wood gas (output), mol/sec; m_9 – specific content of resin in wood gas (output) , mol/sec; λ – coefficient characterizing the nitrogen content in the air (λ=3.76); x – the number of carbon molecules in the fuel mole; y – the number of hydrogen molecules in the fuel mole; z – the number of oxygen molecules in the fuel mole; n – the number of nitrogen molecules in the fuel mole; x_{tar} – the number of carbon molecules in the resin mole; y_{tar} – the number of hydrogen molecules in the resin mole; z_{tar} – the number of oxygen molecules in the resin mole.

---

[1] *Genadii Golub, Prof.Dr.; Savelii Kukharets, Prof.Dr.; Jonas Čėsna, Dr.; Oleh Skydan, Prof.Dr.;*
Yaroslav Yarosh, Dr.; Mykolai Kukharets, As.

Taking into account the equivalence ratio (*ER*) which determines the ratio of the oxygen amount supplied to the gasifier to the oxygen amount required according to the stoichiometric combustion of fuel *(Maneerung et al, 2018; Yan et al, 2018)* we obtain: $ER = 0.21m_3 / (xm_1 + 0.25ym_1 + 0.5zm_1)$, the value of the air flow will be:

$$m_3 = 4.76ER(xm_1 + 0.25ym_1 + 0.5zm_1).$$ (2)

Substituting the equation 2 in 1 and taking into account that the coefficient characterizing the nitrogen content in the air is *λ*=3.76, we obtain:

$$m_1 \left(\begin{array}{c} C_x H_y O_z N_n + 4.76ER(x + 0.25y + 0.5z)(0_2 + 3,76N_2) - \\ -(n + 17.9ER(x + 0.25y + 0.5z)N_2 \end{array} \right) + m_2 H_2 0 =$$ (3)

$$= m_4 CO + m_5 H_2 + m_6 C0_2 + m_7 H_2 0 + m_8 CH_4 + (nm_1 + 3.76m_3)N_2 + m_9 C_{xtar} H_{ytar} O_{ztar}.$$

If we take into account the molar masses of the chemical components included in equation (4), it can be written as the calculated material balance:

$$\mu_1 m_1 \left(\begin{array}{c} C_x H_y O_z N_n + 4.76ER(x + 0.25y + 0.5z)(0_2 + 3,76N_2) - \\ -(n + 17.9ER(x + 0.25y + 0.5z)N_2 \end{array} \right) + 18m_2 H_2 0 =$$

$$= 28m_4 CO + 2m_5 H_2 + 44m_6 C0_2 + 18m_7 H_2 0 +$$ (4)

$$+ 16m_8 CH_4 + 28(nm_1 + 3.76m_3)N_2 + \mu_9 m_9 C_{xtar} H_{ytar} O_{ztar},$$

where: μ_1 – molar mass of fuel, g/mol; μ_9 – molar mass of resin, g/mol.

Obviously, in equation 5, the product $\mu_1 m_1$ is the fuel consumption rate or the rate of plant biomass gas generation. Nevertheless, the study of biomass gasification rate is difficult for theoretical research due to the complexity of interaction, diversity and transience of the corresponding processes *(Yan et al, 2018; Ali et al, 2016)*. This complexity prevents theoretical models from achieving the necessary accuracy to optimize the gasification process *(Mazaheri et al, 2018)*. In addition, the insufficient amount of experimental data on the rate of biomass gasification also does not allow the developed theoretical models of the gasification process to achieve the required accuracy *(Gu et al, 2019).* Therefore, it is necessary to accumulate experimental data in the real range of parameters of gasifiers and create simple mathematical models that adequately describe the biomass gasification rate.

MATERIALS AND METHODS

A specially designed research plant was used for experimental studies of biomass gasification rate (Fig. 1 a, b). The structure of the plant included a gasifier of the reverse process. The diameter of the recovery zone was 200 mm; the height of the recovery zone was 110 mm and was determined according to the studies described in (*Golub et al, 2019)*. The number of tuyere holes was 12; their diameter was 10 mm. The flow of air into the gasifier was carried out by a blower and was varied in the range of 0.0009 m³/sec and 0.012 m³/sec. The performance of the blower was adjusted by frequency converter. The gasifier was installed on the scales, loaded with fuel and put into operation. Operating mode was fixed by steady burning of gas torch.

a)   b)
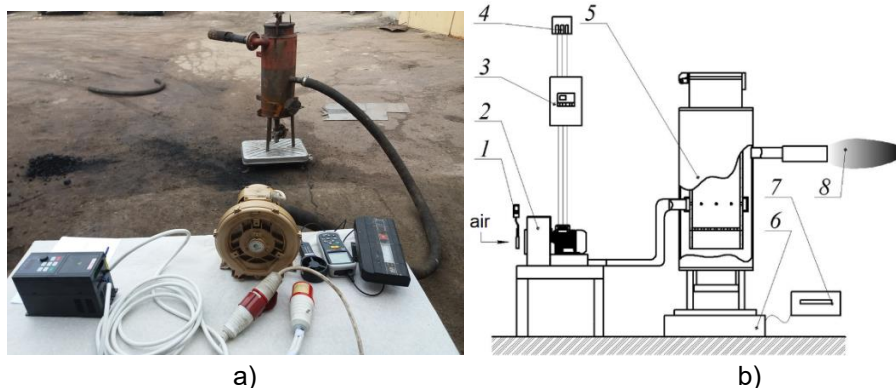
**Fig.1 - Appearance (a) and scheme (b) of the plant for the study of changes in the fuel mass
in the process of combustible gas production**
*1 – anemometer Tenmars TM-402; 2 – blower Goorui GHBH-0D5-34-1R2; 3 – frequency converter Hitachi-3G3JX-A4075-EF;
4 – socket 0.4 kV; 5 – gasifier GG-1; 6 – scale; 7 – scale indicator; 8 – wood gas torch*

Straw pellets, wood pellets, wood pieces and peat pieces were used as fuel. With the help of scales, the mass of fuel remaining in the gasifier was fixed at equal intervals. For the final moment of time, it was accepted the moment when the torch of combustible gas extinguished. Further, the mass of fuel remaining in the gasifier and the mass of ash were recorded.

RESULTS
Theoretical studies

Assuming that the rate of gas generation of plant biomass is proportional to the amount of plant biomass that can still be gasified, three models with the following assumptions can be used to analyse the change in fuel mass during the operation of the gasifier for a certain period of time: the change in fuel mass is inversely proportional to fuel mass and time; the change in fuel mass is inversely proportional to the fuel mass; the change in fuel mass is inversely proportional to time.

The first model is based on the assumption that the fuel mass change $dM/d\tau$ is inversely proportional to the fuel mass M and time τ:

$$\frac{dM}{d\tau} = -k_{M\tau} M \tau , \tag{5}$$

where:

M – the fuel mass, kg; τ – gasifier operating time, sec; $k_{M\tau}$ – the speed ratio of the fuel gasification according to mass and time.

The solution of the equation (5) will be as follows:

$$\frac{dM}{M} = -k_{M\tau} \tau d\tau; \quad \ln M - \ln M_0 = -\frac{k_{M\tau}}{2}(\tau^2 - \tau_0^2).$$

Considering that $\tau_0 = 0$, we will obtain:

$$\ln \frac{M}{M_0} = -\frac{k_{M\tau}\tau^2}{2}, \quad \frac{M}{M_0} = \exp\left(-\frac{k_{M\tau}\tau^2}{2}\right),$$

$$M = M_0 \exp\left(-\frac{k_{M\tau}\tau^2}{2}\right), M_g = M_0\left(1 - \exp\left(-\frac{k_{M\tau}\tau^2}{2}\right)\right); \tag{6}$$

where:

M_0, M, M_g – initial, final, and the mass of the gasified fuel, %.

In this case, the rate coefficient of fuel gasification based on research data can be determined by the formula:

$$k_{M\tau} = \frac{2}{\tau^2} \ln \frac{M_0}{M} . \tag{7}$$

The second model is based on the assumption that the fuel mass change $dM/d\tau$ is inversely proportional to the fuel mass M:

$$\frac{dM}{d\tau} = -k_M M ; \tag{8}$$

where:

k_M – the speed ratio of the fuel gasification according to the mass.

The solution of the equation (8) will be as follows:

$$M = M_0 \exp\left(-k_M \tau\right), \ M_g = M_0\left(1 - \exp\left(-k_M \tau\right)\right). \tag{9}$$

In this case, the rate coefficient of fuel gasification based on research data can be determined by the formula:

$$k_M = \frac{1}{\tau} \ln \frac{M_0}{M} . \tag{10}$$

The third model is based on the assumption that the change in fuel mass $dM/d\tau$ is inversely proportional to the operating time of the gasifier τ:

$$\frac{dM}{d\tau} = -k_\tau \tau; \qquad (11)$$

where:

k_τ – the speed ratio of gasification according to the time.

The solution of the equation (11) will be as follows:

$$M = M_0 - \frac{k_\tau}{2}\tau^2, \quad M_g = M_0 - \left(M_0 - \frac{k_\tau}{2}\tau^2\right). \qquad (12)$$

In this case, the rate coefficient of fuel gasification based on research data can be determined by the formula:

$$k_\tau = 2\frac{M_0 - M}{\tau^2}. \qquad (13)$$

Experimental studies

Experiments on the gasification rate of straw pellets at different modes of oxidizer (air) supply to the gasifier oxidation zone at the optimum height of the reduction zone were carried out and the results given in table 1 were obtained.

Table 1

Experimental values of fuel mass change in the process of straw pellets gasification

Indicator	Mass of gasified fuel, kg					
	0	1	2	3	4	4.8
The air supply to the gasifier 0.012 m³/sec						
Ash mass, kg	0	0.04	0.08	0.12	0.16	0.2
Gasifier operation time, sec	0	135	250	415	620	840
Current fuel mass, kg	5	3.96	2.92	1.88	0.84	0
Ash content, %	0	0.8	1.6	2.4	3.2	4.0
The air supply to the gasifier 0.006 m³/sec						
Ash mass, kg	0	0.04	0.08	0.12	0.16	0.2
Gasifier operation time, sec	0	150	300	475	740	1015
Current fuel mass, kg	5	3.96	2.92	1.88	0.84	0
Ash content, %	0	0.8	1.6	2.4	3.2	4
The air supply to the gasifier 0.0009 m³/sec						
Ash mass, kg	0	0.04	0.08	0.12	0.16	0.2
Gasifier operation time, sec	0	315	621	1040	1630	2100
Current fuel mass, kg	5	3.96	2.92	1.88	0.84	0
Ash content, %	0	0.8	1.6	2.4	3.2	4

Substituting the value of the initial and final mass and time (from table 1) in formulas 9, 13 and 1, the coefficients of the gasification rate of straw granules were determined and the change in the fuel mass was calculated according to the above three models (table 2).

Since the calculated coefficient of determination is the highest for the model with the assumptions that the change in fuel mass is proportional to the fuel mass, it is the closest to the experimental values of the change in the mass of straw granules during the operation of the gasifier for a certain period of time. The obtained dependences are shown in Fig. 2.

Similar calculations were also performed for other values of air supply to the gasifier.
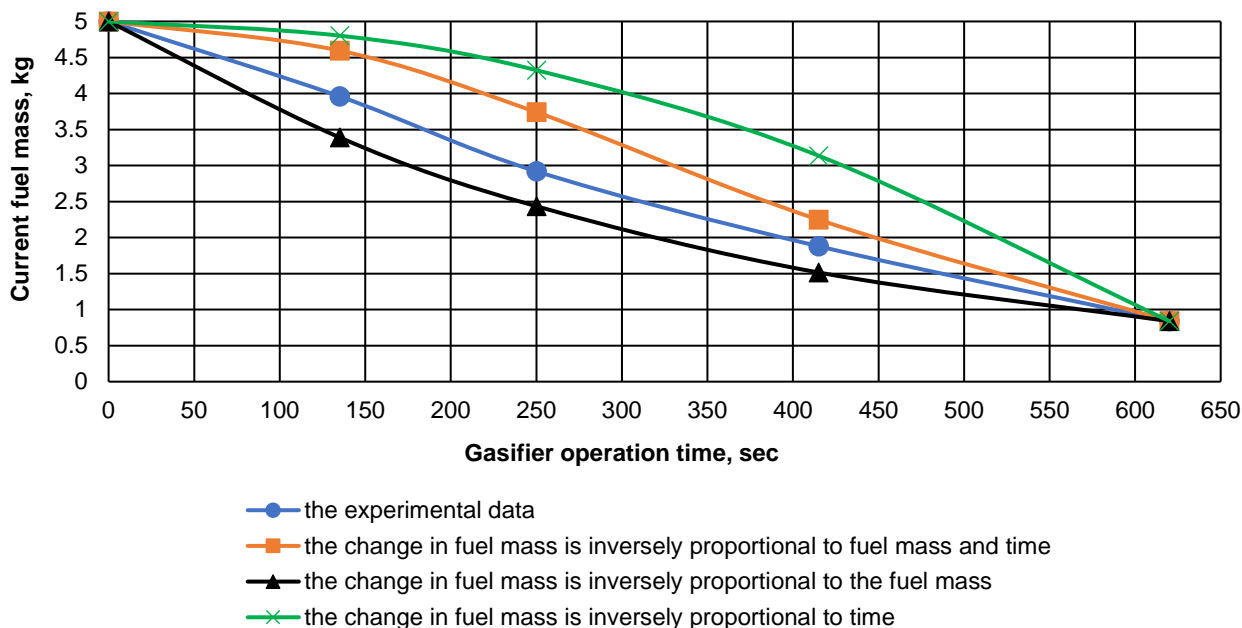
Fig. 2 - Change of fuel mass in the process of straw pellets gasification during air supply 0.01169 m^3/sec

Table 2

Calculated values of fuel mass change in the process of straw pellets gasification (initial fuel mass 5 kg, air supply to the gasifier 0.012 m^3/sec, time 620 sec)

Indicator	Gasifier operation time, sec					The sum of the values
	0	**135**	**250**	**415**	**620**	
Experimental data						
Current fuel mass, kg	5	3.96	2.92	1.88	0.84	14.6
The square of deviation of experimental values from the general arithmetic mean	1.8225	0.0961	0.5329	3.1329	7.8961	13.4805
The change in fuel mass is inversely proportional to fuel mass and time						
The ratio of gasification rate, sec^{-2}	9.2809·10^{-6}					
Current fuel mass, kg	5	4.59	3.74	2.25	0.84	16.42
Square of deviation of experimental data from theoretical one	0	0.3969	0.6724	0.1369	0	1.2062
Coefficient of determination	0.955					
The change in fuel mass is inversely proportional to the fuel mass						
The ratio of gasification rate, sec^{-1}	0.002877					
Current fuel mass, kg	5	3.39	2.44	1.52	0.84	13.19
Square of deviation of experimental data from theoretical one	0	1.44	1.69	0.5329	0	3.6629
Coefficient of determination	0.973					
The change in fuel mass is inversely proportional to time						
The ratio of gasification rate, kg·sec-2	2.1644·10^{-6}					
Current fuel mass, kg	5	4.8	4.32	3.14	0.84	18.1
Square of deviation of experimental data from theoretical one	0	0.7056	1.96	1.5876	0	4.2532
Coefficient of determination	0.848					

Similarly to the study of the rate of straw pellets gasification, the experiments on the rate of gasification of wood pellets, wood pieces and peat pieces were conducted (table 3-5).

Table 3

**Experimental parameters of fuel mass change in the process of pellets and wood gasification
(air supply to the gasifier 0.012 m³/sec)**

Indicator	Mass of gasified fuel, kg					
	0	1	2	3	4	4.85
Ash mass, kg	0	0.03	0.05	0.08	0.1	0.15
Gasifier operation time, sec	0	105	230	390	580	785
Current fuel mass, kg	5	3.97	2.95	1.92	0.9	0
Ash content, %	0	0.6	1	1.6	2	3

Table 4

**Experimental parameters of fuel mass change in the process of gasification of wood pieces
(air supply to the gasifier 0.012 m³/sec)**

Indicator	Mass of gasified fuel, kg					
	0	1	2	3	4	4.8
Ash mass, kg	0	0.04	0.08	0.12	0.16	0.2
Gasifier operation time, sec	0	125	235	405	615	830
Current fuel mass, kg	5	3.96	2.92	1.88	0.84	0.00
Ash content, %	0	0.8	1.6	2.4	3.2	4.0

Table 5

**Experimental parameters of fuel mass change in the process of gasification of peat pieces
(air supply to the gasifier 0.012 m³/sec)**

Indicator	Mass of gasified fuel, kg					
	0	1	2	3	4	4.65
Ash mass, kg	0	0.07	0.14	0.21	0.28	0.35
Gasifier operation time, sec	0	109	222	375	595	800
Current fuel mass, kg	5	3.93	2.86	1.79	0.72	0
Ash content, %	0	1.4	2.8	4.2	5.6	7

According to the results of experimental studies, the values of the gasification rate coefficients depending on the air supply to the gasifier were calculated (Fig. 3). It was established that for other types of biomass the closest to the experimental values of the fuel mass change and during the operation of the gasifier for a certain period of time was a model with the assumptions that the fuel mass change was proportional to the fuel mass. Empirical equations for determining the coefficient of fuel gasification rate by mass depending on the air supply to the gasifier are given in table. 6.
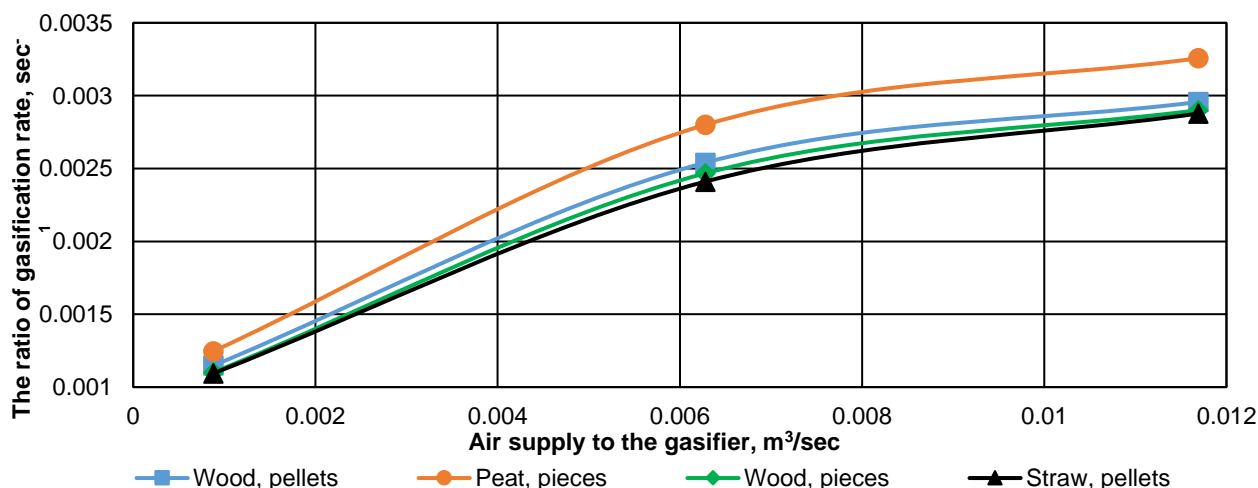
Fig. 3 - Change in the speed of gasification depending on the air supply

Table 6

The values of the speed ratio of biomass gasification

Fuel type	Air supply q_g, m³/sec			Empirical equation
	0.0009	**0.006**	**0.012**	
Wood, pellets	0.001148	0.00254	0.002957	$k_M=-16.733q_g^2+0.3776q_g+0.0008$
Peat, pieces	0.001246	0.0028	0.003257	$k_M=-18.819q_g^2+0.4226q_g+0.0009$
Wood, pieces	0.001101	0.002467	0.0029	$k_M=-15.994q_g^2+0.3675\ q_g+0.0008$
Straw, pellets	0.001094	0.002411	0.002877	$k_M=-14.57q_g^2+0.3481q_g+0.0008$

According to the values of the coefficient of biomass gasification rate, peat pieces have the highest gasification rate, and straw pellets – the lowest one. The proposed method of biomass gasification rate estimation can be used for other types and sizes of gasifiers.

CONCLUSIONS

Mathematical models of fuel mass change in the gasifier in the process of wood gas depending on the air supply to the gasifier are developed.

In mathematical models, the following assumptions were made: change in fuel mass is inversely proportional to the mass of fuel and time; change in the mass of the fuel is inversely proportional to the mass of fuel; change in the mass of the fuel is inversely proportional to time.

It is found that the closest to the experimental values of the fuel mass change during the operation of the gasifier for a certain period of time is the model of the fuel mass change proportional to the fuel mass.

On the basis of experimental studies, it was found that peat pieces have gasification coefficient of 0.0033 sec^{-1}, wood pellets – 0.003 sec^{-1}, wood pieces and straw pellets – 0.0029 sec^{-1} when the air supply to the tuyere belt of the gasifier equals 0.012 m³/sec.

REFERENCES

[1] Ali D.A., Gadalla M.A., Abdelaziz O.Y., et al., (2016), Co-gasification of coal and biomass wastes in an entrained flow gasifier: Modelling, simulation and integration opportunities, *Journal of Natural Gas Science & Engineering*, Vol.37, pp.126-137, Netherlands;

[2] De La Hoz C.K., Pérez J.F., Chica Arrieta E.L., (2017), Design of a Top-Lit Up-Draft Micro-gasifier Biomass Cookstove by Thermodynamic Analysis and Fluent Modeling, *International Journal of Renewable Energy Research*, Vol.7, No.4, pp.2172-2187, Ankara / Turkey;

[3] Fani Mostafa M., Niri H., Joda F., (2018), Simplified Dynamic Thermokinetic-Based Model of Wood Gasification Process, *Process Integration and Optimization for Sustainability*, Vol.2, Is.3, pp.269-279, Malaysia;

[4] Golub G., Kukharets S., Tsyvenkova N., et al., (2018a), Experimental study into the influence of straw content in fuel on parameters of generator gas, *Eastern-European Journal of Enterprise Technologies*, Vol.5/8(95), pp.76-86, United Arab Emirates;

[5] Golub G., Kukharets S., Yarosh Y., Chuba V., (2019), Method for Optimization of the Gasifier Recovery Zone Height, *Journal of Sustainable Development of Energy, Water and Environment Systems*, Vol.7(3), pp.493-505, Croatia;

[6] Golub G.A., Kukharets S.M., Tsyvenkova N.M., et al., (2018b), Research on a boiler furnace module effectiveness working on small fracture wastes, *INMATEH – Agricultural Engineering*, Vol.55, Issue 2, pp.7–16, Bucharest / Romania;

[7] Gu H., Tang Y., Yao J., Chen F., (2018), Study on biomass gasification under various operating conditions, *Journal of the Energy Institute*, Vol.92, is.5, pp.1329-1336, London / U.K.;

[8] Jia J., Xu L., Abudula A., Sun B., (2018), Effects of operating parameters on performance of a downdraft gasifier in steady and transient state, *Energy Conversion and Management*, Vol.155, pp.138-146, London / U.K.;

[9] La Villetta M., Costa M., Massarotti N., (2017), Modelling approaches to biomass gasification: A review with emphasis on the stoichiometric method", *Renewable and Sustainable Energy Reviews*, Vol.74, pp.71-88, Netherlands;

[10]   Maneerung T., Li X., Li C., Dai Y., Wang C.-H., (2018), Integrated downdraft gasification with power generation system and gasification bottom ash reutilization for clean waste-to-energy and resource recovery system, *Journal of Cleaner Production*, Vol.188, pp.69-79, Netherlands.

[11]   Mazaheri N., Akbarzadeh A.H., Madadian E., Lefsrud M., (2019), Systematic review of research guidelines for numerical simulation of biomass gasification for bioenergy production, *Energy Conversion and Management*, Vol.183, pp.671-688, London / U.K.;

[12]   Melgar A., Perez J., Laget H., Horillo A., (2007), Thermochemical equilibrium modelling of a gasifying process, *Energy Conversion and Management*, Vol.48, Issue 1, pp.56–67, London / U.K.;

[13]   Patra T. K., Sheth P. N., (2015), Biomass gasification models for downdraft gasifier: A state-of-the-art review, *Renewable and Sustainable Energy Reviews*, Vol.50, pp.583–593, Netherlands;

[14]   Thiagarajan J., Srividya P.K., Balasubramanian P., (2018), Thermal Kinetics and Syngas Production on Co-gasification of Deoiled Jatropha Seed Cake Residues with Wood Chips", *International Journal of Renewable Energy Research*, Vol.8, No.2, pp.1105-1111, Ankara / Turkey;

[15]   Yan W.-C., Shen Y., You S., et al., (2018), Model-Based Downdraft Biomass Gasifier Operation and Design for Synthetic Gas Production, *Journal of Cleaner Production*, Vol.178, pp.476-493, Netherlands;

[16]   Zainal Z., Ali R., Lean C., Seetharamu K.N., (2001), Prediction of performance of a downdraft gasifier using equilibrium modeling for different biomass materials, *Energy Conversion and Management*, Vol.42, Issue 12, pp.1499-1515, London / U.K.

ONLINE PARAMETER IDENTIFICATION OF RICE TRANSPLANTER MODEL BASED ON IPSO-EKF ALGORITHM
/
基于 *IPSO-EKF* 算法的插秧机模型参数在线辨识

Yibo Li *[1]**, Hang Li** [1]**, Xiaonan Guo** [2]
[1] College of Automation, Shenyang Aerospace University, Shenyang / China;
[2] Shenyang Aviation Xinxing Electromechanical Co., Ltd. Shenyang / China;
Tel: +86 13998825712; E-mail: stulihang@163.com
DOI: *https://doi.org/10.35633/inmateh-61-03*

ABSTRACT

In order to improve the accuracy of rice transplanter model parameters, an online parameter identification algorithm for the rice transplanter model based on improved particle swarm optimization (IPSO) algorithm and extended Kalman filter (EKF) algorithm was proposed. The dynamic model of the rice transplanter was established to determine the model parameters of the rice transplanter. Aiming at the problem that the noise matrices in EKF algorithm were difficult to select and affected the best filtering effect, the proposed algorithm used the IPSO algorithm to optimize the noise matrices of the EKF algorithm in offline state. According to the actual vehicle tests, the IPSO-EKF was used to identify the cornering stiffness of the front and rear tires online, and the identified cornering stiffness value was substituted into the model to calculate the output data and was compared with the measured data. The simulation results showed that the accuracy of parameter identification for the rice transplanter model based on the IPSO-EKF algorithm was improved, and established an accurate rice transplanter model.

摘要

为了提高插秧机模型参数辨识精度，提出了一种基于改进的粒子群算法(IPSO)和扩展卡尔曼滤波算法(EKF)的插秧机模型参数在线辨识方法。建立了插秧机动力学模型，用于确定插秧机模型参数。针对 EKF 算法中噪声矩阵难以选取而影响最佳滤波效果的问题，该算法在离线状态下应用 IPSO 算法对 EKF 算法的噪声矩阵进行优化。根据实车试验，采用 IPSO-EKF 对前后轮胎的侧偏刚度进行在线辨识，将辨识的侧偏刚度值代入模型中计算得到输出数据与测量数据进行对比。试验和仿真结果表明,基于 IPSO-EKF 算法提高了插秧机模型参数的辨识精度，建立了准确的插秧机模型。

INTRODUCTION

With the intelligent and modernized development of agricultural machinery, a rice transplanter with autonomous navigation has played a key role in rice planting. However, an accurate dynamic model must be established before the model-based rice transplanter control algorithm is designed. The accuracy and real-time of parameters for the dynamic model directly affect the path tracking control of the rice transplanter (*Kayacan E., et al., 2019*). The cornering stiffness of the front and rear tires for a rice transplanter is an important parameter of the dynamic model, it needs to be accurately identified online. At present, it is difficult for sensors to directly measure the cornering stiffness of tires in real time, so the system identification method is particularly important to identify the parameter of vehicle models.

The least square algorithm is widely used in parameter identification. The non-linear least squares algorithm is used to identify the vehicle parameter, namely, the cornering stiffness of the front and rear tires (*Kayacan E., et al., 2015*). The offline least squares algorithm is used to identify tire cornering stiffness by real vehicle tests (*Li L., et al., 2016*). They don't consider that the cornering stiffness is a time-varying parameter. The variable forgetting factor recursive least squares algorithm is used to identify online parameters such as the vehicle mass and the rotational inertia (*Khaknejad M B., et al., 2011*). Although the algorithm meets the requirements of online identification, it is only suitable for simple linear models and can't be directly used for nonlinear models. The modern intelligent optimization algorithms are also applied to parameter identification.

The eight unknown parameters of the semi-trailer train model are identified by genetic algorithm and L-M optimization algorithm (*Liang Q.Z., 2016*). The improved genetic algorithm is presented to optimize the parameters of the inertia for three coordinate axes (*Zhang Q.C.,2007*). The genetic algorithm can identify multiple parameters at the same time and can reach the global optimal solution, but the calculation is large and complicated, and the identification of time-varying parameters can't be well applied. Considering the real-time nature of the algorithm, the EKF algorithm is used to identify the vehicle's mass and the cornering stiffness of front and rear tires online (*Wang J., 2019*). The EKF is used to identify the cornering stiffness of the front and rear tires of vehicle (Reina et al., 2019). As the noise matrices are selected according to experience, the filtering didn't reach the expected effect. A method is presented for identifying parameters of a vehicle dynamic model (*Best., et al., 2007*). They used an adaptive EKF with variable fading factor to identify vehicle's mass, the rotational inertia and wheelbase parameters online, but this algorithm was more complicated and adjusted more parameters.

Considering the above-mentioned problems, this paper proposes an online parameter identification algorithm based on IPSO-EKF. As the selection of the process noise matrix Q and the measurement noise matrix R determines the convergence for EKF algorithm, and the true value of the Q and R can't be obtained directly, combined with PSO algorithm, Q and R matrices are identified offline to determine the optimal noise matrices. This algorithm not only solves the difficult problem of determining the noise matrices in traditional EKF, but also doesn't need to change the original EKF algorithm. Therefore, the IPSO-EKF algorithm is used to identify the cornering stiffness of the front and rear tires for the rice transplanter online.

MATERIALS AND METHODS

Dynamic model of the rice transplanter

According to motion characteristics of rice transplanter, the two degrees of freedom of the bicycle model with only lateral and yaw motion are established. In the range of small angles, the lateral tire forces are assumed to be proportional to the slip angles. The front wheel of the rice transplanter is steered and the front wheel has a small angle. The bicycle model is shown in Fig.1.
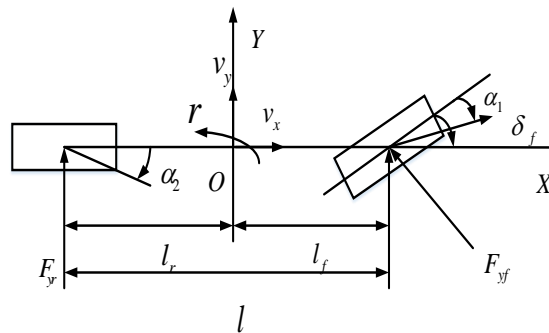
Fig. 1 - Two degrees of freedom of the bicycle dynamic model

According to Newton's second law of motion, the lateral and yaw motion of the rice transplanter is written as follows (Xu Y., et al., 2019):

$$\begin{cases} \sum F_Y = (m\dot{v}_y + mrv_x) = 2F_{yf}cos\delta_f + 2F_{yr} \\ \sum M_Z = I_z\dot{r} = 2F_{yf}l_f - 2F_{yr}l_r \end{cases} \tag{1}$$

Where m - is the mass of the rice transplanter, kg; v_x - the longitudinal velocity, m/s; $\dot{v}_y$ - the lateral acceleration, m/s²; v_y - the lateral velocity, m/s; $\dot{r}$ - the yaw acceleration, rad/s²; r - the yaw rate, rad/s; F_{yf} - the lateral force on the front wheels, N; F_{yr} - the lateral force on the rear wheels, N; δ_f - the steering angle of the front wheels, rad; I_z - the moment of inertia around the vertical axis, Kg·m²; l_f - the distance between the front axle and the centre of gravity, m; l_r - the distance between the rear axle and the centre of gravity, m.

The lateral tire forces are calculated in a linear model in which they are assumed to be proportional to the slip angles, and they are written as follows:

$$\begin{cases} F_{yf} = C_f \alpha_1 \\ F_{yr} = C_r \alpha_2 \end{cases} \tag{2}$$

$$\begin{cases} \alpha_1 = \delta_f - \dfrac{v_y + l_f r}{v_x} \\ \alpha_2 = \dfrac{l_r r - v_y}{v_x} \end{cases} \tag{3}$$

Where C_f - is the cornering stiffness of the front tires, N/rad; C_r - the cornering stiffness of the rear tires, N/rad; α_1 - the side slip angles of the front tires, rad; α_2 - the side slip angles of the rear tires, rad. By combining equations (1), (2) and (3), the state-space model of the rice transplanter can be written as follows:

$$\begin{bmatrix} \dot{v}_y \\ \dot{r} \end{bmatrix} = \begin{bmatrix} -\dfrac{2C_f + 2C_r}{mv_x} & -v_x - \dfrac{2C_f l_f - 2C_r l_r}{mv_x} \\ \dfrac{2C_r l_r - 2C_f l_f}{I_z v_x} & -\dfrac{2l_f^2 C_f + 2l_r^2 C_r}{I_z v_x} \end{bmatrix} \begin{bmatrix} v_y \\ r \end{bmatrix} + \begin{bmatrix} \dfrac{2C_f}{m} \\ \dfrac{2C_f l_f}{I_z} \end{bmatrix} \delta_f \tag{4}$$

An approximate value for the rotational inertial can be calculated as follows:

$$I_z = ml_f l_r \tag{5}$$

In equation (4), m, l_f, l_r and I_z are invariant parameters of the rice transplanter, I_z can be approximated by (5), δ_f is steering angle of the front wheel as input variable, v_x can be approximately equal to the speed of the rice transplanter on the ground, C_f and C_r are the cornering stiffness to be identified. In this paper, the cornering stiffness of tires for the rice transplanter will be changed for the complexity of the road surface. Therefore, the cornering stiffness is regarded as a time-varying parameter for online identification. Equation (4) can be equivalently expressed as:

$$\dot{x}(t) = f(x(t), \delta(t)) \tag{6}$$

In order to collect the data, the steering angle of the front wheel is set to 20 degrees step, and the rice transplanter is driven counter clockwise on the asphalt ground at a low speed, as shown in Fig. 2. The rice transplanter uses RTK system for precise positioning. The speed and heading angle of the rice transplanter are obtained by the M600 receiver, and the data collection frequency is 5 Hz. The lateral velocity v_y and yaw rate r of the rice transplanter are obtained by coordinate transformation.

The measurement vector $z = [v_y, r]^T$ is introduced as the measurement equation of the system, which is equivalently expressed as:

$$z(t) = h(x(t)) \tag{7}$$

Fig. 2 - The actual vehicle test of the rice transplanter

EKF algorithm for online identification parameters

The EKF algorithm can be used as a parameter online identification algorithm of nonlinear systems which can be transformed into a linear problem by Taylor decomposition, and be the same as linear Kalman filtering (*Battistelli G., 2016*). In the process of parameter identification, the state vector $x = [v_y, r]^T$ and the cornering stiffness of the front and rear tires to be identified are combined into a joint state vector, and the EKF algorithm is used to make the optimal estimation of the parameters by combining the joint state vector. When the value of the parameter to be identified converges, the convergent value is used as the value of the optimal parameter. EKF is widely used for online identification of model parameters due to its small amount of calculation and high real-time performances.

In this paper, EKF is applied to the online identification of the parameters for the rice transplanter's dynamic model, C_f and C_r are added to the state vector x. The equations (6) and (7) can be expressed as a nonlinear system.

$$\begin{cases} \dot{x}(t) = f(x(t), \delta(t)) + w(t) \\ z(t) = h(x(t)) + v(t) \end{cases} \tag{8}$$

Where $w(t)$, $v(t)$ - the process noise and the measurement white Gaussian noise with zero mean, respectively. First, the above continuous-time nonlinear equations need to be converted in a discrete-time state-space representation.

$$\begin{cases} x_{k+1} = f(x_k, \delta_k) + w \\ z_k = h(x_k) + v \end{cases} \tag{9}$$

Where $f(.)$ - the state evolution function represents the rice transplanter dynamics, $h(.)$ - the relationship between the state vector and measurement, $x_k = \left[v_{y_k}, r_k, C_{f_k}, C_{r_k} \right]^T$ - the joint state vector at time k, δ_{f_k} - the steering angle of the front wheel, and $z_k = [v_{y_k}, r_k]^T$ - the measurement vector at time k. If the sampling period is dt, the discrete system is represented by a first-order difference quotient, $f(.)$ is expressed as follows:

$$f_1 : v_{y_{k+1}} = (1 - \frac{2C_{f_k} + 2C_{r_k}}{mv_x} dt)v_{y_k} + (-v_x - \frac{2C_{f_k}l_f - 2C_{r_k}l_r}{mv_x})dtr_k + \frac{2C_{f_k}}{m} dt\delta_k$$

$$f_2 : r_{k+1} = \frac{2C_{r_k}l_r - 2C_{f_k}l_f}{I_z v_x} dtv_{y_k} + (1 - \frac{2l_f^2 C_{f_k} + 2l_r^2 C_{r_k}}{I_z v_x} dt)r_k + \frac{2C_{f_k}l_f}{I_z} dt\delta_k \tag{10}$$

$$f_3 : C_{f_{k+1}} = C_{f_k}$$

$$f_4 : C_{r_{k+1}} = C_{r_k}$$

Similarly, $h(.)$ can be obtained as:

$$h_1 : v_{y_{k+1}} = v_{y_k}$$

$$h_2 : r_{k+1} = r_k \tag{11}$$

The EKF algorithm can be given by the following recursive equations:

$$\begin{cases} \bar{x}_{k+1} = f(\hat{x}_k, \delta_k) \\ \bar{P}_{k+1} = A_k P_k A_k^T + Q \\ K_{k+1} = \bar{P}_{k+1} H_k^T (H_k \bar{P}_{k+1} H_k^T + R)^{-1} \\ \hat{x}_{k+1} = \bar{x}_{k+1} + K_{k+1}(z_{k+1} - H_{k+1}\bar{x}_{k+1}) \\ P_{k+1} = (I - K_{k+1}H_{k+1})\bar{P}_{k+1} \end{cases} \tag{12}$$

Where $\bar{x}_{k+1}$ - the priori state vector prediction; $\bar{P}_{k+1}$ - the posteriori error covariance matrix prediction; Q - the process noise matrix; R - the measurement noise matrix; K_{k+1} - the Kalman gain; $\hat{x}_{k+1}$ - the posteriori state vector prediction; z_{k+1} - the measurement vector; I - the identity matrix; P_{k+1} - the posteriori error covariance matrix prediction; In these equations, A_k, H_k - the Jacobian matrix of the state vector and the Jacobian matrix of the measurement vector, respectively.

$$A_K = \left[\frac{\partial f(x_k, \mathbf{u}_k)}{\partial x_k}(\hat{x}_k)\right] = \begin{bmatrix} A_{11} & A_{12} & A_{13} & A_{14} \\ A_{21} & A_{22} & A_{23} & A_{24} \\ 0 & 0 & 1 & 0 \\ 0 & 0 & 0 & 1 \end{bmatrix} \tag{13}$$

$$H_k = \left[\frac{\partial h(x_k)}{\partial x_k} \,|\, (\overline{x}_{k+1})\right] = \begin{bmatrix} 1 & 0 & 0 & 0 \\ 0 & 1 & 0 & 0 \end{bmatrix} \tag{14}$$

Where:

$$A_{11} = 1 - \frac{2\hat{C}_{f_k} + 2\hat{C}_{r_k}}{mv_x} dt, \; A_{12} = (-v_x - \frac{2\hat{C}_{f_k}l_f - 2\hat{C}_{r_k}l_r}{mv_x})dt$$

$$A_{13} = -\frac{2v_{y_k}dt + 2r_kl_fdt}{mv_x} + \frac{2\delta_kdt}{m}, \; A_{14} = \frac{2l_rr_kdt - 2v_{y_k}dt}{mv_x}$$

$$A_{21} = \frac{2\hat{C}_{r_k}l_r - 2\hat{C}_{f_k}l_f}{I_zv_x} dt, \; A_{22} = 1 - \frac{2l_f^2\hat{C}_{f_k} + 2l_r^2\hat{C}_{r_k}}{I_zv_x} dt$$

$$A_{23} = -\frac{2l_fv_{y_k}dt + 2l_f^2r_kdt}{I_zv_x} + \frac{2l_f\delta_kdt}{I_z}, \; A_{24} = \frac{2l_rv_{y_k}dt - 2l_r^2r_kdt}{I_zv_x}$$

The initial values $P(0)$ and $x(0)$ are selected by experience, and the measurements of the vehicle's response (v_y, r) are input into the extended Kalman filter that recursively outputs the vector (C_f, C_r) according to equation (12). Then the optimal state estimate is obtained, and model parameters of the rice transplanter are obtained in real time.

Parameter identification algorithm of IPSO-EKF

The Q and R matrices corresponding to the statistical characteristics of noise w and v have a greater impact on the convergence of EKF. In this paper, IPSO combined with the EKF algorithm is used to optimize Q and R offline. Particle swarm optimization (PSO) is a population-based stochastic search algorithm inspired by the social behaviour of bird flocking. It was first introduced by Kennedy and Eberhart in 1995. Each particle in the PSO algorithm represents a feasible solution, and the particle has two properties: velocity and position. In the search space, individual particles compare the optimal positions they pass with the optimal position of all the particles and adjust their speed continuously so that they can move closer to the global optimal position. The velocity and position of each particle are updated according to the following equations (Liu W.X., et al., 2011):

$$v_{i,d}(k+1) = wv_{i,d}(k) + c_1r_1(p_{i,d} - x_{i,d}(k)) + c_2r_2(g_d - x_{i,d}(k)) \tag{15}$$

$$x_{i,d}(k+1) = x_{i,d}(k) + v_{i,d}(k) \tag{16}$$

Where i - the number of the particle; d - the dimension of the particle; k - the number of iterations; c_1, c_2 - the acceleration coefficient; r_1, r_2 - two random numbers uniformly distributed in the interval [0,1]; $p_{i,d}$ - the historically optimal position of particle i; g - the optimal position experienced by all particles in the population; w - the inertia decreasing weight. In order to increase the new space solution for more extensive search, an adaptive detection radius is proposed (Zhang Q., et al.,2019).

$$R(k) = \frac{(x_{max}^d + x_{min}^d)}{2} + \frac{(x_{max}^d - x_{min}^d)}{2} \cdot e^{-\lambda t} \cdot \cos(2\pi u) \tag{17}$$

Where λ is a variable parameter ($\lambda > 2$), u represents the random numbers uniformly distributed in the interval [0,1]. x_{max}^d and x_{min}^d are the upper and lower bounds of the variables, respectively. The IPSO velocity equation is updated according to the following equation:

$$v_{i,d}(k+1) = wv_{i,d}(k) + c_1r_1(p_{i,d} - x_{i,d}(k)) + c_2r_2(g_d - x_{i,d}(k)) + c_3r_3(R(k) - x_{i,d}(k)) \tag{18}$$

Because the standard PSO algorithm is easy to fall into the local optimal value, chaotic search is introduced into the PSO algorithm. After updating the velocity and position of each particle according to

equations (15) and (16), the fitness function f of each particle is updated accordingly. When the particle i satisfies $|f(x_i) - f(p_i)| < \delta$ for N consecutive times, it is judged that the particle has a stagnation state. So, the chaotic sequence generated by Logistic is used to search again; it is expressed as follows:

$$y_{k+1,d} = 4y_{k,d}(1 - y_{k,d}) \tag{19}$$

Each component of the initial value y_0 is randomly generated in a uniform distribution in the interval [0,1]. In a carrier-like manner, the particles expanded to an area with R_d radius centred on the current position.

$$x_{i,d}^k = x_{i,d} + R_d(2y_{k,d} - 1) \tag{20}$$

When $f(x_{i,d}^k) < f(x_{i,d})$ is satisfied, the current particle position is updated. When $k > N_{max}$ is satisfied, chaotic iteration ends. By increasing the adaptive detectable radius and chaotic sequences generated by stagnation, the IPSO algorithm solves the problem which falls into a local optimal solution, and greatly improves the reliability of global optimization.

IPSO optimizes the noise matrices

The parameters optimized by the IPSO algorithm are Q and R noise matrices in EKF. The sequence of lateral speed, the yaw rate and the steering angle of the front wheel collected by the above M600 receiver were input into a discrete rice transplanter model. IPSO randomly generates $F \times D$ dimensional matrices, and uses equations (15) and (16) to update the position and velocity of particles and chaotic search for stagnant particles. The random Q and R noise matrices are input into EKF, and the optimal Q and R matrices are obtained according to the objective function until the maximum number of iterations is met. The selection of fitness function is a core part of the PSO algorithm. If it is not adopted properly, it will affect the global optimization performance of the algorithm. The optimized noise matrices Q and R in EKF are designed to minimize the cumulative absolute error between the sampled measurement data y_{k+1} and the filtered output $H\overline{x}_{k+1}$. The objective function is defined as follows (Xiang Y., et al., 2016):

$$f = \frac{1}{N}\sum_{k=1}^{N}|y_{k+1} - H\overline{x}_{k+1}| \tag{21}$$

Where N - the number of the measurement data. The two degree of freedom dynamic model of the rice transplanter established in this paper has four state variables and two output variables, where the matrices corresponding to the Q and R are as follows:

$$Q = diag(q_{11}, q_{22}, q_{33}, q_{44})$$
$$R = diag(r_{11}, r_{22}) \tag{22}$$

The structure of the noise matrices for the EKF algorithm identified by the IPSO algorithm is shown in Fig.3.
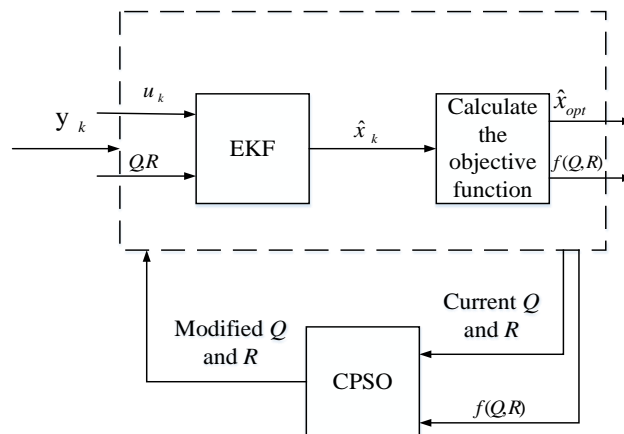
Fig. 3 - Structure diagram of IPSO optimized noise matrices

The parameters of the identification algorithm are set as: $F = 20$, $D = 6$, $N_c = 20$, $c_1 = 1$, $c_2 = 1.5$, $c_3 = 2$, $k_{max} = 40$, $N_{max} = 10$, $N = 5$, $R_d = 10$, $\lambda = 4$, $\delta = 10^{-6}$, w decreases linearly at [0.9,0.4]. When the IPSO algorithm is run, the change curve of the global optimal objective function value for population is shown in Fig.4. It can be known that about 13 iterations tend to stabilize in the search process. Chaotic search and adaptive detection radius are introduced to solve the problem that the PSO algorithm is easy to fall into the local optimal value, and the global optimal solution can be searched. The identified Q and R noise matrices will be used in the online identification algorithm based on IPSO-EKF in the next chapter.
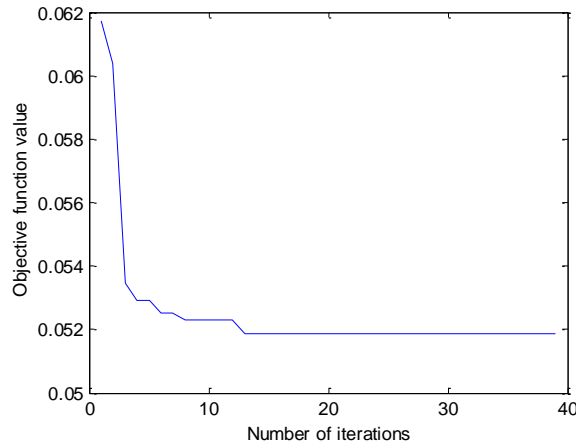
Fig. 4 - Evolution of the objective function

RESULTS

Simulation of parameters setting

This simulation uses MATLAB to verify the accuracy of the IPSO-EKF algorithm. The model parameters of the rice transplanter PZ60-DT are shown in Table 1. The ground speed and course angle of the rice transplanter come from the M600 receiver, and the yaw rate and lateral acceleration are calculated by coordinate transformation.

Table 1

Simulation model parameters of the rice transplanter

Parameters	m	l_f	l_r	I_z	δ_f
	[Kg]	[m]	[m]	[Kg·m²]	[°]
Values	720	0.7	0.4	201.6	20

Online identification of cornering stiffness based on IPSO-EKF

The data collected by the above M600 receiver and the Q and R noise matrices identified by IPSO-EKF are input into dynamic simulation model of the rice transplanter. The initial value of the cornering stiffness is set to $C_f = C_r = 1000$N/rad, the simulation results of the cornering stiffness of the front and rear tires for the rice transplanter are shown in Fig.5, which shows the evolution in the cornering stiffness of the front and rear tires at each sampling time. Considering the unevenness of the test field and the serious side slip of the front wheels during driving, the change in the cornering stiffness of tires is obvious. In order to more intuitively verify the accuracy of the identification results, the identified cornering stiffness of the front and rear tires are substituted into the dynamic model of the rice transplanter, and the model output obtained is compared with the measurement data collected by M600 receiver as shown in Fig.6. It can be seen from Fig.6 that the cornering stiffness and yaw rate response curves of the model output after IPSO-EKF identification are basically consistent with the collected data. In what follows and for comparison purposes, our proposed method will be compared with trial-error method for standard EKF. As shown in Fig.7, it can be known that model output identified based on EKF algorithm doesn't match the measured value. There is a large error between the model output calculated from the identified model parameters and the measured data in Table 2. The simulation results show that the noise matrices optimized by IPSO have a better optimization effect on the online identification algorithm of EKF, and can accurately identify the model parameters.
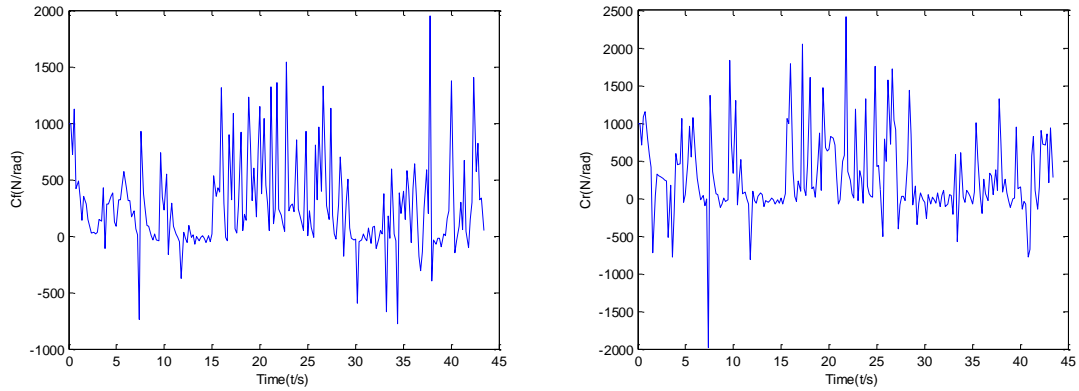
Fig. 5 - The cornering stiffness of the front and rear tires under 20-degree step condition
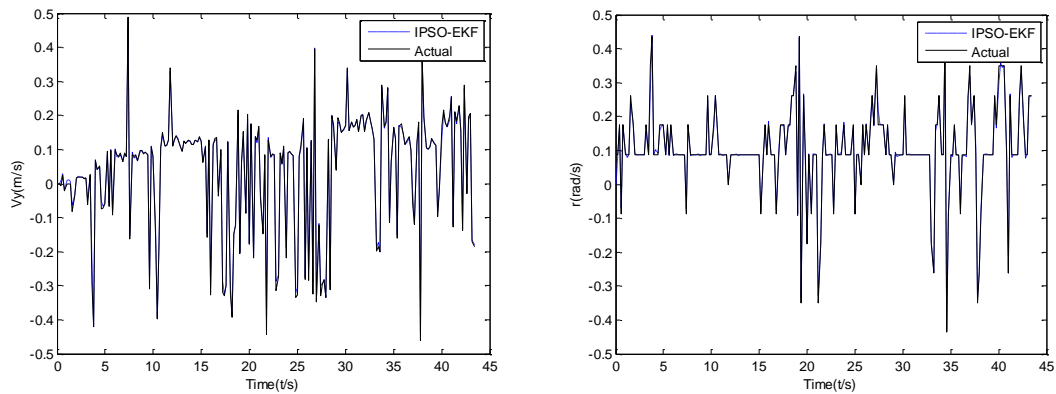
Fig. 6 - The value of model output and measured value obtained by IPSO-EKF algorithm under 20-degree step condition
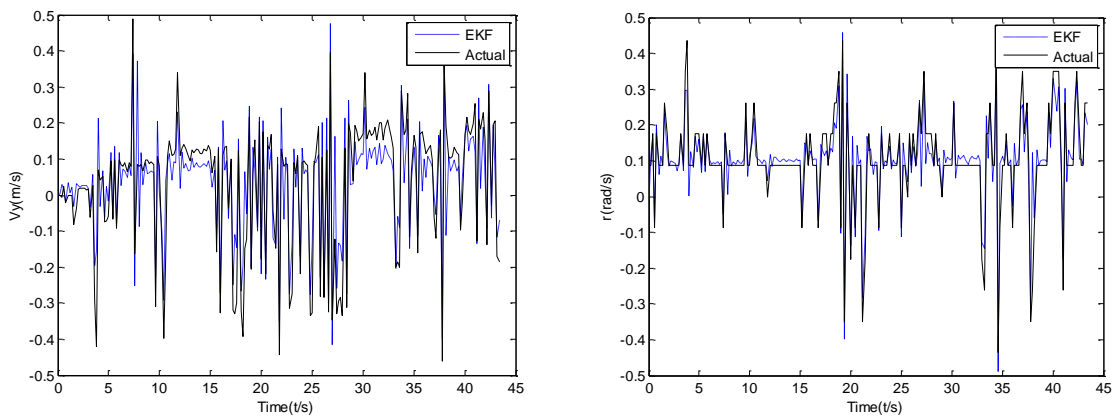
Fig. 7 - The value of model output and measured value obtained by EKF algorithm under 20-degree step condition

Table 2

The statistics of lateral velocity and yaw rate for errors under 20-degree step condition

Identification algorithm	Maximum error v_y	Maximum error r	Average error v_y	Average error r
	[m/s]	[rad/s]	[m/s]	[rad/s]
IPSO-EKF	0.0672	0.0873	0.0064	0.0050
EKF	0.3050	0.3841	0.0595	0.0316

Simulation verification under different operating conditions

In order to verify the consistency of the algorithm, the data under different working conditions are used to simulate the IPSO-EKF algorithm. The steering angle of the front wheels for the rice transplanter is set to

30 degrees, and it is driven clockwise at low speed along the field. Similarly, the collected longitudinal velocity, lateral velocity and yaw rate are input into the dynamic model of the rice transplanter. The cornering stiffness of the front and rear tires are identified by the EKF algorithm, as shown in Fig.8. The comparison between the output data calculated by the model and the data measured by M600 receiver is shown in Fig.9. Fig.9 shows that the data calculated by the model are basically consistent with the measured data, although there are some errors which are small and can better match the measured data, and the overall curve trend is consistent.
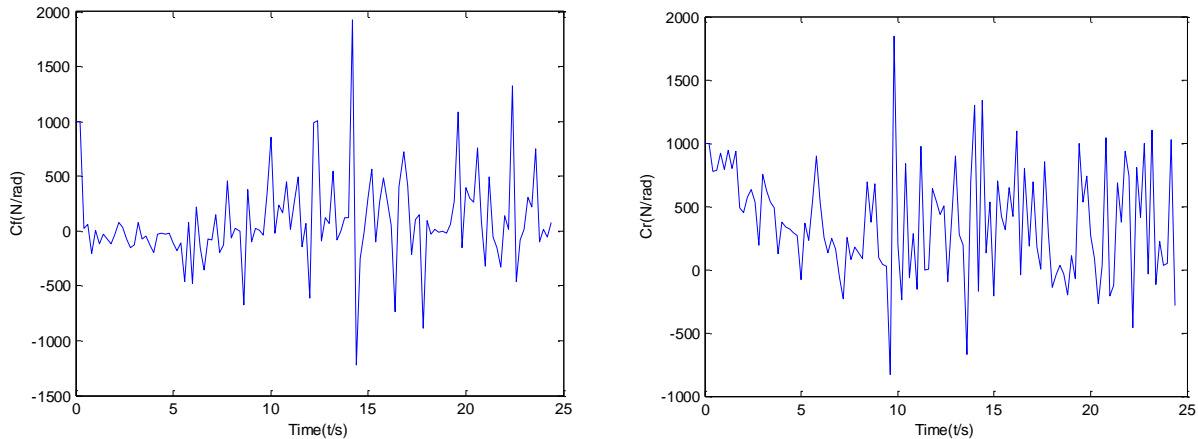
Fig. 8 - The cornering stiffness of the front and rear tires under 30-degree step condition
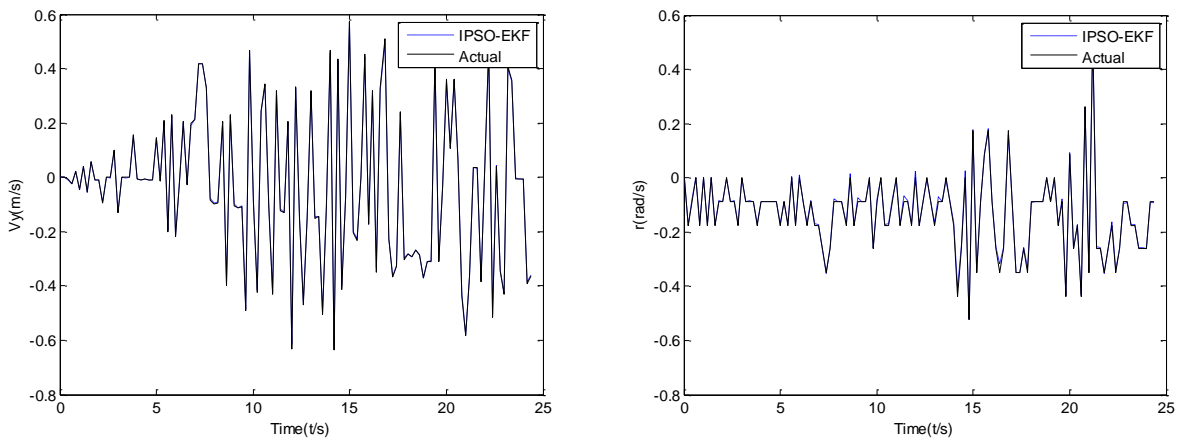
Fig. 9 - The value of model output and measured value obtained by IPSO-EKF algorithm under 30-degree step condition

CONCLUSIONS

In this paper, through the dynamic analysis of the rice transplanter, a lateral dynamic model of the rice transplanter was established. In order to accurately identify the parameters of the rice transplanter dynamic model, the IPSO-EKF algorithm was proposed. In the offline state, combined with data collected by M600 receiver, the noise matrices in EKF were optimized by IPSO algorithm. The optimized noise matrices are selected as the best matrices, and the cornering stiffness of the front and rear tires for the rice transplanter model was identified online based on the IPSO-EKF algorithm. The simulation results showed that the output data calculated by the model was basically consistent with the data collected by M600 receiver. Compared with the EKF algorithm, the IPSO-EKF algorithm greatly improved the accuracy of the identification. In order to verify the consistency of the algorithm proposed in this paper, the data collected under different operating conditions of the rice transplanter were used to verify the algorithm. The simulation results showed that the algorithm can better describe the dynamic characteristics of the rice transplanter and accurately realize the online identification of the parameters for the rice transplanter model. This algorithm lays the foundation for the design of a rice transplanter based on a dynamic model control algorithm.

REFERENCES

[1]   Kayacan E., Chowdhary G., (2019), Tracking error learning control for precise mobile robot path tracking in outdoor environment, *Journal of Intelligent & Robotic Systems*, vol.95, issue 3-4, pp.975-986;

[2]   Kayacan E., Kayacan E., Romon H., et al., (2015), Towards Agrobots: Identification of the yaw dynamics and trajectory tracking of an autonomous tractor, *Computers and Electronics in Agriculture*, Vol.115, pp.78-87;

[3]   Li Ling, Ma Li, Mu Yu, Xu Chao, Li Wenru, Shi Shuming, (2016), Parameter identification method for the tire cornering stiffness of model vehicle(模型车轮胎侧偏刚度的参数辨识方法), *Automotive Engineering*, vol.36, issue 12, pp.1508-1514;

[4]   Khaknejad M B., Kazemi R., Azadi S., (2011), Identification of vehicle parameters using modified least square method in ADAMS/Car, I*nternational Conference on Modelling, Identification and Control. IEEE*, pp.98-103;

[5]   Liang Qunzhang, (2016), Research on rollover control system of semi-trailer train based on parameter identification(基于参数辨识的半挂汽车列车侧翻控制系统的研究), Guangxi University/China;

[6]   Zhang Qingchun, (2007), Identification of the key parameters in vehicle dynamics(车辆动力学关键参数辨识研究), Huazhong University of Science and Technology/China;

[7]   Wang Jie, (2019), Vehicle parameter identification based on extend Kalman filter(基于扩展卡尔曼滤波的车辆参数辨识), *Modern Machinery*, Issue.03, pp.4-9;

[8]   Reina G., Messina A., (2019), Vehicle dynamics estimation via augmented extended Kalman filtering, *Measurement,* Vol.133, pp.383-395;

[9]   Best M C., (2007), Parametric identification of vehicle handling using an extended Kalman filter, *International Journal of Vehicle Autonomous Systems*, Issue 5, pp.256–273;

[10]   Xu Yang, Lu Liping, Chu Ruifeng, Huang Zichao, (2019), Unified modelling of trajectory planning and tracking for unmanned vehicle(无人车辆轨迹规划与跟踪控制的统一建模方法), *Acta Automatica Sinica,* Vol.45, Issue 4, pp.799-807;

[11]   Battistelli G., Chisci L., (2016), Stability of consensus extended Kalman filter for distributed state estimation, *Automatica,* Vol.68, pp.169-178;

[12]   Liu W.X., Liu L., et al., (2011), Real-time particle swarm optimization based on parameter identification applied to permanent magnet synchronous machine, *Applied Soft Computing*, Vol.11, Issue 2, pp.2556-2564;

[13]   Zhang Qi, Jia Hongping, (2019), Predictive current control based on improved particle swarm optimization(基于改进粒子群算法的预测电流控制), *Information Technology*, Vol.43, Issue 8, pp.66-70;

[14]   Xiang Yu, Liu Chunguang, Li Jiaqi, (2016), Model parameters estimation of lithium batteries based on Kalman filtering(基于卡尔曼滤波的锂离子电池模型参数辨识), *Journal of Ordnance Equipment Engineering*, Vol.37, Issue 10, pp.147-151;

AN OMNI-DIRECTIONAL ELECTRIC PRUNING SAW FOR FOREST TENDING
/
全方位电动打枝锯研究

Qingqing Shang*, Bin Wang, Jiawei Yang, Yizhi Lu, Tongming Yin   [1]
Nanjing Forestry University, Nanjing 210037, China
Tel: +8613813990580; E-mail: qqshang@njfu.edu.cn

ABSTRACT

This paper attempts to design a universal, easy-to-use pruning tool suitable for taller branches. For this purpose, the author proposed an omni-directional electric pruning saw. The saw has a 360° rotatable head, which can prune branches in all directions. Under the saw blade, a V-shaped groove was added so that the branches can be introduced, cut and released stably. A telescopic rod was included in the design to prune branches at different heights. To facilitate the retraction and release of wire, a winding reel was provided to make the wire change with the length of the rod. In addition, there is a deadlock device at the handle, which prevents the manmade safety hazards. The proposed pruning saw was tested through an experiment. The results show that the saw could be used for various branches and was 4 times more efficient than the traditional hand saw.

摘要

本文研究一种全方位电动打枝锯，其旋转锯头实现了 360 度全方位打枝作业；锯片下方设计的 V 型槽，方便了枝条的导入，保证了锯切打枝的稳定性；伸缩杆满足了高度不同树种打枝的需求；绕线盘使导线在伸缩杆的收缩和拉伸的过程中，随杆长变化而变化，解决了导线收放不便的问题；手柄处设计的锁死装置，有效避免了由于人为操作误失而造成的安全隐患。实验结果证明：该打枝据可应用于多种枝条，相比普通手工锯，效率提高了 4 倍。

INTRODUCTION

China has made great progress on land afforestation. In 2017, China planted 7.362 million hectares of trees and tended 8.302 million hectares of forest, making a great contribution to the ecological protection in the country *(Li and Wang, 2006)*. One of the main measures for forest tending lies in tree pruning. Rational pruning keeps the trees straight, tough and bending-resistant and facilitates the upper photosynthesis; it is very important for the growth of trees *(Cheng, 1981; Ji, 1990; Liu, 1975)*. Traditional pruning tools like saw and machete are relatively backward. These tools require high labour intensity and only apply to lower branches, failing to achieve desirable pruning effect. China is located in East Asia, in the north of the distribution centre of bamboo plants in the world. There are more than 30 genera of bamboos, accounting for about 45% of the world's bamboos. The total area of bamboo forest is about 3.4 million hectares, the total volume is about 71.2234 million tons, and the total annual cutting volume of commercial bamboo is about 5 million tons. In the paper (*Yu, 2019*), a cluster bamboo selective cutting machine featuring operation in a small space, small size, light weight and a reciprocating saw-based cutting mode was designed. The preliminary test shows that the surface cut by the reciprocating saw is very relatively smooth, with no serious tearing phenomenon of bamboo outer skin, able to meet the basic requirements for selective cutting of cluster bamboo, the saw was 4-6 times more efficient than the traditional hand saw. Bosch GSA18V compact reciprocating saw (*Jeremy, 2018*) did everything the operator wanted to do. Cordless, portability and convenience with high electrical storage capacity of 6.3 Ah, makes the instrument more competitive on the market. One V-type bamboo cutting program with double cylindrical helical cutter was proposed in his paper (*Wang, 2016*). Two experiments about the efficiency of cutting bamboo and impact resistance capacity show that the cylindrical cutter can be used for cutting bamboo, and its cross section is similar to conical surface which is formed by the chopper. Considering the huge demand for forest pruning in China and the poor

---

[1] *Qingqing Shang, M.S.; Bin Wang, B.S.; Jiawei Yang, M.S.; Yizhi Lu, M.S.; Tongming Yin, Ph.D.*

capacity of traditional pruning tools *(Chen, 2018; Deng, 2017; Shen, 2010)*, this paper attempts to design a universal, easy-to-use pruning tool suitable for taller branches.

MATERIALS AND METHODS
Determination of pruning saw working mode

At present, most of pruning saws at home and abroad are circular saw, chain saw and hand saw. The circular saw has simple operation and high rotational speed, but its feeding is difficult and the safety is poor. The cutting thickness of the chain saw is large and the maintenance can sometimes be difficult. The hand saw needs pure manpower for operation with high labour intensity, low work efficiency and high risk, which is not suitable for large-area pruning operation (*Wang et al., 2017; Tang, 2015; Lin, 1985*).

In the omni-directional electric pruning saw, a high-power charged lithium battery is taken as power supply, a worm gear reducer is provided, and a small teeth space saw blade is used for reciprocating cutting, ensuring sufficient power and increasing working stability. Charged machine is light, environmental and energy-saving. By increasing the extension length of the equipment and the rotation degree of the saw head, it can be well adapted to the change of the height and orientation of tree branches, highlighting its strong application value (*Michael and Jin, 2014*).

Overall design and parameters of pruning saw

The pruning saw consists of a locking device, a telescopic device, a rotating device, a cutting device, and an introduction device, as shown in Fig.1. The winding device is composed of a winding reel, a winding reel and electric wire. The wire can be retracted or released according to actual requirements to avoid enwinding of the electric wire (*Liu et al., 2018*).
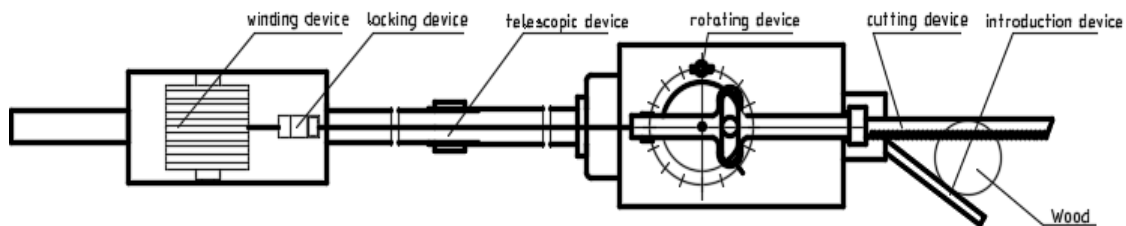
Fig. 1 - Schematic diagram of omni-directional pruning saw

The locking device is composed of a power dead lock button and a power switch button. The telescopic device is composed of n (n>=3) one-meter-long steel pipes and n-1 connection heads. The telescopic device can be adjusted over two meters in length, and the connection heads are used to fix the position of the steel pipes.

The rotating device consists of a shell, a bayonet lock and an annular support which can rotate within 360 degree, and the bayonet lock is responsible for fixing its position.

The cutting device is mainly composed of a slider-crank mechanism, which converts the rotary motion of the motor into the reciprocating linear motion of the saw blade.

The introduction device is mainly a V-shaped groove structure composed of a saw blade and a frame, which is convenient for locking the branches and stabilizing the sawing operations.

Operation force analysis of pruning saw

The force analysis of V-shaped groove structure is shown in Fig.2. $\vec{V}$ is the moving direction of the saw blade, $\overrightarrow{F1}$ is the force of the frame to the wood, $\overrightarrow{F2}$ is the vertical force of the knife saw to the wood, $\overrightarrow{F3}$ is the horizontal force of the cutter to the wood. Therefore, the resultant force received by the wood is $\vec{F}$, so the wood will move in the direction of $\vec{F}$ in the process of being cut, which is conducive to fixing the cut branches.

As shown in Fig.3, $\vec{V}$ is the moving direction of the saw blade, $\overrightarrow{F1}$ is the force of the frame to the wood, $\overrightarrow{F3}$ is the horizontal force of the cutter to the wood, and $\overrightarrow{F2}$ is the vertical force of the knife saw to the wood. The resultant force received by the wood is $\overrightarrow{F2}$, so the wood will move downward and leave the saw blade in the process of being cut, which is not favourable for the operator to perform the pruning operation.
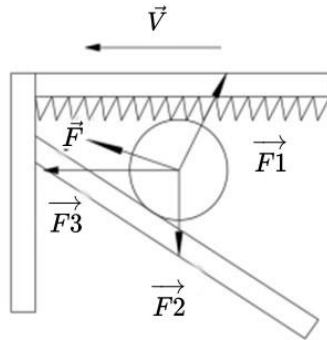
Fig. 2 - Force analysis 1
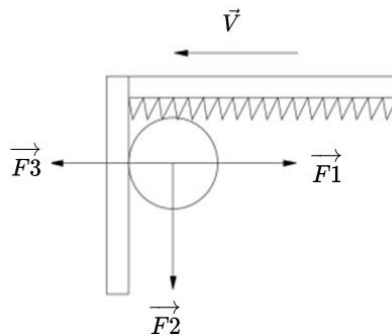
Fig. 3 - Force analysis 2

The following symbols are used in this paper:

$\vec{V}$ =The moving direction of the saw blade;

$\vec{F}$ =The resultant force received by the wood;

$\overrightarrow{F1}$ =The force of the frame to the wood;

$\overrightarrow{F2}$ =The vertical force of the knife saw to the wood;

$\overrightarrow{F3}$ =The horizontal force of the cutter to the wood

Pruning saw parameters

For the users of electric power tools, efficiency and running time are the most important to evaluate whether a pruning saw is excellent or not besides the comfortable holding and exquisite design, so it is important to set the parameters of the pruning saw correctly.

Worm gear reducer. When using tools for wood sawing, one of the basic characteristics of cutting machine under load is power. The correct selection of worm gear reducer determines the cutting force of pruning saw. Specific parameters include the structure type of the motor, output speed, power, voltage, and diameter specifications. Technical parameter range and selection parameters of small worm gear reducer are as follows:

Table 1

Technical parameter range and selection parameters of small worm gear reducer

Parameters	Range	Selection parameters
Voltage (V)	3-24	18
Power (W)	0.5-50	24
Reduction	1:17, 1:31, 1:50	1:31
Output	5-1,000	260
Gear	Metal and plastics	Metal
Motor	Motor, DC, Step-by-	DC motor

Lithium battery. The battery pack with high mA hour rating can maintain the reciprocating saw for a longer time than the battery pack with low mA hour rating. According to the number of branches cut by the saw after one charge, the voltage of the worm gear reducer and the weight of the whole machine, the

pruning saw is equipped with 2 to 3 lithium batteries with a voltage of 18 (V) and battery capacity of 3.0 (Ah) for one day's work (*Zhang et al., 2018; Katuril and Gorantla, 2018*).

Saw blade. In daily life and industrial production, there are numerous examples of interchangeability, and saw blades are produced and sold according to the requirements of interchangeability. Therefore, the selection of the saw blade in this study is based on the parameters existing on the market, and can be replaced with each other in the same specification. (1) Choice of materials. According to the processing object, using strength and processing precision, the cutting object of the pruning saw is wood, the strength requirement is lower than in the case of metal, and the precision requirement is lower. At present, there are duplex metal saw blades (*Jia et al., 2017*), high-speed steel saw blades and carbon steel saw blades. Carbon steel saw blades are low in cost and hardness, so they are more generally used. (2) Selection of dimensions. The maximum cutting width of the saw blade is equal to the total length (mm) of the saw blade minus 70 (mm). The thicker the material is, the larger the teeth spacing is. In accordance with the load capacity of the battery and the power analysis provided by the worm gear reducer, the larger the teeth spacing is, the larger the saw feed amount is, the larger the battery power consumed by the sawing process is. When the electric quantity is small, the saw blade is easy to be blocked (*Li, 2017*). A saw blade with length of 150 (mm) and teeth spacing of 2.6 (mm) is selected in combination with market research and experiment.

EXPERIMENTAL TEST OF PRUNING

Experimental test of pruning is carried out on three kinds of common trees, poplar, plane tree and pine in Fig.4. The hand saw with teeth spacing of 6 mm and omni-directional pruning saw with teeth spacing of 4.3 mm, 2.6 mm and 1.4 mm are used to conduct pruning on the trees with different diameters and their time is counted. Each experiment group is carried out for three times. Finally, the average value is taken. The results are shown in Table 2.

Table 2

Statistical table of data

Type of tree	Poplar			Plane tree			Pine		
Branch diameter (mm)	25	30	35	25	30	35	25	30	35
Pruning time with teeth spacing of 6 mm (s)	28.3	39.1	69.7	15.6	51.6	98.1	22.6	29.6	49.3
Pruning time with teeth spacing of 4.3 mm (s)	7.8	18.5	20.3	6.3	15.0	22.2	6.0	11.7	17.6
Pruning time with teeth spacing of 2.6 mm (s)	5.3	9.2	14.9	3.5	10.4	12.5	6.9	9.4	12.1
Pruning time with teeth spacing of 1.4 mm (s)	10.8	15.5	36.8	5.9	15.6	19.6	11.2	13.7	20.5

Experimental analysis: as a whole (take Fig.5 as an example), the larger the diameter is, the longer the pruning time of different cutters is. Under the condition of the same tree diameter, the pruning time of omni-directional pruning saw is obviously shorter than that of the hand saw. In the case of the same tree diameter, the pruning time of saw blade of 2.6 teeth spacing is significantly shorter than that of the other two kinds of teeth spacing. And we also cut the bamboo with this experimental equipment and saw blade. In this case, compared with the time taken for hand saw, the omni-directional pruning saw of 2.6 saw blade is approximately 1/4 of the time, that is, its efficiency is approximately 4 times that of the hand saw.

Fig. 4 - Experimental test of pruning
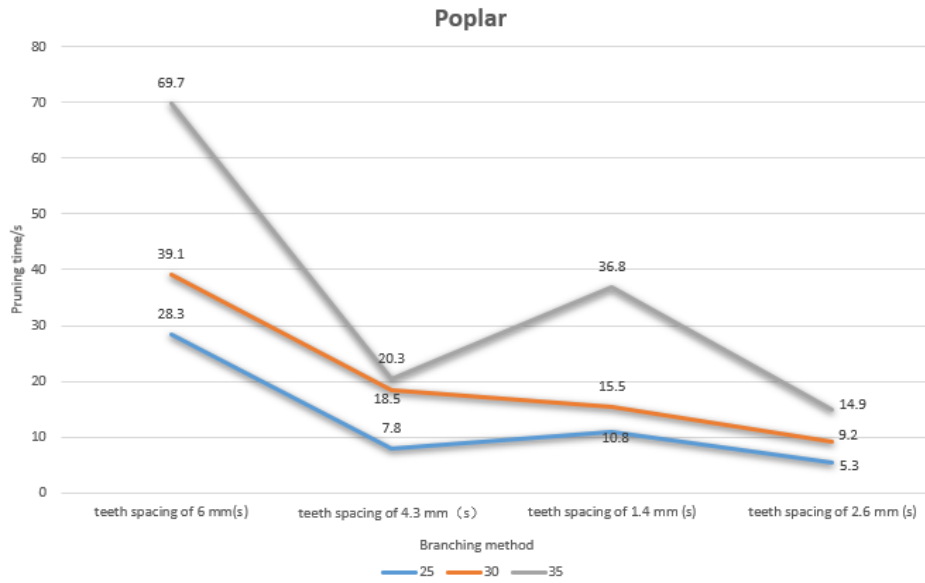
Fig. 5 - Line chart of poplar
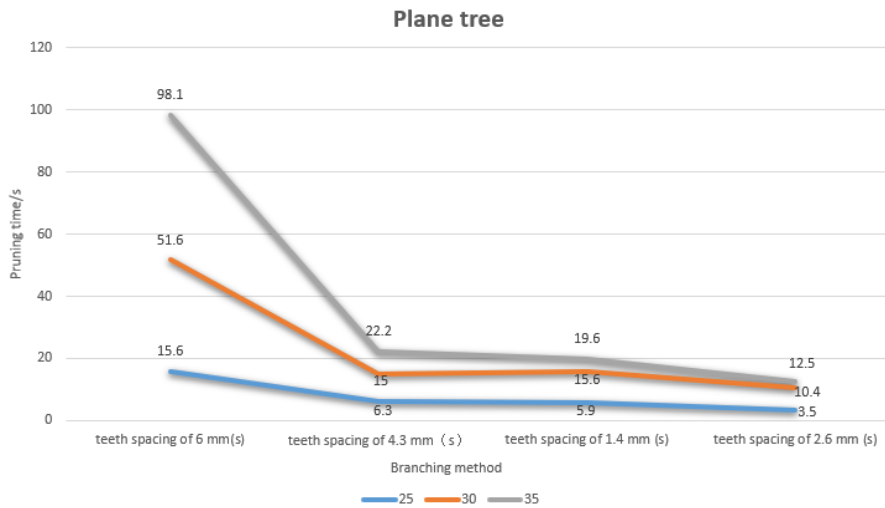
Fig. 6 - Line chart of plane tree
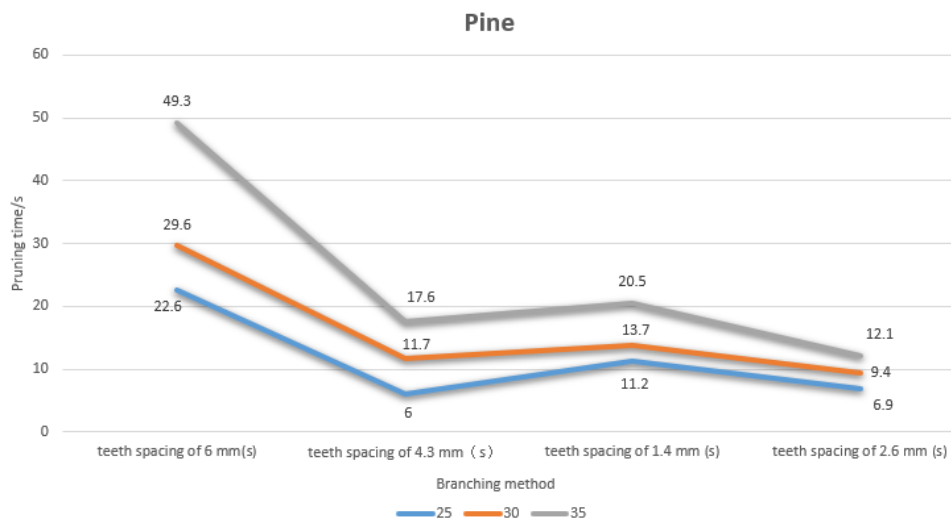
Fig. 7 - Line chart of pine

CONCLUSIONS

The study researches a type of omni-directional electric pruning saw with 360-degree rotary saw head, V-shaped groove under saw blade, telescopic rod, winding reel and head lock device at the handle. The experiment shows that the saw can be used for various branches; compared with ordinary hand saw, the efficiency is improved four times and the present manual labour mode is completely replaced, reducing the field labour intensity and the risk of high-altitude operation and improving the overall work efficiency of the existing high-altitude operation. In addition, the pruning operation cost is reduced and the pruning economic benefit is improved.

ACKNOWLEDGEMENT

REFERENCES

[1] Chen H.J., (2018), Study on type and application of forestry mining and transportation, *China Academic Journal Electronic Publishing House*, issue 2, pp. 24-25;

[2] Cheng F., (1981), New technique of pruning, *Forestry Abroad*, issue 3, pp. 55-56;

[3] Deng Z.F., (2017), Discussion on types and applications of forestry harvesting and transportation machinery, *Green Technology*, issue 13, pp.168-169;

[4] Ji H., (1990), Automatic cutting saw, *Forestry Abroad*, issue 2, pp. 59-60;

[5] Jia Y.Z., Wu Y.P., Kuang X.G., Liu G.Y., Chen G., (2017), Research progress in manufacturing process of bimetal band saw blade, *Tool technology*, vol. 51, issue 10, pp. 3-10;

[6] Katuril R., Gorantla S., (2018), Comparative analysis of controllers for a smooth switching between battery and ultracapacitor applied to E-vehicle, *European Journal of Electrical Engineering*, vol. 20, issue 1, pp. 47-75;

[7] Katuril R., Gorantla S., (2018), Performance analysis of hybrid controller for automatic switching between energy sources of hybrid energy storage system, *European Journal of Electrical Engineering*, vol. 20, issue 5-6, pp. 617-630;

[8] Li X.X., (2017), Design and cutting performance simulation of bimetal band saw blade, *Dalian University of Technology;*

[9] Lin S., (1985), Study on cutting conditions of chain Saw for logging, *Journal of Nanjing Forestry University (Natural Science Edition)*, issue 4, pp. 124-137;

[10] Liu D., Tang P., Guo J., Song S.Q., (2018), Design of bundling system for electric vegetable harvester, *China Journal of Agricultural Machinery Chemistry*, vol. 39, issue 7, pp. 11-15;

[11] Liu J.H., Wang D., (2006), The actuality and development trend of plantation tending machines at home and abroad, *Forest Engineering*, issue 3, pp. 12-14;

[12] Liu T., (1975), Stumpage saw, *Forestry Abroad*, issue 3, pp. 32-36;

[13] Michael S., Jin Y., (2014), Review--18 V cordless RECIP saws, *Power Tools*, issue 5, pp. 23-29;

[14] Shen J.F., (2010), Research on forestry felling & cultivation machine executive mechanism and load-sending hydraulic system, *Beijing Forestry University;*

[15] Tang K.X., (2015), Basic research on hand saw design, *Literary Life (Art China)*, issue 6, pp. 136-138;

[16] Wang Z., Song Y.P., Gao D.S., Liu, H.J., Fan G.J., Zhang T., (2017), Dynamic simulation analysis and experiment of apple branch sawing process, *China Journal of Agricultural Machinery Chemistry*, vol. 38, issue 9, pp.44-50;

[17] Zhang Y., Sun Y.M., Cao H.X., Du S.S., Yuan J.L., (2018), Application trend of high-performance lithium battery materials, *Contemporary Chemical Research*, issue 11, pp. 20-21.

[18] Wang J.P., Yu J., Zhou H. P., Zhou F. F., Tao L., Chen J. W. (2016) Research on bamboo cutting mode with double V-type cylindrical helical cutters, *Journal of Forestry Engineering,* issue 1, pp.124-129;

[19] Yu H., Fu W.S., Zhang C.Q., Li C.W., Zhu B.H., (2019), Design of Cluster Bamboo Selective Cutting Machines Based on Reciprocating Saws*, Forestry Machinery & Woodworking Equipment,* issue 4, pp.11-14;

[20] Jeremy K., (2018), Experience of the Bosch GSA18V*, Power Tools*, issue 5, pp. 23-25.

LABORATORY-FIELD RESEARCH RESULTS FOR ONION CLEANING
/
РЕЗУЛЬТАТЫ ЛАБОРАТОРНО-ПОЛЕВЫХ ИССЛЕДОВАНИЙ МАШИНЫ ДЛЯ УБОРКИ ЛУКА

Alexey Semyonovich Dorokhov, **Aleksey Viktorovich** Sibirev, **Alexander Gennadievich** Aksenov,
Maxim Alexandrovich Mosyakov [1]
FSBSI "Federal Scientific Agronomic and Engineering Centre VIM"/ Russian
Telephone: 89645843518; E-mail: sibirev2011@yandex.ru
DOI: https://doi.org/10.35633/inmateh-61-05

ABSTRACT

In the machine technology for cultivation and harvesting of root crops and onions, one of the most important quality indicators determining the duration of root crops storage is the presence of soil and plant impurities in the heap to be stored. The impossibility to separate soil lumps from the heap of root crops and onions is due to the fact that the majority of harvesters use slotted separating executive devices, while the inter-rod distance of the separating conveyor, in order to eliminate the loss of root crops, is made smaller than the minimum size of the separated root crop, which leads to the impossibility of their cleaning on the separating executive devices of harvesters, and, consequently, to the damage of a significant part of commercial products and loss of a significant part of the crop grown during storage. The modern technologies and technical means for harvesting root crops and onions are not capable of providing high-quality commercial products with minimal labour, due to falling behind or a lack of development of technological foundations, technologies and executive devices for harvesting root crops and onions, capable of reducing or excluding the content of soil lumps in commercial products under various soil and climatic conditions. Therefore, development of mechanization tools for harvesting root crops and onions, which would allow reducing or eliminating the content of mechanical impurities in commercial products under various soil and climatic conditions, is a scientific problem, the solution of which will contribute to the innovative development of the domestic agricultural market, Russia's stable position on the foreign market.

РЕЗЮМЕ

В машинной технологии возделывания и уборки корнеплодов и лука одним из важнейших показателей качества, определяющего длительность хранения корнеплодов является наличие в закладываемом на хранение ворохе почвенных и растительных примесей. Невозможность отделения почвенных комков из вороха корнеплодов и лука обусловлена тем, что на большинстве уборочных машин применяют щелевые сепарирующие рабочие органы, при этом межпрутковое расстояние сепарирующего транспортера с целью исключения потерь корнеплодов выполнено меньше минимального размера сепарируемого корнеплода, что приводит к невозможности их очистки на сепарирующих рабочих органах уборочных машин, а следовательно, к травмированию значительной части товарной продукции и потерям при хранении значительной части выращенного урожая. Современные технологии и технические средства уборки корнеплодов и лука не способны обеспечить получение качественной товарной продукции при минимальных трудозатратах, что обусловлено отставанием или отсутствием в разработке технологических основ, технологий и рабочих органов уборки корнеплодов и лука, позволяющие снизить или исключить содержание почвенных комков в товарной продукции в различных почвенно-климатических условиях. Следовательно, разработка средств механизации для уборки корнеплодов и лука, позволяющих снизить или исключить содержание механических примесей в товарной продукции в различных почвенно-климатических условиях представляет научную проблему, решение которой будет способствовать инновационному развитию внутреннего рынка сельскохозяйственной продукции, устойчивому положения России на внешнем рынке.

---

[1] *Dorokhov Alexey Semyonovich, Prof. PhD. Eng.Sc.; Sibirev Aleksey Viktorovich, PhD. Eng.Sc.;*
Aksenov Alexander Gennadievich, PhD. Eng.Sc.; Mosyakov Maxim Alexandrovich, PhD. Eng.Sc.

INTRODUCTION

Creation and implementation of machines of a new, intellectual type is the determining component of the agricultural engineering development strategy in the Russian Federation *(Aldoshin N.V. et al., 2015; Aldoshin N.V. et al., 2014; Kukharev O.N. et al., 2018; Kurdyumov V.I. et al., 2019; Kurdyumov V.I. et al., (2016))*. The harvesting productivity and efficiency depends on the optimal solution to the problem of controlling the technological process of machine harvesting of root crops and onions *(Bashkirtsev V.I. et al., 2017; Lobachevsky Ya.P. et al., 2016; Laryushin N.P. et al., 2015).*

When solving many problems related to the improvement of technological processes and executive devices of agricultural machines, the main goal is to increase crop yields and improve the harvesting quality of the grown crops *(Zykin E.S. et al., 2017; Kukharev O.N., 2006; Kalinin A.B. et al., 2015; Kalinin A.B. et al., 2016; Kukharev O.N. et al., 2018).*

The main task to be achieved by mechanized harvesting of root crops and onions, as well as other crops, is to increase the completeness of collection, reduce damage to the products, which can be achieved by creating higher-performance harvesters.

When harvesting root crops and onions, a large volume of soil passes through the separating devices of root and onion harvesters on each hectare, from which root crops and bulbs must be extracted with minimal damage. Because of this, the productivity of harvesters is determined mainly by the throughput capacity of the separating devices *(Kukharev O.N. et al., 2018; Sibirev A.V. et al., 2018).*

At the same time, separating devices, and in particular the most common ones - rod elevators, are unable to ensure the required completeness of separation and sufficient performance under various conditions of their use.

To eliminate these deficiencies, various intensifiers with various drive designs are used on harvesters.

The disadvantages of separation intensifiers of various designs include the fact that, as a result of force impact on the material being processed, the product is damaged, moreover, during harvesting, soil impurities come together with root crops and bulbs, which leads to the clogging of the product, so additional processing is required for its cleaning at the site, which entails additional costs.

It is known that the separating ability of a rod elevator depends on the inclination angle α_1 and the elevator speed v_{EL}.

The separation coefficient ε at any inclination angle α_1 increases as the speed of the rod elevator v_{EL} increases, to a certain maximum value, after which it starts decreasing. The optimal movement speed v_{EL} of a rod elevator is an interval between 2 m/s and 2.5 m/s.

Moreover, to avoid unloading a heap of root crops and onions on the surface of the rod elevator, the following conditions must be met (*Sorokin A.A., 2006*):

$$v_{\mathrm{EL}} = v_{\mathrm{Me}} = v_{\mathrm{K}} \cdot \mathrm{A} \tag{1}$$

where v_{K} − is the progressive speed of the harvester movement, m/s; A − coefficient (A=1.3).

Therefore, an increase in the productivity of the technological process of harvesting root crops and onions will lead to a decrease in the separation quality and increase in the damage to commercial products.

MATERIALS AND METHODS

Based on the functional diagram of the control system with a perturbation control principle, an intelligent technology for harvesting root crops and onions was developed, with the development of a separating rod elevator with an adjustable blade inclination angle.

The separating rod elevator with an adjustable inclination angle (RF patent No. 2679734) ensures damage reduction and improves the quality of the separated products by minimizing the impact of the vertical component of the gravity of root crops and bulbs, while also increasing the uniformity of distribution of the heap of root crops and bulbs across the separating surface when changing angle α of the rod elevator inclination as a result of changes in soil and climatic conditions of harvesting root crops and onions *(Sibirev A.V. et al., 2019)*. To adjust the inclination angle of the blade of rod elevator *1*, weight sensors *2* mounted on digging plough share *3* (Figure 1) are used.

Weight sensors *2* measure the weight of the incoming heap of root crops on digging plough share *3* and send the readings to microcontroller *4* during the root crops and onion heap separation and bar elevator *1* inclination angle α_1 adjustment.

The linear drive, represented by electric cylinders *5*, moves the linear drive rod to the required distance S_1 or S_2 changes the α_1 inclination angle of the blade of rod elevator *1* depending on the readings of weight sensors *2* after receiving a signal from microcontroller *4*.
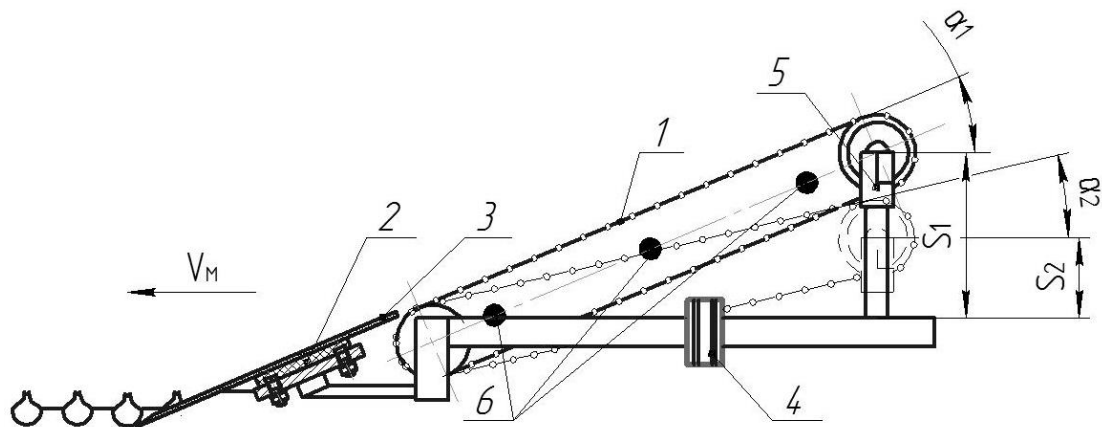
Fig. 1 – Diagram of changes in the inclination angle of the rod elevator:
1 – rod elevator; 2 – digging plough share weight sensor; 3 – digging plough share; 4 – microcontroller;
5 – electric cylinder; 6 – inertial sensor

When a heap of root crops passes across the surface of rod elevator *1*, the soil is screened through slotted holes formed by adjacent rods of the blade (Figure 2). The screened soil is registered by means of inertial sensors *6* installed along the length of rod elevator *1*. When evaluating the efficiency of separation by inertial sensor 6, the oscillation frequency will also be characterized by the movement speed of rod elevator *1* (interchanging gaps and rods above the sensor).
However, the amount of the screened soil will be characterized by peak amplitude values. Therefore, the separation efficiency of the elevator is estimated according to the amplitude values *(Sibiryov A.V. et al., 2019)*.

If the soil is screened on the rod elevator below the required value set by microcontroller *4*, inclination angle α_1 of rod elevator *1* is adjusted in the specified range of values. After determining the mass of the root crop and onion heap on the digging plough share, the controller, with time delay *T*, along with the movement of the rod elevator, sends a control signal to move the actuator rod.

Fig. 2 – General view of the machine for harvesting root crops and onions, equipped with a separating rod elevator with adjustable blade inclination angle and receiving plough share for digging/collecting root crops and bulbs
1— frame; 2 – receiving plough share for digging/collecting root crops and bulbs; 3 – supporting wheels; 4 – main separating rod elevator; 5 – additional rod elevator; 6 – bed-forming roller; 7 – shaker adjusting plate; 8 – narrowing tray; 9 – electric cylinders; 10 – weight sensor of the digging plough share; 11 – microcontroller

The aim of the studies was to substantiate the possibility of using a separating rod elevator with an adjustable blade inclination angle for harvesting root crops and onions, as well as to establish the optimal values of its process parameters under laboratory and field conditions, ensuring high-quality separation of onion heaps from soil and plant impurities.

Fig. 3 – General view of the harvester for root crops and onions, equipped with separating rod elevator with an adjustable blade inclination angle and receiving plough share for digging/collecting root crops and bulbs
1 – Tractor MTZ 1221; 2 – root and onion harvester

Field studies of a separating rod elevator with adjustable blade inclination angle of root and onion harvester (Figure 3) were carried out on the fields owned by Tsirulev E.P. peasant farm enterprise in the Samara region in 2019, when harvesting Stuttgarter Riesen breed onions.

Production studies were carried out in accordance with STO AIST 8.7-2013 "Machines for harvesting vegetables and gourds. Methods for assessing functional indicators".

When conducting studies of separating rod elevator with an adjustable blade inclination angle installed on a UKL-1.3 root and onion harvester, the physical and mechanical properties of the soil were determined, as well as the onion heap separation quality indicators. The soil in the plot selected for the studies is medium loamy black earth soil, the field relief is flat, the field contour is close to a rectangular shape, the pass (furrow) length is 350 m.

The quality of the technological process performance was assessed according to the following indicators:

– damage P to the bulbs;

– separation completeness v of an onion heap *(Sibirev A.V. et al., 2018; Sibirev A.V. et al., 2019).*

When determining the optimal value of the studied factor during production studies, the other factors remained unchanged, i.e. equal to the optimal values determined during laboratory and field studies. In the process of laboratory and field studies of a root and onion harvester equipped with separating rod elevator with an adjustable blade inclination angle, process parameters were set in the above specified range of values.

Progressive speed v_{EL} of the rod elevator blade varied from 1.0 m/s to 1.8 m/s with a variation interval of 0.2 m/s.

The only exceptions are the factors, the optimal values of which could not be investigated under laboratory conditions; these factors include depth h_L of immersion into the soil of the digging plough share and progressive v_K speed of the root and onion harvester. In addition, in order to study the influence of the amount of onion heap supply Q_{BEL} on the quality of separation of the rod elevator with an adjustable blade inclination angle, the progressive speed v_P of the root and onion harvester, as well as the depth h_L of immersion of the digging plough share into the soil, were changed.

The progressive speed v_K of the root and onion harvester varied from 1.0 m/s to 1.8 m/s with a variation interval of 0.2 m/s, the immersion depth h_L of the digging plough share into the soil varied in the range of 0.02 m to 0.06 m, in increments of 0.01 m.

The performance quality of the rod elevator with an adjustable blade inclination angle was determined as follows. At the start of the registration plot, with self-propelled combine *1* moving non-stop (Figure 3), canvas was placed under the separating rod elevator upon a signal, in which all the harvested mass was collected.

In the process of passing the plot, canvas was unrolled behind the harvester, on which the heap dropped after separation.

Then samples were taken from the canvas surface from the entire territory of the registration plot. In so doing, the fractional composition of the heap was determined, taking into account: bulbs, loose soil and soil attached to bulbs.

RESULTS AND DISCUSSION

When conducting laboratory studies of a rod elevator with adjustable blade inclination angle, the optimal values of the studied factors were determined, to be investigated for quality indicators of work in a production environment. The study of the technological process of the work of a rod elevator with adjustable blade inclination angle under laboratory field conditions was carried out with factors varying within (Figure 4):

– depth of the digging plough share immersion into the soil $h_L =$ was 0.02 m to 0.06 m;

– progressive speed of the root and onion harvester $v_K =$ was 1.0 m/s to 1.8 m/s;

– the progressive speed of the rod elevator blade $v_{EL} = 1.55$ m/s to 1.67 m/s.

According to the results of processing the experimental data, dependence graphs were plotted with regard to the completeness of separation of onion heap v in % and damage to bulbs D in % vs. the operating and process parameters of the harvester (h_L and v_P) and the separating rod elevator (v_{EL}) with an adjustable blade inclination angle.
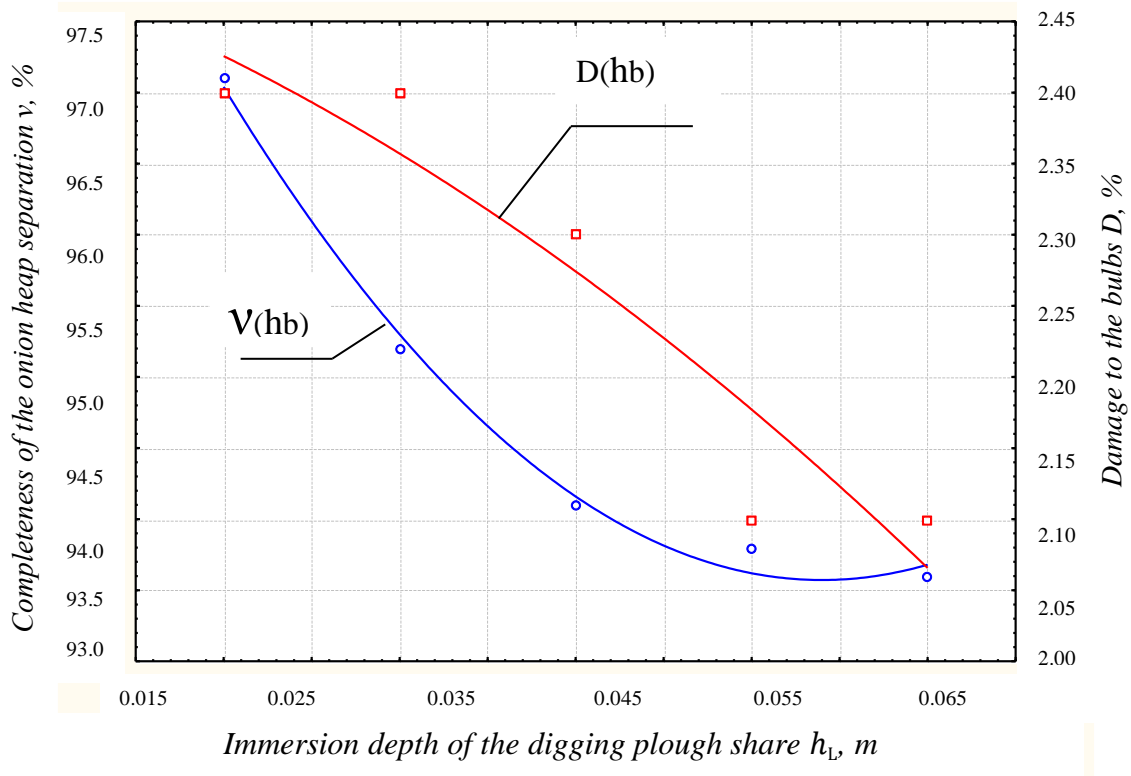
Fig. 4 – Dependence of separation completeness v and damage to bulbs D of a separating rod elevator with an adjustable blade inclination angle vs. depth h_L of the digging plough share immersion into the soil

The correlation between the quality indicators of the technological process of operation of a root and onion harvester equipped with rod elevator with an adjustable blade inclination angle from the immersion depth h_L of the digging plough share into the soil is expressed by an equation of parabolic functions:

$$\begin{cases} v = 102.32 - 3.24 \cdot h_L + 0.28 \cdot h_L^2, \\ D = 2.52 - 3.28 \cdot h_L - 0.71 \cdot h_L^2. \end{cases} \qquad (2)$$

Analysing the graph (Figure 5), we can say that high quality of onion heap separation exceeding 98 % is ensured when the digging depth of the digging plough share is 0.02 m, and when the digging depth is increased, the completeness of onion heap separation is significantly reduced.

This circumstance is explained by an increase relative to the optimal onion heap supply determined under laboratory conditions for the rod elevator studied.

The lowest indicators of damage to onion bulbs, i.e. less than 2.5%, are achieved with the greatest digging depth of the digging plough share into the soil equal to 0.06 m/s, which is explained by the presence of a soil layer between the elevator rods and the separated onion products.
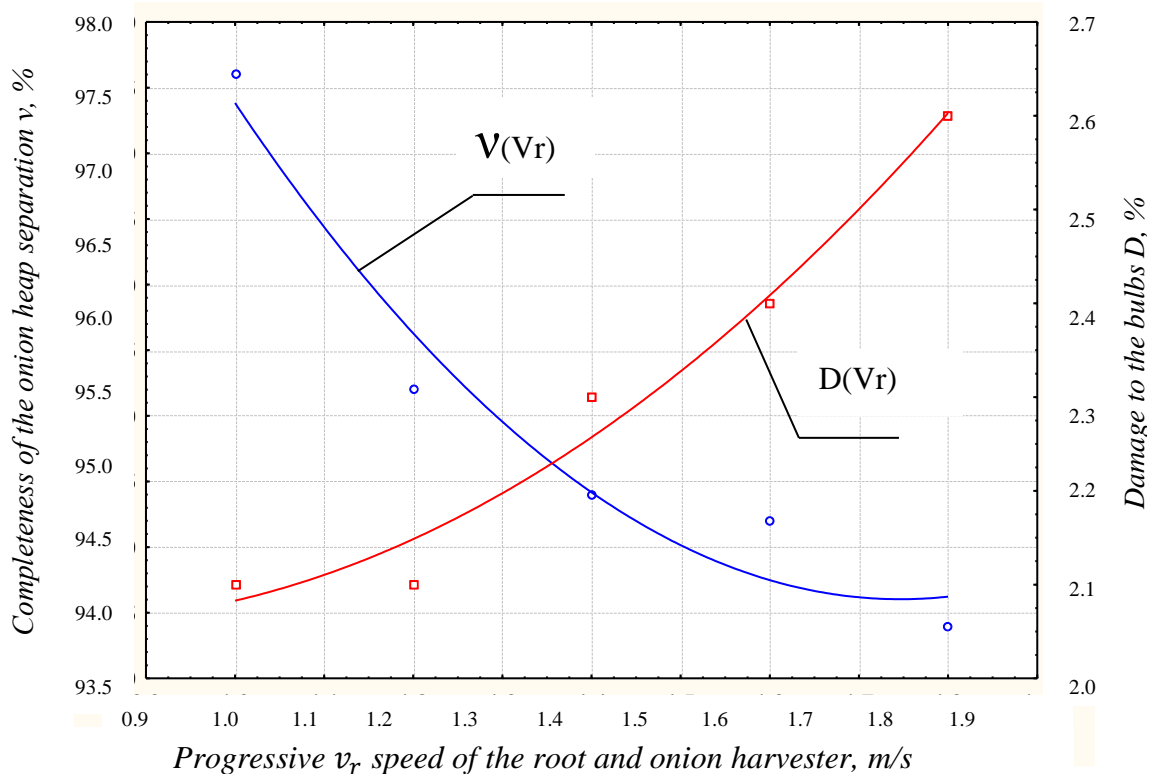
Fig. 5 – Dependence of the completeness of separation v **and damage to bulbs** D
of separating rod elevator with adjustable blade inclination angle vs. the progressive v_r
speed of the root and onion harvester

When determining the quality indicators of the technological process of operation of a rod elevator with adjustable blade inclination angle, we obtained a correlation dependence of the separation completeness of the onion heap v in % and damage to the bulbs D in % on the progressive speed of the seed onion harvester:

$$\begin{cases} v = 114.29 - 2.37 \cdot v_K + 0.67 \cdot v_K^2, \\ D = 2.39 + 0.85 \cdot v_K + 0.53 \cdot v_K^2. \end{cases} \qquad (3)$$

An analysis of quality indicators of operation of the root and onion harvester equipped with rod elevator with adjustable blade inclination angle depending on changes in the progressive v_K speed of the root and onion harvester shows that the completeness of separation and damage to the bulbs drop with an increase in the technological indicator under study.

According to the graph shown in figure 6, it follows that the optimal ratio of onion harvesting quality indicators is ensured when crossing curves approximating the separation completeness of 95.7 % and bulb damage of 2.6 % at a progressive speed of the root and onion harvester equal to 1.38 m/s.

The results of studies of progressive speed v_{EL} of the rod elevator with adjustable blade inclination angle with regard to quality harvesting indicators in the field indicate that the optimal value of the studied factor corresponds to 1.6 m/s with separation completeness of 98.5 % and production damage of 2.3 %.

The correlation between quality indicators (v and D) of onion harvesting and progressive speed v_{EL} is determined by a correlation dependence, which is expressed by an equation of parabolic functions:

$$\begin{cases} v = 82.79 + 12.2 \cdot v_{EL} - 2.14 \cdot v_{EL}^2, \\ D = 0.45 + 0.05 \cdot v_{EL} + 0.53 \cdot v_{EL}^2. \end{cases} \tag{4}$$
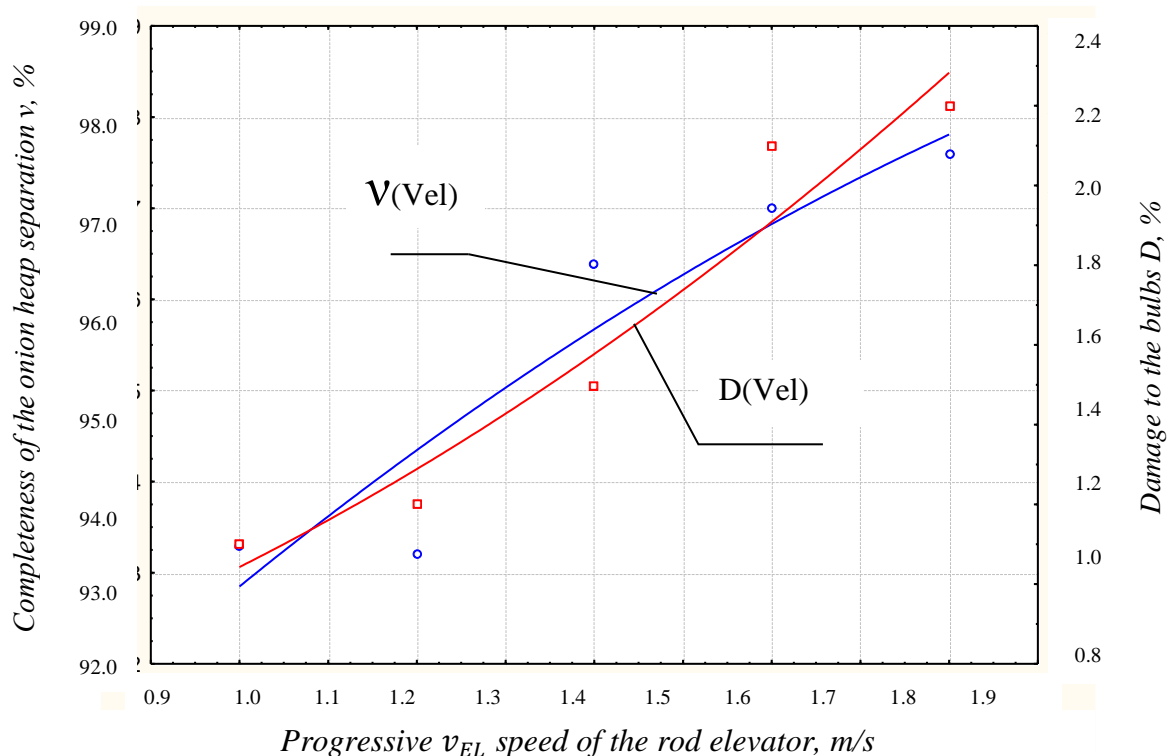
Fig. 6 – Dependence of the completeness of separation v and damage to bulbs D of separating rod elevator with adjustable blade inclination angle vs. the progressive speed v_{EL} of the rod elevator blade

CONCLUSIONS

The results of production studies performed on a root and onion harvester equipped with rod elevator with adjustable blade inclination angle demonstrated high-quality performance of the technological process of separation of an onion heap with optimal values of parameters:

– progressive speed v_{EL} of the rod elevator with adjustable blade inclination angle of 1.6 m/s, with separation completeness of 98.5 % and product damage of 1.3 %;

– movement speed v_K of the root and onion harvester 1.38 m/s, with separation completeness of 95.7 % and damage to the bulbs of 1.6 %;

– digging depth h_L of the digging plough share equal to 0.02 m with onion heap separation completeness exceeding 98 % and damage to the products less than 1.5 %.

REFERENCES

[1]   Aldoshin N.V., Didmanidze O.N., (2015), *Engineering and technical support for the quality of mechanized work: Monograph*, State Agrarian University - Moscow Agricultural Academy named after K.A. Timiryazev. 188 p. Moscow / Russia;

[2]   Aldoshin N.V., Gorbachev I.V., Zolotov A.A. and others. (2014), *Agricultural machines,* State Agrarian University - Moscow Agricultural Academy named after K.A. Timiryazev. 149 p. Moscow / Russia;

[3]   Bashkirtsev V.I., Aldoshin N.V., (2017), *Mechanized work quality assurance during the operation of agricultural machinery*, State Agrarian University - Moscow Agricultural Academy named after K.A. Timiryazev. 96 p. Moscow / Russia;

[4]   Kalinin A.B., Smelik V.A., Teplinsky I.Z., Pervukhina O.N., (2015), *Selection and substantiation of the parameters of an agroecosystem ecological state for monitoring technological processes of crop cultivation*, no. 39. pp. 315-319. St. Petersburg / Russia;

[5]   Kalinin A.B., Teplinsky I.Z., Kudryavtsev P.P., (2016), Soil condition in intensive technology. *Potatoes and vegetables*. no. 2. pp. 35–36. St. Petersburg / Russia;

[6]   Kukharev O.N., (2006), *Energy-saving technologies for oriented planting of crops (by the example of onions and sugar beets)*: dis. Ph. D. in Eng. Science. 414 p. Penza / Russia;

[7]   Kukharev O.N., Larushin N.P., (2018), A device for guiding bodies of irregular shape, *Research Journal of Pharmaceutical, Biological and Chemical Sciences*. vol. 9. no 3. pp. 30–33. India;

[8]   Kukharev O.N., Laryushin N.P., (2018), Analysis of the existing methods and means of collecting seed onions from rolls, Resource-saving technologies and technical means for the production of crop and livestock products, *Collection of articles of the IV International Scientific and Practical Conference*. pp. 86 - 89. Penza /Russia;

[9]   Kurdyumov V.I., Zykin E.S., Lazutkina S.A., (2019), Universal roller attachment, Materials of the National Scientific-Practical *Conference "Agricultural science and education at the present stage of development: experience, problems and solutions"*. pp. 39-42. Ulyanovsk / Russia;

[10]   Kurdyumov V.I., Zykin E.S., Sharonov I.A., Martynov V.V., Tatarov G.L., (2016), Experimental studies of a ridge forming roller, Materials of the *VII International Scientific-Practical Conference "Agricultural science and education at the present stage of development: experience, problems and solutions"*. pp. 110 -114. Ulyanovsk / Russia;

[11]   Laryushin N.P., Kukharev O.N., Kiryukhina T.A., (2015), Initial provisions in the design of onion harvesters, *Science in Central Russia*. no. 6 (18). pp. 48–58. Tambov / Russia;

[12]   Lobachevsky Ya.P., Emelyanov P.A., Aksenov A.G., Sibirev A.V., (2016), Onion production machine technology, *Monograph, FSBSI "Federal Scientific Agronomic and Engineering Centre VIM"*.168 p. Moscow / Russia;

[13]   Patent no. 2679734 Russia, IPC A01 D33/00. *Separating conveyor of a root and bulb harvester* / A.V. Sibirev, A.G. Aksenov, N.G. Kynev, N.V. Sazonov. no. 2018117525; Application 11.05.2018; Publ. 12.02.2019, Bull. No. 5;

[14]   Sibirev A.V., Aksenov A.G., Mosyakov M.A., (2019), Results of experimental studies of separation of head of onion-seed on a bar elevator with asymmetrically installed shakers, *Engineering technologies and systems*. vol. 29. no. 1. pp. 91-107. Saransk / Russia;

[15]   Sibirev A.V., Aksenov A.G., Mosyakov M.A., (2018), Experimental Laboratory Research of Separation Intensity of Onion Set Heaps on Rod Elevator, *Journal of Engineering and Applied Sciences*. no. 23. pp. 10086–10091. Islamabad / Pakistan;

[16]   Sibirev A.V., Aksenov A.G., Dorokhov A.S., (2019), Results of laboratory investigations of soil screening ability of a chain digger with asymmetric vibrator arrangement, *INMATEH — Agricultural Engineering*. no.1. (57), pp. 9–18. Bucharest / Romania;

[17]   Sorokin A.A., (2006), Theory and calculation of potato harvesters, Monograph, VIM.159p. Moscow / Russia;

[18]   Zykin E.S., Kurdyumov V.I., (2017), Energy efficiency of ridge technology for cultivating row crops. *Bulletin of the Ulyanovsk State Agricultural Academy*. no. 1 (37). pp. 160 - 166. Ulyanovsk/Russia.

AN EXPERIMENTAL INVESTIGATION OF SOIL LAYER COUPLING FAILURE CHARACTERISTICS ON NATURAL GRASSLAND BY PASSIVE SUBSOILER-TYPE OPENERS
/
深松铲型开沟部件作用下的天然草地耦合失效试验研究

Changbin He [1,2), Yong You *2), Decheng Wang *2,3), Hongjian Wu 2,4), Bingnan Ye 2) 1]
1) Inner Mongolia Agricultural University, College of Mechanical and Electrical Engineering, Hohhot / China;
2) China Agricultural University, College of Engineering, Beijing / China;
3) China Agricultural University, Key Laboratory of Grassland Management and Rational Utilization, Beijing / China;
4) Tsinghua University, Department of Mechanical Engineering, State Key Laboratory of Tribology, Beijing / China;
Tel: +86 10 010-62737977; +86 10 010-62737208; E-mail: youyong@cau.edu.cn; wdc@cau.edu.cn
Corresponding authors: Yong You, Decheng Wang
DOI: https://doi.org/10.35633/inmateh-61-06

ABSTRACT

Unclear soil layer coupling failure characteristics on natural grassland impeded the design and optimization of appropriate tillage tools. The coupling failure characteristics including surface disturbance and profile, disturbed cross-section area, soil over-turning rate, and coupling forces between the soil layer of natural grassland and selected passive subsoiler-type openers were investigated in this paper. Three single-shoot openers (i.e. CO, AO and WAO) and a test unit were designed, and furrow opening experiments under different working depths were conducted. Results showed that, along the passages, U-shaped disturbed cross-sections were usually created with soil-root clods overturned along the furrows. The roots were usually broken in a pulling or dragging way underground. Both disturbed cross-section area and draft force values increased with the working depth increasing linearly ($R^2 \geq 0.93$), contrary to the tendency of the specific draft force with the depth. Winged opener (i.e. WAO) had larger draft forces and disturbed soil layer cross-section areas than no-winged openers (i.e. AO and CO). The soil layer failure processes of the natural grassland were affected by its composite soil layer structure and the geometry parameters of the openers. The results provide original references for designing novel furrow openers applicable to improve degraded natural grassland.

摘要

为研究耕作部件作用下的天然草地耦合失效特性，设计了三种深松铲型开沟部件，通过搭建试验台进行了不同作业深度下的草地开沟失效试验，对草地土层失效过程、扰动情况、扰动截面积、翻垡率和作业阻力进行了分析。试验结果表明，深松铲型开沟部件作业时产生 U 形扰动截面，同时沿沟易产生翻垡的土壤-根系复合结构土块；开沟部件作业时主要通过拉扯的方式使根系拉断；开沟扰动截面积和水平方向的作业阻力均随着作业深度的增加呈线性增加的趋势（$R^2 \geq 0.93$）；而沟形面积比阻随着作业深度的增加而减少。具有双翼的开沟部件产生较大的牵引阻力和土层扰动截面积，草地土层失效过程受其复合土层结构和开沟部件的形状参数的影响。试验结果为退化草地改良用专用开沟部件的研发和优化设计提供了参考。

INTRODUCTION

Natural grasslands are important ecological screens of Northern China. Leymus chinensis (Trin.) Tzvel. (abbreviated as L-C hereafter), as a popular fodder grass, due to its good palatability and high forage value, widely spread in the natural grasslands of Northern China (*MOA, 1996*). However, the natural grasslands have been showing degradation trends including vegetation cover reducing, productivity decreasing, and ecosystem conditions deteriorating etc. recently, mainly caused by irrational management (e.g. overgrazing and over-cultivation) and climate change (*Zhao et al., 2006; Han et al., 2008; Li et al., 2018*).

---

[1] *Changbin He, Lecturer Ph.D. Eng.; Yong You, As. Prof. Ph.D. Eng.; Decheng Wang, Prof. Ph.D. Eng.; Hongjian Wu, Ph.D. Eng.; Bingnan Ye, Dr. Stud. Eng.*

Mechanical improvement methods including aerating, fertilizing, shallow ploughing, soil gashing and root cutting, loosening, and reseeding have been applied to improve degraded natural grassland in recent years (*You et al., 2012; He et al., 2015; De Boer et al., 2018*). Among those methods, drilling or reseeding practice was one of effective and long-standing recommendation means (*Liu et al., 2015; Zhou et al., 2017*).

A furrow opener is an irreplaceable component for a planter, which is very important for building a suitable seedbed. In general, it moves in the soil layer underground and breaks the soil layer structure, creating a furrow and allowing the seeds to be deposited before being partially covered with the soil. Furrow openers such as hoe, shovel, shoe, runner, single disc, double disc, and chisel types have been widely used for many years in conventional tillage system (*Chaudhuri, 2001*). With the conservation agriculture technique developed, no-tillage farming system has been accepted and adopted gradually, openers such as disc, tine, chisel, shank types etc. have been applied, seeds are placed into crop fields by opening a narrow furrow, or hole of only sufficient width and depth to obtain appropriate seed placement and coverage (*Derpsch et al., 2014*). Numerous investigations around the furrow openers in agricultural tillage system have been conducted in recent years. Performance of various furrow openers of seed drills or planters were studied in the laboratory, and compared with the results obtained through the experiments in the field (*Chaudhuri et al., 2001*). The disturbance caused by selected furrows and related working forces was also investigated under various different soil properties, operating conditions, and geometry structures (*Sánchez-Girón et al., 2005; Solhjou et al., 2013; Matin et al., 2016; Barr et al., 2020*). In addition, the interaction relationships between the soil and furrow openers were also investigated, to supply suitable indexes for evaluating the performance or design novel tillage tools (*Hasimu and Chen, 2014; Qin et al., 2018*).

The natural grassland forms undisturbed soil layer structure underground, different from the usually cultivated crop field due to composite tangled and outspread L-C roots underground, which bring about different soil layer failure characteristics from that of crop fields. However, the coupling failure characteristics caused by tillage tools were still undefined, affecting the development of appropriate tillage tools used for degraded natural grassland restoration. The mechanism, type and degree of soil disturbance of the natural grassland must be considered for the design and optimization of suitable tillage tools, related coupling forces should also be considered. However, almost all related studies and experiments about the openers focused on common crop fields, limited research or reports about specific furrow openers applied for natural grassland were found. This paper was a new attempt, aimed to investigate the soil coupling failure characteristics caused by selected passive subsoiler-type openers (i.e. chisel opener, arrow opener, and winged arrow opener) operated under different working depths on natural grassland, to provide original references and support for designing novel and specialized furrow openers applicable to natural grassland. The visual analysis of grassland surface disturbance, soil over-turning rate, and cross-section area of disturbed soil layer were used for describing the coupling failure characteristics, and the failure mechanism was analysed. The coupling horizontal and vertical resistances from the soil (defined as draft force and vertical force in this paper) were also recorded as well. Working depth and its uniformity were measured so that the results could be compared at the same controlled situation.

MATERIALS AND METHODS

- **Experimental site description**

The experimental site was located in a typical natural grassland with the area of over 80 ha in Chabei district of Hebei province (41°28'31.649″N, 115°1'28.733″E). L-C was the dominant grass species of this area. No conventional tillage practices were used in this area before and no livestock grazing was allowed in recent three years. The bulk density, moisture content, and porosity of the soil layer within the depth range of 0-15 cm on natural grassland were obtained based on the survey method as He et al. (2016) reported, listed in Table 1.

Table 1

Soil physical properties of the experimental site

Depth (cm)	Bulk density (g/cm^3)	Moisture content (g/(100g), d.b.)	Soil cone index (MPa)
0-5	1.04±0.05	9.99±2.43	2.92±0.53
5-10	1.26±0.13	13.68±2.42	2.38±0.62
10-15	1.34±0.12	17.18±2.35	2.20±0.56

- **Experimental openers and test unit**

Three single-shoot subsoiler-type openers were selected. They were chisel (CO), arrow (AO), and winged arrow (WAO) openers, as shown in Fig. 1. The front working surface of the chisel opener consisted of a flat and a shank adapter, the arrow opener resembled a sweep, and the winged arrow opener had a similar configuration, but with two additional wings. These openers were designed based on typical subsoilers commonly used in conventional tillage system in China. A shared shank was designed without any cutting edges. In the experiments, the openers were mounted on the same shank. The other parameters of the openers and the shank were similar to those listed in the MOMI standard (*MOMI, 1999*).
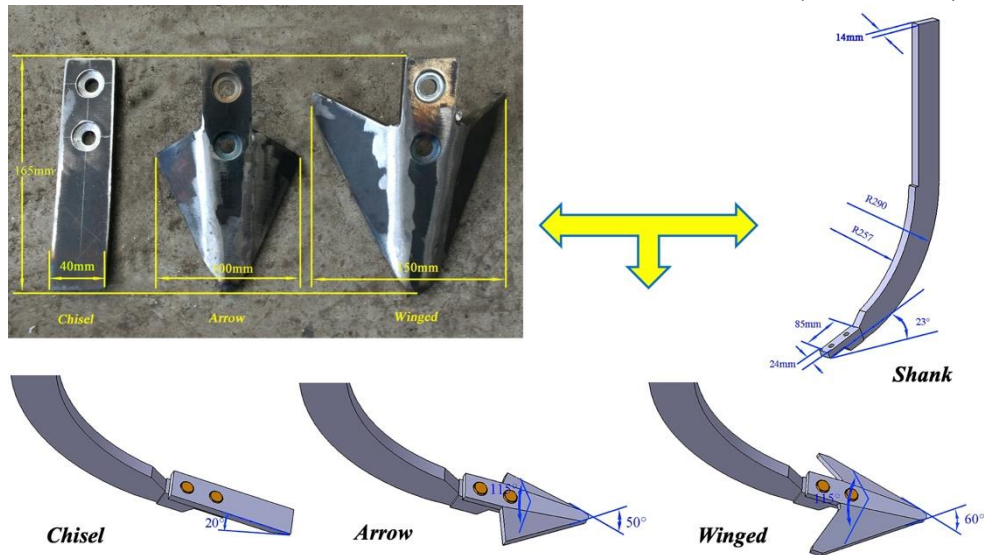
Fig. 1 - Selected openers used in the experiments

A test bench (Fig. 2) was designed and applied in the experiments, which was mainly composed of a data collection system, an image collecting device, frames and depth limiting device. The test bench was linked with a tractor by three-point hydraulic suspension frames. The openers were fixed on the frame in an articulated connection way. Two tension-pressure sensors (BK-2B, China Academy of Aerospace Aerodynamics) used for monitoring force data were fixed on the frame in horizontal and vertical directions, respectively. A data collector (SQ 2020, Grant Squirrel) was placed on the frame, which could gather the data from the two sensors. During the experiments, the data was reserved by the collector, then was exported to the laptop when the experiments were finished. An image collecting device (GoPro video) was fixed on the frame to capture the images, moving processes and interactive behaviours between the openers and soil layer on the natural grassland.
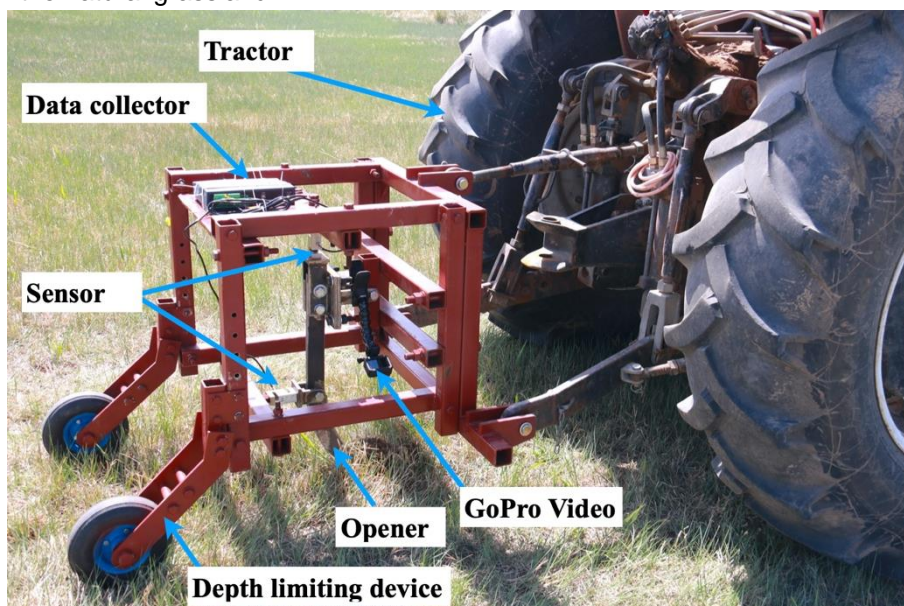
Fig. 2 - The photograph of the test facility

A profile metering device was used to measure the surface profile of disturbed soil-layer, as shown in Fig. 3. The spirit level was placed on the fixed plate to keep the horizontal ruler overlapping with the horizontal line. Coordinate value of a point of the disturbed area could be confirmed through the readings of the two rulers, then the cross-section profile could be drawn by Computer Aided Design (CAD) software through the coordinate values.
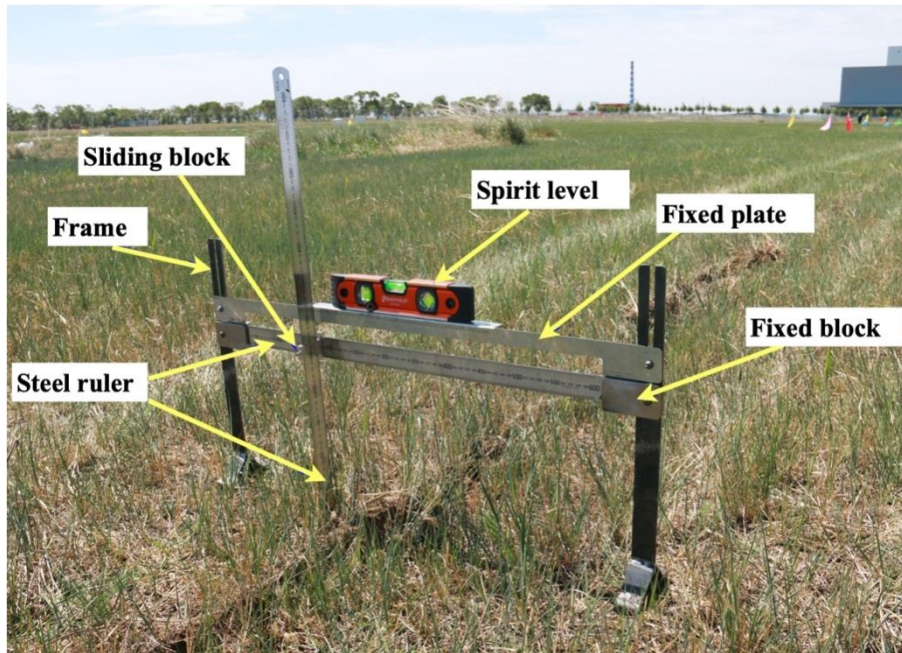
Fig. 3 - Profile meter

- **Experimental procedure and calculation**

Based on the pre-experiments, the openers always went through two phases when they were working, i.e. the phases of penetrating into the soil and moving stably. The dimensions of the experimental field area were 25 m ×18 m (length × width). The openers usually entered the soil layer gradually at the first distance of 1 meter along the moving direction, then kept on-the-go movements stably underground along the last distance of 24 meters. During the stable movement phase, the results were obtained from every 8 meters along the length. There were 3 repetitions for each opener. The openers were operated at a forward speed of 1.08±0.14 km/h pulled by the tractor moving at a slow speed of No.2 level. The operating depth was 5 cm, 10 cm, and 15 cm, respectively.

The depth uniformity was used to describe the stability of working depth during the tillage movements of the openers, taking the Chinese NY standard (MOA, 2003) as a reference, calculated as follows:

$$U = \left(1 - \frac{V}{100}\right) \times 100\% \tag{1}$$

$$V = \frac{S}{h} \times 100\% \tag{2}$$

$$S = \sqrt{\frac{\sum_1^n (h_i - h)^2}{N - 1}} \tag{3}$$

where:

U is the uniformity of working depth;

V is the coefficient of variation;

S is the standard deviation of depth;

h is the average value of depth;

h_i is the measured depth value at the point i;

N and n are the numbers of the measurement points.

The soil over-turning rate was defined as the total length of overturned soil clods divided by the travel distance of the opener (MOMI, 2007), calculated by:

$$F_L = \frac{L_f}{bL} \times 100\% \tag{4}$$

where:

F_L is soil over-turning rate;

L_f is the average value of the total length of overturned soil clods;

b is the numbers of opener while working, L is the travel distance.

The disturbance range of soil layer underground caused by the openers was described by the value of disturbance cross-section area, which was defined as Askari (2013) reported, calculated by equation (5) as follows:

$$A = [(2\sum_{i=1}^{n} d_i) - (d_1 + d_n)] \times \frac{l}{2} \tag{5}$$

where:

A is disturbance cross-section area;

d_i is profile meter reading, which represented the depth from the disturbed bottom surface underground to the grassland surface;

d_1 and d_n are the first and the last profile meter readings for every section of the profile, respectively;

l is the interval distance of every two adjacent measurement points, which was controlled at 10 mm along horizontal direction in this study.

The specific draft force was calculated using the following equation:

$$S.D = \frac{F}{A} \tag{6}$$

where:

$S.D$ is specific draft force;

F is the draft force of tillage openers. Average draft force and disturbed soil layer area were used to calculate the specific draft force.

RESULTS

- **Working depth and its uniformity**

Table 2 showed that the actual working depths of all openers were basically located in the range of 0-5 cm, 5-10 cm, and 10-15 cm as desired. The actual working depth had no significant differences between the three openers within the depth range of 10-15 cm. In the range of 0-5 cm and 5-10 cm, significant differences existed between the depth values of CO and AO at the significance level of 0.05, but no significant differences were found between CO and WAO. There were three gradients in the working depths, implying that the working performance of the same opener could be compared under various working depths.

The working depth uniformity was obtained based on equations from equation (1) to (3).

All openers had good working depth uniformities with the value of exceeding 76%, especially it went over 85% for WOA within the depth range of 0-15 cm. The results demonstrated that the openers had stable movements when they were working.

Table 2

The actual working depth of all openers

Tines	Desired depth of 0-5 cm	Desired depth of 5-10 cm	Desired depth of 10-15 cm
	Actual working depth (cm)		
CO	3.23±0.15bC	8.17±1.94bB	12.33±2.61aA
AO	5.37±1.27aC	11.3±0.72aB	14.63±0.23aA
WAO	4.23±0.45abC	8.37±0.45bB	15.03±2.22aA

Note: Different lowercase letters (i.e. a, and b) in each column represented the significant difference at the significance level of 0.05 by the Duncan Multiple Range Test. Different capital letters (i.e. A, B, and C) in each row represented the significant difference at the significance level of 0.05 by the Duncan Multiple Range Test.

- **Soil layer coupling failure characteristics on the grassland**

The L-C roots in the horizontal direction were mainly distributed in the subsoil layer at the depth of around 5 cm, and there were almost no roots that could be observed clearly beyond the depth of 10 cm underground. The rhizomes and soil formed composite structure underground. The disturbed soil layer surface profile was measured via the profile meter aforementioned; it could be concluded that it usually formed a "U" type disturbed cross-section profile underground after the opener making a furrow. Three main disturbed grassland surfaces remained after working, one was that big clods were overturned along the furrow, another one was only small over-turning clods left after working, the other one was that the soil layer on the grassland surface was ruptured, and bulged but not overturned after the opener moving. These selected openers easily caused the soil-root clods overturning when they were moving underground on the natural grassland. The soil over-turning rate was more than 5% for all openers calculated by measuring the

over-turned clods with the diameter of more than 5 cm along the furrows. Within the depth range of 5-10 cm, the soil over-turning rate even reached 26.08 %.

Among all the disturbed results, the situation with big clods overturned occupied most, and it was hard to produce soil backfill. The typical disturbed situations were as shown in Fig. 4.

| (a) | (b) | (c) | (d) |
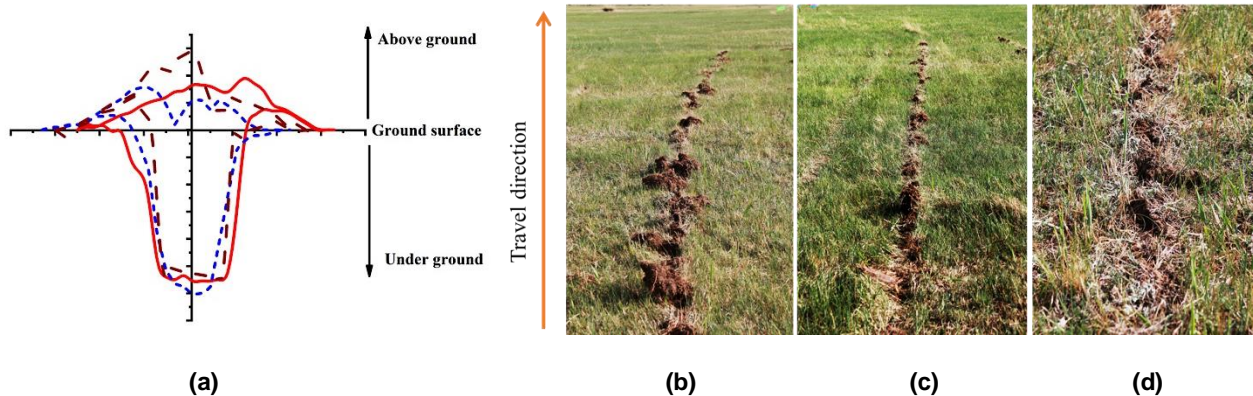
Fig. 4 - Soil disturbance on grassland: (a) typical profile of disturbed soil layer cross-section (b) big clods along the furrow; (c) small clods along the furrow; (d) soil layer bulged without overturning

When the opener was moving underground, the front surfaces of the opener lifted up the soil-root complicated layer structure and push them laterally, as shown in Fig. 5 (a). In addition, it was observed that the roots in the soil layer were broken by the openers in a pulling or dragging way. The aboveground part of the shank was usually wrapped by the composite structure of soil and roots, clods and dry grass during on-the-go movements.

| (a) | (b) |

Fig. 5 - Soil disturbance underground: (a) schematic diagram of the coupling failure mechanism between opener and soil layer, (b) broken roots caused by openers

Two kinds of actions of the soil layer usually generated with the opener moving along the passage. a) When the opener was moving in the soil layer, the front surface contacted with the soil layer, producing disturbance and fracture. During the experiments, the fracture line of the soil layer was usually created randomly, not always along the symmetry line of the shank and front surface. The soil root clod was disturbed and lifted up, then moved along the front surface of the shank. Under the connecting function by the rhizomes with the undisturbed soil layer, the disturbed soil root clod moved laterally, and fell back subsequently. This coupling mechanism resulted in the surface disturbance characteristic with bulged soil layer but not overturning. The coupling procedure was as shown in Fig. 6 (a). b) The soil layer was lifted up by the front contact surface of the opener, then it moved along the shank, under the action of the shank, the soil layer was separated into two soil-root clods. Due to the tangled rhizomes, the two clods were still connected and went forward with the shank. With the opener moving underground, the soil layer ahead the front surface was lifted up again, and higher rising height following, the disturbed and uplifted soil layer prevented the two clods from moving forward. The tangled roots were pulled apart and broken by the ongoing shank, and the clods were overturned along the passage. Related coupling procedure was as shown in Fig. 6 (b).

(a)

(b)
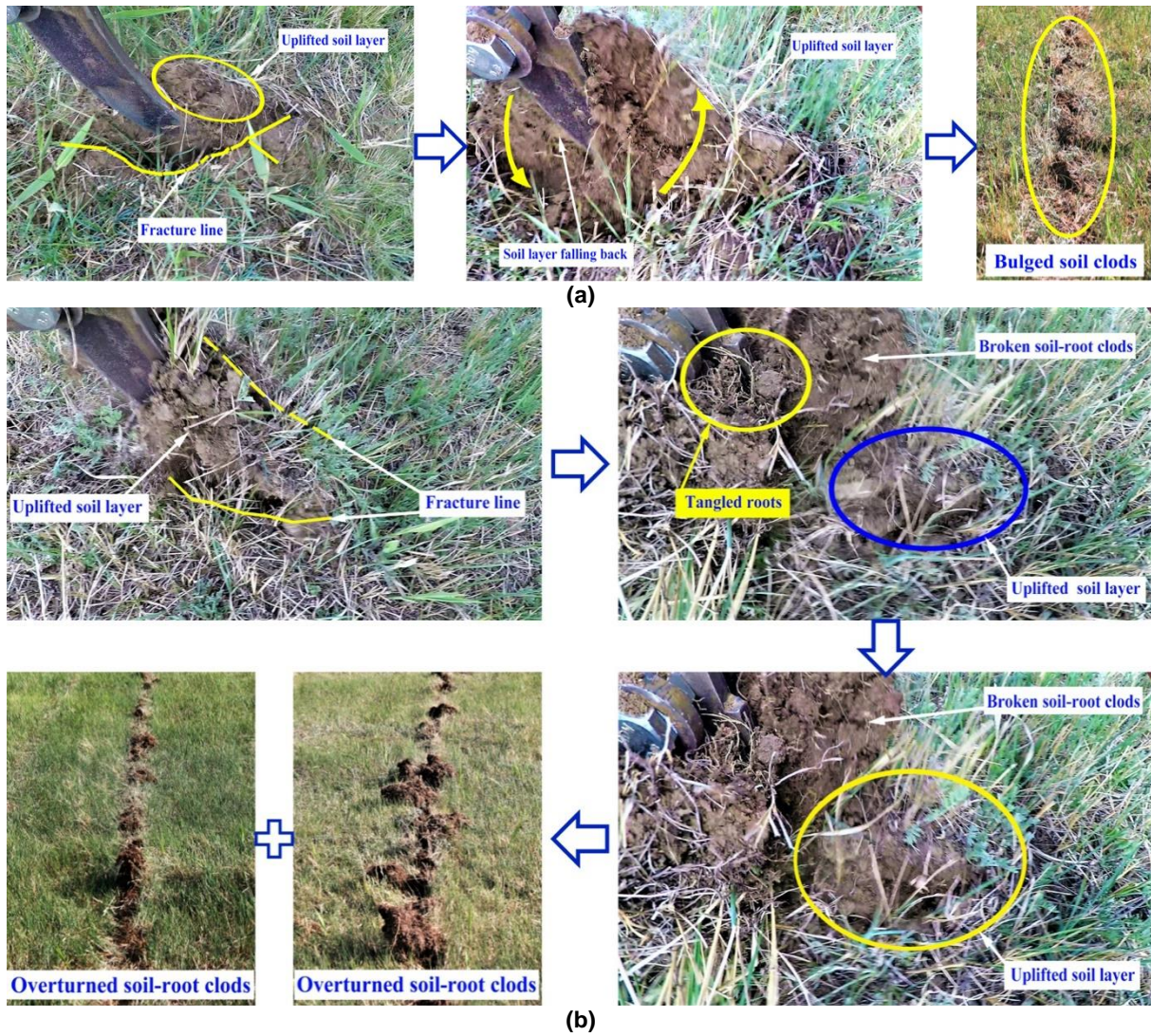
Fig.6 - Coupling procedure between the grassland surface and opener. (a) coupling procedure for disturbed surface with overturning soil clods, (b)coupling procedure for disturbed surface with bulged soil layer

The area of disturbed soil layer cross-section underground was calculated by equation (5), listed in Fig.7.
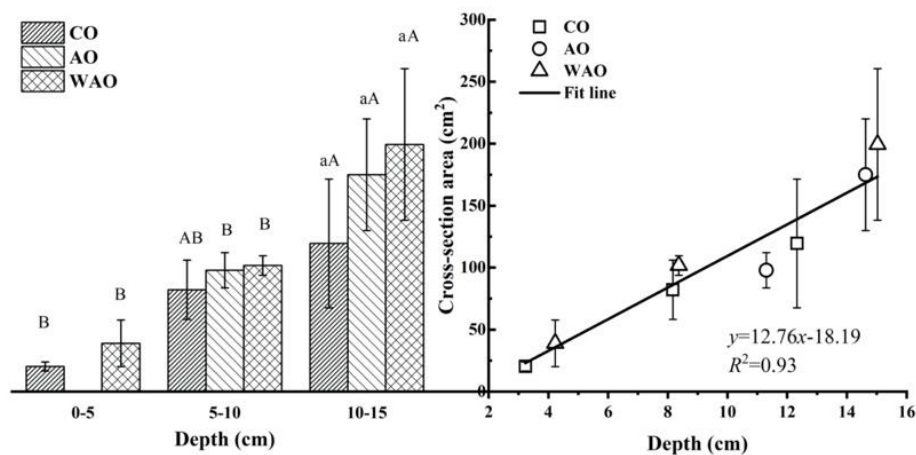
Fig. 7 - Cross-section area of disturbed soil layer underground

Note: The different lowercase letters reflected the significant differences between cross-section areas of different openers at the same depth range at the significance level of 0.05 by the Duncan Multiple Range Test. The different capital letters represented the significant differences between cross-section areas at different depth ranges of the same opener at the significance level of 0.05 by the Duncan Multiple Range Test.

It presented that the disturbance cross-section area increased with the working depth increasing linearly with the R^2 value of 0.93. WAO had the largest value, the second place was AO, and CO produced the lowest cross-section area underground, within the depth range of 5-10 cm and 10-15 cm. However, no significant differences were found between these three openers at the depth of 10-15 cm. For the same opener, the disturbed cross-section areas within the depth ranges of 0-5 cm and 5-10 cm, showed differences from that at the depth of 10-15 cm significantly. Although the disturbed cross-section area of CO was lower than that of WAO, no significant differences could be found within the depth range of 0-5 cm and 5-10 cm through the method of Independent Samples Test at the significance level of 0.05 within the depth range of 0-5 cm and 5-10 cm, respectively, as shown in Table 3.

Table 3

Independent Samples Test of disturbed soil layer cross-section area for CO and WAO

Depth (cm)		Levene's Test for Equality of Variances		t-test for Equality of Means		
		F	Sig.	t	df	Sig. (2-tailed)
0-5	Equal variances assumed	6.017	.070	-1.692	4	.166
	Equal variances not assumed			-1.692	2.149	.224
5-10	Equal variances assumed	1.670	.266	-1.357	4	.246
	Equal variances not assumed			-1.357	2.432	.287

- **Soil cutting forces**

Within the depth range of 0-15 cm, CO had the lowest draft force of all the selected openers, WAO had the largest values, approximately twice larger than CO. All the horizontal force data increased with the working depth increasing linearly with the R^2 values of exceeding 0.99 (Fig.8(a)). Significant differences existed between the draft forces of the same opener with the working depth varying. For the vertical resistance data, it varied with the working depth and opener geometry. The vertical force of CO increased with the working depth increasing. However, for AO and WAO, the sensor was in a compression situation in the depth range of 0-5 cm, but under stretch within the depth range of 5-15 cm.

The specific draft forces were calculated through equation (6), and the relationship between specific draft force and working depth was obtained and drawn in Fig. 8(b). The lines showed the specific draft forces of the openers decreased with the working depth increasing. CO always had the lowest specific draft force when it operated at different working depths, smaller than that of WAO.

(a) (b)
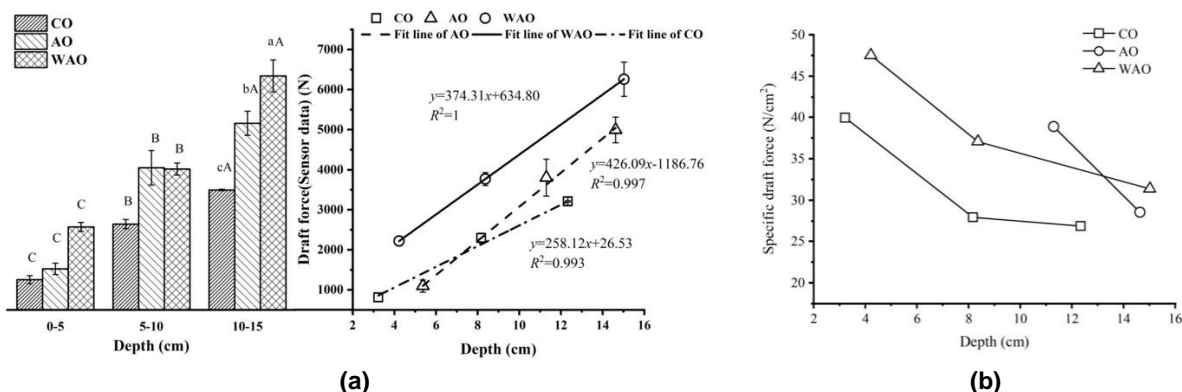
Fig. 8 - Typical soil resistance curves: (a) horizontal sensor data with depth, (b) specific draft force with depth

Note: Different lowercase letters reflected the significant differences between the forces of different openers at the same depth range at the significance level of 0.05 by the Duncan Multiple Range Test. Different capital letters represented the significant differences between the forces at different depth ranges of the same opener at the significance level of 0.05 by the Duncan Multiple Range Test.

CONCLUSIONS

(1) The selected subsoiler-type openers could break the soil layer underground and create disturbance on natural grassland. The manners of opener penetrating into the soil layer and its on-the-go movements, the geometry parameters of the front surfaces and shank of the openers, affected the ways of roots fracture and the translocations of soil underground a lot. Wings or wider working width could increase the draft forces and create larger soil disturbance area. However, the differences of disturbed soil layer cross-section areas between the winged opener and no-winged opener is not significant.

To obtain the same disturbance effect, using a no-winged or a narrow opener could be an effective choice compared with the winged opener.

(2) Tangled L-C roots and the soil underground, and withered grass on the surface, formed a complicated structure on natural grassland, brought about large soil over-turning rate (maximum value of 26.08%) and little soil backfill for the typical subsoiler-type openers (i.e. CO, AO, and WAO) during their passages, making them not suitable to be used to create necessary furrows for drilling or reseeding because of the possibility of resulting in severe soil erosion problems and improper roots damage. Adding cutting chamfers or adjusting appropriate structure parameters may be alternatives for subsoiler-type openers to achieve desirable soil loosening or soil fragmentation situations, but needs further research.

(3) The soil layer failure processes of the natural grassland were affected by its composite soil layer structure and the geometry of tillage tool. Coupling failure mechanism, working resistance, soil over-turning rate, area of disturbed cross-section, and specific draft force reflected the working performance of these subsoiler-type openers well, may become the evaluation indicators of the specialized tillage tools used for natural grassland, and supportive references for designing and optimizing related tillage tools for grassland.

ACKNOWLEDGEMENT

REFERENCES

[1]   Askari, M., Shahgholi, G., Abbaspour-Gilandeh, Y., Tash-Shamsabadi, H., (2013). The Effect of New Wings on Subsoiler Performance. *Applied Engineering in Agriculture*. Vol.32, pp. 353-362, America.

[2]   Barr, J., Desbiolles, J., Ucgul, M., & Fielke, J. M. (2020). Bentleg furrow opener performance analysis using the discrete element method. *Biosystems Engineering*, Vol.189, pp. 99-115, San Diego/ America.

[3]   Chaudhuri, D., (2001). Performance evaluation of various types of furrow openers on seed drills: a review. *Journal of Agricultural Engineering Research*, Vol. 79, pp.125-137, London/ England.

[4]   De Boer, H. C., Deru, J. G. C., Van Eekeren, N., (2018). Sward lifting in compacted grassland: effects on soil structure, grass rooting and productivity. *Soil and Tillage Research*, Vol. 184, pp. 317-325, Amsterdam/Netherlands.

[5]   Derpsch, R., Franzluebbers, A. J., Duiker, S. W., Reicosky, D. C., Koeller, K., Friedrich, T., Sturny, W.G., Sa, J.C.M., Weiss, K., (2014). Why do we need to standardize no-tillage research?. *Soil & Tillage Research*, Vol. 137, pp. 16-22, Amsterdam/Netherlands.

[6]   Han, J. G., Zhang, Y. J., Wang, C. J., Bai, W. M., Wang, Y. R., Han, G. D., Li, L.H., (2008). Rangeland degradation and restoration management in China. *The Rangeland Journal*, Vol.30, pp. 233, Cotteslow/ Australia.

[7]   Hasimu, A., Chen, Y., (2014). Soil disturbance and draft force of selected seed openers. *Soil and Tillage Research*, Vol.140, pp. 48-54, Amsterdam/Netherlands.

[8]   He C., You Y., Wang D., Wang G., Wu H., Gong S., (2016). Mechanical characteristics of soil-root composite and its influence factors in degenerated grassland (退化草地复合体力学特性与影响因素研究). *Transactions of the Chinese Society for Agricultural Machinery*, Vol.47, pp. 79-89, Beijing/China.

[9]   He, C., Wang, D., Wang, G., You Y., Liang F., Liu L., Shao C., (2015). The development of grassland mechanical restoration technology research (天然草地机械化改良技术研究进展). *Journal of Agricultural Mechanization Research*, Vol. 37, pp. 258-263, Heilongjiang/China. (in Chinese with English abstract)

[10] Li, L., Yang, H., Liu, P., Ren, W., Wu, X., Huang, F., (2018). Combined impact of heat stress and phosphate deficiency on growth and photochemical activity of sheepgrass (Leymus chinensis). *Journal of plant physiology*, Vol.231, pp.271-276, Munich/ Germany.

[11] Liu, G. X., He, F., Wan, L. Q., Li, X. L., (2015). Management Regimen and Seeding Rate Modify Seedling Establishment of Leymus chinensis. *Rangeland ecology & management*, Vol.68, pp.204-210, Lakewood/ America.

[12] Matin, M. A., Desbiolles, J. M. A., Fielke, J. M., (2016). Strip-tillage using rotating straight blades: Effect of cutting edge geometry on furrow parameters. *Soil and Tillage Research*, Vol. 155, pp. 271-279, Amsterdam/Netherlands.

[13] MOA (Ministry of Agriculture of the People's Republic of China), (1996). *Chinese Grassland Resource* （中国草地资源）. Chinese Science and Technology Press, Beijing/China.

[14] MOA (The Ministry of Agriculture of the People's Republic of China), (2003). *Chinese Standards. NY/T 740-2003: Field operation quality of ditchers* （田间开沟机械作业质量）. MOA, Beijing/China.

[15] MOMI (Ministry of Machinery Industry of the People's Republic of China), (1999). *Chinese Standards. JB/T 9788-1999: Subsoiler and share shaft* （深松铲和深松铲柄）. MOMA, Beijing/China.

[16] MOMI (Ministry of Machinery Industry of the People's Republic of China), (2007). *Chinese Standards. JB/T 7135-2007: Subsoiling plow for leymus chinensis land* （羊草地潜松耕犁）. MOMA, Beijing/China.

[17] Qin, K., Ding, W., Ahmad, F., Fang, Z., (2018). Design and experimental validation of sliding knife notch-type disc opener for a no-till combine harvester cum seed drill. *International Journal of Agricultural and Biological Engineering*, Vol. 11, pp. 96-103, Beijing/ China.

[18] Sánchez-Girón, V., Ramırez, J. J., Litago, J. J., Hernanz, J. L., (2005). Effect of soil compaction and water content on the resulting forces acting on three seed drill furrow openers. *Soil and Tillage Research*, Vol. 81, pp. 25-37, Amsterdam/Netherlands.

[19] Solhjou, A., Desbiolles, J. M., Fielke, J. M., (2013). Soil translocation by narrow openers with various blade face geometries. *Biosystems engineering*, Vol. 114, pp. 259-266, San Diego/ America.

[20] You, Y., Wang, D., Liu, J., (2012). A device for mechanical remediation of degraded grasslands. *Soil and Tillage Research*, Vol. 118, pp. 1-10, Amsterdam/Netherlands.

[21] Zhao, H. L., Zhou, R. L., Zhang, T. H., Zhao, X. Y., (2006). Effects of desertification on soil and crop growth properties in Horqin sandy cropland of Inner Mongolia, north China. *Soil and Tillage Research*, Vol.87, pp. 175-185, Amsterdam/Netherlands.

[22] Zhou, J., Zhang, Y., Wilson, G. W., Cobb, A. B., Lu, W., Guo, Y., (2017). Small vegetation gaps increase reseeded yellow-flowered alfalfa performance and production in native grasslands. *Basic and Applied Ecology*, Vol. 24, pp. 41-52, Jena/ Germany.

PREDICTION MODEL OF AMMONIA CONCENTRATION IN YELLOW-FEATHER BROILERS HOUSE DURING WINTER BASED ON EEMD-GRU
/
基于 EEMD-GRU 的黄羽鸡舍冬季氨气浓度预测模型

Zeying Xu [1)], Xiuguo Zou *), Zhengling Yin, Shikai Zhang, Yuanyuan Song, Jie Zhang, Jingxia Lu [1]
[1)] College of Engineering, Nanjing Agricultural University / China
Corresponding author: Xiuguo Zou
Tel: +862558606585; E-mail: xiuguozou@gmail.com
DOI: https://doi.org/10.35633/inmateh-61-07

ABSTRACT

In winter, the poor ventilation conditions in broiler houses may lead to high ammonia concentration, which affects the health of yellow-feather broilers or even causes the death of many broilers. This research used a machine learning model to predict the ammonia concentration in a broiler house during winter. After analysis, it was found that the ammonia generation in the broiler house was a gradual accumulation featured by non-linear data. After the broilers entered the broiler house for several days, and the ammonia concentration reached a certain value, a ventilation system was used for regulating the concentration. Firstly, the back-propagation (BP) neural network model and gated recurrent unit (GRU) model were used for predicting the ammonia concentration, respectively. Then, ensemble empirical mode decomposition (EEMD) was performed on the time series data of ammonia concentration in the broiler house. After that, the EEMD-GRU prediction model has been established for the intrinsic mode function (IMF) components and the temperature and humidity data in the broiler house. Finally, all component results were summarized to obtain the final prediction result. A comparison was conducted among the prediction results obtained by the above three models. The results show that the root mean square errors of the above three models are 6.2 ppm, 4.4 ppm, and 2.4 ppm, respectively, and the average absolute errors were 4.9 ppm, 2.8 ppm, and 1.6 ppm, respectively. It could be seen that the EEMD-GRU model had higher accuracy in predicting the ammonia concentration in the broiler house. The EEMD-GRU model can effectively predict the ammonia concentration in broiler houses, facilitating the feedback to the central system for timely adjustment.

摘要

　　针对冬季鸡舍通风限制，舍内氨气浓度高，轻则影响黄羽鸡健康，重则导致大量鸡死亡的问题，本文采用机器学习模型对冬季黄羽鸡舍内的氨气浓度进行预测。分析发现鸡舍内氨气生成是一个逐渐累积的过程，数据具有非线性，在鸡只进入鸡舍氨气浓度达到一定值后，鸡舍内采用通风系统进行调控。本文首先选择 BP 神经网络模型和 GRU 模型进行预测，再对鸡舍氨气浓度时间序列数据进行集合经验模态分解，并分别对分解得到的 IMF 分量和鸡舍内对应时间的温度湿度数据建立 EEMD-GRU 预测模型，最后对每个分量结果求和得到最终的预测结果。通过三种模型的预测结果对比，得到预测结果的均方根误差分别为 6.2 ppm ，4.4 ppm ，2.4 ppm，平均绝对误差分别为 4.9 ppm，2.8 ppm，1.6 ppm。由此可见基于 EEMD-GRU 模型的鸡舍氨气浓度预测精度更高，更准确，在鸡舍中应用可以有效预测未来的氨气浓度，反馈给系统及时调控。

INTRODUCTION

　　As the living standards of the Chinese people are improving, the demand for meat consumption is also becoming diversified. This has accelerated the development of China's breeding industry. As the basic meat in people's lives, broiler meat deserves much attention from the breeding industry in terms of the quality and health of broilers. In broilers' breeding, environmental factors in broiler houses have important effects on the health and production of broilers, such as ammonia concentration. Ammonia is a colourless, poisonous gas with a strong pungent odour. The ammonia in a broiler house is mainly produced by the decomposition of broiler manure and nitrogen-containing organic matters.

---

[1]*Zeying Xu, Ms.; Xiuguo Zou, Assoc. Prof. Ph.D.; Zhengling Yin, Ms.; Shikai Zhang, MAE. Stud.;*

Yuanyuan Song, MAE. Stud.; Jie Zhang, MAE. Stud.; Jingxia Lu, Assoc. Prof. Ph.D.

The high concentration of ammonia can not only affect the broiler's feed intake, feed conversion ratio (FCR) and productivity, but also cause damage to the broiler's respiratory system, which may reduce the quality of broiler (*Yao Z., 2008*). Therefore, it is of great significance to reasonably, timely, and accurately analyse and predict the ammonia concentration in broiler houses, so as to provide a reference for breeders to take corresponding measures.

Liu et al. (*Liu W., 2019*) implemented structural partitioning of a broiler house in Shandong Province along with horizontal and vertical directions. Based on the ammonia concentration data at each point monitored from 2014 to 2015, the single factor analysis method was used to obtain the daily ammonia concentration change in the broiler house and the ammonia gas distribution pattern between different cross-sections. They also proposed corresponding measures to reduce the ammonia concentration. Shen et al. (*Shen D., 2018*) used the statistical data of environmental indicators such as ammonia concentration detected in a broiler house to obtain the statistical characteristics of the distribution of air pollutants in the broiler house and the main sources of pollutants. Zilio et al. (*Zilio M., 2020*) determined the main contributor to the ammonia emissions of livestock farms using the seasonally sampled feces and ammonia data from four livestock farms in Italy from 2015 to 2017 through partial least squares (PLS) regression. They found that temperature was the main predictor of ammonia concentration. In summary, researchers have conducted extensive research on the poisonous gas emissions and distribution patterns in broiler houses. Multivariate statistical analysis and empirical models have played a very important role in the above research. However, the concentration data of various environmental factors in a broiler house are mostly non-stationary. This means that statistical methods cannot accurately predict the concentration of pollutants in a broiler house in a timely manner, and cannot provide a more accurate reference on breeding schemes for breeders.

With the development of artificial neural networks (ANN), traditional machine learning algorithms have been widely used in many research fields. Huo (*Huo C., 2018*) used a gray neural network algorithm and corrected the residual error through BP neural network to predict the ammonia concentration in a piggery, with a prediction accuracy of 94%. In the same year, Richardson et al. (*Ribeiro R., 2019*) established the ANN-Bayesian regularization model, and used the historical environment data of a broiler house to generate a set of parameters for the controller to make a correct response, which reduced the labour cost of poultry management. Xie (*Xie Q., 2015*) used the ANFIS-based algorithm to establish a model for ammonia concentration prediction in pig houses in different seasons, and analysed and obtained the correlation between ammonia concentration and various environmental factors in pig houses. The smallest relative error of the predicted ammonia concentration was 0.0858. This model provides a reliable reference for the control of the environment in a pig house.

Researchers have made considerable improvements to the structure of neural networks in recent years to improve the training effect of neural networks. Deep learning networks and the various learning frameworks they generate have gradually become popular and applied in various fields, especially on the research of air pollutant concentration. Guo et al. (*Hao G., 2019*) used a deep neural network to predict the concentrations of $PM_{2.5}$ and PM_{10} in Beijing, and proposed a prediction method of spatial conversion. They investigated the spatial correlation between air pollutants, which provided new ideas for air quality prediction models. Wei et al. (*Xu W., 2011*) developed a soft sensor for predicting the ammonia concentration at the outlet of a factory using BP neural network. They proposed an improved particle swarm algorithm to optimize the BP neural network model. Compared with the other two models, this model showed higher accuracy and better generalization ability. Due to the strong memory function and the ability to effectively process time-series data, the long short term memory (LSTM) network has been widely used in various practical problems, e.g., human action recognition (*Majd M., 2019*), water level prediction for nuclear reactor pressurizer (*Zhang J., 2019*), and short-term economic load forecasts (*Muzaffar S., 2019*), etc. The GRU model is a variant of the LSTM model, which is simpler in structure and can reduce the iteration time to a certain extent. GRU has also been used in sentiment classification(*Pu M., 2019*), and travel pattern recognition (*Guo M., 2019*), etc.

In previous research, we have used the computational fluid dynamics (CFD) method to establish a 3D model of the broiler house designed in this paper, which proved that the ventilation system of the broiler house met the requirements for cooling, ventilation and comfortable breeding (*Zhang S., 2019*). The proposed method of using an inverter to control the negative pressure fan has been accepted by some breeding bases, and has a good prospect for further application (*Yao H., 2018*). In terms of the research on the temperature inside a broiler house, we used the optimized least squares support vector machine model

based on the improved particle swarm optimization algorithm to predict the temperature in a broiler house. The average absolute error was 0.787 °C (*Zhang X., 2019*).

Based on the BP neural network and GRU model, this paper constructs an EEMD-GRU model to predict the ammonia concentration in the broiler house. The EEMD-GRU model effectively uses the historical time series data in the broiler house, considers the non-stationarity of the environmental data, and can determine the information forgotten and retained at each step according to the activation function. The results show that the EEMD-GRU model can improve the prediction accuracy and reduce the iteration time.

MATERIALS AND METHODS
Data Acquisition

In this experiment, the ammonia concentration of the yellow-feather broiler house located in Jinniuhu Street, Luhe District, Nanjing City, Jiangsu Province, China, was used as the research object. Environmental monitoring sensors were installed in the broiler house, and environmental data were collected in real-time every 1 min and transmitted through the RS485 serial network. The broiler house is 1.9 m wide and 2.9 m long. Fig. 1 shows the internal scene of the broiler house. The experiment had 45 broilers in the broiler house, and 50833 pieces of environmental data and broilers situation data from December 5, 2019 to January 12, 2020 were used as experimental data in this paper, including ammonia concentration, temperature, humidity, age of broilers and time for broilers to enter the broiler house. Because the ammonia concentration, temperature and humidity inside and outside the broiler house would not change greatly within 1 h, this research used the average of minutely data within 1 h as the hourly data. A model was established using experimental data to predict the ammonia concentration of the broiler house in the next hour. The increase of ammonia concentration in the broiler house was a gradual process, as the ammonia concentration would change with the growing days of the broilers and the environmental factors inside and outside the broiler house. Table 1 shows some of the data in this experiment. Table 2 exhibits the result of the statistical analysis.

Fig. 1 – Internal scene of the broiler house

Sensors, cameras, and wind speed inverters, etc. were installed in the experimental broiler house to detect the environmental data in real-time and take corresponding measures. The temperature and humidity sensors were purchased from Shandong Renke Measurement & Control Technology Co., Ltd., with an accuracy of ±0.5 ℃ and ±3% RH, respectively, and with a resolution of 0.1 ℃ and 0.1% RH, respectively. The PM$_{2.5}$ sensor was also purchased from this company with an accuracy of ± 10%. The ammonia concentration sensor was also purchased from this company with a resolution of 0.1 ppm (parts per million, 1 ppm = 1 ml/m^3). The above sensors all had a dimension of 110 mm x 85 mm x 44 mm.

Experimental data from December 15 to December 31, 2019

Time	Ammonia concentration (ppm)	Outside temperature (℃)	Outside relative humidity (%)	Inside temperature (℃)	Inside relative humidity (%)	Age of broiler (day)	Time for broilers to enter the broiler house(hour)
2019-12-15 00:00	2.3	13.6	77.9	15.1	69.7	84	202
2019-12-15 01:00	2.2	14.4	78.1	14.8	70.6	84	203
2019-12-15 02:00	2.2	14.2	74.6	14.1	66.4	84	204
2019-12-15 03:00	2.2	13.9	73.6	13.7	65.8	84	205
2019-12-15 04:00	2.1	13.7	73.9	13.7	68.3	84	206
⋮	⋮	⋮	⋮	⋮	⋮	⋮	⋮
2019-12-31 06:00	29.6	0.4	65.4	3.9	66.6	100	592
2019-12-31 07:00	29.0	0.2	66.0	3.9	67.0	100	593
2019-12-31 08:00	28.1	1.9	67.3	4.9	65.9	100	594
2019-12-31 09:00	27.1	3.2	63.0	6.1	64.1	100	595
2019-12-31 10:00	25.3	3.8	62.0	7.0	61.5	100	596

Statistical analysis of environmental data

Parameter	Data volume	Mean value	Standard deviation	Maximum value	Minimum value
Ammonia	883	15.5	12.5	50	0
Outside temperature	883	10.8	3.9	23.3	0.2
Inside temperature	883	12.7	3.2	23.2	3.8
Outside relative humidity	883	81.7	11.4	97.8	36.2
Inside relative humidity	883	76.0	9.3	90.1	40.7

Data Processing Methods
- **Data Normalization**

Data normalization is to make the eigenvalues of different dimensions on the data set comparable to a certain extent, and to eliminate the dimensional and order of magnitude differences between the eigenvalues. If there is a large difference in the value of features on a data set, the features with larger values often make a greater contribution to the model's results. Therefore, in order to improve the convergence speed and accuracy, the ammonia concentration, temperature and humidity values in this research need to be normalized.

The normalization method adopted in this paper is the min-max scaling method. All the values are concentrated to 0-1 according to

$$x^* = \frac{x - x_{min}}{x_{max} - x_{min}} \tag{1}$$

where x^* is the normalized data, x is the original data, x_{min} and x_{max} are the minimum and maximum values of the eigenvalues of the original data, respectively.

- **Data Interpolation**

In the experiment, the data is collected every 1 min, and data missing often occurs due to the failure of the data acquisition device. The data set is interpolated by summing and averaging the data of one hour before and after the missing time as the missing data to make the time series of the data set more complete.

Establishment of the Model

TensorFlow is a powerful open-source software library developed for deep neural networks (DNN). It supports all popular languages, such as Python, C ++, and Java, etc., with the ability to work on multiple platforms, and has good visualization of computing charts. Based on the TensorFlow framework, the following three models are established in this research for prediction.

• **BP Neural Network Model**

Back propagation (BP) neural network is a multilayer feedforward neural network using an error back-propagation algorithm and consists of an input layer, a hidden layer, and an output layer. The basic steps of a BP neural network are as follows:

(1) The kth output value y of output layer neuron is calculated forward by:

$$y_k = f\left(\sum_{h=1}^{q} w_h \times b_h - \theta\right) \tag{2}$$

where w_h represents the weight matrix from the hth neuron of the hidden layer to the output layer, θ represents the threshold of neurons in the output layer, b_h represents the output of the hth neuron in the hidden layer. f
represents the activation function.

$$b_h = f\left(\sum_{i=1}^{d} v_{iq} \times x_i - \theta_h\right) \tag{3}$$

where v_{iq} represents the weight matrix from the ith neuron of input layer to hidden layer, x_i represents the input of the ith neuron in the input layer, θ_h represents the threshold value of the hth neuron in the hidden layer.

$$v_{iq} = [v_{i1} \quad v_{i2} \quad v_{i3} \dots v_{iq}] \tag{4}$$

where d represents the number of neurons in the input layer, q represents the number of neurons in the hidden layer. In this paper: $d = 14$.

Final output value y of output layer:

$$y = [y_1 \quad y_2 \dots y_k \dots y_n] \tag{5}$$

where n is the number of forecast samples.

The structure of the BP neuron model is shown in Fig. 2.
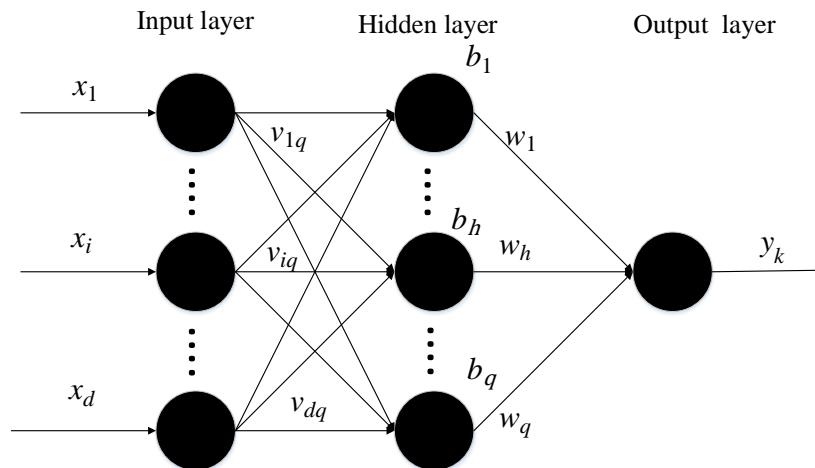
Fig. 2 – Structure diagram of BP neuron model

(2) If there is an error between the output value and the expected output value, the error term is back propagated.

$$E = \frac{1}{2}(y - y_r)^2 \tag{6}$$

where E represents the output error, y_r represents the expected output value.

(3) The gradient descent method is used to continuously iterate each neuron's weights to reduce the error term until it reaches the acceptable error range.

In this research, the ammonia concentration, temperature, and humidity of the broiler house in the previous two hours are used as input data. The ammonia concentration at the current moment is used as a label to construct a BP neural network sample.

The parameters of the BP model designed in this paper are shown in Table 3.

Table 3

BP model's parameters

Parameter	Parameter value
Training set	70% of all data sets
Test set	30% of all data sets
Optimizer	Adam adaptive moment estimation optimizer
Exponential decay rate of first-order moment estimation	0.9
Exponential decay rate of second-order moment estimation	0.999
Epsilon	10^{-8}
Hide layer activation function	ReLU( )
Number of Network layer	3
Number of hidden layer nodes	10, 15
Output layer activation function	ReLU()
Learning rate	0.001

- **GRU Model**

The gated recurrent unit (GRU) model uses a recurrent neural network. The structure of the recurrent neural network is similar to that of a shallow neural network, which is composed of an input layer, a hidden layer, and an output layer. The difference is that the recurrent neural network is composed of multiple hidden layers, which deepens the depth of the network structure to a certain extent. The nodes in the hidden layer are connected to each other. When processing time-series data, the output result of each node is not only related to the current information input to the node, but also depends on the output result of the previous node, which means a function of memorizing. So, the recurrent neural networks are suitable for processing time series-data (*Hu M., 2019*). The LSTM recurrent neural network adds forget gate, input gate, and output gate to the original recurrent neural network structure. The opening and closing of these gates are determined by the activation function, which can determine whether the information of the upper layer is added to the calculation of this layer. However, its ability to learn complex long-sequence data is poor, and there will be the problems of gradient disappearance and gradient explosion during the learning process. The GRU model is a variant structural model of LSTM, but simpler in structure, which reduces the iteration time. There are only two gates in the GRU structure, namely, update gate and reset gate. The update gate can be seen as a combination of the forget gate and input gate in the LSTM model. The GRU network structure is shown in Fig. 3.
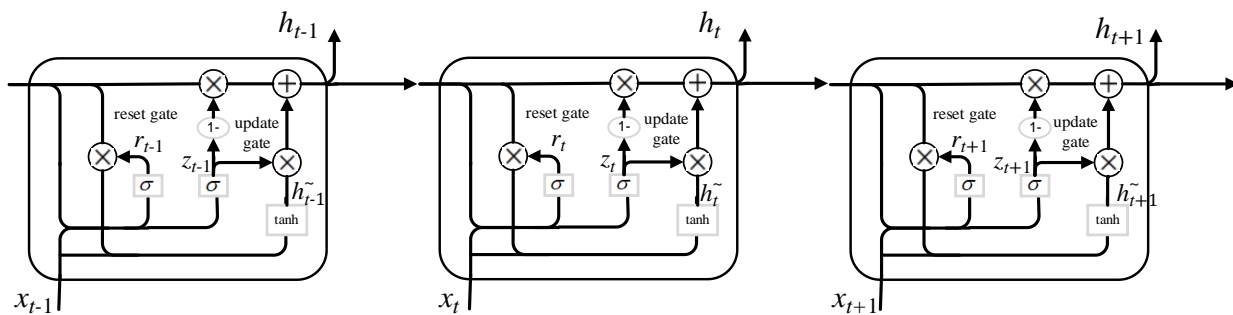
Fig. 3 – GRU network structure

As shown in Fig. 3, x_{t-1}, x_t and x_{t+1} represent the input of the previous moment, the current moment, and the next moment, respectively, h_{t-1}, h_t and h_{t+1} represent the hidden state of the previous node, the current node, and the next node, respectively, $\tilde{h_{t-1}}$, $\tilde{h_t}$ and $\tilde{h_{t+1}}$ represent the candidate hidden states, r_t and z_t represent the reset gating and update gating, respectively, and σ represents the activation sigmoid function.

The states of the reset gate and update gate at time *t* are defined as:

$$\begin{cases} r_t = \sigma(w_r x_t + u_r h_{t-1}) \\ z_t = \sigma(w_z x_t + u_z h_{t-1}) \end{cases} \tag{7}$$

where w_r, u_r, w_z and u_z represent the weight matrixes.

The hidden state h_t and the candidate hidden state $h_t^{\sim}$ at time t are defined as:

$$\begin{cases} h_t=(1-z_t)h_{t-1}+z_t h_t^{\sim} \\ h_t^{\sim}=tanh(w_h x_t+u_t(r_t \cdot h_{t-1})) \end{cases} \tag{8}$$

where

$$\begin{cases} \sigma(x)=\dfrac{1}{1+exp(x)} \\ tanh(x)=\dfrac{1-exp(2x)}{1+exp(2x)} \end{cases} \tag{9}$$

In the output layer:

$$y_t=h_t \cdot w \tag{10}$$

where w is the weight matrix of the output layer.

The training process of the GRU model is as follows:

(1) Learning weight matrix parameters by the forward propagation.

(2) Calculate the sample loss in the transmission by the forward network.

(3) Learn network update parameters by the backward error propagation.

The GRU model's parameters in this research are shown in Table 4.

Table 4

GRU model's parameters

Parameters	Parameter value
Training set	70% of all data sets
Test set	30% of all data sets
Optimizer	SGD random gradient descent optimizer
Momentum parameter	0.8
Learning rate attenuation	10^{-5}
Regularization of random deactivation	0.1
Hide layer activation function	Sigmoid( )
Input dimension	3
Number of Network layer	30
Output layer activation function	tanh( )
Learning rate	0.001

- **EEMD-GRU model**

    The empirical mode decomposition (EMD) method can decompose a signal into several IMFs and one RES that reflects the overall trend of the signal based on the local characteristics of the original signal. EMD method does not need to select any function as the base, and has the adaptive capability, which is suitable for the data processing of non-linear and non-stationary signals. The decomposition formula is given by

$$x(t)=\sum_{i=1}^{n} c_i(t)+r_n(t) \tag{11}$$

where c_1, c_2,····· ·· , c_n represent the IMFs obtained by the decomposition of the original signal $x(t)$, with each IMF containing a single time scale, and $r_n(t)$ represents the residue (RES).

    The ensemble empirical mode decomposition (EEMD) is an improvement to the EMD method, which overcomes the phenomenon of modal aliasing in the EMD method. If there is a sudden change in the time scale of a signal, there will be an IMF component containing different time scales. By adding white noise to the original signal sequence, EEMD performs smoothing processing on the abrupt changes in the time scale, and uses the uniform distribution of white noise spectrum to make the signals of different scales adaptively map to the appropriate reference scale. At the same time, by adding white noise multiple times to perform EMD and obtain the average result, the influence of noise is eliminated. Finally, the IMF component containing a single time scale is obtained. The decomposition steps of EEMD are as follows (*Chen R., 2012*):

     (1) Add M Gaussian white noise $n_i(t)$ (i =1~M) with an amplitude of 0 and constant amplitude standard deviation to the original signa $x(t)$ to obtain $x_i(t)$, as shown below.

$$x_i(t)=x(t)+n_i(t) \tag{12}$$

(2) Perform EMD on $x_i(t)$ respectively to obtain the IMFs and RES, and record the jth IMF as $c_{ij}(t)$ and the RES as $r_i(t)$.

 (3) Perform average calculation on the IMFs, and obtain the final result of EEMD, as shown below.

$$c_j(t) = \frac{1}{M} \sum_{i=1}^{n} c_{ij}(t) \tag{13}$$

The flow chart of EEMD is shown in Fig. 4.

By performing EEMD on the time series data of ammonia concentration in the broiler house, the ammonia concentration series are decomposed into 8 IMF components and 1 RES component, which achieves the separate processing for different characteristic components, thereby improving the prediction accuracy. Then, the GRU model is established for each component, and finally, the prediction results of the components are summed to obtain the final prediction result. The flow chart of the EEMD-GRU model is shown in Fig. 5.
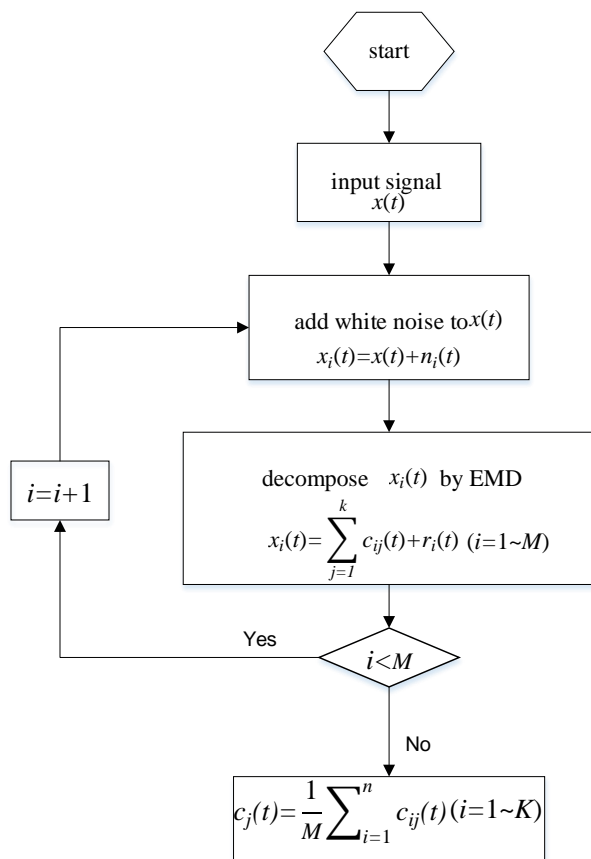
Fig. 4 – Flow chart of EEMD model   **Fig. 5 - Flow chart of EEMD-GRU model**
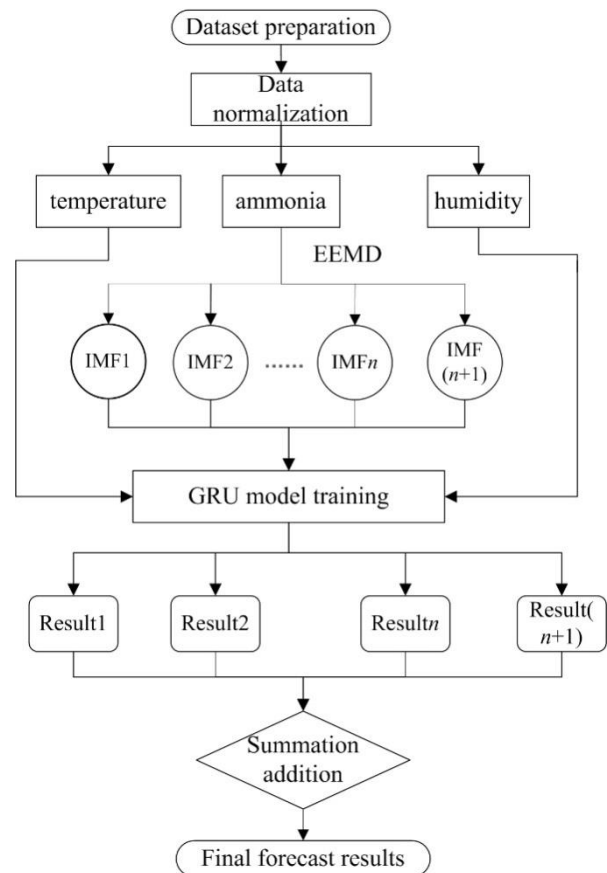
RESULTS AND DISCUSSION
Data Trends

Based on the data set used in the experiment, the trend of the environmental data in the broiler house is obtained, as shown in Fig. 6.

It can be seen from Fig. 6 that the temperature inside and outside the broiler house was maintained at about 15°C during the experimental period from December 5 to January 12. After 16 days from the start of the experiment (December 21), the temperature inside and outside the broiler house gradually decreased and fluctuated around 10°C. It can be seen from the figure that the humidity of the broiler house changed greatly during a whole day, with higher humidity at night, and lower humidity in the daytime.
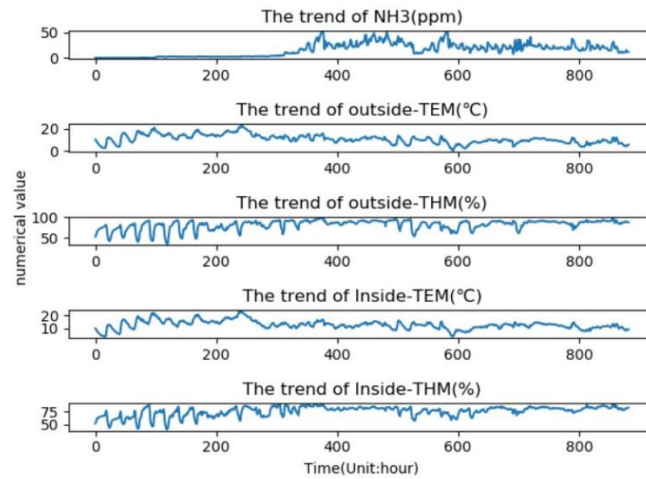
Fig. 6 - Trend of the environmental data

The highest relative humidity is about 90% and the lowest is about 40%. The temperature and humidity inside and outside the broiler house had the same change trend. For the trend of ammonia concentration, it can be clearly seen that the change in the ammonia concentration underwent a cumulative process. At the beginning of the experiment, there was no ammonia in the house and the ammonia concentration is 0. As the experiment went on, ammonia gas was generated, and the concentration continued to increase with the increase of the experimental time. The ammonia concentration reached the maximum value of 50 ppm at about 15 days after the broilers entered the chicken house. In order to protect the health of the broiler, the ventilation system started to regulate the ammonia concentration. It can be seen that the ventilation system had well controlled the ammonia concentration in the broiler house.

EEMD Results

The ammonia concentration data in the broiler house has obvious non-linear and unstable characteristics. In this paper, the EEMD algorithm is performed on the ammonia concentration data collected in 38 days, from December 5, 2019 to January 12, 2020. The ammonia concentration data in the broiler house is used as the input and the components and residuals of the ammonia concentration data are used as the output, as shown in Fig. 7.
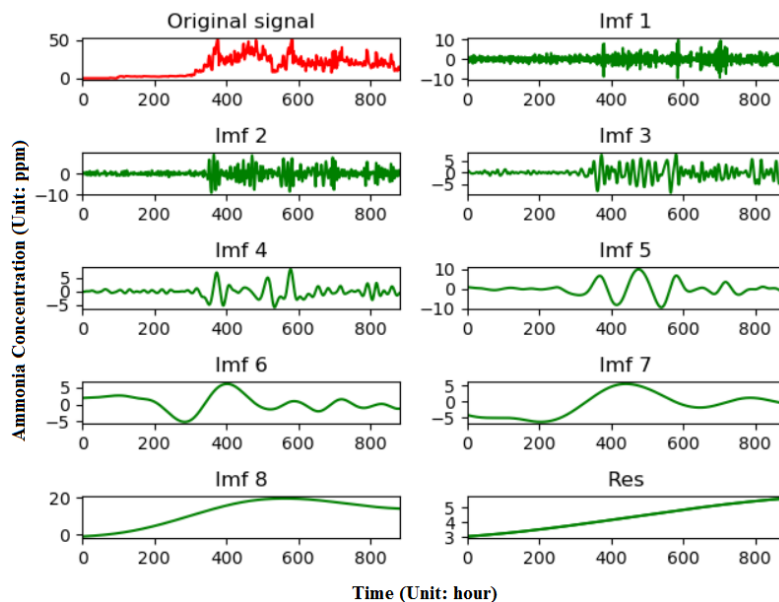
Fig. 7 - Decomposition results of EEMD algorithm

It can be seen from the decomposition results in Fig. 7 that the EEMD algorithm decomposes the ammonia concentration data into 8 IMF components and 1 RES component. Specifically, the IMF1-IMF3 components have a high frequency and have a certain random disorder, which reflects the influence of random uncertain factors inside and outside the house on the characteristics of the ammonia concentration

in the house. As the decomposition goes on, the volatility and frequency of the IMF component decrease in order. The RES component is a low-frequency component, which reflects the overall change trend of the original ammonia concentration data during the experiment. The original data sequence can be obtained by adding each component.

Prediction Results

In this research, the ammonia concentration is predicted according to the parameters of the BP model, GRU model, and EEMD-GRU model. A comparison is conducted on the prediction results of the three models. The prediction results are shown in Fig. 8, Fig. 9, and Fig.10.
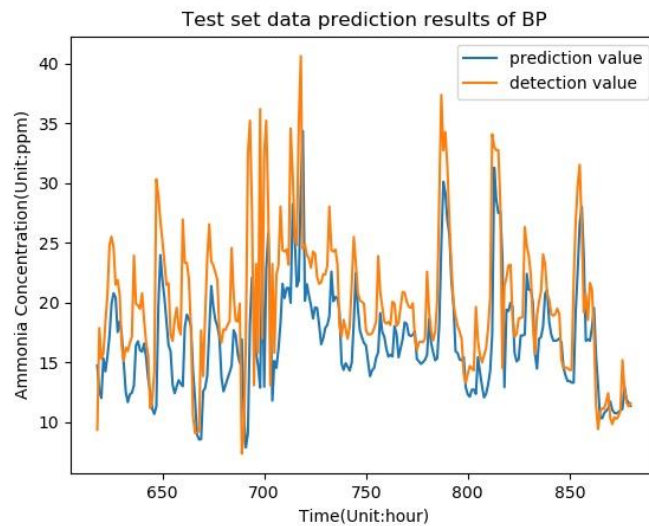
Fig. 8 - Prediction result curve of the BP model

From Fig. 8, it can be seen that the ammonia concentration fluctuates greatly during the experiment, showing strong instability and fluctuation. The prediction result of the BP model is roughly consistent with the true curve. However, it can also be observed that the prediction result curve by the BP model is slightly lagged behind the true curve, and the difference between the two is larger on the vertical axis, especially in the range of 630 h to 670 h and 725 h to 800 h. The maximum difference reaches about 20 ppm. In the final prediction result, Test RMSE is 6.2 ppm and Test MAE is 4.9 ppm.
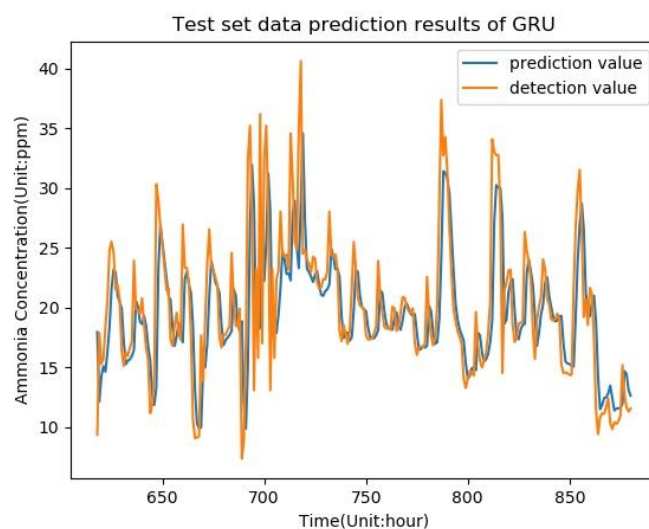
Fig. 9 - Prediction result curve of the GRU model

From Fig. 9, it can be seen that the prediction result curve of the GRU model is more consistent with the true curve than the BP model. The problem of lag in the two curves disappears, and the error is reduced. Especially in the range of 680 h to 710 h and at the time of about 850 h, the two curves can basically

coincide. The curves from 630 h to 670 h and 725 h to 800 h are also close, better than the result by the BP model. However, it can be seen that the maximum error is still around 17 ppm, and the prediction accuracy needs to be further improved. In the final prediction result, Test RMSE is 4.4 ppm and Test MAE is 2.8 ppm.
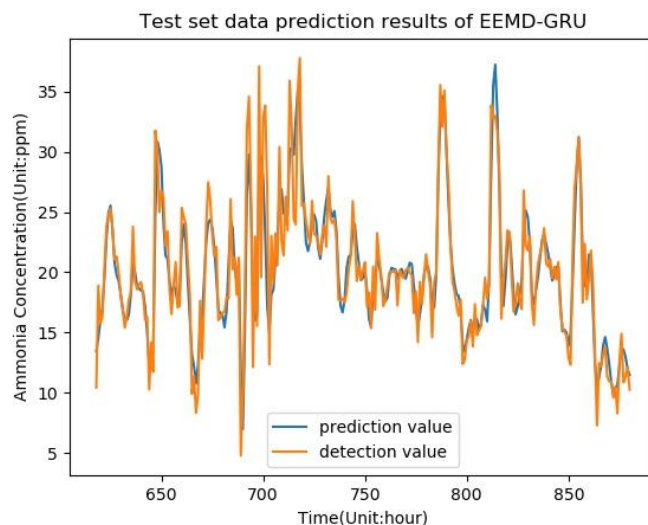
Fig. 10 - Prediction result curve of the EEMD-GRU model

From Fig. 10, it can be clearly seen that the prediction result using the EEMD-GRU model are more accurate than the previous two models. The two curves can basically coincide at more points in time, and the maximum error is also reduced to about 4 ppm. In the final prediction result, Test RMSE is 2.4 ppm and Test MAE is 1.6 ppm. From the perspectives of both intuitive judgment and the final error, the EEMD-GRU model has fewer errors and better accuracy than the BP model and GRU model.

Table 5 shows the comparison of the prediction errors of the three models.

Table 5

Comparison of the prediction errors of the three models

Model	Root mean square error(ppm)	Mean absolute error(ppm)
BP	6.2	4.9
GRU	4.4	2.8
EEMD-GRU	2.4	1.6

CONCLUSIONS

In this paper, the EEMD-GRU model has been used to predict the ammonia concentration in a broiler house for yellow-feather broilers. The experimental data of the broiler house from December 5, 2019 to January 12, 2020 were used as the data set. The generation of ammonia concentration has a strong correlation with the age of broilers entering the house. When the number of broilers in the house was 45, the ammonia concentration reached the highest concentration 15 days after the broilers entered the house. After that, the ammonia concentration decreased through the ventilation control system. The first 70% of the data set was used as the training set, and 30% was used as the test set. After 1000 iterations of the model, the prediction results were obtained. For the EEMD-GRU model results, the root mean square error is 2.4 ppm, and the mean average error is 1.6 ppm, which are higher than 6.2 ppm and 4.4 ppm of the BP mode and 4.9 ppm and 2.8 ppm of the GRU model. The EEMD-GRU model has shown the highest accuracy.

The EEMD-GRU model proposed in this paper can decompose the data with large volatility and non-stationarity to obtain relatively stable data, which effectively improves the prediction accuracy. The accurate and timely prediction of the ammonia concentration data in the broiler house will help breeders make accurate judgments on the environment of broiler houses, effectively reduce the damage of harmful gases to broilers, and improve the yield and quality.

ACKNOWLEDGEMENT

REFERENCES

[1] Chen R., Tang B. and Ma J., (2012), Adaptive de-noising method based on ensemble empirical mode decomposition for vibration signal, *Journal of Vibration and Shock*, Vol. 31, Issue 15, pp. 82-86, London/England;

[2] Guo M., Wang P. and Zhao L., (2019), Research on recognition method of transportation modes based on deep learning, *Journal of Harbin Institute of Technology*, Vol. 51, Issue 11, pp. 1-7, Haerbin/China;

[3] Hao G., (2019), Research and implementation on air quality prediction method deep learning based, Beijing University of Posts and Telecommunications, Beijing/China;

[4] Hu M., Lu W., Xu C., et al., (2019), Satellite RCS anomaly detection using the GRU model, Journal of *Xidian University*, Vol. 46, Issue 06, pp. 125-130, Xian/China;

[5] Huo C., (2018), Research of remote monitoring system of piggery environment based on LoRa and prediction model of ammonia concentration, *Jiangsu university*, Zhenjiang/China;

[6] Liu W., Han H., Gao J., et al., (2019), Study on distribution rule of atmospheric ammonia in standardized broiler house, *Shandong Agricultural Sciences*, Vol. 51, Issue 08, pp. 79-83, Jinan/China;

[7] Majd M. and Safabakhsh R., (2019), Correlational convolutional LSTM for human action recognition, *Neurocomputing*, Available online 24 April, https://doi.org/10.1016/j.neucom.2018.10.095, Amsterdan/Netherlands;

[8] Muzaffar S. and Afshari A., (2019), Short-term load forecasts using LSTM networks, *Energy Procedia*, Vol. 158, pp. 2922-2927, Hongkong/China;

[9] Pu M. and Ge Y., (2019), Attention based GRU network for domain adaptation in sentiment classification, *International Conference on Computation and Information Sciences*, Chengdu/China;

[10] Ribeiro R., Casanova D., Teixeira M., et al., (2019), Generating action plans for poultry management using artificial neural networks, *Computers and Electronics in Agriculture*, Vol. 161, pp. 131-140, Oxford/England;

[11] Shen D., Dai P., Wu S., et al., (2018), Distribution of particles, ammonia and carbon dioxide as well as physicochemical property of pm2.5 in an enclosed broiler breeder house in winter, *Chinese Journal of Animal and Veterinary Sciences*, Vol. 49, Issue 06, pp. 1178-1193, Beijing/China;

[12] Xie Q., (2015), Environmental suitability assessment and control model development for a swine house based on fuzzy theory, *Northeast Agricultural University*, Haerbin/China;

[13] Xu W., Zhang L. and Gu X., (2011), Soft sensor for ammonia concentration at the ammonia converter outlet based on an improved particle swarm optimization and BP neural network, *Chemical Engineering Research and Design*, Vol. 89, Issue 10, pp. 2102-2109, Rugby/England;

[14] Yao H., Sun Q., Zou X., et al., (2018), Research of yellow-feather chicken breeding model based on small chicken chamber, *INMATEH - Agricultural Engineering*, Vol. 56, Issue 3, pp. 91-100, Bucharest/Romania;

[15] Yao Z., (2008), Effects of different ammonia concentrations on growth, immunity and physiological-biochemical parameters in broiler chickens, *Zhejiang University*, Hangzhou/China;

[16] Zhang J., Wang X., Zhao C., et al., (2019), Application of cost-sensitive LSTM in water level prediction for nuclear reactor pressurizer, *Nuclear Engineering and Technology*, Available online 27 December, https://doi.org/10.1016/j.net.2019.12.025, Daejeon/South Korea;

[17] Zhang S., Ding A., Zou X., et al., (2019), Simulation analysis of a ventilation system in a smart broiler chamber based on computational fluid dynamics, *Atmosphere*, Vol. 10, Issue 6, no. 315, Basel/Switzerland;

[18] Zhang X., Ding A., Zou X., et al., (2019), Prediction of ambient temperature in the chambers for yellow feather chickens based on least squares support vector machine optimized by improved particle swarm optimization algorithm. *International Agricultural Engineering Journal*, Vol. 28, Issue 4, no. 9, Beijing/China;

[19] Zilio M., Orzi V., Chiodini M., et al., (2020), Evaluation of ammonia and odour emissions from animal slurry and digestate storage in the Po Valley (Italy), *Waste Management*, Vol. 103, pp. 296-304, Oxford/England.

TECHNOLOGY FOR TWO SWITCHGRASS MORPHOTYPES GROWING IN THE CONDITIONS OF UKRAINE'S FOREST STEPPE ZONE
/
ТЕХНОЛОГІЯ ВИРОЩУВАННЯ ДВОХ МОРФОТИПІВ СВІТЧГРАСУ В УМОВАХ ЛІСОСТЕПОВОЇ ЗОНИ УКРАЇНИ

Gumentyk M.Ya.[1),] Chernysky V.V.[1),] Gumentyk V.M.[2),] Kharytonov M.M.[3] [1]
[1)] Institute of Energy Crops and Sugar Beet of NASU
[2)] National University of Life and Environmental Sciences of Ukraine
[3)] Dnipro State Agrarian and Economics University, Ukraine
Tel: 0973456227; E-mail: envteam@ukr.net, S.Yefremova st. 25, Dnipro, Ukraine
DOI: https://doi.org/10.35633/inmateh-61-08

ABSTRACT
Different quality adaptive reactions of the "Cave-in-rock" and "Morozko" varieties were found in terms of productivity parameters depending on the method of sowing seeds, the presence of a marker crop and the conditions of vegetation periods. The highest yield of switchgrass for both varieties was for the second and third terms of sowing (first and second decades of May). The method of sowing switchgrass seeds with a row spacing of 45 cm with white mustard as marker crop must be used for effective weed control. Ukrainian variety "Morozko" is a more adapted variety for the conditions of the forest-Steppe of Ukraine.

РЕЗЮМЕ
Різні якісні адаптивні реакції сортів "Cave-in-rock" та "Морозко" виявлено за показниками продуктивності залежно від способу посіву насіння, наявності маркерної культури та періодів вегетації. Найбільша врожайність світчграсу обох сортів була на другий і третій терміни посіву (перша і друга декади травня). Для ефективної боротьби з бур'янами необхідно використовувати спосіб посіву насіння світчграсу з міжряддям 45 см з використанням білої гірчиці у якості маркерної культури. Український сорт "Морозко" є більш пристосованим сортом для умов Лісостепу України.

INTRODUCTION

The soil and climatic conditions in the main regions of Ukraine are favourable for energy crops cultivation with high level of biomass energy accumulation (*Kvak et all., 2018*). Switchgrass is a perennial plant similar to a shrub grass, which is propagated by both seeds and rhizomes. This crop uses C4 carbon fixation and has a high capacity to utilize nitrogen and water *(Zhang et al., 2017)*. The advantages of Switchgrass are: little need for the use of pesticides, promoting the preservation of natural conditions and improving the quality of the soil *(Rushing et al, 2013)*. The crop is resistant to diseases and pests, has a low cost and low risks of cultivation, requires little investment, gives high yields of biomass even on low-productive lands *(Smeets et al, 2009)*. Switchgrass requires minimal management, and has a large potential to sequester carbon underground *(Hartman et al, 2011)*. In the last decade, Switchgrass has been considered to be a "model biofuel" crop because of its ability to produce large quantities of biomass on marginal soils *(Scagline et al, 2015)*. Numerous cultivars of switchgrass (*Panicum virgatum L.*) have been assessed in terms of yield potential and adaptability in diverse environments, in different countries. Upland ('Cave-in-Rock' and 'Shelter') and lowland ('Alamo' and 'Kanlow') cultivars were harvested for 3 year under one- or two-cut management at eight sites in the USA (*Fike et al, 2006; Cherney et al., 2018*). Upland cultivars yielded more on average with two harvests rather than one. Lowland varieties grow better in deep moist soils, while upland varieties tend to be better adapted to thinner soils and drier sites (*Parrish and Fike, 2005*). The highest yield, obtained with Cave-in-Rock during the third year, was 9.2 t/ha (*Marra et al., 2013*). Cave-in-Rock and Nebraska 28 had the highest photosynthesis rate. At the same time Nebraska 28 and Pathfinder varieties shown strong drought tolerance (*Ma et al, 2011*).

---

[1] *Gumentyk M.Ya., Dr. Ph.D. Eng.; Chernysky V.V., Dr. Ph.D. Eng.; Gumentyk V.M., BSt; Kharytonov M.M., Prof. Ph.D. Agri.Sci.*

General opinion is that Cave-in-Rock variety and other upland cultivars with a high chromosome ploidy might be optimal choices for biomass plants. Field experiments with two US varieties from the Elsberry Plant Materials Centre conducted in Ukraine last decade gave possibility to select locally adapted Switchgrass varieties (*Kulik, 2016*). Yield of variety Cave-in-Rock in the fifth vegetation year with row-spacing of 45 cm was higher on 1.0 t/ha (10.0%) comparatively with width of 30 cm. Sanburst variety had increase of yield according to row-spacing on 1.2 t/ha (9.4%) and 0.1 t/ha (0.8%). The greatest difficulty in switchgrass growing technology is the increased sensitivity of plants to the conditions of life support in the first year of vegetation. The highest switchgrass yield of dry biomass and the energy output was provided in our earlier conducted field experiments in options with marker crop sowing and the inter-row space width of 30 and 45 cm (*Gumentyk and Kharytonov, 2018*). The main goal of this research was to develop a technology for two switchgrass varieties growing by establishing the optimal terms and methods of sowing and caring for plants during the first year of vegetation.

MATERIALS AND METHODS

Studies of switchgrass cultivation was carried out at the Borschyv experimental field station in Ternopil region for the 2013-2016 period. This area is represented by gray forest soils. The climate of the district is moderate-continental with insignificant amplitudes of temperature fluctuations, characterized by short mild winters, warm humid summers and sufficient precipitation. The period with an average daily temperature of more than 10^0C lasted 160-165 days. The amount of precipitation during the growing season was 370...420 mm. Weather conditions prevailing in the region during 2013-2016 years are shown in Fig. 1 and 2.
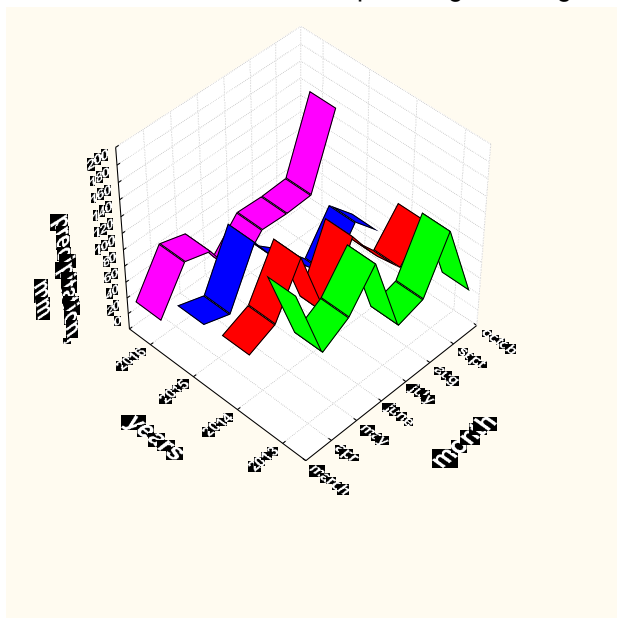
| Fig. 1 - The precipitation during the vegetation periods of 2013-2016, [mm] | Fig. 2 - The temperature regime during the growing periods of 2013-2016, [°C] |
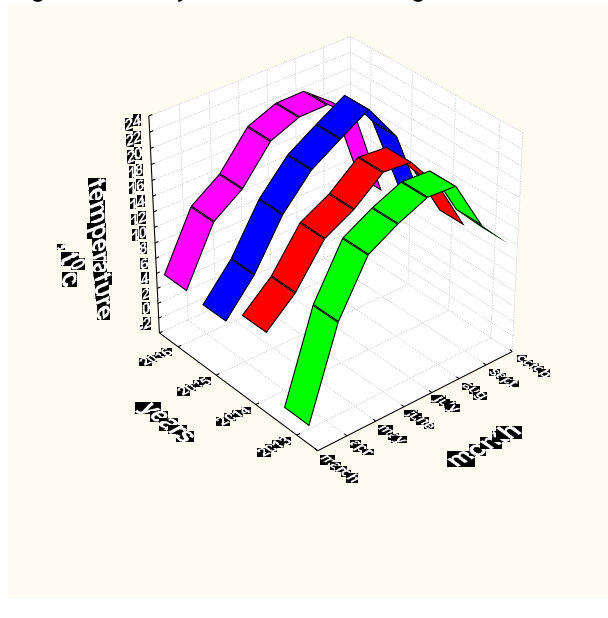
Temperature regimes during the vegetation periods of 2013-2016 were characterized as weighted average without extreme emissions. The year 2016 was the driest during the active vegetation period. The vegetation periods of 2013 and 2014 were the most optimal in terms of moisture content. 2015 was characterized by a lack of moisture in the second half of the growing season. Several factors were taken into account in the field experiment with switchgrass including planting dates (III decade of Apryl, I – II decade of May and III decade of June)*,* method of sowing switchgrass seeds (with and without marker plant), width of inter-row spacing (30 and 45 cm) and two varieties (Cave-in-rock and Morozko) testing. White mustard was used as marker crop. The total area of the experiments was 0.90 ha, four-fold repetition. Switchgrass sowing period was chosen, waiting for the soil temperature at a depth of 10 cm to exceed 10°C. The germination of switchgrass seeds in the forest-Steppe of Ukraine occurred at a temperature of +6-8°C. High level of germination was observed when the soil was heated to +15°C. It was established that the crop can be sown until the end of May in the conditions of Forest-Steppe zone of Ukraine. In our earlier conducted research, the largest switchgrass yield was obtained when a seed sowing was made in the first decade of May (*Gumentyk and Kharytonov, 2018*).

Sowing with marker crop - white mustard, which comes before the main crop and sprouts very quickly, was used to speed up the first row-to-row processing before the emergence of switchgrass seedlings. Marker crop makes it possible to carry out the first inter-row processing before the emergence of seedlings. Seeding rate of marker crop (white mustard) - 1-2 kg/ha. Depth of seeding-1-1.5 cm. Inter-row cultivation was carried out to establish the optimal timing of soil treatment in various phases of plant growth and development of weed control methods. These agrotechnical operations were carried out during the entire vegetation period until the parts of plants closed over the soil surface. The soil was treated as close to the plant as possible to minimize the protective zone and reduce the cost of weeding and loosening the soil in the rows of crops. Cultivator with claws - blades in combination with needle discs, loosens the soil near the plants and cleans the soil from the shoots of annual weeds by 60-70% was used for inter-row tillage. The average width of the protective zone after the passage of the cultivator was 5-6 cm. Ripping needle discs with bent to one side pointed teeth had a diameter of 350 and 450 mm. During the movement of such discs in the aisles and protective zones, the teeth are buried in the ground up to 4-9 cm, loosen it and destroy weeds. The quality of inter-row processing depends on the straightness of the lines. The width of the cultivator working zone should coincide with the seeder width. The working bodies must completely cut the weeds in the rows, not bring the wet soil layer to the surface, not damage the plants more than 1-2%, not deviate from the specified depth by more than 15%.

RESULTS AND DISCUSSIONS

It was established that the terms and methods of switchgrass sowing had a significant impact on seed germination (Table.1).

Table 1

The boundaries of changing the friction angle of the soil on the steel

Variety	Terms of sowing			
	I term (III decade of April)	**II term (I decade of May)**	**III term (II decade of May)**	**IV term (I decade of June)**
Cave-in-rock	42	73	68	60
Morozko	47	75	71	65
LSD$_{95}$	4.0			

The first and second decades of May were the best for sowing. The number of seedlings of switchgrass plants was 75 ... 71 units/line meter for Morozko variety and 73...68 units/line meter - for Cave-in-Rock variety. The lowest number of seedlings was in the third decade of April and the first decade of June - 47 and 65 units/line meter varieties Morozko and Cave-in-Rock. This is due to the low temperature of the soil at the time of sowing. This is also due to the varietal features of the switchgrass. The data on switchgrass plants standing density at the end of the growing season are shown in table 2.

Table 2

Table 2. Density of switchgrass plants standing at the end of the growing season, depending on the timing of sowing and varietal characteristics, mln. unit /ha, (2013-2016).

Variety	Terms of sowing			
	I term (III decade of April)	**II term (I decade of May)**	**III term (II decade of May)**	**IV (I decade of June)**
Cave-in-Rock	3.9	6.7	6.3	3.9
Morozko	3.4	5.2	4.1	3.7
LSD$_{95}$	0.1			

The density of standing switchgrass plants at the end of the growing season was the highest (6.7 mln. units/ha) - for the second term of sowing Cave-in-Rock variety and the smallest (3.4 mln. units/ha) - for the first period of sowing the Morozko variety. It was found that the switchgrass sowing timing had a significant impact on the yield and energy output (table 3). The highest average yield of 16.5 t/ha of switchgrass biomass for both varieties was for the second and third terms of sowing, the lowest-11.0 t/ha - for the fourth term. This is due to the fact that during the first period of switchgrass sowing, the soil temperature has didn't rise to a favourable level for seed germination.

Low reserves of productive moisture led to a decrease in field germination and, as a result, the crop decreased. Accordingly, the energy yield was in the range from 176.0 to 268.8 GJ / ha depending on the sowing period.

Table 3

Productivity of dry switchgrass biomass and energy output in the third year of vegetation depending on the sowing period and varietal characteristics

Variety	Terms of sowing									
	I term (III decade of April)		II term (I decade of May)		III term (II decade of May)		IV (I decade of June)		Average	
	Yield, t/ha	Energy uptake, [GJ/ha]	Yield, [t/ha]	Energy uptake, [GJ/ha]	Yield, [t/ha]	Energy uptake, [GJ/ha]	Yield, [t/ha]	Energy uptake, [GJ/ha]	Yield, [t/ha]	Energy uptake, [GJ/ha]
Cave-in-Rock	14.0	224.0	16.7	267.2	16.8	268.8	9.0	144.0	14.1	225.6
Morozko	14.3	228.8	16.3	260.8	16.1	257.6	13.0	208.0	14.9	238.4
Average	14.2	227.2	16.5	264.0	16.5	264.0	11.0	176.0	14.5	232.0
LSD$_{95}$									1.6	

The most productive variety in the first year of vegetation was Morozko with an average yield of 14.9 t/ha. Different quality adaptive reactions of "Cave-in-rock" and "Morozko" varieties were identified by productivity parameters depending on the method of sowing seeds, the presence of marker crop and terms of vegetation periods (Fig. 3 and 4).
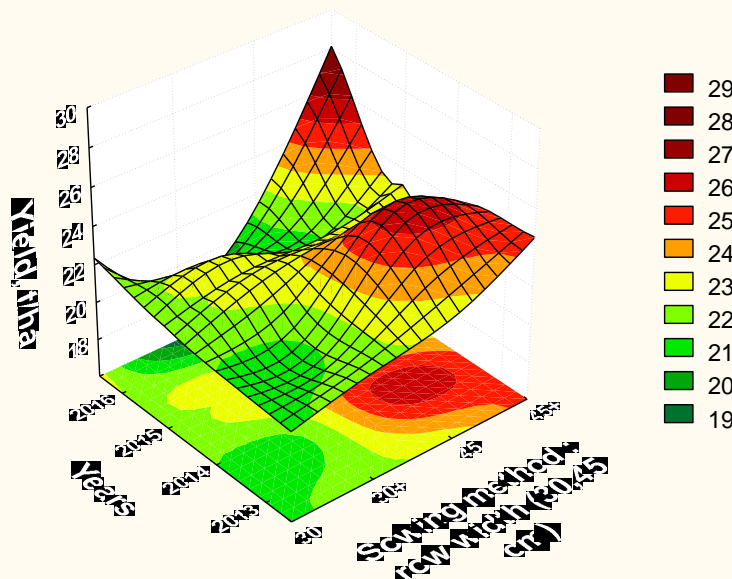
Fig. 3 - Productivity of the "Cave-in-rock" variety biomass, depending on the sowing seeds, the presence of a marker crop and the terms of vegetation periods

In particular, it can be noted, that the adaptive reactions of the "Cave-in-rock" variety concern the method of sowing seeds, the presence of a marker crop and the conditions of vegetation periods. The adaptive reactions of the variety "Morozko" were flexible regarding the parametric levels of productivity relative to the method of sowing seeds, the presence of a marker crop in the conditions of extreme manifestations of 2016 in the growing season. It indicates a wider and optimized rate of adaptive reactions at "Morozko" variety.
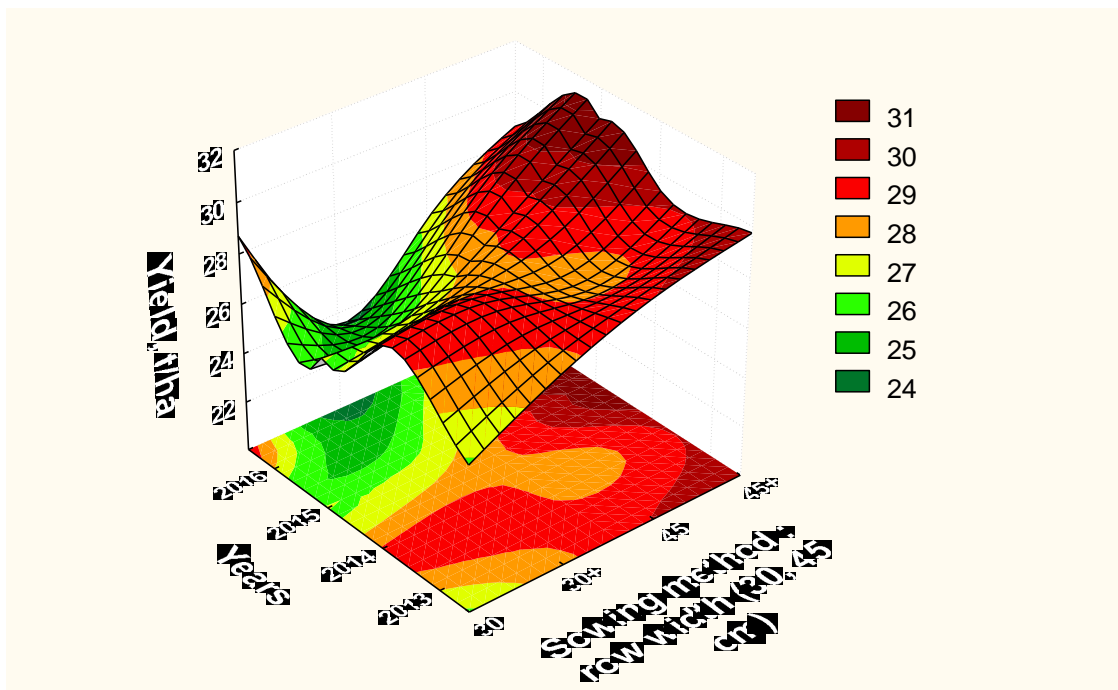
**Fig. 4 - Morozko varieties' productivity of biomass depending on the method of sowing seeds,
the presence of marker crop and terms of vegetation periods, t/h, 2013-2016**

The results of accounting for the yield of Cave-in-Rock and Morozko varieties, depending on the method of sowing seeds, are shown in table 4.

Table 4

Switchgrass yield depending on width of inter raw spacing, t/ha

Trials	Years				Average
	2013	2014	2015	2016	
«Cave-in-Rock»					
Width 30 cm	20.8	21.0	21.4	22.0	21.3
Width 30 см with marker crop	21.4	21.5	22.2	20.4	21.4
Width 45 см	23.8	25.2	22.4	21.0	23.1
Width 45 см with marker crop	24.5	23.8	23.2	25.7	24.3
Morozko					
Width 30 cm	27.0	28.1	26.2	27.0	27.1
Width 30 см with marker crop	28.1	28.3	26.3	24.3	26.8
Width 45 см	28.4	27.7	28.3	27.4	28.0
Width 45 см with marker crop	29.4	29.4	30.7	29.9	29.9
LSD_{95} – 1.08 t/ha					

High yield of switchgrass biomass 29.9 t/ha, in the first year of vegetation was observed in the variety Morozko with white mustard as marker crop and inter raw spacing width of 45cm.

Conventional planting techniques managed in the field experiments in Virginia State of US showed that the best way to get the greatest yields is a choice for width of switchgrass stands from18 to 25 cm (*Parrish and Fike, 2005*). In order to maximize biofuel production in other field experiments managed earlier in the same experimental station in Ukraine it was advisable to plant switchgrass in narrow rows to provide quicker canopy closure and weed control (*Kulik, 2016*). Variety Cave-in-Rock during the first three years and variety Sanburst during four years had the highest phytomass productivity with row - spacing width of 30 cm. However, switchgrass formed considerably high yield during the fifth and the sixth vegetation year with row-spacing width of 45 cm.

CONCLUSIONS

Different quality adaptive reactions of the "Cave-in-rock" and "Morozko" varieties were found in terms of productivity parameters depending on the method of sowing seeds, the presence of a marker crop and the conditions of vegetation periods. The highest yield of switchgrass for both varieties was for the second and third terms of sowing. In particular, it can be noted, that the adaptive reactions of the "Cave-in-rock" variety concern both methods of sowing seeds, the presence of a marker crop and the conditions of vegetation periods. The adaptive reactions of the variety "Morozko" were flexible regarding the parametric levels of productivity relative to the method of sowing seeds, the presence of a marker crop in the conditions of extreme manifestations of 2016 in the growing season. High yield of switchgrass biomass 29.9 t/ha, in the first year of vegetation was observed in the Morozko variety with white mustard as marker crop and inter raw spacing width of 45cm. It indicates a wider and optimized rate of adaptive reactions at "Morozko" variety.

ACKNOWLEDGEMENT

REFERENCES

[1] Cherney J.H., Cherney D.J.R., Paddock K.M., (2018), Biomass Yield and Composition of Switchgrass Bales on Marginal Land as Influenced by Harvest Management Scheme. *Bioenerg. Res.* Vol.11(1): 34–43. https://doi.org/ 10.1007/s12155-017-9875-y;

[2] Fike J.H., Parrish D.J., Wolf D.D., Balasko J.A., Green Jr. J.T., Rasnake M., Reynolds J. H., (2006), Switchgrass production for the upper south-eastern USA: Influence of cultivar and cutting frequency on biomass yields *Biomass and Bioenergy*. Volume 30, Issue 3: 207-213. https://doi.org/10.1016/j.biombioe.2005.10.008;

[3] Gumentyk M., Kharytonov M., (2018), Development and assessment of technologies of Miscanthus and Switchgrass growing in forest-steppe zone of Ukraine. *Agriculture and Forestry Journal*. Vol.64, Issue 2: 137-146 doi: 10.17707/AgricultForest.64.2.10;

[4] Hartman J.C., (2011), Potential ecological impacts of switchgrass (Panicum virgatum L.) biofuel cultivation in the Central Great Plains, USA / J.C. Hartman, J.B. Nippert, R.A. Orozco, C.J. Springer // *Biomass and bioenergy*. Vol. 35: 3415–3421. https://doi.org/10.1016/j.biombioe.2011.04.055;

[5] Kulik M., (2016), Impact of seeding terms and row spacing on yield of switchgrass phytomass, biofuel and energy output. *Annals of Agrarian Science*. Volume 14, Issue 4: 331-334. https://doi.org/10.1016/j.aasci.2016.09.011;

[6] Kvak V., Stefanovska T., Pidlisnyuk V., Alasmary Z., Kharytonov M., (2018), The long-term assessment of miscanthus× giganteus cultivation in the forest-steppe zone of Ukraine. *INMATEH – Agricultural Engineering*, Vol.54, No.1, pp.113-121, http://www.inmateh.eu/INMATEH_1_2018/54-14%20Kvak.pdf;

[7] Marra M., Keene T., Skousen J., Griggs T., (2013), Switchgrass yield on reclaimed surface mines for bioenergy production. *J. Environ. Qual.*, 696–703. doi:10.2134/jeq2012.0453;

[8] Ma Y, An Y, Shui J, Sun Z., (2011), Adaptability evaluation of switchgrass (*Panicum virgatum L.*) cultivars on the Loess Plateau of China. Plant Sci. 181(6):638-43. doi: 10.1016/j.plantsci.2011.03.003

[9] Parrish D.J., Fike J.H., (2005), The biology and agronomy of switchgrass for biofuels. *Crit. Rev. Plant Sci.* Vol.24 (5-6):423–459. https://doi.org/10.1080/07352680500316433;

[10] Rushing, J.B., Baldwin B.S., Taylor A.G., Owens V.N., Fike J.H., Moore K.J., (2013), Seed safening from herbicidal injury in switchgrass establishment. *Crop Sci.* 53:1-8. doi: 10.2135/cropsci2013.01.0050;

[11] Scagline S., Skousen J., Griggs T., (2015), Switchgrass and miscanthus yields on reclaimed surface mines for bioenergy production. *JASMR.* Vol.4(2): 80–90. http://doi.org/10.21000/JASMR15020080

[12] Smeets E.M.W., (2009), The economic and environmental performance of miscanthus and switchgrass production and supply chains in a European setting / E.M.W. Smeets, I.M. Lewandowski, A.P.C. Faaij //*Renewable and Sustainable Energy Reviews*. Vol. 13:1230–1245. https://doi.org/10.1016/j.rser.2008.09.006;

[13] Zhang Fu J., Lin G., Jiang D., Yan X., (2017), Switchgrass-Based Bioethanol Productivity and Potential Environmental Impact from Marginal Lands in China. *Energies* 10, 260; doi:10.3390/en10020260.

ANALYSIS AND CALIBRATION OF QUINOA GRAIN PARAMETERS USED IN A DISCRETE ELEMENT METHOD BASED ON THE REPOSE ANGLE OF THE PARTICLE HEAP
/
基于堆积试验的藜麦离散元参数分析及标定

Fei Liu, Dapeng Li, Tao Zhang※, Zhen Lin [1]

College of Mechanical and Electrical Engineering, Inner Mongolia Agricultural University, Hohhot / China
Tel: +86-471-5964308   E-mail: afei2208@imau.edu.cn
DOI: https://doi.org/10.35633/inmateh-61-09

ABSTRACT

An optimization method based on a regression model was established by combining physical experiments, and an extended distinct element method (EDEM) simulation was proposed to address the difficult problem of obtaining the contact characteristic parameters used in the discrete element method (DEM) model of quinoa grains and for calibrating the parameters of the quinoa DEM model. The Plackett-Burman test was designed using Design-Expert software to screen the parameters of the quinoa DEM model, and the quinoa-quinoa static friction coefficient, quinoa-polylactic acid (PLA) static friction coefficient and quinoa-quinoa rolling friction coefficient were found to have significant effects on the repose angle. The optimal value intervals of the parameters with a significant impact on the repose angle were determined using the steepest ascent test. A regression model of the repose angle and the parameters with a significant impact on the repose angle was then established with the Box-Behnken design and further optimized, and the combination of optimal parameters was as follows: 0.26 for the quinoa-quinoa static friction coefficient (E), 0.38 for the quinoa-PLA static friction coefficient (F), and 0.08 for the quinoa-quinoa rolling friction coefficient (G). Lastly, the optimal combination was used in the verification performed by the DEM simulation, and the error between the simulated repose angle and the target repose angle was 0.86%. These findings indicated that it was feasible to use the response surface optimization to calibrate the parameters required for quinoa DEM simulation and that the combination of optimal parameters can provide a reference for selecting the characteristic contact parameters used in quinoa DEM simulation.

摘要

针对藜麦离散元仿真模型接触参数难以直接获取的问题，提出一种结合物理试验和 EDEM 仿真试验建立回归模型进行寻优的方法，对藜麦离散元仿真模型参数进行标定。应用 Design Expert 软件设计 Plackett-Burman 试验对藜麦离散元模型参数进行筛选，得到藜麦-藜麦静摩擦系数、藜麦-PLA 静摩擦系数和藜麦-藜麦滚动摩擦系数对休止角影响显著；通过最陡爬坡试验确定显著性参数的最优值区间，然后根据 Box-Behnken 设计结果建立休止角与显著性参数的回归模型并对其进行优化，得到显著性参数的最佳组合为：藜麦-藜麦静摩擦系数为 0.26、藜麦-PLA 静摩擦系数为 0.38、藜麦-藜麦滚动摩擦系数为 0.08。最后将最佳参数组合进行离散元仿真验证，仿真休止角与目标休止角的相对误差为 0.86%，表明应用响应面优化标定藜麦离散元仿真中所需的参数是可行的；标定所得的最佳参数组合可为藜麦离散元仿真接触参数的选取提供参考。

INTRODUCTION

Quinoa is resistant to cold, drought, barren soil, and saline-alkaline soil and is thus highly suitable for cultivation in arid and semiarid plateau areas. Due to its complete and rich nutritional content, quinoa is regarded as one of most promising "superfoods" for ensuring global food security and human nutrition in the 21st century, according to the Food and Agriculture Organization of the United Nations (*Chen et al., 2018*). However, quinoa is planted by the hole sowing method, at 5-8 grains per hole, leading to serious grain waste. Quinoa seedlings look very similar to those of Chenopodium album, a common field weed, and both plants belong to the Chenopodiaceae family, making it very difficult to control weeds and thus resulting in high labour costs.

---

[1] *Fei Liu, A/Prof. Ph.D. Eng.; Dapeng Li, As Ph.D. Stud. Eng.; Tao Zhang, Lec. Ph.D. Eng.; Zhen Lin, As M.S. Stud. Eng.*

The mechanization level involved in harvesting quinoa is low, and the use of traditional combines for grain crops leads to high grain loss and high levels of impurities, which are seriously hampering the healthy development of the quinoa industry. Therefore, it is of great practical significance to study key common issues in quinoa mechanization.

In recent years, the discrete element method (DEM) has been increasingly used in research and development (R&D) on agricultural equipment, and good results have been obtained. Investigating the parameters involved in the quinoa DEM simulation can help in the R&D of quinoa production equipment (*Ucgul et al., 2017; Ucgul and Saunders, 2020; Sun et al., 2018; Zhao et al., 2013*). The characteristic physical parameters of quinoa grain include its intrinsic parameters and contact characteristic parameters, which can be obtained through direct measurement. In EDEM, the intrinsic parameters can directly adopt measured values, but the established model and the actual grains have specific differences with one another, causing a simulation distortion when using measured contact characteristic parameters directly. Therefore, it is necessary to calibrate the contact characteristic parameters of quinoa grains.

These characteristic parameters include the static friction coefficient, rolling friction coefficient, and collision restitution coefficient (*Zeng et al., 2017; Bart et al., 2014; González et al., 2012*). Scholars in China and abroad have investigated the parameter measurements of DEM simulations extensively. Han et al. constructed a linear equation for the rolling friction coefficient and repose angle, and they simulated the heaping process for ellipsoidal particles using the DEM, performed virtual experimental calibration on the measured parameters of loose materials, and obtained the rolling friction coefficient of granular materials, thereby providing approximate numerical measurements (*Han et al., 2014*). Using rice grains as an example, Jia et al. simulated rice grain heaping in a bottomless cylinder using DEM and MATLAB graphic image processing techniques, demonstrating that this method was suitable for measuring the repose angle of rice grains; they were able to predict the repose angle of ellipsoidal granular materials with known physical and mechanical parameters (*Jia et al., 2014*).

In many cases, the response surface design is integrated into the calibration and optimization of particle parameters. Li et al. obtained the repose angle of wheat kernels using the cylindrical lifting method, established and optimized a second-order regression model of the repose angle based on the static friction coefficient and rolling friction coefficient by response surface design, and compared the measured values with the simulated ones for model verification, thus providing a reference for the parameter calibration of granular materials, such as wheat kernels, in DEM simulations (*Li et al., 2016*). Based on the DEM, Santos et al. obtained the dynamic repose angle of dried cherry fruits using a central combination experimental design and a rotating drum test and calibrated the parameters needed in DEM simulations (*Santos et al., 2015*).

In this study, by using the Plackett-Burman, steepest ascent, and Box-Behnken tests, we calibrated the contact characteristic parameters of quinoa grains and polylactic acid (PLA), a new biobased, biodegradable, renewable material used for 3D printing, in the DEM model. We obtained the combination of optimal parameters and verified this combination by comparing the simulated repose angle and the target repose angle to provide a reference for the parameter calibration of quinoa grains in the DEM simulation.

MATERIALS AND METHODS
Basic parameters of quinoa grains

The quinoa used in this study was "Mengli No. 1" that was harvested in Liangcheng County, Ulanqab City, Inner Mongolia, China, with a density of 870 kg/m3, a water content of 8%, and a thousand-kernel weight of 2.27-2.35 g. Using an outside micrometre with an accuracy of 0.01 mm, the average length, width, and thickness of the quinoa grains were determined to be 1.803, 1.711, and 1.150 mm, respectively, with a sphericity of 0.85.

Test method

We first measured the repose angle of the quinoa grain using the injection method during the physical test, in addition to the contact characteristic parameters (collision restitution coefficient, static friction coefficient and rolling friction coefficient) to determine the value ranges. We then constructed a simulation model using SolidWorks software, which was added to EDEM for simulation, and we screened the contact characteristic parameters of the quinoa grains used in the DEM simulation using the Plackett-Burman test to determine the parameters that significantly affected the repose angle. Using the steepest ascent test, we obtained the optimal value intervals of the parameters that were significantly affecting the repose angle. We further established a regression model of the repose angle for the quinoa grain heap and the parameters that

significantly affect the repose angle by performing an analysis of variance (ANOVA) as part of the Box-Behnken test, and the regression model was optimized to obtain the optimal value for each significant parameter. Lastly, we performed verification by simulation using the calibrated parameters and compared the deviation between the simulated repose angle and the actual repose angle to verify the accuracy of the calibrated parameters. The effects of the repose angles of different materials on the parameters of the DEM model vary; because the regression model that was established using the response surface analysis method is continuous, the optimum value obtained through the optimization is more accurate (*Yuan et al., 2018*).

Parameter calibration process and analysis

Determination of the repose angle

During this study, we calibrated the contact characteristic parameters of the quinoa grain and PLA, a new biobased, biodegradable, and renewable 3D printing material. In reference to *Surface active agents – Powders and Granules – Measurement of angle of repose* (GB11986-89), the national standard (GB/T 16913.5-1997) and the existing literature (*Peng et al., 2018*), the repose angle of the quinoa grains was measured by the injection method using FT-104B powder and a particle repose tester. The setup is shown in Fig. 1. To obtain accurate measurements and calibrated parameters, the funnel and the cylinder chassis were manufactured with PLA by 3D printing. The inner diameter of the lower opening in the funnel was 10 mm; the diameter of the cylindrical chassis was 50 mm; and the distance between the lower opening of the funnel and the upper surface of the cylindrical chassis was 50 mm. During the measurement, the instrument was placed and levelled on the table and ensured the centre of the chassis and the centre of the funnel in the same axis through the alignment of the concentric circles on the chassis. Then, a specific amount of grain was weighed and poured into the funnel. The height of the heap was measured sometime after the grains stopped flowing. The repose angle of the quinoa grains was calculated using Eq. (1), and 10 measurements were averaged, for a repose angle of 28.14°.

$$\theta = \arctan \frac{2l}{R}$$

(1)

where: θ is the repose angle, [°];

R is the diameter of the cylindrical chassis, [mm];

l is the height of the heap, [mm].
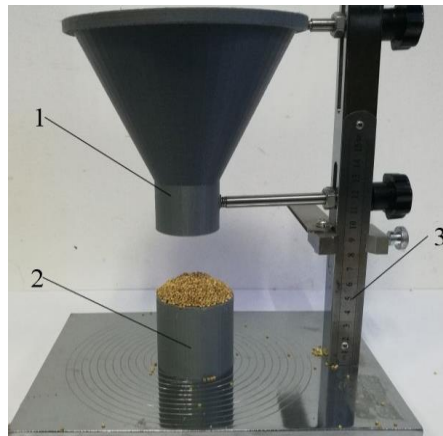
Fig. 1 - Angle of repose measuring instrument
1. PLA funnel; 2. PLA cylindrical chassis; 3. Iron stand

Determination of the friction coefficient

The friction coefficient was determined based on the inclined plane mechanics principle using the CNY-1 Inclined Plane Tester, as shown in Fig. 2. Because the grains roll on the plane, the quinoa grains were attached to the plane surface through adhesion, and the PLA plate and the adhesive plate for quinoa grains were used (*Zhang et al., 2017*). The seeds are placed on the inclined surface, as the inclination angle of the inclined surface gradually increases, when the grain is just about to start sliding on the inclined surface, the inclination angle of the inclined surface at this moment is defined as static friction angle, and the corresponding static friction coefficient of the quinoa grain is calculated using Eq. (2), which is the friction

coefficient formula. The measurement was repeated 20 times, and the obtained average static friction coefficients were 0.468 between quinoa grains and 0.545 between quinoa grains and PLA.

Fig. 2 - Friction coefficient tester

$$\mu = \tan \beta \tag{2}$$

where: μ is the static friction coefficient, [-];

β is the static friction angle, [°];

Similarly, to measure the rolling friction coefficient, a single quinoa grain was placed on the test material; when the grain was just about to roll, the inclination angle of the inclined surface was defined as the rolling friction angle of the grain, and the rolling friction coefficient of the grain was calculated using Eq. (2). The measurement was repeated 20 times, and the average rolling friction coefficients were 0.141 between quinoa grains and 0.124 between quinoa grains and PLA.

Determination of the restitution coefficient

The collision restitution coefficient reflects the ability of an object to retake its form following deformation during a collision, and it is only related to the materials in the collision. During testing, the grain was dropped and allowed to free-fall from fixed height H, and it collided with the test material to rebound. This process was videotaped with a camera using a test system, as shown in Fig. 3. After the test, the video was analysed and the grains that experienced a direct collision were analysed; rebounding height of the grain after its collision with the test material was determined. The restitution coefficient of quinoa grain was calculated using Eq. (3). The measurement was repeated 20 times, and the obtained average restitution coefficients were 0.347 between quinoa grains and 0.455 between quinoa grains and PLA.

$$e = \sqrt{\frac{h}{H}} \tag{3}$$

where: e is the restitution coefficient, [-];

h is the seed bounce height, [mm];

H is the seed falling distance, [mm].
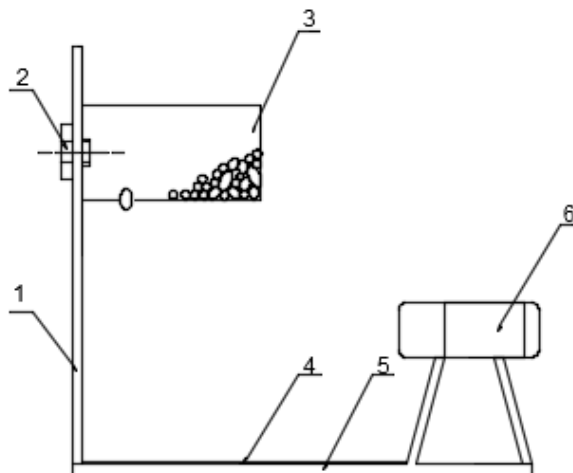
Fig. 3 - Collision recovery coefficient tester
1. Calibration plate 2. Fixed bolt 3. Blanking box 4. Test material plate 5. Base 6. Camera

DEM model of quinoa grains

Quinoa grains assume the form of a round tablet without an adhesive surface. For this study, we adopted the Hertz-Mindlin (no slip) contact model in the EDEM software and used the 6-ball combination method to construct a DEM model of the quinoa grains, as shown in Fig. 4. In the simulation model, the quinoa grain was 1.8 mm long, 1.7 mm wide, and 1.1 mm thick, with a relative size error of 1.57%.

Fig. 4 - Quinoa seed particle model

Simulation parameters

By combining the existing physical characteristic parameters of the quinoa grain with the measured parameters, we determined the variation ranges of the simulation parameters, as shown in Table 1. During the simulation, we set the time step to 20% of the Rayleigh time step and the grid size to five times the minimum spherical element size.

Table 1

Parameters required in DEM simulation

Parameters	Value
Poisson's ratio of quinoa	0.2-0.3 [a]
Poisson's ratio of PLA	0.25-0.47 [a]
Young's modulus of quinoa [MPa]	390.00
Young's modulus of PLA [MPa]	2 350.00
Density of quinoa [kg·m^{-3}]	0.87
Density of PLA [kg·m^{-3}]	1.23
Quinoa-quinoa restitution coefficient	0.22-0.54 [a]
Quinoa-PLA restitution coefficient	0.32-0.68 [a]
Quinoa-quinoa static friction coefficient	0.24-0.70 [a]
Quinoa- PLA static friction coefficient	0.32-0.66 [a]
Quinoa-quinoa rolling friction coefficient	0.05-0.19 [a]
Quinoa- PLA rolling friction coefficient	0.03-0.19 [a]

Note: a shows the term is variable.

Simulation model of the repose angle

The Hertz-Mindlin (no slip) contact model in the EDEM software was adopted, and the inner diameters and heights of the funnel and the cylinder chassis were identical to those in the repose angle test, as shown in Fig. 5. The particles formed a particle plant at the top of the funnel. The Dynamic particle generation method was used, and 7,000 particles were generated. The fixed time step was 25% of the Rayleigh time step. After all the particles in the funnel fell into the chassis, they were left to rest for a period of time, a stable particle heap was formed on the chassis, and then the repose angle was measured.
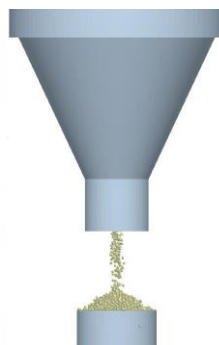
Fig. 5 - Simulation of quinoa seed particle accumulation

Response surface design for simulation parameters

To calibrate the repose angle parameters accurately, the grain contact characteristic parameters were screened based on their significance. In this study, the Plackett-Burman test was performed using Design-Expert 8.0.6 software, and eight true parameters and three virtual parameters, each having two levels (high and low), were chosen. The test parameters are shown in Table 2.

Table 2

Test parameters

Symbol	Parameters	Low level	High level
A	Poisson's ratio of quinoa	0.2	0.3
B	Poisson's ratio of PLA	0.25	0.47
C	Quinoa-quinoa restitution coefficient	0.22	0.54
D	Quinoa-PLA restitution coefficient	0.32	0.68
E	Quinoa-quinoa static friction coefficient	0.24	0.70
F	Quinoa- PLA static friction coefficient	0.32	0.66
G	Quinoa-quinoa rolling friction coefficient	0.05	0.19
H	Quinoa- PLA rolling friction coefficient	0.03	0.19
J, K, L	Virtual parameters	-1	1

The Plackett-Burman test design designs were coded as -1 and +1, with one centre point, over a total of 13 tests. After the parameters with a significant impact on the repose angle were screened out using the Plackett-Burman test. The steepest ascent test was used to determine the optimal value interval for each parameter rapidly. Based on the steepest ascent test results and the response surface design principle, Box-Behnken test was performed and three levels, i.e., low (-1), medium (0) and high (1), were chosen for each parameter with a significant effect. The medium level was chosen for each parameter with a nonsignificant effect, and three centre points were designed to assess the error.

RESULTS AND DISCUSSION

Plackett-Burman test

The results are shown in Table 3. The ANOVA was performed on the test results using Design-Expert software, and the effect of each parameter is shown in Table 4, indicating that the quinoa-quinoa static friction coefficient (*E*), quinoa-PLA static friction coefficient (*F*) and quinoa-quinoa rolling friction coefficient (*G)* had a significant effect on the repose angle of the grains, while other parameters only had a nonsignificant effect. Thus, in the steepest ascent test and the Box-Behnken test, only the above three parameters with a significant impact were considered, and for the parameters with a nonsignificant effect, an intermediate value was chosen (i.e., the Poisson's ratio of quinoa: 0.25; the Poisson's ratio of PLA: 0.36; quinoa-quinoa restitution coefficient: 0.38; quinoa-PLA restitution coefficient: 0.50; and quinoa-PLA rolling friction coefficient: 0.11).

Table 3

Design and results of Plackett-Burman test

No.	A	B	C	D	E	F	G	H	J	K	L	Angle of repose [°]
1	1	-1	-1	-1	1	-1	1	1	-1	1	1	45.23
2	-1	1	1	-1	1	1	1	-1	-1	-1	1	36.34
3	1	1	-1	-1	-1	1	-1	1	1	-1	1	29.42
4	1	-1	1	1	1	-1	-1	-1	1	-1	1	30.46
5	0	0	0	0	0	0	0	0	0	0	0	38.38
6	1	1	1	-1	-1	-1	1	-1	1	1	-1	28.55
7	1	1	-1	1	1	1	-1	-1	-1	1	-1	34.22
8	-1	1	1	1	-1	-1	-1	1	-1	1	1	22.39
9	-1	-1	1	-1	1	1	-1	1	1	1	-1	35.60
10	-1	1	-1	1	1	-1	1	1	-1	-1	-1	42.24
11	1	-1	1	1	-1	1	1	1	-1	-1	-1	33.42
12	-1	-1	-1	-1	-1	-1	-1	-1	-1	-1	-1	22.00
13	-1	-1	-1	1	-1	1	1	-1	1	1	1	33.58

Analysis of significance of parameters in Plackett-Burman test   Table 4

Parameters	Effect	Sum of squares	Contribution [%]	Significance
A	-0.14	0.06	0.01	8
B	0.48	0.69	0.10	7
C	-1.62	8.22	1.16	6
D	-1.80	9.77	1.38	5
E	10.79	349.16	49.14	1
F	3.62	39.28	5.53	3
G	9.21	254.56	35.82	2
H	2.19	14.41	2.03	4

Steepest ascent test

The results are shown in Table 5, and the results showed that as the *E*, *F*, and *G* increased, the repose angle gradually increased. The relative error was the lowest at Level 2, and it decreased first and then increased when changed from Level 1 to Level 3. This finding indicated that the optimal value interval was close to Level 2, which was then chosen as the centre point, and Levels 1 and 3 were designated as the low and high levels, respectively, to set up the subsequent response surface design.

Design and results of steepest ascent test   Table 5

No.	Test factors			Angle of repose [°]	Relative error [%]
	E	F	G		
1	0.2	0.31	0.04	21.41	23.93
2	0.3	0.38	0.07	28.72	2.07
3	0.4	0.45	0.10	37.23	32.32
4	0.5	0.52	0.13	41.35	46.94
5	0.6	0.59	0.16	44.07	56.60
6	0.7	0.66	0.19	45.57	61.93

Box-Behnken test

The Box-Behnken test results are shown in Table 6. A second-order regression model of the repose angle for parameters with a significant effect was established using Design-Expert software, and the quadratic polynomial equation is as follows:

$$\theta = -9.63 + 36.74E + 123.53 - 69.64G + 72.50 + 175.83EG + 101.19FG - $$

$$64.79E^2 - 169.98F^2 + 247.53G^2 \qquad (4)$$

Design and results of Box-Behnken test   Table 6

No.	Test factors			Angle of repose [°]
	E	F	G	
1	-1 (0.20)	0(0.38)	-1(0.04)	23.56
2	1(0.40)	0	-1	30.46
3	0(0.30)	-1(0.31)	1(0.10)	28.72
4	-1	0	1	25.83
5	0	1(0.45)	1	32.13
6	-1	1	0(0.07)	25.27
7	1	1	0	33.42
8	0	0	0	29.07
9	0	0	0	28.90
10	0	1	-1	27.93
11	0	0	0	29.25
12	-1	-1	0	22.78
13	0	-1	-1	25.27
14	1	0	1	34.84
15	1	-1	0	28.90

The ANOVA results of the model are shown in Table 7. The *E*, *F*, *G*, and the quadratic term of *F* (*F*²) showed a highly significant effect on the repose angle. The quadratic term of *E* (*E*²) and the interaction terms of *E* and *F* (*EF*) and *E* and *G* (*EG)* showed a significant effect on the repose angle. The linear regression

model had a $P < 0.01$, indicating that the relationship of the repose angle with the obtained regression equation was statistically significant. The lack-of-fit item showed $P = 0.21 > 0.05$, indicating that the equation had a good fit. In the test, the coefficient of variation CV = 1.30%, indicating that the test had high reliability. The determination coefficient $R^2 = 0.996$, the correction determination coefficient $R^2_{adj} = 0.989$, and the prediction determination coefficient $R^2_{pre} = 0.940$, all of which were close to 1, indicating that the model can truly reflect the actual situation. The test precision of Adep Precision = 39.962, indicating that the model had good accuracy.

ANOVA of quadratic polynomial model of Box-Behnken test   **Table 7**

Source of variation	Sum of squares	df	Mean square	P-value
Model	167.45	9	18.61	＜0.0001
E	113.85	1	113.85	＜0.0001
F	21.06	1	21.06	＜0.0001
G	25.92	1	25.92	＜0.0001
EF	1.03	1	1.03	0.0406
EG	1.11	1	1.11	0.0357
FG	0.18	1	0.18	0.3025
E^2	1.55	1	1.55	0.0200
F^2	2.56	1	2.56	0.0075
G^2	0.23	1	0.23	0.2555
Residual	0.68	5	0.14	
Lack of fit	0.62	3	0.21	0.1313
Pure error	0.06	2	0.03	
Total	168.13	14		
R^2=0.996；R^2_{adj}=0.989；R^2_{pre}=0.940；CV=1.30%； Adep Precision=39.962				

Based on the results in Table 7, under the objective of ensuring that the model was significant and the lack-of-fit term was not significant, the terms (FG, G^2) without a significant effect on the repose angle were excluded and the ANOVA results of the optimized model are shown in Table 8. The lack-of-fit term showed $P = 0.135 > 0.05$, indicating that the equation fit well. In the test, CV = 1.390%, indicating that the test had high reliability. The $R^2 = 0.994$, $R^2_{adj} = 0.987$, and $R^2_{pre} = 0.955$, indicating that the model can truly reflect the actual situation. The test precision of Adep Precision = 41.084, indicating that the model was improved after the optimization. The regression equation after optimization is as follows:

$$\theta = -14.25 + 37.88E + 133.56F + 7.25G + 72.50EF + 175.83EG - 66.69E^2 - 173.86F^2 \qquad (5)$$

ANOVA of modified model of Box-Behnken test   **Table 8**

Source of variation	Sum of squares	Freedom	Mean square	P value
Model	167.04	7	23.86	＜0.0001
E	113.85	1	113.85	＜0.0001
F	21.06	1	21.06	＜0.0001
G	25.92	1	25.92	＜0.0001
EF	1.03	1	1.03	0.0396
EG	1.11	1	1.11	0.0318
E^2	1.65	1	1.65	0.0139
F^2	2.70	1	2.70	0.0042
Residual	1.09	7	0.16	
Lack of fit	1.03	5	0.21	0.1347
Pure error	0.06	2	0.03	
Total	168.13	14		
R^2=0.994；R^2_{adj}=0.987；R^2_{pre}=0.955；CV=1.39%；Adep Precision=41.084				

Analysis of the interaction terms in the regression model

The ANOVA results of the optimized regression model indicated that two interaction terms, i.e., EF and EG, had a significant effect on the repose angle of the quinoa grains ($P < 0.05$). When G was 0.07 and F was 0.38, the response surfaces of three parameters (E, F, and G) under the interactions of EF and EG were plotted using Design-Expert software, as shown in Fig. 6, to describe the effect of the interaction term on the

repose angle in a visual manner. Fig. 6A and Fig. 6B show that compared to those of *F* and *G*, the response surface of *E* was steeper, indicating that it had a more profound effect on the repose angle.

a)   Interaction between *E* and *F*   b)   Interaction between *E* and *G*
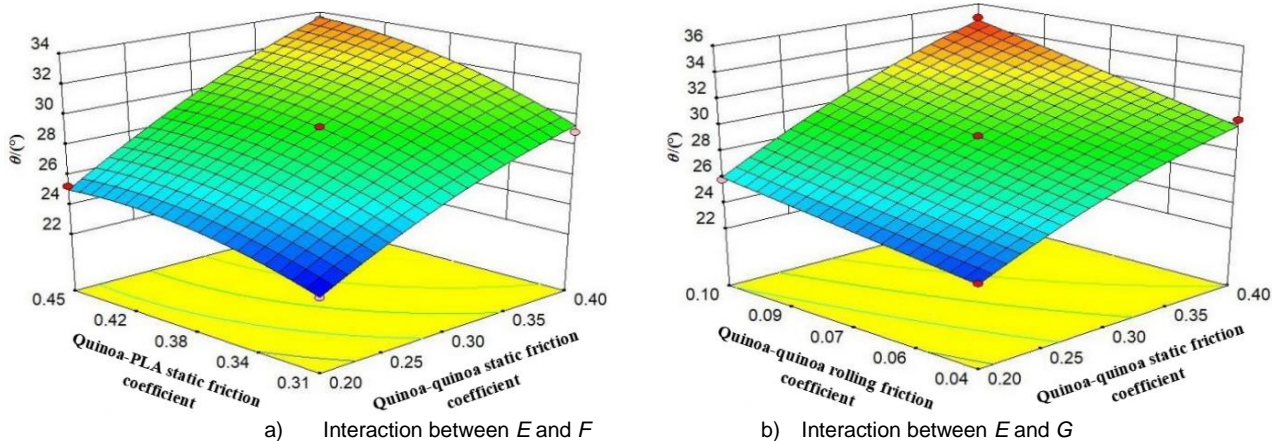
Fig. 6 - Interaction effect diagram of *EF* and *EG*

Determination of the optimal parameter combination and its simulation verification

    With Design-Expert software, the optimized regression equation was solved with the actual repose angle of quinoa grains as the target, and the results showed that when *E*, *F*, and *G* were 0.26, 0.38, and 0.08, respectively, and the parameters with a nonsignificant effect were set to the medium level, the minimal deviation between the simulated repose angle and the experimental repose angle was obtained. The simulation on the repose angle was then performed with the combination of the above optimal parameters, and the comparison of the simulation and physical test is shown in Fig. 7. The repose angle values obtained through three repeated simulations were 28.55°, 28.05°, and 28.37°, with an average error of 0.86%, indicating the feasibility of the optimization of physical characteristic parameters for the quinoa grains used in the simulation by combining the significance analysis and the response surface method.

a)   Physical test   b)   Simulation test

Fig. 7 - Comparison of simulation and physical tests

CONCLUSIONS

    In this study, based on the reported experiments, we calibrated and optimized the simulation parameters of quinoa grains and the 3D printing material PLA using the DEM. Using Design-Expert software with the significance analysis and the response surface methods, we optimized and solved the simulation parameters with the repose angle as the response value, screened those with a significant impact on the repose angle, determined the optimum value range for each parameter, established a regression model, and analysed the interactions between the parameters to determine the optimal parameters. We then verified the accuracy of the quinoa grain simulation model through the simulation and drew the following conclusions:

    1) The Plackett-Burman test results showed that *E*, *F*, and *G* had a significant effect on the repose angle, while the other parameters showed no significant impact on the repose angle of the quinoa grains.

    2) The optimal value interval of the parameters with a significant effect on the repose angle was determined through the steepest ascent test. Based on the Box-Behnken test results, a second-order regression model of the repose angle on the parameters with a significant impact was established and optimized. The ANOVA results for the optimized model showed that in addition to the linear terms of the three parameters with a significant impact on the repose angle (*E*, *F*, and *G*), the interaction terms *EF* and *EG* and the quadratic terms F^2 and E^2 showed a significant effect on the repose angle.

    3) The above regression equation was optimized and solved using the actual repose angle of quinoa grains as the target value, and the combination of the optimal parameters with a significant effect was obtained, i.e., *E* was 0.26, *F* was 0.38, and *G* was 0.08. The experimental comparison showed that the repose

angle obtained from the simulation was not significantly different from the actual repose angle (P > 0.05), indicating that the response surface analysis was feasible for calibrating the parameters used in the DEM simulation.

4) A simulation on the repose angle was performed using the obtained combination of optimal parameters, and the repose angle of the quinoa grains obtained through the simulation was 28.32°, which had an error of 0.86% under the experimentally measured repose angle (28.14°) and was not significantly different, indicating that the contact characteristic parameters obtained during the calibration can be used in the DEM simulation.

ACKNOWLEDGEMENT

REFERENCES

[1] Guang Chen, Yang Sun, Gang Wang, Huan Chen, Shanshan Tang, Xiaoxuao Yu. (2018). Comprehensive utilization and development prospect of whole-plant chenopodium quinoa. *Journal of Jilin Agricultural University*, Vol. 40, issue 1, pp. 1-6;

[2] Ucgul, M., Saunders C., Fielke, J. M. (2017). Discrete element modelling of tillage forces and soil movement of a one-third scale mouldboard plough. *Biosystems Engineering*, Vol 155, issue 3, pp. 44-54;

[3] Ucgul, M., Saunders, C. (2020). Simulation of tillage forces and furrow profile during soil-mouldboard plough interaction using discrete element modelling. *Biosystems Engineering*, Vol190, issue 2, pp.58-70;

[4] Zhao Z., Li Y., Liang Z., Gong Z. (2013). DEM simulation and physical testing of rice seed impact against a grain loss sensor. *Biosystems Engineering*, Vol 116, issue 4, pp. 410-419;

[5] Sun J., Wang Y., Ma Y., Tong J., Zhang Z. (2018). DEM simulation of bionic subsoilers (tillage depth > 40 cm) with drag reduction and lower soil disturbance characteristics. *Advances in Engineering Software*, Vol 119, issue 5, pp. 30-37;

[6] González-Montellano, C., Fuentes, J. M., Ayuga-Téllez, E., Ayuga, F. (2012). Determination of the mechanical properties of maize grains and olives required for use in DEM simulations. *Journal of food engineering*, Vol 111, issue 4, pp. 553-562;

[7] Zeng Z., Chen Y., Zhang X. (2017). Modelling the interaction of a deep tillage tool with heterogeneous soil. *Computers & Electronics in Agriculture*, Vol 143, issue 12, pp. 130-138;

[8] Lenaerts, B., Aertsen, T., TijskensE, Ketelaere B. D., Ramon, H., Baerdemaeker, J. D., Saeys, W. (2014). Simulation of grain–straw separation by Discrete Element Modeling with bendable straw particles. *Computers & Electronics in Agriculture*, Vol 101, issue 2, pp. 24-33;

[9] Yanlong Han, Fuguo Jia, Yurong Tang, Yang Liu, Qiang Zhang. (2014). Influence of granular coefficient of rolling friction on accumulation characteristics. *Acta Physica Sinica*, Vol 63 , issue 17, pp. 173-179;

[10] Fuguo Jia, Yanlong Han, Yang Liu, Yinping Cao, YuFei Shi, Lina Yao, Hui Wang. (2014). Simulation prediction method of repose angle for rice particle materials. *Transactions of the Chinese Society of Agricultural Engineering*, Vol 30, issue 11, pp. 254-260;

[11] Fanyi Li, Jian Zhang, Bo Li, Jun Chen. (2016). Calibration of parameters of wheat required in discrete element method simulation based on repose angle of particle heap. *Transactions of the Chinese Society of Agricultural Engineering*, Vol 32, issue 12, pp. 247-253;

[12] Santos, K .G.，Campos, A.V .P., Oliveira ,O .S, Ferreira L V. (2015). Dem simulations of dynamic angle of repose of acerola residue: a parametric study using a response surface technique. *Blucher Chemical Engineering Proceedings*, Vol 1, issue 2, pp. 11326－11333;

[13] Quanchun Yuan, Liming Xu, Jiejie Xing, Zhuangzhuang Duan, Shuai Ma, Changchang Yu, Chen. (2018). Parameter calibration of discrete element model of organic fertilizer particles for mechanical fertilization. *Transactions of the Chinese Society of Agricultural Engineering*, Vol 34 , issue 18, pp. 21-27;

[14] Fei Peng, Hongying Wang, Fang, Yude Liu. (2018). Calibration of Discrete Element Model Parameters for Pellet Feed Based on Injected Section Method. *Transactions of the Chinese Society for Agricultural Machinery*, Vol 49, issue 4, pp. 140-147;

[15] Tao Zhang, Fei Liu, Manquan Zhao, Yueqin Liu, Fengli Li, Qian Ma, Yong Zhang, Peng Zhou. (2017). Measurement of physical parameters of contact between soybean seed and seed metering device and discrete element simulation calibration. *Journal of China Agricultural University*, Vol 22 (9), pp. 86-92.

EXPERIMENT ON IMPACT DAMAGE OF CASTOR CAPSULE AND ITS INFLUENCING FACTORS OPTIMIZATION
/
蓖麻蒴果冲击损伤试验及影响因素优化研究

Hou Junming, Yang Yong, Zhu Hongjie, Hu Weixue [1]
Shenyang Agricultural University, College of Engineering / China
Tel: +8618202412618; E-mail: junming_hou@163.com
DOI: https://doi.org/10.35633/inmateh-61-10

ABSTRACT

Castor is an important oil crop. Impact damage is critical in the process of castor capsule shelling, directly affecting the shelling effect of castor seeds. An experiment was taken to investigate it. To study the damage degree of castor capsule under the impact, water content, impact height, and impact angle were taken as test factors, and the maximum impact force and normal deformation were taken as test indexes. The combination optimization was carried out through the multi-objective genetic algorithm. The results show that the impact height has a significant effect on the maximum deformation (p<=0.01), and the water content and impact angle have a significant impact on the impact force (p<=0.05). The height and angle have a significant impact on the deformation (p<=0.01), and the water content has a significant impact on the deformation (p<=0.05).

摘要

蓖麻是重要的油料作物。蓖麻种子脱壳过程中大量存在冲击现象，直接影响蓖麻种子的脱壳效果。为研究蓖麻蒴果冲击时的损伤程度，以含水率、冲击高度、冲击角度为为试验因素，最大冲击力和法向变形量为试验指标，进行试验。通过多目标遗传算法进行组合优化。结果表明，碰撞高度对最大变形量的影响极显著(p<=0.01)，含水率和碰撞角度对冲击力的影响显著(p<=0.05)；碰撞高度和碰撞角度对变形量的影响极显著(p<=0.01)，含水率对变形量的影响显著(p<=0.05)。

INTRODUCTION

Castor is an important biomaterial, which is widely used in medicine, aviation, and other engineering fields. It is an essential oil crop in China, with a total output of ten million tons in China. During the process of shelling, repeated impacting occurs between the castor capsule and the shelled part. This directly leads to its damage in the process of shelling. The shelling damage affects the yield of crops for about 6% *(Sun et al., 2012)*. Therefore, it is vital to study the impact damage of the castor capsule.

At present, the research on the damage theory of agricultural materials is pervasive. *Huang et al. (2013)* regarded castor bean seeds as approximate spheres and analysed the mechanical model of castor bean under concentrated force by using the elastic thin shell theory. Based on the finite element theory *(Liu et al., 2012)*, numerical simulation of the compression load on the castor capsule was studied and the damage position, deformation, and stress of it was obtained. Based on the explicit dynamic simulation, PETRU M et al. (2012) conducted a static compression load test on jatropha seeds. They obtained the relationship between force, deformation, and energy of fruits with different maturity. ROMULI S et al. (2015) used the energy method to analyse the influence of the physical characteristics of jatropha seeds on the energy consumption of the shelling mode. Based on the collision exfoliation test, the mechanism of peanut seed shelling under the collision exfoliation method is complex *(Yang et al., 2017)*, experimental analysis on the variety, collision location, moisture content, and other factors was studied. Based on the discrete element method, *Zhao et al. (2013)* established the ellipsoid model of rice grains for simulation and used sensors for experimental analysis. The results showed that the normal force of rice grains in the collision test increased with the change of particle size ratio. To explore the damage degree of a cherry collision, *Zhou et al. (2016)* conducted a collision test on cherry to study the collision of collision materials, impact height, and collision

---

[1] *Hou Junming, Associate Prof., Ph.D. Eng.; Yang Yong., MS. Stud. Eng.; Zhu Hongjie, MS. Stud. Eng.; Hu Weixue, MS. Stud. Eng.*

angle on the damage. *Wang et al. (2018)* reconstructed the corn model by 3D reverse scanning technology and conducted collision analysis.

Although *Cao et al. (2010)* used the thin shell theory and the finite element method to analyse the effects of the physical and mechanical properties of castor seeds on the shelling, the studies on the collision characteristics of castor seeds are still relatively few. Because the material properties and geometric characteristics of castor seeds are different, the deformation and stress change dynamically in the process of shelling. Therefore, this study focuses on the damage theory of the castor capsule and its influence factors on the maximum impact force and normal deformation.

MATERIALS AND METHODS
Test materials

The typical castor capsule variety of ZheBi 4 and TongBi 17 are widely planted in the Tongliao areas of China. They were selected as the experimental material, which is shown in Fig.1. The test instrument is Vernier calliper, which is to measure the geometric dimension of castor seed. The mass of castor seed was measured by electronic balance. One hundred samples of castor capsules were taken for measurement. Through the statistical analysis of the geometrical dimensions of the castor capsule. It is concluded that the triaxial dimensions of the castor capsule are D_x=13.65~18.75mm, D_y=14.40~15.90mm, D_z=15.50~17.90mm.

The embedded drop impact testing bench is used for the experiment. Test machine includes USB-6009 data acquisition card, QLMH-P collision sensor (power supply 5-12 V, measuring range 0-1000N, output voltage 2 mV, strain gauge amplifier (power supply 5-9 V, amplification factor k=470).

(a) TongBi 17   *(b) ZheBi 4*

Fig. 1 - Different castor varieties

Test method

In the test of impacting, the sensor was placed in the centre of the test plate. And the castor capsule was placed on the centre of the sensor. In the beginning, the TLB-30B falling darts impact loading test bench was activated to adsorb iron impact block onto the drop darts. And then it was raised to a specified height. When the drop dart and the iron were at rest, the release button is pushed, the iron block would drop to the castor capsule. At the same time, the data of the collision force was transmitted to the signal analysis system through the USB6009 acquisition card and the strain gauge amplifier. The value of the output voltage of each collision force was recorded. By comparing the relationship between the maximum value of the collision force sensor and the test value, the collision force of the castor capsule would be obtained, as shown in Eq.(1).

$$F = k \frac{F_{max} v_{real}}{v_{max}} \tag{1}$$

Where: *F* is the maximum collision force received by the castor, [N]. *K* is the amplification factor of the amplifier circuit, *k*=470. F_{max} is the maximum range of the collision sensor, [N]. V_{real} is the actual measured output voltage, [mv]. V_{max} is the maximum output voltage of the amplifier, [mv]. V_{max} = 2 [mv].
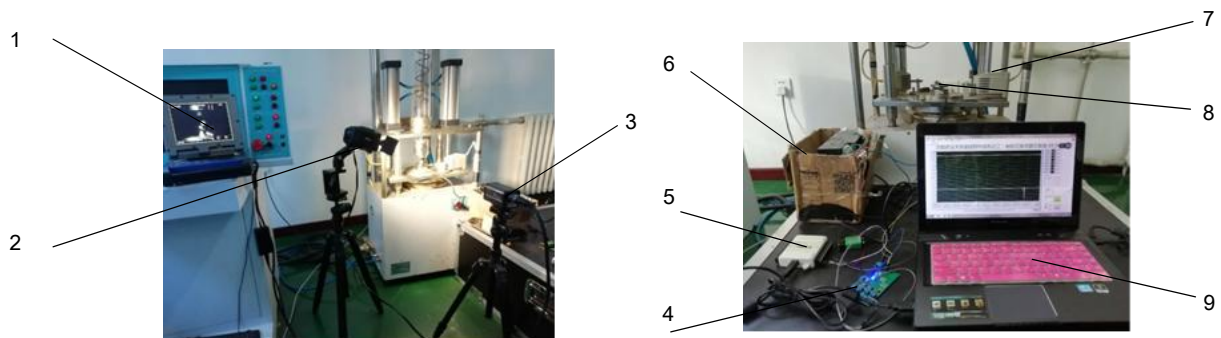
Fig. 2 - Castor capsule impact test device
1. display panel; 2. camera; 3 light sources; 4.USB transmission line; 5. collection card; 6. battery;
7. dart impact load test bench; 8. sensor; 9. signal analysis system

The impact process of the castor capsule was recorded by high-speed photographic equipment. Through image and video processing, the changes in normal deformation of castor fruit were analysed. The normal deformation of castor fruit was obtained through the conversion of pixel distance and actual distance. The impact test device of castor fruit is shown in Fig.2.

Based on the change of reasonable deformation amount of castor capsule, the deformation amount is:

$$u_z = \frac{|L_2 - L_1|}{|L_0|}$$

(2)

Where: u_z is the normal deformation quantity [mm]. L_0 is the large diameter of the castor capsule. L_1 and L_2 are the pixel distances initiation and end of the collision respectively [mm].

(a)   (b)
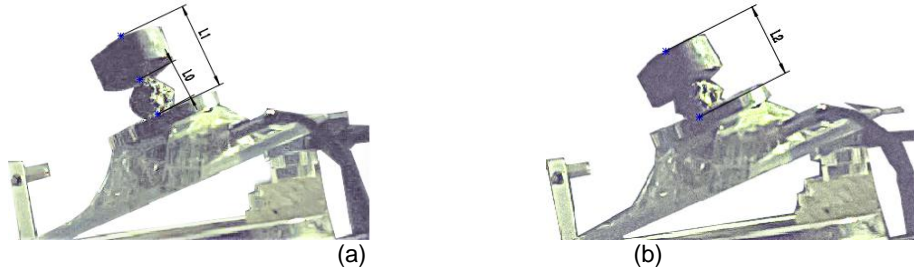
Fig. 3 - Variation of normal deformation before and after the collision of castor

(a) Initiation of the collision contact   *(b) End of the collision contact*

Test methods

The main factors affecting the impact of breaking shells include impact force, moisture content, impact angle, material parameters (thickness, elastic modulus), variety, etc. Considering the limitations of the TLB-30B falling impact load test bench, the moisture content, impact height, and the angle were selected as experimental factors. The maximum impact force and normal deformation of castor capsule were selected as experimental indexes. The impact experiment was carried out by using the standard ternary quadratic general rotation combination regression test, which is shown in Table 1.

In the experiment, the castor capsules of different varieties were gradually dried and evenly divided into five parts to measure the moisture content, which was 4.01%, 9.26%, 16.97%, 24.67%, and 29.92%, respectively. With the increase of impact angle, its maximum impact force and normal deformation are smaller. Therefore, the collision angle was selected as 4°-15°. According to the secondary general rotation combination regression test, the voltage peak data and video of each test data acquisition were recorded. The sampling frequency of the data acquisition system is 1024Hz, and the sampling time is 0.5s.

Table 1

Castor capsule collision test factor level coding

Coding space	Factor levels		
	Moisture content	Fall height	Collision Angle
	[%]	[mm]	[°]
-1.682	4.01	160	4
- 1	9.26	237	6
0	16.97	350	9
1	24.67	463	12
1.682	29.92	540	14

RESULTS

Castor TongBi 17 collision test

Based on the standard ternary quadratic universal rotating combination regression test scheme, an impact test was conducted on the castor TongBi 17. The maximum collision force y_1 and normal deformation y_2 were obtained, as shown in table 2.

Table 2

TongBi 17 castor experiment design plan and results

Water content x_1	Collision height x_2	Collision Angle x_3	The maximum collision force y_1	The normal deformation y_2
[%]	[m]	[°]	[N]	[mm]
1	1	1	370.692	2.246
1	1	- 1	383.245	2.405
1	- 1	1	332.766	0.981
1	- 1	- 1	344.202	1.035

Water content x_1	Collision height x_2	Collision Angle x_3	The maximum collision force y_1	The normal deformation y_2
- 1	1	1	410.021	1.935
- 1	1	- 1	413.521	2.147
- 1	- 1	1	310.734	0.904
- 1	- 1	- 1	350.523	1.121
1.682	0	0	365.585	1.785
1.682	0	0	325.479	1.805
0	1.682	0	313.617	0.627
0	1.682	0	459.575	2.548
0	0	1.682	371.021	1.681
0	0	1.682	345.473	1.402
0	0	0	366.223	1.532
0	0	0	369.787	1.427
0	0	0	351.649	1.498
0	0	0	353.457	1.544
0	0	0	356.543	1.475
0	0	0	364.202	1.526

According to the results in table 2, the regression model of the maximum impact force y_1, moisture content x_1, impact height x_2 and impact angle x_3 were obtained based on the principle of the least square method, as equation (3):

$$y_1 = 297.95 - 6.34x_1 + 38.89x_2 - 6.42x_3 - 9.87x_1x_2 + 8.05x_2^2 \tag{3}$$

To study the significant relationship between the maximum impact force and the indicators, variance analysis was performed on the test data in table 2. The significance level α was 0.05. The analysis results are shown in Table 3. It can be seen that $F=33.19>F_{0.01}(9,10)=4.95$ and $P<0.0001$, which indicates that the proxy model is very significant. The impact height has an extremely significant effect on the maximum impact force, while moisture content and collision angle have a significant effect on the maximum impact force. The interaction between moisture content and collision height has a significant effect on the maximum impact force.

Table 3

Analysis of maximum collision force variance for TongBi 17

Source	Sum of squares	Degrees of freedom	The mean square	The F value	P values
model	23538.4	9	2615.38	33.19	0.0001 * *
x_1	549.41	1	549.41	6.97	0.0247 *
x_2	20653.9	1	20653.9	262.1	< 0.0001 * *
x_3	563.38	1	563.38	7.15	0.0233 *
x_1x_2	765.23	1	765.23	9.71	0.0109 *
x_1x_3	0.53	1	0.53	0.006	0.9365
x_2x_3	23.06	1	23.06	0.29	0.6004
x_1^2	95.93	1	95.53	1.22	0.2957
x_2^2	934.91	1	934.91	11.86	0.0063 * *
x_3^2	24.91	1	24.91	0.32	0.5864
Residual item	788.06	10	78.81		
Loss of quasi item	651.94	5	130.39	4.79	0.0553
Error term	136.12	5	27.22		
Total error	24326.5	19			

Note: R=0.96, correction R=0.93.   Extremely significant level (p<0.01, significant level (p<0.05), not significant (p>0.05).

To further study the fitting accuracy of the agent model, the residual distribution curve of the maximum striking force test value, and the distribution diagram of the test value are shown in Fig.4. The predicted value obtained is shown in Fig.5. Among them, the biggest maximum residual value is 2.607, and the minimum residual value is 0.046. The biggest collision force of experiment and predicted values are on a straight line, which shows that the agent regression model can well reflect on the relationship of the factors.

According to the test data in table 2 and based on the principle of the least square method, the standard ternary-quadratic polynomial regression proxy model of castor TongBi 17 normal deformation was established as follows:

$$y_2 = 1.70 + 0.04x_1 + 0.6x_2 + 0.08x_3 + 0.068x_1x_2 + 0.093x_1^2 \tag{4}$$
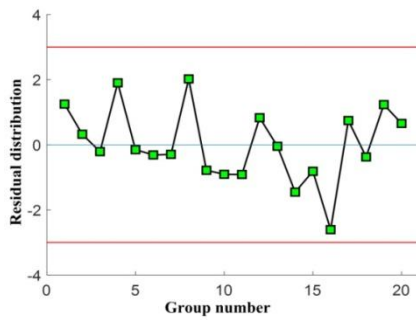
Fig. 4 - Maximum collision residual distribution of TongBi 17
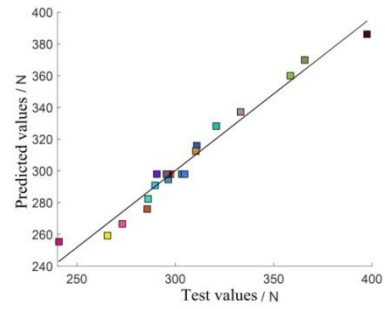
Fig. 5 - Distribution of test values and predicted values for TongBi 17

To study the significant relationship between the normal deformation y_2 and various test factors, variance analysis was conducted on the test data of castor TongBi 17. The significance level α was 0.05. The results are shown in Table 4.

Table 4

Analysis of the normal deformation variance of castor TongBi 17

Source	Sum of squares	Degrees of freedom	The mean square value	The F value	P values
model	5.25	9	0.58	147.4	< 0.001 * *
x_1	0.023	1	0.023	5.84	0.0363 *
x_2	4.96	1	4.96	1254	< 0.001 * *
x_3	0.091	1	0.091	22.93	0.0007 * *
$X_1 x_2$	0.037	1	0.037	9.42	0.0118 *
$X_1 x_3$	0.0075	1	0.0075	1.91	0.1967
$X_2 x_3$	0.0005	1	0.0005	0.15	0.7102
x_1^2	0.12	1	0.12	31.47	0.0002 * *
x_2^2	0.0055	1	0.0055	1.39	0.2650
x_3^2	8×10^{-7}	1	8.2×10^{-7}	2×10^{-4}	0.9888
Residual item	0.04	10	0.0039		
Loss of quasi item	0.03	5	0.0059	3.12	0.1185
Error term	0.0095	5	0.0019		
Total error	5.28	19			

Note: R=0.98, correction R=0.96, Extremely significant level (p<0.01), significant level (p<0.05). not significant (p>0.05).

Analysis of the normal deformation variance of castor TongBi 17 is shown in Table 4. The regression proxy model F=147.38 >F(9,10)=4.95, P<0.0001, which indicated that the proxy model is very significant. The correlation coefficient R=0.98 and the misfit term P=0.1185>0.05 indicate that the agent model had high fitting accuracy. The influence of impact height and angle on the normal deformation of castor ZheBi 17 is very significant. The influence of moisture content on the normal deformation of castor TongBi 17 is significant. The interaction of moisture content and impact height on the normal deformation is significant.
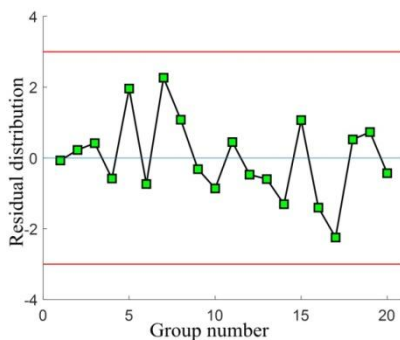
Fig. 6 - Residual distribution of normal deformation of Tongbi 17
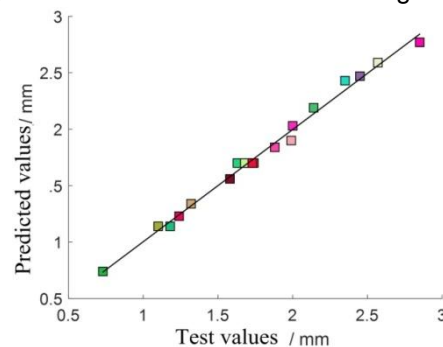
Fig. 7 - Distribution of the test value and the predicted value of the TongBi 17 deformation

The residual distribution curve of the standard deformation test value is shown in Fig.6. The distribution diagram of the test value and the predicted value are shown in Fig.7. It can be seen that the maximum residual is 2.266, and the minimum residual is 0.021. The experimental value and predicted value of the normal deformation are distributed on a straight line, which indicates that the regression agent model can well reflect the relationship between the normal deformation and the test factors.

Based on the same experimental scheme, the test factors of the castor ZheBi 4 castor fruit were at the same level as those of castor TongBi 17. The test factors of castor ZheBi 4 and castor TongBi 17 were the same. Among them, the test results of the maximum impact force y_3 and the normal deformation y_4 of castor ZheBi 4 are shown in Table 5.

Table 5

Castor TongBi 4 impact experiment design and results

Water content x_1	Collision height x_2	Collision Angle x_3	Maximum collision y_3	Normal deformation y_4
[%]	[m]	[°]	[N]	[mm]
1	1	1	350.732	2.331
1	1	- 1	367.136	2.474
1	- 1	1	300.031	1.083
1	- 1	- 1	316.104	1.149
- 1	1	1	380.426	2.033
- 1	1	- 1	390.734	2.255
- 1	- 1	1	300.484	1.047
- 1	- 1	- 1	310.695	1.258
1.682	0	0	345.866	1.186
1.682	0	0	315.732	1.984
0	1.682	0	275.819	0.627
0	1.682	0	430.214	2.748
0	0	1.682	343.381	1.802
0	0	1.682	323.692	1.202
0	0	0	330.293	1.632
0	0	0	325.764	1.567
0	0	0	320.466	1.705
0	0	0	336.047	1.655
0	0	0	320.732	1.579
0	0	0	326.415	1.603

Based on the principle of the least square method, the standard ternary quadratic polynomial regression model between the maximum impact force and water content, impact height and impact angle of castor capsule was established in equation (5)

$$y_4 = 1.62 + 0.053x_1 + 0.59x_2 - 0.12x_3 + 0.07x_1x_2 + 0.098x_1^2 \tag{5}$$

To study the significant relationship between the maximum impact force and the test factors, variance analysis was carried out for the test data of the maximum impact force in Table 5. The significance level α is 0.05, and the analysis result is shown in Table 6.

Table 6

Analysis of the variance for castor ZheBi 4

Source	Sum of squares	Degrees of freedom	The mean square value	The *F* value	*P values*
model	22876.3	9	2541.81	32.48	< 0.001 * *
x_1	717.88	1	717.88	9.17	0.0127 *
x_2	19904.4	1	19904.4	254.4	< 0.001 * *
x_3	542.93	1	542.93	6.94	0.0250 *
x_1x_2	424.10	1	424.10	5.42	0.0422 *
x_1x_3	17.87	1	17.87	0.23	0.6430
x_2x_3	0.023	1	0.023	0.002	0.9867
x_1^2	28.55	1	28.55	0.36	0.5593
x_2^2	1236.41	1	1236.41	15.80	0.0026 * *
x_3^2	81.31	1	81.31	1.04	0.3321
Residual item	782.50	10	78.25		
Loss of quasi item	606.83	5	121.37	3.45	0.0999
Error term	175.67	5	35.13		
Total error	23658.8	19			

Note: R=0.96, correction R=0.93, extremely significant level (p<0.01). 22* significant level (p<0.05). not significant (p>0.05).

It can be seen in Table 6 that the regression model $F=32.48 > F_{0.01}(9,10)=4.95$, $P<0.0001$. It suggested that the agent model is very significant. The influence of impact height on the maximum impact force of castor ZheBi 4 is very significant. The influence of moisture content on the maximum impact force of castor Zheri 4 is significant. The influence of impact angle on the maximum impact force is significant, and the interaction of moisture content and impact height on the maximum impact force is significant.
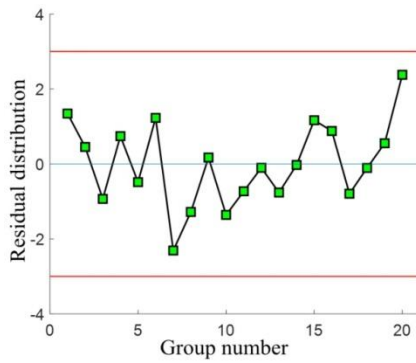
Fig. 8 - Distribution of the maximum residual of ZheBi 4
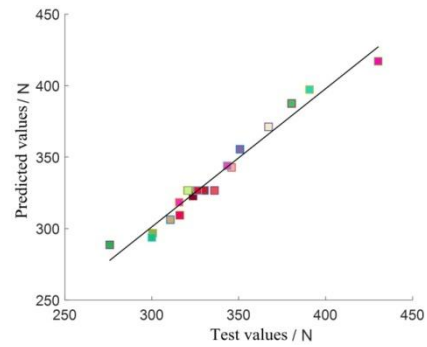
Fig. 9 - Distribution of the maximum collision force test value and the predicted value of ZheBi 4

To further study the fitting accuracy of the agent model, the residual distribution curve of the maximum striking force test value and the distribution diagram of the test value and the predicted value were obtained as shown in Fig.8 and Fig.9. The results indicated that the regression agent model could well reflect the relationship of the factors. Based on the principle of the least square method, the regression model of the standard ternary quadratic polynomial between the normal deformation y_2 and the moisture content x_1, the collision height x_2 and the collision angle x_3 are obtained as equation (6):

$$y_4 = 1.62 + 0.053x_1 + 0.59x_2 - 0.12x_3 + 0.07x_1x_2 + 0.028x_1x_3 - 0.011x_2x_3 + 0.098x_1^2 + 0.023x_2^2 - 0.042x_3^2 \qquad (6)$$

The significant relationship between the normal deformation and the experimental factors was studied. Analysis of normal deformation variance is shown in table 7.

Analysis of normal deformation variance for castor ZheBi 4   Table 7

Source	Sum of squares	Degrees of freedom	The mean square value	The F value	P values
model	5.30	9	0.59	101.9	< 0.0001 **
x_1	0.039	1	0.039	6.64	0.0276*
x_2	4.83	1	4.83	829.6	< 0.0001 **
x_3	0.20	1	0.20	34.27	0.0002 **
x_1x_2	0.044	1	0.044	7.47	0.0211*
x_1x_3	6×10^{-3}	1	6.2×10^{-3}	1.08	0.3238
x_2x_3	9×10^{-4}	1	9.6×10^{-4}	0.17	0.6921
x_1^2	0.14	1	0.14	23.93	0.0006**
x_2^2	7×10^{-3}	1	7.7×10^{-3}	1.33	0.2749
x_3^2	0.026	1	0.026	4.44	0.0613
Residual item	0.058	10	5.8×10^{-3}		
Loss of quasi item	0.045	5	8.9×10^{-3}	3.38	0.1038
Error term	0.013	5	2.6×10^{-3}		
Total error	5.36	19			

Note: R=0.98, correction R=0.97, extremely significant level (p<0.01);22Significant level (p<0.05); not significant (p>0.05).

It can be seen that $F=101.9 > F_{0.01}(9,10)=4.95$, $P<0.0001$, which suggested that the agent model is very significant. The correlation coefficient $R^2=0.98$ and lost quasi item $P=0.1038>0.05$, which shows that the fitting accuracy is higher. The influence of impact height on the normal deformation is very significant, the influence of impact angle and moisture content on the normal deformation is very significant, and the interaction of water content and impact height on the normal deformation is significant.

Effect of interaction on collision damage of castor fruit

Based on experiment results, it can be seen that the interaction of water content and falling height had a significant effect on the maximum impact force and normal deformation. The interaction of moisture content and angle had no significant effect on the maximum impact force and deformation, while the interaction of impact height and impact angle has no significant effect on the maximum impact force and normal deformation. Therefore, the response surface of the interaction of water content and impact height of castor TongBi 17 and castor ZheBi 4 on their maximum impact force and normal deformation is shown in Fig.12 and Fig.13.

In the process of impacting, the interaction between moisture content and impact height affected the maximum impact force and normal deformation.

When the impact height was constant, with the increase of moisture content, the maximum impact force increased first and then decreased, and the normal deformation increased slightly. It is because the impact force increases before the shell is broken. When the shell is broken, the impact force becomes smaller. When the water content was constant, the maximum impact force and normal deformation increased significantly with the increase of impact height. Therefore, reasonable control of the maximum impact force can improve the shelling result. It is of considerable significance to reduce the shelling damage rate.
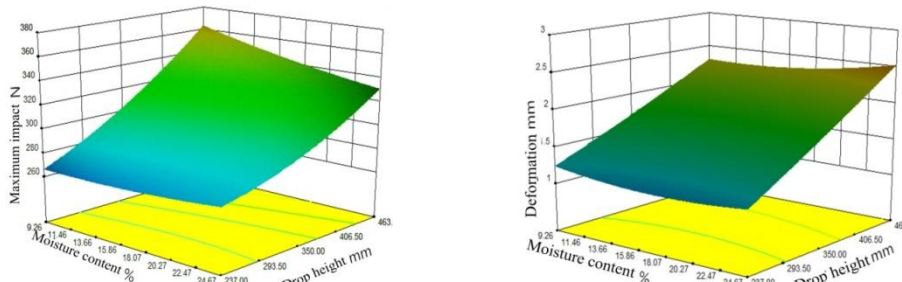
Fig.12- Effect of moisture content and drop height interaction on TongBi 17
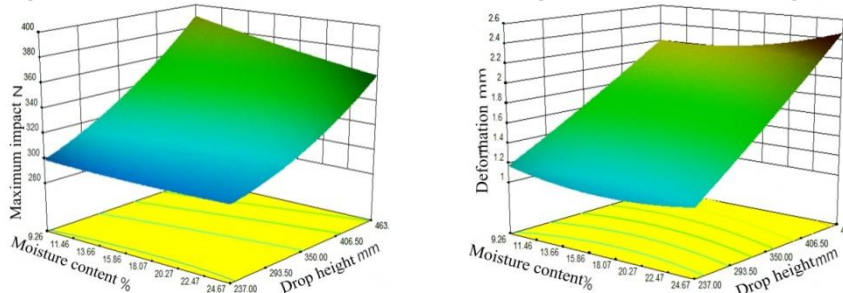
Fig. 13 - Effect of moisture content and drop height interaction on ZheBi 4

Evaluation of collision damage and multi-objective optimization

To study the sensitivity of parameters to break the shell, the optimal ratio of shelling parameters was determined. The moisture content x_1, impact height x_2 and collision angle x_3 were taken as optimization variables. The maximum impact force and normal deformation were carried for optimization, and the multi-objective genetic algorithm was used to calculate the optimal value. The multi-objective optimization model is shown in equation 7.

$$\begin{array}{c} max\ Y_1=f_1(x) \\ min\ Y_2=f_2(x) \\ S.t.\ \ l_b{\leq}x_i{\leq}u_b\ \ i=1....n \\ S.t.\ l_b\ x\ or\ less\ u_b\ or\ less\ I=1..._i\,n \end{array} \qquad (7)$$

where: Y_1-normal deformation amount [mm]. Y_2- maximum collision force [N], l_b-parameter lower bound; u_b - upper bound of parameters. n - parameter dimension.

Evaluation index of castor capsule collision damage

The damage degree of castor under different experimental conditions was used as the damage index to make the classification. Then the best parameters of the breaking shell of castor capsule were found. The classification of damage degree is shown in Table 8, and the actual impact results are shown in Fig.14.

Evaluation criteria for collision damage of castor   **Table 8**

Varieties	Collision force [N]	Normal deformation [mm]	Damage index	Damage level number
TongBi 17	[0, 290]	[0,1.1]	Undamaged (elastic deformation)	I
	[290, 350]	[1.1, 2.3]	Moderate injury (three ventricular ruptures)	II
	[350 ~]	[2.3 ~]	Severe injury (complete rupture)	III
ZheBi 4	[0, 310]	[0,1.2]	Undamaged (elastic deformation)	I
	[310, 360]	[1.2, 2.1]	Moderate injury (three ventricular ruptures)	II
	[360 ~]	[2.1 ~]	Severe injury (complete rupture)	III

| (a) Damage level Ⅰ | (b) Damage level Ⅱ | (c) Damage degree Ⅲ |

Fig. 14 - Classification of collision damage levels of castor

Multi-objective genetic algorithm optimization

In the actual collision of the castor capsule, the collision of falling height on the maximum collision force and deformation of castor fruit is very significant. To improve the efficiency of the castor shelling machine, reduce the damage rate, the maximum collision force of castor fruit must be smaller. Based on the strategy of elitist rapid nondominated sorting genetic algorithm (NSGA-II), the maximum collision force and deformation of combination optimization is the following.
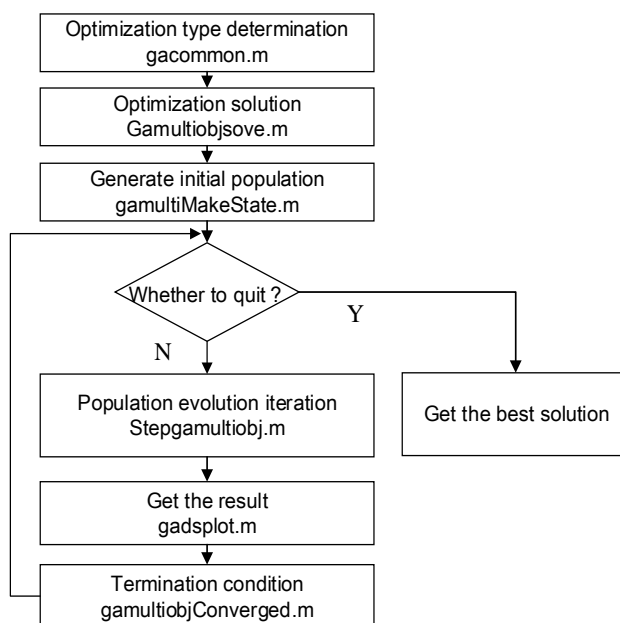
Fig. 15 - Multi-objective genetic algorithm optimization process

The optimal front-end individual coefficient ParetoFraction is 0.3, the Population size is 100, the maximum evolutionary algebra is 200, the stop algebra is 200, and the deviation of the fitness function is 1e-100.

Table 9

Optimal combination of the parameters for collapsing and shelling of castor

Varieties	The moisture content	Collision height	Collision Angle	Maximum collision force	Normal deformation
	[%]	[mm]	[°]	[N]	[mm]
ZheBi 4	4.2494	361.72	5.9906	351.0137	1.9627
TongBi17	4.3006	353.51	0.2433	347.9855	2.2786

The multi-objective optimization results are shown in Table 9. Under the optimum condition of castor capsule breaking, the difference between the maximum impact force of TongBi 17 and ZheBi 4 is 1.67% and 0.86% respectively. When the water content, collision height, and collision angle are similar, the maximum impact force of TongBi 17 is smaller, and the normal deformation is the larger. Therefore, castor ZheBi 4 is more difficult to shell than castor TongBi 17.

CONCLUSIONS

From the analysis of the experiment, it can be seen that the impact height has a significant impact on the maximum deformation($p <= 0.05$), and the moisture content and impact angle have a significant impact on the force($p <= 0.05$). The influence of impact height and angle on deformation is very significant($p <= 0.01$), and the influence of moisture content on deformation is significant($p <= 0.01$).

According to the response surface analysis, when the impact height is constant, with the increase of moisture content, the maximum impact force increases first. It then decreases, and the normal deformation rises slightly. When the moisture content is constant, the maximum impact force and normal deformation increase significantly with the increase of impact height. The difference between the maximum impact force of the castor capsule between castor TongBi 17 and castor ZheBi 4 was 7.63%, and the difference between the maximum normal variation was 3.51%.

The difference between the maximum impact forces of castor Tongli 17 and castor ZheBi 4 was 1.67% and 0.86% respectively. In the case of similar water content, collision height, and collision angle, the impact force of TongBi 17 is the smallest, and the normal deformation is the largest. Therefore, castor ZheBi 4 is more accessible to shell than castor TongBi 17.

ACKNOWLEDGEMENT

REFERENCES

[1] Sun Z.J., Lv L.Y., Wu Y.P., (2012), Development of castor bean industry: from planting to utilization. *Journal of China agricultural university*, Vol. 17, Issue 06, pp.204-214;

[2] Huang Z.H., Cheng X.X., Li C.Z., Xiao Z.H., Shi L.L., (2013), Research on mechanical model of castor bean nut husking and its main influencing factors. *Journal of Shenyang agricultural university*, Vol. 44, Issue 02, pp. 185-189;

[3] Liu R.K., Cheng X.X., Xiao Z.H., Li C.Z., Huang Z.H., Ye H.Q., (2015), Finite element simulation of mechanical properties of capsule of castor. *Chinese journal of cereals and oils*, Vol. 30, Issue 05, pp. 62-66;

[4] Petru M., Novák O., Herák D., et al., (2012), Finite element method model of the mechanical behaviour of Jatropha curcas L. seed under compression loading. *Biosystems Engineering*, Vol.111, Issue 04, pp.412-421;

[5] Romuli S., Karaj S., Müller J., (2015), Influence of physical properties of Jatropha curcas L. seeds on shelling performance using a modified disc mill. *Industrial Crops and Products*, Vol. 77, pp.1053-1062;

[6] Yang Y.Z., Gu B.L., Liu S.S., Zhang Y.H., Liang T.H., (2017), Impact mechanical properties test of peanut pod. *Chinese journal of agricultural mechanization*, Vol. 38, Issue 04, pp.53-57;

[7] Cheng X.L., Gao L.X., Liu M.G., Wang R.L., Na X.J., (2009), Mechanical properties test of peanut shell-shock. *Journal of Shenyang agricultural university*, Vol. 40, Issue 01, pp.111-113;

[8] Zhao C., Li Y.M., Chen Y., et al., (2013), Study on the Collision Mechanical Properties of Rice Grains. *Chinese Journal of Agricultural Machinery*, Vol. 44, Issue 06, pp.88-92;

[9] Zhou J., He L., Karkee M. et al, (2016), Effect of catching surface and tilt angle on bruise damage of sweet cherry due to mechanical impact. *Computers & Electronics in Agriculture*, Vol. 121, Issue C, pp.282-289;

[10] Hoffmann C., (2018), Sugar beet from field clamps - harvest quality and storage loss. *Zuckerindustie*, Vol. 143, Issue 11, pp. 639-647, Berlin/Germany;

[11] Wang J.X., Zheng D.C., Cui Q.L., Xu S.H., Jiang B.Y., (2019), Study on Tensile Mechanical Property and Microstructure of Fruit and Vegetable Peels. *INMATEH Agricultural Engineering*, Vol. 59, Issue 03, pp.227-236;

[12] Singh H., Meghwal M., (2019), Physical and thermal properties of various ajwain (Trachyspermum ammi L.) seed varieties as a function of moisture content, *Journal of Food Process Engineering*, pp.e13310.

[13] Iyilade I.A., Aviara N.A., Aremu A.K., Oyeniyi S.K., (2019), Effect of moisture content on physical properties of bush mango (Irvingia gabonensis) nut, *Agricultural Engineering International: CIGR Journal,* Vol.20(4), pp.221-226.

PIG FACE IDENTIFICATION BASED ON IMPROVED ALEXNET MODEL
/
基于改进 *AlexNet* 模型的生猪脸部识别

Hongwen Yan, Qingliang Cui*, Zhenyu Liu [1]

College of Information Science and Engineering, Shanxi Agricultural University, Taigu / China
Tel: +86-0354-6289253; E-mail: qlcui@126.com
DOI: https://doi.org/10.35633/inmateh-61-11

ABSTRACT

Individual pig identification technology is the precondition of precise breeding. Taking pig face as the study point, this article puts forward a pig face identification method based on improved AlexNet model and explores the influence of training batch size on the performance of the model. Spatial attention module (SAM) is introduced in AlexNet model to compare the performance of the AlexNet model and the improved model on the training set and the validation set. The study shows that the improved AlexNet model can achieve higher precision rate under different training batch sizes and has higher convergence rate and robustness, with an identification precision rate reaching 98.11%, and a recall rate and f1 value reaching 98.03% and 98.05%. When the training batch sizes are 16, 32, and 64 respectively, the test time of the model, which represents its operating efficiency, improves by 1.99%, 2.36% and 10.31%, respectively, showing better performance in pig face identification. The test results show that different batch sizes have a certain influence on the prediction results of the model, while no fixed relationship.

摘要

生猪个体识别技术是实现精准养殖的前提，本文以猪脸为研究点提出基于改进 AlexNet 模型的猪脸识别方法并探究训练批大小对模型性能影响，在 AlexNet 模型中引入空间注意力模块（SAM），比较 AlexNet 与其改进模型在训练集及验证集上的性能，研究表明，改进的 AlexNet 模型在不同训练批大小情况下均可取得较高准确率，具有更快的收敛速度与鲁棒性，识别准确率达到 98.11%，召回率与 f1 值分别达到 98.03%、98.05%，其在训练批大小分别为 16、32、64 情况下，表征其运行效率的模型测试时间分别提高了 1.99%，2.36%、10.31%，可对生猪脸部进行更有效识别，试验结果表明，不同的批大小对模型预测结果有一定影响，不存在固定关系。

INTRODUCTION

Effective individual pig identification is the precondition of intelligent pig breeding. Pig face includes pig's eyes, pig's nose and other biological characteristics that are of natural identifiability. Based on these characteristics, pigs can be individually identified. The face identification technology has been widely used in the field of individual identification for its advantages such as non-invasiveness, low cost and operability.

Radio-frequency identification (RFID) is a widely-used technology in the field of individual pig identification *(Maselyne et al., 2014; Hahnel et al., 2016)*. With its shortcomings becoming increasingly prominent, researchers turned to the machine learning method to conduct contour extraction and behavioural detection to study the pigs, laying emphasis on the aspects such as contour extraction *(Ma et al., 2016; Guo et al., 2015, Li et al., 2017)*, climbing and attacking behaviours *(Chen et al., 2017)*, standing and lying posture *(Kim et al., 2017)*, and behaviour tracking *(Peter et al., 2011)*.

Recently, some scholars have used deep learning technology to conduct image segmentation and individual target detection to pigs *(Psota et al., 2019; Zhang et al., 2018, Ju et al., 2018)*.

However, as for individual pig identification based on convolution network, only *Wang et al. (2018)* effectively fused the feature integration method with features extracted from deep convolutional neural network such as DPN131 *(Chen et al., 2017)*, InceptionV3 *(Szegedy et al., 2016)* and Xception *(Chollet, 2017)* based on transfer learning method, achieving an identification precision rate of 96.41%.

---

[1] *Hongwen Yan, As. Ph.D. Lect. Eng.; Qingliang Cui*, Prof. Ph.D. Eng.; Zhenyu Liu, Prof. Ph.D. Eng.*

Hansen et al. (2018) combined the feature extraction results of VGG-Face model *(Parkhi et al., 2015)* and used Grad-CAM *(Ramprasaath et al., 2016)* activation-resembling mapping to distinguish the adhered pigs, achieving an identification precision rate of 96.7%. There is a lack of open data set in the studies of this direction, and no complete research direction has been formed yet.

Based on these, this paper used the principle of convolutional neural network to build and improve the AlexNet model, so as to explore the impact of batch size on performance of the model, and have individual identification of the pigs with pig face as the study point to provide reference for accurate breeding of pigs.

MATERIALS AND METHODS
Sample collection

As shown in Figure1, the experimental materials of this study were collected on a small farm in Wujiazhuang, Taigu County, Shanxi Province, China (112º53′ E, 37º42′ N), and the sampling date was in March 2018.

Pictures of a total of 10 pigs were collected, including 684 training samples, 77 validation samples and 254 test samples.

Fig. 1 - Pig Samples

To avoid memory overflow, batch training method was taken to compare the AlexNet model and its improved model on the training set and validation set. The training batch size was set to be 16, 32 and 64 respectively, and the batch size of validation set and that of training set were synchronous. The iteration round number was set to be 100. After each round of iteration, the model evaluation index values were calculated on the test set.

Structure of base model

With an accuracy rate of 57.1% and a top-5 identification rate of 80.2%, AlexNet *(Krizhevsky et al., 2012)* proposed by Alex Krizhevsky won the first prize in ImageNet competition in 2012. The structure of AlexNet model is as shown in Figure 2.

The model contained four layers, and each level was composed of different amounts of convolution layer and pooling layer. A total of 9 weight layers were there, among which 5 convolution layers and 4 fully connected layers were included.

AlexNet jointed the LRN layer after the 1st and 2nd convolution layer so as to do local normalization processing to the area near the activated neurons, but follow-up studies indicated that after joining LRN layer, the effect got reduced rather than increased.

Therefore, the LRN layer was removed in this experiment, the model's convolution and pooling layer feature map uses an effective filling mode, and the final convolution layer at each level was connected to the maximum pooling layer, and the each weight layer used ReLU activation function to nonlinearize linear operations after completion of the corresponding operation.

Since the fully connected layer contained many parameters, dropout mechanism was introduced in the fully connected layer to prevent model overfitting.
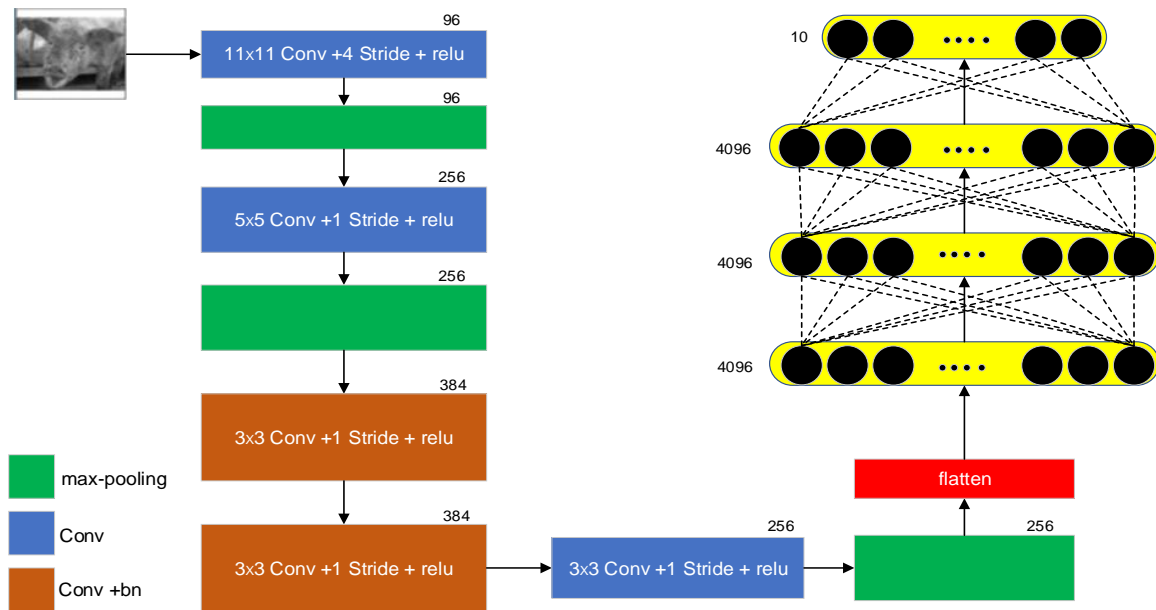
Fig. 2 - Structure of AlexNet Model

Note: max-pooling in the figure refers to the maximum pooling operation, conv refers to the conventional convolution operation, conv+bn refers to jointing normalized operation in batch behind at the end of the conventional convolution operation, and figures above each module show the number of feature maps after the convolution operation is used. The Inside of each convolution module is represented in the form of 11×11 conv+4 stride+relu, in which 11×11 means both the width and the height of the convolution kernel are 11, while 4 means the step size of convolution operation, relu means that the linear result after convolution operation is nonlinearized by using relu activation function. The numbers 4,096 and 10 on the upper right indicate the number of nodes in the fully connected layer.

SAM module, the improved part of the model

      Deep web contains rich semantic information and can guide surface web in choice of information, so it can get more accurate resolution ratio information. SAM module combined with soft attention mechanism can capture rich information associated to context, also it can give different weight values to different positions on a feature map to strengthen the effective features. As shown in Figure 3, its specific operation went through the following three stages.
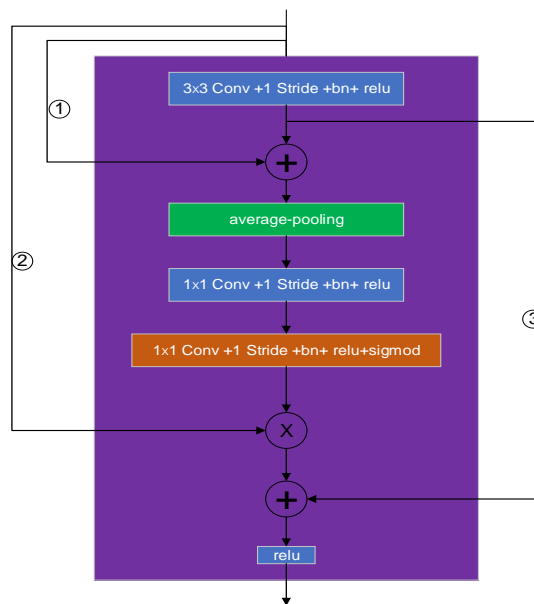
Fig. 3 - Spatial Attention Module (SAM)

*Note: ① shows the residual of the original feature, ② shows the product between the original feature and the weighted feature map, which may recalibrate the original feature, ③ shows the original feature after one 3*3 convolution, bn processing as well as relu nonlinear processing.*

(1) The surface web input went through 1 operation of convolution with a size of 3×3 and a step size of 1, batch normalization and activation function before the output of the middle layer was obtained. The surface layer input and the middle layer output were superimposed in operation *1* to be the input of step (2);

(2) After the global average pooling operation of output feature map in (1), the values at the same position of different channels were added and averaged to obtain the feature map with channel dimension of 1 and resolution size that was consistent with input to be the weight map of input feature map. In order to nonlinearize the global average pooling operation, the operations of two steps of 1×1 convolution, batch normalization and activation function were introduced. In step 1, the number of convolution kernels took any value. In the test, the values taken were the same as the number of channels in the input feature map in step (2), and ReLU was used as the activation function. In step 2, for the 1×1 convolution operation, Sigmoid activation function was selected to generate different regional characteristics. The number of convolution kernels must be the same as the number of channels of the input feature map in step (2) so as to facilitate the multiplication of subsequent feature maps. The final output result was taken as the output weight information of the middle layer, and the weighted surface layer input information was obtained by multiplying the weight information with the surface input via operation *2*;

(3) Finally, via operation *3*, the output of the middle layer and the result of step (2) were superimposed to get the output of SAM module, which was used as the input of subsequent operations.

Improved AlexNet module

Inspired by the application of attention mechanism in natural language processing and image segmentation field, SAM was introduced in the AlexNet model in the test to form the Attention-AlexNet model, so as to further improve the predictive performance of the model, whose structure is as shown in Figure 4.
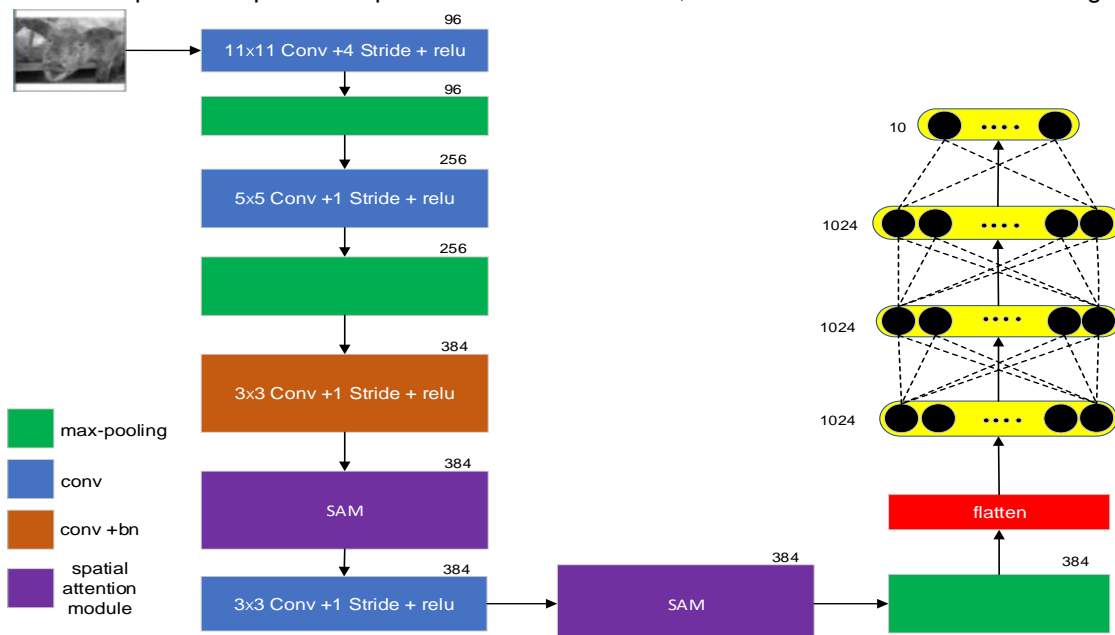
Fig. 4 - Structure of Attention-AlexNet Module

In Attention-AlexNet model, the structure of two levels in the front was the same as that of AlexNet model. After the front two-level operation, the input image was converted into 256 feature maps of size of 26×26. The Attention-AlexNet model contained 1 maximum pooling, 2 basic convolution operations and 2 SAM modules in the third level, where the second-level output was first made, a maximum pooling operation whose pooling kernel size was 3 and pooling step size was 2 before 256 feature maps of size of 12×12 were obtained. Then, 384 conventional convolutions whose convolution kernel size was 3×3 and step size was 1 were jointed, thus the feature map was converted to be 384 feature maps of size of 10×10 to be the first SAM module input. After SAM processing, the feature map was consistent with the input in size and number. After the first SAM output, 384 conventional convolutions whose size was 3×3 and step size was 1 were jointed to get 384 feature maps of size of 8×8.

In order to further strengthen the obviously characteristic area, SAM module was jointed again after the operation.

After the fourth layer, the flattening operation was jointed and three fully connected layers on which the number of neuron nodes was 1024, 1024 and 10 respectively, were jointed behind so as to greatly reduce the training parameters and improve the training speed.

Tests and result s analysis
Test parameter setting

In this study, python v3.5 language was used to construct the convolution network AlexNet and Attention-AlexNet models under the Keras framework with a video memory capacity of 6G. The construction was carried out in the GPU environment where the graphics card chipset was GeForce GTX TITAN, and the system adopted CentOS7.0.

Categorical_crossentropy in Keras was adopted as cost function; dropout mechanism was introduced to restrain neuron nodes from participating in the process of back propagation at probability of 0.4; EarlyStopping mechanism was used to prevent overfitting; Adam optimization model was adopted and the initial value of learning rate parameter was set to be 0.0001; ModelCheckpoint mechanism was used, thus it was able to judge whether the precision rate got improved when a training was completed. If improved, the current parameters shall be saved, otherwise the next round of training shall be carried out. To automatically modify the learning rate, ReduceLROnPlateau was introduced, and it was set that the learning rate would be reduced to 0.9 times the current learning rate when the loss function value of the validation set did not reduce in the 5 rounds of iteration process. The optimal parameters and structure could be obtained at the end of the training, and the pig face identification test could be carried out by using the training results.

RESULTS AND DISCUSSION

Figure 5 shows the relation curve between precision rate and loss functions of AlexNet model and Attention-AlexNet model under training set and validation set of different batch sizes, where Figure (5a)~Figure (5c) represents the performance of AlexNet model under batch sizes of 16, 32 and 64 respectively, and Figure (5d) ~ Figure (5f) represents the performance of Attention-AlexNet model under batch sizes of 16, 32 and 64 respectively.
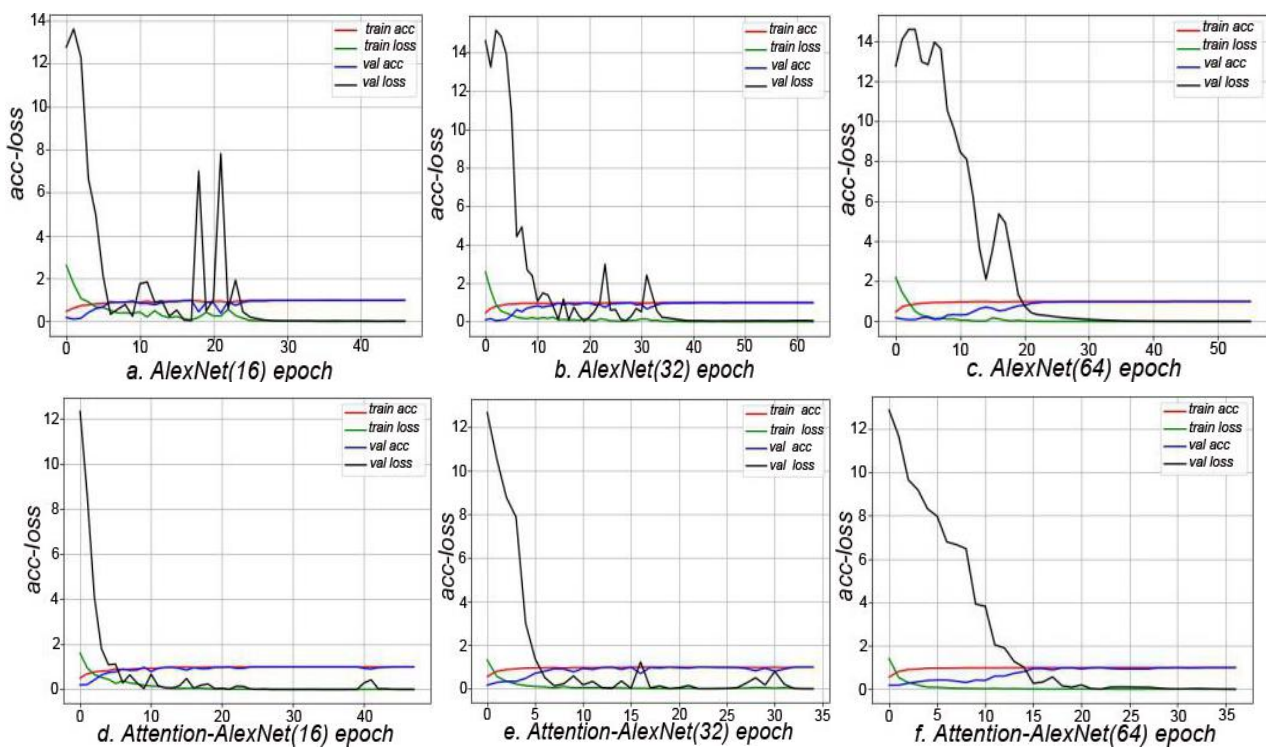
Fig. 5 - Iteration curve of AlexNet, Attention-AlexNet modules under different batch sizes

Note: 'acc–loss' represents the accuracy rate and loss function curve, 'train acc' represents the accuracy rate of the model on the training set, 'val acc' represents the accuracy rate of the model on the validation set, 'train loss' represents the loss rate of the model on the training set, and 'val loss' represents the loss rate of the model on the validation set, 'val' represents validation set and 'train' represents the training set.

As can be seen in Figure (5a), Figure (5c), for AlexNet model, in early iterations, the precision rate of training sets was all relatively low at the beginning but well above the validation precision rate. With the iteration going on, the precision rate of training set quickly reached the convergence condition. In Figure (5a), the 5th round of iteration tended to be smooth and stable; and in Figure (5b), the 4th round tended to be stable; in Figure (5c), the convergence rate of AlexNet became faster, and in the third round it had tended to balance. For the precision rate of validation set, the iteration converged after a certain number of rounds. In the early stage of the convergence, fluctuations were there, but they tended to be stable on the whole, and the stationary value finally held the line with the precision rate of training set, which showed that the AlexNet model applied to the data set of pig face in this test. For loss function, the loss function values of the validation set were far higher than those of training set at the beginning of the training iteration, and in the iteration process, drastic fluctuation appeared. The greater the fluctuation was, the more obvious the fluctuation of precision rate on the corresponding validation set was. With the iteration going on, when the batch sizes were 16, 32 and 64 respectively, convergence took place on the 25th, 35th and 30th rounds.

However, for loss function values in the training set, in the whole iteration process, under different batch sizes, excessive fluctuation did appear, and the trend had been in the direction of a decrease in its value. It can be seen from the relationship between precision rate and the value of the loss function that in the iteration rounds where the precision rate changed significantly, the value of loss function had significant change correspondingly and the two went in opposite directions.

As can be seen in Figure (5d)~Figure (5f), for Attention-AlexNet model, the precision rate of training set and the precision rate of validation set were increasing in the whole iteration process, and compared with AlexNet model, it converged more quickly. In terms of value change of loss function, in three kinds of cases, its value changed greatly in some parts in the iterative process, though compared with the AlexNet model, its fluctuation amplitude was relatively small, showing that the Attention-AlexNet model could achieve convergence condition much faster and it owned a small fluctuation amplitude.

Model efficiency analysis

In the performance evaluation of deep learning models, recall ratio, precision ratio and f1-score measurement indexes were adopted. In the classification task, the results were usually divided into true positive cases (TP), false positive cases (FP), true negative cases (TN) and false negative cases (FN). With the number of samples corresponding to TP, FP, TN and FN given, the precision ratio was defined as:

$$precision = \frac{TP}{TP + FP} \tag{1}$$

Recall ratio was defined as

$$recall = \frac{TP}{TP + FN} \tag{2}$$

Recall ratio was also called recall rate. Recall ratio and precision ratio changed in opposite trend. fl-score can measure the different preferences of these two indexes, and the formula was as follows:

$$f1 - score = 2 \times \frac{precision \times recall}{precision + recall} \tag{3}$$

where: *TP* represents the number of positive samples that are actually positive samples, [a];

FP represents the number of positive samples that are actually negative samples, [a];

FN represents the number of negative samples that are actually positive samples, [a].

The model was tested on the test set. In order to effectively measure the operating efficiency of different models, the training and test time was counted, and the results were as shown in Table 1.

Precision Rate, Recall Ratio, f1 Value, Training and Testing Time of Each Model   Table 1

Model	Precision [%]	Recall [%]	*f1-score* [%]	Test time[ms]	Training time[ms]
AlexNet(16)	97.19	98.03	98.05	5,123	211,951
AlexNet(32)	95.53	95.28	95.29	4,926	203,674
AlexNet(64)	97.48	97.24	97.28	4,518	198,631
Attention-AlexNet(16)	98.11	98.03	98.05	5,021	255,283
Attention-AlexNet(32)	97.48	97.24	97.29	4,810	194,913
Attention-AlexNet(64)	97.48	97.24	97.27	4,052	217,527

It can be seen in Table 1 that, in terms of precision rate, recall ratio and f1 value, under the same batch size, Attention-AlexNet model performed better than or not weaker than AlexNet model, and under the batch size of 16, the three evaluation indexes reached optimum, which benefited from the introduction of SAM module in Attention-AlexNet module. This module was able to give different weight values to element values at different locations in the feature map, so as to filter out the effective features for identification. In terms of operating efficiency, although the Attention-AlexNet model increased the training time of the model, after the Attention-AlexNet model is introduced into the SAM module, the model training time increases by 43,332ms, -8,761ms, and 18,896ms when the batch is 16, 32, and 64. However, the test time has been reduced by 102ms, 116ms, and 466ms under the three batch sizes. We can use the test time of the model to express its operating efficiency. The test efficiency of the model has been increased by 1.99%, 2.36%, and 10.31%, achieving good results.

CONCLUSIONS

In this study, the AlexNet model was constructed and improved to form the Attention-AlexNet model. The pig face identification results were compared between the two models, also the impact of batch size on the model performance was discussed. The conclusions are as follows:

(1) With the improved Attention-AlexNet model, pig face identification test was carried out, and its precision rate, recall ratio and f1 value reached 98.11%, 98.03% and 98.05% at most, increasing by 0.92 percentage points, 0.0% and 0.0% respectively than that of the AlexNet model, also its operating efficiency got increased under different batch sizes, increasing by 10.31% at most, showing that the improved Attention-AlexNet model can be used to identify the pig face more effectively.

(2) The batch size had a certain influence on the prediction result of the model, but there was no fixed relationship between the batch size and the performance of the model.

ACKNOWLEDGEMENTS

REFERENCES

[1]   Chen C., Zhu W.X., Cao J., Ma C.H., Huang W.J., Ruan C.Z., (2017), Image motion feature extraction for recognition of aggressive behaviours among group-housed pigs. *Computers and Electronics in Agriculture*, Vol.142, pp.380-387, Oxford/England;

[2]   Chen Y.P., Li J.A., Xiao H.X., Jin X.J., Yan S.C., Feng J.S., (2017), Dual path networks. *Advances in Neural Information Processing Systems*, pp.4470-4478, New York/USA;

[3]   Chollet F., (2017), Xception: Deep learning with depthwise separable convolutions. *Proceedings of the IEEE conference on computer vision and pattern recognition*, pp. 1251-1258, Hawaii/USA;

[4]   Guo Y.Z., Zhu W.X., Jiao P.P., Ma C.H., Yang J.J., (2015), Multi-object extraction from topview group-housed pig images based on adaptive partitioning and multilevel thresholding segmentation. *Biosystems Engineering*, Vol.135, pp.54-60, San Diego/USA;

[5]   Hahnel D, Burgard W, Fox D, Fishkin K., Philipose M., (2004), Mapping and localization with RFID technology. *IEEE International Conference on Robotics and Automation*, pp. 1015-1020, New Orleans, LA/USA;

[6]   Hansen M F, Smith M L, Smith L N, (2018), Towards on-farm pig face recognition using convolutional neural networks. *Computers in Industry*, Vol.98, pp. 145－152, Elsevier B.V. /Netherlands;

[7]   Ju M, Choi Y, Seo J, (2018), A Kinect-Based Segmentation of Touching-Pigs for Real-Time Monitoring. *Sensors*, Vol.18, Issue 6, pp.1746, Basel/ Switzerland;

[8]   Kim J, Choi Y, Ju M, (2017), Lying-Pig Detection using Depth Information. *ICACS '17 Proceedings of the International Conference on Algorithms, Computing and Systems*, pp.40-43, New York/USA;

[9]   Krizhevsky A, Sutskever I, Hinton G E., (2012), ImageNet classification with deep convolutional neural networks. *Advances in Neural Information Processing Systems 25 (NIPS 2012)*, pp.1097-1105, New York/USA;

[10]   Li Y, Sun L.Q., Zou Y.B., (2017), Detection method of moving object pig based on difference method and energy minimization. *International Agricultural Engineering Journal*, Vol.26, pp.428-438, Issue 3, Beijing/P.R.C.;

[11]   Ma C.H., Li M., Zhu W.X., Li H., Li X.C., (2016), Pig target extraction based on adaptive elliptic block and wavelet edge detection. *ICSPS 2016 Proceedings of the 8th International Conference on Signal Processing Systems*, pp.11-15, New York/USA;

[12]   Maselyne J, Saeys W, Ketelaere B D., (2014), Validation of a High Frequency Radio Frequency Identification (HF RFID) system for registering feeding patterns of growing-finishing pigs．*Computers and Electronics in Agriculture*, Vol.102, pp.10-18 , Oxford/England;

[13]   Parkhi O M, Vedaldi A, Zisserman A., (2015), Deep face recognition. *Proceedings of the British Machine Vision Conference (BMVC)*, Vol.1, Issue 3, pp.1-12, Swansea/UK;

[14]   Peter A, Gregersen T, Karstoft H., (2011), Development of a real-time computer vision system for tracking loose-housed pigs. *Computers and Electronics in Agriculture*, Vol.76, Issue 2, pp.169-174, Oxford/England;

[15]   Psota E T, Mittek M, Pérez L C., (2019), Multi-Pig Part Detection and Association with a Fully-Convolutional Network. *Sensors*, Vol.19, Issue 4, pp.852, Basel/ Switzerland;

[16]   Ramprasaath R S, Das A, Vedantam R., (2016), Grad-CAM: Why Did You Say That?. *arXiv preprint arXiv.* 1611.07450, New York/USA;

[17]   Szegedy C, Vanhoucke V, Ioffe S., (2016), Rethinking the inception architecture for computer vision. *The IEEE Conference on Computer Vision and Pattern Recognition (CVPR)*, pp.2818-2826, Las Vegas/USA;

[18]   Wang J.Z., Liu A.Z., Xiao J., (2018), Video-Based Pig Recognition with Feature-Integrated Transfer Learning. *Biometric Recognition*, pp.620-631, Basel/Switzerland;

[19]   Zhang L., Gray H, Ye X.J., (2018), Automatic individual pig detection and tracking in surveillance videos. *arXiv preprint arXiv*, 1812.04901, New York/USA.

TEST RESEARCH ON THE IMPACT PEAK FORCE
AND DAMAGE DEPTH OF POTATO
/
马铃薯碰撞峰值力与损伤深度试验研究

Weigang Deng, Chunguang Wang*, Shengshi Xie [1]
College of Mechanical and Electrical Engineering, Inner Mongolia Agricultural University, Hohhot, China
Tel: +86 13948815406; E-mail: nndjdwcg@126.com
DOI: *https://doi.org/10.35633/inmateh-61-12*

ABSTRACT

To analyse the influence factors of impact peak force (IPF) and damage depth (DD) on potatoes, the orthogonal test and single factor test were carried out on two potato varieties. The results showed that the IPF of Xiabodi was smaller and DD was greater than those of Gaoyuanhong. Potato mass had the greatest effect on IPF, and that of drop height on DD. The equations between IPF, DD and potato mass, drop height were obtained. Both IPF and DD impacting with steel were the largest, and the smallest with steel- rubber. With the increase of impact times, IPF decreased first and then increased, and DD increased gradually.

摘要

　　为了分析各因素对马铃薯碰撞峰值力和损伤深度的影响，分别对两个品种马铃薯进行了正交试验和单因素试验。结果表明：夏波蒂的碰撞峰值力小于高原红，损伤深度大于高原红。马铃薯质量对碰撞峰值力影响最大，下落高度对损伤深度影响最大。试验得出了碰撞峰值力和损伤深度与马铃薯质量和下落高度之间的方程式关系。马铃薯与不锈钢碰撞的峰值力和损伤深度最大，与不锈钢-橡胶最小。随着碰撞次数的增加，碰撞峰值力先减小后增大，损伤深度逐渐变大。

INTRODUCTION

Impact damage to potatoes is a common phenomenon during harvesting and post-harvesting operations (*Nikara et al, 2018; Yingwang Gao et al, 2018*), and it seriously affects the potato yield and causes a dual decline of potato appearance and quality that affect the development of the entire potato industry (*Romano et al, 2018; Strehmel et al, 2010*). Lots of studies have been performed to analyze the potato impact damage factors. Upon the research, many scholars have adopted testing as the main research method, and some scholars have used the finite element analysis method (*Caglayan et al, 2018；Celik et al, 2019; Yingwang Gao et al, 2018*). In the field of test research, Some researchers have used a pendulum impact device to study the potato impact response with different tuber temperature, tuber mass, initial height, and impact material, and described the equation of the damage depth and volume of the bruise spots (*Mathew and Hyde,1997; Shengshi Xie et al, 2018*). Other researchers have used the free fall device to study the speed, force, respiration and bruise volume of potatoes after impacting with different objects under different conditions (*Geyer et al, 2009; Qi Lu,2016; Rady and Soliman, 2015; Zhizhen Liu,2016*). Some researchers have used an instrumented potato to record the extent of impact and predicted the tissue discoloration in order to find the relationship between potato damage and harvest parameters (*Bentini et al, 2006; Canneyt et al, 2004*).

Based on these papers, the main research contents are the influence factors of potato impact damage and the evaluation indexes after potato injury, such as drop height, potato mass, potato temperature, impact material, potato variety, cultivation conditions, collision pressure, impact acceleration, potato damage volume, damage area, damage depth, and respiratory rate (*Shengshi Xie et al, 2018*). In the research of potato collision tests, the impact force was usually obtained by force sensor (*Qi Lu, 2016; Zhizhen Liu, 2016*), or by the signal measured by acceleration sensors (*Bentini et al, 2006; Geyer et al,*

---

[1] *Weigang Deng, As. Prof. Ph.D. Stud. Eng.; Chunguang Wang*, Prof. Ph.D. Eng.; Shengshi Xie, Lect. Ph.D. Eng.*

2009; Rady and Soliman, 2015). There has been no research on direct force measurements of potato impacts by hammers' force.

The study both researching on IPF and DD is rare and the relationship between IPF and DD has not been reported. No relevant information is available on the evaluating of significant factor to IPF. Therefore, this article aims to directly test the impact force by a force hammer, find the relationships between IPF and DD, and analyze the primary and secondary sequences of factors that affect both IPF and DD.

MATERIALS AND METHODS

- **Potato impact test system**

The potato impact test system is shown in Figure 1. The testing device included a bracket, height ruler, light rod and fixture. The testing system consists of a data acquisition device (AVANT - MI7016, Hangzhou Yiheng Technology Co., Hangzhou, China), an impact hammer (5800B5, 1.12 mv/N, DYTRAN Instruments Co., Ltd., USA) and a computer with a data acquisition software (Dynamic Signal Analysis, Hangzhou Yiheng Technology Co., Hangzhou, China). During the test, the potato was lifted to a certain height and released to collide with the hammer tip. The test system could detect the change of force during the collision process.
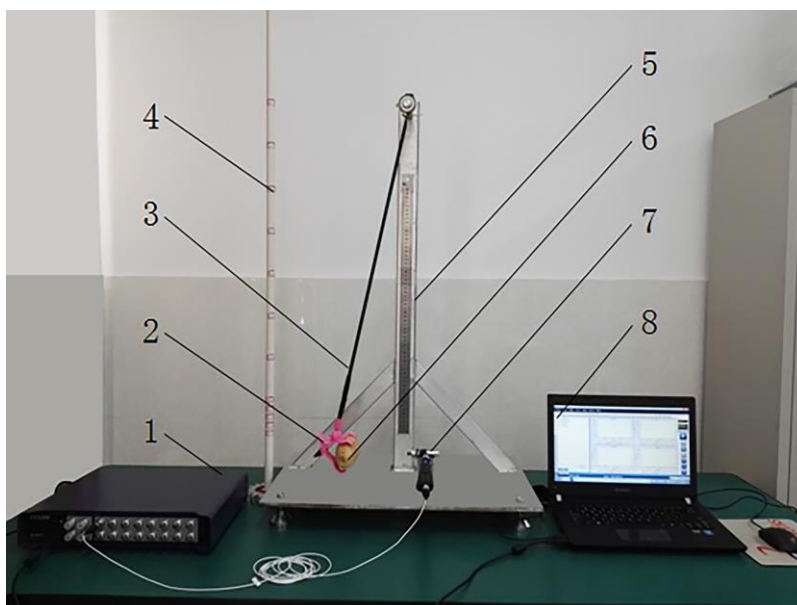
Fig.1 - Test equipment
1. Data acquisition device 2. Fixture 3. Light rod 4. Height ruler
5. Bracket 6.Potato 7. Impact hammer and fixing device 8. Computer

The original tip materials of the 5800B5 impact hammer are aluminum (m = 2.1 g), aluminum-hard plastic (m = 2.7 g) and aluminum-soft plastic (m = 2.7 g). The connection between the tip and the hammer body is threaded. During a mechanized potato harvest, the potato-soil separator is usually made of steel. To simulate field harvest conditions during the impact process, the steel tip of the impact hammer was covered with 3 mm either soft plastic, rubber or leather. The main factor influencing the test results was the mass of the hammer tip. Fine wire was wound on the hammer tip to make the mass close to that of the original. The tip masses of steel, steel-soft plastic, steel-rubber and steel-leather hammers were 2.11 g, 2.72 g, 2.69 g and 2.68 g, respectively.

- **Accuracy of hammer tips**

In order to check the accuracy of the changed hammer, the light rod and fixture shown in Figure 1 were removed, and a standard weight (m = 500 g) was connected to the test bracket with nylon wire and fine iron wire. An acceleration sensor with dimensions of Φ10 mm × 22 mm (1A102E, Jiangsu Donghua Testing Technology Co. Jiangsu, China) was attached to the weight. When the weight was lifted to a certain height and released, it collided with the impact hammer. The collision process followed the integral expression of Newton's second law.

$$\int_{t_1}^{t_2} F(t)\, dt = m \int_{t_1}^{t_2} a(t)\, dt \tag{1}$$

where:

t_1 is the impact start time; t_2 is the impact end time; $F(t)$ is the impact force; m is the impact mass; $a(t)$ is the impact acceleration.

From the beginning to the end of the collision, the data acquisition system detected the acceleration and force signals simultaneously. According to equation (1), the error between the impact hammer and the acceleration sensor was obtained. The test errors of the steel, steel-soft plastic, steel-rubber and steel-leather hammer tips were 4.25%, 4.7%, 5.17% and 4.77%, respectively.

● **Theoretical analysis of the collision process**

According to the kinetic energy theorem, the following relation is satisfied before collision.

$$mgh = \frac{1}{2} m v_1^2 \tag{2}$$

where:

m is the potato mass; g is the acceleration of gravity; h is the drop height; v_1 is the initial impact speed.

The impulse theorem is also satisfied during the collision process.

$$\int_{t_1}^{t_2} F\,dt = m\Delta v = m\,(v_1 - v_2) \tag{3}$$

where:

t_1 is the loading start time; t_2 is the impact contact time; F is the impact force; and v_2 is the potato impact speed in t_2.

When v_2 is zero, the potato compression displacement reaches its maximum, and t_s is the corresponding time. Equation (4) is derived from (2) and (3).

$$\int_{t_1}^{t_s} F\,dt = m v_1 = m\sqrt{2gh} \tag{4}$$

A potato can be characterized as a type of nonlinear viscoelastic material. According to the generalized Hertz theory, during a collision contact, the relationship between impact force and displacement can be written as follows (*Jankowski, 2006; Wenxi Wang et al, 2017*).

$$F = k\delta^n + c\dot{\delta} \tag{5}$$

where: F is the impact force; δ is the compression displacement; $\dot{\delta}$ is the compression speed; k is the stiffness coefficient and c is the damping coefficient.

The value of k and c depends on potato varieties and impact materials. Based on the above equations, both the IPF and DD of potato are related to the potato mass, drop height, potato varieties and impact materials.

● **Orthogonal tests**

In order to clarify the significance of the various factors on the impact force and damage depth of potato, the orthogonal test was conducted. The IPF and DD were taken as the evaluation index. Meantime, the potato mass (A), drop height (B), impact material (C), and impact times (D) with four levels were selected as factors in the experiments. Considering that the potato mass was mainly distributed in the range of 200-250g during harvest, the level ranges of factor A were determined. The level ranges of factor B were determined by the impact of potato dropping from different heights with the tip of hammer in the pre-test. The test factors and levels were shown in Table 1.

Table 1

Factors and levels

Level	Factor			
	Potato mass *A* [g]	Drop height *B* [mm]	Impact material *C*	Impact times *D*
1	150	40	steel	1
2	200	60	steel-soft plastic	2
3	250	80	steel-rubber	3
4	300	100	steel-leather	4

16 groups of orthogonal tests were designed with $L_{16}(4^5)$ program, and the test scheme was shown in Table 2. In order to analyze the influence of potato varieties on the test results, two potato varieties, Xiabodi and Gaoyuanhong, were selected for comparative test. The peel of Xiabodi is yellow and it is one of the main varieties planted in Inner Mongolia Autonomous Region. Gaoyuanhong is red, which is one of the main varieties planted in Ningxia Hui Autonomous Region.

According to the scheme in Table 2, three repeated impact tests were carried out. In each impact test, each group was repeated 5 times, and the average value of IPF was taken as the final result. After collision, the potato was left at room temperature for 48 hours, and the average of DD in each group, which was measured by slice method (*Baritelle et al, 2000; Blahovec, 2006*), was taken as the test result. To reduce the influence of curvature difference on the impact force, a flat surface with a small curvature in the middle part of potato was selected as the impact site. The results of repeated orthogonal tests were shown in table 3.

Table 2

Scheme of orthogonal experiments

Test number	Potato mass *A*	Drop height *B*	Impact material *C*	Impact times *D*	Free
1	1	1	1	1	1
2	1	2	2	2	2
3	1	3	3	3	3
4	1	4	4	4	4
5	2	1	2	3	4
6	2	2	1	4	3
7	2	3	4	1	2
8	2	4	3	2	1
9	3	1	3	4	2
10	3	2	4	3	1
11	3	3	1	2	4
12	3	4	2	1	3
13	4	1	4	2	3
14	4	2	3	1	4
15	4	3	2	4	1
16	4	4	1	3	2

Table 3

Results of orthogonal tests

Test number	IPF-Xiabodi F [N]			IPF-Gaoyuanhong F [N]			DD-Xiabodi S [mm]			DD-Gaoyuanhong S [mm]		
	F1	F2	F3	F1	F2	F3	s1	s2	s3	s1	s2	s3
1	54.08	50.46	59.61	61.31	66.64	64.46	3.24	3.74	3.12	1.9	1.88	1.78
2	42.80	44.98	47.17	52.82	53.05	45.18	3	4.20	3.14	1.3	1.7	1.66
3	43.17	39.95	35.55	49.66	50.54	50.12	3.35	3.58	3.93	2.86	2.76	2.7
4	66.67	63.53	64.94	72.35	71.86	66.55	5.44	4.88	4.62	4.4	4.22	4.3
5	49.03	47.82	42.75	66.89	57.16	69.13	2.74	2.56	2.68	2.2	2.38	2.06
6	56.04	52.02	76.26	79.29	80.55	73.40	4.12	4.38	4.88	4.22	4.18	4
7	48.90	46.31	55.44	58.01	64.06	62.91	4.42	3.44	3.66	1.8	1.52	1.22
8	63.68	55.85	57.19	60.06	57.96	62.26	5.26	5.12	5.58	3.44	4.16	3.8
9	80.18	74.64	77.79	82.98	88.46	83.8	3.44	3.22	3.38	1.4	1.66	1.26

Results of orthogonal tests

Test number	IPF-Xiabodi F [N]			IPF-Gaoyuanhong F [N]			DD-Xiabodi S [mm]			DD-Gaoyuanhong S [mm]		
	F1	F2	F3	F1	F2	F3	s1	s2	s3	s1	s2	s3
10	79.42	72.74	69.83	82.6	74.51	79.18	4.92	5.00	4.28	3.56	4	3.92
11	74.27	72.00	77.92	80.74	75.27	93.25	5.4	5.46	5.88	4.1	4.16	4.3
12	73.48	68.44	69.89	73.83	77.13	67.34	4.84	4.44	4.32	4.06	4.2	4.08
13	64.66	65.89	67.15	80.30	75.09	76.04	2.36	2.38	2.24	1.28	1.18	1.4
14	85.88	75.91	68.23	85.34	85.34	90.07	3.22	3.16	3.6	1.7	1.26	1.7
15	94.83	98.18	107.05	106.38	114.34	101.82	5.8	5.92	5.58	5.6	5.5	5.9
16	114.94	105.00	103.70	125.27	130.14	133.64	7.76	6.98	6.94	6.02	5.75	6.92

- **Single factor tests**

In order to obtain the mathematical model between potato mass, drop height and IPF, DD, a single factor test was designed. The evaluation index was IPF and DD. Each group of the test was repeated 10 times and the average value was taken as the test result. Considering the planting and distribution characteristics of potato in Inner Mongolia Autonomous Region, Xiabodi was selected as the experimental potato variety. The test schemes and results were shown in Table 4.

Test schemes and results

Test number	Potato mass / g	Drop height / mm	Impact material	Evaluation index	
				IPF [N]	DD [mm]
1	100	60	steel	40.53	1.53
2	150			61.76	2.53
3	200			71.09	3.1
4	250			86	3.83
5	300			108	4.87
6	200	20	steel	44.17	0
7		40		62	1.9
8		60		71.09	3.1
9		80		89.25	3.87
10		100		96.97	4.53

RESULTS

- **Orthogonal test results**

The range analysis results were shown in table 5. The order of influencing factors for IPF of Xiabodi was found to be: potato mass >impact times > drop height > impact material. For Gaoyuanhong, the order was as follows: potato mass > impact material >impact times > drop height. The orders for DD of both Xiabodi and Gaoyuanhong were the same as: drop height > impact material>impact times> potato mass.

It can be seen from the range analysis that the larger the potato mass and drop height of the two potato varieties, the greater the IPF and DD. Equation (4) showed that the impulse of the collision process was determined by the potato mass and drop height. The larger the potato mass and drop height was, the greater the impulse was. Based on the research of some scholars, it can be inferred that under the same impact material, the trend of potato impact force and the contact time were little affected by the changes of potato mass and drop height (*Bajema and Hyde, 1999; Qi Lu, 2016; Zhizhen Liu, 2016*).

Therefore, the larger the impact impulse was, the larger the IPF was. So, with the increase of potato mass and drop height, the IPF will increase correspondingly. Geyer M. O. analysed the influence of potato mass and drop height on the IPF through acceleration sensor (*Geyer et al, 2009*), which was consistent with the results in this paper. Xie Shengshi developed a model to predict the potato impact damage depth, which showed that DD increased with the increase of potato mass and drop height (*Shengshi Xie et al, 2018*). Baritelle found that the larger the potato mass was, the larger the DD was (*Baritelle et al, 2000*). Mathew and Hyde also found that the DD increased with the drop height (*Mathew and Hyde, 2013*).

The potato mass was the most significant factor to IPF and drop height was the most significant to DD. When potato mass and drop height increased, both IPF and DD increased. Therefore, during the cultivation of potato varieties, the moderate potato mass will be helpful to reduce the impact force during the harvest. In the process of potato harvesting, reasonable working parameters of the harvesting machine can reduce the drop height of potato on the separating device and effectively reduce the DD.

According to the range analysis in Table 5, the IPF of two potato varieties decreased in turn when they collided with steel, steel-soft plastic, steel-leather and steel-rubber.

Table 5

Range analysis of orthogonal experiment results

Evaluation object	Range source	Potato mass A	Drop height B	Impact material C	Impact times D
IPF-Xiabodi F [N]	K1	612.91	734.04	896.31	756.63
	K2	651.28	771.27	786.40	733.55
	K3	890.59	793.56	758.01	803.87
	K4	1051.40	907.31	765.47	912.13
	R	109.62	43.32	34.58	44.65
	Factor order	A>D>B>C			
IPF-Gaoyuanhong F [N]	K1	704.54	872.26	1063.97	856.44
	K2	791.68	881.33	885.07	812.02
	K3	959.09	907.10	846.59	968.84
	K4	1203.77	998.39	863.46	1021.78
	R	124.81	31.53	54.34	52.44
	Factor order	A>C>D>B			
DD-Xiabodi S [mm]	K1	46.24	35.10	61.90	45.20
	K2	48.84	47.90	49.22	50.02
	K3	54.58	56.42	46.84	54.72
	K4	55.94	66.18	47.64	55.66
	R	2.43	7.77	3.77	2.62
	Factor order	B>C>D>A			
DD-Gaoyuanhong S [mm]	K1	31.46	20.38	49.21	27.10
	K2	34.98	33.20	40.64	32.48
	K3	40.70	42.42	28.70	45.13
	K4	44.21	55.35	32.80	46.64
	R	3.19	8.74	5.13	4.89
	Factor order	B>C>D>A			

The stiffness of the impact material affected the impact contact time. When the impact impulse was the same and the impact force had a certain trend, the greater the stiffness of the impact material, the shorter the impact contact time, and so the larger the IPF. Among the four types of impact materials, the stiffness of steel was the largest and that of rubber was the smallest. Therefore, the IPF was the largest impacted with steel and that of steel-rubber was the smallest.

The results of range analysis showed that impact materials had the same influence rule on IPF and DD. It can be inferred that the impact force and damage of potato during harvest can be reduced by covering the surface of potato-soil separator with leather, rubber and other cushions. Geyer M. O. found that in comparison to bare steel, the maximum force and maximum acceleration due to drops from 25 cm were almost halved by both cushions (Poron 20250 and PVC foam) (*Geyer et al, 2009*) Mathew and Hyde considered that the cushioning materials performed well in reducing impact damage occurring in the potatoes (*Mathew and Hyde, 2013*).

With the increase of the impact times, the IPF of the two potato varieties decreased first and then increased, and the second time IPF was the minimum. It was because in the second collision, the potato damage caused by the previous impact made the contact time longer and so the IPF reduced. However, with the increase of impact times, the influence of the previous damage on the contact time of the next impact decreased, so the IPF increased again. The results also showed that the DD of two potato varieties increased gradually when the impact times increased. It was caused by the cumulative damage of the same site after multiple collisions. Researchers found that with each successive impact, the potato bruise size increased until it stabilized after more than 4 impacts (*Bajema and Hyde, 1999; Baritelle and Hyde, 2003*). It can be inferred that when the impact times increase from 1 to 4, the DD will gradually increase, which is consistent with the results of this study.

● **The effect of potato varieties on IPF and DD**

The average values of the three repeated test results in each group in Table 3 were taken to draw the graphs of IPF and DD, as shown in Figure 2 and 3. The trends of IPF and DD of the two potato varieties were the same. The IPF of Xiabodi was smaller than that of Gaoyuanhong but DD was larger than that of Gaoyuanhong. The results showed that potato varieties had an effect on both IPF and DD. The average dry matter content of Xiabodi was 21% (*Haiying Qi and Chun Yang, 2006*), and that of Gaoyuanhong was 24.5% (*Hongyuan Huang et al, 2010*). So, the internal tissue of Xiabodi was softer, which could absorb and buffer the impact force. And Gaoyuanhong was relatively denser, so it had a better damage resistance effect.
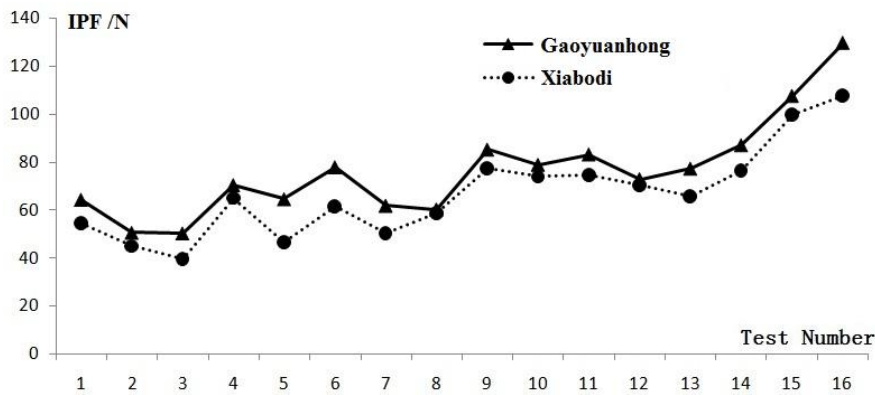
Fig. 2 - The graph of IPF for Xiabodi and Gaoyuanhong
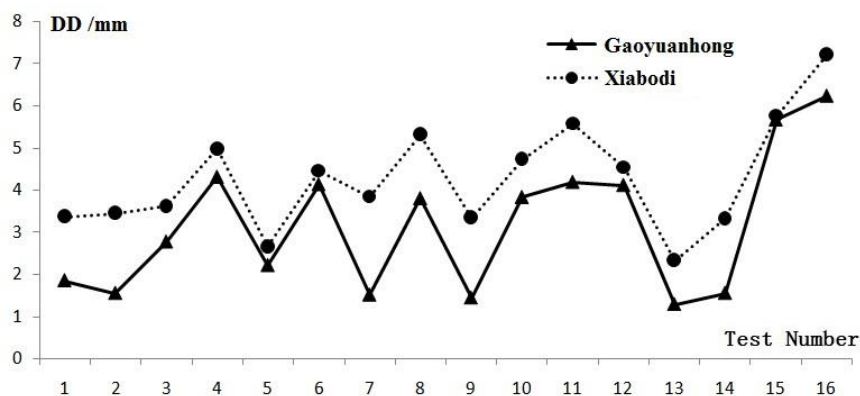
Fig. 3 - The graph of DD for Xiabodi and Gaoyuanhong

● **Single factor test results**

➢ **The effect of potato mass(m) on IPF(F) and DD(s)**

According to the test results in Table 4, the curves of s-m and F-m were drawn, as shown in Figure 4. The results showed that the equation between the potato mass and either IPF or DD was linear. With the increase of potato mass, both IPF and DD increased linearly.
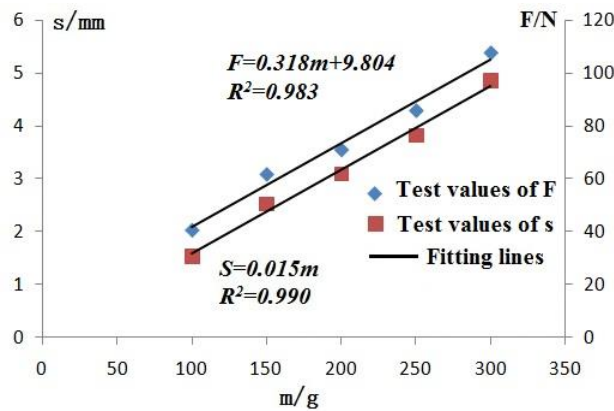
Fig. 4 - The curves of *s-m* and *F-m*

➢ **The effect of drop height(h) on IPF(F) and DD(s)**

The curves of s-h and F-h were shown in Figure 5. The results showed that the equation between the IPF and drop height was linear, and it was logarithmic between DD and drop height. With the increase of drop height, both IPF and DD increased gradually.
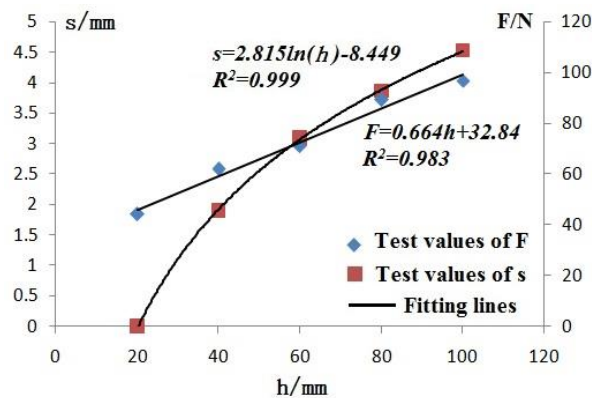
Fig. 5 - The curves of *s*-h and *F-h*

➢ **The relationship between DD(s) and IPF(F)**

The curve of s-F was shown in Figure 6 based on the results in Table 4. The curve of s-F_1 corresponds to the results of No.1 to 5 in table 4 and s-F_2 corresponds to that of No.6 to10.
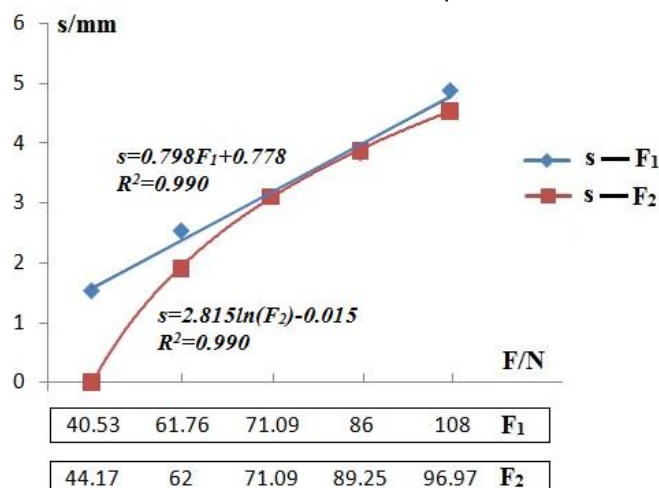
Fig. 6 - The curve of *s-F*

The figure showed that when potato collided with steel and the drop height was a constant, the equation between DD and IPF was linear, and both of them increased linearly. If the potato mass was a constant, the equation was logarithmic, and the larger the IPF was, the greater the DD was.

CONCLUSIONS

In this paper, the effects of potato mass, drop height, impact material, impact times and potato varieties on the IPF and DD were studied by orthogonal tests and single factor tests. Based on the orthogonal tests, the order of influencing factors for IPF of Xiabodi was found to be: potato mass >impact times > drop height > impact material, and that of potato mass > impact material >impact times > drop height for Gaoyuanhong. The orders of influencing factors for DD of both Xiabodi and Gaoyuanhong were the same as: drop height > impact material>impact times> potato mass. Both IPF and DD of two potato varieties increased with the increase of potato mass and drop height, and decreased in turn when they collided with steel, steel-soft plastic, steel-leather and steel-rubber. With the increase of impact times, IPF decreased first and then increased, and DD increased gradually. Under the same conditions, the IPF of Xiabodi was smaller than that of Gaoyuanhong, but DD was greater than that of Gaoyuanhong. The results of single factor tests showed that the relationship between the IPF and either potato mass or drop height was linear equation. The DD and potato mass equation was linear, and the DD and drop height equation was logarithmic. When potato collided with steel and the drop height was a constant, the relationship between DD and IPF was linear equation. If the potato mass was a constant, the relationship turned to be logarithmic equation.

ACKNOWLEDGEMENT

REFERENCES

[1] Bajema, R.W., Hyde, G.M., (1999), Instrumented pendulum for impact characterization of whole fruit and vegetable specimens, *Transactions of the ASAE*, Vol.41, Issue 5, pp.1399-1405, ST. JOSEPH / U.S.A.;

[2] Baritelle, A.L., Hyde G.M., (2003), Specific gravity and cultivar effects on potato tuber impact sensitivity, *Postharvest Biology and Technology*, Vol.29, pp.279-286, ISSN: 0925-5214, Elsevier, Amsterdam/Netherland;

[3] Baritelle, A., Hyde, G., Thornton, R., et al., (2000), A Classification System for Impact-Related Defects in Potato Tubers, *Am. J. Potato Res*, Vol.77, pp.143-148, New York/U.S.A.

[4] Bentini, M., Caprara, C., Martelli, R., (2006), Harvesting Damage to Potato Tubers by Analysis of Impacts Recorded with an Instrumented Sphere, *Biosystems Engineering*, Vol.94, pp.75-85, Academic Press INC Elsevier Science, San Diego/U.S.A.;

[5] Blahovec, J., (2006), Shape of bruise spots in impacted potatoes, *Postharvest Biology and Technology*, Vol.39, Issue 3, pp.278-284, ISSN: 0925-5214, Elsevier, Amsterdam/Netherland;

[6] Caglayan, N., Oral, O., Celik, H. K., et al., (2018), Determination of time dependent stress distribution on a potato tuber during drop case，*Journal of Food Process Engineering*, Vol.41, Issue 7, Wiley-Blackwell, Malden/ U.S.A.;

[7] Canneyt, T. V., Tijskens, E., Ramon, H., et al., (2004), Development of a Predictive Tissue Discolouration Model Based on Electronic Potato Impacts, *Biosystems Engineering*, Vol.88, pp.81-93, Academic Press INC Elsevier Science, San Diego/U.S.A.;

[8] Celik, H. K., Cinar, R., Yilmaz, D., et al., (2019), Mechanical collision simulation of potato tubers，*Journal of Food Process Engineering*, Vol.42, Issue 5, Wiley-Blackwell, Malden/ U.S.A.;

[9] Geyer, M. O., Praeger, U., König, C., et al., (2009), Measuring Behaviour of an Acceleration Measuring Unit Implanted in Potatoes，*Transactions of the ASABE*, Vol.52, Issue 4, pp.1267-1274, ST. JOSEPH / U.S.A.;

[10] Hongyuan Huang, Jinhua Wang, Qingnan Shi, et al., (2010), Quality analysis and utilization of potato (马铃薯的品质分析及利用评价), *Guizhou Agricultural Sciences*, Vol.11, pp.32-36, Gui Zhou/China;

[11] Jankowski, R., (2006), Analytical expression between the impact damping ratio and the coefficient of restitution in the non-linear viscoelastic model of structural pounding, *Earthquake Eng. Struct. Dyn.*, Vol.35, pp.517-524, Chichester / U.K.;

[12] Mathew, R., Hyde, G. M., (1997), Potato Impact Damage Thresholds，*Transactions of the ASAE,* Vol.40, pp.705-709, ST. Joseph / U.S.A.;

[13] Nikara, S., Ahmadi, E., Nia, A. A., (2018), Scanning electron microscopy study of microstructure damage and micromechanical behaviour of potato tissue by impact during storage, *Journal of Food Process Engineering*, Vol.41, Issue 6, Wiley-Blackwell, Malden/ U.S.A.;

[14] Qi Lu, (2016), *Experimental research on damage mechanism of potato and combine harvester design(马铃薯损伤机理试验研究及联合收获机设计)*, MSc Thesis, Northwest A＆F University, ShanXi/China;

[15] Rady, A.M., Soliman, S.N., (2015), Evaluation of mechanical damage of lady rosetta potato tubers using different methods，*International Journal of Postharvest Technology & Innovation*，Vol.5, Issue 2, pp.125-148, Geneva / Switzerland;

[16] Romano, A., Masi, P., Aversano, R., et al., (2018), Microstructure and tuber properties of potato varieties with different genetic profile，*Food Chemistry*，Vol.239, pp.789–796，Elsevier, Oxford/U.K.;

[17] Shengshi Xie, Chunguang Wang, Weigang Deng, (2018), Model for the prediction of potato impact damage depth, *International Journal of Food Properties*, Vol.21, Issue 1, pp.2517-2526, Taylor & Francis INC., Philadelphia/U.S.A.;

[18] Strehmel, N., Praeger, U., Konig, C. et al., (2010), Time course effects on primary metabolism of potato (Solanum tuberosum) tuber tissue after mechanical impact, *Postharvest Biology and Technology*，Vol.56, pp.109–116, Elsevier, Amsterdam/Netherland;

[19] Wenxi Wang, Xugang Hua, Xiuyong Wang, (2017), Advanced Impact Force Model for Low-Speed Pounding between Viscoelastic Materials and Steel, *Journal of Engineering Mechanics*, Vol.143, Issue 12, ASCE，Virginia/U.S.A.;

[20] Yingwang Gao, Chenbo Song, Xiuqin Rao, et al., (2018), Image processing-aided FEA for monitoring dynamic response of potato tubers to impact loading. *Computers and Electronics in Agriculture*, Vol.151，pp.21–30, Elsevier, Oxford/U.K.;

[21] Zhizhen Liu, (2016), *Research on potato collision problem and key mechanism of sorting equipment (马铃薯碰撞问题及分选装备关键机构研究)*，MSc Thesis, Zhejiang University, Zhejiang/China.

RESEARCH ON DESIGN AND HYBRID SLIDING MODE CONTROL OF HIGH CLEARANCE SELF-PROPELLED SPRAYER CHASSIS AIR SUSPENSION
/
高地隙自走式喷雾机底盘空气悬架设计与混合滑模控制研究

Yu Chen[1], Jun Chen[1], Wei Li[2], Shuo Zhang[*1], Hui Xia[3], Yahui Zhu[3], Jiajun Wang[3]
[1] College of Mechanical and Electronic Engineering, Northwest A&F University, Yangling 712100, China;
[2] College of Engineering, China Agricultural University, Beijing 100083, China;
3) Jiangsu World Agriculture Machinery Co., Ltd, Danyang 212300, China;
Tel: +86 18829225579; E-mail: zhangshuo@nwafu.edu.cn
DOI: *https://doi.org/10.35633/inmateh-61-13*

ABSTRACT

According to the operation characteristics of high clearance self-propelled sprayer, an independent vertical shaft air suspension system with auxiliary chamber was designed. On the basis of the damping characteristic analysis and experiment of the air suspension with auxiliary chamber, the sprayer suspension control strategy was developed. Aiming at strong non-linearity and hysteresis for air suspension with auxiliary chamber, and when the sprayer performed road transportation and spraying operation, there was a contradiction between ride comfort and road friendliness, a hybrid sliding mode control method for sprayer chassis suspension based on skyhook reference sliding mode and ground-hook reference sliding mode was proposed. Finally, Matlab/Simulink was used to analyse the effect of the control method in different mixing coefficients. The simulation results showed that according to the requirements of different working conditions of the sprayer, by properly selecting the mixing coefficient γ value, the hybrid sliding mode control could simultaneously take into account the sprayer ride comfort and road friendliness, which was important to improve the sprayer overall performance and operating efficiency.

摘要

针对喷雾机特殊的作业特点和要求，设计了一种带附加气室的独立式立轴空气悬架系统，并在前期对带附加气室空气悬架阻尼特性分析与实验的基础上，制定了喷雾机悬架的基本控制策略。然后针对带附加气室空气悬架具有较强非线性和滞后性，且喷雾机道路转场运输和喷雾作业时，存在行驶平顺性和道路友好性之间矛盾的问题，提出了一种基于天棚参考滑模和地棚参考滑模的悬架混合滑模控制方法。最后应用 Matlab/Simulink 对不同混合系数下的控制效果进行了分析。仿真结果表明，根据喷雾机不同工况要求，合理地选择 γ 值，混合滑模控制可以同时兼顾喷雾机行驶平顺性和道路友好性，对提高喷雾机整机性能和作业效率具有重要意义。

INTRODUCTION

Large scale high clearance self-propelled sprayer plays a very important role in promoting food security production. However, because of the complex working conditions and unique working characteristics of the spray machine, special suspension system is needed to meet its requirements of high ground clearance, large vibration reduction stroke, convenient for four-wheel steering and wheelbase adjustment. In terms of how to reduce the dynamic load of the sprayer tire, improve the its spraying quality and ride comfort, the sprayer designers have proposed a variety of beneficial measures. For example, the designed sprayer is equipped with low-pressure, large-ground-area vacuum meridian cultivator tires, and adopts an independent chassis air suspension or hydropneumatic suspension with less unsprung mass and good nonlinearity (*Wu X H et al., 2018*). John Deere (*Carlson B C et al., 2011; Wubben T M et al., 2007*), AGCO (*Slawson J, 2013; Steffensen C et al., 2012*), HAGIE (*Schaffer J A, 2002*), AgriFac (*Blaauw D, 1999; Ehlen V and Voth R, 2011*) and other sprayer companies have applied for patents on air suspension, and their newly produced sprayers are also equipped with independent air suspension system. However, due to structural and spatial limitations, the independent air suspension system has not been equipped with damper, and only relies on the damping of tires and springs to attenuate the vibration (*Chen Y et al., 2016; 2020*). When the sprayer is running at a high speed or on the rough road conditions, the suspension vibration reduction effect will be

greatly affected. Therefore, in order to better adapt to the sprayer complex working conditions, the design of the new sprayer chassis suspension system is imminent.

In recent years, air suspension with auxiliary chamber, which uses air damping to reduce vibration, has gradually gained the attention of scholars (*Liu H and Lee J C, 2011*). Compared with traditional air suspension, air suspension with auxiliary chamber has the advantages of less heat, low manufacturing and maintenance cost (*Quaglia G et al., 2012*), better vibration reduction effect for the most sensitive frequency segment of human body (4~8Hz) (*Todkar R G, 2011*), which has been widely used in vibration reduction of commercial vehicles (*Kat C J and Els P S, 2009; Porumamilla H et al., 2008*) and rail vehicles (*Docquier N et al., 2007*). The introduction of auxiliary chamber into the sprayer's independent air suspension system can solve the problem that the suspension cannot be equipped with a damper due to structural and space constraints. Research scholars have carried out a lot of simulation and experimental research on the air suspension with auxiliary chamber structure (*Quaglia G and Sorli M, 2001; Vogel J M and Kelkar A G, 2013*), mathematical model (*Wang J, 2012*), dynamic characteristics (*Nieto A J et al., 2008; Toyofuku K et al., 1999*), control methods (*Robinson W D et al., 2012; 2013*) and so on.

Currently, there are mainly three control forms for air suspension with auxiliary chamber. One is to adjust the stiffness of the suspension by switching the auxiliary chamber with different volumes. For example, Li Z X (*2015*) applied decision control method to control the adjustable volume of the air suspension with auxiliary chamber. In this way, the suspension needed to be equipped with an adjustable shock absorber so that the suspension relative damping coefficient could be adjusted when the system stiffness changed, so as to re-matched the suspension parameters. Another method is to change the damping ratio of the system by adjusting the opening diameter of the throttle valve. Such as the research of *Porumamilla H.* (*2007*) and *Robinson W D et al.* (*2012*). The sliding mode variable structure control and linear quadratic optimal control were used to control the air spring seat suspension with auxiliary chamber. This method needed to select a suitable variable throttle valve diameter to make the system air damping have good switching performance, and to ensure that the suspension stiffness and the natural frequency changed less during the change of the system damping ratio. Another control method is to adjust the auxiliary chamber volume and the variable throttle valve diameter. For example, Jerald M V et al. (*2013*) designed a device for continuous adjustment of auxiliary chamber volume and variable throttle valve diameter. Due to the complex structure and the large number of changing parameters of the suspension system, this control method is rarely studied.

Based on this, according to the special operating characteristics and requirements of the sprayer, an independent vertical axis air suspension system with auxiliary chamber was designed. On the basis of the damping characteristic analysis and experiment of the air suspension with auxiliary chamber, the sprayer suspension control strategy was developed. Aiming at strong non-linearity and hysteresis for air suspension with auxiliary chamber, and traditional passive suspension could not take into account both road friendliness and ride comfort, a hybrid sliding mode control method for sprayer chassis suspension based on skyhook reference sliding mode and ground-hook reference sliding mode was proposed. Finally, Matlab/Simulink was used to analyse the effect of the control method in different mixing coefficients.

MATERIALS AND METHODS
Suspension structure design and vibration reduction strategy formulation
● **Suspension structure design**

The sprayer operation condition is complicated, so it not only needs to complete the transportation operation on the ordinary road, but also needs to complete the plant protection operation in the field. Two different working conditions have different requirements for suspension vibration reduction. During sprayer transportation operation, the sprayer speed is high (generally 20–40 km/h), the road conditions are good. The driver's riding comfort and the sprayer operation stability are the performance indexes that should be given priority to. Meanwhile, due to the sprayer large mass, the road friendliness should be taken into account to reduce the impact and damage to the road surface. During sprayer plant protection operation, the tire's dynamic load should be minimized to prevent soil compaction and damage. In addition, although the sprayer speed is low (less than 20 km/h) during plant protection operation, due to the complicated road conditions in the field and the wide width of the boom, the slight tilt and vibration of the sprayer body will cause the boom to vibrate, swing and rotate, which greatly reduces Spray effect. Therefore, the sprayer ride comfort is also an important index to be considered during the its plant protection operation. In accordance with the special operating characteristics and requirements of the sprayer, based on the existing suspension

system, an independent vertical axis air suspension system with auxiliary chamber was designed, and its structural assembly wad shown in Fig.1. In the process of suspension vibration reduction, the vibration caused by the road surface is first transmitted to wheel *1*, and then transmitted to motor protection housing welding *3*, and then reaches to vertical shaft 6. Guided by the internal shaft sleeve of Beam support column welding *7*, the vibration through spring bottom support welding *21*, air spring *10*, spring top support welding *17*, guide post *19*, steering arm welding 15, positioning ring *14*, and beam *9* in order. Finally, the vibration is transmitted to the sprayer body. Air spring 10, variable throttle valve *18*, compressed air hose *11* and auxiliary chamber *12* form the suspension damping adjustment device. According to the driving conditions of the sprayer, by adjusting the opening degree of the variable throttle valve, the suspension damping is changed, and the impact load transmitted from the ground to the vehicle body is more effectively absorbed to ensure the ride comfort of the driver.

(a) Overall structure   *(b) Local large map*
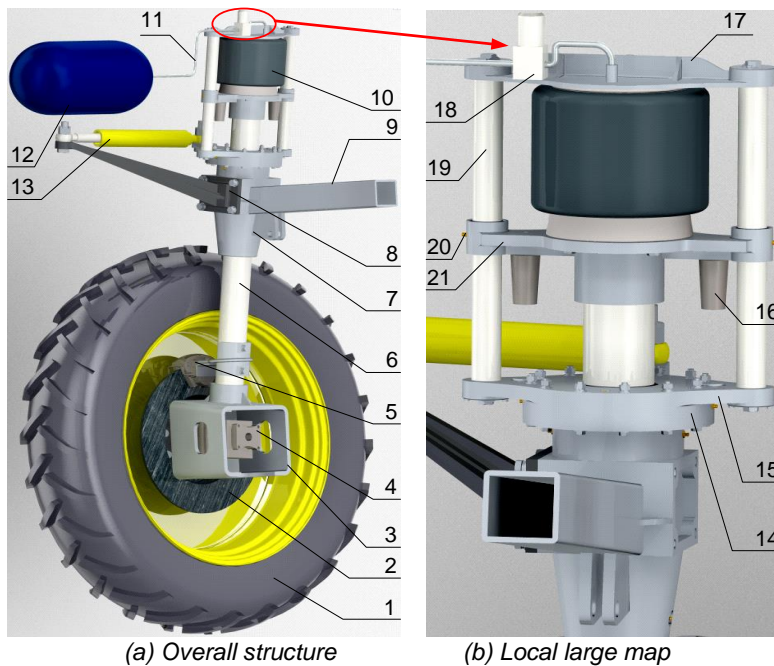
Fig. 1 – The structure of sprayer chassis independent vertical axis air suspension system with auxiliary chamber
1. Wheel; 2. Brake disc; 3. Motor protection housing welding; 4. Hydraulic motor; 5. Brake caliper installation welding; 6. Vertical shaft; 7. Beam support column welding; 8. Steering cylinder support arm welding; 9. Beam; 10. Air spring; 11. Compressed air hose; 12. Auxiliary chamber; 13. Steering cylinder; 14. Positioning ring; 15. Steering arm welding; 16. Rubber limit block; 17. Spring top support welding; 18. Variable throttle valve; 19. Guide post; 20. Lubrication mouth; 21. Spring bottom support welding

● **Vibration reduction strategy formulation**

By abstracting air spring *10*, compressed air hose *11*, auxiliary chamber *12* and variable throttle valve *18* in Fig.1, the vibration damping mechanism of the sprayer chassis air suspension is shown in Fig.2. Where *1* is sprung mass, *2* is air spring, *3* is variable throttle valve, *4* is auxiliary chamber, and *G* is an air mass flow rate. p_1 and p_2 are the absolute pressures of the air spring and the auxiliary chamber, respectively. V_1 and V_2 are the volumes of the air spring and the auxiliary chamber, respectively. m_b is sprung mass, x_b and w are displacements of the sprung mass and excitation, respectively. When the suspension vibrates, the air mass is exchanged between the air spring and the auxiliary chamber under the action of the excitation force. The pressure difference between the two ends of the variable throttle valve makes the air flowing through the variable throttle valve to produce damping and dissipates vibration energy.
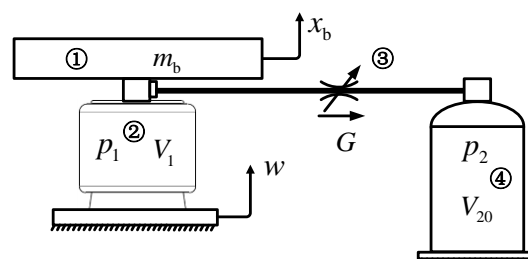
Fig. 2 - Schematic diagram of air suspension with auxiliary chamber

According to the author's previous analysis and experimental results on the damping characteristics of the sprayer chassis air suspension with auxiliary chamber (*Li W et al., 2018*), the variation relationship between the damping coefficient ζ of the air suspension with auxiliary chamber and the natural frequency ω_n and the throttle valve orifice diameter d is obtained as shown in Fig.3.

(a) Variable relationship between ζ and d   *(b) Variable relationship between ω_n and d*
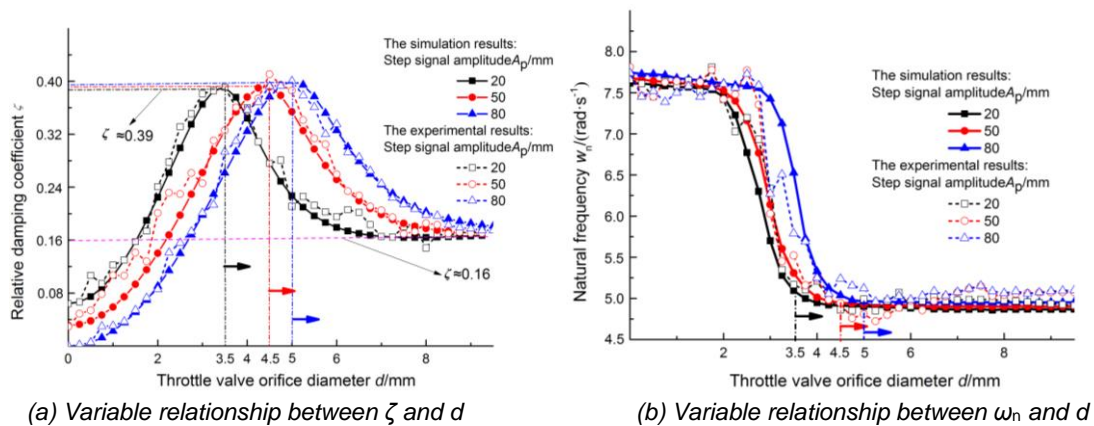
Fig. 3 - the variation relationship between ζ and ω_n, d

In Fig.3(a), in the area to the left of the maximum value point of relative damping coefficient, although the relative damping coefficient changes continuously with the throttle valve orifice opening, the change process is very drastic. Moreover, the spring natural frequency has a step change in this area (see Fig.3(b)), the system shows a strong nonlinearity. On the contrary, in the area to the right of the maximum value point of the relative damping coefficient, the relative damping coefficient changes continuously with the throttle valve orifice opening, and finally reaches the same value (0.16). At this point, the spring natural frequency basically remains unchanged. Therefore, when damping control is carried out on the air suspension with auxiliary chamber, the sprayer road conditions can be divided into flat road surface, uneven road surface and bad road surface. These road conditions can be simulated with step excitation amplitude of 0.02m, 0.05m and 0.08m respectively. Adjust the throttle valve opening according to different road conditions to ensure that the suspension damping ratio ζ changes between 0.39 and 0.16. Therefore, the specific control strategy of the air suspension with auxiliary chamber is as follows: when the sprayer is running on the flat road, make the throttle valve orifice opening diameter d switch between 3.5 mm and full open;When the sprayer is running on uneven road, make the throttle throttle valve orifice opening diameter d switch between 4.5mm and full open. Switch throttle valve orifice opening diameter d between 5.0 mm and full open when the sprayer is running on bad road. During the switching process of the throttle valve orifice opening, the suspension system natural frequency ω_n remains basically unchanged. This strategy will reduce the impact of changes in the parameters (such as static stiffness, natural frequency, et al.) of the air suspension system with auxiliary chamber on the system control effect.

Due to the contradiction between the ride comfort and road friendliness of the sprayer during its transportation condition and spraying condition, a trade-off must be made between the two performances. By developing appropriate suspension control strategy, the sprayer can be manually controlled or automatically controlled between ride comfort and road friendliness according to different driving conditions, so as to take into account the performance requirements of both. Meanwhile, the air suspension with auxiliary chamber has strong nonlinear and hysteresis, while the sliding mode control has high robustness to the uncertainty of model parameters and external disturbances (*Zirkohi M M et al., 2014; Assadsangabi B et al., 2009*). In order to ensure that the sprayer has good ride comfort and road friendliness under complex working conditions (*Mulla A et al., 2014*). In this paper, based on the basic control strategy of air suspension with auxiliary chamber, a hybrid control strategy combining skyhook reference sliding mode and ground-hook reference sliding mode is proposed to control the sprayer chassis air suspension.

Mathematical modeling

● **Mathematical model of suspension**

The 3D model of the sprayer independent vertical axis air suspension in Fig. 1 could be represented by the structural model of Fig. 4. The structure model in Fig. 4(a) was simplified as follows: According to the Taylor series theory, the small deviation linearization method was used to linearize the suspension stiffness k_s. The damping of air spring rubber, the damping caused by suspension element friction and other

unlabelled damping were expressed by c_s. The damping force adjusted by switching the throttle valve orifice opening between the air spring and the auxiliary chamber was represented by the suspension equivalent control force F_d. The suspension equivalent model obtained by simplification was shown in Fig. 4(b).

(a) Suspension structure   *(b) Suspension equivalent model*
Fig. 4 - 2-DOF quarter-car suspension dynamic model
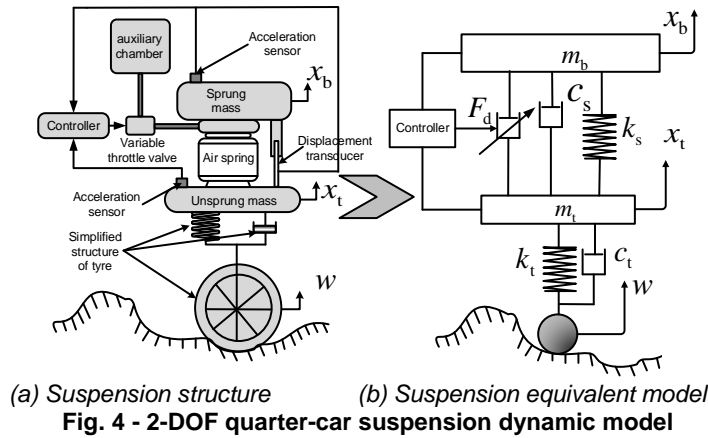
In Fig. 4: k_t – tire stiffness, N/m; c_t – tire damping, N·s/m;

  m_b – sprung mass, kg; m_t – unsprung mass, kg;

  x_b – sprung mass displacement, m; x_t – unsprung mass displacement, m;

  w – road excitation displacement, m.

The vibration differential equation of the suspension system is:

$$\begin{cases} m_b\ddot{x}_b = -k_s\left(x_b - x_t\right) - c_s\left(\dot{x}_b - \dot{x}_t\right) - F_d \\ m_t\ddot{x}_t = k_s\left(x_b - x_t\right) + c_s\left(\dot{x}_b - \dot{x}_t\right) + F_d - k_t\left(x_t - w\right) - c_t\left(\dot{x}_t - \dot{w}\right) \\ k_s = anP_{10}A_e/\left(V_{10} + V_2\right) \end{cases} \quad (1)$$

In equation (1): α – the rate at which the volume of an air spring changes with height;

  V_{10} – the volume of the air spring at the initial equilibrium position, and $V_{10} = V_2/3$;

  V_2 – auxiliary chamber volume, m³;

  $\ddot{x}_b$ – sprung mass acceleration, m/s²;

  $\dot{x}_b$ – sprung mass speed, m/s;

  $\ddot{x}_t$ – unsprung mass acceleration, m/s²;

  $\dot{x}_t$ – unsprung mass speed, m/s;

  $\dot{w}$ – road excitation speed, m/s.

● **Reference model**

The ideal skyhook control mainly aims at ride comfort (*Ahmadian M et al., 2004; Poussot-Vassal C et al., 2006; Priyandoko G et al., 2009*). When the dynamic load of tires deteriorates, the vehicle's handling stability becomes worse, and the large dynamic load of tires will destroy the road surface. The ideal groundhook control can reduce the dynamic load of tires by sacrificing ride comfort (*Valášek M et al., 1997; Viet L D et al., 2014*) and reduce the impact and damage of vehicles on the road surface. The ideal skyhook control model and groundhook control model are shown in Fig. 5.

(a) The ideal skyhook control model   *(b) The ideal groundhook control model*
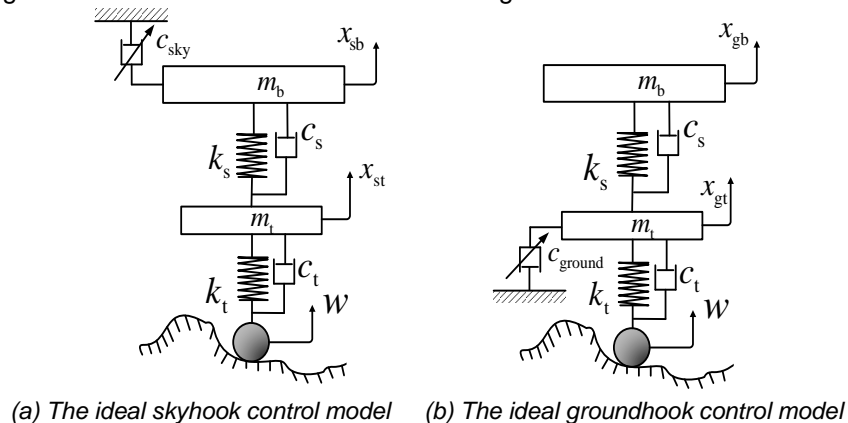
Fig. 5 - The ideal skyhook control model and groundhook control model

The vibration differential equation of skyhook and groundhook reference control model could be expressed by equations (2) and (3). When subscript $i = s$, the equation is skyhook control.

When subscript $i = g$, the equation is groundhook control.

$$\begin{cases} m_b \ddot{x}_{sb} = -k_s \left(x_{sb} - x_{st} \right) - c_s \left(\dot{x}_{sb} - \dot{x}_{st} \right) - c_{sky} \dot{x}_{sb} \\ m_t \ddot{x}_{st} = k_s \left(x_{sb} - x_{st} \right) + c_s \left(\dot{x}_{sb} - \dot{x}_{st} \right) - k_t \left(x_{st} - w \right) - c_t \left(\dot{x}_{st} - \dot{w} \right) \end{cases}$$ (2)

$$\begin{cases} m_b \ddot{x}_{gb} = -k_s \left(x_{gb} - x_{gt} \right) - c_s \left(\dot{x}_{gb} - \dot{x}_{gt} \right) \\ m_t \ddot{x}_{gt} = k_s \left(x_{gb} - x_{gt} \right) + c_s \left(\dot{x}_{gb} - \dot{x}_{gt} \right) - c_t \left(\dot{x}_{gt} - \dot{w} \right) - k_t \left(x_{gt} - w \right) - c_{ground} \dot{x}_{gt} \end{cases}$$ (3)

In equation (2) and equation (3) : $\ddot{x}_{ib}$ – sprung mass acceleration of reference model, m/s²;

$\dot{x}_{ib}$ – sprung mass speed of reference model, m/s;

x_{ib} – sprung mass displacement of reference model, m;

$\ddot{x}_{it}$ – unsprung mass acceleration of reference model, m/s²;

$\dot{x}_{it}$ – unsprung mass speed of reference model, m/s;

x_{it} – unsprung mass displacement of reference model, m;

c_{sky} – damping coefficient of ideal skyhook control;

c_{groung} – damping coefficient of ideal groundhook control.

c_{sky} and c_{groung} can be expressed by the relation (4).

$$\begin{cases} c_{sky} = \begin{cases} 2\xi_{max} m_s \omega_n & \text{if } \dot{x}_{sb} \left(\dot{x}_{sb} - \dot{x}_{st} \right) \geq 0 \\ 2\xi_{min} m_s \omega_n & \text{if } \dot{x}_{sb} \left(\dot{x}_{sb} - \dot{x}_{st} \right) < 0 \end{cases} \\ c_{ground} = \begin{cases} 2\xi_{max} m_s \omega_n & \text{if } \dot{x}_{gt} \left(\dot{x}_{gb} - \dot{x}_{gt} \right) \geq 0 \\ 2\xi_{min} m_s \omega_n & \text{if } \dot{x}_{gt} \left(\dot{x}_{gb} - \dot{x}_{gt} \right) < 0 \end{cases} \end{cases}$$ (4)

In relation (4) : ζ_{max} – the maximum damping ratio that the suspension system can achieve when switching the variable throttle valve orifice;

ζ_{min} – the minimum damping ratio that the suspension system can achieve when switching the variable throttle valve orifice;

ω_n – Natural frequency of air suspension system with auxiliary chamber, rad/s.

Design of hybrid sliding mode controller
● **Controller design**

The air suspension with auxiliary chamber has strong nonlinearity and hysteresis. Sliding mode control is highly robust to the uncertainty of model parameters and external disturbances. In order to ensure that the sprayer has good ride comfort and road friendliness under complex working conditions, a hybrid control algorithm for the sprayer chassis suspension that combined the skyhook reference sliding mode and groundhook reference sliding mode was proposed, as shown in Fig. 6. A mixing coefficient γ was introduced into the controller to adjust the mixing degree of the two control strategies. The value of γ was [0,1]. When $\gamma = 0$, the controller was the skyhook reference sliding mode control. When $\gamma = 1$, the controller was the groundhook reference sliding mode control. The value of γ was between 0 and 1 to synthesize the characteristics of skyhook reference sliding mode control and groundhook reference sliding mode control.

The hybrid sliding mode real-time control force F_d can be expressed as:

$$F_d = \gamma F_{ssmc} + \left(1 - \gamma \right) F_{gsmc}$$ (5)

Where: F_{ssmc} - skyhook reference sliding mode control force, N;

F_{gsmc} - groundhook reference sliding mode control force, N.
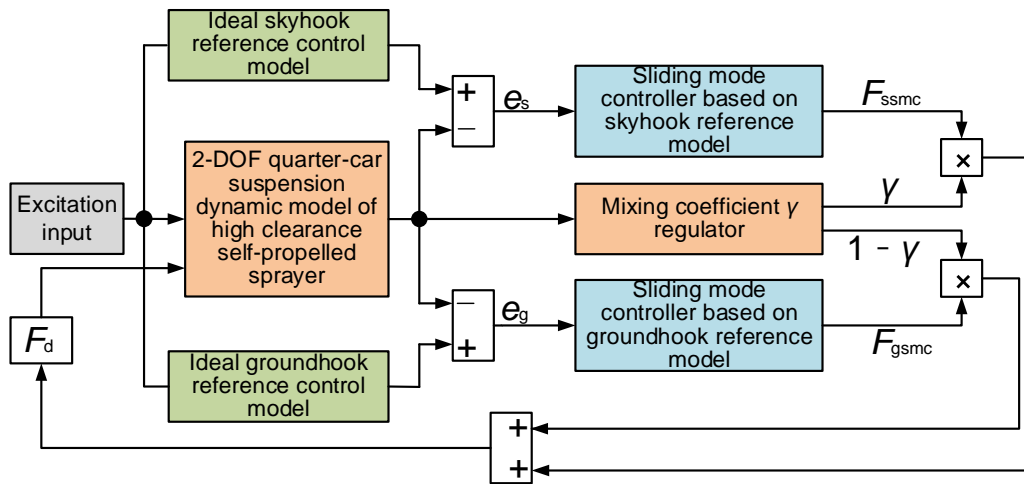
Fig. 6 - Schematic diagram of hybrid sliding mode control

● **Error dynamics model**

Because the design process of the two references sliding mode control algorithms were similar, this article took the groundhook reference sliding mode control design as an example. In order to reduce the steady-state error of the system, the integral error of unsprung mass displacement was introduced. Unsprung mass displacement integral error, unsprung mass displacement error and unsprung mass velocity error together formed the groundhook reference sliding mode control model tracking error vector e_g. The error dynamics equation of groundhook reference sliding mode control was

$$\dot{e}_g = A_g e_g + B_g u_g + G_g X + H_g X_g \tag{6}$$

Where: $X=[x_b\ x_t\ \dot{x}_b\ \dot{x}_t]$, $X_g=[x_{gb}\ x_{gt}\ \dot{x}_{gb}\ \dot{x}_{gt}]$, $u_g=F_d$, $e_g=[e_{g1}\ e_{g2}\ e_{g3}]^T=[\int(x_t - x_{gt})\ (x_t - x_{gt})\ (\dot{x}_t - \dot{x}_{gt})]^T$, $\dot{e}_g=[\dot{e}_{g1}\ \dot{e}_{g2}\ \dot{e}_{g3}]^T=[(x_t - x_{gt})\ (\dot{x}_t - \dot{x}_{gt})\ (\ddot{x}_t - \ddot{x}_{gt})]^T$,

$$A_g = \begin{bmatrix} 0 & 1 & 0 \\ 0 & 0 & 1 \\ 0 & -\dfrac{k_s+k_t}{m_t} & -\dfrac{c_s+c_t+c_{ground}}{m_t} \end{bmatrix},\ B_g = \begin{bmatrix} 0 \\ 0 \\ \dfrac{1}{m_t} \end{bmatrix},\ G_g = \begin{bmatrix} 0 & 0 & 0 & 0 \\ 0 & 0 & 0 & 0 \\ \dfrac{k_s}{m_t} & 0 & \dfrac{c_s}{m_t} & \dfrac{c_{ground}}{m_t} \end{bmatrix},\ H_g = \begin{bmatrix} 0 & 0 & 0 & 0 \\ 0 & 0 & 0 & 0 \\ -\dfrac{k_s}{m_t} & 0 & -\dfrac{c_s}{m_t} & 0 \end{bmatrix}.$$

Integral sliding mode variable structure control was performed on the error dynamic system, and the integral sliding mode surface was obtained as:

$$s = \lambda_{g2}\int_0^t e_{g2}\,\mathrm{d}r + \lambda_{g1}e_{g2} + \dot{e}_{g2} = \varGamma e_g \tag{7}$$

Where: $\varGamma$ was a coefficient matrix, and $\varGamma = [\lambda_{g2}\ \lambda_{g1}\ 1]$, λ_{g1}, $\lambda_{g2}> 0$.

Using the pole placement method to select the coefficient matrix $\varGamma$, the system could quickly reach the sliding mode. Assuming the system dynamic error was in the sliding mode plane, we got $s = \dot{s} = 0$. Bring $\dot{e}_{g3}$ into $\dot{s} = 0$, when the system entered the sliding mode, the equivalent control force F_{geq} could be gotten as:

$$F_{geq} = \left(c_s + c_t + c_{ground} - \lambda_{g1}m_t\right)e_{g3} + \left(k_s + k_t - \lambda_{g2}m_t\right)e_{g2} - c_{ground}\dot{x}_t - k_s\left(x_b - x_{gb}\right) - c_s\left(\dot{x}_b - \dot{x}_{gb}\right) \tag{8}$$

According to equation (8), the equivalent control was essentially the feedback control of partial states. F_{geq} was closely related to the system state. Due to the strong non-linearity of the air suspension with auxiliary chamber, in order to satisfy the sliding condition and enhance the robustness of the system, when the control system reached the sliding mode surface s, a discontinuous term $\varepsilon sgn(s)$ was added on F_{geq}. The actual system control F_{gsmc} was:

$$F_{gsmc} = F_{geq} + \left(-\varepsilon\,\mathrm{sgn}(s)\right) \quad \varepsilon > 0 \tag{9}$$

In formula (9), ε represented the velocity of the system's motion point approaching the switching plane $s=0$. Reasonable selection of ε value could satisfy the system's good dynamic quality under large interference conditions.

● **System stability analysis**

Selecting Lyapunov function $V(s) = s^2/2$ and deriving it, inequality (10) could be obtained.

$$\dot{V}(s) = \frac{1}{2}\frac{d}{dt}s^2 = s\dot{s} \leq -\eta |s| \tag{10}$$

In inequality (10), $\eta > 0$. According to the stability theory of Lyapunov, if the inequality (11) was true, the system converged. Assuming the system was stable, we could get equation (11) by introducing equations (6), (7), and (8) into equation (10).

$$s\dot{s} = \boldsymbol{\Gamma}\left(A_g e_g + G_g X + H_g X_g + B_g F_{geq}\right)s - \boldsymbol{\Gamma}B_g \varepsilon \operatorname{sgn}(s)s \leq -\eta |s| \tag{11}$$

Since $\varepsilon sgn(s)s = \varepsilon |s|$, and the first term of equation (11) was 0 when the system moved in the sliding mode surface, equation (11) could be rewritten as

$$-\boldsymbol{\Gamma}B_g \varepsilon |s| \leq -\eta |s| \tag{12}$$

namely

$$\varepsilon \geq \eta m_t \tag{13}$$

The inequality (13) showed that the control system was stable. By substituting (13) into (9), F_{gsmc} could be obtained as

$$F_{gsmc} = F_{geq} + \left(\eta m_t\right)\operatorname{sgn}(s) \tag{14}$$

In order to ensure that the variable damping force dissipated energy in real time under sliding mode control and prevented vibration deterioration, F_{gsmc} was switched by reference to groundhook logic switch control. In order to reduce the system chattering and improve the control quality, a continuous saturation function sat (s/ψ) was used instead of the discontinuous symbol function *sgn (s)*. The real-time variable damping force F_{gsmc} of the groundhook reference sliding mode control was obtained as

$$F_{gsmc} = \begin{cases} F_{geq} - \left(\eta m_t\right)\operatorname{sat}\left(s/\psi\right), & \left(F_{geq} - \left(\eta m_t\right)\operatorname{sat}\left(s/\psi\right)\right)\left(\dot{x}_b - \dot{x}_t\right) \leq 0 \\ 0, & \left(F_{geq} - \left(\eta m_t\right)\operatorname{sat}\left(s/\psi\right)\right)\left(\dot{x}_b - \dot{x}_t\right) > 0 \end{cases} \tag{15}$$

Where: ψ - boundary layer thickness, the value was 0.1.

Similarly, the real-time control force F_{ssmc} of the skyhook reference sliding mode was obtained as shown in equation (16).

$$F_{ssmc} = \begin{cases} F_{seq} + \left(\eta_s m_b\right)\operatorname{sat}\left(s_s/\psi_s\right), & \left(F_{seq} + \left(\eta_s m_b\right)\operatorname{sat}\left(s_s/\psi_s\right)\right)\left(\dot{x}_b - \dot{x}_t\right) \geq 0 \\ 0, & \left(F_{seq} + \left(\eta_s m_b\right)\operatorname{sat}\left(s_s/\psi_s\right)\right)\left(\dot{x}_b - \dot{x}_t\right) < 0 \end{cases} \tag{16}$$

In equation (16), F_{seq} was skyhook reference sliding mode equivalent control force. F_{seq} could be calculated by formula (17).

$$F_{seq} = \left(\lambda_{s2}m_b - k_s\right)\left(x_b - x_{sb}\right) + \left(\lambda_{s1}m_b - c_{sky} - c_s\right)\left(\dot{x}_b - \dot{x}_{sb}\right) + c_{sky}\dot{x}_b + k_s\left(x_t - x_{st}\right) + c_s\left(\dot{x}_t - \dot{x}_{st}\right) \tag{17}$$

RESULTS

Matlab/Simulink was applied to establish the control system simulation model. The simulation time interval was set as 0.005s, the simulation duration was set as 100s. Applied filtering white noise to generate a typical road excitation signal (*Popp K and Schiehlen W, 2010*). The sprayer crossed the c-class road surface at a speed of 40 km/h. The low-frequency cut-off frequency of road signal was 0.1 Hz. The road roughness coefficient was $256 \times 10^{-6} m^3$. Other simulation parameters were set as follows: $m_s = 3000$ kg, $m_t = 300$ kg, $c_s = 2400$ N·m/s, $k_t = 560$ KN/m, $c_t = 5700$ N·m/s, $\lambda_{g1} = \lambda_{s1} = 3.96$, $\lambda_{g2} = \lambda_{s2} = 36.08$, $\eta_s = 3$, $\eta_g = 30$, $\zeta_{max} = 0.39$, $\zeta_{min} = 0.16$, $\omega_n = 6$ rad/s, $\alpha = 0.0564$, $V_2 = 0.0507 m^3$. Sprayer body acceleration and tire dynamic load root mean square value were selected as the evaluation indexes of ride comfort and road friendliness respectively. The influence of sliding mode control on suspension performance was analysed by changing the value of mixing coefficient γ.

The simulation results were shown in Tab. 1, Fig. 7, Fig. 8 and Fig. 9. In Tab. 1, the passive suspension referred to the simulation results when the variable throttle valve was in the optimal opening and remained unchanged, and the suspension damping coefficient $\zeta = 0.39$.

Table 1

Comparison with simulation results

Performance indicators (RMS)	Sprung mass acceleration (m·s^{-2})	Tire dynamic load (N)	S_{sky}	S_{ground}
Passive suspension	1.56444	12430.9	——	——
γ=0	1.69968	4834.4	——	0.0081
γ=0.2	1.57673	5995.3	0.1731	0.0313
γ=0.4	1.31196	7668.8	0.07109	0.0589
γ=0.6	1.14915	9459.8	0.0436	0.09542
γ=0.8	0.87060	11990.6	0.0224	0.2146
γ=1	0.58458	13060.1	0.0065	——
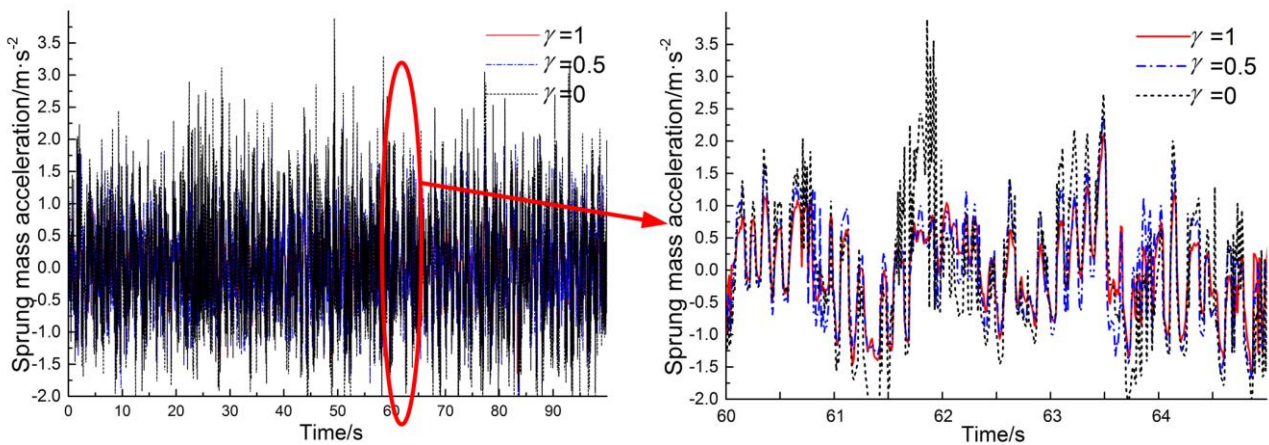
(a) Variation curve of sprung mass acceleration in time domain *(b) Local amplification*

Fig. 7 - Response curve of sprung mass acceleration in time domain
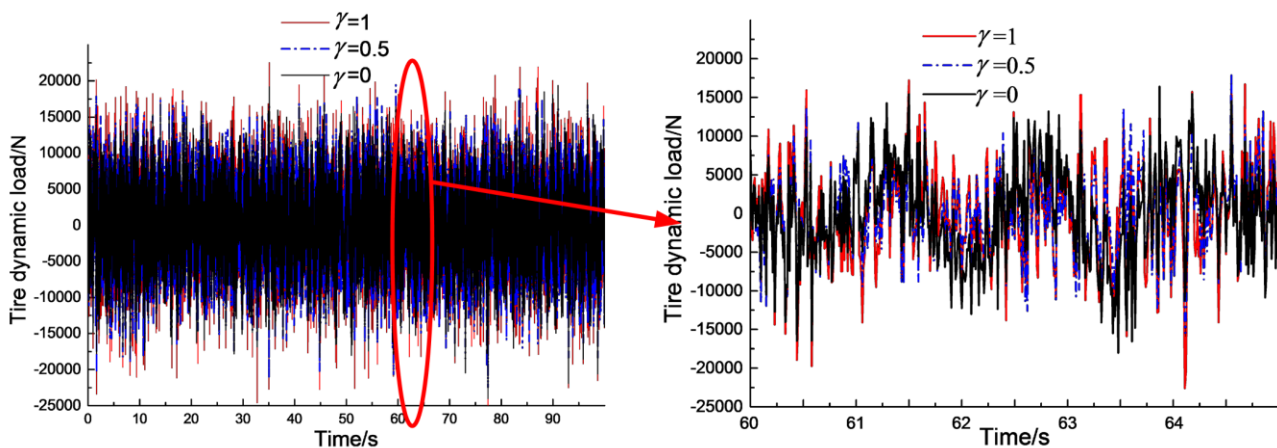
(a) Variation curve of tire dynamic load in time domain *(b) Local amplification*

Fig. 8 - Response curve of tire dynamic load in time domain

It could be seen from Tab. 1 that when the mixing coefficient γ value changed, the root mean square values of the sliding surface S_{ground} and S_{sky} were both small. It showed that the control system could track the ideal skyhook reference model and ideal groundhook reference model well. When γ =0, the hybrid sliding mode control was equivalent to the groundhook reference sliding mode control. At this time, the tire dynamic load was small and the sprayer had good road friendliness. When γ =1, the hybrid sliding mode control was equivalent to the skyhook reference sliding mode control. At this time, the sprung mass acceleration was

123

small and the sprayer had good ride comfort. The γ value was larger, the hybrid sliding mode control was closer to skyhook reference sliding mode control, and the sprayer ride comfort was better. The γ value was smaller, the hybrid sliding mode control was closer to groundhook reference sliding mode control, and the sprayer road friendliness was better.

When the values of γ were 0, 0.5 and 1, the corresponding responses in time and frequency domain of the sprung mass acceleration and the tire dynamic load were obtained, as shown in Fig. 7, Fig. 8 and Fig. 9. In Fig. 7, when γ =0.5, the corresponding peak - peak of sprung mass acceleration increased compared with γ =1, and decreased compared with γ =0. The sprayer ride comfort could be improved by increasing γ value. In Fig. 8, when γ value was reduced, the tire dynamic load was also reduced and the sprayer road friendliness was effectively improved.

(a) Sprung mass acceleration frequency domain   *(b) Tire dynamic load in frequency domain*
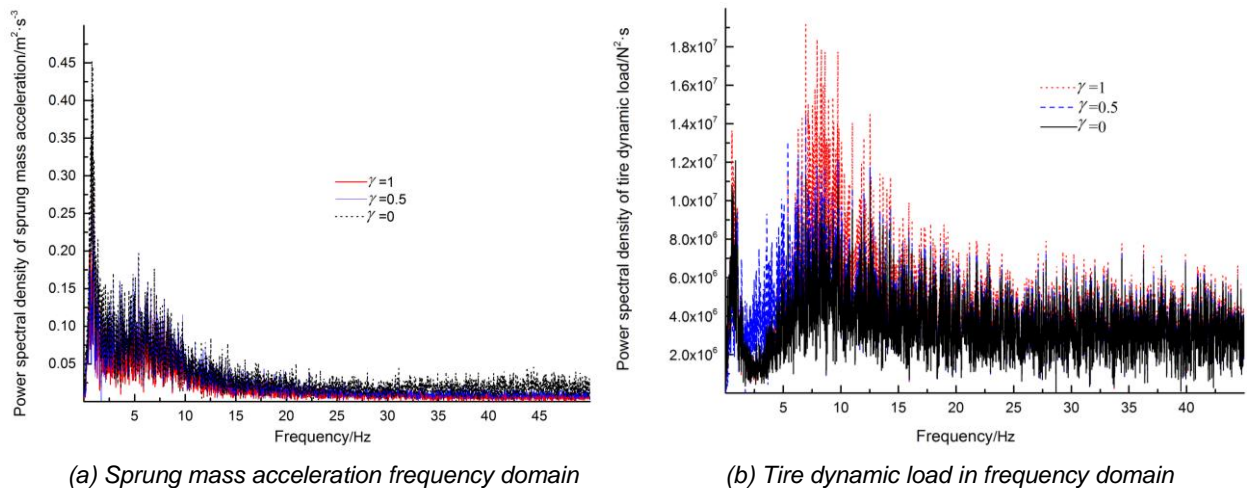
Fig. 9 - The curve of power spectral density

The Fig. 9 showed that in the vicinity of 1.2 Hz and 9 Hz, the sprung mass acceleration power spectrum density corresponding to γ = 0.5 was smaller than that when γ = 0 and bigger than that when γ = 1. The tire dynamic load power spectral density corresponding to γ = 0.5 was bigger than that when γ = 0, and smaller than that when γ = 1. It showed that the hybrid sliding mode control could combine the advantages of skyhook sliding mode control and groundhook sliding mode control, and had good comprehensive performance.

As could be seen from Tab. 1, Fig. 7, Fig. 8 and Fig. 9, although the hybrid sliding mode control could not achieve the effect of groundhook reference sliding mode control in terms of road friendliness, and could not achieve the effect of the skyhook reference sliding mode control in terms of ride comfort, but according to the sprayer different requirements, the mixing coefficient γ was reasonably selected, and the hybrid sliding mode control could take into account both ride comfort and road friendliness.

CONCLUSIONS

(1) According to the special operation characteristics and requirements of sprayer, an independent vertical shaft air suspension system with auxiliary chamber was designed.

(2) A damping control strategy for the sprayer suspension was presented. According to the different road surface, the variable throttle valve orifice opening was adjusted, the designed suspension system damping ratio ζ changed between 0.39 and 0.16. During the whole valve orifice being adjusted process, the system natural frequency ω_n basically remained unchanged.

(3) A hybrid sliding mode control method which combined skyhook reference sliding mode and groundhook reference sliding mode was proposed to control the sprayer suspension. When the mixing coefficient γ value was changed, the root mean square values of S_{ground} and S_{sky} were both small, the established control system could track the ideal skyhook reference model and groundhook reference model well.

REFERENCES

[1] Ahmadian M, Song X, Southward S C., (2004), No-jerk skyhook control methods for semiactive suspensions, *J. Vib. Acoust.*, vol.126, pp.580-584;

[2] Assadsangabi B., Eghtesad M., Daneshmand F. et al., (2009), Hybrid sliding mode control of semi-active suspension systems, *Smart Materials and Structures*, vol.18, pp.406-414.

[3] Blaauw D., (1999), *Spring-mounted spreading device*, EP, 0919124 A1;

[4] Carlson B.C., Young D.E., Baxter G.E. et al., (2011), *Suspended axle for sprayer*, US, 7938415;

[5] Chen Y., Chen S.Y., Du Y.F. et al., (2016), Damping characteristics of chassis suspension system of high clearance agricultural machinery based on friction damper（基于摩擦阻尼的高地隙农机底盘悬架减振特性），*Transactions of the CSAE*, vol.34, pp.51-57;

[6] Chen Y., Zhang S., Mao E.R. et al, (2020), Height stability control of a large sprayer body based on air suspension using the sliding mode approach, *Information Processing in Agriculture*, vol.7, pp.20-29;

[7] Docquier N., Fisette P., Jeanmart H., (2007), Multiphysics modelling of railway vehicles equipped with pneumatic suspensions, *Vehicle System Dynamics*, vol.45, pp.505-524;

[8] Ehlen V., Voth R., (2011), Suspension for self-propelled spreading machine, EP, 2388157 A1;

[9] Kat C.J., Els P.S., (2009), Interconnected air spring model, *Mathematical & Computer Modelling of Dynamical Systems*, vol.15, pp.353-370;

[10] Liu H., Lee J.C., (2011), Model development and experimental research on an air spring with auxiliary reservoir, *International Journal of Automotive Technology*, vol.12, pp.839-847;

[11] Li W., Chen Y., Zhang S. et al., (2018), Damping characteristic analysis and experiment of air suspension with auxiliary chamber, *IFAC-PapersOnLine*, vol.51, pp.166–172;

[12] Li Z.X., Ju L.Y., Jiang H. et al., (2015), Parameter optimization and control of air suspension with adjustable auxiliary chamber [J]. *Automotive Engineering*, vol.37, pp.941-945;

[13] Mulla A., Jalwadi S., Unaune D., (2014), Performance analysis of skyhook, groundhook and hybrid control strategies on semiactive suspension system, *International Journal of Current Engineering and Technology*, vol.3, pp.265-269;

[14] Nieto A.J., Morales A.L., González A. et al., (2008), An analytical model of pneumatic suspensions based on an experimental characterization, *Journal of Sound & Vibration*, vol.313, pp.290-307;

[15] Popp K., Schiehlen W., (2010), Ground vehicle dynamics, Berlin: Springer publisher；

[16] Porumamilla H., Kelkar A.G., Vogel J.M., (2008), Modeling and verification of an innovative active pneumatic vibration isolation system, *Journal of Dynamic Systems Measurement & Control*, vol.130, pp.1750-1753;

[17] Porumamilla H., (2007), *Modeling, analysis and non-linear control of a novel pneumatic semi-active vibration isolator: A concept validation study*, Ames: Iowa State University;

[18] Poussot-Vassal C., Sename O., Dugard L. et al., (2006), Optimal skyhook control for semi-active suspensions, *IFAC Proceedings Volumes*, vol.39, pp.608-613;

[19] Priyandoko G., Mailah M., Jamaluddin H., (2009), Vehicle active suspension system using skyhook adaptive neuro active force control, *Mechanical systems and signal processing*, vol.23, pp.855-868;

[20] Quaglia G., Sorli M., (2011), Air suspension dimensionless analysis and design procedure, Vehicle System Dynamics: *International Journal of Vehicle Mechanics & Mobility*, vol.35, pp.443-475;

[21] Quaglia G., Scopesi M., Franco W., (2012), A comparison between two pneumatic suspension architectures, *Vehicle System Dynamics*, vol.50, pp.509-526;

[22] Robinson W.D., Kelkar A.G., Vogel J.M., (2013), Semi-active control methodology for control of air spring-valve-accumulator system, *ASME 2013 Dynamic Systems and Control Conference*;

[23] Robinson W.D., (2012), *A pneumatic semi-active control methodology for vibration control of air spring based suspension systems*, Ames: Iowa State University;

[24] Schaffer J.A., (2002), *Steering system for variable height agricultural sprayer*, US, 6371237 B1;

[25] Schaffer J.A., (2002), *Wheel support system for agricultural sprayer*, US, 6491306 B2;

[26] Slawson J., (2013), *Independent strut suspension*, US, 8534686;

[27] Steffensen C., Michels E., Kleven J.E., (2012), *Suspension assemblies with bump steer control*, US, 8136824;

[28] Todkar R.G., (2011), Design, development and testing of an air damper to control the resonant response of a SDOF quarter-car suspension system, *Modern Mechanical Engineering*, vol.1, pp.84-92;

[29] Toyofuku K., Yamada C., Kagawa T. et al., (1999), Study on dynamic characteristic analysis of air spring with auxiliary chamber, *Jsae Review*, vol.20, pp.349-355;

[30] Valášek M., Novak M., Šika Z. et al., (1997), Extended ground-hook-new concept of semi-active control of truck's suspension, *Vehicle system dynamics*, vol.27, pp.289-303;

[31] Viet L.D., Nghi N.B., Hieu N.N. et al., (2014), On a combination of ground-hook controllers for semi-active tuned mass dampers, *Journal of Mechanical Science and Technology*, vol.28, pp.2059-2064;

[32] Vogel J.M., Kelkar A.G., (2013), *Continuously variable natural frequency and damping vibration isolation system*, US, US8490952 B1;

[33] Wang J., (2012), *Nonlinear modeling and h-infinity model reference control of pneumatic suspension system*, Ames: Iowa State University;

[34] Wubben T.M., Maiwald M.A., Carlson B.C. et al., (2007), *High clearance vehicle suspension with twin spindles for transferring steering torque*, US, 7168717 B2;

[35] Wu X.H., Qin J.H., Du Y.F. et al., (2018), Experiments of vibration control for active pneumatic suspension system in high clearance self-propelled sprayer（高地隙喷雾机主动空气悬架减振控制与实验）, *Transactions of the Chinese Society for Agricultural Machinery*, vol.49, pp.60-67;

[36] Zirkohi M.M., Lin T.C., (2014), Interval type-2 fuzzy-neural network indirect adaptive sliding mode control for an active suspension system, *Nonlinear Dynamics*, vol.79, pp.513-526.

DESIGN AND ANALYSIS OF AN EFFICIENT SHOCK ABSORPTION SYSTEM FOR AN AGRICULTURAL ELECTRIC TRICYCLE
/
PROIECTAREA ȘI ANALIZA UNUI SISTEM EFICIENT DE ABSORBȚIE A ȘOCURILOR PENTRU UN TRICICLU AGRICOL ELECTRIC

Albert Suvac [1 2], Vasilica Stefan[2], Cristian-Gabriel Alionte[3], Liviu-Marian Ungureanu[4]

[1] University Politehnica of Bucharest, Bucharest / Romania; [2] INMA Bucharest / Romania;
[3] University Politehnica of Bucharest / Romania; [4] University Politehnica of Bucharest / Romania
Tel: 0721853715; E-mail: albertsuvac @gmail.com

ABSTRACT

Ecological transport systems must be provided with efficient vibration damping systems for the comfort and safety of the user. This paper analyses a shock absorption system that can be used in an individual three-wheeled transport vehicle. The vehicle has a complex structure, with an equal size of the front and rear wheels. This uniformity of dimensions between the rear and front wheels makes it easier to travel on rough terrain and manoeuvre in a folded shape. The tricycle allows aggregation with different agricultural equipment and can be used in small farms, greenhouses, solariums, meadows, orchards, etc. In this paper we simulate several models of absorption systems with different construction parameters. The strength of the system and the efficiency of shock absorption were taken into account. The best result of the simulation test for absorption systems will be the comparison with the actual physical model used by the electric vehicle.

REZUMAT

Sistemele de transport ecologic trebuiesc prevăzute cu sisteme eficiente de amortizare a vibrațiilor pentru confortul si siguranță utilizatorului. In lucrarea prezenta se analizează un sistem de absorbție a șocurilor care poate fi utilizat într-un vehicul individual de transport pe trei roți. Vehiculul are o structură complexă, cu o dimensiune egala a roților din față și din spate. Această uniformitate a dimensiunilor dintre roțile din spate și cele din față face mai ușoară deplasarea pe teren accidentat și manevrarea într-o formă pliată. Tricicleta permite agregarea cu diferite echipamente agricole și poate fi folosită în mici ferme, sere, solarii, pajiști, livezi etc. În această lucrare se realizează simularea mai multor modele de sisteme de absorbție cu diferiți parametri constructivi. S-a avut în vedere rezistența sistemului și eficiența absorbției de șoc. Cel mai bun rezultat al testului de simulare pentru sistemele de absorbție va fi comparația cu modelul fizic real utilizat de vehiculul electric.

INTRODUCTION

The need for agricultural equipment caused by the growth of the world's population is more than obvious. Current agricultural equipment has reached its limits of optimization in terms of complexity and efficiency with current technology. Moreover, improvements in the field of drive technology today, mainly mechanical or hydraulic drives, are limited. Therefore, the focus in this area will be on electric units in the future.

Reducing pollutant emissions and dependence on fossil fuels is a global goal. In many countries, governments promote the use of efficient vehicles such as electric and hybrid vehicles. The development of electric agricultural equipment has advantages in terms of increased energy efficiency and extended functionality. Greater efficiency means reducing fuel consumption and subsequently reducing CO_2 emissions. The new functionalities improve the quality of work and increase the comfort of the operator. The major advantages of electrifying agricultural machinery are: electric motors can have an efficiency of about 90% compared to diesel engines powered by diesel, a maximum torque from time 0, lower maintenance costs, noise reduction, low pollution and a more flexible design.

Such a vehicle can be the electric tricycle, with low production and maintenance costs, reliability for transport, its mechanics being relatively simple, having better stability than the motorcycle and possibilities of adaptation for multiple utilities such as, in this case, operation in small farms, greenhouses, solariums, meadows, orchards etc. (*Suvac A, 2019*)

The systems for suspension that integrate in their structure the rubber is encountered in many studies because this optimizes the control of the shocks and the vibrations. For example, we can mention the study conducted by *Zhao L.L. et al., (2018),* where, for improving the performance of a vehicle's seat, was created a new type of suspension composed of springs made of composite material based on rubber. This implementation has led to a low-frequency vibration attenuation generated by difficult terrain.

For vehicles used for rail transport are used, more and more often, as secondary suspension system, pneumatic elastic elements that contain rubber *(Spiroiu M.A, 2018).* For trucks, the rubber elements are designed to provide a reduction of the engine vibration and the transmission of the vibrations to passengers. (*Hur S, 2017*).

In aeronautics, the problem of complex setup can be solved by generating new models based on qualitative semantic models. The approach of this analysis requires the development of new models and methods for obtaining information regarding the shape of the modeled object, which captures greater importance than its structure (*Tomilov I., 2015*)

In the case of autonomous vehicles, in order to improve the comfort and handling achieved through the dissipation of the energy induced by terrain, have been designed other types of suspension systems. The relevant results in scientific literature, for example studies made by (*Nielens H., 2004*) are focused on mechanical simulations, as well as on structures that have a better energy absorption. Other studies (*Nielens H., 2001*) indicate that we should be cautious before using multiple suspensions regardless of terrain because the handling becomes more difficult. Also, since these systems ensure a good efficiency of shocks absorption generated by the terrain irregularities, and, as a consequence, a greater comfort is obtained, they can generate, an increase in passenger's effort, especially for cyclists.

Unfortunately, studies show that the passive vibration absorption systems, which use viscoelastic materials due to their non-linear characteristics with temperature, frequency and mechanical stress, lead to nonlinear dynamic properties (*Neto F.P.L., 2012*). Thus, in the design of the reliable vibration isolator system from the point of view of the mathematical model and of the optimal design, it is necessary to determine the degree of rigidity and absorption of the viscoelastic material influenced by shape and structure.

MATERIALS AND METHODS

In this paper, three different vibration damping structures and the mechanical vibration damping intended for use in an individual electric tricycle vehicle (Fig. 1) were analysed. The systems are used basically at the level of the foot sustaining parts, but they can be used at the direction.

a)   b)   c)
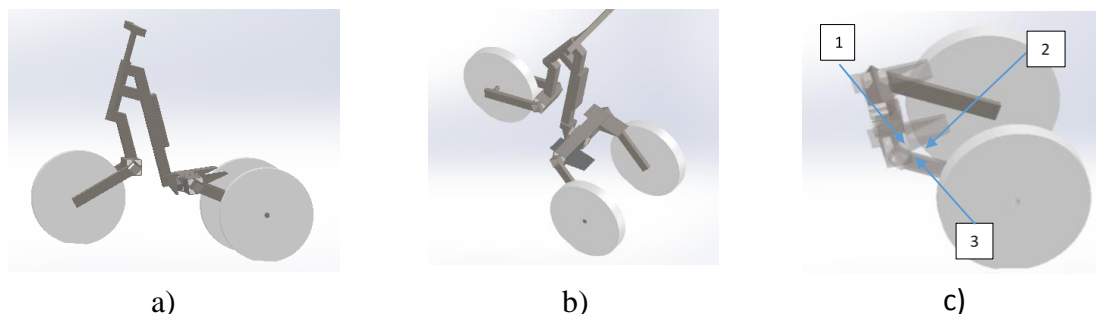
Fig. 1 - 3D model of the individual electric tricycle vehicle:
a) lateral view; b) isometric view; c) system structure
1 -external part, 2 – rubber, and, 3- central part

The three constructive solutions are presented structurally and physically in Fig. 2.
The characteristic elements are:
- exterior part is a rectangular shell with hexagonal solid central part, see Fig. 2a;
- exterior part is a rectangular shell with round shell central part, see Fig. 2b;
- exterior part is a round shell with rectangular shell central part, see Fig. 2c.

| a) | b) | c) |
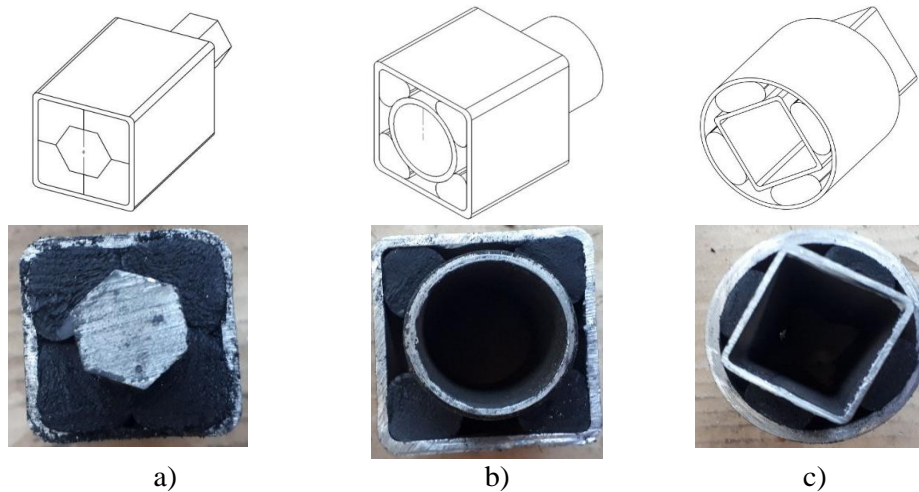
Fig. 2 - Different constructive solutions for vibration damping structures
a) exterior part is a rectangular shell with hexagonal solid central part; b) exterior part is a rectangular shell with round shell central part;
c) exterior part is a round shell with rectangular shell central part

All the solutions for static mechanical load were tested with the sole purpose of validation of the absorption system design structure. In this first step, the performance of the system isn't taken into account, because we were interested only in the functional mechanical load, which means applying a moment of torsion on the central part. For this purpose, a testing stand was built (Fig. 3).

Three shape details were presented in Fig. 4a, 4b and 4c. Element 1 is fixed on the Table 4 and the element *2* is a bar with the length of 1m which has a system for measuring the angle *5* (considering the horizontal line as reference). The calibrated weight 3 is similar with the user's distributed weight on the legs. After a set of preliminary tests, a maximum mechanical load corresponding to 30kg was used. For this purpose, a fastening part was constructed to allow the installation of each exterior elements of the tested structures. On the central part a lever with 1m length was fastened, and to the free end we attached gauges with pre-set weights.
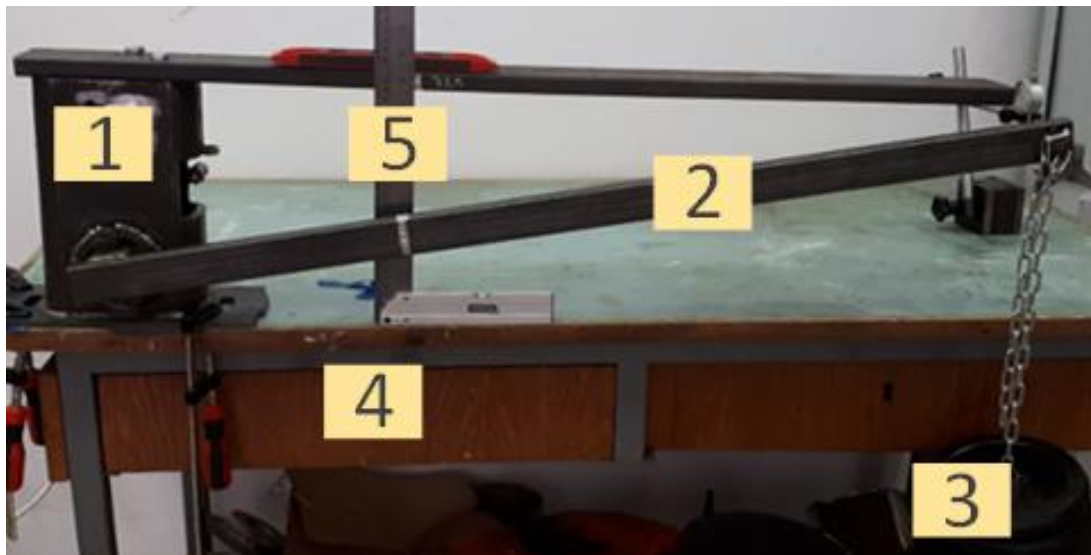
Fig. 3 - Experimental testing stand for static mechanical load (physical view)
1) fastening device for the structure to be tested; 2) bar with the length of 1m; 3) calibrated weights;
4) table; 5) system for measuring the angle of the bar (considering the horizontal as reference) and the height

In the first case, the external part is a rectangular and the central part is the solid hexagon (Fig 4a). Due to the compact structure, neither the external part, nor the central part is deforming and thus the rubber will have a large deformation under mechanical load considered and has a null elastic characteristic.

a)   b)   c)
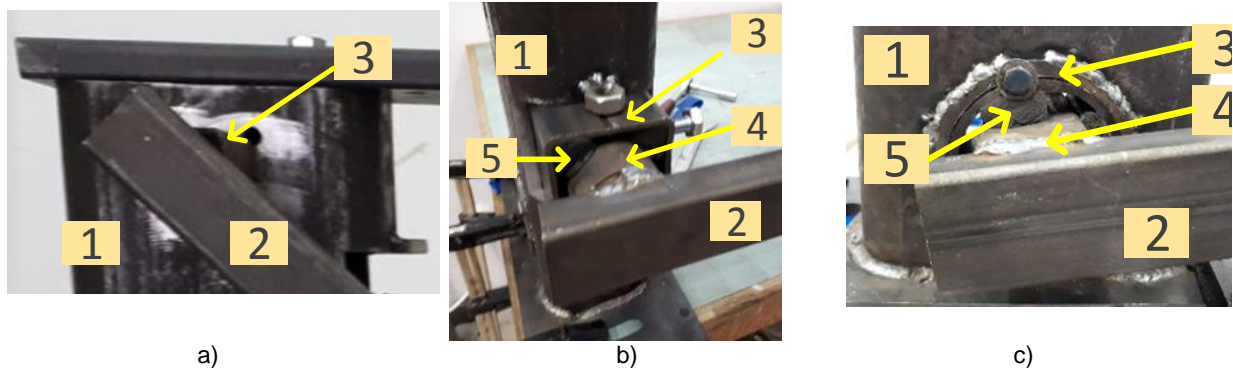
Fig. 4 - Experimental testing stand for static mechanical load
a) exterior part is a rectangular shell: 1) fastening part of the absorption structures;
2) bar used for applying the moment to the inner part; 3) hexagonal solid central part (hidden);
b) exterior part is a rectangular shell: 1) fastening part of the absorption structures; 2) bar used for applying the moment to the inner part; 3) the outer part of the damping system; 4) round shell central part; 5) rubber;
c) 1) fastening part of the absorption structures; 2) bar used for applying the moment to the inner part; 3) exterior part is a round shell;
4) with rectangular shell central part; 5) between the parts there is rubber

Considering the structure where the exterior part is a rectangular shell with a round shell central part (Fig. 4b), we didn't achieve the expected results. We expected the central part to return to the initial position. But, because the structure does not permit to the central part to have an elastic deformation, this part slides on the rubber part and the whole structure isn't returning to the initial position, as can be seen in Fig. 5.

Figure 5 is used only to demonstrate this behaviour, using a white paint on the exterior part and another on the central part.

a)   b)
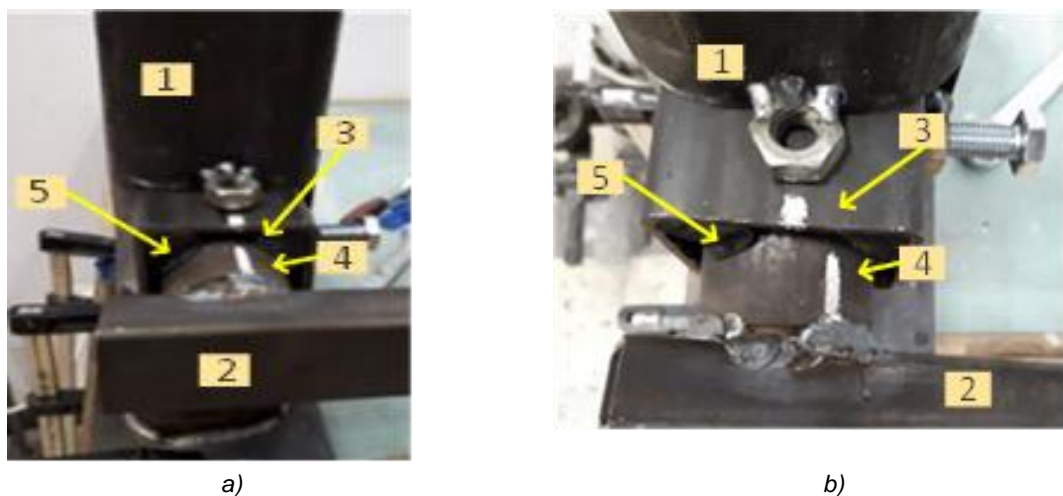
Fig. 5 - Experimental testing stand for static mechanical load
a)   Before applying loads;   b) Testing stand under stress conditions
1) fastening part of the absorption structures; 2) bar used for applying the moment to the inner part;
3) exterior part is a rectangular shell; 4) round shell central part; 5) rubber

In the third case, the structure is made by a round shell as exterior part and rectangular shell as central part. This structure had the best results in the first mechanical test. This is the reason why a dynamic theoretical analysis was realized only for this structure. The experimental tests have been confirmed by the finite elements simulation results. For this test, a 3D model using an automated fine meshing with 12524 nodes and 4623 elements was used. Each type of elements is tetrahedral. The exterior part is fixed and a mechanical load of 300Nm was applied on the rubber central part. Fig.6 shows how the central part deforms by adding, as effect, an elastic component to the structure.

a)   b)   c)
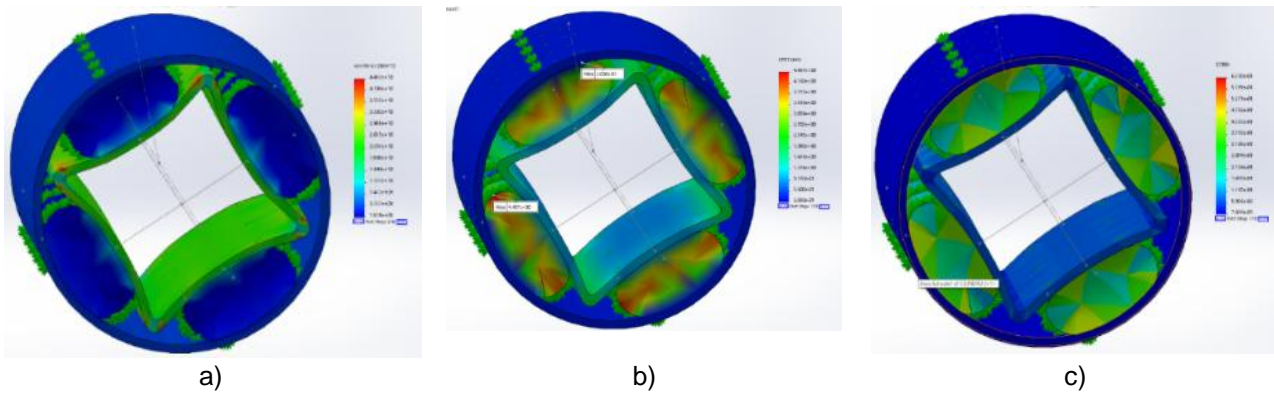
Fig. 6 - Finite elements simulation results
a) mechanical strain; b) deformation, c) mechanical

Dynamic analyses

Due to the mechanical structure of the vehicle, the shape of the user's weight (dumping part which can be put under the feet sustaining part as can be seen in Fig. 7 and the oscillation of terrain level, three types of mechanical load were identified:
- compression of rubber elements;
- bending of the exterior part when the central part is fixed;
- bending of the central part when the exterior part is fixed;
- torsion of the central part when the exterior part is fixed, as in static tests and FEM presented in Figure 6.

The first case analysed is the compression caused by the system itself. The system is much longer than the dimensions of the section of the frame. The load of the user's body is uniformly distributed by the feet sustaining part (position 1 and 2, Fig. 7) which has, at the central part, a connection to the direction system. We will consider this harmonic load because although the mass is unchanged when the terrain is flat, but it has some roughness, due to the dynamics of the system the load varies because of its vertical displacement.
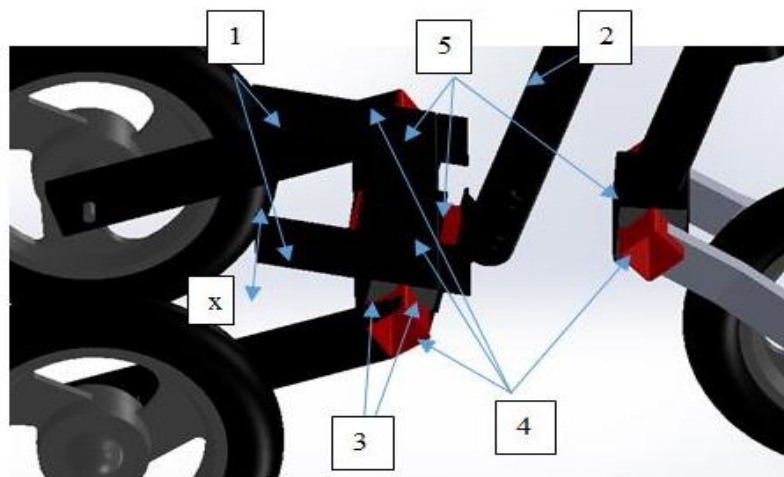
Fig. 7 - The components of the absorbing system
1) position of feet; 2) the body support part; 3) rubber;
4) central part (the profile can be: hexagonal, rectangular or round); 5) exterior part

Since the structure has no bearing and no clearance, we can say that we are dealing with a system with linear cubic rigidity. We can write, in this case, from a mathematical point of view the elastic component of the system (*Radeş M., 1985):*

$$f_e = k(x + \mu x)^3 \tag{1}$$

where f_e is the elastic force;
    x - vertical deformation of the system;
    k – stiffness;

μ - coefficient of negative nonlinearity since the tests showed that the system has a descending slope so, it has soft feature of the elastic component.

We consider that, when the vehicle is in motion, the force generated by the weight of the passenger is harmonic with the magnitude F_0 and a small pulse ω because of a very low frequency of the several Hz that will result in a harmonic displacement. Since we have separated the types of mechanical load, we can consider having a system with a degree of freedom consisting of a nonlinear spring because of the central part deformations and a dissipative part consisting of rubber elements.

The motion equation in the form considering only the transversal vibration of the central part is *(Radeş M., 1985)*:

$$m\ddot{x} + \frac{g \cdot k}{\omega} \cdot \dot{x} + k(x + \mu x^3) = F_0 e^{i\omega t} \tag{2}$$

In Eq. 2, g is an equivalent structural absorption factor. We're interested only in the first harmonic and the displacement can be described in function of vector of the movement which has real component (a_R) and imaginary component *(a_I):*

$$x = \tilde{a}e^{i\omega t} = (a_R + ia_I)e^{i\omega t} = ae^{i(\omega t + \theta)} \rightarrow x^3 \cong \frac{3}{4}a^2 x \tag{3}$$

The real component (a_R)and imaginary component (a_I)of the system are:

$$a_R = \left(1 + \frac{3}{4}\frac{\omega}{\omega_n}a^2 - \frac{\omega}{\omega_n}\right)\frac{k}{F_0}a^2 = F\sqrt{a^{2-\left(\frac{gka^2}{F_0}\right)^2}} \tag{4}$$

$$a_I = -g\frac{k}{F_0}a^2 \tag{5}$$

Considering that the displacement amplitude and the phase θ angle we can describe the vector of the movement:

$$a = \sqrt{a_R^2 + a_{R1}^2} \tag{6}$$

$$tg(\theta) = \frac{g}{\eta^2 - 1\frac{3}{4\mu}\mu a^2} = \frac{g}{\pm\sqrt{\frac{F_0^2}{k^2 a^2} - g^2}} \tag{7}$$

Where η is the loss factor defined as the ratio between the energy dissipated in a vibration cycle and the maximum potential energy, accumulated by the system in that cycle *(Radeş M., 1985)*.

We rewrite the equations according to the imaginary and the real part, and we obtain:

$$\left(\frac{\omega}{\omega_n}\right)^2 = 1 + \frac{3}{4}\mu\frac{F_0}{k}(-a_I) \pm g\sqrt{\frac{F_0}{gk}\frac{1}{(-a_I)} - 1} \tag{8}$$

$$\left(\frac{\omega}{\omega_n}\right)^2 = 1 + 3\mu\left(\frac{F_0}{2gk}\right)^2 - \frac{3\mu\left(\frac{F_0}{2gk}\right)^2 a_R^2 + \frac{F_0}{k}a_R}{2\left(\frac{F_0}{2gk}\right)^2\left[1 \pm \sqrt{1 - \left(\frac{2gk}{F_0}\right)^2 a_R^2}\right]} \tag{9}$$

Equations describing a family of curves above the curve leaning towards the low frequencies:

$$\omega^2 = \omega_n^2\left(1 + \frac{3}{4}\mu a^2\right) \tag{10}$$

The pulsation of the system should be different from the natural pulsation of the system which is $\omega_n = \sqrt{\frac{k}{m}}$. In our case we obtained from the finite element model that its value was 0.07234.

We can define the stability limit as:

$$\left(\frac{\omega}{\omega_n}\right)^2 = 1 + \frac{3}{4}\mu a^2 \pm \sqrt{\frac{9}{16}\mu^2 a^4 - g^2} \tag{11}$$

$$\eta\left(\frac{\omega}{\omega_n}\right)^2 = 1 + \frac{g}{2}\left(tg(\theta) + \frac{3}{tg(\theta)}\right) \tag{12}$$

The following type of load is torsional for the entire structure. In our case the motion equations are *(Cârdei P, 2010)*:

$$\ddot{\beta} + k_{0i}1 \cdot \beta + k_{1i} \cdot \beta^3 + c\beta' = M(t) \tag{13}$$

where $i = \begin{cases} 1 \text{ at charging} \\ 2 \text{ at discharging} \end{cases}$

with the original conditions

$$\beta(t_0) = 0 \text{ and } \quad \dot{\beta}(t_0) = 0 \tag{14}$$

Experimentally, we obtain the values between the moment of torsion and torsion angle and, based on these values, the chart presented in figure 8 was build. It can be seen, in figure 8, that there is a small hysteresis, which hasn't been taken into account, and using only the trend line, the resistant moment *M(t)* was identified:

$$M(t) = 7.345\beta - 15.387 \tag{15}$$
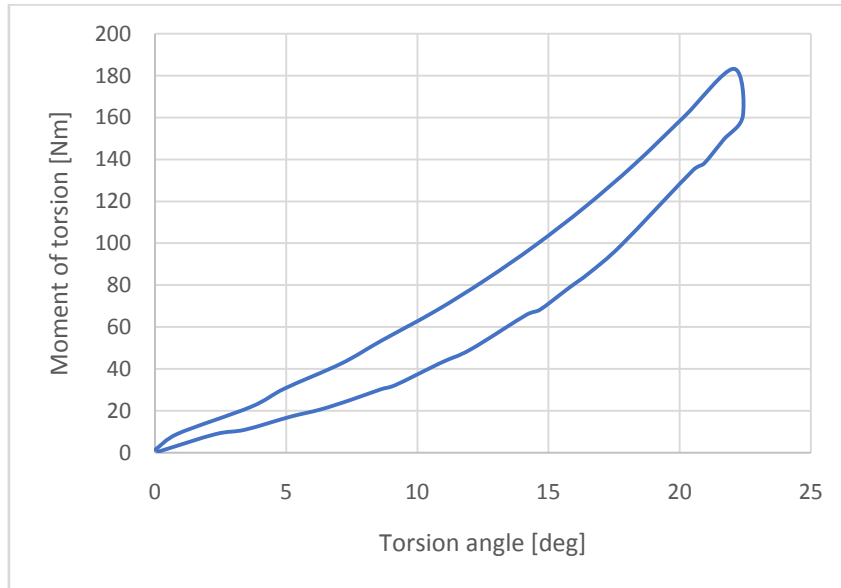
Fig. 8 - Diagram of the torsion moment vs torsion angle

CONCLUSIONS

In the article were presented three systems that can be used in individual electric vehicles, designed to absorb the mechanical shock and to reduce vibrations. The experimental tests with static mechanical loads identified the most efficient structure and it was validated by the finite element analysis. Also, for this structure were analysed different types of simple dynamic load which will be integrated into a complex mathematical model that can be used into other similar structures.

In the following research we will consider the bending and we'll analyse the simplified case in which a wheel does not move and the other moves under the action of the force generated by the deformations of the land when the vehicle is in the movement and the third type of mechanical load in the case of which we'll consider the effect of the central part.

a)

b)

Fig. 9 – 3D tricycle rendering

a)   *Used for a small trailer traction*   b) *Used for a mower traction*

Fig. 10 – Testing tricycle prototype

REFERENCES

[1]   Zhao L.L., Yu Y.W., Zhou C.C., Yang FX, (2018), Modelling and validation of a seat suspension with rubber spring for off-road vehicles. *Journal of Vibration and Control,* vol. 24(18), pp. 4110-4121;

[2]   Spiroiu MA, (2018), Railway Vehicle Pneumatic Rubber Suspension Modelling and Analysis, *Material Plastic Journal* , vol. 55(1), pp.24-27;

[3]   Hur S., Woo C.S., (2017), FEA Simulations and Tests of Rubber Insulator for Truck Suspension. *Elastomers and Composites Journal,* vol.52(4), pp. 303-308;

[4]   Tomilov I.N., Dostovalov D.N., Klokova E.A., (2015), Analysis of the Two-chamber Shock-absorption System of Landing Gear Based on Hybrid Methodology 2015, *International Siberian Conference on Control and Communications (SIBCOM),* DOI: 10.1109/SIBCON.2015.7147241;

[5]   Nielens H., Lejeune T., (2004), Bicycle shock absorption systems and energy expended by the cyclist. *Sports Medicine Journal*, vol.34(2), pp.71-80;

[6]   Nielens H., Lejeune T.M., (2001), Energy cost of riding bicycles with shock absorption systems on a flat surface. *International Journal of Sports Medicine* 22(6), pp. 400-404;

[7]   Neto F.P.L., dos Santos M.B., (2012), A Procedure for the Parametric Identification of Viscoelastic Dampers Accounting for Preload, *Journal of the Brazilian Society of Mechanical Sciences and Engineering,* vol.34(2), pp. 213-218;

[8]   Radeș M., (1985), Frequency domain experimental modal analysis techniques. *Shock and Vibration Digest*, vol.17(6), pp. 3-15;

[9]   Cârdei P., Munteanu Al., Muraru V., Sfiru R., (2010), Elementary Non-Linear with Linear Damping Mathematical Model for Neidhart Suspension, *INMATEH - Agricultural Engineering,* vol.10(1), pp.31-34;

[10]   Suvac A.M., Ganea-Christu I., (2019), *Electrically powered tricycle to be aggregated with small agricultural equipment*. Patent application no. A-00625 / 2019, Bucharest / Romania;

[11]   Suvac A.M., Ganea-Christu I., (2019), Electrically powered tricycle aggregated with agricultural Equipment, Proceedings of *The International Symposium ISB-INMA TEH' 2019*, Bucharest / Romania.

INVESTIGATION ON DATA COLLECTION AND FRACTAL CHARACTERISTICS OF SOIL SURFACE ROUGHNESS
/
土壤表面粗糙度数据采集及分形特性研究

Yi Qiu, Zhi Chen, Zhanfeng Hou*), Haiyang Liu, Fang Guo, Nianzu Dai
Inner Mongolia Agricultural University, College of Mechanical and Electrical Engineering, Inner Mongolia, China
*Tel: 04714309215; *)Corresponding author E-mail: njauhzf@163.com*

ABSTRACT

It is of great significance to acquire the soil surface roughness accurately for the study of the interaction between tractors and soil. Based on the laser sensor, this paper proposed the non-contact measuring instrument of the soil surface roughness with the data acquiring system by using Lab-View software. By using W-M theory, three commonly used fractal dimension calculation methods are compared and analyzed.. The result showed that the Root-mean-square method has the highest accuracy and clear physical meaning, which is ideal method to calculate the soil surface roughness characteristics. When the fractal dimension is between 1.4 and 1.6, the acquired data is analysed by the Root-mean-square method to obtain the fractal features of the soil surface roughness. The experiment results indicated that the fractal dimension of the ploughed surface is 1.39, that of disc harrow surface is 1.550, and that of rolled surface is 1.46-1.54. Obviously, the fractal dimension can accurately distinguish the soil surface roughness with the different treatments. However, the fractal dimension selected from different scales showed an obvious instability during calculations. The surface roughness index combined with the two parameters can effectively represent the soil surface roughness, and the larger the surface roughness index is, the greater the surface roughness is.

摘要

　　准确获取土壤表面粗糙度对于研究拖拉机与土壤的相互作用具有重要意义。基于激光传感器，利用软件 Lab View的数据采集系统，提出了一种非接触式土壤表面粗糙度测量仪。利用W-M理论的分形曲线对3种常用的分形维数计算方法进行了比较分析。结果表明，均方根法具有较高的精度和明确的物理意义，是计算土壤表面粗糙度特性的理想方法。当分形维数在 1.4～1.6 之间时，用均方根法对采集的数据进行分析，得到土壤表面粗糙度的分形特征。试验结果表明，犁耕表面的分形维数为 1.390，圆盘耙耕作表面的分形维数为 1.550，驱动耙耕作表面的分形维数为 1.460-1.540。可见，分形维数可以准确区分不同处理的土壤表面粗糙度。然而，选取不同尺度得到的分形维数在计算过程中表现出明显的不稳定性。结合分形维数与标准差这两个参数的表面粗糙度指数可以有效地表征土壤表面粗糙度，且表面粗糙度指数越大，表面粗糙度越大。

INTRODUCTION

Soil surface roughness plays an important role on the formation of soil particles, soil surface abrasion, wind erosion (*Shu, 2016; Lin, 2019*).Through the soil surface roughness analysis, predictions of soil erosion and soil moisture and distribution maps of soil moisture content can be drawn (*Zeng, 2017*). In addition, the interaction between the soil and the tire and the soil deformation can be simulated according to the surface roughness (*Mark, 2015; Hambleton, 2008*). Therefore, the soil roughness is the object the agricultural engineers and the automotive engineering personnel have studied since long (*Per, 2010*). This indicates that research to characteristic of soil surface irregularity has the great significance.

Since the 1980s, fractal theory has been widely used in surface topography feature recognition, which has good applicability for describing the natural phenomena of scale rate characteristics (*Altun, 2016; Fernández, 2016*). Therefore, regarding the randomness of spatial and temporal variability of agricultural soil, the use of fractal analysis can better describe the soil surface irregularities and supply the information that the traditional parameters cannot provide. So far, it has introduced a number of different methods of calculating fractal dimension, such as the box counting method, variation method, power spectrum method, the Root-mean-square method and the structure function method, these methods have their own characteristics and

the applicable scope (*Alsaidi, 2015; Tao,2020*). If the fractal dimension calculated and the actual types of fractal sets are incompatible, big calculation errors will be caused.

In this paper, several commonly used methods to calculate the fractal dimension of the rough surface are compared and studied to find a suitable characterization method for the fractal characteristics of the soil surface roughness.

MATERIALS AND METHODS

METHODOLOGY

Fractal, as a novel mathematical concept, is widely applied in processing and analysing natural phenomena of the complex minutiae characteristic. In the process of fractal attribute of surface roughness, the first step is to choose the appropriate fractal dimension calculation method. If the calculated fractal dimension is not compatible with the actual fractal set type, it will cause a large calculation error.

Measuring the spectral index β of a section is a common method to measure the fractal dimension. Fractal dimension D can be evaluated by plotting the power spectrum P in a logarithmic graph.

$$\left.\begin{array}{l} P(\omega) = B \cdot \omega^{-\beta} \\ D = (5-\beta)/2 \end{array}\right\} \tag{1}$$

where: D-the fractal dimension, [-];

   β-the slope, [-]

   ω-the frequency, [Hz];

   B-a constant, [-];

Hurst method is a simple and direct method applied to self-affine profile data. This method finds the maximum difference $R(\tau)$ in the window τ, and displays the difference in a $log–log$ plot as a function of 'window' width. $R(\tau)$ is calculated as follows.

$$R(\tau) = \max_{1\langle t \langle \tau} X(t,\tau) - \min_{1\langle t \langle \tau} X(t,\tau) \tag{2}$$

$X(T, \tau)$ is the data set. By dividing $R(\tau)$ by 'window' width $S(\tau)$, the R/S value will be a dimensionless number, which can be used to compare different phenomena and data sets. The slope H will give the fractal dimension according to $D = 2\text{-}H$. However, one disadvantage of this method is that transient noise may hide "real" data, although Hurst method has been proved to be one of the more accurate methods when tested on simulated isotropic noise-free sections.

The Root-mean-square (*RMS*) surface roughness describes the variation in surface elevation. It is also known as the standard deviation of the surface height. The *RMS* is the most basic form of profile description. The method of *RMS* height statistics h_{RMS} is as follows:

$$h_{RMS} = \sqrt{\frac{1}{n} \sum_{x=0}^{n} [s(x) - \bar{s}(x)]^2} \tag{3}$$

Where: n-the observation times of each sample, [-];

   $S(x)$-the height of the surface, the point X in the surface contour, [m];

   $\bar{s}(x)$-the average height of the surface contour, [m];

The fractal dimension is obtained from the $log–log$ plot of the *RMS* /variance values versus the perimeter length or box size. In this study we divide the profiles or the surfaces into equal-sized lengths or boxes, and calculate the variance or the square of the *RMS*, as:

$$S(h) = \frac{1}{N_h} \sum_{u=1}^{N_h} \left\langle \frac{1}{m_h} \sum_{i \in h} \left[z(x_i) - \bar{z}(h) \right]^2 \right\rangle^{1/2} \tag{4}$$

$$= ch^{2-D_{RMS}}$$

Where: N_h-the total number of boxes of size h, [-];

   m_h-the number of points in a box of size h, [-];

   $z(x_i)$-the measured value of profile curve that correspond to the x_i position, [m];

   $\bar{z}(x)$-average elevation value for all points in its box, [m];

   c-scale parameter, [-];

   D_{RMS}-fractal dimension, [-];

Changing equation (4) into the logarithm style, the form of linear equation is as follows:

$$\log S(h) = \log c + (2 - D_{RMS}) \log h \tag{5}$$

Assuming fractal behaviour, the slope of the *log-log* plot of the structural function, $S(h)$, against the distance, h, gives an estimation of the D_{RMS}.

The *RMS*/variance method is useful since it combines traditional roughness measurements with fractal analyses, and emphasizes the fact that *RMS*/variance values are scale dependent and can only be used as qualitative measurement.

W-M function

The soil surface roughness has statistical self-affine property, which can be simulated by the ideal fractal curve W-M which is continuous everywhere but not differentiable everywhere and has self-affine property. Its expression is as follows (*Deng, 2017*):

$$Z(x) = G^{D-1} \sum_{n=n_1}^{M} \frac{\cos(2\pi \gamma^n x)}{\gamma^{(2-D)n}} \quad (1 < D < 2, \ \gamma > 1) \tag{6}$$

Where: $Z(x)$-random surface profile height, x-profile position coordinates, [m];

G-amplitude correction, reflecting the amplitude of $Z(x)$, which determines the specific size of $Z(x)$, [-];

D-fractal dimension, [-];

γ^n-profile spatial frequency, to determine the surface roughness spectrum, [-];

In this paper, calculating methods of the fractal dimension of surface roughness were compared using the standard functions. The fractal dimension of four W-M function curve was tested by using software programming of Matlab 7.0 (taking $D = 1.2, 1.4, 1.6, 1.8$; $G = 0.01$, $\gamma = 1.5$); the results are shown in Table 1.

Comparison with four methods   **Table 1**

Theoretical dimension	RMS method		Power spectrum method		Variation method		Weighted RMS method	
	Fractal Dimension	Accuracy	Fractal Dimension	Accuracy	Fractal Dimension	Accuracy	Fractal Dimension	Accuracy
	[-]	[%]	[-]	[%]	[-]	[%]	[-]	[%]
1.2	1.317	90.3	0.703	58.6	1.262	94.8	1.086	94.9
1.4	1.457	95.9	1.078	77.0	1.342	95.8	1.455	96.2
1.6	1.592	99.0	1.433	89.6	1.469	91.8	1.597	99.8
1.8	1.619	89.9	1.761	97.8	1.501	83.4	1.794	98.9

Analysis of results

It can be seen from the above computed results, for the simulated profile curve, that power spectrum method increases its precision unceasingly along with the rise of fractal dimension. When the fractal dimension is 1.8, the precision is higher than other methods. Variation method has the high precision when the fractal dimension is small compared to other calculation methods, but the precision drops sharply along with the rise of fractal dimension; the method is suitable for dimension analysis of less than 1.4 in profile curves. Root-mean-square method has high computational accuracy in the theory fractal dimension of 1.4 to 1.6.

As physical meaning of the Root-mean-square method is clear, this method has very good function of characterization to the surface profile curve. Simultaneously, pass through calculation of each kind of soil data, it can be found that its fractal dimension value is smaller than 1.6, therefore the root-mean-square method was used to calculate soil surface roughness in this article.

Root-mean-square weighting method

In the computational analysis, it is found that the fractal curve in the scale domain of the measure does not strictly meet the fractal scaling rates. In different scale domain estimate of the fractal dimension, there are still some differences, which makes difficult to eliminate subjective defects of fractal dimension.

It is observed from Equation (5) that, (2-*D*) is the slope of the straight line obtained from the statistical regression in the double logarithmic graph, so that (2-*D*) is equal to *ε*, which is called the fractal dimension scale factor. If the time series strictly satisfies the fractal scaling rate, the scaling factor should be constant. However, in the actual calculation of the fractal dimension of soil surface roughness, if the calculation of time-domain value is known as the growth measure, and because calculation of the selected growth scale is different, it will lead to the difference between the corresponding scale factors. Their standard deviation can be expressed as:

$$\sigma_c = \mathrm{E}\left(\varepsilon - \bar{\varepsilon}\right)^2 \tag{7}$$

The smaller the value of δ_C is, the closer the scale coefficient ε is, the higher the precision of fractal dimension is. On the other hand, if the value of δ_C is larger, the deviation of fractal dimension scale factor ε will increase, and the accuracy of fractal dimension will be lower. In a certain confidence level, the confidence limit of scale coefficient of these growth measure is:

$$\varepsilon_u = \bar{\varepsilon} + K\sigma_c \tag{8}$$

K is the ratio of scale factor, when K is discrete normal distribution and confidence level is 0.995 in the case, K=2.99. The value of ε_u is substituted into (5), obtaining:

$$\log S(\tau) = \log c + \varepsilon_u \log \tau \tag{9}$$

See Table 1 for the standard fractal dimension value calculated by standard function *W-M* method. The results show that the accuracy of this method is obviously higher than that of the original Root-mean-square method.

RESULTS AND DISCUSSIONS
Surface roughness testing device Design Solutions

The testing device of road surface asperity designed in this paper. This device uses laser distance measuring sensor to collect the data information about the distance between the uneven ground and sensor. From a light source L, a light beam is issued onto the surface of measured object O_1 in Fig.1. The light beam will hit the surface of the measured object at point A. The scattered light reflection is focussed through a lens at a point A' on the detector. If the distance from the gauge probe to the measured surface is changed by X, the light beam from the light source will hit the source O_2 of the measured object at a new point B. The image of point B on the detector at point B' is displaced from the previous point A' by X'. The relation between the distance change X and the translation of X' by the light spot on the detector is determined by the geometrical arrangement between the light source and the detector. This relation is not linear. Since the light source, the lens and the detector are mechanically and solidly attached together, the relation between X and X' is known and can be used to linearize the measured results.
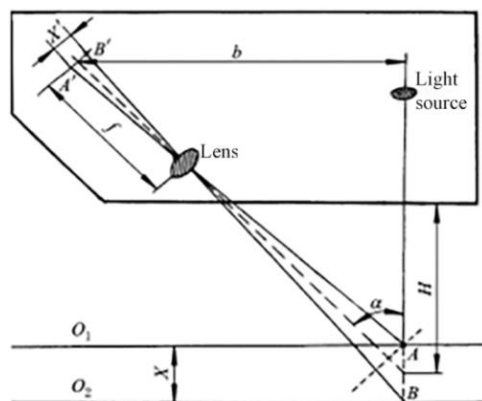
Fig. 1 - The measurement principle of the laser profiler

The test system consists of the hardware control and software data processing in Fig.2. The hardware control system is established on the ball screw slipway with the length of 1.2 m and lead of 5 mm. The rack is 0.6 to 1 m higher above the ground, which is equipped with 42HD1403 two phase four-wire stepping motor and high-subdivision stepper motor drives 2HD403 with a stepping angle of 1.8°. The laser distance measuring sensor has a range of measurement of 0.2m to 2m with a resolution rate of 1mm and data interface of RS232 USB. In the process of measuring, the laser sensor is fixed on the sliding block and moves back and forth along with the screw on the horizontal direction. The data transmission interface is connected with the USB interface. The controller adopts STC89C52 single-chip as the central processing unit and programming adopts the integrated development environment of Keil-µVision4. The serial port break method is utilized to receive the control order from the upper monitor and control the working condition of stepper motor driver module. The working voltage of stepper motor driver is DC 24V (external power source) and that of the single-chip control system is direct current 5V (computer serial port power supply).

Fig. 2 - The test equipment

A laser profiler was applied to measure agricultural soil roughness. The profiler is capable of acquiring roughness profiles of up to 1 m long at one time. The spatial resolution of the instrument is 1 mm. The instrument is thus well suited for capturing accuracy roughness information. The software control system adopts the virtual instrument software development platform LabVIEW2014 and the modular design method. The module is independent, and realizes the functions of parameter setting, control instruction sending, data acquisition and analysis processing, graph drawing and data display. The data processing software interface and system flow chart are shown in Fig.3 and Fig.4.

Under the "measurement mode", first, it is demanding to reset the laser sensor location and click on the button of "Start Calibration". Send "3" to the single-chip controller through the software. After receiving the instruction, the controller will reverse the stepping motor and the sliding block drives the laser sensor to move left to the "zero". Click on this button after it reaches "zero" and the software system will send "zero" to the single-chip controller. The stepping motor will enter the "forward state", indicating the completion of calibration and entry into the state of waiting for the instructions.

Click on the button of "start processing". The software will send "0x4F" to the laser sensor; after the laser sensor is started, "0x43" is sent after 3s so as to place it under the continuous collection mode (at this time, the laser sensor has already started sending the collected data to the serial port; however, the software system does not read this data). At last, click on the button of "collecting data". After setting the save path, the stepping motor is driven for operation according to the parameter that has been set' meanwhile, the upper computer software reads the data collected by laser sensor and exercises the real-time display and storage. When the measuring point reaches 1024, the software system stops data storage. At the same time, the MCU names a new measuring file according to the time and stores the data in the file. The single-chip controller is also started to drive the stepping motor.
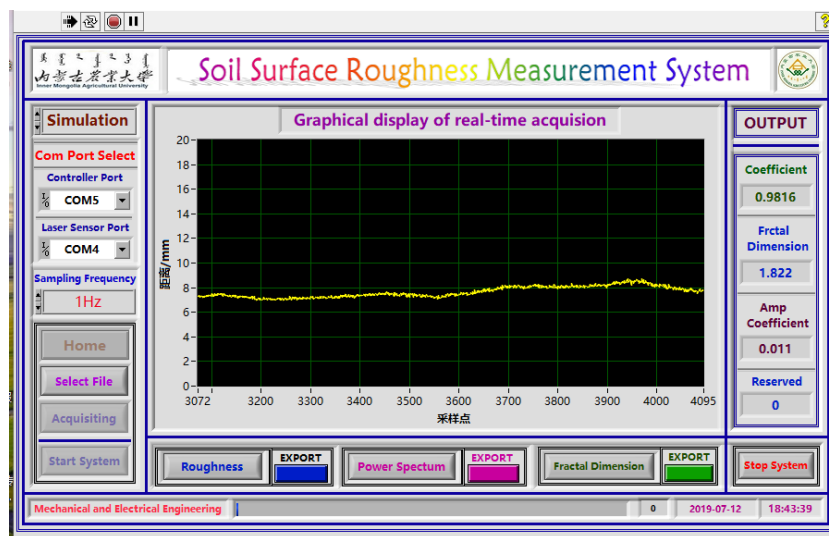
Fig. 3 - Data processing interface
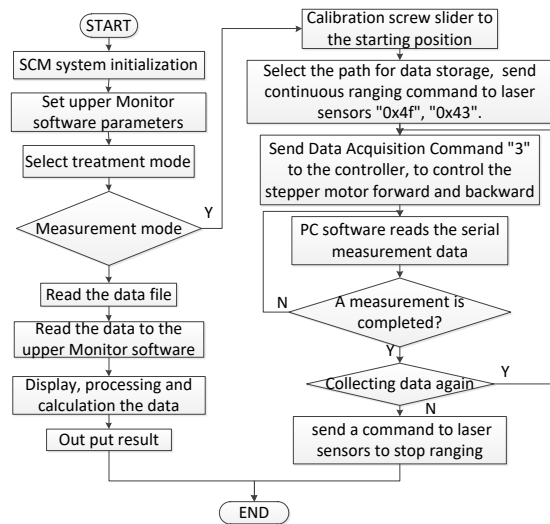
Fig. 4 - The system work flow chart

Three types of tillage surfaces, that is ploughed, harrowed and rolled surface, are tested, details concerning this database are showed in Fig.5. Profiles are acquired at 0 (parallel), 45 and 90 (perpendicular) degrees with respect to the tillage direction. The measuring length is 5 m.
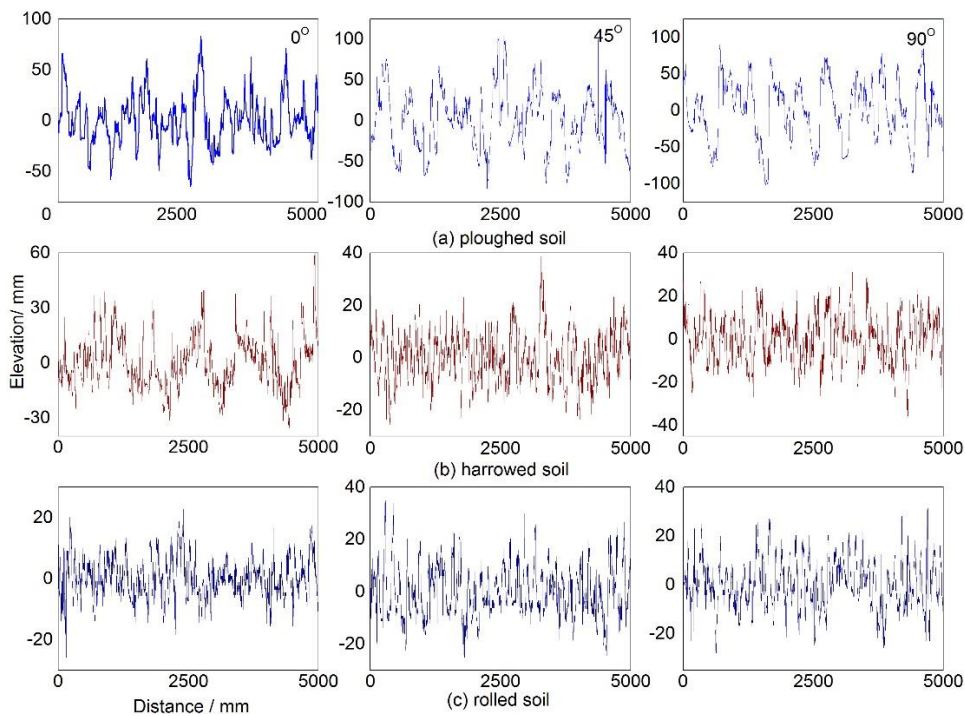
Fig. 5 - Profiles of different tillage soil surface

Calculation of fractal dimension

Three kinds of soil surface roughness are analysed with root-mean-square weighting method and the result is shown in Table 2. The fractal features of the three soil surface asperity of the data are presented in Fig.6.

RMS height, fractal dimension and surface roughness parameter   **Table 2**

Tillage method	Ploughed soil			Harrowed soil			Rolled soil		
	0°	45°	90°	0°	45°	90°	0°	45°	90°
D	1.340	1.391	1.362	1.471	1.534	1.497	1.622	1.552	1.578
RMS	22.395	37.294	40.773	11.941	9.014	10.214	6.689	10.984	8.485
R^*	103.55	181.86	231.59	29.13	17.58	22.30	10.42	21.94	15.03

Table 2 shows that fractal dimension can distinguish the different tillage states. There is a good correspondence between tillage state and fractal dimension. For instance, the ploughed surface exhibit D less 1.40, rolled surfaces exhibit D more than 1.55, whereas the harrowed surfaces have D values between 1.40

and 1.55. So, fractal dimension can be considered as a reliable parameter to describe local irregular structure of soil surface. The more non-uniform the surface roughness profile, the higher the fractal dimension.
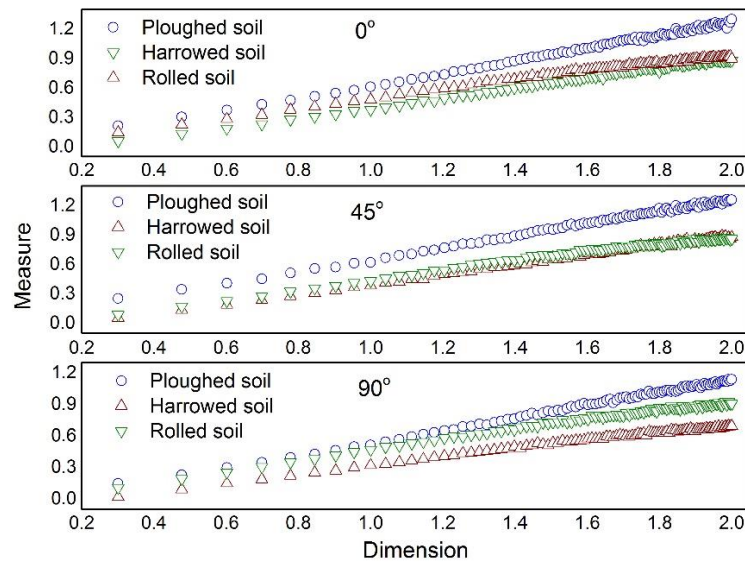
Fig. 6 - Fractal features of different soil surface

Fig. 6 shows that measure $S(\tau)$ and scale τ display good linear relation in the bi-logarithmic diagram, a phenomenon that eloquently demonstrates that the curve of soil surface asperity is of typical fractal features. The irregularity of the soil surface could be described by the fractal dimension.

At the same time, it can be found that fractal dimension is the slope coefficient of the straight line between $logS(h)$ and $log(h)$. If two scale lines are parallel, it can be gotten the equal fractal dimension. Surface with the same profile shapes but with different profile heights have the same fractal dimensions. However, properties of such surfaces are completely different. In general, only the fractal dimension cannot express the character of soil surface's roughness. Therefore, a new parameter is still necessary. In the following, we will show that combining local fractal structure with classical parameters (*RMS* height) leads to satisfying description of soil surfaces. The overall statistics for *RMS* height as a function of fractal dimension are summarised in Fig.7.
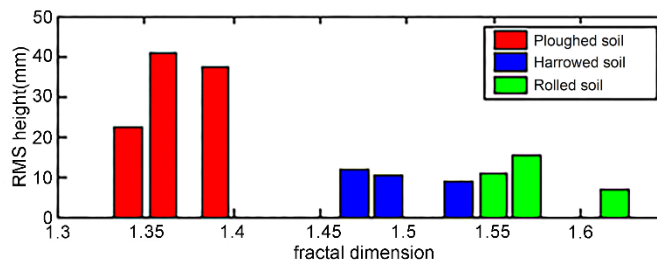
Fig. 7 - Effect of vibration frequency on the quality of pelleting

The Fig.7 shows that the linear relationship of *RMS* height h_{RMS} and fractal dimension D_{RMS} is not very obvious. For our database, the greater the *RMS* height is, the smaller the fractal dimension is. In fact, observation of our test soils show that for small *RMS* height, local structure is often described by small clods and then introduces a very high variability in the surface leading to a high fractal dimension.

The Equation(5) indicates that when the size of h is a unit, the dimension parameter $logC$ is the intercept of the regression line in $logS(h)$ -$logh$ plot. In other words, it is the height deviation of the profile in unit scale, and it has the same physics sense with the profile mean root square deviation value h_{RMS}. Therefore, we defined roughness index as a combinative parameter of fractal dimension D and mean root square deviation h_{RMS}, with the form as following:

$$R^* = h_{RMS}^{\frac{1}{D_{RMS}}}$$

(10)

When D_{RMS} keeps invariable, the increase or decline of h_{RMS} reflects the flat grade of the surface. increases or declines with h_{RMS} changes. So, we can apply to identify the complexity roughness surface. For instance, Table 2 shows that h_{RMS} value between the harrowed and rolled surfaces is basically the same. But

value of the ploughed soil, harrowed soil and rolled soil has a big difference. So, roughness index has high resolution capability to express the soil surface roughness.

CONCLUSIONS

1) The self-made soil surface asperity tester is utilized to collect the relevant information, which could provide a rapid and efficient method for the engineers to collect the data information about the soil surface asperity.

2) For cultivated soils, the fractal dimension is 1.3 to 1.6; calculating its fractal dimension using Root-mean-square method has high precision; Root-mean-square measure directly reflects the dynamic level of the surface profile roughness in the different scales, its physical meaning is clear, the fractal attribute is intuitive, after all, it is an effective way for soil surface fractal.

3) Calculating fractal dimension by modified Root-mean-square method can get right dimensions of division ratio with the growth measure; any scale of the fractal dimension has little influence on the results, so it is very stable and accurate to calculate fractal dimension of soil surface using this method.

4) The relationship between *RMS* height of the traditional statistical parameters and the farming way is not as obvious as the relationship between the fractal dimension and farming way of soil. Linear relationship between *D* and *RMS* is not very obvious, but as a whole, *RMS* height decreases as the fractal value increases gradually.

5) Describing the surface roughness with surface roughness index has higher resolution power than with *RMS*; it retains not only the characteristics of multi-scale fractal measurement, but also retains the advantages of traditional roughness parameters intuitive and simple. The greater the surface roughness index, the greater the surface roughness, and vice versa.

ACKNOWLEDGEMENTS

REFERENCES

[1]   Alsaidi N., Abdulaal J., (2015), An Improved Differential Box Counting Method to Estimate Fractal Dimension. *Eng. & Tech. Journal.* Vol 33, Issue 4, pp. 714-722, University of Technology /Baghdad;

[2]   Altun S., Sezer A., Goktepe A., (2016), Effect of fractal dimension on the strain behaviour of particulate media. *Fractals*, Vol 24, Issue 4, pp.165, Ege University/Turkey;

[3]   Deng K., Liu Z., Deng J., Zhao Y., (2017), Variation of Surface Profile Topography Based on W-M Function Model. *Mechanical design and manufacturing*, Vol 1, Issue 1, pp. 47-50, Jiangxi/China;

[4]   Fernández M., Nowak M., Sánchez M., (2016), Counterexamples in theory of fractal dimension for fractal structures, *Chaos Solitons and Fractals*, Vol.89, Issue 1, pp.210-223, Spain;

[5]   Hambleton J., Drescher A., (2008), Modelling wheel-induced rutting in soils: Indentation. *Soil & Tillage Research*, Vol 45, Issue 1, pp. 201-211, Minneapolis/USA;

[6]   Lin J., (2019), Study on the influencing factors and prediction model of wind erosion in the north sand covered loess area. *Water Conservancy Technical Supervision*, Vol 1, Issue 5, pp. 16-19, Liaoning/China;

[7]   Mark M., Frank V., Bernhard P., (2015), DEM–FEM coupling simulations of the interactions between a tire tread and granular terrain, *Computer Methods in Applied Mechanics and Engineering*, Vol 289, Issue 6, pp. 227-248, University of Luxembourg/ Luxembourg;

[8]   Per S., Mathieu L., (2010), A note on the vertical stresses near the soil-tyre interface. *Soil& tillage Research*, Vol 108, Issue 1, pp. 77-82, Aarhus University/ Denmark;

[9]   Shu T., Wang X., (2016), Correlation between topographic relief and regional soil erosion based on 3S technology. *Soil and water conservation research*, Vol 24, Issue 4, pp. 127-132, Guizhou/China;

[10]   Tao Q., (2020), Analysis of variation characteristics of soil organic matter in Chuzhou based on topographic relief. *Anhui agronomy bulletin*, Vol 26, Issue 1, pp. 95-97, Anhui/China;

[11]   Zeng J., Chen K., (2017), A Comprehensive Analysis of Rough Soil Surface Scattering and Emission Predicted by AIEM With Comparison to Numerical Simulations and Experimental Measurements. *IEEE Transactions on Geoscience & Remote Sensing*, Vol 55, Issue 3, pp. 1696-1708, Beijing/China.

SIMULATION AND TEST OF CUTTING MECHANICAL CHARACTERISTICS OF MILLET STALK BASED ON ANSYS/LS-DYNA
/
基于 ANSYS/LS-DYNA 的谷子茎秆切割力学特性仿真与试验

Yanqing Zhang, Qingliang Cui[*], Hongbo Li, Zhiyong Zhang, Yongqiang He, Deng Sun [1]
College of Engineering, Shanxi Agriculture University, Taigu/China
Tel: +86-0354-6288254; E-mail: qlcui@126.com

ABSTRACT

In order to find the variations of mechanical properties of millet stalk during dynamic cutting, a three-dimensional model of cutting parts and a double-layer flexible model of millet stalk were established in this study. The mechanical cutting properties of millet stalk at different cutting speeds and blade oblique angles were investigated based on ANSYS/LS-DYNA, while the verification tests were carried out based on the self-made cutting test bench. Simulation results showed that the maximum Von Mises stress was concentrated on the contact point of the stalk and the moving blade. The maximum Von Mises stress of stalk during extrusion, cutting, and after cutting were 60.03 MPa, 60.72 MPa, and 39.87 MPa, respectively, and the cutting energy of stalk epidermal tissue was greater than that of inner tissue. The cutting stress and the unit area cutting energy decreased first and changed steadily as cutting speed was increased when the cutting speed was 0.5-1.5 m/s. When the blade oblique angle was 0°-48°, the cutting stress decreased as the blade oblique angle was increased, while the unit area cutting energy decreased first and then increased. Verification tests showed that the cutting speed and the blade oblique angle had significant effects on the cutting mechanical properties (P < 0.05), which was consistent with the simulation test results. Research results can be used to optimize the cutting parameters of millet stalk.

摘要

为探究谷子茎秆动态切割过程中的力学特性参数变化规律，本文建立了切割部件三维模型与谷子茎秆双层柔性模型，以切割速度与刀片斜角为影响因素，基于 ANSYS/LS-DYNA 对谷子茎秆进行动态切割力学仿真，并采用自制切割试验台进行验证试验。仿真结果表明：茎秆切割过程分为挤压与切割茎秆两个阶段，且最大 Von Mises 应力集中于茎秆与动刀片接触部位，挤压过程、切割过程与切割完成后茎秆最大 Von Mises 应力分别为 60.03 MPa、60.72 Mpa 和 39.87 MPa，且茎秆表皮层较内层切割功耗大。当切割速度为 0.5—1.5 m/s 时，切割应力、单位面积切割功耗随切割速度的增大而减小后呈现平稳变化的趋势：当刀片斜角度 0°—48° 时，切割应力随刀片斜角的增大而减小，而单位面积切割功耗随刀片斜角的增大先减小后增大。验证试验表明：切割速度与刀片斜角均对其切割应力、单位面积切割功耗影响显著（P<0.05），与仿真试验结果吻合。研究结果可为谷子茎秆切割参数优化提供借鉴。

INTRODUCTION

Cutting is one of the necessary processes of crop mechanical harvesting. The cutter is one of the key parts of the harvester, and its performance parameters not only is a prerequisite for smooth progress of the harvester operation, but has great significance for reducing cutting force and energy *(Wang et al., 2017; Liu et al.,2018)*. Millet, a *graminaceous* plant, is mainly grown in the temperate and tropical regions of Eurasia, and it has gradually become an important crop for adjusting the structure of the planting industry and improving dietary habit with the improvement of people's living standards *(Annor, et al., 2017; Li, et al., 2018)*. Nowadays, most researches mainly focus on the mechanical threshing, separating, cleaning and other mechanical harvesting issues to reduce grain loss *(Liang, et al., 2015)*.

---

[1] *Yanqing Zhang, As Lec. Ph.D. Eng.; Qingliang Cui[*], Prof. Ph.D. Eng.; Hongbo Li, Prof. Ph.D. Eng.; Zhiyong Zhang, Prof. Ph.D. Eng.; Yongqiang He, M.S. Stud. Eng.; Deng Sun, M.S. Stud. Eng.*

Imminently, due to the large diameter and high hardness of millet stalk, how to reduce the stalk cutting force and energy is an urgent problem to be solved under the background of energy conservation.

Our research group performed a quasi-static cutting mechanical test of millet stalk previously *(Zhang, et al., 2018)*. In order to obtain the cutting mechanical parameters more accurately, it is necessary to consider the dynamic cutting mechanical characteristics because of the faster cutting speed during mechanical harvesting. ANSYS/LS-DYNA is an explicit solution software that can solve highly nonlinear structural dynamic questions, and using it can greatly shorten the cycle of development *(Zhang, et al., 2010)*. The mechanical model of cutting stalk belongs to a typical high-speed erosion model, and adopting ANSYS/LS-DYNA can clearly express the interaction between the stalk and the cutter to explore the failure form and the change laws of mechanical properties of the stalk under different cutting parameters. Most Scholars had used this software to simulate the cutting experiments of stalks such as Chinese Cabbage, sweet sorghum, corn and sugarcane, and the stalk failure stress during dynamic cutting was found *(Zhang, et al., 2010; Diao, et al., 2011; Huang, et al., 2011)*. Many scholars also analysed the regular patterns of cutting mechanical properties of stalk with different cutting speeds and blade oblique angles *(Igathinathane, et al., 2010; Johnson, et al., 2012; Song, et al. 2015)*, but there are few studies about the dynamic cutting mechanical characteristics of millet stalk.

In this study, the material model of millet stalk and mechanical cutting simulation test based on ANSYS/LS-DYNA were carried out, and the simulation results were compared with the verification test based on the cutting test bench. The change rules of stress during mechanical cutting and the effect of cutting parameters on its properties were analysed. These results not only provide a modelling method for millet stalk, but supply a reference for optimization of cutting parameters of millet stalk.

MATERIALS AND METHODS
Sample preparation
The millet stalk was taken from the test field of millet planting in Taigu County, Shanxi Province, China (112º55′ E, 37º43′ N). After the stalks without lodging, diseases and pests were randomly taken back, the stalks were cut about 15 cm from the root. The moisture content (w.b.%) of the stalks were measured at 67.83% by the standard method *(ASABE, 2008)*. The cross section of millet stalk was similar to hollow ellipse, and the average length axis D_1, short axis D_2, and wall thickness T of stalks were about 12.50 mm, 7.75 mm, and 3.17 mm, respectively, as shown in Fig. 1.

Cutting model
In this study, the millet stalk was regarded as an elastomer, and the node load, node displacement, node speed, and node acceleration can be expressed by the following general dynamic equation in the process of analysing the elastomer *(Liu et al., 2018)*:

$$[M]\{\ddot{X}\}+[C]\{\dot{X}\}+[K]\{X\}=\{F(T)\} \tag{1}$$

where: $[M]$ is the structural mass matrix; $[C]$ is the structural damping matrix; $[K]$ is the structural stiffness matrix; $\{X\}$ is the node position vector; $\{\dot{X}\}$ is the node velocity vector; $\{\ddot{X}\}$ is the node accelerated velocity vector; F is the load; T is the time.

Millet stalk is composed of epidermal tissue, basic tissue and vascular bundle *(Zhang et al., 2018)*. The physical properties of millet stalk were shown in Table 1. Specifically, the wall thickness, density, elasticity modulus and shear modulus of epidermal tissue and inner tissue (basic tissue and vascular bundle) of stalks were measured in biomechanical test before this study *(Zhang, 2019)*, and the Poisson's ratio was taken from the references about agricultural material *(Ma et al., 2015)*. According to the modelling method *(Cui et al., 2010)*, the stalk was simplified into a hollow elliptic cylinder with equal section, as shown in Fig. 1.

Table 1

The size and mechanical parameters of the cutting model

Material	Wall thickness [mm]	Density [g/cm³]	Elasticity modulus [MPa]	Shear modulus [MPa]	Poission's ratio
Epidermal tissue	0.28	0.77	$8.79×10^3$	$9.54×10^3$	0.30
Inner tissue	2.89	0.72	$4.93×10^3$	$3.71×10^3$	0.30
Moving blade	/	7.85	$1.98×10^5$	$7.86×10^4$	0.35
Guard	/	7.30	$1.51×10^5$	$6.10×10^4$	0.25

The standard type II cutter (including the type II moving blade and the type IV guard) commonly used in harvester were selected, and its structural parameters and physical properties were determined according to the national standard of China *(China National standardizing committee, 2009)*.

The stalk cutting model is shown in Fig.2, and the mechanical parameters of the cutter are also shown in Table 1.
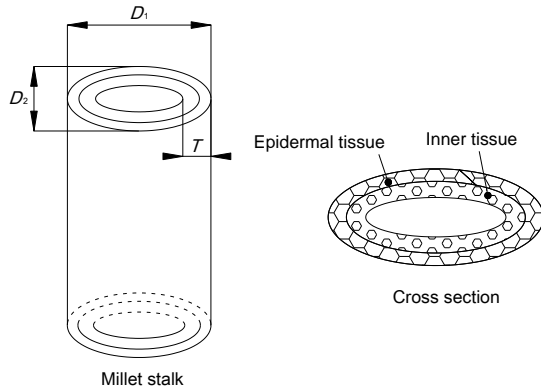
Fig. 1 Simplified stalk model
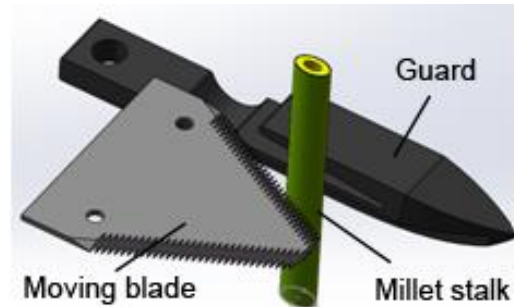
Fig. 2 Cutting model

Simulation test

HyperMesh Desktop 14.0 was adopted for pre-processing of the cutting model, including the following steps:

Cutting model meshing: Tetrahedral solid unit was selected to mesh the cutter and the stalk. The contact area of the cutter and the stalk and the non-contact area were meshed in turn, and the grid size of the contact area and the non-contact area were 2 mm and 5 mm, respectively. In this way, there were 2263, 8621, 58032 units for the moving blade, cutter and stalk, respectively.

Material parameter setting: The material parameters were determined according to the Table 1.

Contact condition and constraint condition setting: The contact forms of millet stalk with moving blade and guards were erosion contact and face contact, respectively，and the dynamic friction and static friction were 0.12 and 0.24, respectively *(Xue, 2018)*. The moving blade was set to translational freedom in the cutting direction, and the guard and the bottom stalk were fully constrained.

Initial condition of simulation setting: In order to analyse the influence of cutting speed and blade oblique on mechanical properties of millet stalk, different cutting speed (0.5-1.5 m/s) and blade oblique angle (0°- 48°) were set in the simulation test. Meanwhile, the solution time and the simulation interval time were set to 0.04s and 0.0008s, respectively.

The pre-processing file was saved as a .k file, and then loaded into ANSYS / LS-DYNA to solve.

The stalk cutting energy and the reaction force received by the moving blade were recorded during the simulation cutting process, and the cutting stress and the unit area cutting energy were calculated by equation (2) and equation (4).

Verification test

The self-made cutting test bench was used to stalk cutting test (Fig.3). The cutting test bench is powered by a speed-regulating motor, and the slider-crank mechanism drives the moving blade to move in a straight line to complete the stalk cutting. The cutting force was measured by the force sensor, and the sensor signals were recorded by the TST5000 data acquisition instrument (Fig.4).

The motor speed can be controlled by the inverter to adjust the average cutting speed of the moving blade (0-2 m/s). The moving blade is provided with a central hole and an arc-shaped hole surrounding the central hole, so the angle of the moving blade can be adjusted from 0 ° to 48 ° (Fig.5).

Fig. 3 - Cutting test bench
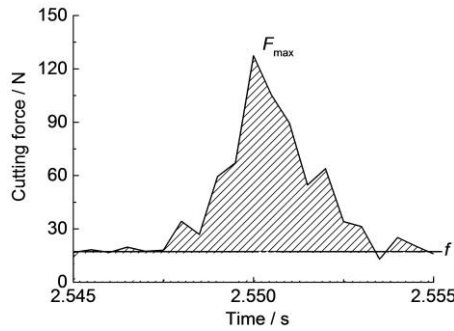
Fig. 4 - Curve of cutting force with time of millet stalk in verification test

Fig. 5 - Adjustment of blade oblique angle

The stalk cutting force during the verification test was recorded by force sensor, and the cutting stress, cutting energy and the unit area cutting energy were calculated as follows:

$$\tau = \frac{F_{max} - f}{A} \tag{2}$$

$$W = \int_0^t F \cdot v \cdot dt (-) \int_0^t f \cdot v \cdot dt \tag{3}$$

$$W_A = \frac{1000 \cdot W}{A} \tag{4}$$

where: τ is the cutting stress, [MPa]; A is the area of stalk cross section, [mm^2]; F_{max} is the maximum cutting force, [N]; f is the No-load resistance of moving blade in the verification test, [N]; F is the cutting force during the cutting test, [N]; W is the cutting energy, [J]; W_A is the unit area cutting energy, [mJ·mm^{-2}]; v is the average cutting speed, [m/s]; t is the cutting time, [s].

RESULTS
Stress distribution of millet stalk during cutting

The stress-strain cloud diagram of millet stalk from simulation test is shown in Fig.6. When the cutting speed was 1 m/s and the blade oblique was 30°, the stalk was squeezed first, and the maximum Von Mises stress of stalk at the contact point with the moving blade increased rapidly to 60.03 MPa. This is due to the tougher epidermal tissue of the millet stalk, and the moving blade had a certain impact force, resulting in Von Mises stress rising rapidly. Then the moving blade cut into the stalk, and the Von Mises stress changed dynamically, and the maximum Von Mises stress was 60.72 MPa. After cutting, the stalk was cut off and there was a certain residual stress of stalk, and the maximum Von Mises stress decreased to 39.87 MPa. Similar rules were found in other simulation tests at different cutting speeds and blade oblique angles.

Before cutting   **During cutting**   **After cutting**
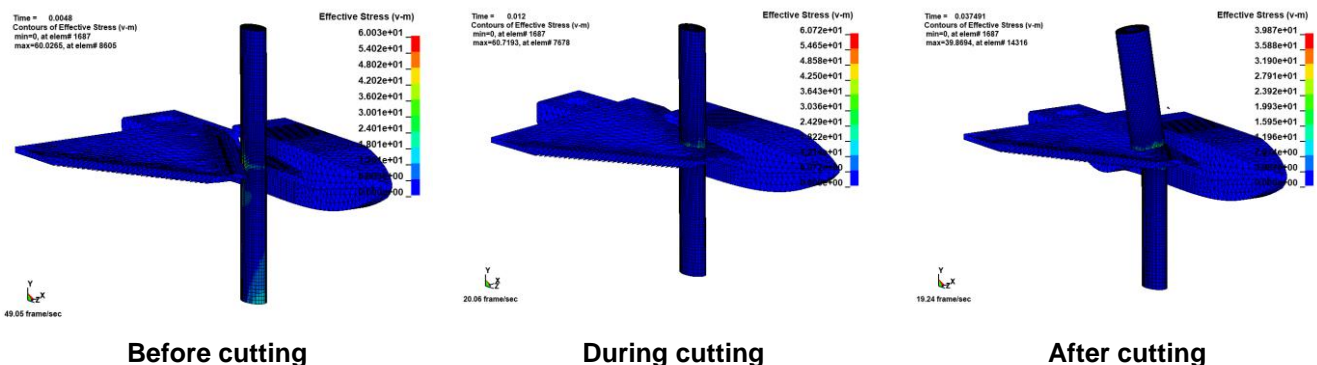
Fig. 6 - Stress and strain cloud diagram of the millet stalk during cutting

The variations of the cutting force, the cutting energy of stalk epidermal tissue and the inner tissue were shown in Fig.7, Fig.8 and Fig.9, respectively. In the cutting process, the cutting force increased intermittently until the stalk was cut off, the cutting force dropped to 0 N.
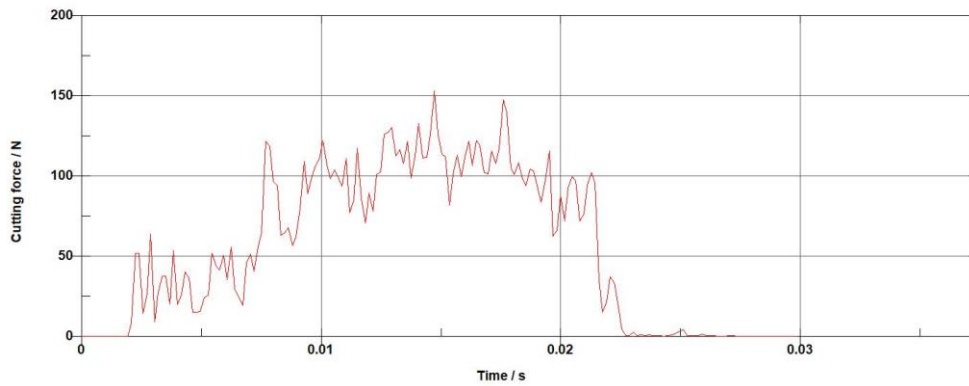
Fig. 7 - Curve of cutting force with time of millet stalk in simulation test
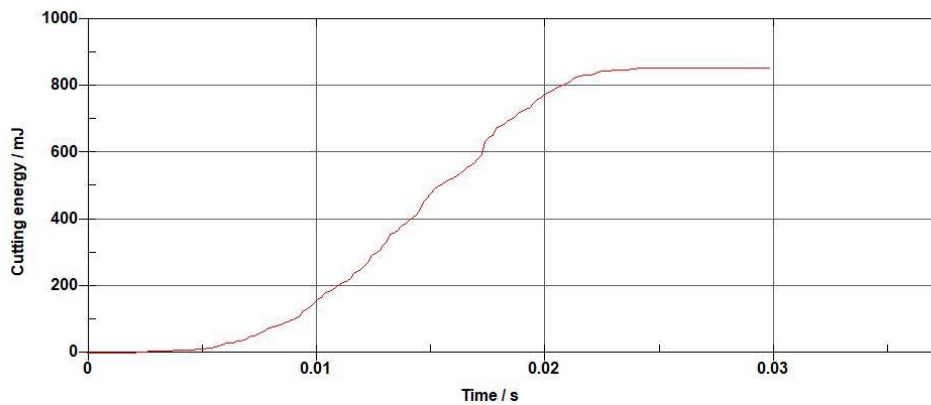
Fig. 8 - Curve of cutting energy with time of epidermal tissue of stalk in simulation test
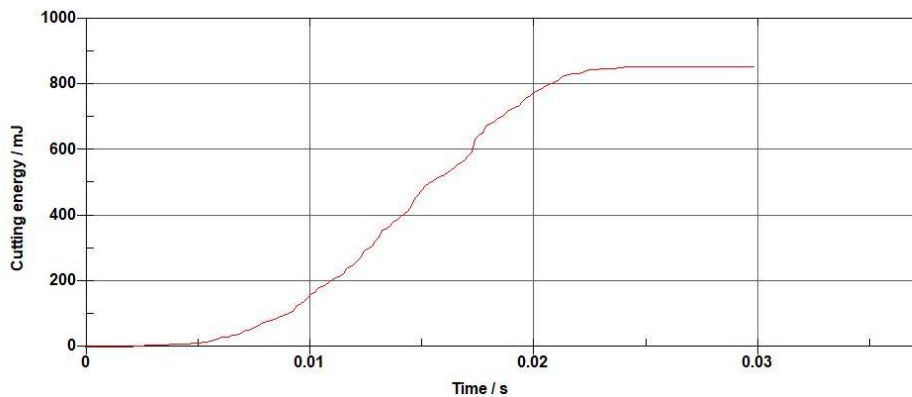
Fig. 9 - Curve of cutting energy with time of inner tissue of stalk in simulation test

The cutting energy of the epidermal tissue and inner tissue of stalk increased first and then presented a stable change trend. When the cutting speed was 1 m/s and the blade oblique angle was 30°, the maximum cutting force and the whole cutting energy (cutting energy of epidermal tissue and inner tissue) were 153.02 N and 1.07 J, respectively. The cutting energy of epidermal tissue and inner tissue of stalk were 0.86 J and 0.21J, respectively. Obviously, the epidermal tissue is stronger than the inner tissue of stalk, and similar rules in other simulation tests at different cutting speeds and blade oblique angles.

Effect of cutting speed on mechanical cutting characteristics of millet stalk

Simulation tests were conducted at five average cutting speeds of 0.5, 0.75, 1.0, 1.25 and 1.5 m/s. The variations of cutting stress and unit area cutting energy of stalk are shown in Fig.10. From Fig.10, we can find that the cutting stress and unit area cutting energy of stalk showed a trend of first decrease and then steady change with increasing average cutting speed.
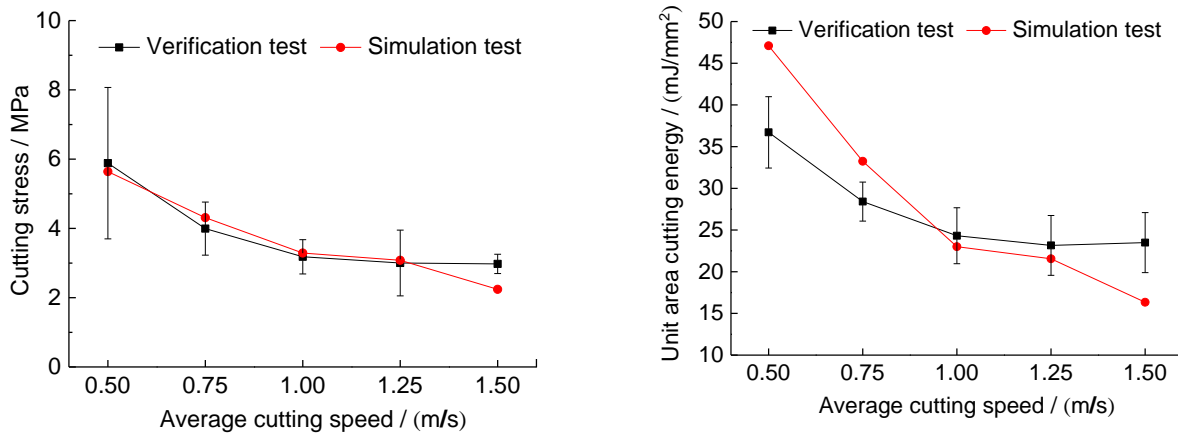
Fig. 10 - Variation of cutting mechanical properties with cutting speed

The reason was that the cutting process was divided into extrusion process and cutting process. When the cutting speed was slow, the stalk had a compression deformation under the action of cutter, but the time to transfer the stalk compression deformation gradually decreased with the increasing cutting speed. As a result, the amount of compression deformation does not change significantly, that is, the moving blade can easily cut into the stalk to complete the cutting at a higher speed. These results were consistent with the cutting tests previously mentioned by *Li et al.* (2011) and *Song et al.* (2015).

Verification tests at different cutting speeds were also carried out in this study, and similar rulers were found in verification tests. When the average cutting speed was 0.5-1 m/s, the cutting stress and the unit area cutting energy of stalk decreased significantly ($P<0.05$), but the cutting mechanical characteristics did not change significantly when the average cutting speed was 1-1.5 m/s ($P> 0.05$). The cutting stress and unit area cutting energy were the smallest when the average cutting speed was about 1 m/s. Therefore, the cutting simulation model established in this study was effective and could be used to reflect the cutting mechanical properties of millet stalk to a certain extent.

Effect of blade oblique angle on mechanical cutting characteristics of millet stalk

Simulation tests were conducted at five blade oblique angles of 0°, 12°, 24°, 36° and 48°. The variations of cutting stress and unit area cutting energy of stalk are shown in Fig.11. As can be seen, the cutting stress decreased with the increasing blade oblique angle, but the unit area cutting energy decreased first and then increased with the increasing blade oblique angle. These results were also consistent with studies by *Mathanker et al.* (2015) and *Song et al.* (2015). The reason can be attributed to the fact that the stalk was firstly clamped and fixed by the cutter, and the blade oblique played the role of sliding cutting the stalk. The actual wedge angle of moving blade is decreased with increasing blade oblique angle when sliding cutting the stalk *(Pang et al., 1982)*. Thus, the normal force used to cut stalk is reduced, and the cutting stress and unit area cutting energy decreased. However, the relative distance between the stalk and the moving blade increased when the blade oblique angle was too large. So, the cutting energy is not only used to cut the stalk, but also for the friction power consumption between the stalk and the moving blade, leading to an increase in unit area cutting energy of stalk.
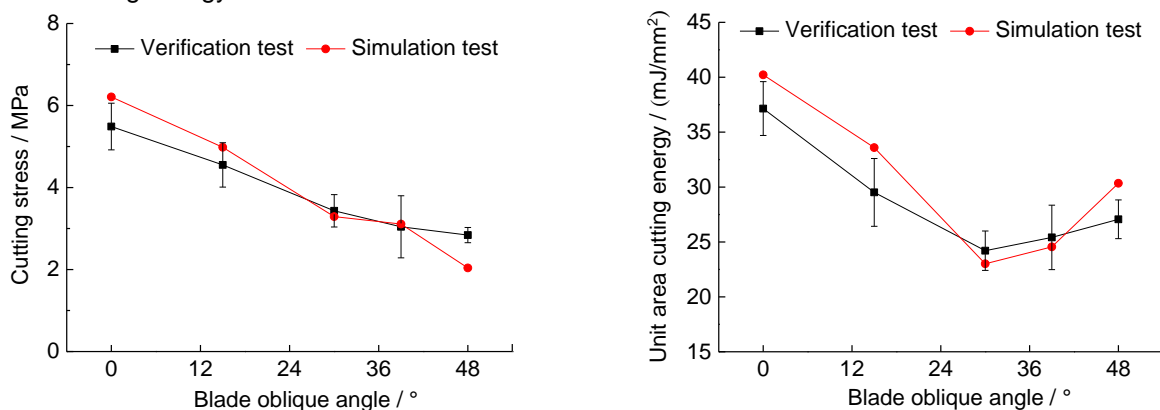
Fig. 11 - Variation of cutting mechanical properties with blade oblique angle

148

Verification tests at different blade oblique angle were also carried out in this study, and similar rulers were found in verification tests. Multiple comparisons of the mean values showed that the blade oblique angle had a significant effect on the cutting stress and the unit area cutting energy of stalk ($P > 0.05$), and the unit area cutting energy was smallest when the blade oblique angle was about 30°. These results were different from the previous quasi-static cutting test results *(Zhang et al., 2018)*, which is caused by high-speed cutting, and the high-speed cutting was much closer to the actual working conditions of harvest.

CONCLUSIONS

The simulation tests and verification tests of dynamic cutting of millet stalk were carried out, and the following conclusions were obtained:

(1) Dynamic cutting process of millet stalk could be divided into extrusion process and cutting process, and the maximum Von Mises stress was concentrated on the contact point of the stalk and the moving blade.

(2) The cutting energy of stalk epidermal tissue was greater than that of inner tissue.

(3) The verification test results were consistent with those of the simulation test. The cutting speed and the blade oblique angle had significant effects on the cutting mechanical properties ($P < 0.05$). When the average cutting speed was 0.5-1.5 m/s, the cutting stress and the unit area cutting energy decreased first and changed steadily with the increasing cutting speed. When the blade oblique angle was 0°- 48°, the cutting stress decreased with increasing blade oblique angle, while the unit area cutting energy decreased first and then increased.

(4) The average cutting speed and the blade oblique angle suitable for millet stalk dynamic cutting were about 1 m/s and 30°, respectively.

ACKNOWLEDGEMENTS

REFERENCES

[1] Annor G. A., Tyl C., Marcone M., et al., (2017), Why do millets have slower starch and protein digestibility than other cereals?, *Trends in Food Science & Technology*, Vol. 2017, Issue 66, pp. 73-83, Ed. Elsevier, London/England;

[2] Cui H.L., Shen H.S., (2010), Nonlinear elastic buckling of plant stems under various loading conditions(植物茎秆在各种荷载作用下的非线性弹性屈曲), *Bulletin of science and technology,* Vol. 26, Issue 6, pp. 874-878, Hangzhou/ P.R.C.;

[3] Diao P.S., Yuan C.Y., Zhang D.L., et al., (2011), Experiment of the rotor cutter chop stalk on ANSYS/LS-DYNA（基于 ANSYS/LS-DYNA 的转子铣刀茎秆切割试验）, *Journal of Agricultural Mechanization Research*, Vol.2011, Issue 12, pp.116-119, Haerbin/P.R.C.;

[4] Huang H.D., Wang Y.X., Tang Y., et al., (2011), Finite element simulation of sugarcane cutting (甘蔗切割过程的有限元仿真), *Transactions of the Chinese Society of Agricultural Engineering,* Vol.27, Issue 2, pp.161-166, Beijing/P.R.C;

[5] Igathinathane C., Womac A.R., Sokhansanj S., (2010), Corn stalk orientation effect on mechanical cutting. *Biosystems Engineering*, Vol. 107, Issue 2, pp. 97-106, Ed. Elsevier, San Diego/USA;

[6] Johnson P.C., Clementson C.L., Mathanker S.K., et al., (2012), Cutting energy characteristics of miscanthus x giganteus stems with varying oblique angle and cutting speed. *Biosystems Engineering*, Vol. 112; Issue 1; pp. 42-48, Ed. Elsevier, San Diego/USA;

[7] Li S.G., Liu F., Liu M., et al., (2018), Technology Need and Prospect of Foxtail Millet Industry Development in China in the New Era(新时期中国谷子产业发展技术需求与展望), *Journal of Agriculture*, Vol.8, Issue 6, pp.96-100, Beijing/P.R.C;

[8] Liang S.N., Jin C.Q., Zhang F.F., et al., (2015), Design and experiment of 4LZG-3.0 millet combine harvester (4LZG-3.0 型谷子联合收获机的设计与试验), *Transactions of the Chinese Society of Agricultural Engineering*, Vol.31, Issue 12, pp.31-38, Beijing/P.R.C.;

[9]   Liu D., Xiao H.R., Jin Y., et al., (2018), Finite element analysis of stalk cutting of Chinese little greens based on ANSYS and verification test (基于 ANSYS 的鸡毛菜茎秆切割的有限元分析及验证试验), *Journal of Agricultural Science and Technology*, Vol. 20, Issue 11, pp.85-93, Nanjing/P.R.C.;

[10]   Li Y.M., Qing T.D., Chen J., et al., (2011), Experiments and analysis on mechanical property of corn stalk reciprocating cutting (玉米茎秆往复切割力学特性试验与分析), *Transactions of the Chinese Society of Agricultural Engineering*, Vol.27, Issue 1, pp.160-174, Beijing/P.R.C.;

[11]   Ma Y.S., Zhang J. B., Wu Y. L., (2015), Agricultural material (农业物料学), Chemical Industry Press Co. Ltd., Beijing/P.R.C.;

[12]   Mathanker S.K., Grift T.E., Hansen A.C., (2015), Effect of blade oblique angle and cutting speed on cutting energy for energycane stems. *Biosystems Engineering*, Vol. 2015, Issue 133, pp. 64-70, Ed. Elsevier, San Diego/USA;

[13]   Pang S.H., (1982), Theory of sliding cutting and the choice of its angle (关于滑切理论与滑切角的选用). Journal of Huazhong Agricultural College, Vol. 1982, pp. 64-69, Wuhan/P.R.C.;

[14]   Song Z.H., Song H.L., Geng A.J., et al., (2015), Experiment on cutting characteristics of cotton stalk with double supports(棉花秸秆双支撑切割性能试验), *Transactions of the Chinese Society of Agricultural Engineering*, Vol.31, Issue 8, pp.37-45, Beijing/P.R.C.;

[15]   Wang S., Zhang B., Li X.W., (2017), Research status on thick stalk crop cutting device and its problems and development proposals (粗茎秆作物切割装置研究现状、存在问题及发展建议), *Journal of Agricultural Mechanization Research*, Vol. 2017, Issue 8, pp. 263-268, Haerbin/P.R.C.;

[16]   Xue Z., (2018), Cutting mechanical characteristics and simulation analysis of cassava stalk (木薯茎秆切割力学特性与仿真分析), Doctor dissertation, *Huazhong Agricultural University*，Wuhan//P.R.C.;

[17]   Zhang X.W., (2012), Current situation and problems of millet harvesting machinery (谷子收获现状与存在问题), *Agricultural Technology & Equipment*, Vol. 2012, Issue 20, pp. 32-34, Beijing/P.R.C.;

[18]   Zhang Y.Q., Cui Q.L., Li H.B., et al., (2018), Effects of stem region, moisture content and blade oblique angle on mechanical cutting of millet stems, *INMATEH-Agricultural Engineering*, Vol. 55, Issue 2, pp.105-112, Bucharest/Romania;

[19]   Zhang Y.Q., (2019), Experimental study on cutting mechanical properties of coarse cereals stem related to mechanical harvest (杂粮作物机械收获切割力学特性试验研究), Doctor dissertation, Shanxi Agriculture University, Taigu/ P.R.C.;

[20]   Zhang Z.Z., Liang S., Li H.P., et al. (2010), Dynamic simulation analysis of sugarcane cutting on ANSYS/LS-DYNA (基于 ANSYS/LS-DYNA 的甘蔗切割动力学仿真分析), *Journal of Agricultural Mechanization Research*, Vol.2010, Issue 1, pp.64-67, Haerbin/P.R.C.;

[21]   ***ASABE Standards, 2008. S358.2. Moisture Measurement-Forages. American Society of Agricultural and Biological Engineers, St. Joseph, MI, Spokane/USA;

[22]   ***Ministry of Industry and Information Technology, (2009), Agricultural machinery-cutter bars-part 3: knife sections, ledger plates and knife backs, GB/T 1209.3-2009, China Machine Press, Beijing/P.R.C.;

TECHNOLOGICAL DEVELOPMENT OF ROBOTIC APPLE HARVESTERS: A REVIEW
/
苹果收获机器人技术发展综述

LingXin Bu[1], ChengKun Chen[1,2], GuangRui Hu[1], Adilet Sugirbay[1,3], Jun Chen*[1] [1]

[1] College of Mechanical and Electronic Engineering, Northwest A&F University, Yangling 712100, China;
[2] Guizhou University of Traditional Chinese Medicine, Guiyang, 550025, China;
[3] Technical faculty, S. Seifullin Kazakh Agro Technical University, Astana 010000, Kazakhstan
Tel: +86 135721917773; E-mail: chenjun_jdxy@nwsuaf.edu.cn

ABSTRACT

Apple harvesting in orchards is a challenging task due to its dependence on manual labour. In addition, the reduction in skilled farmers and increasing employee costs have popularized mechanical harvesting. As a highly optimal apple picking method, apple harvesting robots integrate machine vision, image processing, robot kinematics, and multi-sensor fusion. This article reviews the vision system and mechanical structure of apple harvesters and evaluates the performance of robotic apple harvester prototypes from 2010 to 2018. Moreover, horticultural adaptability is also discussed in order to facilitate the expansion of orchard structures suitable for mechanized operations. We find that to solve the difficulties faced by apple harvesters, the development of mechanized apple harvesting and modern orchard structure applications must be accelerated. Furthermore, research into anthropomorphic control strategies has the potential to optimize picking patterns, while improvements in environment reconstruction and semantic segmentation can improve harvesting efficiency. Finally, the challenges and strategies based on the development status of robotic apple harvester are also analysed. The review is intended to assist researchers in structure design, sensor choice and adaptability improvement of agricultural machinery and horticulture, and to influence the direction of the development of robotic apple harvester.

摘要

苹果收获是一项极具挑战性的工作，并具有劳动密集型的特点。劳动力减少和劳动力成本的增加促进了机械化收获的发展。作为一种高度优化的收获方法，苹果收获机器人集成了机器视觉、图像处理、机器人运动学以及多传感器融合。本文对苹果收获机器人的视觉系统和机械结构进行了综述，并对 2010 至 2018 年间的苹果收获机器人的样机性能进行了评估。此外讨论了苹果收获机器人的园艺适应性，以促进果园结构适应机械化作业的发展。为解决苹果收获机器人所面临的困难，除园艺与农机适应性之外，拟人化的控制策略具有优化采摘方法的潜力，而环境重建技术和语义分割的应用可能提高采摘效率。最后，根据苹果收获机器人的发展现状，分析了其面临的挑战和策略。本文旨在为研究人员在机器人的结构设计、传感器选择以及园艺适应性改进方面提高参考，并对苹果收获机器人的发展方向产生一定影响。

INTRODUCTION

Apple is one of the most valuable agriculture products across the globe. According to the United States Department of Agriculture (USDA), global fresh apple production between 2018-2019 was approximately 68.7 million tons (*USDA, 2019*). As the world's biggest apple producer, according to China Agricultural Yearbook of 2016, the apple planting area in China covered 2.32 million hectares, accounting for 17.9% of the global total planting area. Furthermore, apple production reached 43.882 million metric tons, accounting for 24.2% of the total. Since the 20th century, the development of agricultural mechanization technology has fundamentally changed modern agriculture, allowing for the mechanization of farming to harvesting in the main food crops (e.g. wheat and corn). However, the harvest of fresh fruit, such as apple, pear and peach, which is easily prone to bruising and damage, remains as a complicated task for farmers (*Bac et al., 2014*).

---

[1] *LingXin Bu, Ph.D. Stud. Eng.; ChengKun Chen, M.S. Stud. Eng.; GuangRui Hu, M.S. Stud. Eng.;*

Adilet Sugirbay, Ph.D. Stud. Eng.; Jun Chen, Prof. Ph.D. Eng.

In particular, apple harvesting is highly labour intensive, with manual labour making up 35-40% of the total orchard production process during harvest (*Sanders, 2005*), and approximately 25% of labour cost used during the harvest process (*Gallardo and Brady, 2015*).

The 21st century has seen a reduction in the agriculture-related workforce, placing a serious challenge in many countries. Mechanization has the potential to overcome this obstacle faced by the fruit industry (*Fennimore and Doohan, 2008*).

Robotic and platform-assisted mechanical apple harvesting technology focuses on semi-automatic harvesting technology (also known as bulk technology) (*Zhang et al., 2016; De Kleine and Karkee, 2015*). For the application of this type of technology, a worker is initially required to drive the machine to the target location, whereby the machine then generates external excitation in order to detach the apples from the limbs. This basic principle can be employed for both single tree vibration harvesting (*McHugh et al., 1981*) and over-the-row continuous harvesting (*Monroe, 1982; Peterson, 1982a*). However, harvesting machines based on the shake-and-catch (*Peterson et al., 1985*), combing principle (*Le Flufy, 1983*), rod press (*Peterson, 1982b*), and air jet (*Berlage, 1973*) approaches are easily damaged and thus cannot be used for the harvest of fresh apples. Apple harvesting robots integrate machine vision, image processing, robot kinematics, and multi-sensor fusion. Relevant research on the identification, picking and placing of the fruit in order to reduce the damage rate and improve efficiency is still in the laboratory and orchard trial phase. Platform-assisted harvesting concepts integrate the working platform, conveyor and fruit collecting systems (*Peterson and Miller, 1996*). In contrast to manual harvesting, where climbing a ladder is required, workers are placed on a platform in order to pick apples from trees, depositing them in an automatic fruit delivery mechanism that subsequently delivers the fruit to fruit-collecting boxes. Although commercial platform-assisted products are available, they are expensive and require workers of high quality.

Apple harvesting robots have been the focus of research for over three decades. Despite this, commercial apple harvesting robot systems are unavailable on the market. This is attributed to high manufacturing costs, low harvesting efficiency and poor horticultural adaptability to environment complexity. Thus, we aim to review the state of apple harvesters in terms of their vision system and mechanical structure, as well as the performance of robotic apple harvester prototypes, from 2010 to 2018. Furthermore, we also investigate the theme of horticultural adaptability, thus facilitating the expansion of orchard structures for mechanized operations. Finally, we evaluate the current development status of apple harvesting robots, and predict possible trends and challenges for the future.

VISION SYSTEM

Machine vision systems are widely employed in agricultural robotics applications, including yield estimation, path planning and vision-based control. Previous studies have achieved fruit grasping by driving the robot to the target position (*Barth et al., 2016*). The visual system simultaneously recognizes the fruit and acquires depth information. Depth information can be determined directly via time-of-flight (TOF) methods, including the deployment of laser range finders and 3D-cameras, or indirectly using colour images, such as monocular and binocular depth. Recent reviews on recognition algorithms present a comprehensive evaluation of such methods (*Wang et al., 2017*). In the current paper, we focus on the hardware requirements and their performances of the following four methods.

Laser range finder

A laser range finder is able to perform scene reconstruction through horizontal and vertical scanning. (*Jiménez et al., 2000b*) developed a laser-based computer vision system for the picking of spherical fruit by a harvesting robot. More specifically, the contour, crown, convex and reflectance primitives generated by the range and reflectance information were applied to determine the 3D position, radius and surface reflectivity of the fruit. The study was able to achieve a 100% and 74% detection rate of the red and green fruit, respectively. This system proved to perform well under scenarios with shadows, occlusions, and overlaps. However, the scanning speed (20s) and processing time (60s) limited its application (*Jimenez et al., 1999; Jiménez et al., 2000a*).

Liu et al. (2010) designed a three-dimensional vision sensor based on reflectance spectra variations across Fuji apple tree components. Laser reflection at the wavelengths of 685 nm and 830 nm were used to distinguish apples from branches and leaves, with depth information determined from the reflection at 830nm.

Experimental results indicated a stable output signal of the system, ranging from 150 mm to 750 mm, and a maximum error of 13 mm.

Furthermore, previous work has integrated machine vision and laser ranging sensors into a fruit detection system based on an apple picking robot. This real-time system employs CCD camera image feedback to drive the robotic arm, such that the camera mounted on the end-effector was aligned with the target fruit in 2D space, and the laser measured the fruit centre. The detection accuracy of this system lies within 3 mm (*Bulanon and Kataoka, 2010*).

Monocular camera scheme

Parrish et al. (1977) presented a camera model that mapped plane coordinates to spatial coordinates via a perspective transformation that calculates location information in natural scenes. More specifically, a single-camera moving with the end-effector (eye-in-hand) can locate the fruit (*Zhao et al., 2011*). The location process is similar to that of laser ranging sensors in that the setting position is based on information derived from the image, while the distance between the target fruit and the camera is determined via the camera parameters and geometrical relationships. Triangulation is then used to calculate the additional distance to the target apple, and is updated in real-time as the camera approaches the target apple (*Baeten et al., 2008*).

Binocular vision system

Binocular visual localization calculates the parallax of image pairs that can be potentially matched together. The distance to objects from the camera is converted using relative camera locations and orientations, and built-in parameters of the cameras. Therefore, calibration is necessary prior to fruit recognition.

Li et al. (2016a) used a Bumblebee2 binocular camera mounted on the manipulator of the system to detect apples in a single tree canopy. Limited by the vision of the camera, the robotic arm moved in front of the canopy, stopping to collect images in order to localize all apples. At least six images were required to cover the region of the canopy to be harvested.

Binocular vision imaging sensors can also be applied in global vision systems. (*Si et al., 2015*) used two complementary metal-oxide semiconductor (CMOS) cameras to implement a recognition algorithm, with distance estimation errors observed to be less than 20 mm in the range of 400-1500 mm. In order to overcome lighting issues, (*Hohimer et al., 2019*) fused stereo image pairs at five exposure values collected via a Bumblebee XB3 industrial stereo vision imaging sensor to form a single image.

Ji et al. (2017a) constructed an experimental platform with an MV-VS220 binocular stereo vision system in order to locate branches. The platform was based on skeleton feature extraction, and was able to avoid branch obstacles during apple picking with the harvesting robot manipulator. Errors of just 1.5 mm were associated with distances of 1000 mm between the object and binocular camera.

Wang et al. (2013) integrated two high-resolution monocular Nikon D300s cameras with wide-angle lenses into an autonomous orchard vehicle for yield estimation. The global location of apples was calculated from image sequences taken by the two cameras at either side of the tree row. Each single apple was matched in the different images, merged and subsequently registered on the global map. However, navigation system errors and stereo triangulation bias led to inaccurate position information.

3D-camera system

A 3D-camera is a type of time-of-flight detector, whereby the lens collects the reflected light and images it onto the sensor or focal plane array. Such a camera is able to detect the intensity, distance and 3D coordinates of the fruit (*Gongal et al., 2015*). Previous research has implemented a 3D-camera as the single sensor for a vision system. Features of the target were extracted from 3D point clouds, and were subsequently used to reconstruct the fruits, such that apples could be separated from branches and leaves. (*Nguyen et al., 2016*) used the colour feature to test a Kinect sensor system, resulting in 100% and 80% detection rates for fully and partially visible apples, respectively. Location errors were reported to be less than 10 mm, with a 50 ms processing time per apple. (*Tao and Zhou, 2017*) evaluated five features for the recognition of apples, branches and leaves, observing that a support-vector machine, optimized by a genetic algorithm (GA) and trained using Colour-FPFH (combined colour features with Fast Point Feature Histogram), was associated with a high recognition accuracy and performance.

Wang et al. (2012) tested a vision system consisting of a Kinect sensor positioned on the manipulator and a camera mounted under the gripper allowing for long-distance observations to locate targets as the

system approached them. Kinect sensor errors for distances of 240 cm and 150 cm were reported as 4.9 cm and 2.4 cm, respectively.

Gongal et al. (2016) constructed a sensor system consisting of a PMD CamCube 3D camera, a Prosilica GigE colour camera and a LED light mounted on an over-the-row platform with a tunnel structure. Apples were identified in 2D images, while distances and coordinates were determined by intersecting the 2D and 3D images. The system was able to achieve a detection rate of 87.0% for repeated apples.

As a stage summary, there is a characteristic that the vision sensor could move with the manipulator or be fixed on the platform to provide a global view. As two different ways of visual servo, the "eye-in-hand" configuration is referred to as the end-point closed-loop, while the additional configuration is referred to as the end-point open-loop. In particular, open-loop servo control falls into the category of position-based visual servos (PBVS), whereby the robot pose is calculated by the target position. Hence, the accuracy of this "looking then moving" system depends on the precision of the robot kinematic model as well as the calibration of the camera. Moreover, closed loop servo control is a type of image-based visual servo (IBVS), employing continuous images to estimate current robot pose by comparing the current image to the desired image. This avoids the requirement of a complex camera calibration process (*Zhao et al., 2016*). Closed-loop control is considered to be more accurate than open-loop control, yet the former requires a longer operation time due to the highly non-linear image features of the camera pose (*Corke, 2013*). Despite high data acquisition and processing speeds, as a relatively new product, the vulnerability of the 3D camera to light and heat limits its adaptability to daytime operation.

MECHANICAL STRUCTURE

Manipulator

A robotic arm is typically employed as the manipulator in robotic apple harvesters. The manipulator generally consists of several links and joints, including revolute (R) and prismatic (P), which have one degree of freedom (DOF). In addition, the Denavit–Hartenberg (D-H) parameters can be used to describe the forward kinematics of the manipulator (*Denavit and Hartenberg, 1955*). Moreover, the control of the manipulator is closely related to inverse kinematics, that is, the desired pose of the end effector is solved for each joint pose, which consequently completes the path planning.

The working reachability of the robot arm is affected by the degrees of freedom. The number of joints of the underactuated robot arm is generally less than six, thus the pose of the end effector is limited. Moreover, although a redundant robot arm (excessive number of joints) can theoretically reach the desired position in any Cartesian coordinate system, due to conditions such as joint limitation and singularity, this is not always true in real applications (*Corke, 2013*).

Hence, the forward and inverse kinematics of the manipulator are usually pre-verified via simulations. Robotic apple harvester simulations performed by the Washington State University determined apple fruit reachability rates of 69.9%, 77.6% and 81.8% for robotic arms with 5-DOF，7-DOF and 8-DOF, respectively (*Wang et al., 2018; Hohimer et al., 2019*). (*Bloch et al., 2018*) developed a methodology to optimize robot systems according to tree shape.

Simulated results indicate the optimal frames of a 3-DOF robotic arm for Central Leader, Tall Spindle, and Y-trellis apple trees to be RRR, RRR, and RRP, respectively. (*Vougioukas et al., 2016*) evaluated linear fruit reachability (LFR) via simulation tools and concluded that more than 90% of fruits were reachable with the employment of suitable approach angles following three "harvesting passes". (*Nguyen et al., 2013*) applied nine algorithms including RRT, RRTConnect, KPIECE, BKPIECE, LBKPIECE, SBL and EST to a 9-DOF robotic arm in Gazebo for motion planning. All algorithms were able to perform tasks within 5s due to the high DOF, with RRTConnect as the most efficient algorithm, independent of running and planning time.

End-effector

The end-effector is a crucial component of the detachment of the fruit from the tree by the robotic apple harvester. This is usually performed via vacuum gripping or grasping, with the aim of mimicking the functionality of the human hand. (*Napier, 1956*) classified the end-effector grasp into the power grasp and precision grasp based on human grasp taxonomy. The power grasp results in a large contact surface when the fingers and palm envelop the object, while just the finger and thumb tips are used to hold the object in the precision grasp (*Rodriguez et al., 2013*). In general, the power grasp is appropriate for a large load, whereas the precision grasp is always applied to smaller loads (*Feix et al., 2014*).

The shape and size of the target object determine grasping postures and the choice of grasp type (*Lee and Jung, 2014*). Power and precision grasp can be adapted to prismatic- and circular-shaped objects, the general shapes of most fruit and vegetables. For prismatic (i.e. long) shapes, the thumb is used such that the object is picked up like two virtual fingers, while for circular (i.e. radially symmetric) shapes, all fingers are used, picking the object like three virtual fingers (*Rodriguez et al., 2013*). (*Cutkosky, 1989*) analyzed 16 grasp types used in manufacturing and proposed the spherical power grasp robot hand for sphere objects. Table 1 reports the gripper characteristics of robotic apple harvesters.

Table 1

Summary of apple harvesting robot gripper characteristics

References	Grasp classification	Major structure	Accessory	Transmission system
(*Setiawan et al., 2004*)	Power grasp	Cylinder cup with rubber bladders inside	NA	Pneumatics
(*Bulanon and Kataoka, 2010*)	Precision grasp	Two parallel rigid fingers	NA	DC motor
(*Zhao et al., 2011*)	Power grasp	Two angular spoon-shaped fingers	electric cutting knife	NA
(*Gu et al., 2012*)	Precision grasp	Two parallel rigid fingers	NA	NA
(*Davidson and Mo, 2014)*	Power grasp	Three 2-joint fingers and a palm	NA	Tendons and reset spring
(Davidson and Mo, 2015); (*Silwal et al., 2017*)	Power grasp	Three 2-joint fingers and a palm	a stem gripper	Tendons driven by DC motor
(*Quan et al., 2017*)	Power grasp	Six 3-joint fingers	NA	Tendons driven by servo motor
(*Hohimer et al., 2019*)	Power grasp	Three pneumatic fingers	NA	Pneumatics

Cutkosky additionally pointed out that the power grasp is more suited for apple picking (*Cutkosky, 1989*). Furthermore, the robustness of the gripper increases with the number of fingers. In particular, for precision grasp, the two finger grippers tend to require accessories during the grasping and picking process, such as a cutting knife and suction pad. This is attributed to the lack of necessary force to break the joint between the stem and branch (*Kataoka et al., 1998*).

Detecting the apple stem and detaching the fruit is an alternative strategy for precision grasping, yet it requires a complex algorithm and an uncontrolled environment (*Bulanon and Kataoka, 2010*).

Direct contact force detection is widely used in the controller of grippers with stiff fingers using press sensors to avoid the occurrence of surface bruises in real-time (*Zhao et al., 2011; Ji et al., 2015; Ji et al., 2017b*). A simpler and more effective way to eliminate the effects of fruit size and environmental changes is to embed elastomeric materials on the surface of the fingers. However, the soft pneumatic gripper is currently the most compliant end-effecter in fruit protecting, providing adequate grasp force and avoiding bruise. The flexible gripper with simple structure and easy control should be the focus of further research.

ROBOTIC APPLE HARVESTER PERFORMANCE

Despite the development of the robotic apple harvester MAGALI over three decades ago (*D'Esnon et al., 1987*), there are no commercial robotic systems available for apple picking. A substantial amount of research on individual harvesting system components has been performed due to their relative independence, yet work on the whole system performance is limited. Table 2 reports robotic apple harvesters tested during 2010-2018, with the corresponding prototype photos presented in Figure 1. The areas of concern include the structure configuration and test metrics.
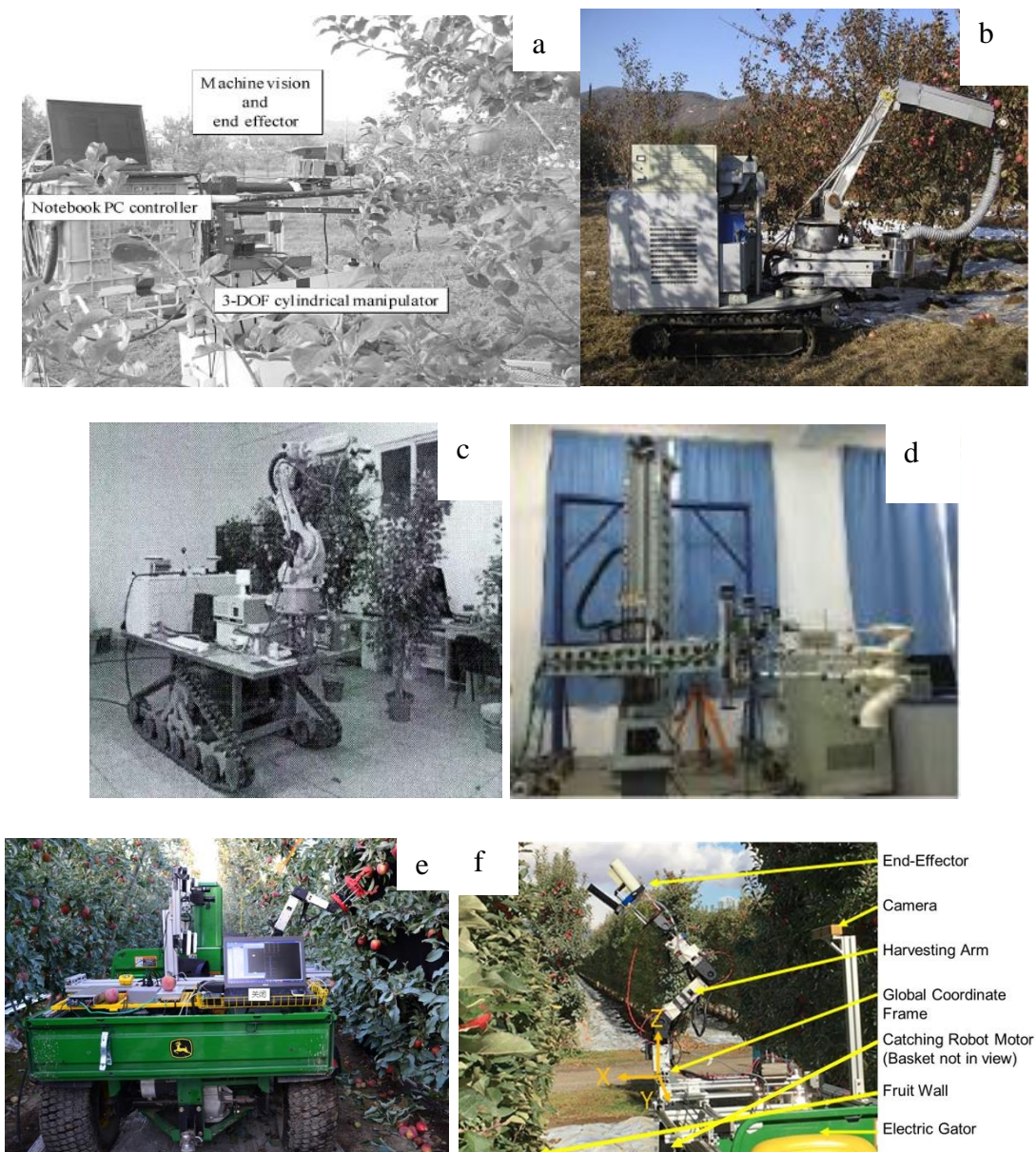
Fig. 1 - Six robotic apple harvester prototypes tested during 2010-2018
(a) Apple harvesting robot from (*Bulanon and Kataoka, 2010*); (b) mobile fruit robot designed by (*Zhao et al., 2011*), reprinted with permission from Elsevier; (c) intelligent mobile fruit robot reported by (*Gu et al., 2012*); (d) apple harvesting robot manipulator with multiple end-effectors (*Li et al., 2016a*); (e) robotic apple harvester tested in Washington State University (*Silwal et al., 2017*), reprinted with permission from Wiley; and (f) robotic system with soft pneumatic gripper (*Hohimer et al., 2019*).
Copyright 2019 ASABE. Used with permission.

Table 2

Robotic apple harvester configuration characteristics and performance metrics

References	Servo method	Sensors	Manipulator	End-effector	Picking method	Localization time/ success rate	Picking time per fruit [s]	Success rate [%]
Baeten et al., 2008	Closed-loop	Monocular CMOS camera	6-DOF	Soft suction gripper	Vacuum suction	NA/ approximately 80%	8-10	80
Bulanon and Kataoka, 2010	Closed-loop	CCD camera and laser range finder	4-DOF	2-parallel-finger peduncle holder	Stem bending	NA/100%	7.1	90
Zhao et al., 2011	Closed-loop	Monocular CCD camera	5-DOF	Gripper shaped like 2 angular spoons with	Stem cutting	NA	15.4	77

References	Servo method	Sensors	Manipulator	End-effector	Picking method	Localization time/ success rate	Picking time per fruit [s]	Success rate [%]
				a cutting knife				
Gu et al., 2012	Closed-loop	Binocular camera	Industry robotic arm	2-parallel-finger gripper	Fruit grasping	NA/81.73%	9.5	86.92
Li et al., 2016a	Open-loop	Binocular camera	One main robotic arm (3-DOF) with three accompanying arms (2-DOF)	collectors with cutting devices connected to conveying pipes	Stem cutting	NA	NA	82.14
Silwal et al., 2017	Open-loop	CCD camera and 3D camera	7-DOF	3-finger gripper	Fruit grasping	1.5s/NA	6	84
Hohimer et al., 2019	Open-loop	Binocular camera	5-DOF	Pneumatic 3-finger gripper	Fruit grasping	NA	7.3±0.78 s[*]	67

*This time accounts for the entire picking process, from apple identification to storage bin.

The picking method determines the mechanical structure hence the design of the robotic harvester is embodied in the structural characteristics of the system. Previous work employed a laser ranging sensor as a camera collaborator to measure the distance to the target fruit and to confirm the end-effector's reaching working space. This is followed by the tripping and twisting of the stem by the end-effector when the required distance is reached. Though the system presented high localization and harvesting success rates, the localization time was not reported, and an ideal environment was also required (*Bulanon and Kataoka, 2010*). The robot systems reported by (*Zhao et al., 2011*) and (*Gu et al., 2012*) employ an end-point closed-loop visual servo for navigation in a traditional orchard. Field tests faced obstructions when approaching the detected fruit and light interference. (*Li et al., 2016a*) presented a regionalization strategy for parallel harvesting that can extend design ideas. Spatial interference is one of the difficulties in the synchronization control of multi-manipulator system. The partitioned fruit tree picking strategy could reduce control difficulty and improve efficiency.

Researchers from Washington State University developed the 7-DOF robotic apple harvester designed for V-trellis fruiting walls. They were able to maintain the end-effector speed at 0.15 m/s as it approached the target apple, which it subsequently detected and detached from the branch (*Silwal et al., 2017*). (*Hohimer et al., 2019*) further developed the robotic apple harvester system by designing a new tendon-driven end-effecter prototype to replace the pneumatic gripper to avoid bruising. The kinematic model was also applied to reduce backtracking and translation, and an inexpensive vision sensor was employed to reduce costs. Field tests indicated that clustered apples, calibration and position errors caused by the harvesting system and the branch pendulum phenomenon were the main reasons leading to picking failure.

(*Baeten et al., 2008*) evaluated the AFPM robotic harvester with vacuum suctioning, demonstrating that stem-pull apples accounted for 30% of all picked apples, which proved to reduce storage time (*Janisiewicz and Peterson, 2004*). Recently, a new automated vacuum harvester system has been presented in Agricultural Robotics (*Vougioukas, 2018*), including a global vision sensor, a delta robot with a vacuum gripper connected to running piping and a fruit bin positioned on the mobile platform. Other technical details were not reported by the authors.

HARVESTING METHODS AND HORTICULTURAL ADAPTABILITY

The adaptability of agricultural machinery and horticulture is crucial for the development and popularization of agricultural machinery. Compared to traditional orchards, factors such as complex fruit tree structures, fruit clusters, fruit shape and size differences across varieties, as well as sensitivity to mechanical damage, exert high adaptability requirements for picking machinery (*Robinson, 2008*).

At the early development stage of mechanized apple harvesting, (*Tennes and Brown, 1985*) determined the shake-and-catch method to be highly suitable for high-yield, structured trees, and also suggested that the orchard structure should be adapted to the harvester structure. Following on from this, semi-automatic harvesters for the narrow hedgerow systems, with the Y-trellis, T-trellis, and double-layer T-trellis structure, were developed (Figure 2). Table 3 compares these harvesters.
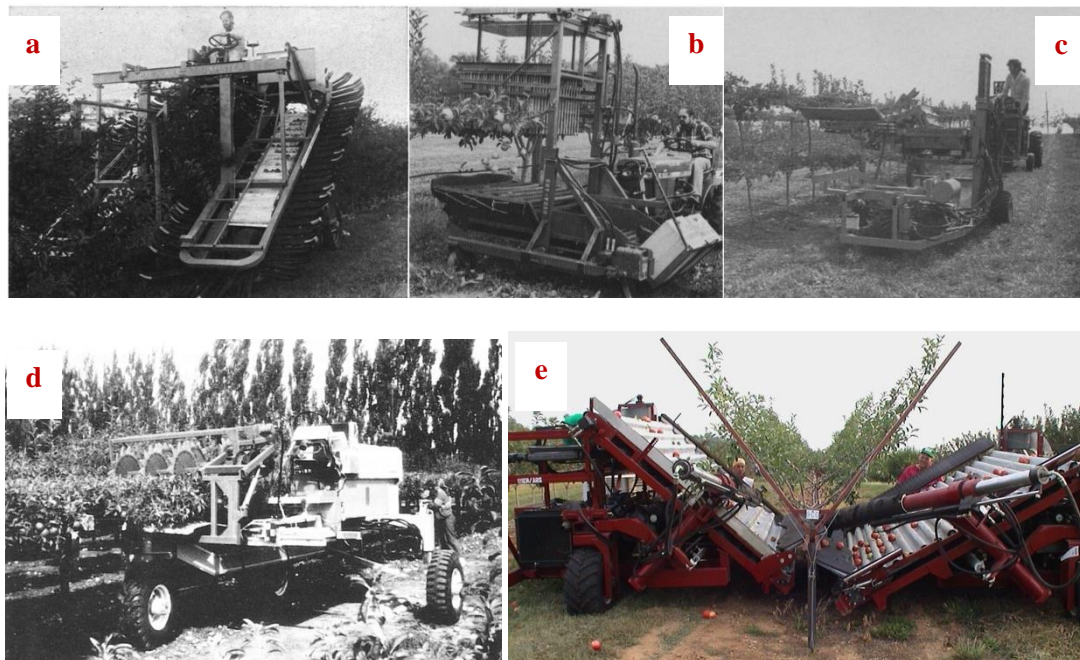
Fig. 2 - Five typical mechanized apple harvesting prototypes for different tree shapes
(a) Combine principle harvester for narrow hedgerow systems (*Le Flufy, 1982a,b; Le Flufy, 1983*), reprinted with permission from Elsevier; (b) harvester with rod press fruit removal mechanism for T-trellis canopies (*Peterson and Kornecki, 1987*). Copyright 1987 ASABE. Used with permission; (c) catch-shake harvester for double-T trellis (Domigan et al., 1988), reprinted with permission from Elsevier; (d) self-propelled NZAEI (New Zealand Agricultural Engineering Institute) machine with shaking units for T-trellis (*Láng, 1989*), reprinted with permission from Elsevier; and (e) two-sided scaffold-shaking harvester for trees trained to Y-trellis (*Peterson and Wolford, 2003*), Copyright 2003 ASABE. Used with permission

Table 3

Comparison of semi-automatic apple harvesters for typical tree structures

Reference	Tree shape	Harvest method	Damage rate*
LeFlufy, 1982a,b; 1983	Narrow hedgerow system	Combine principle (Figure 2a)	23%[a]
Peterson and Kornecki, 1987	T-trellis	Rod press mechanism (Figure 2b)	15%[b]
Domigan et al., 1988	Double "T" trellis	Shake and catch harvest (Figure 2c)	3%[c]
Láng, 1989	T-trellis	Canopy shake harvest (Figure 2d)	15%-31%[d]
Peterson and Wolford, 2003	Y-trellis	Fruiting wall shaking harvest (Figure 2e)	9.9%-33.1%[e]
(a) Damaged fruit is defined as any fruit exhibiting broken skin (i.e. a cut or a puncture) or bruising greater than 1 cm^2, assessed at least 3 d after harvesting. (b) Graded by the 1964 USDA grade standards. (c) Apple graded into not "fancy and extra fancy" (1987). (d) New Zealand Standard, issued by the Apple and Pear Board. Apple graded into "Bruised". (e) USDA fresh market standards. Apple graded into "Bruised" and "Cuts and Punctures".			

The emergence of apple harvesting robots also placed new demands on the orchard structure, as the obstruction by branches and leaves results in difficulties in fruit recognition and localization. Thus, scholars have attempted to eliminate the influence of fruit occlusion by improving the visual system hardware and upgrading algorithms, subsequently enhancing recognition and positioning accuracy (*Silwal et al., 2014; Wang et al., 2016; Niu et al., 2017*).

However, thus far, the occlusion of branches has not been entirely eliminated. (*Robinson et al., 2013*) reported seven simple, narrow, accessible, and productive (SNAP) canopies suitable for assisted-platform operations and high tree densities (900-2200 trees/acre), projected to attain very high yields (1500 bu/acre), as shown in Figure 3.

The apple picking robot developed by (*Silwal et al., 2017*) has been demonstrated as a feasible system for the V-trellis fruiting wall. Here, the branches are fixed on the trellis wire, allowing for the fruit to be distributed along the same wire, significantly avoiding the occlusion by branches and leaves, and consequently, improving the recognition efficiency and accuracy. This indicates that the modern orchard structure should evolve with the development of different harvesting methods.

Due to limited land resource availability and the need to simplify technology and save labour, most new orchards in China are densely planted dwarfed orchards. This increases the yield per unit and also improves fruit quality. In order to increase the bearing capacity of the fruit trees, spindle-shaped trees with fewer branches are widely promoted. However, the early cultivation and management costs of the fruit tree wall have restricted its development. Therefore, changes in fruiting wall or V-trellis require further comprehensive evaluation in terms of their economic applicability.
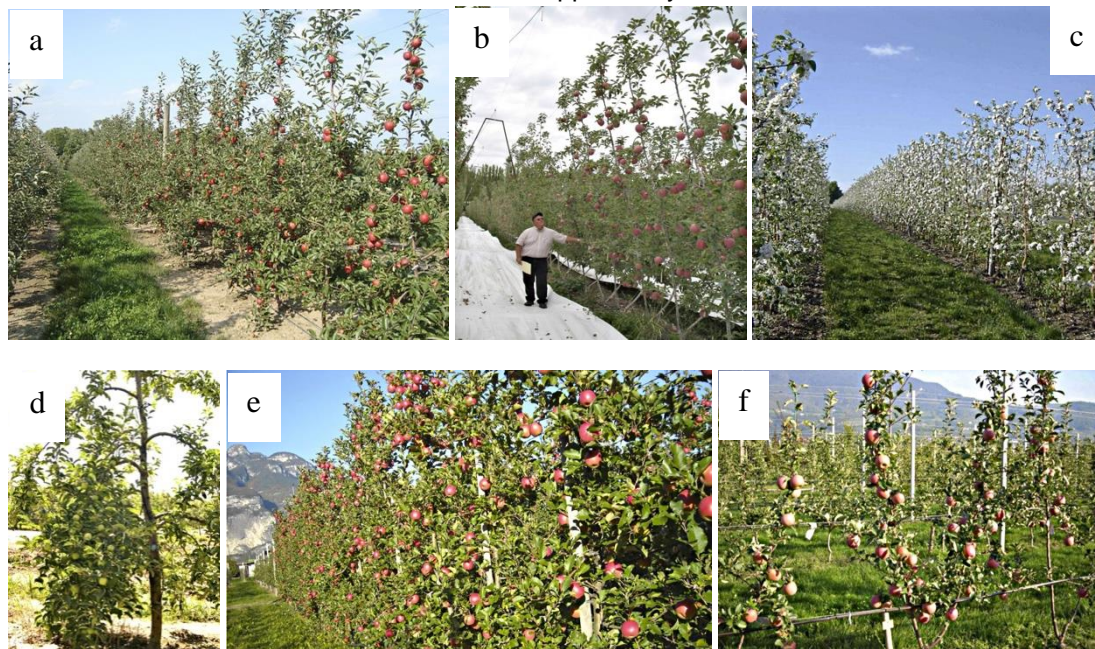
Fig.3 - Six leading global orchard systems:
(a) Tall spindle; (b) V-trellis; (c) super spindle; (d) solaxe; (e) fruiting wall; and (f) bi-axis
(*Robinson et al., 2013*)

DISCUSSION

Analysis and summary

The robotic apple harvester system had developed rapidly over the recent years. Much of the research in robotic apple harvesting presented in the previous sections is still in the course of development and can thus not be fully reviewed. The performance gains of apple robotic harvesters resulted in two factors: "simplifying the task" and "enhancing the robot".

Modern cultivation systems have been able to reduce the computational scale of fruit recognition and also avoid obstacles during the recognition and grasping process compared to traditional orchards. Therefore, position-based look-and-move becomes the main method of visual servo in apple picking. The eye-to-hand model improves harvesting efficiency and allows for the accurate estimation of the localization time, yet high-performance cameras are required. Moreover, eye-in-hand robots boast autonomous navigation and fruit detection capabilities to deal with complex environments. The localization of fruit within an independent tree using the image-based vision servo (IBVS) control method requires multiple successive iterations, while scanning surrounding canopies is necessary when searching for potential targets. This may explain the missing data in the "Localization time" column in Table 2. In addition to the temporal factor, the failure to detect target apples due to branch obstacles in the canopy also impacts the performance evaluation of the harvesting robots.

The simplification of the apple harvesting task calls for a robot-friendly orchard environment, while enhancements in robot performance depend on technological improvements and the update of hardware. Vision sensors developed from RGB cameras and laser range finders, and 3D cameras enhance sensor output and improve performances. Furthermore, commercial sensors involved in the previously mentioned robotic harvesters have undergone substantial updates, for example Bumblebee 2 to Bumblebee XB3. Numerous sensor technologies provide more choices for the design and development of robots, and highlight the potential of multi-sensor fusion.

Challenges and strategies

High robot manufacturing and maintenance costs, insufficient speeds and the complexity of agricultural environments have limited the promotion of harvesting robots. Traditional orchards have been unable to adapt to the requirements of the modern fruit industry because of mechanical adaptability. Tall fruiting walls with simple narrow canopies at an optimum planting density is the trend for future orchards. Despite the proved advantages of such an orchard design, the economic gain from yield improvements may take at least three years to materialize following orchards remould. If the evolution of orchards is to be popularized, issues relating to initial investment and loss compensation should be prioritized.

Early apple harvesters applied the "optimum technique" (*Nguyen et al., 2012; Tong et al., 2014*) or "standard method" (*Davidson et al., 2016*), whereby the orientation and stem of the fruit are initially detected, followed by cutting of the stem. Since the gripper was only required to limit the movement of the fruit, a small force was necessary to support. Ensuring minimum damage was prioritized, which consequently increased picking time due to too many necessary moving steps. Compared to the apple harvesting robot reported by (*Zhao et al., 2011*), (*Silwal et al., 2017*) attempted to detach apples by grasping them directly via a three-finger end-effecter, demonstrating the potential to reduce picking time. In terms of direct grasping, the harvesting effect is largely determined by the motion characteristics of the manipulator picking patterns of the robotic apple harvester. Several anthropomorphic methods have been explored to develop control strategies. (*Davidson et al., 2016*) used a sensing glove to evaluate four picking techniques and determined that the optimum picking method (i.e. with the lowest stem loss rate) depended on the apple variety. (*Li et al., 2016b*) evaluated four three-finger examples to measure the detachment angle, movements, and patterns of stem bending using sensing glove, and presented that pull with a bending moment could reduce the required grasping pressure for fruit detachment. These results appeared to have been applied to the control of their robotic apple harvesters, and yet they are associated with unexpected circumstances resulting in picking failure (e.g. pendulum apples with long branches) (*Hohimer et al., 2019*). Additional research in anthropomorphic methods can help to overcome these common picking failures.

As shown in figure 1, all prototypes are the serial structure apple harvesting robot, whereby a working cycle is completed after reaching a working position. In this case, the visual system recognizes and obtains the 3D coordinates of the fruit, determines the picking order according to the relative position of the fruit from the end effector and completes the inverse of the Kinematics solution of the mechanical arm. Following this, the actuator completes the fruit picking and confirms whether the picking has been successful. Finally, it moves to the next working position, continuing the cycle. However, the vision system enters the idle state following the completion of the fruit position feedback, providing for room for potential efficiency improvements. Fruit detection and separation in orchards requires multi-sensor fusion. Environment reconstruction is a rapidly-developing technology based on machine vision, and is used widely in horticulture phenotyping and yield evaluation. This technology can be potentially applied to fruit harvesting. Double-side views of orchard rows were matched using global features and semantic information in order to reconstruct 3D row models and the spatial distribution of the fruit (*Yao et al., 2010; Dong et al., 2020*). A possible solution of efficiency improvement is to divide the serial robot into two separate components: a visual recognition robot and a picking robot. The visual recognition robot detects the position of the fruit and determines their location on a fruit map. Fruit maps make the visual system redundant in the harvesting robot system, while only eye-in-hand cameras are required to compensate for position errors. According to the fruit map, the path planning of the picking robot is performed and the robot is driven to complete the picking action. This is expected to achieve continuous positional movement and fruit grabbing. However, it is worth noting that the accuracy of the fruit positioning, the positioning error of the visual robot and environmental changes may lead to the "blind" picking robot missing the target. Thus, a "hand eye" can be included in order to correct this error. An exceptional equipment performance usually means high prices; thus, farmers have to

decide between performance and cost. For researchers, if function implementation and promotion are the main goals, then the application of cheap equipment to achieve acceptable performance levels for farmers should be the next step for consideration.

CONCLUSIONS

We have presented a comprehensive review of the robot harvesting techniques published during 2010-2018. Based on our analysis of these strategies, we determine the development of harvesting robots to be a function of the modern orchard structure, anthropomorphic research, and environmental reconstruction. In particular, the development of constructed orchards should be popularized as this orchard system can be easily adapted to the mechanization requirements of robotic harvesters. In addition, further anthropomorphic foundation testing should be performed on direct grasping to optimize the control strategy of the robot during the harvesting process. Lastly, we propose that the application of environmental reconstruction during harvesting can promote the efficiency of robotic harvesters. Robotic fruit harvesting has proven to be a highly challenging task due to environmental complexities, sensor reliability, and robot stability. In order to improve the accuracy and efficiency of harvest mechanization applications in fruit, the orchard structure and environment, harvesting robot, and horticultural technology must all be optimized accordingly.

Overall, the review is intended to assist researchers in structure design, sensor choice and adaptability improvement of agricultural machinery and horticulture, and to influence the direction of the development of robotic apple harvester. As the proposed solution of efficiency improvement, the eye-hand separated harvesting system requires multi-sensor fusion. The accuracy of fruit map depends on semantic mapping for orchard environments, which is still difficult due to technical limitations and the complexity of the orchard. Therefore, semantic segmentation and environmental reconstruction are important directions for agricultural robots to enhance their environmental awareness and precise operation.

ACKNOWLEDGEMENT

REFERENCES

[1] Bac C.W., Van Henten E.J., Hemming J. et al., (2014), Harvesting robots for high-value crops: State-of-the-art review and challenges ahead. *Journal of Field Robotics*, vol.31, pp.888-911.

[2] Baeten J., Donné K., Boedrij S., Beckers W., Claesen E., (2008), Autonomous fruit picking machine: a robotic apple harvester, In: Laugier, C., Siegwart, R. (Eds.), Field and Service Robotics: Results of the 6th International Conference. *Springer Berlin Heidelberg*, Berlin, Heidelberg, pp. 531-539.

[3] Barth R., Hemming J., van Henten E.J., (2016), Design of an eye-in-hand sensing and servo control framework for harvesting robotics in dense vegetation. *Biosystems Engineering*, vol.146, pp.71-84.

[4] Berlage A.G., (1973), Apple Harvesting Trials with Oscillating Air Jets. *Transactions of the ASAE*, vol.16, pp. 460-461.

[5] Bloch V., Degani A., Bechar A., (2018), A methodology of orchard architecture design for an optimal harvesting robot. *Biosystems Engineering*, Vol.166, pp.126-137.

[6] Bulanon D.M., Kataoka T., (2010), Fruit detection system and an end effector for robotic harvesting of Fuji apples. *Agricultural engineering international: CIGR journal*, vol.12, pp. 203-210.

[7] Corke P., (2013), Robotics, Vision and Control: Fundamental Algorithms in MATLAB. Springer Publishing Company, Incorporated.

[8] Cutkosky M.R., (1989), On grasp choice, grasp models, and the design of hands for manufacturing tasks. IEEE Transactions on Robotics and Automation, vol.5, pp.269-279.

[9] D'Esnon A.G., Rabatel G., Pellenc R., Journeau A., Aldon M.J., (1987), MAGALI: A self-propelled robot to pick apples, *ASAE Annual International Meeting*, Baltimore, MD, ASAE Paper No.87-1037.

[10] Davidson J., Mo C., (2014), Conceptual design of an end-effector for an apple harvesting robot, *International Conf. on Automation Technology for Off-Road Equipment*.

[11] Davidson J., Mo C., (2015), Mechanical Design and Initial Performance Testing of an Apple-Picking End-Effector, 2015 *ASME International Mechanical Engineering Congress and Exposition*, Houston, Texas, USA.

[12] Davidson J., Silwal A., Karkee M., Mo C., Zhang Q., (2016), Hand-picking dynamic analysis for undersensed robotic apple harvesting. *Transactions of the ASABE*, vol.59, pp.745-758.

[13] De Kleine M.E., Karkee M., (2015), A semi-automated harvesting prototype for shaking fruit tree limbs. *Transactions of the ASABE*, vol.58, pp.1461-1470.

[14] Denavit J., Hartenberg R.S., (1955), A kinematic notation for lower-pair mechanisms based on matrices. *Journal of Applied Mechanisms*, vol.22, pp.215-221.

[15] Domigan I.R., Diener R.G., Elliott K.C., Blizzard S.H., Nesselroad P.E., Singha S., Ingle M., (1988), A fresh fruit harvester for apples trained on horizontal trellises. *Journal of Agricultural Engineering Research*, vol.41, pp.239-249.

[16] Dong W., Roy P., Isler V., (2020), Semantic mapping for orchard environments by merging two-sides reconstructions of tree rows. *Journal of Field Robotics*, vol.37, pp.97-121.

[17] Feix T., Bullock I.M., Dollar A.M., (2014), Analysis of human grasping behaviour: Object characteristics and grasp type. *IEEE Transactions on Haptics*, vol.7, pp.247-252.

[18] Fennimore S.A., Doohan D.J., (2008), The challenges of specialty crop weed control, future directions. *Weed Technology*, vol.22, pp.364-372.

[19] Gallardo R.K., Brady M.P., (2015), Adoption of labour-enhancing technologies by specialty crop producers: The case of the Washington apple industry. *Agricultural Finance Review*, vol.75, pp.514-532.

[20] Gongal A., Amatya S., Karkee M., Zhang Q., Lewis K., (2015), Sensors and systems for fruit detection and localization: A review. *Computers and Electronics in Agriculture*, vol.116, pp.8-19.

[21] Gongal A., Silwal A., Amatya S., Karkee M., Zhang Q., Lewis K., (2016), Apple crop-load estimation with over-the-row machine vision system. *Computers and Electronics in Agriculture*, vol.120, pp.26-35.

[22] Gu B., Ji C., Wang H., Tian G., Zhang G., Wang L., (2012), Design and experiment of intelligent mobile fruit picking robot. *Transactions of the Chinese Society for Agricultural Machinery*, vol.43, pp.153-160.

[23] Hohimer C.J., Wang H., Bhusal S., Miller J., Mo C., KarkeeM., (2019), Design and field evaluation of a robot apple harvesting system with 3D printed soft-robotic end-effector. *Transactions of the ASABE*, vol.62, pp.404-415.

[24] Janisiewicz W.J., Peterson D.L., (2004), Susceptibility of the stem pull area of mechanically harvested apples to blue mould decay and its control with a biocontrol agent. *Plant Disease*, vol.88, pp.662-664.

[25] Ji W., Li J., Yang J., Ding S., Zhao D., (2015), Analysis and validation for mechanical damage of apple by gripper in harvesting robot based on finite element method. *Transactions of the Chinese Society of Agricultural Engineering*, vol.31, pp.17-22.

[26] Ji W., Meng X., Qian Z., Xu B., Zhao D., (2017a), Branch localization method based on the skeleton feature extraction and stereo matching for apple harvesting robot. *International Journal of Advanced Robotic Systems*, vol.14, 172988141770527.

[27] Ji W., Qian Z., Xu B., Tang W., Li J., Zhao D., (2017b). Grasping damage analysis of apple by end effector in harvesting robot. *Journal of Food Process Engineering*, vol.40, e12589.

[28] Jiménez A.R., Ceres R., Pons J.L., (2000a). A Survey of Computer Vision Methods for Locating Fruit on Trees. *Transactions of the ASAE*, vol.43, pp.1911-1920.

[29] Jiménez A.R., Ceres R., Pons J.L., (2000b), A vision system based on a laser range-finder applied to robotic fruit harvesting. *Machine Vision and Applications*, vol.11, pp.321-329.

[30] Jimenez A.R., Jain A.K., Ceres R., Pons J.L., (1999), Automatic fruit recognition: a survey and new results using Range/Attenuation images. *Pattern Recognition*, vol.32, pp.1719-1736.

[31] Kataoka T., Hiroma T., Ota Y., (1998), Development of a harvesting hand for apples. *Advanced Robotics*, vol.13, pp.293-294.

[32] Láng Z., (1989), Lincoln canopy apple harvester using a continuous horizontal shaking method. *Journal of Agricultural Engineering Research*, vol.44, pp.267-273.

[33] Le Flufy M.J., (1982a), The design of a prototype apple harvester. *Journal of Agricultural Engineering Research*, vol.27, pp.51-60.

[34] Le Flufy M.J., (1982b), Harvest trials with a prototype apple harvester. *Journal of Agricultural Engineering Research*, vol.27, pp.415-420.

[35] Le Flufy M.J., (1983), Apple harvesting by a combing technique. *Transactions of the ASAE*, vol.26, pp.661-664,668.

[36] Lee K.S., Jung M.C., (2014), Common patterns of voluntary grasp types according to object shape, size, and direction. *International Journal of Industrial Ergonomics*, vol.44, pp.761-768.

[37] Li G., Ji C., Gu B., Xu W., Dong M., (2016a), Kinematics analysis and experiment of apple harvesting robot manipulator with multiple end-effectors. *Transactions of the Chinese Society for Agricultural Machinery*, vol.47, pp.14-29.

[38] Li J., Karkee M., Zhang Q., Xiao K., Feng T., (2016b), Characterizing apple picking patterns for robotic harvesting. *Computers and Electronics in Agriculture*, vol.127, pp.633-640.

[39] Liu Z., Liu G., Qiao J., (2010), Development of a 3-dimension vision sensor in apple harvesting robot. *Transactions of the Chinese Society for Agricultural Machinery*, vol.41, pp.171-175.

[40] McHugh C.M., Webb B.K., Hood C.E., Garrett T.R., (1981), A compact, single operator tree crop harvester. *Transactions of the ASAE*, vol.24, pp.26-30.

[41] Napier J.R., (1956), The prehensile movements of the human hand. *The Journal of bone and joint surgery*, vol.38, pp.902-913.

[42] Nguyen T.T., Kayacan E., De Baedemaeker J., Saeys W., (2013). Task and Motion Planning for Apple Harvesting Robot. *IFAC Proceedings*, vol.46, pp.247-252.

[43] Nguyen T.T., Van Eessen D., Baerdemaeker J., Saeys W., (2012), Optimum detaching movement for apples-harvesting robot, *Infomation Technology, Automation & Precision Farming International Conference of Agricultural Engineering-CIGR-AgEng: Agriculture & Engineering for A Healthier Life. CIGR-EurAgEng*, Valencia, Spain.

[44] Nguyen T.T., Vandevoorde K., Wouters N., Kayacan E., De Baerdemaeker J.G., Saeys W., (2016), Detection of red and bicoloured apples on tree with an RGB-D camera. Biosystems Engineering, vol.146, pp.33-44.

[45] Niu L., Zhou W., Wang D., He D., Zhang H., Song H., (2017), Extracting the symmetry axes of partially occluded single apples in natural scene using convex hull theory and shape context algorithm. Multimedia Tools and Applications, vol.76, pp.14075-14089.

[46] Parrish E.A. Jr., Goksel A.K., (1977), Pictorial pattern recognition applied to fruit harvesting. *Transactions of the ASAE*, vol.20, pp.822-827.

[47] Peterson D.L., (1982a), Continuously moving over-the-row harvester for tree crops. *Transactions of the ASAE*, vol.25, pp.1478-1483.

[48] Peterson D.L., (1982b), Rod press fruit removal mechanism. *Transactions of the ASAE*, vol.25, pp.1185-1188.

[49] Peterson D.L., Kornecki T.S., (1987), Mechanical apple harvester for T-trellis canopies. *Transactions of the ASAE*, vol.30, pp.597-600.

[50] Peterson D.L., Miller S.S., (1996), Apple harvesting concepts for inclined trellised canopies. *Applied Engineering in Agriculture*, vol.12, pp.267-271.

[51] Peterson D.L., Miller S.S., Kornecki T.S., (1985), Over-the-row harvester for apples. *Transactions of the ASAE*, vol.28, pp.1393-1397.

[52] Peterson D.L., Wolford S.D., (2003), Fresh-market quality tree fruit harvester part II: apples. *Applied Engineering in Agriculture*, vol.19, pp.545-548.

[53] Quan L., Zhao L., Li X., Zhang C., Wang J., Cheng G., (2017), Design and test of multifunctional dragonfly claws form bio-mimetic end effector. *Transactions of the Chinese Society for Agricultural Machinery*, vol.48, pp.33-42,52.

[54] Robinson T., (2008), The evolution towards more competitive apple orchard systems in the USA. *Acta Horticulturae*, vol.772, pp.491-500.

[55] Robinson T., Hoying S., Sazo M.M., Marree A.D., Dominguez L., (2013), A vision for apple orchard systems of the future. *New York Fruit Quarterly*, vol.21, pp.11-16.

[56] Rodríguez F., Moreno J.C., Sánchez J.A., Berenguel, M., (2013), Grasping in Agriculture: State-of-the-Art and Main Characteristics, In: Carbone, G. (Ed.), *Grasping in Robotics*. Springer London, London, pp.385-409.

[57] Sanders K.F., (2005), Orange harvesting systems review. *Biosystems Engineering*, vol.90, pp.115-125.

[58] Setiawan A.I., Furukawa T., Preston A., (2004), A low-cost gripper for an apple picking robot, Robotics and Automation, 2004. *Proceedings. ICRA '04. 2004 IEEE International Conference on*, pp.4448-4453.

[59] Si Y., Liu G., Feng J., 2015. Location of apples in trees using stereoscopic vision. *Computers and Electronics in Agriculture* 112, 68-74.

[60] Silwal A., Davidson J.R., Karkee M., Mo C., Zhang Q., Lewis K., (2017), Design, integration, and field evaluation of a robotic apple harvester. *Journal of Field Robotics*, vol.34, pp.1140-1159.

[61] Silwal A., Gongal A., Karkee M., (2014), Identification of red apples in field environment with over the row machine vision system. *Agricultural Engineering International: CIGR journal*, vol.16, pp.66-75.

[62] Tao Y., Zhou J., (2017), Automatic apple recognition based on the fusion of colour and 3D feature for robotic fruit picking. *Computers and Electronics in Agriculture*, vol.142, pp.388-396.

[63] Tennes B.R., Brown G.K., (1985), A sway-bar shaker for apples. *Transactions of the ASAE*, vol.29, pp.60-64.

[64] Tong J., Zhang Q., Karkee M., Jiang H., Zhou J., (2014), Understanding the dynamics of hand picking patterns of fresh market apples, *ASABE and CSBE/SCGAB Annual International Meeting*. ASABE, Quebec Canada, p. 1.

[65] USDA, (2019), *Fresh Apples, Grapes, and Pears: World Markets and Trade*. Foreign Agricultural Service, https://apps.fas.usda.gov/psdonline/circulars/fruit.pdf (accessed on 22 August 2019).

[66] Vougioukas S.G., (2018), Agricultural Robotics. Annual Review of Control, *Robotics, and Autonomous Systems*, vol.2.

[67] Vougioukas S.G., Arikapudi R., Munic J., (2016), A study of fruit reachability in orchard trees by linear-only motion. *IFAC-PapersOnLine*, vol.49, pp.277-280.

[68] Wang D., Song H., He D., (2017), Research advance on vision system of apple picking robot. *Transactions of the Chinese Society of Agricultural Engineering*, vol.33, pp.59-69.

[69] Wang D., Song H., Tie Z., Zhang W., He D., (2016), Recognition and localization of occluded apples using K-means clustering algorithm and convex hull theory: a comparison. *Multimedia Tools and Applications*, vol.75, pp.3177-3198.

[70] Wang H., Hohimer C.J., Bhusal S., Karkee M., Mo C., Miller J.H., (2018), Simulation as a tool in designing and evaluating a robotic apple harvesting system. *IFAC-PapersOnLine*, vol.51, pp.135-140.

[71] Wang H., Mao W., Liu G., Hu X., Li S., (2012), Identification and location system of multi-operation apple robot based on vision combination. *Transactions of the Chinese Society for Agricultural Machinery*, vol.43, pp.165-170.

[72] Wang Q., Nuske S., Bergerman M., Singh S., (2013), Automated crop yield estimation for apple orchards, In: Desai, J.P., Dudek, G., Khatib, O., Kumar, V. (Eds.), Experimental Robotics: The 13th International Symposium on Experimental Robotics. *Springer International Publishing*, Heidelberg, pp. 745-758.

[73] Yao B.Z., Yang X., Lin L., Lee M.W., Zhu S.-C., (2010), I2t: Image parsing to text description. *Proceedings of the IEEE*, vol.98, pp.1485-1508.

[74] Zhang Z.H., Heinemann P., Liu J.A., Baugher T.R., Schupp J., (2016), The development of mechanical apple harvesting technology: a review. *Transactions of the ASABE*, vol.59, pp.1165-1180.

[75] Zhao D.A., Lv J., Ji W., Zhang Y., Chen Y., (2011), Design and control of an apple harvesting robot. *Biosystems Engineering*, vol.110, pp.112-122.

[76] Zhao Y., Gong L., Huang Y., Liu C., (2016), A review of key techniques of vision-based control for harvesting robot. *Computers and Electronics in Agriculture*, vol.127, pp.311-323.

ENGINEERING MANAGEMENT OF MACHINE FOR FORMATION OF ARTIFICIAL SHELL ON SEED VEGETABLE CULTURES
/
ІНЖЕНЕРНИЙ МЕНЕДЖМЕНТ МАШИНИ ДЛЯ ФОРМУВАННЯ ШТУЧНОЇ ОБОЛОНКИ НА НАСІННІ ОВОЧЕВИХ КУЛЬТУР

Rogovskii I.L.[1)], Titova L.L.[1)], Trokhaniak V.I.[1)], Marinina, L.I.[1,2)], Lavrinenko, O.T.[1], Bannyi O.O.[1)] [1]
[1)] National University of Life and Environmental Sciences of Ukraine / Ukraine;
[2)] Scientific Organization "Leonid Pogorilyy Ukrainian Scientific Research Institute of Forecasting and Testing of Machinery and Technologies for Agricultural Production" / Ukraine
Tel: +380673513082; E-mail: Trohaniak.v@gmail.com
DOI: https://doi.org/10.35633/inmateh-61-18

ABSTRACT

The article analyses the universalization of the seed material by its physical and mechanical properties by means of pre-sowing treatment, resulting in the formation of an artificial shell. As a result of the generalization, a technological scheme of obtaining an encapsulated seed and a design of a seed coating machine was proposed. A simulation model of the sowing accuracy process from the internal friction coefficient of seeds at different root mean square deviations of seed sizes is proposed. The regression equation for the influence of the dynamic mode of operation of the developed experimental sample of seed coating machine is established. According to the experimental studies' results, the static and dynamic friction coefficients of the encapsulated vegetable seeds on the steel and plastic working surfaces of seed coating machine were established. Under the production conditions, experimental tests were conducted to compare the seedlings of untreated, coated, branded and encapsulated seeds of vegetables by the quality of prepared seed material and sowing time.

РЕЗЮМЕ

В статті виконано аналіз універсалізації посівного матеріалу за фізико-механічними властивостями шляхом передпосівного оброблення в результаті чого утворюється штучна оболонка. В результаті узагальнення запропоновано технологічну схему отримання капсульованого насіння та конструкцію дражиратора. Запропоновано імітаційну модель процесу точності сівби від коефіцієнта внутрішнього тертя насіння при різних середньоквадратичних відхиленнях розмірів насіння. Встановлено рівняння регресії з впливу динамічного режиму роботи розробленого експериментального зразка дражиратора. За результатами експериментальних досліджень встановлено статичний і динамічний коефіцієнти тертя капсульованого насіння овочевих культур по сталевих і пластмасових робочих поверхнях дражиратора. У виробничих умовах проведено експериментальні випробування з порівняння сходів необробленого, дражированого фірмового та капсульованого насіння овочевих культур за якістю підготовленого насіннєвого матеріалу і часу посіву.

INTRODUCTION

The process of coated seeds is a perspective, but compared with inlaid less common way of coating seeds (*Arsenoaia V.N. et al, 2019*). Coated seeds are characterized by the fact that the shape and size of the seeds changes significantly (*Dihingia P.C. et al, 2017*). The weight of the seeds can be increased 10 - 25 times (mini pill) or 15 - 100 times (standard pill) (*Gaganpreet K. et al, 2011*). Coating helps unify the seeds in shape and size (*Kroulík M. et al, 2016*), which allows for even and accurate sowing (*Pruteanu A. et al, 2020*) and also reduces seed costs and the costs of thinning the seedlings (*Vlăduţ D.I. et al, 2018*).

Studies have shown that the yield of standard root crops is increased by 40% by sowing with coated beet seeds (*Hevko B.M. et al, 2018*).

---

[1] *Rogovskii I.L., Prof. Ph.D. Eng.; Titova L.L., Assoc. Prof. Ph.D. Eng.; Trokhaniak V.I., Assoc. Prof. Ph.D. Eng.; Marinina L.I., Ph.D. Eng.; Lavrinenko, O.T., Assoc. Prof. Ph.D. Eng.; Bannyi O.O., Assoc. Prof. Ph.D. Eng.*

Therefore, modern seedling growing technologies in many countries are based on the use of coated seeds (*Pedrini S. et al, 2017*). In this case, the yield of cucumbers, lettuce and tomatoes can increase by 15% (*Tolvaly-Roşca F. et al, 2017*). According to research (*Stroescu Gh. et al, 2018*), coated vegetable seeds reduce the rate of seeds by 3 - 4 times and increase the yield by 25%.

The organic and mineral mixture for coating as filler includes 50 - 90% expanded perlite particle size of 0.01 - 0.25 mm with a bulk density of 70 - 150 kg/m^3 (*Amirkhani M. et al, 2019*). The prepared components of the mixture are mixed with water in a ratio of 10:1 to obtain a homogeneous mass with moulding humidity (*Halber A. et al, 2018*).

The mixture is then provided into a seed coating machine with seeds and pumped with seeds mixed with the mixture (*Rogovskii I. et al, 2019*). In the process of pumping in the seed coating machine, a light bulk dragee with a kernel-seed is formed (*Belc N. et al, 2016*). The mixture is provided using an auger. The process of pumping takes 15 - 20 minutes; 1 - 2 minutes before the end of the process in the seed coating machine is provided bentonite clay to obtain a smooth outer shell of the dragee (*Hevko R.B. et al, 2017*). Ready dragee is sent for drying (*Rogovskii I.L. et al, 2019*).

The author of the method of "clay balls" - Masanabu Fukuoka (1913-2008), a Japanese farmer, creator of "natural farming" was looking for a way to sow rice without filling the fields, without digging and without fertilizing the soil (*Tutunaru L.F. et al, 2014*). Fukuoka came to think of making a clay shell for seeds. Subsequently, Fukuoka organized a large campaign to green the desert soils and personally tested the method of "clay balls" in Africa, Southeast Asia, Australia, America and others. In Greece, the "greening" case continues with Panos Manikis, Fukuoka's student. The essence of the method of "clay balls". Seeds of perennial and annual plants are mixed with clay and water. From the resulting mixture, by hand or concrete mixer, make small balls. They are dried in the sun, harvested, manually or airborne scattered over a desert area. The cost of this method is around EUR 250 per hectare (including the cost of seeds, clay and food for volunteers). Fig. 1 presents a scheme for obtaining vegetable seeds encapsulated in clay.
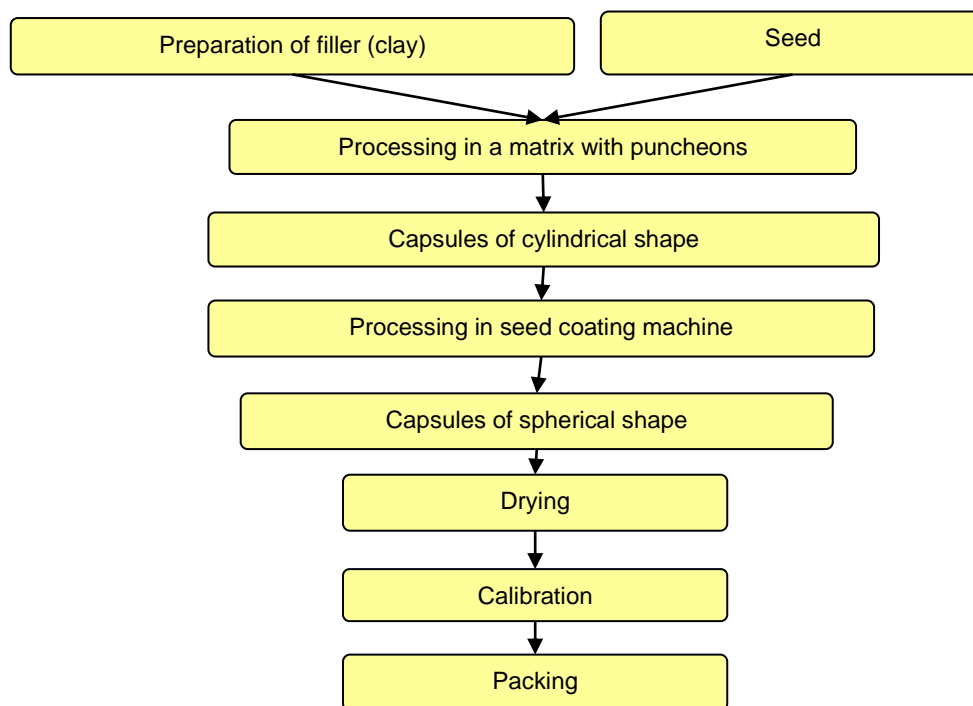
Fig. 1 - Technological scheme of obtaining encapsulated seeds

The development of modern designs of machines for pre-sowing seed treatment with the application of artificial shell on it is a result of improvement of the most common machines for the implementation of this technological operation – seed coating machines. Despite the benefits of seed coating machines, there are many unresolved issues (*Rogovskii I.L. et al, 2019*).

The main of these issues is the influence of the design and mode parameters of the seed coating machine on the formation of artificial shell on seed surface in the case of small-seeded vegetable crops.

As a result of the analysis of research and design works, it can be concluded that the creation of theoretical foundations and the development of a machine for the pre-sowing treatment of vegetable crop seeds with the formation of artificial shell on their surface, is current.

The purpose of the study is to increase the efficiency of the artificial shell formation process on the seed surface by reasoning the technological process, parameters and operation modes of the seed coating machine.

MATERIALS AND METHODS

Theoretical studies were conducted using mechanical-mathematical modeling and are based on the provisions of theoretical mechanics, methods of mathematical analysis, methods of multivariate experiment planning and statistical processing of experimental data using Statistica 7.

To obtain cylindrical capsules containing seeds, a device (matrix with puncheon) was developed. To obtain spherical capsules, it is necessary to carry out the treatment of cylindrical capsules in the working unit of the experimental installation (Fig. 2 a).

a)   b)   c)
Fig. 2 - General views of the experimental installation (a, b) and production model of the seed coating machine (c)
a: 1 - drawer; 2 - hydrostation; 3 - electric engine; 4 - hydraulic motor; 5 - control unit; 6 - manometer; 7 - adjustable throttle;
8 - device for controlling the speed of rotation; 9 - a box block; b: 1 - bedplate; 2 - drum; 3 - board; 4 - bracket; 5 - hinge;
6 - mechanism for adjusting the angle of the drum

The main tasks of developing the installation:
- providing the possibility of varying the speed of the seed coating machine drum;
- providing the ability to measure the speed of the drum;
- providing the possibility of changing the angle of inclination of the drum;
- ensuring the efficiency of the process of artificial shell formation on the seed surface due to the additional working elements of the installation.

To intensify the process of forming the shell in the drum *2* (Fig. 2 b), a slope board *3* is placed, which with the help of the bracket *4* is secured to the bedplate *1* and is intended to increase the surface for forming an artificial shell on the seeds. The position of the slope board is adjustable by the hinge *5* (Fig. 2 b), which allows you to change the angles relatively to the axis of rotation and relatively to the bottom of the drum of the seed coating machine. To investigate the influence of the drum angle of inclination on the formation of encapsulated seeds in the design of the experimental setup, there is a mechanism *6* to change the position of the seed coating machine drum.

To determine the static and dynamic coefficients of friction, the measuring device was developed, and the methodology provided for the use of video equipment and the computer program Movie Maker.

The movement of the encapsulated seeds in the seed coating machine drum is a waterfall mode. The working areas on which the artificial shell is formed are *AB* and *EA* (Fig. 3). Thus, to increase the performance of seed coating machine, it is necessary to increase the diameter of the drum, and as a consequence, it will increase its size and cost. We suggest installing an additional working element in the seed coating machine drum - a slope board. Section *CD* (Fig. 3) is an additional working surface for forming capsules of spherical shape.

When the drum is tilted, the conditions $\omega^2 R/g$ and the conditions of detachment of the capsules change slightly (*Dugaesescu I. et al, 2019*).

Since the drum of seed coating is angled, and in analytical studies we found that the efficiency of seed coating machine is affected by the angle of the drum, we considered the movement of the capsules in an inclined drum (Fig. 4).

a)   b)
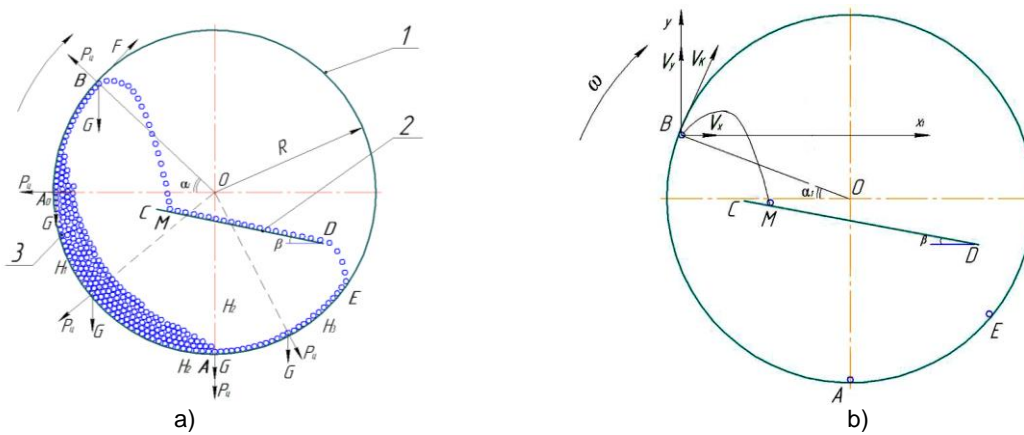
Fig. 3 - The scheme of the seed coating machine and the various positions of the capsules:
1 - drum; 2 - board; 3 - lifting capsule
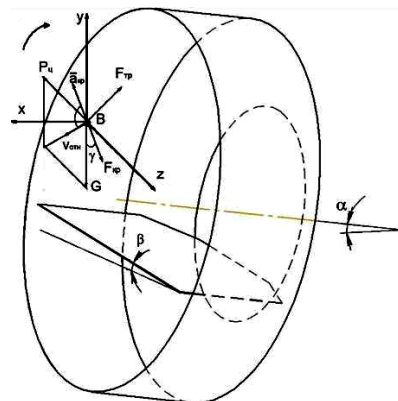
**Fig. 4. - The calculated scheme of the forces of seed coating machine at an angle
to the horizon and the flight path of the capsule**

Equation of the separation condition of the capsule from the drum's inner wall:

$$P_c \sin\beta - mg - \overline{F}_{cor} \cos\gamma = 0 , \tag{1}$$

$$m\omega^2 R\sin\cdot\sin\beta - mg - F_{cor}\cdot\cos\gamma = 0 , \tag{2}$$

where F_{cor} – Coriolis force, H; β – the installation angle of the slope board, deg.; γ – the angle between the Coriolis force and the gravity, deg.

$$\sin\alpha_1 = \frac{mg + F_{cor}\cos\gamma}{m\omega^2 R\sin\beta} = \frac{mg + ma_{cor}\cos\gamma}{m\omega^2 R\sin\beta} = \frac{g + a_{cor}\cos\gamma}{\omega^2 R\sin\beta} . \tag{3}$$

Then the angle at which the capsule rises is:

$$\alpha_1 = \arcsin\frac{(g + a_{cor}\cos\gamma)}{\omega^2 R\sin\beta} \tag{4}$$

where a_{cor} – Coriolis acceleration, m/s².

At the point of separation, the free flight begins in the plane of the forces acting: gravity, inertia, and friction (*Fan G.J. et al, 2017*). Because part of the initial data is almost very difficult and, even, it is not possible to determine mathematically - we choose the way to solve the problem by the method of multivariate experiment.

In view of the above, we will theoretically consider the motion of the capsule in the horizontal drum of the seed coating machine (Fig. 3 a).

Consider the motion of a single capsule in sections (Fig. 3):

I) AB - the area on which the capsules with seeds from the resting state move on the inner surface of the drum; II) *BC* - the area on which the encapsulated seed breaks away from the drum wall and falls on a slope board along the parabolic trajectory; III) *CD* - movement of capsules on an inclined plane - a slope board; IV) *DE* - the area on which the encapsulated seed breaks away from the slope board and falls on the drum wall; V) *EA* - the movement of the capsules on the inner wall of the drum.

The external forces applied to the material point - units of the capsule are: gravity *mg,* friction force *F*. As can be seen from Fig. 3 a, the drum *1* rotates clockwise and captures the capsules that hit the lower part of the drum. Before the drum rotation, only the gravitational force *G* acted on the capsules vertically downwards. For each capsule, the force of gravity *G* directed downwards, the friction force *F*, and the centrifugal inertia force P_c are directed from the centre of rotation *O* to act upon the rotation of the drum. Upon further rotation of the drum, the new position of the capsule will be at point B after rotation of the radius OA_0 and its transition to the position *OB*. Such a change in the position of the capsule may detach it from the surface of the drum. This separation will occur by the equality of the geometric sum of the forces $\overline{P}_c + \overline{G} + \overline{F}$ with zero.

In position B, the capsule will be in relative rest, if the sum of these forces' projections on the horizontal and vertical is zero, then we have:

$$\left. \begin{array}{l} mR\cos\alpha_1 - F\sin\alpha_1 = 0 \\ -mg + F\cos\alpha_1 + mR\omega^2\sin\alpha_1 = 0 \end{array} \right\}, \tag{5}$$

where *g* – the acceleration of free fall, m/s²; α_1 – the angle A_0OB (Fig. 3)*.*

After making a number of transformations we get:

$$R\omega^2\cos^2\alpha_1 = g\sin\alpha_1 + R\omega^2\sin\alpha_1. \tag{6}$$

Then:

$$\frac{R\omega^2}{g} = \sin\alpha_1. \tag{7}$$

Denote $\omega^2 R/g$ the relation by *k* and call it an indicator of the dynamic mode of the seed coating machine.

After separation of the capsule from the inner surface of the drum, the capsule flies free on a slope board to point *M* (Fig. 3 b). To derive the flight equations of the capsule on a slope board, we make the coordinate system *xBy* starting at point *B*. Let the capsule fall along the parabolic curve. The capsule is subjected to a force *G*, equal *mg*; air resistance is not taken into account. Let`s make the differential equations of capsule motion for this case:

$$\dot{y} = \omega R\cos\alpha_1 - gt, \tag{8}$$

$$y = \omega Rt\cos\alpha_1 - gt^2/2. \tag{9}$$

Excluding *t,* we obtain the equation of the capsule flight trajectory:

$$y = x\,ctg\,\alpha_1 - \frac{gx^2}{2\omega^2 R^2\sin^2\alpha_1}. \tag{10}$$

The capsule speed, taking into account the indicator of the dynamic mode of operation of the seed coating machine is equal to:

$$v_x = v\sin\alpha_1 = \omega R\cdot k, \tag{11}$$

$$v_y = v\cos\alpha_1 = \omega R\cdot\sqrt{1-k^2}. \tag{12}$$

Then the equation of the flight path of the capsule in the coordinate system *xOy*, taking into account the indicator of the dynamic mode of operation of the seed coating machine will be:

$$y = \frac{R(1+k)\sqrt{1-k^2}}{k} - \frac{x^2(R\cos\alpha_1 + x)^2}{2k^3\cdot R}. \tag{13}$$

Immediately after the fall, the capsule moves on the slope board *CD* to the right, starting from point *M* (Fig. 3). In this case, there is an overcoming of resistance due to rolling friction, but provided that this rolling occurs on an inclined plane at an angle *β* (Fig. 3).

Determine the equation of motion on the slope board *CD* (Fig. 3):

$$y_c = R\sin\alpha + R = R(1+k), \tag{14}$$

$$y_c = R(1+k). \tag{15}$$

The following condition needs to be done for constant movement on a slope board:

$$\beta \geq f, \tag{16}$$

where *f* – the coefficient of friction of the capsules.

Then, the equation of motion on the slope will look like:

$$y = y_0 - (R\cos\alpha_1 + x) \cdot f .$$ (17)

After making the conversion, we obtain the equation of motion of the capsule on the slope board, taking into account the indicator of the dynamic mode of operation of the seed coating machine:

$$y = R(1 + k) - f(R\sqrt{1 - k^2} + x) .$$ (18)

The speed of movement of the capsule on the slope board (Fig. 5) is determined by:

$$v = gt(\cos\beta - f\sin\beta) + R\omega k\cos\beta + \sqrt{2g(h_{max} - y_m)} \cdot \sin\beta ,$$ (19)

where h_{max} – the maximum capsule rise during parabola drop, m; y_m – the coordinate of the capsule at the point M (Fig. 3) falling on the slope.
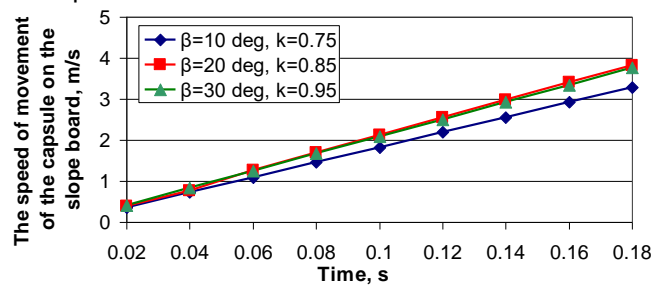
Fig. 5 - The speed of the capsule movement on a slope board

RESULTS

Requirements for dimensional characteristics and coefficients of friction of the seed material, that ensure the high quality of sowing. The main thing is based on simulation modeling for a mesh-disk seeding machine. As a result of simulation, a graph was obtained (Fig. 6), the analysis of which shows that the accuracy of sowing is practically ensured under the condition of obtaining seeds, the coefficient of friction equal to 0.5 and the standard deviation of the sizes of capsules σ + 0.1…0.2 mm. Thus, we formulated requirements for encapsulated seeds for accurate sowing of the mesh-disk seeding apparatus: the coefficient of friction shouldn't be more than 0.6, and the coefficient of variation of capsule sizes shouldn't be more than 5…8 %.

According to the experimental research programme, a second-order Box-Behnken plan was drawn up for the implementation of the experiments (Table 1). During the experimental studies, the effect of the dynamic mode of the seed coating machine k, the angle α of the drum slope to the horizon, and the angle β of the slope board installation β on the output of 6 - 6.5 mm spherical capsules were studied.
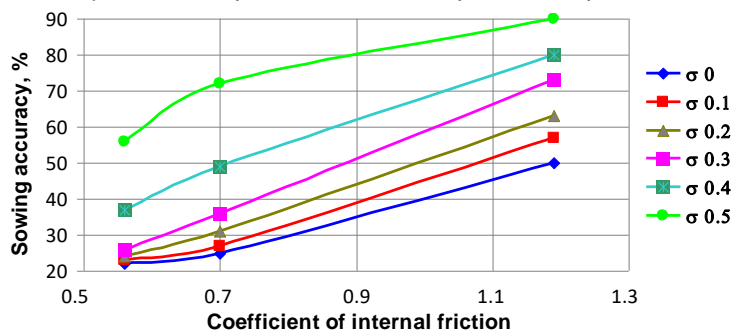
Fig. 6 - Dependence of sowing accuracy on the coefficient of internal friction of seeds at various standard deviations of seed sizes

Table 1

Levels of variation by factors

Levels and interval of variation	The coded value	Factors and their designation		
		Dynamic mode indicator, k (x₁)	Tilt angle of the seed coating machine α, deg. (x₂)	Angle of installation of the slope board β, deg. (x₃)
Upper level	+1	0.95	27	30
Basic level	0	0.85	18	20
Lower level	-1	0.75	9	10
Variation interval		0.10	9	10

At the end of the experiments, the obtained data were processed on PC using application packages Statistica 7. The result is a regression equation:

$$Y = 94.21 + 0.34x_1 + 0.59x_2 - 0.69x_3 + 0.86x_1x_2 + 2.2x_1x_3 + 0.75x_2x_3 - 1.99x_1^2 + 0.06x_2^2 - 0.92x_3^2. \qquad (20)$$

The response surfaces of the dependence of the output of capsules with a 6 - 6.5 mm diameter on the controlled parameters are presented in Fig. 7.

a   b

c
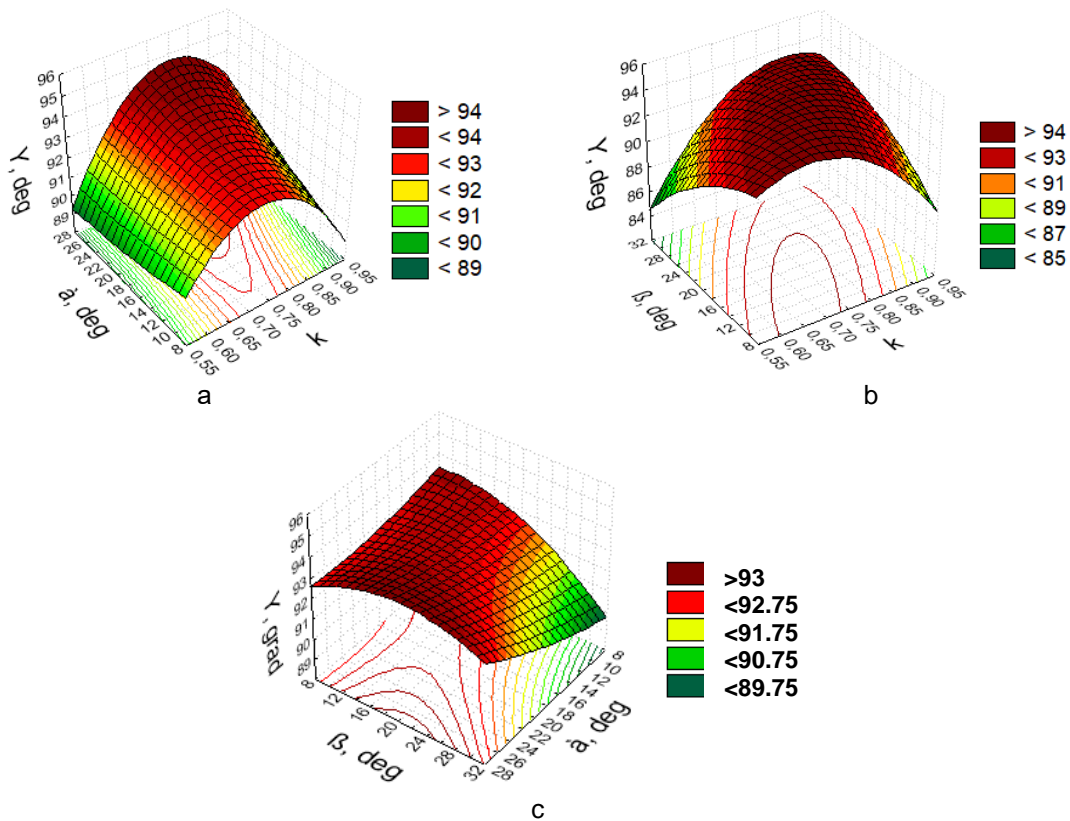
Fig. 7 - The dependence of the output of seed capsules with a diameter of 6-6.5 mm:
(a) - on k - dynamic mode and α - the angle of inclination of the drum; (b) on k - the dynamic mode of operation and β - the angle of installation of the slope board; (c) on α - the angle of inclination of the drum and β - the angle of installation of the slope board

The statistical analysis made it possible to make a regression equation, which normally describes the process of forming a capsular seed with 95% probability. The analysis of theoretical data with experimental data is presented in Fig. 8.
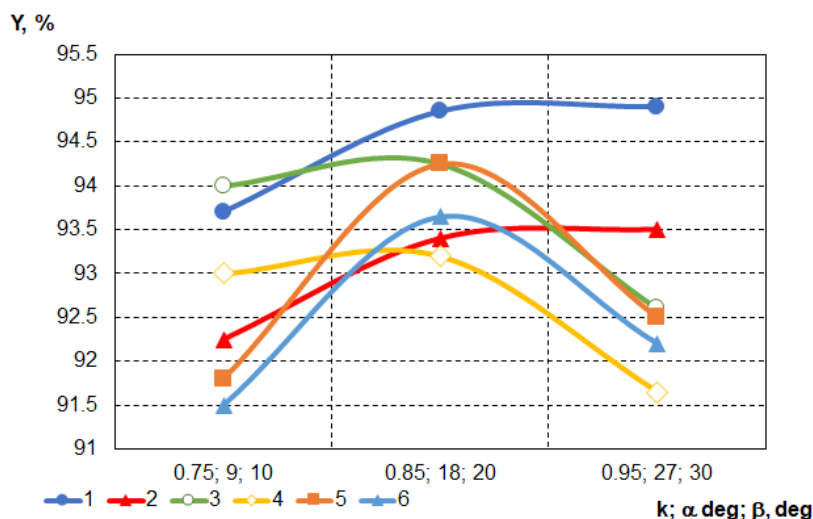
Fig. 8 - Comparison of experimental data with theoretical ones (dependence of the dynamic indicator of the seed coating machine k, the angle of drum installation, the angle of the slope board installation from Y, %:
1 - the dependence of the angle of installation of the drum α on Y, % (k=0.85; β=200); 2 - experimental data of the dependence of the dynamic operation indicator of the seed coating machine on Y,%; 3 - theoretical data of the slope board angle of installation on Y, % (k=0.85; α=180); 4 - experimental data of the dependence of the slope board angle of installation on Y,%; 5 - theoretical data of the dependence of the dynamic indicator of the seed coating machine k on Y, % (α=180; β=200);
6 - experimental data of the dependence of the operation dynamic indicator of the seed coating machine k on Y,%

In the process of seed encapsulation, cylindrical capsules of the same volume are used for the purpose of obtaining capsules of the spherical shape of the same size, but during the processing of

cylindrical capsules in the drum of the seed coating machine, they can be erased against the walls of the drum or rolled as a result of connection with clay residues. This leads to the distribution of capsules by size (Fig. 9).
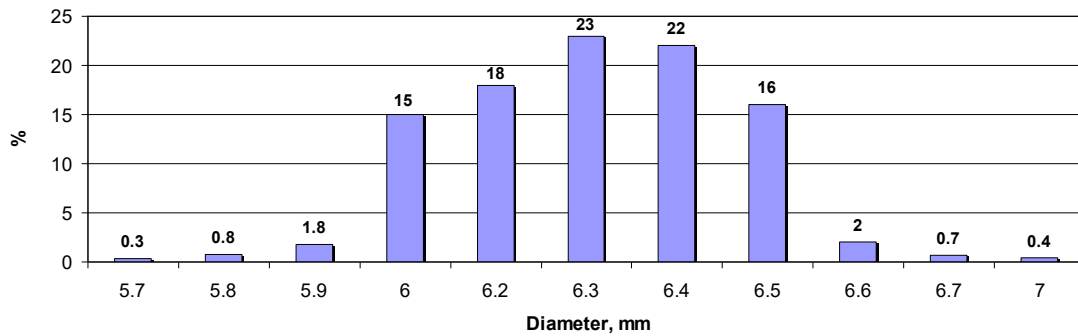
Fig. 9 - The distribution of the capsular seeds depending on the diameter

The absolute mass of seeds in the artificial shell, depending on the diameter is 36 - 42 times greater than the weight of ordinary seeds (Fig. 10), so the seeds in the capsule provide the exact distribution of the sowing mechanism in the row, as the probability of seed drift by wind is reduced.

$$y = 3.7143x + 184.43$$
$$R^2 = 0.9919$$
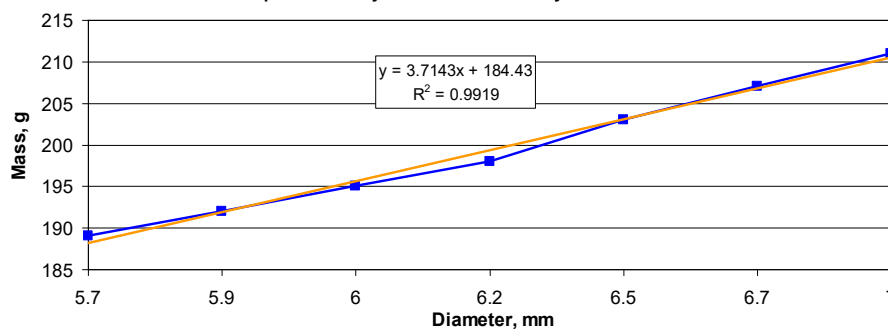
Fig. 10 - Dependence of the mass of the encapsulated seeds on the diameter

Static and dynamic coefficients of friction on steel and plastic (Fig. 11-12) were determined during the study of seeds in artificial shell (Figs. 11-12). The graph shows that the static coefficient of friction of the encapsulated seeds decreased in comparison with the untreated seeds of vegetable crops 2 - 3.8 times (depending on the culture). The comparative graph shows that the dynamic coefficient of friction of seeds in the artificial shell has decreased 4.5 - 8 times (depending on the culture) compared to ordinary seeds. Thus, the reduction of friction coefficients to one value makes it possible to universalize the working units of the planter.
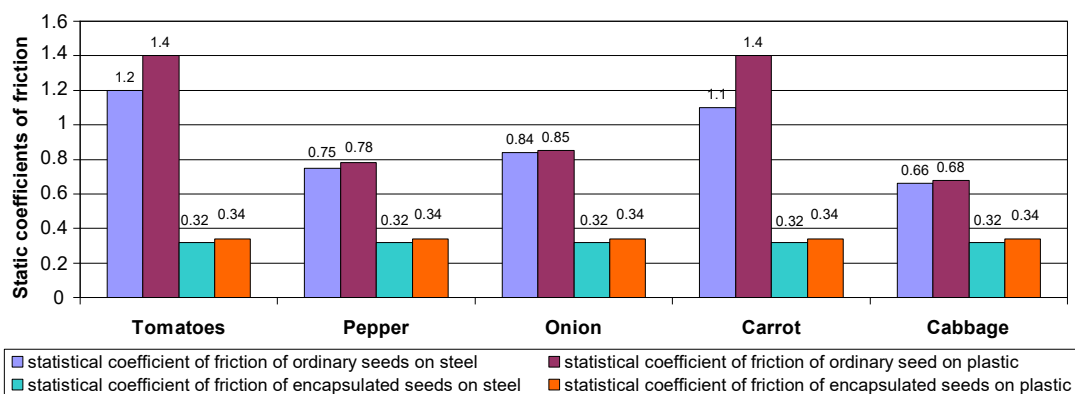
Fig. 11 - Static coefficients of friction of conventional and encapsulated vegetable seeds

The experimental research programme provided for the determination of the dynamics of the appearance of the seed capsules. As a result of researches, the dynamics of seedling emergence was determined: carrots, peppers, tomatoes of untreated seeds, coated company seeds and capsular seeds, and comparative graphs of the percentage of seedlings of plants (carrots) from the time of sowing were obtained (Fig. 13). Studies have shown that seedlings in clay capsules appeared faster than unprocessed seeds, carrots, tomatoes by 20%, and peppers by 32%. This is due primarily to the fact that the clay shell has hygroscopic properties, the ability to absorb soil moisture and provide reliable aeration, and as a result, to provide better seed germination.
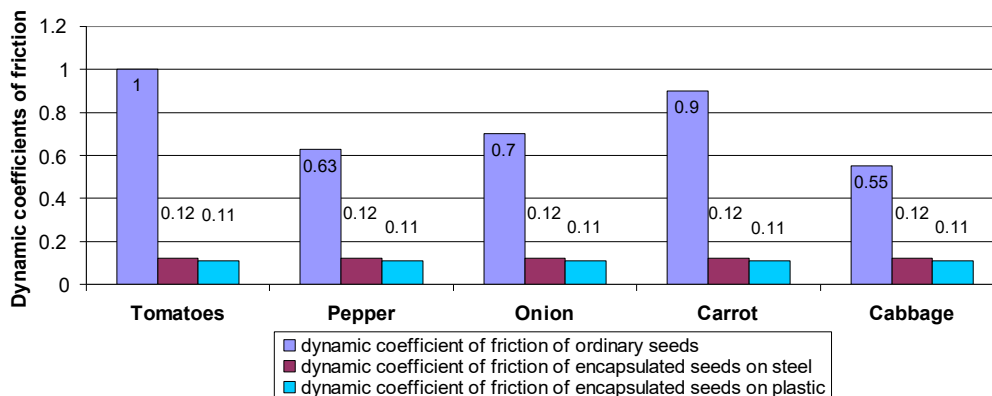
Fig. 12 - Dynamic coefficients of friction of conventional and encapsulated vegetable seeds
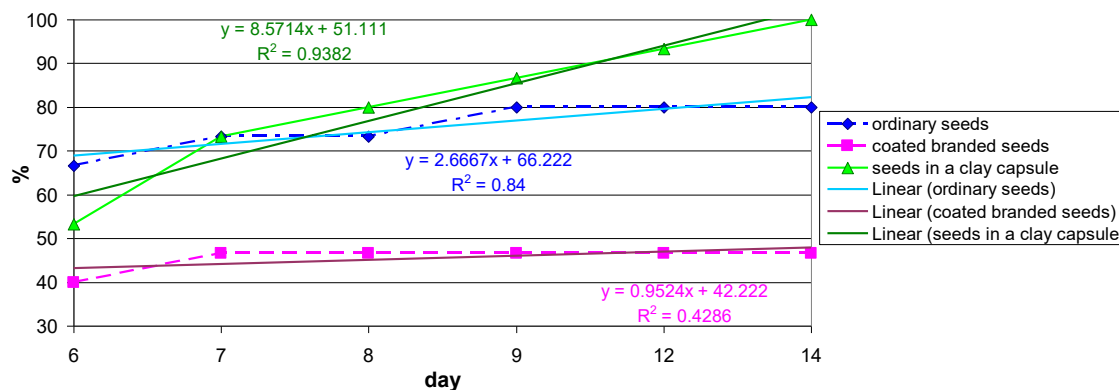
Fig. 13 - Dynamics of carrot seedlings

a – behaviour of spring shank response to the external impacts; b – autocorrelation function;
c – density of distribution; d – spectral analysis.

CONCLUSIONS

1. As a result of the simulation application, the requirements for encapsulated seeds were formulated for accurate sowing by the mesh-disk seeding apparatus: the coefficient of friction should be no more than 0.6, and the coefficient of variation of capsule sizes no more than 5…8 %.

2. The optimum parameters of the experimental setup are substantiated: dynamic mode of the seed coating machine k=0.85, angle of installation of the seed coating machine drum - 190 degrees to the horizontal and angle of installation of the slope board - 140 degrees to the horizontal.

3. Physical-mechanical properties of the encapsulated seeds were investigated. The static coefficient of friction in comparison with untreated seeds decreased 2 - 3.8 times (depending on the culture) and is 0.32, the dynamic coefficient of friction decreased 4.5 - 8 times (depending on the culture) and is 0.12.

4. As a result of studies of encapsulated seeds quality, the seedling emergence dynamics of encapsulated seeds of tomatoes and carrots was 20% higher than of untreated seeds and pepper by 32%.

REFERENCES

[1]   Amirkhani M., Mayton H.S., Netravali A.N., Taylor A.G., (2019), A seed coating delivery system for bio-based biostimulants to enhance plant growth. *Sustainability*, vol. 11, no 5304, pp. 1-16, Basel/Switzerland, (doi:10.3390/su11195304);

[2]   Arsenoaia V.N., Vlăduț V., Țenu I., Voicea I., Moiceanu G., Cârlescu P.M., (2019), Mathematical modeling and numerical simulation of the drying process of seeds in a pilot plant. *INMATEH Agricultural Engineering*, vol. 57, issue 1, pp. 55-62, Bucharest/Romania;

[3]   Belc N., Mustatea G., Apostol L., Iorga S., Vlăduț V., Mosoiu C., (2016), Cereal supply chain waste in the context of circular economy. *E3S Web of Conferences,* vol. 112, pp. 1-8, Bucharest/Romania, (doi:10.1051/E3sconf/201911203031);

[4]   Dugaesescu I., Popa L., Moise S., Moise V., Stefan V., Rotaru A., (2019), Kinematic analysis of mono-mobile mechanical system actuated by motor tetrad RRR-TA-RRR. *Proceedings of 18th International Scientific Conference "Engineering for rural development"*, May 22-25, Latvia University of Agriculture. Faculty of Engineering, vol. 18, pp. 648-654, Jelgava/Latvia, (doi:10.22616/ERDev2019.18.N404);

[5] Dihingia P.C., Prasanna Kumar G.V., Sarma P.K., Neog P., (2017), Production of soil block seedlings in plug trays for mechanical transplanting. *International Journal of Vegetable Science*, vol. 23, issue 5, pp. 471-485, Haworth/USA, (doi:10.1080/19315260.2017.1319889);

[6] Fan G.J., Wang Y.Z., Zhang X.H., Zhao J.Y., Song Y.P., (2017), Design and experiment of automatic levelling control system for orchards lifting platform. *Transactions of the Chinese Society of Agricultural Engineering*, vol. 33, issue 11, pp. 38-46, Beijing/China, (doi:114.255.9.31/iaej.2018.V27.I4.3);

[7] Gaganpreet Kaur and Udai R. Bishnoi, (2011), Effect of polymer and pesticide seed coatings on winter canola seed germination at various osmotic potentials. *World Journal of Agricultural Sciences,* vol. 7 (5), pp. 591-598, Kansas/USA;

[8] Halber A., Chakravarty D., (2018), Investigation of wireless tracking performance in the tunnel-like environment with particle filter. *Mathematical Modelling of Engineering Problems*, vol. 5, issue 2, pp. 93-101, Toronto/Canada, (doi:10.18280/mmep.050206);

[9] Hevko B.M., Hevko R.B., Klendii O.M., Buriak M.V., Dzyadykevych Y.V., Rozum R.I., (2018), Improvement of machine safety devices. *Acta Polytechnica,* vol. 58, no 1, pp. 17-25, Prague/Czech Republic, (doi:10.14311/AP.2018.58.0017);

[10] Hevko R.B., Yazlyuk B.O., Liubin M.V., Tokarchuk O.A., Klendii O.M., Pankiv V.R., (2017), Feasibility study of the process of transportation and stirring of mixture in continuous-flow conveyers. *INMATEH: Agricultural engineering*, vol. 51, issue 1, pp. 49-58. Bucharest/Romania;

[11] Kroulík M., Húla J., Rybka A., Honzík I., (2016), Pneumatic conveying characteristics of seeds in a vertical ascending airstream. *Research in Agricultural Engineering*, vol. 62, pp. 56-63, Prague/Czech Republic, (doi:10.17221/32/2014-RAE);

[12] Pedrini S., Merritt D.J., Stevens J., Dixon K., (2017), Seed Coating: Science or Marketing Spin. *Trends in Plant Science*, February, vol. 22, no 2, pp. 106-116, London/UK, (doi: 10.1016/j.tplants.2016.11.002);

[13] Pruteanu A., Vladut V., Cardei P., Bordean D., (2020), General tendencies of the behaviour of vegetables developed in a soil contaminated with heavy metals. *Revista de Chimie*, vol. 71, pp. 13-22, Bucharest/Romania, (doi:10.1007/s10661-013-3472-0);

[14] Rogovskii I., Titova L., Trokhaniak V., Trokhaniak O., Stepanenko S., (2019), Experimental study on the process of grain cleaning in a pneumatic microbiocature separator with apparatus camera. *Bulletin of the Transilvania University of Brasov, Series II: Forestry, Wood Industry, Agricultural Food Engineering*, vol. 12 (61), issue 1, pp. 117-128, Brasov/Romania, (doi:10.31926/but.fwiafe.2019.12.61.1.10);

[15] Rogovskii I.L., Titova L.L., Trokhaniak V.I., Rosamaha Yu.O., Blesnyuk O.V., Ohiienko A.V., (2019), Engineering management of two-phase coulter systems of seeding machines for implementing precision farming technologies. *INMATEH Agricultural Engineering*, vol. 58, issue 2, pp. 137-146, Bucharest/Romania, (doi:10.35633/INMATEH-58-15);

[16] Rogovskii I.L., Titova L.L., Trokhaniak V.I., Solomka O.V., Popyk P.S., Shvidia V.O., Stepanenko S.P., (2019), Experimental studies of drying conditions of grain crops with high moisture content in low-pressure environment. *INMATEH Agricultural Engineering*, vol. 57, issue 1, pp. 141-146, Bucharest/Romania;

[17] Stroescu Gh., Păun A, Matache A., Persu C., Dumitrașcu A., Dumitru I., Iuga D., Epure M., Fătu V., (2018), Technology for obtaining environmentally-friendly seeds and sowing material for vegetable species, *Proceedings of international Symposium ISB-INMATEH– Agricultural and Mechanical Engineering*, 1-3 Nov., pp. 467-472, Bucharest/Romania;

[18] Tolvaly-Roșca F., Máté M., Forgó Z., Kakucs A., (2017), Development of helical teethed involute gear meshed with a multi-edge cutting tool using a mixed gear teeth modelling method. *Procedia Engineering*, vol. 181, pp. 153-158, Oxford/UK, (doi:10.1016/j.proeng.2017.02.421);

[19] Tutunaru L.F., Nagy E.M., Coţa C., (2014), Influence of tillage tools cutting edge wear over technical and economic indicators. *INMATEH Agricultural Engineering*, vol. 44, issue 3, pp. 5-12, Bucharest/Romania;

[20] Vlăduţ D.I., Biriş S., Vlăduţ V., Cujbescu D., Ungureanu N., Găgeanu I., (2018), Experimental researches on the working process of a seedbed preparation equipment for heavy soils. *INMATEH Agricultural Engineering*, vol. 55, issue 2, pp. 27-34, Bucharest/Romania.

DETERMINATION OF TECHNICAL-AND-ECONOMIC INDICES OF ROOT CROP CONVEYER-SEPARATOR DURING THEIR MOTION ON CURVED PATH
/
ВИЗНАЧЕННЯ ТЕХНІКО-ЕКОНОМІЧНИХ ПАРАМЕТРІВ ТРАНСПОРТЕРА-СЕПАРАТОРА КОРЕНЕПЛОДІВ ПРИ ЇХ ПЕРЕМІЩЕННІ КРИВОЛІНІЙНОЮ ТРАСОЮ

Hevko R.B.[1], Tkachenko I.G.[1], Khomyk N.I.[1], Gumeniuk Y.P.[2], Flonts I.V.[3], Gumeniuk O.O.[2]
[1]Ternopil Ivan Puluj National Technical University / Ukraine;
[2]Ternopil National Economical University / Ukraine;
[3]National University of Life and Environmental Sciences of Ukraine / Ukraine;
E-mail: r_hevko@ukr.net
DOI: https://doi.org/10.35633/inmateh-61-19

ABSTRACT

The results of theoretical and experimental study of the process of root crops carrying by a conveyer-separator of a three-row trailed root crop harvester whose rubber belt with rods is equipped with scrapers and has a sign-variable direction of transportation to minimize the machine length have been described in the article. Some analytical dependencies describing the impact of design and kinematic parameters of the conveyer-separator on the root crops motion pattern have been given and analysed. The results of the research including the key factors identification affecting the process of root crops transportation on the curvilinear path between the conveyer-separator members are presented in the experimental part. The theoretical and experimental studies have been compared and the boundaries of the most efficient design and kinematic parameters choice of the conveyer-separator under discussion have been suggested.

РЕЗЮМЕ

У статті наведені результати теоретичних і експериментальних досліджень процесу переміщення коренеплодів транспортером-сепаратором трирядної причіпної коренезбиральної машини, пруткове полотно якого обладнане скребками і має знакозмінний напрямок транспортування для зменшення повздовжніх габаритів машини. Наведено аналітичні залежності впливу конструктивних і кінематичних параметрів транспортера-сепаратора на характер руху коренеплодів та проведений їх аналіз. В експериментальній частині представлено результати досліджень з визначенням домінуючих факторів на процес переведення коренеплодів на криволінійній ділянці між ланками транспортера-сепаратора. Здійснено порівняння теоретичних і експериментальних досліджень та запропоновано межі вибору раціональних конструктивно-кінематичних параметрів транспортера-сепаратора

INTRODUCTION

To solve the problem of root crops quality cleaning and simultaneous keeping to the allowable level of their damage at harvesting under difficult soil-climatic conditions it would be quite reasonable to use the principle of root crops cleaning along their entire route from digging to unloading. Here, the intensity of tools impact on the thrashed heap has to decrease towards its transportation by the tools as during separation the possibility of immediate interaction of working surfaces with root crops is increasing. First of all, the problem is connected with the modernization of rod and scraper conveyers as they should have some additional functions on simultaneous root crops transportation and after-cleaning.

It allows to provide the maximum possible soil separation from the root crops and to minimize its transportation to the raw material processing points.

The theoretical study of a material particle motion and flow motion including the determination of tools parameters and operation modes impact on the process of their displacement in different environments has been described in the papers (*Baranovsky V.M., Potapenko M.V., 2017; Baranovsky V.M., et.al., 2017, 2018; Bratucu Gh., Paunescu D.D., 2015; Bulgakov V., et.al., 2017; Hevko R.B., et.al., 2018; Lyashuk O.L., et.al., 2018, 2019; Pylypaka S.F., et.al., 2019; Rogovskii I.L., et.al., 2019; Tsarenko O.M., et al. 2003).*

The increase of transport-technological tools performance characteristics can be achieved due to the simultaneous carrying out of different operations, namely transportation and mixing of different components that has been paid attention to in the papers (*Hevko R.B., et al., 2017, 2018)*. Such approach describing the simultaneous transportation and cleaning of root crops has been implemented in the developed conveyer-separator and the results of its study are presented in the article under consideration.

The study of parameters impact of different types of root crop harvesters tools on the process of crops harvesting and storage prior to their processing has been highlighted in the papers *(Dumitru I., et.al., 2017, Becker M., et.al., 2016; Dumych.V., Salo, Ya., 2017; Liebe S., Varrelmann M., 2014)*. The results of theoretical and experimental study of similar types of conveyers-separators have been presented in the papers *(Pavelchak O.B., et al., 2000; Synii S.V., et al., 2018; Tkachenko I.G., et al., 2000; Tunik I.G., et al., 1998)*. The materials in the article under discussion are the follow-up study of previous research described in the papers *(Hevko R.B., et.al., 2016, 2018, 2019)*.

The purpose of the article under discussion is to find the most efficient design and kinematic parameters of a root crop scraper conveyer-separator during their curvilinear motion prior to the unloading into the harvester hopper so that to provide the maximum cleaning of the root crops from soil and plant remains with their minimal damage.

MATERIALS AND METHODS

To achieve the purpose in view a design-technological scheme of a root crop two-wheeler harvester with increased separating effect has been developed whose design model is presented in fig. 1
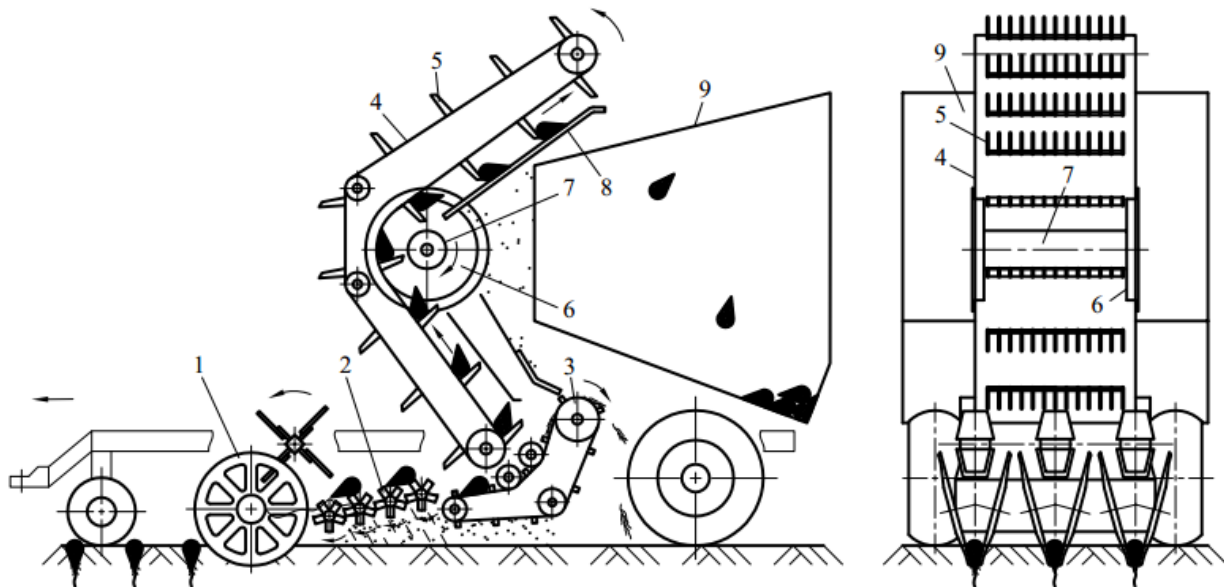
Fig. 1 – Design-technological scheme of a three-row trailed root crop harvester

It contains a disk digger *1*, from which the dug-out thrashed heap of root crops is supplied to the main cleaning unit *2* (auger or beater), where basic separation of the root crops from the soil takes place. After that the root crops are transported to the two-section conveyer *3*, where the remains are thrown away by its unloading link (*Hevko R.B. et.al, 2019)*. In the transfer area of the two-section conveyer *3,* the root crops are selected and transported to the unloading section by the scrapers *5* of the rubber belt with rods *4*. The change of root crops transportation direction and their after-cleaning takes place in the curved section where the elastic sides of the rubber belt with rods are interacting with side disks *6*, connected to each other by a hollow shaft *7*. Longitudinal rods *8* with a clearance Δ relative to the external surface of the hollow are placed under the groups of scrapers shaft towards the root crops transportation to the bunker *9*. Root crops are carried by the scrapers on the longitudinal rods and simultaneously their after-cleaning off tare takes place.

To determine the most efficient design and kinematic parameters of the unloading conveyer-separator of a root crop harvester the design model is presented in fig. 2 a. A picture of the conveyer-separator is on fig.2 b.

The conveyer-separator operation is going on in the following way. At first, in the area *I* the root crops are being transported towards the curved section *II* and are in contact both with the rubber belt with rods *4* and with scrapers *5*. In the curved section due to the action of centrifugal forces the root crops are retained against the rubber belt with rods surface but the soil and plant remains whose mass is much smaller than the

root crops mass are in the area approaching the hollow shaft surface. After that, the root crops are moving to the unloading area on the rectilinear path *III*. In this way, due to the gravitation force the root crops are being displaced on the scrapers surface towards the longitudinal grate but the soil and plant remains are thrown away through the clearance Δ, on the harvested field. Then the root crops are being transported by the scrapers on the longitudinal grate 8 that also contributes to their better cleaning from the sticky soil.

The aim of theoretical calculation is to determine the most efficient value of the clearance Δ to provide the maximum separation of the root crops thrashed heap from soil and plant remains.

Let's consider the forces acting on a root crop in the curved section *II.* The root crop is circulating in a random point M between points A and B.

Figure 1a includes the following symbols: mg – gravitation force; F_f – force of friction of the scraper-root crop couple; F_c – centrifugal force acting on the root crop in the curved section area; N_1 – normal force acting on the root crop from the web side; N_2 – normal force acting on the root crop from the groups of scrapers side; f – friction coefficient between a root crop and a scraper; α – rubber belt with rods inclination angle with horizon in section *I*; β – inclination angle of the unloading section of the rubber belt with rods with horizon; r – radius of the hollow shaft; R – radius of side discs; l – scrapers height; V – linear velocity of the web; ω – angular velocity of the hollow shaft; R_{rc} – equivalent radius of a root crop; D_g – distance from the centre of the hollow shaft rotation to the point of root crop interaction with the longitudinal grate; δ – clearance value between the scraper and external surface of the hollow shaft; γ – variable angle of a root crop displacement in the curved section area. Centrifugal force in the curved section area: $F_c = m\omega^2(R - R_{rc})$.
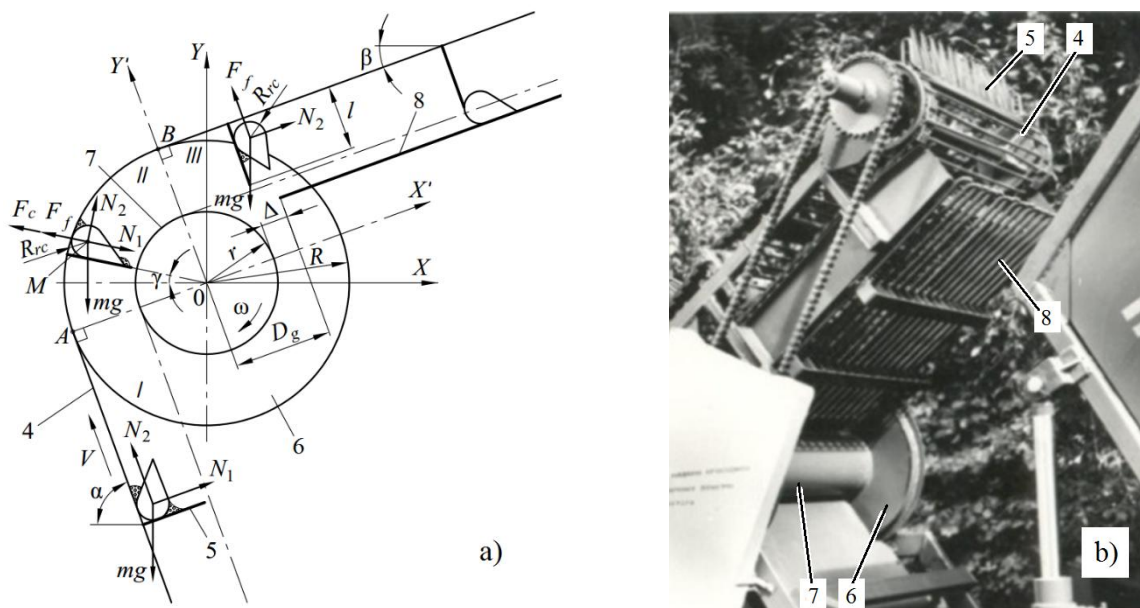
Fig. 2 – Design model to determine the design and kinematic parameters of an unloading transporting-separating tool of a root crop harvester (a) a picture of the conveyer-separator (b)

The equilibrium equations in projections on the axes X and Y are written as:

$$N_1 \cos\gamma + N_2 \sin\gamma - N_2 f \cos\gamma - \frac{mV^2}{R^2}(R - R_{rc})\cos\gamma = 0;$$

$$- N_1 \sin\gamma + N_2 \cos\gamma + N_2 f \sin\gamma - mg + \frac{mV^2}{R^2}(R - R_{rc})\sin\gamma = 0.$$

(1)

The condition when a root crop is retained against the rubber belt with rods: $N_1 > 0$.

Under the boundary condition (minimal velocity of the web when a root crop isn't displaced on the scrapers surface $(N_1 = 0)$ the equations (1) will be written as:

$$N_2(\sin\gamma - f\cos\gamma) = \frac{mV^2}{R^2}(R - R_{rc})\cos\gamma;$$

$$N_2(\cos\gamma + f\sin\gamma) - mg = \frac{mV^2}{R^2}(R - R_{rc})\sin\gamma. \tag{2}$$

After transformations of the system of equations (2) we obtain:

$$\frac{N_2(\sin\gamma - f\cos\gamma)}{N_2(\cos\gamma + f\sin\gamma)} = \frac{\dfrac{mV^2}{R^2}(R - R_{rc})\cos\gamma}{mg - \dfrac{mV^2}{R^2}(R - R_{rc})\sin\gamma};$$

$$(\sin\gamma - f\cos\gamma)R^2 g - (\sin\gamma - f\cos\gamma)V^2(R - R_{rc})\sin\gamma = V^2(R - R_{rc})\cos\gamma(\cos\gamma + f\sin\gamma);$$

$$\frac{V^2(R - R_{rc})}{R^2} = g(\sin\gamma - f\cos\gamma). \tag{3}$$

From the equation (3) we find the minimal velocity $V_{\min}$, where a root crop is pressed against the web surface

$$V_{\min} = R\sqrt{\frac{g(\sin\gamma - f\cos\gamma)}{(R - R_{rc})}}. \tag{4}$$

In this case, the condition must be satisfied

$$(\sin\gamma - f\cos\gamma) > 0. \tag{5}$$

When a root crop enters the unloading section area *III* it starts sliding along the scraper surface on the longitudinal grate. Therefore, the further calculations will involve the determination of the time period when the root crop covers the distance so that its bottom edge has a coordinate l.

During this period of time the web should travel over the distance bigger than the value D_g, which means:

$$S = r + \Delta + R_{rc}. \tag{6}$$

Projections of forces on the axes X and Y, acting on the root crop in the third section of transportation are written as:

$$N_2\cos\beta - F_{mp}\sin\beta = m\ddot{X};$$

$$N_2\sin\beta + F_{mp}\cos\beta - mg = m\ddot{Y}, \tag{7}$$

and projections of forces on the natural axes X' and Y' are written in the following way:

$$mg\cos\beta - N_2 f = m\ddot{l};$$

$$N_2 = mg\sin\beta. \tag{8}$$

Upon integrating the equation (8) we find the time when the lower end of the root crop head receives the coordinate l:

$$t = \sqrt{\frac{2(l - 2R_{rc})}{g(\cos\beta - f\sin\beta)}}. \tag{9}$$

If $\cos\beta - f\sin\beta < 0$, a root crop does not displace, i.e. $\cos\beta < f\sin\beta$; $\text{ctg}\beta < f$; $\text{tg}\beta > 1/f$; $\beta > \text{arctg}(1/f)$ are the conditions of root crop motionlessness.

The height of scrapers group l is found from the equation: $l = R - r - \delta$, where $\delta = 10...20$ mm.

While a root crop is traveling along the scrapers group towards the coordinate Y' one should take into consideration the most unfavourable case when the central axis of the root crop is parallel to the rubber belt with rods surface. In this case, its displacement is taking place with a coefficient of rolling friction which is lower than a coefficient of sliding friction and results in time t decrease.

Thus, taking into account the above-mentioned pattern of the root crop location, the condition when $S = Vt$ and dependencies (6) and (9), the equation to find the clearance value Δ in longitudinal grate is written as

$$\Delta = V\sqrt{\frac{2(R - r - \delta - 2R_{rc})}{g(\cos\beta - f\sin\beta)}} - R_{rc} - r. \tag{10}$$

Before the analytical dependence (10) analysis the minimal velocity of the rubber belt with rods V_{min} was found when the root crop was pressed to the web surface (formula 4). Afterwards, taking into account the certain value V_{min}, the maximum possible value of the longitudinal grate location relative to the hollow shaft Δ has been calculated.

In the analysis of dependencies (4) and (10) the boundaries of variable parameters' values were as follows: $R = 0.25...0.35$ m; $R_{rc} = 0.02...0.06$ m; $r = 0.08...0.12$ m; $\beta = 30...50°$; where $\beta = (90° - \gamma)$. The values: $f = 0.3$; $\delta = 15$ mm; $\beta = 30...50°$ have been assumed as constant ones.

While studying the impact of one of the parameters on the values V_{min} and Δ the other ones remained constant, and their absolute values were as follows: $R = 0.3$ m; $R_{rc} = 0.05$ m; $r = 0.1$ m; $\beta = 40°$.

Figure 3 represents the curves describing dependencies of parameters R, R_{rc} and β impact on the minimal velocity of the web V_{min} (a) and parameters V, R, r and β impact on the value of the clearance Δ (b).
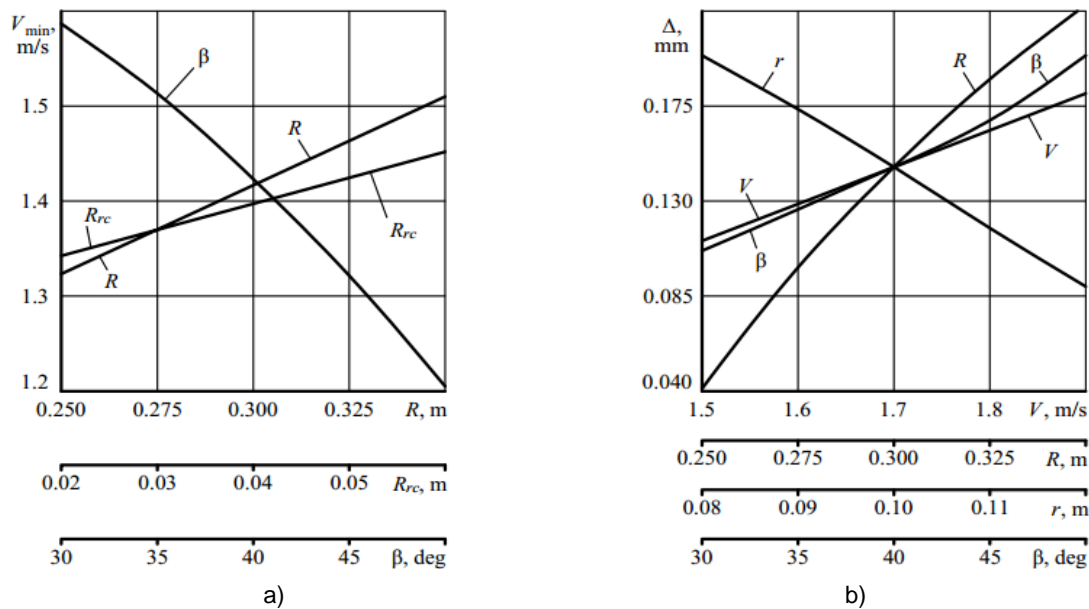
Fig. 3 – Curves describing dependencies of parameters R, R_{rc} and β impact on the minimal velocity of the web V_{min} (a) and parameters V, R, r and β impact on the value of the clearance Δ (b)

The analysis of the curves has proved that angle β (Figure 3a) has the biggest influence on the value V_{min}. The maximum value $V_{min} = 1.59$ m/s corresponds to the angle $\beta = 30°$, whereas minimal $V_{min} = 1.21$ m/s – $\beta = 50°$. It can be explained by the increased value of the angle γ, whose maximum value is determined from the condition $\gamma = (90° - \beta)$.

The second one according to the impact on the value V_{min} is the radius of side disks R, whose range of value change 0.25...0.35 m causes the increase of V_{min} from 1.325 to 1.514 m/s respectively.

A root crop radius is an uncontrolled factor so, while choosing the most efficient design-kinematic parameters of a conveyer-separator one must take into account the most unfavourable options, namely providing the transportation of standard root crops with minimal radius of a root crop head $R_{rc} = 0.02$ m. As we can see from the curves the parameter under discussion has a minimal impact on the value V_{min} and when its value changes from 0.02 to 0.06 m the increase of V_{min} equals only 0.11 m/s. Thus, while studying the impact of design-kinematic parameters on the value Δ we'll accept an average value $R_{rc} = 0.05$ m, which corresponds to satisfactory harvest of sugar beet root crops.

Figure 3 (b) presents the curves of parameters V, R, r and β impact on the clearance value Δ.

While studying one of the parameters the others were given their average values. That is why all curves are crossed in one central point. It makes possible to evaluate both the absolute value change of the required parameter within the certain range and to determine its influence degree on the value Δ as well, due to the comparison with the impact degree of other parameters. Having analysed the obtained dependencies it was found that the value Δ is most of all influenced by the radius of side disks R whose increase from 0.25 to 0.35 m enables to increase the clearance value Δ from 0.04 to 0.223 m. Next, according to the impact degree on the value Δ is the radius of hollow shaft r, whose range of value increase 0.08…0.12 m causes the decrease of value Δ from 0.2 to 0.09 m. The third one, according to the impact degree on the value Δ, is the inclination angle of the unloading section of the rubber belt with rods with horizon β, whose range of value increase 30…50° causes the increase of value Δ from 0.115 to 0.198 m.

The minimal impact on the value Δ is made by the conveyer web velocity V, whose pattern of change is of linear behaviour. So, the increase of V from 0.15 to 0.19 m/s results in the 0.07 m/s increase of Δ.

The purpose of experimental study is to determine the degree of separated dirt and plant remains while using the boundaries of the parameters under discussion and also to check how the results of the theoretical investigation conform to the experimental data on different values of clearance Δ determination.

RESULTS

In comparing the theoretical and experimental studies on observing the root crop displacement prior to its contact with the longitudinal grate (finding the value of clearance Δ) the conventional photo fixation devices (cameras, mobile phones) were used. The discrepancy between the obtained results in determining the value Δ did not exceed 17%.

Moreover, some experimental study has been done to determine the mass of separated dirt and plant remains under the longitudinal grate. The technique of conducting the experimental study under discussion is a standard one and was described in the paper (*Hevko R.B., et al., 2016, 2019).* The obtained data of separated dirt and plant remains mass have been found with 10 m distance of a root crop harvester motion.

While conducting the experimental research, factor fields of variable parameters have the following boundaries: $1.4 \leq V \leq 1.8$ m/s; $30° \leq \beta \leq 40°$; $0.1 \leq \Delta \leq 0.16$ m.

After the necessary statistical manipulations, the regression equation to determine the change of separated dirt and plant remains mass is written as:

$$S_i = -7.46 - 0.98 \cdot V + 1.01 \cdot \Delta + 0.58 \cdot \beta - 0.03 \cdot V \cdot \Delta - 0.1 \cdot 10^{-3} \cdot V \cdot \beta - 0.67 \cdot \Delta \cdot \beta - 0.510^{-2} \cdot V^2 + 166.7 \cdot \Delta^2 - 0.4 \cdot 10^{-2} \cdot \beta^2.$$

The response surfaces of separated dirt and plant remains mass S_i are presented in Figure 4.

While conducting the statistical analysis, the determination coefficient was $D = 0.978$, correlation coefficient – $R = 0.963$, Fisher's ratio test – $F = 82.399$, standard deviation of assessment – $S = 0.193$.

Having analysed the regression equation and response surfaces, we have found that the value S_i is chiefly influenced by the angle β. The second important making impact on the value S_i is the value of clearance Δ. The conveyer web velocity has a reverse mode and makes a minimum impact on the degree of separation of soil and plant remains. Though the parameter under discussion should conform to the previous transport-technological tools in the layout scheme of a root crop harvester and this parameter must have the maximum value to provide the technological process running.

The separated mass of soil and plant remains by the developed conveyer-separator under discussion with 10 m length of furrow of a three-row trailed root crop harvester is 6…7 kg on average (when inter-row sewing of root crops is 0.45 m). Thus, separated dirt and plant remains will be approximately 4.4…5.2 t per 1 ha. We assume that, the annual load of a three-row trailed root crop harvester during sugar beet root crops harvesting is approximately 80 ra. In this case, the additional mass of separated dirt and plant remains left directly on the fields will be approximately 350…416 t, that has some positive effect both for the ecology and for the economy as it allows to achieve the considerable reduction of transport costs for unseparated soil transportation.

It was also found that under dry working conditions of the machine operation when the clearance value exceeds $\Delta > 0.12$ m (soil humidity ≈ 14%) and maximum humidity $\Delta > 0.16$ m (soil humidity ≈ 22 %) the considerable damage of root crops takes place especially in their tail part.
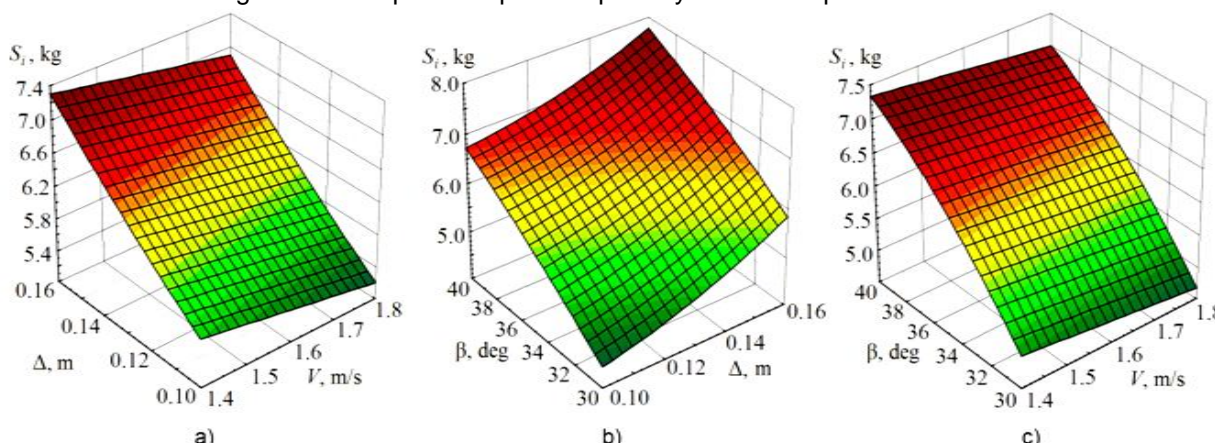
Fig. 4 – Response surfaces of separated dirt and plant remains mass S_i:
a) − $S_i = f(\Delta; V)$; b) − $S_i = f(\beta; \Delta)$; c) − $S_i = f(\beta; V)$

The separated mass of soil and plant remains by the developed conveyer-separator under discussion with 10 m length of furrow of a three-row trailed root crop harvester is 6…7 kg on average (when inter-row sewing of root crops is 0.45 m). Thus, separated dirt and plant remains will be approximately 4.4…5.2 t per 1 ha. We assume that, the annual load of a three-row trailed root crop harvester during sugar beet root crops harvesting is approximately 80 ra. In this case, the additional mass of separated dirt and plant remains left directly on the fields will be approximately 350…416 t, that has some positive effect both for the ecology and for the economy as it allows to achieve the considerable reduction of transport costs spent on unseparated soil transportation.

CONCLUSIONS

The results of theoretical and experimental studies of a root crop conveyer-separator which provides the sugar beet root crops after-cleaning during their transportation to the unloading area have been described in the article.

Due to the results of theoretical investigation it was found that the minimal velocity of the conveyer web should be not less than 1.4 m/s.

The value of clearance Δ must be within the limits 0.12…0.16 m under satisfactory conditions of root crops harvesting (soil humidity 15…20 %; soil hardness 1.6…2.2 MPa). In this regard, one should provide the clearances Δ and δ adjustment when developing the conveyer-separator design to adapt the machine as quickly as possible for the change in soil and climate conditions during sugar beet root crops harvesting.

The conducted theoretical investigation has been proved correct by the results of experimental study and can be applied in similar types of conveyers-separators design.

REFERENCES

[1]   Baranovsky V.M., Potapenko M.V., (2017), Theoretical analysis of the technological feed of lifter root crops, *INMATEH-Agricultural engineering*, vol. 51, no. 1, pp. 29-38, Bucharest/Romania;

[2]   Baranovsky V., Dubchak N., Pankiv M., (2017), Experimental research of stripping the leaves from root crops, *Acta Technologica, Nitra: Slovaca Universitas Agriculturae Nitriae*, vol. 20, no. 3, pp. 69-73, Nitra/Slovakia;

[3]   Becker M., Varrelmann M., Christ D., (2016), Impact of genotype, harvest technology and harvesting conditions on storage rot formation and invert sugar accumulation during long-term storage of sugar beet, *Sugar Industry-Zuckerindustrie*, vol. 141 (5), pp. 322-330, Berlin/Germany;

[4]   Bratucu Gh., Paunescu D.D., (2015), Establishing the optimum operating mode of sugar beet head cutting equipment using a cylindrical palpator, *Bulletin of the Transilvania University of Braşov*, Series II, vol. 8, pp. 51-56, Braşov/Romania;

[5]   Bulgakov V., Adamchuk V., Nozdrovicky L. et al., (2017), Theory of the interaction of flat sensing organ with the head of the sugar beet root, *Journal of Agricultural Engineering*, vol. 48, no. 4, pp. 235-244, Bologna/Italy. https://doi.org/10.4081/jae.2017.676;

[6]   Dumitru I., Voicea I., Găgeanu I. et al. (2017), Technical considerations regarding the harvesting potatoes and carrots equipment, Annals of the University of Craiova - Agriculture, Montanology, Cadastre Series, vol. XLVII, pp. 317-323, Craiova/Romania;

[7]   Dumych V., Salo Ya., (2013), Analysis of structures of technical means for combine harvesting of potatoes, *Engineering and Technology AIC*, vol. 41, no. 2, pp. 19-22, Kyiv/Ukraine;

[8]   Hevko R.B., Tkachenko I.G., Synii S.V., Flonts I.V., (2016), Development of design and investigation of operation processes of small-scale root crop and potato harvesters*, INMATEH-Agricultural engineering*, vol. 49, no. 2, pp. 53-60, Bucharest/Romania;

[9]   Hevko R., Brukhanskyi R., Flonts I., Synii S., Klendii O., (2018), Advances in methods of cleaning root crops, *Bulletin of the Transilvania University of Braşov*, Series II*, vol. 11(60), pp. 127-138, Braşov/Romania;

[10]   Hevko R.B., Tkachenko I.G., Rogatynskyi R.M., Synii S.V., Flonts I.V., Pohrishchuk B.V., (2019), Impact of parameters of an after-cleaning conveyor of a root crop harvester on its performance*, INMATEH-Agricultural engineering*, vol. 59, no. 3, pp.41-48, Bucharest/Romania;

[11]   Hevko R.B., Yazlyuk B.O., Liubin M.V., Tokarchuk O.A., Klendii O.M., Pankiv V.R., (2017), Feasibility study of mixture transportation and stirring process in continuous-flow conveyors, *INMATEH-Agricultural engineering*, vol. 51, no. 1, pp.49-59, Bucharest/Romania;

[12]   Hevko R.B., Liubin M.V., Tokarchuk O.A., Lyashuk O.L., Pohrishchuk B.V., Klendii O.M., (2018), Determination of the parameters of transporting and mixing feed mixtures along the curvilinear paths of tubular conveyors, *INMATEH-Agricultural Engineering*, vol. 55, no. 2, pp. 97-104, Bucharest/Romania;

[13]   Liebe S., Varrelmann M., (2014), Impact of root rot pathogens on storage of sugar beets and control measure, *Sugar Industry-Zuckerindustrie*, vol. 139 (7), pp. 443-452, Berlin/Germany;

[14]   Lyashuk O.L., Sokil M.B., Klendiy V.M., Skyba O.P., Tretiakov O.L., Slobodian L.M., Slobodian N.O., (2018), Mathematical model of bending vibrations of a horizontal feeder-mixer along the flow of grain mixture, *INMATEH-Agricultural Engineering*, vol. 55, no. 2, pp. 35-44, Bucharest/Romania;

[15]   Lyashuk O.L., Vovk Y.Y., Sokil M.B., Klendii V.M, Ivasechko R.R, Dovbush T.A, (2019), Mathematical model of a dynamic process of transporting a bulk material by means of a tube scraping conveyor, *Agricultural Engineering International*: *CIGR Journal*, vol. 21, no. 1, pp. 74-81; Fengmin Zhao/China;

[16]   Pavelchak O.B., Tkachenko I.G., Hladyo Y.B. et al., (2000), Definition of rational parameters of the conveyor-separator (Вибір раціональних параметрів транспортера-сепаратора), *Collection of scientific works of the National Agrarian University (Збірник наукових праць національного аграрного університету),* vol. 8, pp. 41-47, Kyiv/Ukraine;

[17]   Pylypaka S.F., Klendii M.B., Nesvidomin V.M., Trokhaniak V.I., (2019), Particle motion over the edge of an inclined plane that performs axial movement in a vertical limiting cylinder, *Acta Polytechnica, Journal of Advanced Engineering*, vol. 59, no. 1, pp. 67-76, Prague/Czech Republic;

[18]   Pylypaka S.F., Nesvidomin V.M., Klendii M.B., Rogovskii I.L., Kresan T.A., Trokhaniak V.I., (2019), Conveyance of a particle by a vertical screw, which is limited by a coaxial fixed cylinder, *Bulletin of the Karaganda University. Mathematics series*, vol. 95, no. 3, pp. 108-119, Karaganda/Kazakhstan;

[19]   Rogovskii I.L., Titova L.L., Davydenko O.O., Trokhaniak V.I., Trokhaniak O.M., (2019), Technology of Producing Reinforced Concrete Columns of Circular Cross-Sectional and Investigation of Their Strain-Stress State at Transverse-Longitudinal Bending, *Acta Polytechnica, Journal of Advanced Engineering*, vol. 59, no. 5, pp. 510-517, Prague/Czech Republic;

[20]   Synii S.V., Hevko R.B., Flonts I.V., et al., (2018), Improvement of the root crop cleaning efficiency (Підвищення ефективності очищення коренеплодів), *Agricultural machines. Collection of scientific articles*, vol. 40, pp. 89-100, Lutsk/Ukraine;

[21]   Tkachenko I.G., Hladyo Y.B., Hevko R.B., et al., (2000), Substantiation of the conveyor-separator parameters (Обґрунтування параметрів транспортера-сепаратора), *Scientific notes. Intercollegiate collection (Наукові нотатки. Міжвузівський збірник)*, vol. 7, pp. 260-266, Lutsk/Ukraine;

[22]   Tunik I.G., Hevko R.B., Hladyo Y.B., Synii S.V., (1998), Substantiation of the structural and kinematic parameters of the loading conveyor of the root crop harvesting machine (Обґрунтування конструктивно-кінематичних параметрів завантажувального транспортеру коренезбиральної машини), *Agricultural machines. Collection of scientific articles (Сільськогосподарські машини. Збірник наукових статей)*, vol. 4, pp.135-143, Lutsk/Ukraine;

[23]   Tsarenko O.M., Voityuk L.M., Shvayko M.V. et al., (2003), Mechanical and technological properties of agricultural materials (Механіко-технологічні властивості сільськогосподарських матеріалів), *Textbook (Підручник)*, 448 p, Kyiv/Ukraine.

DETERMINATION OF THE ENERGY EFFICIENT MODES
FOR BARLEY SEEDS DRYING
/
ВИЗНАЧЕННЯ ЕНЕРГОЕФЕКТИВНИХ РЕЖИМІВ
СУШІННЯ НАСІННЯ ЯЧМЕНЮ

Snezhkin Yu.F.[1), Paziuk V.M.2), Petrova Zh. O.3), Tokarchuk O.A.4)   [1]

[1)] Institute of technical thermal physics NAS of Ukraine, [2)] Institute of technical thermal physics NAS of Ukraine,
[3)] Institute of Engineering Thermophysics / Ukraine, [4)] Vinnitsia National Agrarian University/Ukraine
Tel: 0977297585 ; E-mail: tokarchyk08@ukr.net

ABSTRACT

For a more accurate study of the kinetics of the barley seeds drying, a convective drying stand with a computerized system of data acquisition and processing on the change in the mass and temperature of the sample from the drying time was used.

The kinetic curves of the drying process under the action of three factors were constructed: the temperature of the coolant, heating medium movement rate and the initial moisture content of the seeds. Studies were also conducted and the germination of barley seeds under the action of these factors was analysed.

Studies have shown that all factors affect the kinetics of the drying process, but the greatest influence on the germination of seed material comes from the influence of the temperature of the coolant. A three-factor effect on the germination of barley seeds on the 7th day of germination is presented, that indicates the need for low-temperature drying at a coolant temperature of 50°C.

In order to increase the intensification and energy efficiency of the drying process, the proposed two-stage drying mode is 65/50°C, which provides intensive heating and evaporation of moisture from the material at the initial stage of the process. Studies on the germination of barley seeds in a two-stage mode showed that the specified drying mode provides a high germination rate of the material up to 99%, an intensity of 83% and an energy efficiency of 62% compared to a rational single-stage drying mode of 50°C and can be recommended for drying barley seeds.

РЕЗЮМЕ

Для більш точного дослідження кінетики сушіння насіння ячменю був застосований конвективний сушильний стенд із комп'ютерною системою збору та обробки даних про зміну маси та температури зразка від часу сушіння.

Проведено побудова кривих кінетики процесу сушіння від дії трьох факторів: температури теплоносія, швидкості руху теплоносія та початкової вологості насіння. Також проведені дослідження та проаналізована схожість насіння ячменю від дії зазначених факторів

Дослідження показали, що всі фактори впливають на кінетику процесу сушіння, але найбільший вплив на схожість насіннєвого матеріалу відбувається від впливу температури теплоносія. Представлений трьохфакторний вплив на схожість насіння ячменю на 7 день пророщування вказує на необхідність низькотемпературного сушіння при температурі теплоносія 50°С.

З метою підвищення інтенсифікації та енергоефективності процесу сушіння запропонований двохступеневий режим сушіння 65/50°С, що забезпечує інтенсивне прогрівання та випаровування вологи з матеріалу на початковій стадії процесу. Проведені дослідження із схожості насіння ячменю в двохступеневому режимі вказали, що зазначений режим сушіння забезпечує високу схожість матеріалу до 99%, інтенсивність на 83% та енергоефективність процесу на 62% в порівнянні з раціональним одноступеневим режимом сушіння 50°С і може бути рекомендований для сушіння насіння ячменю.

---

[1] *Snezhkin Yu.F., Prof. Ph.D. Eng.; Paziuk V.M., Assoc. Prof. Ph.D. Eng.; Petrova Zh. O., Prof. D.Sc.;*
Tokarchuk O.A., Assoc. Prof. Ph.D. Eng.

INTRODUCTION

Drying is the main technological operation for bringing the seeds to a stable equilibrium condition. The technology of seed drying involves knowledge of the biological properties of the grain as the object for drying, the heat stability of the grain, patterns of moisture evaporation, determining the modes of drying and equipment for the implementation of the process.

The theoretical basis of the agricultural material drying techniques has been formed in the world for two and a half centuries. Nevertheless, despite the multitude of studies well presented in the literature, the industry still lacks universally recognized methods of design calculation for the majority of drying problems (*Bulgakov V., Bandura V., Arak M., Olt J., 2018).* Scientists are investigating different types of drying crops: active ventilation (*Gaponyuk O.I. Ostapchuk M.V, Stankevich G.M., 2014*), in a monolayer tray vibration dryer based on infrared radiation (*Bandura V., Mazur V., Yaroshenko L., Rubanenko O., 2019*), by vibration dryer with electromagnetic energy sources (*Burdo O., Bandura V. , Zykov A., Zozulyak I., Levtrinskaya J. , Marenchenko E. 2017*), intermitted drying *(Kumar C., Karim M. A., & Joardder M. U. H., 2014; Souza e Silva J. S., 2008)*, microwave convective drying *(Ahrné L. M., Pereira N. R., Staack N. & P. Floberg)*, a combination of a convective method of supplying heat with the introduction of ozone drying agent (*Tsurkan O. V. Necheporenko S. A., Blyznyuk M. Ya, 2013).*

Having characterized the grain drying processes, we can roughly divide it into soft and rigid grain drying modes. The first is specified by the relatively low temperature and speed of the drying agent. In the soft mode, the processes of heating and drying the grain are relatively slow. For the rigid mode higher temperatures and the heating medium movement rates are characteristic *(Paziuk, V.M., Liubin, M.V., Yaropud, V.M., Tokarchuk, O.A., Tokarchuk, D.M., 2018).*

From the economic point of view, it is desirable to carry out the process of grain drying in a rigid mode with drying time reduction. However, under the rigid mode due to intensive heating and dehydration, grain quality deterioration takes place: cracking of seeds, discoloration, partial or complete destruction of the embryo, deformation of tissues.

The use of high temperatures at the beginning of the wet grain drying process leads to a rapid dehydration of its surface *(Matkivska I. Ja., Atamanyuk V. M., Symak D., 2014*), which makes the shell less permeable to moisture (the phenomenon of thermal "hardening" of the grain). Under such conditions, water vapor is formed in the surface layer, the output of which becomes difficult.

MATERIALS AND METHODS

Drying of seeds of different crops has certain restrictions. As it is known (*Lykov A.V., 1968; Stankevich G. M., Strahova T. V., Atanazevich V.I. , 1997; Paziuk V.M., Petrova Zh.O., Tokarchuk O.A., Yaropud V.M.; Shchitsov S.V., Tikhonchuk P.V., Krivuta Z.F., Kolzov A.V., 2016*), high temperatures have negative effect on the quality of seeds, reducing their energy for germination and growth thus impairing the quality of material for technological purposes.

By the soft drying mode there is no full confidence in preserving seed properties of the grain, thus durable low temperature drying (depending on environmental parameters) may form the mould on the surface of the grain resulting in the seed material damage.

Soares M., Jorge L., Montanuci F. (2016) in their works studied the kinetics of the barley seeds drying process at a 40-80ºC temperature of the drying agent in continuous and periodic drying mode.

Continuous drying has the advantages of the drying time reduction due to elimination of the loading and unloading operations of the dryer. But it also has its disadvantages: in a continuous heat flow a difference between the moisture on the surface and inside the grain occurs.

In periodic dryers, the product passes through the dryer several times until fully dried. Thus, the grain is subjected to a short-repeated action of heat and rest during drying. During the rest, moisture is moved from the centre to the periphery of the grain, which reduces the occurrence of cracks due to a decrease of internal stresses in the grain.

Studies of the barley seeds drying kinetics described in the work of *Soares M. et al* showed that the maximum duration of drying at a 40ºC temperature of the heating medium for 12 hours corresponds to the 94-95% level of seeds germination. Increasing the temperature to 60-80ºC under different drying methods reduces duration of drying and the level of seed material germination

The influence of the coolant temperature in fluidized bed dryers and infrared radiation on drying kinetics and germination rates of barley seeds is demonstrated in the work of *Markowski M. et al (2007)* Drying of barley seeds in a fluidized bed dryer takes place at a 30-45ºC drying agent temperature, which corresponds to radiation in an infrared dryer with an intensity range of 0.048-0.107 W/cm², seed germination rate was at a 91-93% level.

Stankevich G.M. et al (1997) in their work recommend maximal allowable heating temperature for drying barley seeds in a mine-type dryer with a 40°C drying agent temperature, but does not give data on seed germination rate.

Various authors give recommendations on determining the optimal mode of drying, which need clarification.

Many of the approaches and methods for drying barley seeds are alternative to traditional convective drying. Modern drying equipment with computerized processing of the obtained data allows to determine more precisely the necessary drying modes on the base of germination properties of the seeds.

For determining the kinetics of barley seeds drying, a convective drying stand with a computerized data acquisition and processing system was used, which allows to read experimental data 6 times per minute *(Pazyuk V. Petrova Zn., Chepeliuk O., 2018)*.

Data on the barley seeds heating temperature and the weight of the material changes during the studies were obtained. The graphs of the kinetics of the drying process were built and calculations of the drying rates of barley seeds were made.

RESULTS

Results of the authors' laboratory research on the barley seeds drying are presented in Fig. 1-3.

Shift in the temperature of the drying agent from 50 to 80°C reduces the drying time by 2.67 times.

The obtained temperature curves of heating inside the material caused by the drying agent temperature changes, indicate that it can be intensively heated for 10 minutes.

The increase in the intensity of heating of the material depends on the drying agent temperature increase, which directly affects barley seed properties (Fig. 1).
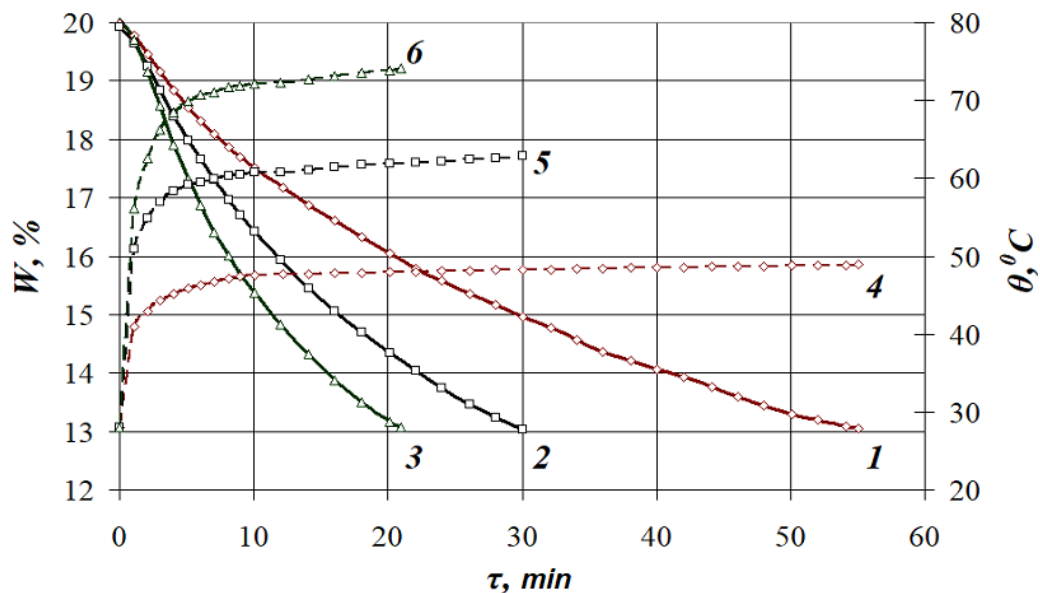
**Fig. 1 - Effect of the coolant temperature and the temperature of
the material heating on the duration of barley seeds drying**
*W_n (initial humidity) = 20%, V (velocity of the coolant) = 1.5 m/s, d (moisture content of dry air) = 10 g/kg d.a.,
δ (grain layer thickness) = 2 mm:
1.4 – 50ºC, 2.5 – 65ºC, 3.6 – 80ºC*

The process of drying barley seeds occurs during the period of decreasing the drying rate on condition of the pre-heating of the material. The maximum drying rate at point K for the 50°C coolant temperature is 0.32% per min, and for the 80°C temperature – 0.63% per min (Fig. 2).
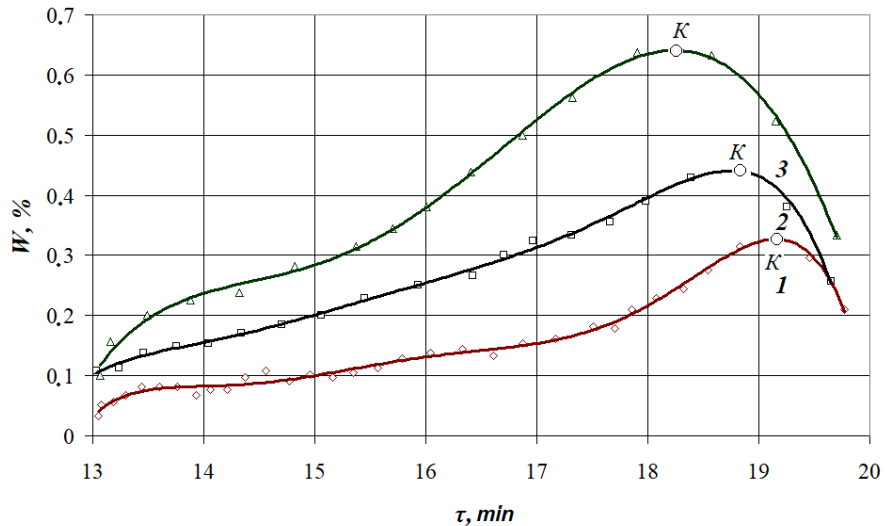
Fig. 2 - Effect of the coolant temperature on the barley seeds drying rate
$W_n = 20\%$, $V = 1.5$ m/s, $d = 10$ g/kg d.a., $\delta = 2$ mm
$1 - 50°C$, $2 - 65°C$, $3 - 80°C$

It has been established that the best germination rate of barley seeds is observed at a 50°C heating medium temperature and 48.9°C temperature of the material heating, namely 96%. Further increase of the drying agent temperature to 80°C considerably reduces barley seed properties (Fig. 3).
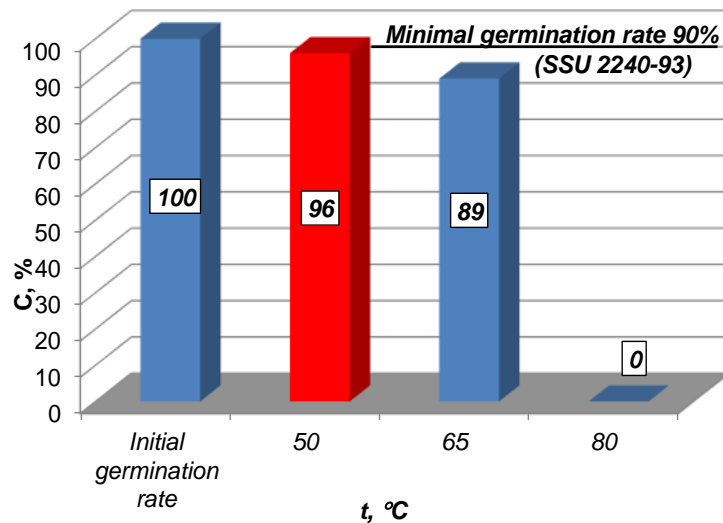
Fig. 3 - Effect of the coolant temperature on the germination rate of barley seeds on the 7th day of germination: $V = 1.5$ m/s, $W_n = 20\%$, $d = 10$ g/kg d.a.

The results of the laboratory studies on the seed germination rate on the 7th day of germination can be seen in Fig. 4, they confirm the data of the experiment on the dependence of germination rates on the drying modes shown in Fig. 3.
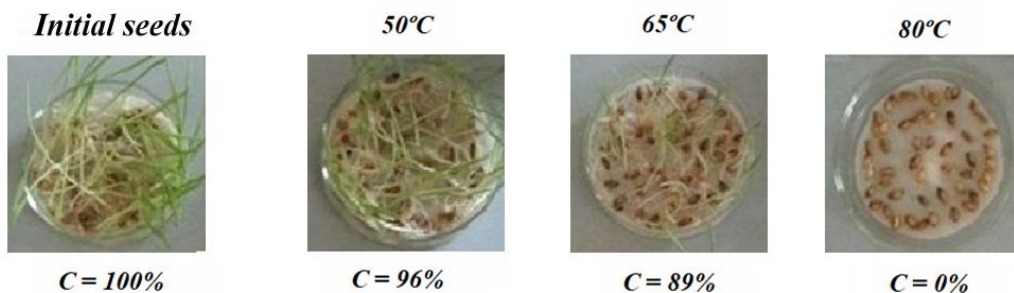
Fig. 4 - Barley seeds germination rates in accordance with drying modes
$V = 1.5$ m/s, $W_n = 20\%$, $d = 10$ g/kg d.a.

Another factor that influences the kinetics of the drying process is the initial moisture content of barley seeds selected in the range of W=16-24%, which corresponds to the moisture content of the seeds when harvested under different climatic conditions.

Kinetics of the barley drying process shows that increase in the initial moisture content from 16% to 24% lengthens duration of drying by 3.29 times (Fig. 5).
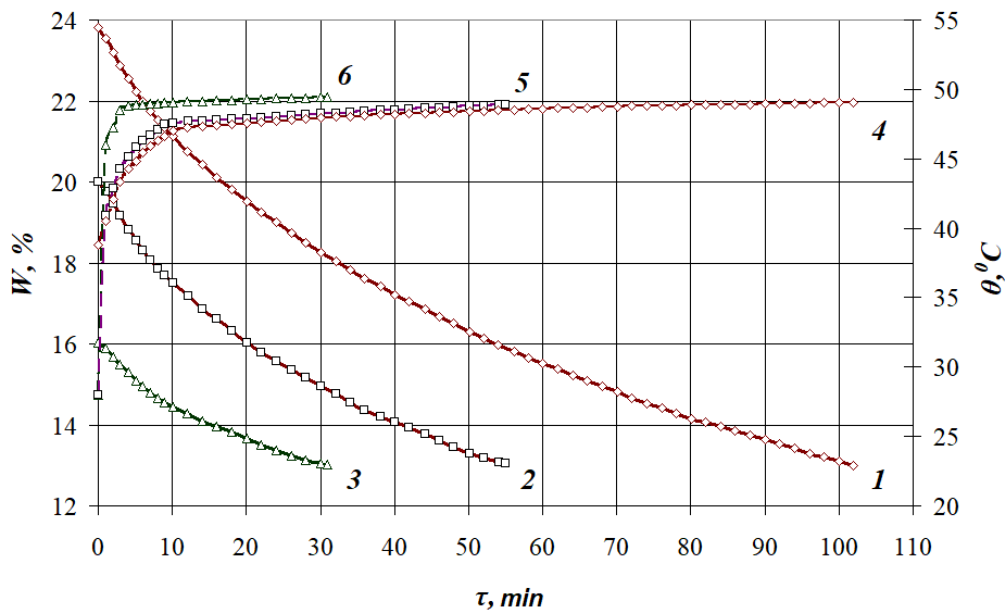
Fig. 5 - Effect of initial moisture content and material heating temperature on duration of barley seeds drying
t = 50ºC, V = 1.5 m/s, d = 10 g/kg d.a., δ = 2 mm:
1 – 24%; 2 – 20%; 3 – 16%

The final barley seeds heating temperature decreases as a result of the initial humidity of the material increase at a temperature of 50ºC and lies within the limits of 48.9-49.6ºC (Fig. 5).

The drying rate curves are similar to the drying curves shown in Fig.2. The rate of the barley seeds drying increases with the increase of the initial moisture content of the material (Fig. 6).
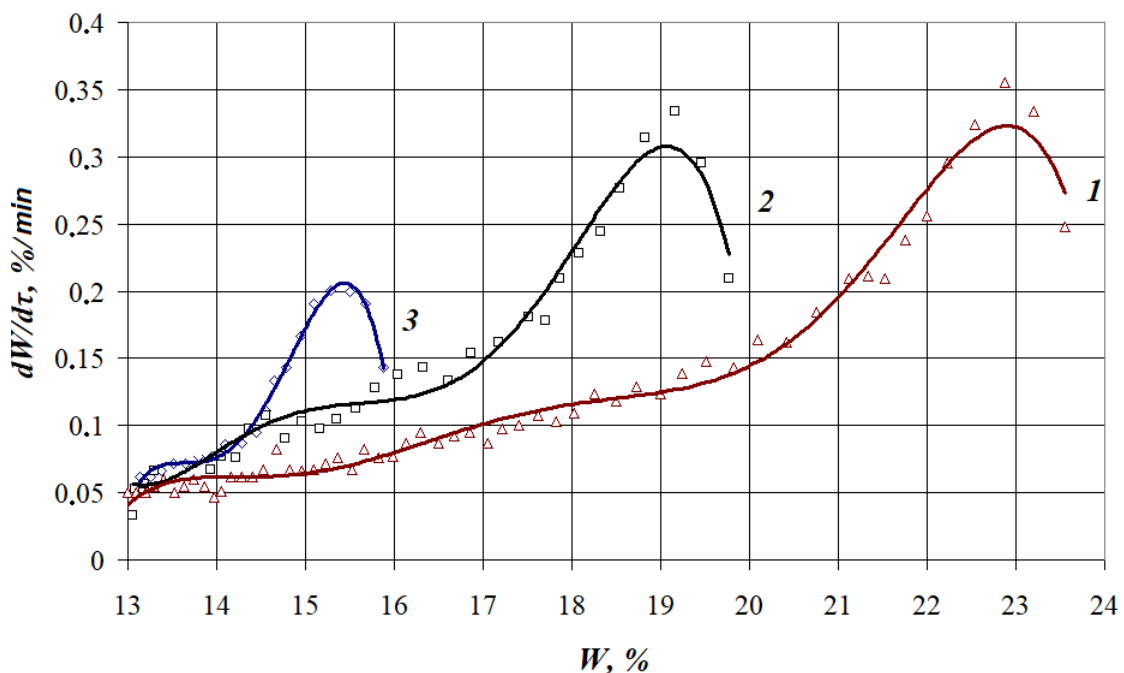
Fig. 6 - Influence of the material initial moisture content on the barley seeds drying rate
t = 50ºC, V = 1.5 m/s, d = 10 g/kg d.a., δ = 2 mm:
1 – 24%; 2 – 20%; 3 – 16%

Increase in the heating medium movement rate from 0.5 to 1.5 m/s increases duration of barley drying by 1.24 times (Fig. 7).
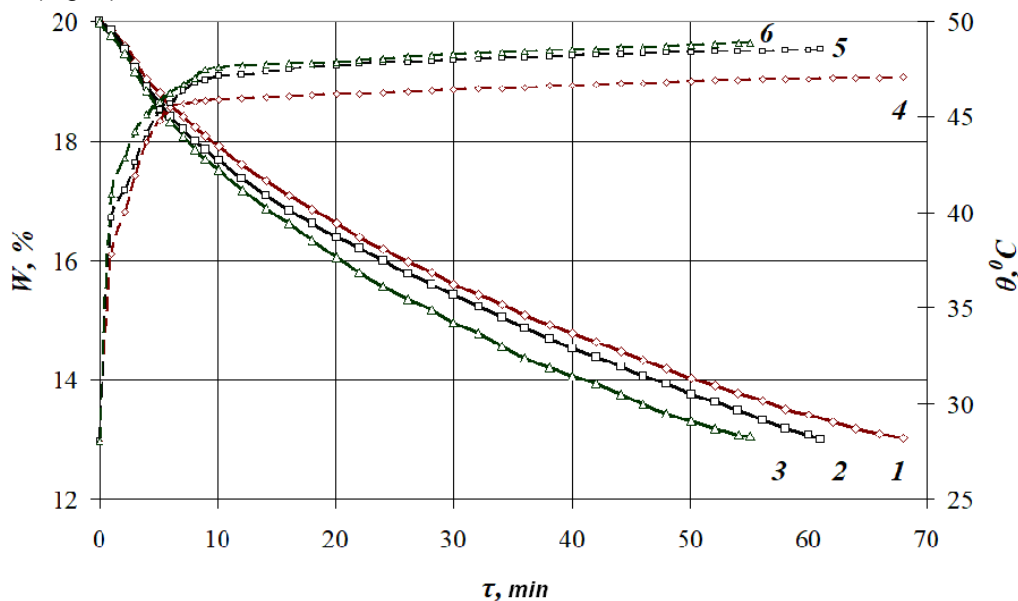
**Fig. 7 - Influence of the heating medium movement rate and
the material heating temperature on the barley seeds drying duration:**
$t = 50ºC$, $W_n = 20\%$, $d = 10$ g/kg d.a., $\delta = 2$ mm:
1 – 0.5 m/s; 2 – 1.0 m/s; 3 – 1.5 m/s

When evaluating and selecting the drying mode, it is necessary to proceed from the qualitative characteristics of seed germination.

The three-factor effect on germination of barley seeds on the 7th day of germination is presented in Table 1.

Table 1

**Influence of drying parameters on germination rates of barley seeds
on the 7th day of germination**

Drying parameters			Germination rates
Temperature of the coolant, [ºC]	Initial moisture content of the seeds [%]	Heating medium movement rate [m/s]	[%]
Output	-	-	100
50	16	1.5	98
50	20	0.5	98
50	20	1.5	98
50	24	1.5	96
65	16	1.5	95
65	20	0.5	90
65	20	1.5	90
65	24	1.5	89
80	16	1.5	18
80	20	0.5	18
80	20	1.5	18
80	24	1.5	0

Drying mode with high seed germination rate is a 50°C heating medium temperature, where the influence of initial moisture content and heating medium movement rate is not significant.

The temperature of the heating medium 65ºC at the initial moisture content above 16% is close to the minimum seed germination rate (92%) and is 89-90%, which does not meet the requirements for seed grain. The influence of the heating medium movement rate on the germination rate of seeds is more significant at the 80ºC temperature mode, and when the initial moisture content makes up 24%, all seed properties of grain disappear.

In order to increase energy efficiency of drying and to improve the rate of barley seeds germination, it is proposed to use a 65/50ºC temperature stepwise drying method. Comparison of the 65/50ºC drying mode with the one-stage modes is demonstrated in Fig. 8.
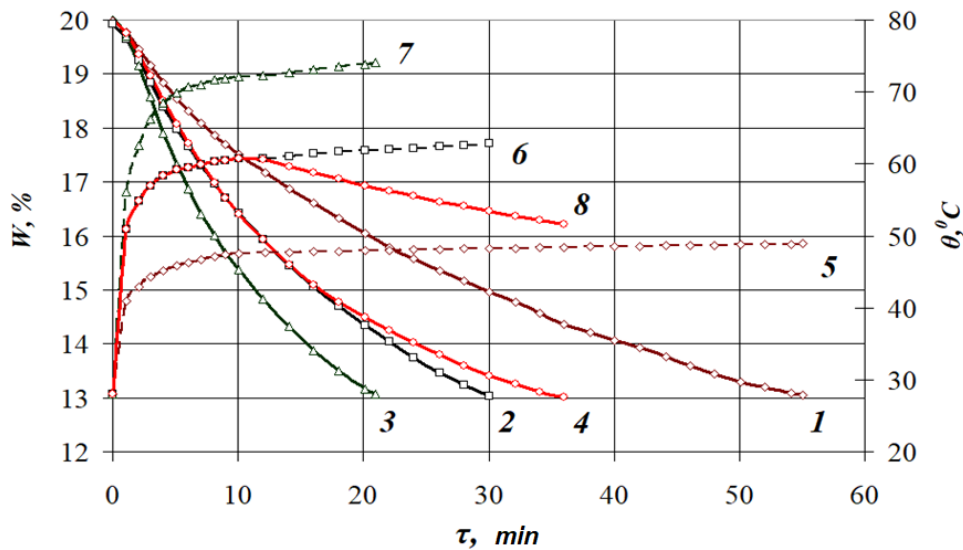
**Fig. 8 - Influence of the heating medium temperature and the
material heating temperature on duration of barley seeds drying**
$W_n = 20\%$, V = 1.5 m/s, d = 10 g/kg d.a., δ = 2 mm:
1.5 – 50ºC, 2.6 – 65ºC, 3.7 – 80ºC, 4.8 – 65/50ºC

As can be seen from Fig. 8, at the beginning of the drying process, the heating temperature of the barley seeds in the two-stage drying mode of 65/50ºC had been keeping for 5 minutes and after that the coolant temperature was sharply reduced to 50°C. The maximum temperature of the material heating at the beginning of the process at a 65°C coolant temperature was 59.18°C and then it gradually decreased to the 51.32°C final value.

Duration of the 65/50ºC two-stage drying process is reduced by 35% compared to the 50ºC drying mode. Low energy consumption for the drying process in the stepwise drying mode is associated with the rapid heating of the material in the drying chamber at a temperature of 65°C and a gradual decrease in the temperature of the coolant to a temperature of 5°C and in duration by 35% (Fig. 9).
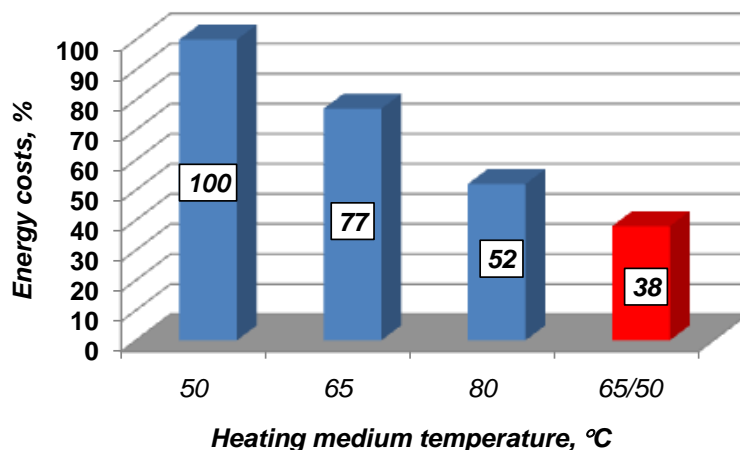
**Fig. 9 - Dependence of the process of barley seeds drying energy consumption
on the heating medium temperature:**
$W_n = 20\%$, V = 1.5 m/s, d = 10 g/kg d.a., δ = 2 mm

To evaluate objectively the stepwise drying modes for barley seed drying, the influence of 65/50, 80/65, and 80/resting/65⁰C modes on the kinetics of the drying process and the qualitative characteristics of the seed material was investigated. The presented drying modes are within the proposed 50-80⁰C range.

Kinetics of the barley seeds drying in stepwise modes indicates the peculiarity of the process and the rate of heating the material with a gradual temperature decrease (Fig. 10).
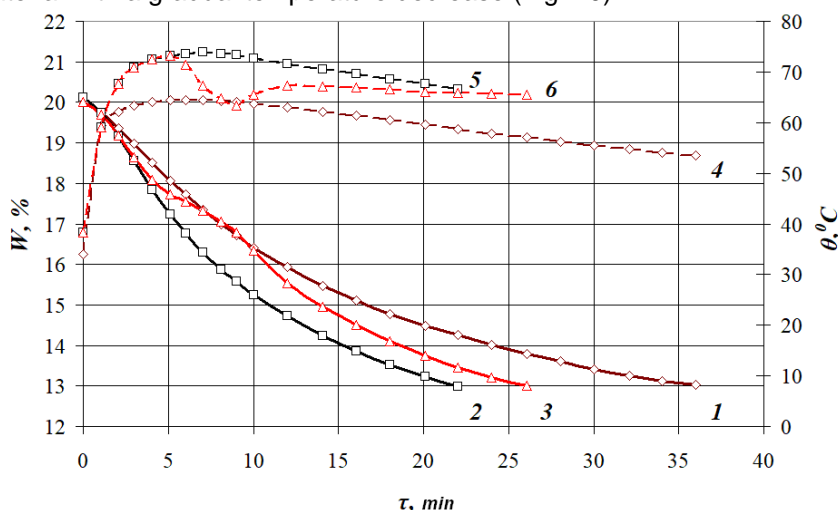
**Fig. 10 - Influence of the heating medium temperature and the heating
of the material temperature on barley seeds drying duration in stepwise modes:**
$W_n = 20\%$, $V = 1.5$ m/s, $d = 10$ g/kg d. a, $δ = 2$ mm:
1.4 – 65/50⁰C, 2.5 – 80/65⁰C, 3.6 – 80/resting/65⁰C

The most intensive 80/65⁰C stepwise drying mode differs from the 80/resting/65⁰C drying mode by 5 minutes, that is, by the time of the seed resting. During the resting movement of the heating medium in the drying chamber stops and a significant slowdown in the removal of moisture from the seeds is observed, while redistribution of heat and moisture in the seed itself becomes the main process. It can also be seen that, in the resting mode, the drying kinetics curve shifts toward the 65/50⁰C drying curve, into the area of high germination rates of the material.

In the 80°C/65°C stepwise drying mode in addition to the other processes, the process of resting is present, which is observed as a "temperature pit" on the curves, the decrease in temperature takes place from the 74⁰C of the seed heating temperature by 15⁰C after 5 min from the start. On the 9th minute it is switched to the 65⁰C drying mode – the temperature rises sharply and then gradually decreases.

The curves of barley seeds drying rate in the stepwise drying modes are presented in Fig. 11.

The nature of the 65/50 and 80/65⁰C drying curves does not differ from the previously described single-stage drying curves. The 80/65⁰C drying mode is the most intensive one, it is more intensive than the 65/50⁰C drying mode by 0.24% per min.

In the 80/resting/65⁰C stepwise drying mode, there is a twofold fall in the heating period and the drying rate with a decrease in the drying rate with critical humidity K1-K3.
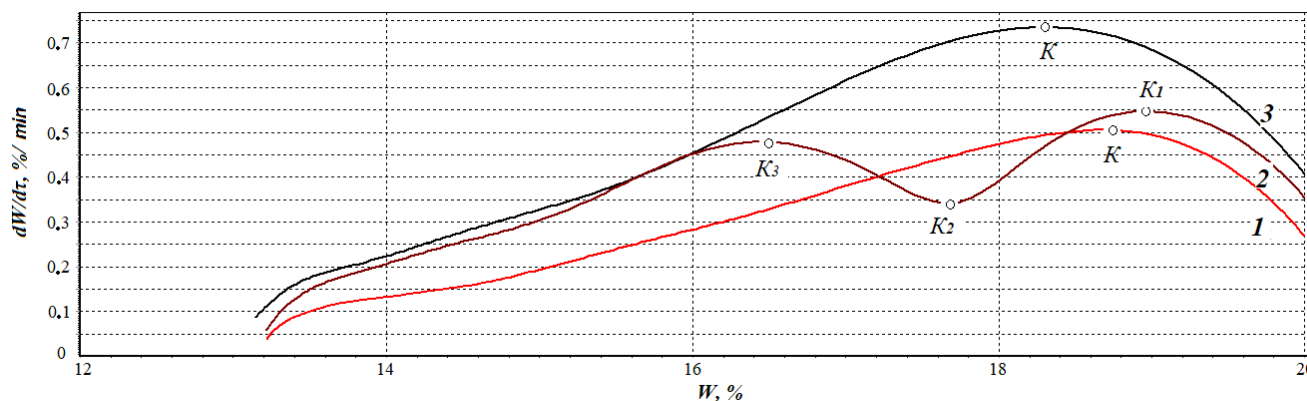
**Fig. 11 - Influence of the heating medium temperature on the barley seeds drying rate
in stepwise modes:**
$V = 1.5$ m/s, $d = 10$ g/kg d.a., $δ = 2$ mm:
1 – 65/50⁰C, 2 – 80/resting/65⁰C, 3 – 80/65⁰C

The barley seeds germination rates in the stepwise drying modes are shown in Fig. 12.
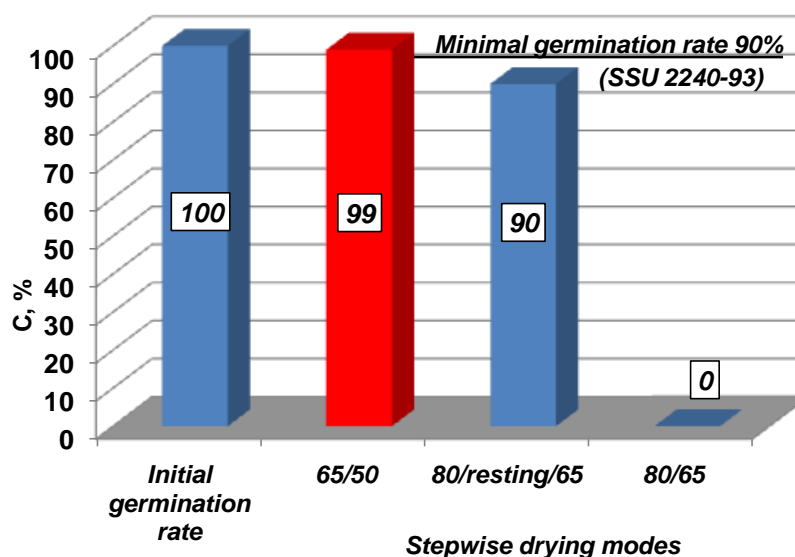
**Fig. 12 - Influence of the stepwise drying modes on the barley seeds germination rates
on the 7th day of germination:**
V = 1.5 m/s, W_n = 24%, d = 10 g/kg d.a.

The results of germination rates prove the effectiveness of drying in the 65/50°C mode. After drying under the 80/65°C mode the seeds of barley do not germinate, but after the stepwise 80/resting/65°C mode of drying there was observed a rather high germination rate at the level of 90%, which testifies to the positive effect of resting on the seed properties of the material.

The strongest sprouts were observed in the 65/50°C stepwise mode of drying. As can be seen from Fig. 13 all seed properties disappear in the 80/65°C stepwise mode. An 80/65°C stepwise drying mode shows that the influence of the 80°C temperature heating medium for 10 minutes completely destroys all seed properties.
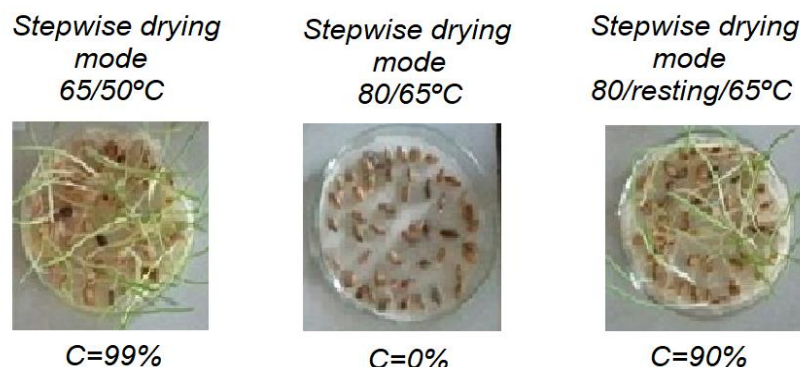
**Fig. 13 - Germination rates of "Barvystyi" variety barley seeds
depending on the drying mode on the 7th day of germination**

CONCLUSIONS

The developed modes of drying allow making the drying of barley seeds more efficient with higher quality of seed material. The most appropriate mode for drying barley seeds is a two-stage drying mode 65/50°C which differs from the drying mode 50°C in that it increases the intensity of the process by 35%, germination rate – by 98% and reduces energy consumption by 62%.

REFERENCES

[1]   Ahrné L. M., Pereira N.R., Staack N., Floberg P., (2007) Microwave Convective Drying of Plant Foods at Constant and Variable Microwave Power, *Drying Technology,* vol. 25:7-8, pp. 1149-1153, London/UK;

[2]   Bandura V., Mazur V., Yaroshenko L., Rubanenko O. (2019) Research on sunflower seeds drying process in a monolayer tray vibration dryer based on infrared radiation, *INMATEH – Agricultural Engineering,* vol. 57, No.1 pp.233-242, Bucharest/Romania;

[3]   Bulgakov V., Bandura V., Arak M., Olt J., (2018), Intensification of rapeseed drying process through the use of infrared emitters. *Agronomy Research.* Vol. 16, No. 2, pp. 349-356, Tartu/Estonia;

[4]   Burdo O., Bandura V., Zykov A., Zozulyak I., Levtrinskaya J., Marenchenko E., (2017), Development of wave technologies to intensify heat and mass transfer processes. *Eastern European Journal of Advanced Technology.* vol. 4 №11(88). pp. 14-18. Kharkiv/Ukraine;

[5]   Gaponyuk O.I., Ostapchuk M.V, Stankevich G.M., (2014), Active ventilation and grain drying (Активне вентилювання та сушіння зерна). Ed. Polygrap. 325 p., Odessa / Ukraine;

[6]   Kumar C., Karim M. A., & Joardder M. U. H. (2014). Intermittent drying of food products: a critical review. *Journal of Food Engineering*, No. 121, pp 48-57. Amsterdam / Netherlands;

[7]   Lykov A.V., (1968), *Drying theory. (Теория сушки)*. Ed. Energia, 472 p, Moscow/Russia;

[8]   Markowski, M., Sobieski, W., Konopka, I. (2007) Drying Characteristics of Barley Grain Dried in a Spouted-Bed and Combined IR-Convection Dryers. *Drying Technology.* №25, pp.1621-1632. London/UK;

[9]   Matkivska I. Ja., Atamanyuk V. M., Symak D., (2014), Basic regularities of the filtration drying of wheat grain. *Eastern European Journal of Advanced Technology.* №5/5 (71). pp. 14-18. Kharkiv/Ukraine;

[10]   Paziuk V.M., Petrova Zh.O., Tokarchuk O.A., Liubin M.V., Yaropud V.M., (2019), Research of rational modes of drying rape seed, *INMATEH–Agricultural Engineering*, vol. 58, no. 2, pp. 330-310, Bucharest/Romania;

[11]   Paziuk V.M., Liubin M.V., Yaropud V.M., Tokarchuk O.A., Tokarchuk D.M., (2018), Research on the rational regimes of wheat seeds drying, *INMATEH–Agricultural Engineering*, vol. 56, no.3, pp. 39- 48, Bucharest/Romania;

[12]   Pazyuk V. Petrova Zn., Chepeliuk O., (2018), Determination of rational modes of pumpkin seeds drying. *Ukrainian Food Journal*. vol. 7, Issue 1. pp. 135-150. Kyiv/Ukraine;

[13]   Souza e Silva, J. S., (2008), *Drying and storage of agricultural products. (Secagem e armazenagem de produtos agrícola)*. Ed. Aprenda Fácil, 560 p. Viçosa / Brasil;

[14]   Shchitsov S.V., Tikhonchuk P.V., Krivuta Z.F., Kolzov A.V. (2016), Research on the influence of kinematic parameters on the optimization of grain drying process, *Far Eastern agrarian messenger. Scientific and practical journal*, №2(38), pp. 98-102, Blagoveshchensk / Russia;

[15]   Soares M., Jorge M., Montanuci F., (2016), Drying kinetics of barley grains and effects on the germination index. *Food Science & Technology.* №36(4), pp. 638-645. Campinas/Brazil;

[16]   Stankevich G.M., Strahova T.V., Atanazevich V.I., (1997), *Drying of grain (Сушіння зерна): textbook*. Ed. Lybid, Moscow/Russia;

[17]   Tsurkan O. V. Necheporenko S.A., Blyznyuk M. Ya., (2013), Modern methods of drying grain materials (Сучасні способи сушіння зернових матеріалів), *Vibratsiyi v tekhnytsi ta tekhnolohiyakh.* №1. pp. 130-134. Vinnytsia/Ukraine.

MODELING OF MOBILE TMR MIXER OPERATION
/
МОДЕЛИРОВАНИЕ РАБОТЫ МОБИЛЬНОГО КОРМОЦЕХА

Kupreenko A.I.[1], Isaev Kh.M.[1], Kuznetsov Yu.A.[*2], Mikhailichenko S.M.[1], Kravchenko I.N.[3], Kalashnikova L.V.[4] [1]

[1] Bryansk State Agrarian University / Russia;
[2] Orel State Agrarian University named after N.V. Parakhin / Russia;
[3] Russian State Agrarian University – Moscow Agricultural Academy named after K.A. Timiryazev / Russia;
[4] Orel State University named after I.S. Turgenev / Russia
Tel: +79208289219; E-mail: kentury@yandex.ru

ABSTRACT

A method for determining the duration of the process of preparation and distribution of feed mixtures by a mobile mixer on cattle farms, based on graph theory, is proposed. A generalized state graph of the mobile mixer is presented and its description is given. The final formula for calculating the probability of the mobile mixer being in the state of distribution of a feed mixture consisting of a different number of components is given. To check the method adequacy, time-lapse measurements were performed in production conditions. The projected durability of the mobile mixer was 92.3% (0.36 h) of the actual recorded time of 0.39 h.

РЕЗЮМЕ

Предложена методика определения продолжительности процесса приготовления и раздачи кормосмесей мобильным кормоцехом на фермах крупного рогатого скота, основанная на теории графов. Представлен обобщенный граф состояний мобильного кормоцеха, дано его описание. Приведена итоговая формула для вычисления вероятности нахождения мобильного кормоцеха в состоянии раздачи кормосмеси, состоящей из различного количества компонентов. Для проверки адекватности методики проведены хронометражные замеры в производственных условиях. Прогнозируемая продолжительность работы мобильного кормоцеха составила 92.3 % (0.36 ч) от фактически зафиксированного времени 0.39 ч.

INTRODUCTION

Preparation and distribution of feed mixtures is one of the most time-consuming processes on cattle farms. For its implementation, the technology based on mobile mixers is widely used. An alternative technology that is becoming more common is the use of automatic feeding systems. A significant number of studies are devoted to comparative estimation of the effectiveness of these technologies (*Belle Z. et al, 2012; Oberschätzl-Kopp R. et al, 2016; Pezzuolo A. et al, 2016*). Automatic feeding systems allow you to achieve a number of advantages compared to the mobile mixers utilization (*Da Borso F. et al, 2017; Kupreenko A.I. et al, 2019*). One of the key advantages is the possibility of increasing the feeding frequency, which is evaluated in many studies on productivity and other indicators of animals (*Crossley R.E. et al, 2018; Hart K.D. et al, 2014; Mattachini G. et al, 2019*). Despite all the advantages, the main drawback of automatic feeding systems is the high cost of acquisition, which hinders their introduction into manufacturing (*Grothmann A. et al, 2010; Tangorra F.M. and Calcante A., 2018*). Therefore, the technology based on mobile mixers is still the main one.

Correctly selected mobile mixer for specific production conditions ensures the efficiency of the process of preparation and distribution of feed mixtures. For this choice, it is necessary to determine the animals feeding time, which must meet the established zootechnical standards in the farm. As practice shows, this time is influenced by a number of factors: load capacity (the volume of the mobile mixer hopper), livestock population maintained, the feeding frequency, the number of components in the feed mixture, the travel distances, etc.

---

1 *Kupreenko A.I., Assoc.Prof.Dr.Eng.Sc.; Isaev Kh.M., Assoc. Prof., Ph.D in Economics; Kuznetsov Yu.A., Prof. Dr. Eng.Sc.; Mikhailichenko S.M., Assistant; Kravchenko I.N., Prof., Dr. Eng.Sc.; Kalashnikova L.V., Prof. Dr. Philology Sc.*

MATERIALS AND METHODS

When working, the mobile mixer spends time on cyclically repeated operations (cycle operating time) and operations related to its setting-up procedures, maintenance, employee rest, and others (off-cycle time). At the same time, due to possible technological violations and technical failures, the time spent on individual operations has probabilistic nature. The time of feed mixtures preparation and distribution on cattle farms, taking into account the probabilistic nature of the components of the operating time balance of the mobile mixer, is determined by the formula:

$$T_{\text{к.мк}} = T_{\text{c}} + T_{\text{oc}} = \frac{Nl_{\text{к}}}{p_p V_p} k_{\text{c}} + T_{\text{oc}} \leq [T_{\text{к}}], \text{ [h]} \tag{1}$$

where: T_{c} – cycle time of one feeding, [h];

T_{oc} – off-cycle time of one feeding, [h];

N – number of animals maintained on the farm, [unit];

$l_{\text{к}}$ – length of one feed space, [km/unit];

k_{c} – coefficient that takes into account the loss of cycle time associated with the management of the technological process of preparation and distribution of feed mixtures;

p_p – the probability of the mobile mixer being in the state of distribution of the feed mixture (corresponds to the state S_{52} in figure 1);

V_p – movement rate of the mobile mixer during distribution, [km/h];

$T_{\text{к}}$ – the time permitted for one feeding according to zootechnical requirements, [h].

To calculate the probability p_p, that is part of the formula (1), a generalized graph of the mobile mixer states (figure 1) is developed. It permits to consider the preparation and distribution of feed mixtures by the mobile mixer at various number of components (parameter "x").

The transition from one state to another occurs under the action of random flows with intensities $\lambda_{i,j}$, indicated in the figure by arrows (for example, the transition from state S_1 to state S_2 is performed under the influence of a random flow with intensity $\lambda_{1,2}$). Their value is inverse ratio to the time spent on the operation performance in the S_i state. The probability of being in the S_i state is equal to p_i.
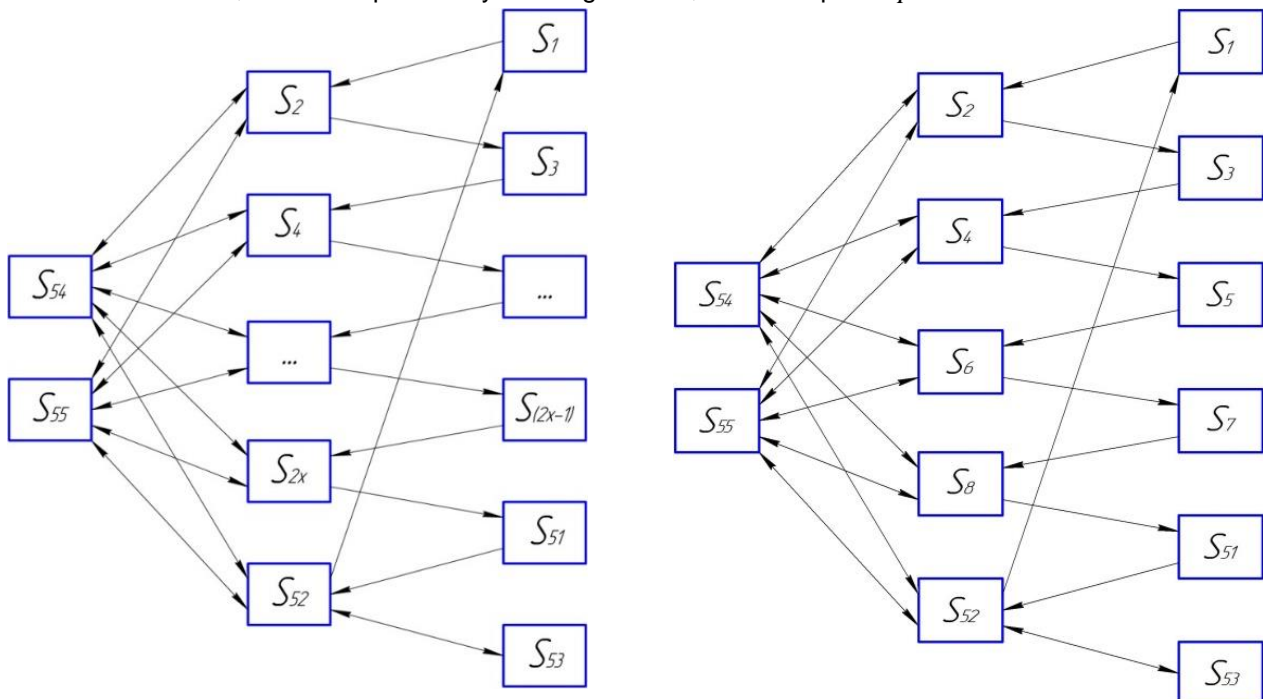
Fig. 1 - Generalized graph of the mobile mixer states (left) and graph for special case at x = 4 (right)

x - the number of components (types of feed) in the feed mix (to 25); S_1 - travel from the parking place to the storage facility with 1 component; S_3… $S_{(2x-1)}$ - travels of the mobile mixer between storages with components; S_2, S_4… S_{2x} - loading of the feed mixture components; S_{51} - travel from storage with the last component to livestock facilities; S_{52} - feed mixture distribution; S_{53} - turning when traveling to another distribution line; S_{54} – technological breakdown; S_{55} - technical failure

$$
\begin{cases}
p_1\lambda_{1,2} = p_{52}\lambda_{52,1} \\
p_2(\lambda_{2,3} + \lambda_{2,54} + \lambda_{2,55}) = p_1\lambda_{1,2} + p_{54}\lambda_{54,2} + p_{55}\lambda_{55,2} \\
p_3\lambda_{3,4} = p_2\lambda_{2,3} \\
p_4(\lambda_{4,5} + \lambda_{4,54} + \lambda_{4,55}) = p_3\lambda_{3,4} + p_{54}\lambda_{54,4} + p_{55}\lambda_{55,4} \\
p_5\lambda_{5,6} = p_4\lambda_{4,5} \\
p_6(\lambda_{6,7} + \lambda_{6,54} + \lambda_{6,55}) = p_5\lambda_{5,6} + p_{54}\lambda_{54,6} + p_{55}\lambda_{55,6} \\
p_7\lambda_{7,8} = p_8\lambda_{8,51} \\
p_8(\lambda_{8,51} + \lambda_{8,54} + \lambda_{8,55}) = p_7\lambda_{7,8} + p_{54}\lambda_{54,8} + p_{55}\lambda_{55,8} \\
p_{51}\lambda_{51,52} = p_8\lambda_{8,51} \\
p_{52}(\lambda_{52,1} + \lambda_{52,53} + \lambda_{52,54} + \lambda_{52,55}) = p_{51}\lambda_{51,52} + p_{53}\lambda_{53,52} + p_{54}\lambda_{54,52} + p_{55}\lambda_{55,52} \\
p_{53}\lambda_{53,52} = p_{52}\lambda_{52,53} \\
p_{54}(\lambda_{54,2} + \lambda_{54,4} + \lambda_{54,6} + \lambda_{54,8} + \lambda_{54,52}) = p_2\lambda_{2,54} + p_4\lambda_{4,54} + p_6\lambda_{6,54} + p_8\lambda_{8,54} + p_{52}\lambda_{52,54} \\
p_{55}(\lambda_{55,2} + \lambda_{55,4} + \lambda_{55,6} + \lambda_{55,8} + \lambda_{55,52}) = p_2\lambda_{2,55} + p_4\lambda_{4,55} + p_6\lambda_{6,55} + p_8\lambda_{8,55} + p_{52}\lambda_{52,55} \\
\sum p_i = 1
\end{cases}
\tag{2}
$$

Expressions of transition intensities have the following form:

$\lambda_{1,2} = \dfrac{V_{emp}}{L_0}$, where: V_{emp} – the speed of the empty mobile mixer, [km/h], L_0 – distance from the parking

place of the mobile mixer to the place of the first component loading;

$\lambda_{2,3} = \dfrac{Q_1}{M_1} \cdots \lambda_{8,51} = \dfrac{Q_4}{M_4}$, where: $Q_1...Q_4$ – loading efficiency of component 1-4, [t/h],

$M_1...M_4$ – corresponding weights of loaded components, [t].

$\lambda_{3,4} = \dfrac{V_l}{L_1} \cdots \lambda_{7,8} = \dfrac{V_l}{L_3}$, where: V_l – speed of loaded mobile mixer, [km/h],

$L_1...L_3$ – corresponding travel distances between storage locations with component 1-3;

$\lambda_{51,52} = \dfrac{V_l}{L_t}$, where: L_t – travel distance from the storage with the last loaded component to the distribution

start point, [km];

$\lambda_{52,53} = \dfrac{2V_p m_p}{G_k l_k}$,   where: V_p – speed of mobile mixer when distributing feed mixture, [km/h], m_p – one-

time feed mixture allowance per head, [kg/head], $G_к$ – load capacity of the mobile mixer / the loaded weight of the feed mixture, [kg], $l_к$ – length of one feed space, [km/head];

$\lambda_{53,52} = \dfrac{1}{t_{tim}}$, where t_{tim} – time of turning when traveling to another distribution line, [h];

$\lambda_{52,1} = \dfrac{V_p m_p}{G_k l_k}$;

$\lambda_{2,54} = ... = \lambda_{52,54} = 1/T_{TH}$, where T_{TH} – running time for technological breakdown, [h];

$\lambda_{2,55} = ... = \lambda_{52,55} = 1/T_{TO}$, where T_{TO} – running time for technical failure, [h];

$\lambda_{54,2} = ... = \lambda_{54,52} = 1/T_{YTH}$, where T_{YTH} – technological breakdown clearing time, [h];

$\lambda_{55,2} = ... = \lambda_{55,52} = 1/T_{YTO}$, where T_{YTO} – technical failure clearing time, [h].

To find a general solution of Kolmogorov equation systems for any number of components in the feed mixture, the systems of equations were compiled for three special cases: $x = 2$, $x = 3$ and $x = 4$ (2 -, 3 - and 4 -component feed mixture).

When solving these systems, to simplify the transformations, we introduced the corresponding coefficients K_i to replace the combinations of intensities $\lambda_{i,j}$. Coefficients K_i make it possible to trace the change of each of them at different amounts of components in the feed mixture to establish the existing pattern. The process of solving these systems of equations as well as the established regularities are reflected in the paper *(Kupreenko A.I. et al, 2017)*.

Only the final formula for calculating the desired probability of finding a mobile mixer in the feed mixture distribution state for any number of components in the feed mixture is presented below:

$$p_{52} = p_{55} \frac{K_{54}^{x\Sigma} \ K_{52}^{x6} + K_{52}^{x_{\text{B}}}}{K_{52}^{xa}}, \tag{3}$$

where:

$$p_{55} = \frac{K_{52}^{xa}}{K_{52}^{xa} + (K_{54}^{x\Sigma} \ K_{52}^{x6} + K_{52}^{x_{\text{B}}})K_{55}^{xa} + K_{54}^{x\Sigma} \ K_{55}^{x6} K_{52}^{xa} + K_{55}^{x_{\text{B}}} K_{52}^{xa}} \tag{4}$$

These expressions are unchanged for any value of x. Herewith, the content of each of the coefficients K_i of expressions (3) and (4) is characterized by the absence of unknown values of incoming variables and with the change of the value of x, it changes in a certain sequence.

The established regularities in the form of a mathematical model are implemented in the MS Excel program. This completely eliminates the need to create graphs of states and the Kolmogorov systems of equations, their further manual solution, and reduces the entire task of determining the duration of the process of preparation and distribution of feed mixtures by the mobile mixer to a simple input of initial data. The correctness of the calculations is confirmed by the convergence of the final values for the 5 - component feed mixture in mathematical modeling in MS Excel and manual solution.

To check the adequacy of the developed methodology, time-lapse measurements of the mobile mixer operation "Storti Husky MT 90" in aggregation with a tractor "Belarus 1221" were carried out at the dairy farm of SEC-Agrofirma "Kultura" in the village of Dobrun, Bryansk region (Russia).

The feed loading time was determined by video recording the process.

The performance of the loading line was determined by dividing the mass of loaded components by the fixed loading time.

Distances and travel times were determined by recording the track of the completed route in the Strava mobile app (fig. 2). Here, in addition, the loading time of components was checked according to the idle time of the unit.

The length of a single feed space was defined as the ratio of the total length of the feed table to the number of animals placed along it.

The one-time feed mixture allowance per head was defined as the ratio of the total mass of feed mixture in the hopper to the number of animals maintained.

The GPS signal required for the mobile application operation was absent in the cowshed. Therefore, the feed table length was determined by the delivery time, which was recorded during the video recording, and the tractor speed, which was constant and was 2 km/h according to the information displayed on the tractor monitor.

In the proposed method, the speed of movement of a loaded mobile mixer is assumed to be constant. In practice, it varies within certain limits. The maximum recorded speed of a loaded mobile mixer when traveling was 9 km/h. In other cases, at a lower recorded speed, the distance for entering data was calculated as the product of the time spent on the move and the maximum speed (9 km/h).

RESULTS

According to the time-metering, the following values are obtained:

1) flour loading in the feed storage facility from the tower hopper (422 kg, 01 min 55 s): $Q = 13.2$ t/h;

2) travel from storage facility (20 m in 00 min 35 s): $V = 2.06$ km/h

3) concentrates loading in the storage facility by a tractor with a bucket (298 kg, 04 min 30 s): $Q = 3.97$ t/h;

4) travel to a silage trench (150 m in 00 min 59 s): $V = 9$ km/h;

5) silage loading from a trench by a tractor with a bucket (3032 kg, 06 min 38 s): $Q = 27.43$ t/h;

6) travel to storage facility with molasses (200 m, 02 min 03 s): $V = 5.85$ km/h;

7) molasses loading (156 kg, 01 min 16 s): $Q = 7.39$ t/h;

8) travel to molasses (230 m, 01 min 52 s): $V = 7.4$ km/h.

The number of the maintained animals is 90 heads, daily allowance of delivery – 43.42 kg/heads.

Duration of single cycle of feed mixture preparation and distribution was 0.39 h (fig. 2): components loading – 0.24 h (61.5 %); travels – 0.09 h (23.1 %); delivery – 0.03 h (7.7 %); cycle time losses – 0.03 h (7.7 %).

The following parameters were used for modeling:

- the load capacity of the mobile mixer G_κ = 3908 kg (numerically equal to the weight of the loaded ration components);

- the component number in the feed mixture x = 4;

- the time of daily maintenance (ETO) of the mobile mixer T_{ETO} = 0.00001 hours (since the division by "0" is not possible in the compiled program, a value close to zero was selected);

a)   b)   c)
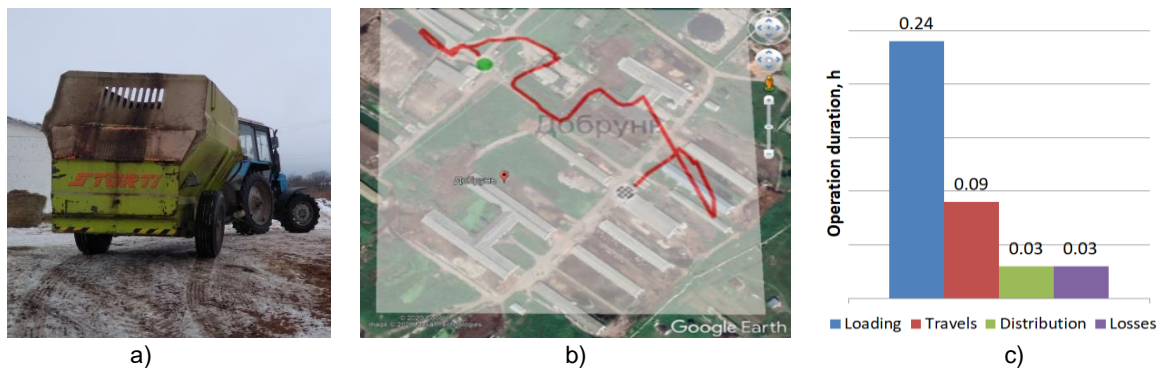
Fig. 2 – Mobile TMR mixer Storti Husky MT 90 (a), Routing track, recorded in mobile application «Strava» (b) and Constituents of time balance of the mobile mixer operating cycle (c)

- the number of the maintained animal (for one cycle) N = 90 heads;

- the speed of the loaded mobile mixer and the speed during delivery correspondingly V_l = 9 km/h and V_p = 2 km/h;

- flour loading efficiency, concentrates, silage and molasses, respectively Q_1 = 13.2 t/h, Q_2 = 3.97 t/h, Q_3 = 27.43 t/h and Q_4 = 7.39 t/h;

- the mass fractions of these components in the feed mixture, respectively m_1 = 0.108, m_2 = 0.076, m_3 = 0.776 and m_4 = 0.04;

- equivalent traveling distances in terms of movement at a speed of 9 km/h: mixer ➔ street L_2 = 87.5 m (traveling distance from the parking place to the loading place of the first component L_1 = 0), street ➔ trench L_3 = 150 m, trench ➔ molasses L_4 = 307.5 m, molasses ➔ cowshed L_p = 280 m;

- one-time feed mixture allowance per head m_p = 43.42 kg;

- length of one feed space l_κ = 0.63 m;

- time of turning for distribution to the second row T_t = 0.000001 h;

- coefficient that takes into account the losses of cycle time k_c = 1;

- in the mean running time for technological breakdown, elimination of technological breakdown; running time for technical failure and elimination of technical failure the following values were accepted: respectively, T_{TH} = 10 h, T_{YTH} = 0.2 h, T_{TO} = 250 h and T_{YTO} = 5 h. The modeling results showed that when changing the values of parameters T_{TH} and T_{YTH} in the range of 1-50 respectively and 0.1-0.5 h the value of feeding time $T_{K.MK}$ is in the range of 0.36-0.38 h; as a result of changing the values of parameters T_{TO} and T_{YTO} within the range of 50-500 and 1-25 h, respectively, the value of the feeding time $T_{K.MK}$ is in the range of 0.36-0.39 h.

According to the results of the modeling (table 1) with the probability of finding a mobile fixer in the state of distribution of feed mixture p_{52} = 0.079 the value of the feeding time $T_{K.MK}$ was 0.36 h (-7.7 % compared to the actual feeding time).

Table 1

Modeling results in MS Excel

p_1	0.00000	p_{51}	0.08596	$T_{K.MK}$ [h]	0.36
p_2	0.08918	p_{52}	0.07915	N [cows]	90
p_3	0.02712	p_{53}	0.00001	n_κ [pc]	0.18
p_4	0.20774	p_{54}	0.00590	$[T_\kappa]$ [h]	2
p_5	0.04628	p_{55}	0.00295	n_c [cycle]	1
p_6	0.30348			Q_{ch} [t/h]	10.85
p_7	0.09379				
p_8	0.05845				

Thus, the adequacy of the proposed mathematical model for determining the time of feeding animals with a mobile mixer on cattle farms is confirmed by the results of timekeeping measurements in production conditions. The study showed that the predicted feeding time was 92.3% of the actual one.

CONCLUSIONS

The use of the proposed method in practice will allow you to make a reasonable choice of appropriate equipment for feeding in specific production conditions, expand the capabilities of personnel in the work organization.

The method adequacy is confirmed by the high accuracy of convergence of timekeeping measurements' results of the mobile mixer in production conditions and modeling. Studies have shown that the predicted feeding time was 92.3% of the actual one.

The main criterion for selecting the required load capacity of the mobile mixer is the permissible duration of animal feeding. The low load capacity of the mobile mixer increases the number of cycles of preparation of feed mixture while reducing the duration of one cycle and vice versa. The next task is to determine the optimal load of the mobile mixer within the possible range of changes in basic input data, the number of animals on the farm, feed mixture allowance.

The further important task is to determine the conditions when the use of two mobile mixers with a small load capacity will be more cost-effective than using one mobile mixer with a high load capacity.

REFERENCES

[1] Belle Z., André G., Pompe J.C.A.M., (2012), Effect of automatic feeding of total mixed rations on the diurnal visiting pattern of dairy cows to an automatic milking system, *Biosystems Engineering,* Vol.111, Issue 1, pp. 33-39, Hexham / UK;

[2] Crossley R.E., Harlander-Matauschek A., DeVries T.J., (2018), Mitigation of variability between competitively fed dairy cows through increased feed delivery frequency, *Journal of Dairy Science*, Vol.101, Issue 1, pp.5188-529, Illinois / USA;

[3] Da Borso F., Chiumenti A., Sigura M., Pezzuolo A., (2017), Influence of automatic feeding systems on design and management of dairy farms, *Journal of Agricultural Engineering (JAE)*, Vol.48, Issue 1s, pp.48-52, Pavia / Italy;

[4] Grothmann A., Nydegger F., Häußermann A., Hartung E., (2010), Automatic feeding system (AFS) – potential for optimisation in dairy farming. *Landtechnik,* Issue 2 (65), pp.129-131, Darmstadt / Germany;

[5] Hart K.D., McBride B.W., Duffield T.F., DeVries T.J., (2014), Effect of frequency of feed delivery on the behaviour and productivity of lactating dairy cows. *Journal of Dairy Science,* Issue 3 (97), pp.1713-1724, Illinois / USA;

[6] Kupreenko A.I., Isaev Kh.M., Grin' A.M., Mikhailichenko S.M., Kolomeichenko A.V., Kuznetsov Y.A., Kalashnikova L.V., (2019), Automated distribution system of feed mixture by using feeding carriage. *INMATEH - Agricultural Engineering*, Vol.58, Issue 2, pp.239-246, Bucharest / Romania;

[7] Kupreenko A.I., Isaev Kh.M., Mikhailichenko S.M., (2017), Solution of the Kolmogorov system of equations for the generalized graph of states of a mobile TMR mixer (Решение системы уравнений Колмогорова для обобщенного графа состояний мобильного кормоцеха), *Tractors and agricultural machinery,* Issue 7, pp.47-52, Moscow / Russia;

[8] Mattachini G., Pompe J., Finzi A., Tullo E., Riva E., Provolo G., (2019), Effects of feeding frequency on the lying behaviour of dairy cows in a loose housing with automatic feeding and milking system, *Animals*, Issue 9, article number 121, Bazel / Switzerland;

[9] Oberschätzl-Kopp R., Haidn B., Peis R., Reiter K., Bernhardt H., (2016), Studies on dairy cow behaviour with automatic feeding in a herd milked by an AMS, *Landtechnik*, Issue 71(2), pp.55-65, Darmstadt / Germany;

[10] Pezzuolo A., Chiumenti A., Sartori L., Da Borso F., (2016), Automatic feeding systems: evaluation of energy consumption and labour requirement in north-east Italy dairy farm, *Engineering for Rural Development*, Issue 15, pp.882-887, Jelgava / Latvia;

[11] Tangorra F.M., Calcante A., (2018), Energy consumption and technical-economic analysis of an automatic feeding system for dairy farms: Results from a field test, *Journal of Agricultural Engineering*, Issue 49(4), pp.228-232, Bologna / Italy.

ADAPTIVE CYBER-PHYSICAL SYSTEM OF THE MILK PRODUCTION PROCESS
/
АДАПТИВНА КІБЕР-ФІЗИЧНА СИСТЕМА ПРОЦЕСУ ВИРОБНИЦТВА МОЛОКА

Dmytriv V.T.[*1)], Dmytriv I.V.[1)], Horodetskyy I.M. [2)], Yatsunskyi P.P.[1)] [1]

[1)] Lviv Polytechnic National University, Institute of Engineering Mechanics and Transport, Lviv / Ukraine
[2)] Lviv National Agrarian University, Faculty of Mechanic and Power Engineering, Lviv-Dubliany / Ukraine
[*] E-mail: Dmytriv_V@ukr.net

ABSTRACT

The basic principles of adaptation of machine milking technical system to the physiology of milk ejection of cows are considered. Main adaptation parameters and conditions of the technical system are grounded, under these parameters and conditions the self-tuning of technical system is possible. The structure of modules of adaptive cyber-physical control system of machine milking is developed, its functionalities are revealed, the method of coordination between discreteness of measurement of information and the quantization period is developed to ensure maximum reliability of the information. The memory size of the operational information about the process parameters is justified, as well as their structure and functional content. Functional content and structure of information about the technological process of the database is formulated. The general view of the main elements of the adaptive cyber-physical system of cows milking is given, as well as the results of work of the experimental adaptive cyber-physical system of the milk production.

РЕЗЮМЕ

Розглянуто основні принципи адаптації технічної системи машинного доїння до фізіології молоковіддачі корови. Наведено основні параметри адаптації та умови за яких можливе самонастроювання параметрів технічної системи. Приведена структура модулів адаптивної кібер-фізичної системи керування технологічним процесом машинного доїння, розкриті функціональні можливості, наведено методику узгодження між дискретністю вимірювання інформації і періодом квантування для забезпечення максимуму достовірності інформації. Обгрунтовано розмір пам'яті оперативної інформації про параметри процесу, їх структуру та функціональний зміст. Наведено функціональний зміст та структуру інформації про технологічний процес бази даних. Наведено загальний вигляд основних елементів адаптивної кібер-фізичної системи доїння корів, результати роботи експериментальної адаптивної кібер-фізичної системи процесу виробництва молока.

INTRODUCTION

The adaptive milk production system of the "man-machine-animal" biotechnical system functionally ensures the realization of the genetic potential of cow productivity through interaction with the technical system. The effectiveness of the system's adaptation depends on the parameters that ensure the quality and efficiency of performing the technological functions.

The milking machine, as the main executor of the milking technological process, adapts the technical system to the physiology of the milk ejection of the cow due to the vacuum pressure of the given parameters and the possibility of their regulation, control at a given level during milking of the cow (*Pirlo G., Abeni F., Capelletti M., et al, 2005*; *Pařilova M., Stadnik L., Ježkova A., 2011*). Pneumatic electromagnetic pulsator, milk concentration meter, microprocessor control unit and other electronic elements are a feature of the milking machine configuration of modified configuration and functionality (*Jędruś A., Lipiński M., 2008; Czarnociński F., 2008*; *Jędruś A., 2010; Juszka H., Tomasik M., Lis S., et all, 2011; Juszka H., Lis S., Tomasik M., 2011*).

---

[1] *Dmytriv V.T., Prof., Dr.Sc.Eng.; Dmytriv I.V., Assoc. prof., Ph.D.Eng.; Horodetskyy I.M., Assoc. prof., Ph.D.Eng.; Yatsunskyi P.P., PhD student*

One of the important factors is the vacuum gauge pressure that directly forms the adaptation parameters of the machine-cow system. To assess the adaptation of the parameters of the milking system, the influence of technological and structural parameters on the operating modes of the system was analysed (*Lis S., Juszka H., Mendyk M., 2016*). Study of vacuum gauge pressure stability, depending on the method of regulation in a vacuum tube or directly in the milking machine (*Pazzona A., Murgia L., Zanini L. et al., 2003*) found that vacuum stabilization by the gravitational type regulator was more dynamic and constant time was twice lower than in the case of the automated system. Such a conclusion was also obtained by the results of study of pulsating vacuum gauge pressure regulators (*Dmytriv V.T. et all, 2017*). Also, oscillations of vacuum pressure were investigated by (*Reinemann D.J., Schuring N., Bade1, R.D., 2007*; *Skalska D., Nejman M., Wiercioch M., et all, 2013*), depending on: a) the configuration of the vacuum and milk tube systems (length of the pipelines, its diameter and other parameters affecting the loss of pressure); b) the rate of milk flow in the milk pipeline; c) the velocity of air in the vacuum pipe. The results of these studies have shown that with a decrease in the intensity of milk ejection, the vacuum pressure increases both in the vacuum and milk tubes and in the under-teat space of teat cups.

The analysis of the research has shown that the parameters substantiation of effective functioning of cows milking biotechnological system requires the development of a concept and methodology for system parameters optimizing and also for its component of the technical system. This is relevant and actual for improving the efficiency of milking machines.

MATERIALS AND METHODS
Concept of adaptive cyber-physical system of milk production

A significant variety of technological schemes of milk production processes forms the appropriate units of control and governing parameters depending on the variant of the technological process.

We propose fundamentally new electronic-mechanical elements of the modular type with the use of microprocessor technology. These elements are developed and integrated into an adaptive cyber-physical system (ACPS) in dairy livestock, which allows for executive, informational, monitoring and diagnostic functions. During the development of such a system, new approaches to the synthesis of mechatronic modules are realized with the possibility of autonomous functioning (using single-chip microcontrollers of K1816BE48 and AT8335 type (by Atmel) at the level of introspection of both the technical system and the biological object which interacts with the machinery. Also, the system has operating mode by the boundary parameters set by the central computer.

ACPS contains software and hardware modules. Software modules include programs for technological objects controlling, the databases formation and management and also simulation of qualitative and quantitative parameters of the technological process of machine milking. The hardware modules include the following already researched and tested modules that are controlled by a central computer: an automated milking machine (with microprocessor control, a thermo-anemometric measurer of milk ejection intensity, the ability to control the pulsation frequency and the ratio of cycles and vacuum-metric pressure, the ability of temperature measurement and electrical conductivity of milk); automated vacuum unit; modular type interface with ACPS system bus, through which the code number forms and adaptive milking machines are connected; automated individual distributor-dispenser of mixed fodders; system of pressure sensors. The general structural scheme of the ACPS of the proposed functional and hardware solution is shown in fig. 1.

According to the needs of the user, the functions of the ACFS are the following: 1) technological information collection, coding, transmission, processing and storage; 2) the database forming and managing; 3) management by technical means and modules; 4) solving of optimization tasks in the system of milk production; 5) the technological information giving on functional request of system modules.

The information functions of the system are ensured in the automatic mode: 1) collecting the information about the dynamics of cow's milk ejection intensity and its maximum value; 2) the value of individual one-time milking; 3) physical time of milking start, machine milking up and milking finish of the cow; 4) time of maximum milk ejection; 5) the temperature of milk of quarters of the udder; 6) electric conductivity of milk; 7) the frequency of pulsation and the ratio of cycles; 8) vacuum pressure in the under-teat space of teat cups; 9) vacuum gage pressure at technological points of the vacuum line and control of the vacuum system; 10) control of the milk pump; 11) collecting information about the condition of the milk filter; 12) collecting the information about milk temperature at the outlet of the cooler and control of the cooler; 13) collecting the information about the washing process of the milking machine and washing process control; 14)

transfer of data to the individual meter-dispenser of mixed fodder; 15) coding the processed information according to the cow number; 16) formation of a database and knowledge, supplementation of it with on-line information; 17) display of the information on the workplace of the machine milking operator.

Objects are surveyed in real time, according to the algorithm of the cyclic survey. Objects are not surveyed if they change the data with interruption (adaptive milking machine, signal of emergency state of the *n*-th object). To implement such an algorithm, the interface is created for receiving and transmitting the data from sensors, as functionally independent elements, and the structural chart of this interface is shown in fig. 2. A structural chart of an adaptive milking machine as to the ACPS is shown in fig. 3.
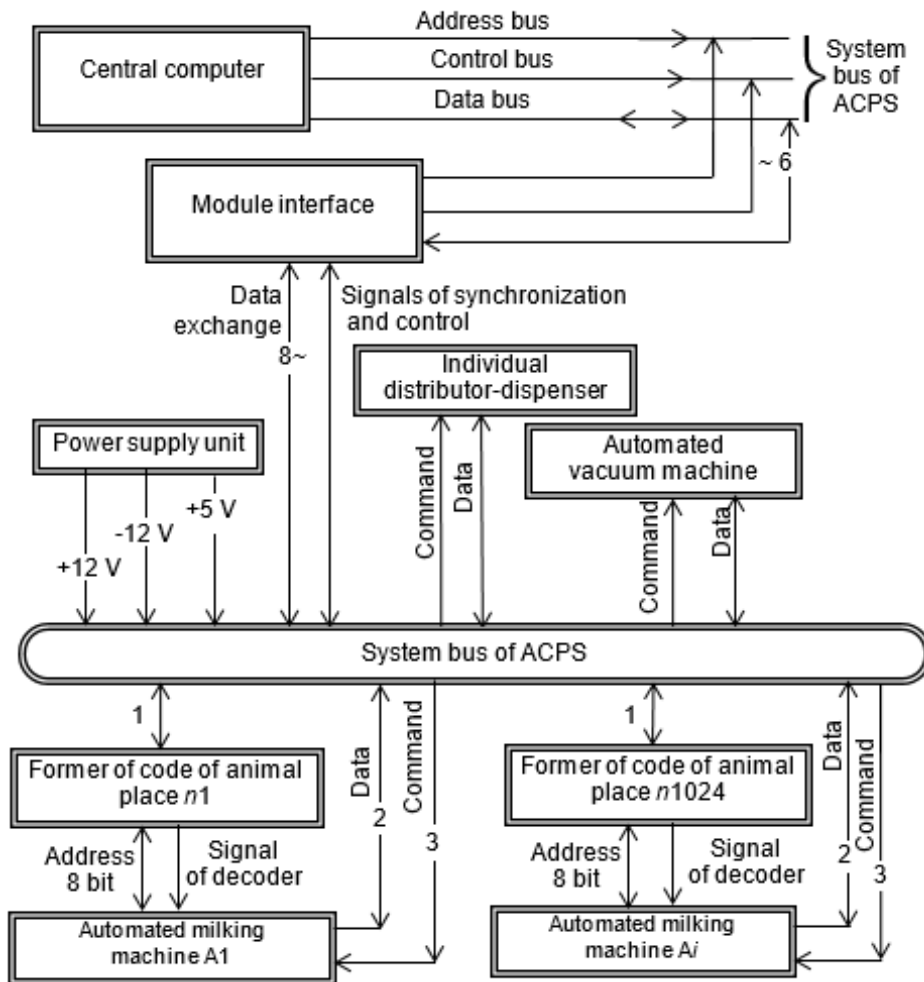
Fig. 1 – Structural scheme of adaptive cyber-physical system of milk production
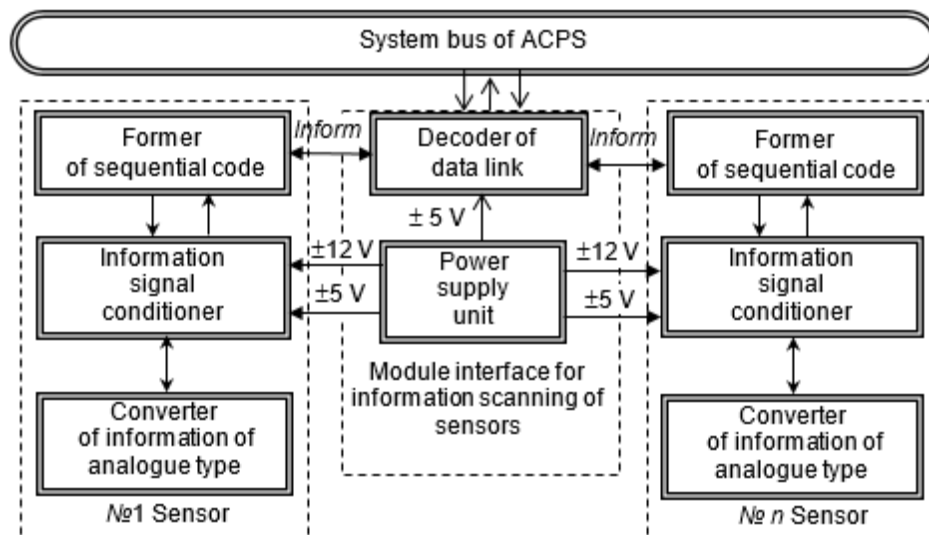
Fig. 2 – The structural chart of the interface for receiving and transmitting the data of ACPS sensors

To implement the operational control of integral characteristics of milk quality the single-frequency express analyser is designed on the principle of dielcometer measuring device of conductivity with modulation of the measuring resonant circuit parameters and the use of a layer-covered insulation of sensors-electrodes of the scattered field. The measuring converter provides important information during the operation of the milking machine. Functional scheme of the measuring converter is shown in fig. 4.
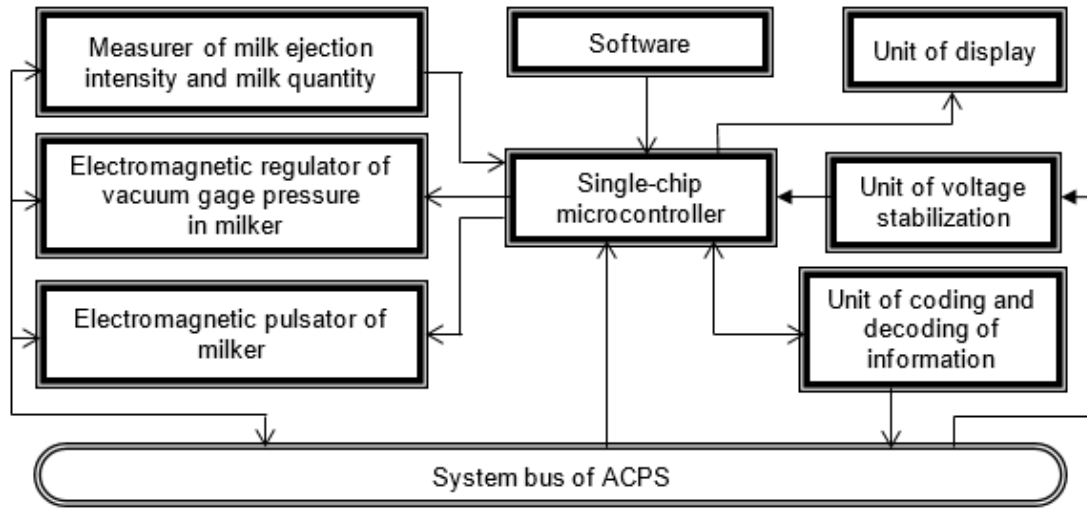
Fig. 3 – The structural chart of an adaptive milking machine as to the ACPS
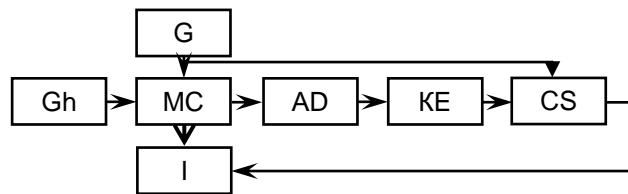
Fig. 4 – Functional scheme of the measuring converter of conductivity of ACPS
Gh – high frequency pulse generator; G – grid; MC – measuring circuit; AD – amplitude detector; KE – key;
CS – coincidence scheme; I – integrator

The peculiarity of the circuit is that the elements are always in dynamic equilibrium mode, and the integrator output voltage is a measure of the actual capacitance of the sensor and, accordingly, the measured conductivity of the medium.

Algorithmization and firmware (soft hardware)
The adaptive cyber-physical system of the milking process provides control and management of the basic technological information about the milk ejection process as well as the state of the machine-animal system in the milking process. For research, an adaptive milking machine with feedback about the cow's milking process was used. According to the algorithm of operation of the pulsator, the feedback was carried out through a thermo-anemometric milk intensity measurer and a sensor of the vacuum gage pressure parameters in the inter wall and under-teat area of the teat cups. The electronic pulsator is controlled by a microcontroller that programmatically generates the f_p frequency and the digital pulse rate. Sensors were used to read the information as to vacuum gage pressure and ripple frequency. The pneumo-electromagnetic pulsator and the electromagnetic pressure regulator are controlled by the PID controller, which is implemented programmatically by the microcontroller.

Using an analog pressure sensor, the information as to vacuum gage pressure and ripple frequency was read. Data exchange was carried out using a bus shaper and an analog key. There is a galvanic isolation in the information lines of data changes with ACPS.

The card of functional distribution of memory cells of the RAM allocated area in the milking machine with microprocessor control is given in table 1.

Table 1

The card of functional distribution of memory cells for generating and storing operational information of the milking machine

16-th code of RAM cell number	Reference designation	PARAMETER
20	n	The cell of cow number forming
21	N	The physical counter
22	ΔM	Intensity of milk ejection
23	N_{start}	Physical time of milking start
24; 25	ΣM	Quantity of milk
26	M_{max}	Maximum intensity of milk ejection
16-th code of RAM cell number	Reference designation	PARAMETER
27	N_{max}	Physical time of occurrence of M_{max}
29	N_{finish}	Physical time of milking finish
2A	N_{1start}	Physical time of milking up start
2B; 2C	ΣM_i	Quantity of milk of the machine milking up
2D	M_{1max}	Maximum intensity of milk ejection of the machine milking up
2E	N_{1max}	Physical time of occurrence of M_{max1}
2F	$N_{1finish}$	Physical time of machine milking up finish
30	--	Complementary marker of the machine milking up
31	T_{finish}	Complementary marker of finish of the machine milking up
32	T_{max}	Maximum duration of milking
33; 34; 35; 36	t_i	Milk temperature by the quarters of the udder
37	$T_{aver. i}$	Average milk temperature
38	$T_{aver.-1}$	Average milk temperature of the pre measuring
39	δ	Electric conductivity of milk
3A	HELP	Indication of the existence of a mastitis
3B	f	Ripple frequency calculated
3C	F	Cycle ratio calculated
3D	P	Level of vacuum gage pressure

Adaptive control module with using the single crystal microcontroller is the main functional module that implements the adapted technological mode of the milking machine. Functional scheme of the adaptive control module with search (expert) self-tuning system is shown in fig. 5. For such a control scheme, the action of disturbing factors F(t) and control signals M(t) = X(t) is characteristic. The system operates these factors with the least error.
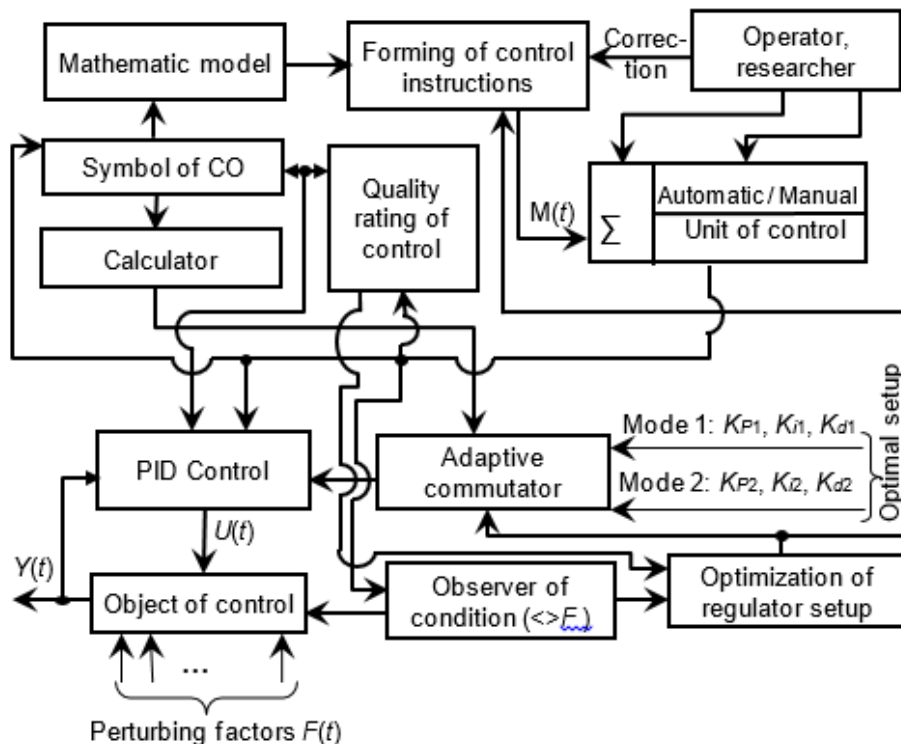
Fig. 5 – Functional scheme of the adaptive control module with search (expert) self-tuning system

The information about system status is collected in a cyclic survey mode. The sensors are interrogated periodically with a specified and clearly defined sequence that corresponds to real-time mode. Each survey cycle occurs at the same time intervals, which is limited by the ω_{max} cut-off frequency. The data of the m series of survey are processed according to a given algorithm. During the implementation of the data exchange algorithm, the procedure of algorithm-hardware correlation of external objects, the interface and the central computer was developed. This procedure enables to determine the duration of measurement and frequency of survey of external objects.

To improve the accuracy, the condition must be met:

$$m = 2^k \, ; \tag{1}$$

by the limitation of

$$m\Delta\tau_{meas.} \leq T_0 ; \tag{2}$$

where T_0 – the period of quantization (measurement time); $k = 0, 1, 2, 3, \ldots$.

Therefore, the measurement discretion must be appropriate:

$$\Delta\tau_{meas} = \frac{T_0}{2^k} \, . \tag{3}$$

The second condition is to minimize the distortion of information during the quantization process. The T_0 quantization period was chosen on the condition that the $N/nT_0]$ discrete function most accurately reflects the $N(\Delta\tau_{meas.})$ continuous function. The faster the $N(\Delta\tau_{meas.})$ continuous function are changed, the T_0 quantization period should be the smaller, i.e. the more often the data is read. Depending on the spectrum of continuous function, we chose the T_0 quantization period on the basis of Kotelnikov's fundamental theorem for the theory of impulse systems. According to the theorem, the $N(\Delta\tau_{meas.})$ time functions, which do not contain harmonic components above the ω_{max} frequency, are completely determined by their values at the $[n \, T_0]$ moments of time that are spaced apart from each other with the period of:

$$T_0 = \frac{\pi}{\omega_{max}} \, . \tag{4}$$

The quantization frequency must be selected according to the condition:

$$\omega_0 = 2\omega_{max} \, . \tag{5}$$

In this case, the $N[nT_0]$ discrete function will accurately reflect the $N(\Delta\tau_{meas.})$ continuous function and there will be no loss of quantization information, i.e.:

$$N(\Delta\tau_{meas.}) = N\left| n\frac{\pi}{\omega_{max}} \right| \, ; \tag{6}$$

The task of optimizing the quantization period is one of the fundamental problems of machine time optimizing, which is directly defined for each digital control loop. As T_0 is decreased, the accuracy of measurement and the PCs utilization are increased, but machine time is not economically used The longer the time period T_0, the reliability of information is decreased. Therefore, the problem of finding a compromise solution occurs in order to satisfy the conflicting requirements. Accordingly, the quantization period should be within:

$$\frac{\pi}{\omega_{max}} \geq T_0 \geq \omega_{tp} \, , \tag{7}$$

where ω_{tp} – the ripple frequency of technological process pulse system;

ω_{max} – the frequency of the functional element operation (control, primary information means, etc.).

The minimum quantization period is determined by the formula:

$$T_{0min} \leq \frac{\varepsilon}{\left|\dfrac{dy(\Delta\tau_{meas.})}{d\Delta\tau_{meas.}}\right|_{max}} \, , \tag{8}$$

where ε – the constant that characterizes the measurement accuracy:

$$\varepsilon \geq N(\Delta\tau_{meas.}) - N[nT_0]; \tag{9}$$

$\left|\dfrac{dy(\Delta\tau_{meas.})}{d\Delta\tau_{meas.}}\right|_{max}$ – the maximum speed of function change.

After assuming $\Delta\tau_{meas.} = 1/T_0 \approx T_0$ and taking into account (9) the $N\varepsilon \approx 0$ is obtained. Between the function rate of change and the frequency of functional element operation, there is the following functional dependence:

$$\left|\frac{dy(\Delta\tau_{meas.})}{d\Delta\tau_{meas.}}\right| \approx \omega_{\max} \tag{10}$$

For a specific milking process, the value of $\omega_{tp} = 1$ [Hz] and ω_{max} depend on the type of milking machine. In two-cycle automated milking machines with a variable ratio of suction and compression cycle, depending on the intensity of milk ejection, the frequency of functional element operation will be of 1.5 Hz $\leq \omega_{max} \leq 3$ Hz. The quantization period will be within $\pi/1.5$ Hz $\geq T_0 \geq 1$ Hz.

Protection of software bit rate exceedance is implemented by including in the data processing algorithm the backup cells and intermediate control. Hardware overflow protection is ensured by software and measurement time limiting.

The developed control system allows to exchange the information between 1024 subscribers in one second. The ACPS database consists of operational information that is placed in modules and stores data only for the period of its operation and permanent information, which is stored in the central computer and is changed due to the data of the operational database and calculations.

The database area for the *i*-th cow is calculated by the formula:

$$N_i = N_{start} + K_i\,(i-1), \tag{11}$$

where N_i – the start number of the memory area cell for the *i*-th cow;

N_{start} – the start number of memory cell allowed by user for the central computer;

K_i – the number of information parameters that need to be formed and stored;

i – the number of cow identification (number of cow or animal location).

Card of the functional distribution of selected area memory cells for *i*-th cow in the central computer database is presented in table 2.

The last three signs of mismatch of the cow's condition (Table 2) are entered by the machine milking operator from the milking machine's keyboard.

The quantities of milk per milking, milk quality, the time of milking, the intensity of milk ejection, the electrical conductivity of milk are integral indicators that characterize following the rules of milk production technology, and especially milking. These indicators are used as the main diagnostic indicators of ACPS.

Table 2

The card of cells functional distribution of database memory area per 1 cow, for generating and storing operational information of the machine milking ACPS

16-th code of cell number	Reference designation	PARAMETER
xx00	n	The cell of cow number
xx01; xx02	∑M	Milk quantity
xx03; xx04	∑Mi	Milk quantity of the machine milking up
xx05	T_{max}	Maximum duration of milking
xx06	$t_{aver.-1}$	Average milk temperature
xx07	δ	Electric conductivity of milk
xx08	HELP	Indication of the existence of a mastitis
xx09	Gcalc.	Calculated quantity of disposable mixed fodder
xx0A	---	Indication of the cow heat period
xx0B	---	Indication of the blood in the cow milk
xx0C	---	Other indication of the cow disparity

The reasons of deviations are analysed according to the algorithm with the output on the screen of the remarks to the administrator. Information row is entered by the milking operator from the console of the automated milking control unit or from the simplified console on the milking machine.

RESULTS

The proposed adaptive cyber-physical system of milk production process and in particular machine milking, is capable to implement the adaptive interaction between the animal and the machine, where milk ejection is a functional parameter. ACPS of milk production process consists of the following subsystems - information, analytical, control, visualization. Let us consider the functioning peculiarities of the developed system main components, as independent elements that can operate both autonomously and within the ACPS.

The experimental laboratory installation of the ACPS (Fig. 6) and individual equipment elements were developed. The nature of the cow milk ejection during the milking process was reproduced by a simulator (2) of milk ejection intensity (Fig. 6). The simulator allows creating a characteristic of milk ejection of different types of cows.

The milk ejection curve is described by the empirical dependence of milk yield on the milking time:

$$q = \frac{a \cdot t^{b}}{e^{ct}},$$

(12)

where a, b, c – research coefficients for a given character of milk ejection curve; t – the time of milking, min.

The c coefficient characterizes the maximum milk ejection, a coefficient – the milk ejection and the time of milking. As a coefficient is increased, the milk ejection and milking time are increased as well. The b coefficient characterizes the rate of maximum milk ejection start. As the b coefficient is decreased ($b = 1.2$), the maximum milk ejection is simulated at the beginning of the first minute, as $b = 2$, the maximum milk ejection is simulated for the second minute from the beginning of milking. The results of the milk ejection curve simulation are shown in Fig. 7.

Fig. 6 – General view of the experimental laboratory complex of ACPS
1 – the reservoir of the milk simulator; 2 – the simulator of milk ejection intensity; 3 – teat cups; 4 – sensors of the pressure in the inter wall and under-teat area of the teat cups; 5 – sensor of the pressure in the milk hose; 6 – measuring device; 7 – the electronic module of milk ejection gauge; 8 – DAC-ADC; 9 – the control system (main computer); 10 – the system of data processing of the pressure sensors; 11 – the electronic module of data-measuring parameters visualization; 12 – blocks of regulated voltage; 13 – the pneumo-electromagnetic pulsator; 14 – the milk tap; 15 – the vacuum hose; 16 – the imitation of udder; 17 – the collector; 18 – the milk hose
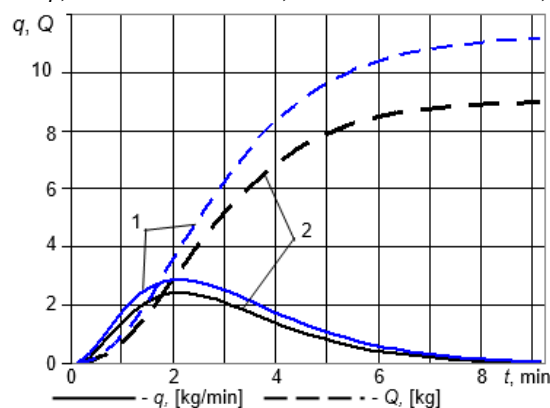
**Fig. 7 – Graphs of simulation of *q* milk ejection intensity and *Q* milk quantity
by simulator of milk ejection intensity during the cow milking period**
$1 - a = 5$; $b = 1.8$; $c = 0.9$; $2 - a = 4.5$; $b = 2$; $c = 1$

Vacuum pressure fluctuations, and in particular the vacuum pressure regulator, were studied using a sensor developed on the basis of the BMP180 sensor (*Dmytriv V.T., Dmytriv I.V., Lavryk Y.M. et all, 2017*). The general view of the sensor with the microprocessor control unit is shown in fig. 8.

Pneumo-electromagnetic pulsators of two types are developed and tested: micro pulsator for each milking cup and pairwise action (Fig. 9) with low power consumption, up to 6 W, variable pulsation frequency (shift between the cycles of pairs of milking cup is 0.2 sec.). The microprocessor unit (Fig. 10) with using of single-chip Atmel microcontroller ensures working algorithm of the central computer. The designed microprocessor unit realizes the following parameters - the step of changing the pulse rate of 0.1 [Hz], the ratio between the cycles of 0.25%, the step of phase shift of 0.1 sec.

General view of the rapid analyser of milk qualitative adjectives is shown in fig. 11.

Functional dependence of the differential sensitivity of the rapid analyser converter as to its execution variant is shown in fig. 12.
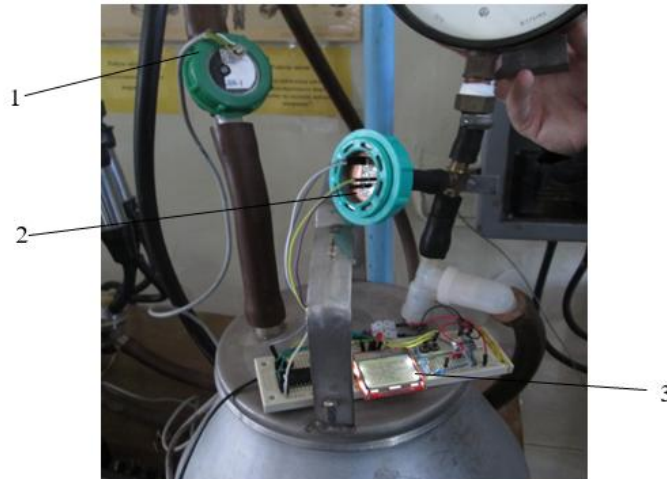
Fig. 8 – General view of the measurement system of vacuum gage pressure fluctuation
1 – the sensor vacuum gage pressure of the line type; 2 – the one-port vacuum gage pressure sensor;
3 – the microprocessor measurement unit

Fig. 9 – General view of the experimental pneumo-electromagnetic pulsator of pairwise interaction

Fig. 10 – General view of the microprocessor unit of the adaptive milking machine

Fig. 11 – General view of rapid analyser of milk qualitative adjectives
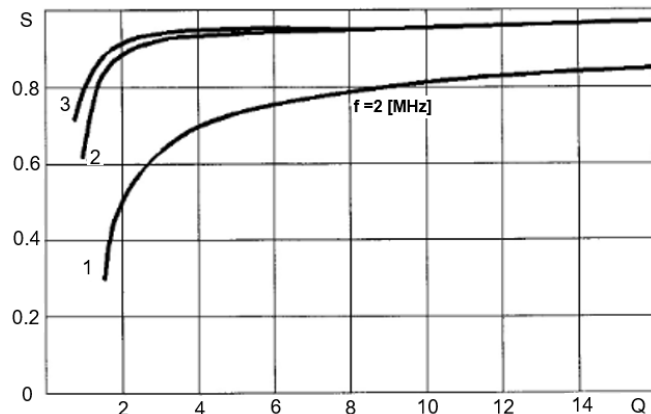
Fig. 12 – Dependence of the differential sensitivity of the converter on its Q-factor
1 – sensor with one-side electrodes ($C_M = 32$ [pF]); 2, 3 – sensor with electrodes of interspersed field at frequency of 2 and 5 [MHz] ($C_M = 144$ [pF] i $C_M = 112$ [pF])

The range of measurement of the Q-factor in the milk by sensors with isolated electrodes is in the range of 1-2, the differential sensitivity varying from 0.5 to 0.9.

CONCLUSIONS

The tried-and-tested adaptive cyber-physical milk production system with an adaptive milking machine with microprocessor control provides regulation of the pulsation frequency depending on the intensity of milk ejection, measures the conductivity of milk, regulates vacuum pressure and displays technological information. Studies of the time characteristics of the transient processes of adaptive milking machine operation with pneumo-electromagnetic pulsators and digital control have shown high efficiency, adaptation of the milking machine to the physiology of milk ejection of cows, stability of technological parameters and indices independence from fluctuations of vacuum pressure.

The use of digital control systems based on single-chip microcontrollers enables the implementation of digital controllers by programming microprocesses, which greatly simplifies the hardware. The optimal parameters for adjusting the regulators are determined in advance by mathematical dependence, which reduces the number of additional adjustments to the parameters of the regulators.

The quantization period of information parameters is chosen based on the frequency characteristics of the machine milking process and it is within 100 [Hz] $\geq T_0 \geq$ 10 [Hz].

Protection against software overflow is realized by entering into the data processing algorithm of backup cells and intermediate control. Hardware overflow protection is provided by software, limiting the duration of measurement.

REFERENCES

[1]   Czarnociński F., (2008), Study of the pressure parameters in selected modern milking apparatuses, *Agricultural Engineering*, vol. 4 (102), pp. 198-202, Poznan / Poland;

[2]   Dmytriv V.T., Dmytriv I.V., Lavryk Y.M. et al, (2017), Study of the pressure regulator work with a spring-damper system applied to milking machine*, INMATEH - Agricultural Engineering*, Vol. 52, No. 2, pp. 61 - 67, Bucharest / Romania;

[3]   Jędruś A., Lipiński M., (2008), Functional analysis of the new quarter milking cluster, *Agricultural Engineering*, vol. 4 (102), pp. 337-345, Poznań / Poland;

[4]   Jędruś A., (2010), Methodology of testing selected metrological properties of thermo-anemometric milk flow indicators with the use of the microprocessor technique, *Agricultural Engineering*, vol. 7 (125), pp. 81-86, Poznań / Poland;

[5]   Juszka H., Tomasik M., Lis S. et al, (2011), Collector of an independent milking machine, *Agricultural Engineering*, vol. 4(129), pp. 93-98, Poznań / Poland;

[6]   Juszka H., Lis S., Tomasik M., (2011), The concept of a two-chamber autonomous claw of the milking unit, *Agricultural Engineering*, vol. 8 (133), pp. 161-165, Poznań / Poland;

[7]   Lis S., Juszka H., Mendyk M., (2016), Modelling of an actuator in the vacuum control system of an autonomous milking machine, *Agricultural Engineering*, vol. 20(3), pp. 95-104, Poznań / Poland;

[8]   Pařilova M., Stadnik L., Ježkova A., (2011), Effect of milking vacuum level and overmilking on cows' teat characteristics*, ACTA Universitatis Agriculturae et Silviculturae Mendelianae Brunensis*, LIX 23 (5), pp. 193-202, Brno / Czech Republic;

[9]   Pazzona A., Murgia L., Zanini L., et al., (2003), Dry tests of vacuum stability in milking machines with conventional regulators and adjustable speed vacuum pump controllers, *ASAE Annual International Meeting*, 27- 30 July, Riviera Hotel and Convention Centre, Paper Num.: 033013, Las Vegas / USA ;

[10]   Pirlo G., Abeni F., Capelletti M., et al, (2005), Automation in dairy cattle milking: experimental results and considerations, *Italian Journal of Animal Science*, vol. 4(3), pp. 17-25, Italy;

[11]   Reinemann D. J., Schuring N., Badel R. D., (2007), Methods for Measuring and Interpreting Milking Vacuum, *Sixth International ASABE Dairy Housing Conference*, 16-18 June, Minneapolis, Minnesota / USA;

[12]   Skalska D., Nejman M., Wiercioch M., et al, (2013), Amplitude of disturbance of the system under pressure in the pipeline milking machine and its impact on the parameters of operation of milking apparatuses of the selected makes, *Agricultural Engineering*, vol. 4 (147), pp. 301-311, Poznan / Poland.

DETERMINATION OF SOWING PRECISION IN SIMULATED LABORATORY CONDITIONS
/
DETERMINAREA PRECIZIEI DE SEMĂNAT ÎN CONDIȚII SIMULATE ÎN LABORATOR

Cujbescu D.[1)], Biriş S.Şt.[2)], Voicu Gh.[2)], Matache M.[1)], Paraschiv G.[2)], Vlăduţ V.[1)], Bularda M [*3,4)], Ungureanu N.[2)] [1]

[1)] INMA Bucharest, [2)] University Politehnica of Bucharest, Faculty of Biotechnical Systems Engineering / Romania;
[3)] SCDA Brăila / Romania; [4)] Univ. Dunărea de Jos Galaţi / Romania;
[*)] *Corresponding author e-mail: marcelbularda@yahoo.com*
DOI: https://doi.org/10.35633/inmateh-61-23

ABSTRACT

In order to obtain a correct and always reproducible image of the performances achieved by a planter (or any agricultural machine), laboratory tests are required, under specified conditions, well controlled, to determine the precision of sowing outside the optimal agricultural periods. The paper presents a theoretical model for estimating sowing precision (feed quality index) as a polynomial function of the second degree, dependent on seed norm per hectare, working speed, depression value, mass of 1000 seeds, as well as combinations thereof.

REZUMAT

Pentru a obține o imagine corectă și oricând reproductibilă a performanțelor atinse de o semănătoare de precizie (sau orice mașină agricolă) se cer inițiate încercări de laborator, în condiții dinainte precizate, bine controlate, pentru determinarea preciziei de semănat în afara perioadelor optime agricole. Lucrarea prezintă un model teoretic pentru estimarea preciziei de semănat (indicele de calitate al alimentării) ca o funcție polinomială de gradul al doilea, dependentă de norma de seminte la hectar, viteza de lucru, valoarea depresiunii, masa a 1000 de seminţe, precum și de combinații ale acestora.

INTRODUCTION

Over time, sowing precision has become a major preoccupation the field of mechanical engineering, with role in optimizing soil processing works and sowing works. Unlike row sowers that conduct seeds distribution in continuous flow on equidistant rows, precision planters achieve the sowing of one or more weeding plant seeds in equally spaced nests on equidistant rows.

In precision agriculture, pneumatic seed meters have been extensively developed to achieve the sowing of different seeds (such as rapeseed, corn, soybean, sugar beet, cotton, etc.), being designed to achieve the introduction of a single seed into the soil at a distance required by agrotechnical norms for precision sowing.

The promotion of researches in the field of sowing precision aim at applying the optimal solutions in the conceptual design of precision planters (precision sowing machines) in order to optimize the qualitative working indices provided in the modern agro-technical norms (*Gângu et al., 2008; Kornienko et al., 2016; Mogilnay et al., 2018*).

The improvement, modernization, simplification of construction and seed distribution adjustment operations are necessary as there are disturbing factors that can affect the precision of sowing due to seed quality: low volume, low weight, and irregular shapes (*Dobre, 2010; Li et al., 2013; Yazgi et al., 2010*), as well as the condition of the sowing machine: clogged row unit, blocked seed meter, broken transmission chain, degraded seed scraper, insufficient pressurization, lack of seed in the hopper.

Karayel et al., (2004) proposes a mathematical model for determining the optimum depression of a precision planting using the physical properties of the weight of 1000 seeds, projection area, sphericity and seed density. All possible combinations of the different variables were tested and included in the mathematical regression analysis. The results have indicated that the developed model can be used to estimate the optimum vacuum pressure for a precision planter with an efficiency of 0.98.

In order to optimize the functional parameters of a seed meter for cotton, *Singh et al., (2005)* analysed its performance through experimental research in the laboratory and in field conditions.

---

[1] *Cujbescu D., Ph.D. Eng.;. Biriş S.Şt., Prof. Ph.D. Eng; Voicu Gh., Prof. Ph.D. Eng.; Matache M., Ph.D. Eng.;*
Paraschiv G., Prof. Ph.D. Eng.; Vlăduţ V., Ph.D. Eng.; Bularda M, Ph.D.Eng.; Ungureanu N., Lecturer Ph.D.Eng.

The influence of the disc's rotation speed, of depression and of the initial shape of the distribution disc orifice were determined by examining the sowing precision (precision in achieving seed spacing, the missing seeds index, and the doubles index).

The performances of the electromechanical drive system and the classic drive system were tested at three different operating speeds (5, 7.5, 10 km/h) and ten different seed spacing from 6 to 29.3 cm in the laboratory. Both systems were compared regarding to the seed spacing uniformity (*Cay et al.,2018).*

To evaluate an acoustic system for online estimation of precision planting indices, a feeding platform was designed being able to apply different patterns of seed spacing with predefined precision planting indices (*Karimi et al., 2018).*

The effects of spatial separation between plants on yields of future crops were studied, the results of research being different, some of them revealing significant effects (*Fanigliulo and Pochi, 2011; Daynard and Muldoon, 1983; Lauer and Rankin, 2004*), while other researchers have achieved reductions in crop yield with increased variability of plant spacing. Even without a consensus, the parameters that influence the performance of precision sowing need to be further studied to guide design engineers' methods of improving future sowing machines (*Kocher et al., 2011; Marin et al., 2014; Miller et al., 2012*).

Glenn and Daynard, (1974), found that a plant spacing reduced by 4.5% resulted in a 5.5% increase in yield of harvested seed, a study conducted on two maize hybrids and two plant densities per hectare.

Nielsen, (2001), conducted researches on large and small parcels obtaining a loss of 62 kg/ha for each 1 cm increase of standard deviation of distances between seeds based on field studies.

Doerge et al. (2002) used spatial analysis to determine the influence of the spacing between maize plant rows on a Midwest farm on yields of future weeding plant crops, concluding that yield could increase by 84 kg/ha for each 1 cm decrease of the standard deviation of the distance between plants.

Liu et al., (2004), states that for each 1 cm increase of standard deviation of distance between plants on a row, the yield decreased by 35.9 kg/ha.

Nielsen, (2004), stated in a later study that the average loss of productivity was 42 kg/ha per cm of standard deviation of distances between seeds in a standard deviation range of 5 to 20 cm.

Fornstrom and Miller, (1989), conducted a study showing that the unevenness of distance between seeds is generally related to the manner in which the seed reaches the channel opened by the coulter and the working speed of the planter.

Liu et al., (2004), conducted a study correlating the degree of soil processing, the working speed of the planter and the type of seed meter. The sowing precision of planters equipped with seed meters with fingers was influenced by the degree of soil processing and the working speed of the planter, while the vacuum seed meters were mainly influenced by the working speed of the planter.

Şerbu, (1998), studied the phenomena governing the distribution process of a pneumatic seed meter by elaborating a mathematical model for determining the time of seed dropping after its detachment from the distribution disc orifice.

Afify, (2009), developed a mathematical model for estimating the optimum vacuum pressure of the seed meter of a precision planter using the properties of onion seeds, vacuum obtaining characteristics, as well as the geometry of the orifices situated on the seed distribution disc.

Xiaoyan, (2010), studied the process of aspirating rapeseed in the distribution disc orifice, aiming at optimizing the parameters that influence it. First, a mathematical model was obtained by minimizing the force of pressing the seed on the orifice, a force that occurs when the seed is aspirated into it. From this model was obtained a relation between the seed diameter, the angle of the orifice walls and the diameter of the orifice.

MATERIALS AND METHODS

In precision agriculture, the field of sowing is thoroughly studied by the realization of mathematical models that characterize the phenomena that govern the seed distribution process in order to achieve the sowing work in due time, to obtain plant densities N (pl/ha) provided by agro-technical norms and to maximize the yield of future crops.

In the analysis of the sowing process, improving the performance of seed meters is a constant concern for researchers in mechanical engineering and beyond. By uniformly spacing the sown seeds, the roots of future plants can reach uniform sizes that will fill the spaces on the sown rows without the risk of being pushed outside of the row of adjacent roots.

The experimental researches were conducted in order to determine the qualitative indices of seed meters (on a fully automated stand) based on the operation principle of the depression created by the exhauster in the seed feeding chamber, for three row units of precision planters, respectively:

  ➢ S1 – row unit with individual drive of the seed meter;
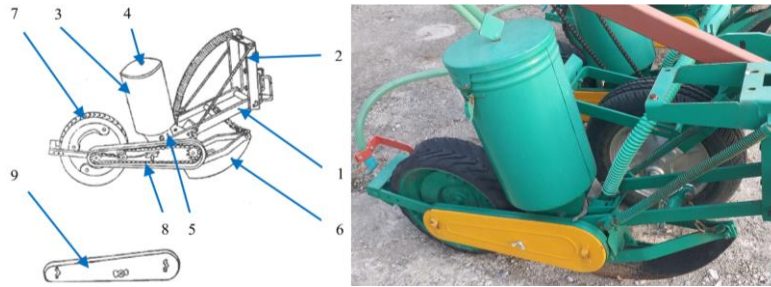
Fig. 1 - S1 row unit with individual driving of the seed meter (*Cujbescu, 2019*)
1-frame; 2-threaded rods; 3-seed supply box; 4-indicator of the level of seeds in the feed box; 5-seed meter with vertical distribution disc with orifices and scarper type - tipping with legs; 6-coulter; 7-drive wheel of the seed meter and soil compaction; 8-chain transmission for driving the seed meter from the compaction wheel; 9-mudguard

  ➢ S2 and S3 – row unit with centralized drive of the seed meters.
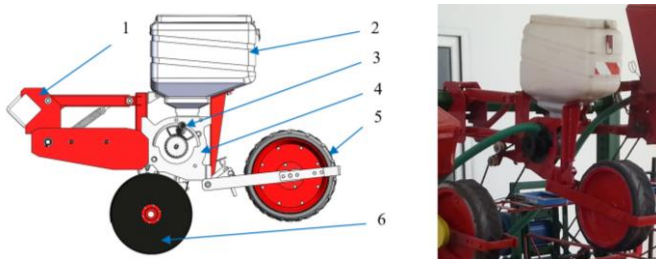
Fig. 2 - S2 row unit (*Cujbescu, 2019*)
1-support; 2-seed hopper; 3-vacuum socket; 4-seed meter with scraper type - fixed serrated; 5-compaction wheel; 6-double disc coulter
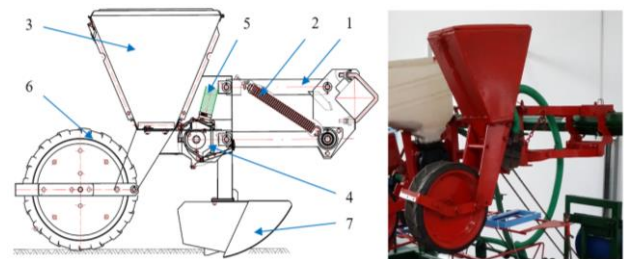
Fig. 3 - S3 row unit (*Cujbescu, 2019*)
1-frame; 2-springs; 3-seed feeding box; 4seed meter with scraper type - lamellar; 5-flexible tube of the vacuum channel; 6-soil compaction wheel; 7-coulter

The methodology for experimental research on the stand involves the following steps: the physical properties of seeds are determined; the physical hopper is fed; the entrance data are introduced (plant density per hectare, distance between rows, number of tested seeds, working speed, number of orifices on the distribution disc); the specialized software calculates (based on the entrance) the theoretical interval between seeds on the row; the motor driving the tested row unit is started; it is waited until the number of seeds tested passes through the transducers; the results are shown in graphic form.

For the experimental determination of the working process indices of pneumatic seed meters, according to ISO 7256/1-92, the theoretical (adjusted) interval between seeds is used as the reference element.

The specialized software for the processing of experimental data is based on a statistical processing system, the reference element being the theoretical (adjusted) interval between the seeds x_{ref} on the row, the real interval between two consecutive seeds x_j being determined on the stand using laser transducers (by transforming the fall time into space by multiplying the falling time with the working speed), considering:

  ➢ double (double sowing) - any real interval: $x_j \leq 0.5 \cdot x_{ref}$

  ➢ normal interval (correct sowing) - any real interval: $0.5 \cdot x_{ref} < x_j \leq 1.5 \cdot x_{ref}$

  ➢ misses (missing sowing) - any real interval: $x_j > 1.5 \cdot x_{ref}$

where:

  x_{ref} – theoretical interval between seeds, obtained by adjusting the planter, [cm];

  x_j – real interval, measured under operating conditions on the stand, [cm].

The percentage frequency of measurements for each type of interval allows the definition of the quality indices that characterize the performance of the planter:

  ➢ A – feeding quality index (percentage of distances correctly sown), %;

$$A = \frac{n_1}{N'} \cdot 100 \quad \%$$ (1)

where:

  n_1 – number of normally sown seeds;

N' – number of theoretical intervals.

➤ D – doubles index, %;

$$D = \frac{n_2}{N'} \cdot 100 \quad \% \tag{2}$$

where: n_2 – number of doubled nests.

➤ M – index of missing seeds, %;

$$M = \frac{n_0}{N'} \cdot 100 \quad \% \tag{3}$$

where: n_0 – number of missing nests.

➤ σ – theoretical deviation;

$$\sigma = \sqrt{\frac{\sum (n_i \cdot X_i^2)}{N_2} - X_{med}^2} \tag{4}$$

➤ CV – variation coefficient, %.

$$CV = \sigma \cdot 100 \quad \% \tag{5}$$

In order to obtain a correct and always reproducible image of the performances achieved by a precision planter (or any agricultural machine), laboratory tests are required, under specified conditions, well controlled, to determine the sowing precision outside the optimal agricultural periods.

Table 1 presents the functional parameters taken into account in determining the quality indices of the studied row units.

Table 1

Functional parameters for determining the qualitative indices of row studied

Crop	Corn		
Sowing norm N **[pl/ha]**	50000	65500	69500
Distance between rows [cm]	70		
Number of tested seeds	500		
Working speed v **[m/s]**	1.18; 1.77; 2.37; 2.96		
Number of orifices on the distribution disc	16		
x_{ref} **[cm]**	28.57	21.81	20.55

The experiments were carried out in 3 repetitions for each working speed, for each plant density (50000, 65500, 69500 pl/ha) and for 4 working speeds (1.18; 1.77; 2, 37; 2.96 m/s).

From the analysis of the experimental data in the table 2, it results that the sowing precision decreases with the increase of the working speed, which is observed for each of the seed meters investigated. The highest value of the feeding quality index of 97.533% was obtained by the seed meter of row unit S3 at a working speed of 1.18 m/s and a density of 50000 pl/ha.

Table 2

Averages of feeding quality indices of the seed meters studied, (*Cujbescu, 2019*)

Working speed [m/s]	Sowing norm N [pl/ha]	S1	S2	S3
		A [%]		
1.18	50000	94.790	96.576	**97.533**
1.77		94.566	95.636	97.028
2.37		94.470	94.151	96.680
2.96		94.152	93.603	95.323
1.18	65500	95.155	95.951	97.309
1.77		94.940	95.423	96.805
2.37		94.209	95.017	96.186
2.96		94.163	94.652	95.860
1.18	69500	95.601	96.143	97.008
1.77		95.119	95.543	96.521
2.37		94.421	95.083	96.327
2.96		94.129	94.693	95.721

Figure 4 shows the variation of the sowing precision according to the working speed, for section S3, observing the decrease of the sowing accuracy with the increase of the working speed.
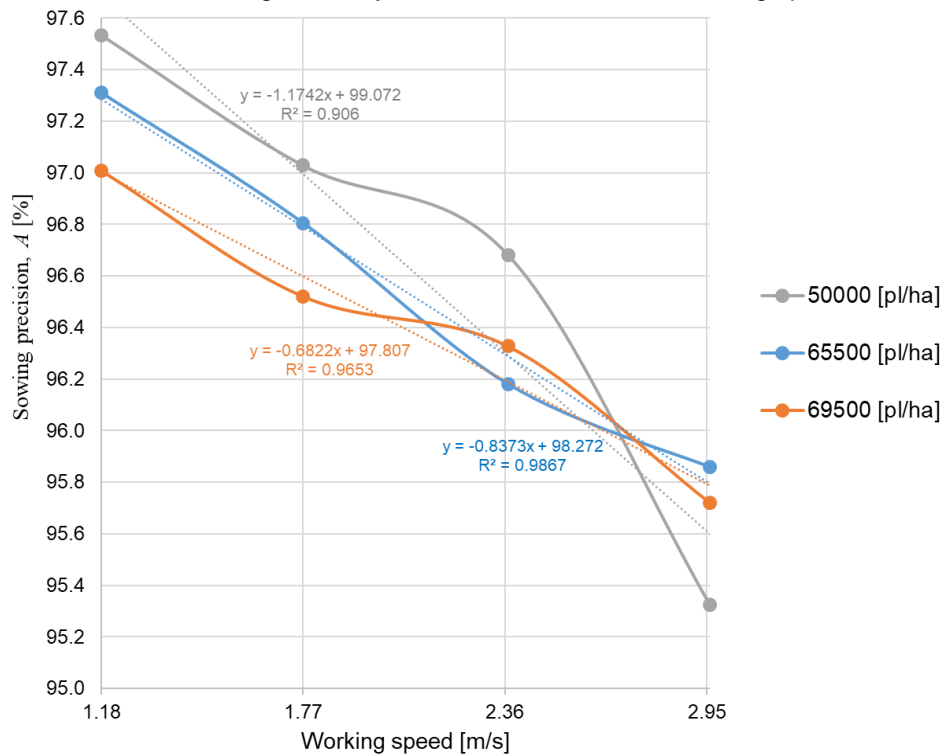
Fig. 4 - Variation of the sowing precision of the S3 row unit depending on the working speed
(*Cujbescu, 2019*)

RESULTS

The development of the mathematical model for the distribution process of the pneumatic seed meter has a key role for a deeper understanding of the phenomena at the basis of this process.

The agricultural technological processes have a special feature that distinguishes them fundamentally from the industrial ones themselves, namely that they are influenced by many disruptive factors, whose study requires complex analysis procedures and mechanisms.

The following equation presents the sowing precision (feeding quality index) as a second-degree polynomial function, dependent on the seed norm per hectare N, working speed v, value of depression Δp, mass of 1000 seeds MMS, as well as combinations between them.

$$A_c = c_0 + c_1 \cdot \Delta p + c_2 \cdot N + c_3 \cdot v + c_4 \cdot MMS + c_{12} \cdot \Delta p \cdot N + c_{13} \cdot \Delta p \cdot v + c_{14} \cdot \Delta p \cdot MMS +$$
$$+ c_{23} \cdot N \cdot v + c_{24} \cdot N \cdot MMS + c_{34} \cdot v \cdot MMS + c_{11} \cdot \Delta p^2 + c_{22} \cdot N^2 + c_{33} \cdot v^2 + c_{44} \cdot MMS^2$$

(6)

where: A_{Ci} represents calculated sowing precision and c_a, c_{ab} regression coefficients ($m = 0..4$), ($n = 1..4$).

To determine the values of the unknown coefficients noted generically c_i by linear mathematical regression, the T-shaped functional was formed, as a sum of the squares of the differences between the values obtained by applying the polynomial equation and the actual values measured at the experiments noted generically z_i from table 3, where z_i can represent any size obtained during the measurements and by means of which the sowing precision A is expressed, $i=1 \div n$, (n represents the number of unknown coefficients and $j=1 \div m$, (m represents the number of measurements measured in table 3):

$$T = \sum_{i=1}^{n} \left(Ac_i(z_j) - A_i \right)^2$$

(7)

where:

A_i − vector of sowing precision measured experimentally;

$Ac_i(z_j)$ − vector of sowing precision calculated using experimentally measured data.

For the determination of the coefficients but by mathematical regression, the method of the smallest squares was used, imposing the condition that the function T is minimal.

The minimum of the function T with respect to c_i is obtained by cancelling the partial derivatives of T with respect to the same coefficients:

$$\frac{\partial T}{\partial c_i} = 0 \tag{8}$$

The partial derivatives of the functional T were determined according to each of them and the unique system determined was created, from n equations with n unknowns (9):

$$\begin{cases} \dfrac{\partial T}{\partial c_i} = 0, \ \ i = 1 \div n \end{cases} \tag{9}$$

For its numerical solution the system equations were explained and the constants eliminated obtaining the equivalent form that can be written as a matrix product:

$$Z \cdot Y = X \tag{10}$$

where:

Z – the system matrix;

X – the matrix of free terms;

Y – the matrix formed by the unknown coefficients k_i, $Y = (k_i)$.

The determination of the vector Y formed by the unknown coefficients, was done by numerically solving by mathematical regression of the equation (11), obtained from the matrix equation (10) by the inverse matrix method, using the data rows obtained from the experiments and presented in the table:

$$Y = Z^{-1} \cdot X \tag{11}$$

The determination of the coefficients of equation (11) was performed using a matrix calculation program in Mathcad, further presenting the coefficients obtained and the numerical form of the polynomial equation:

$$A_c = -1029,29 + 3,233 \cdot \Delta p + 0,005 \cdot N - 5,285 \cdot v + 0,701 \cdot MMS - 0,045 \cdot \Delta p \cdot v -$$
$$-0,004 \cdot \Delta p \cdot MMS - 0,029 \cdot v \cdot MMS - 0,001 \cdot \Delta p^2 + 0,359 \cdot v^2 + 0,002 \cdot MMS^2 \tag{12}$$

The error of the mathematical model was calculated as follows:

$$e = \frac{A_i - Ac_i}{A_i} \cdot 100 \tag{13}$$

where A_i is the vector of sowing precisions determined on the stand, and A_{Ci} is the vector of sowing precisions calculated on the experimentally measured data using relation (12).

Figure 5 shows the diagram representing the experimentally determined sowing precision compared to the calculated sowing precision, (*Cujbescu, 2019*).
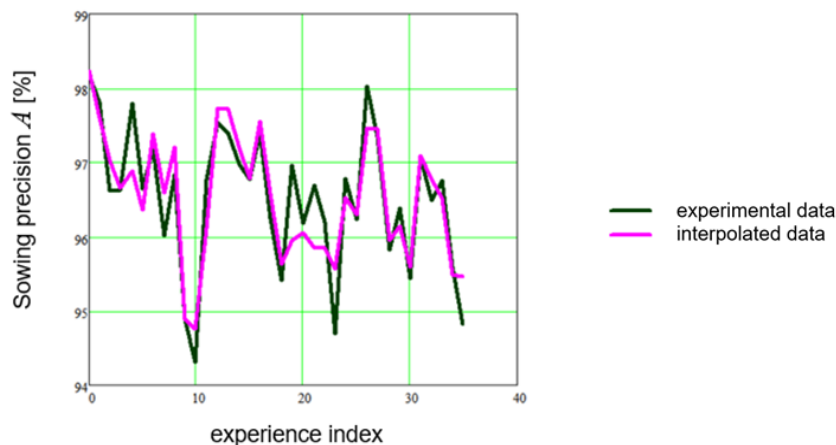
Fig. 5 - Diagram representing experimentally determined (black) and calculated sowing precision (purple)

Figure 6 shows the correlation between the data obtained experimentally and the data obtained by calculation, (*Cujbescu, 2019*).
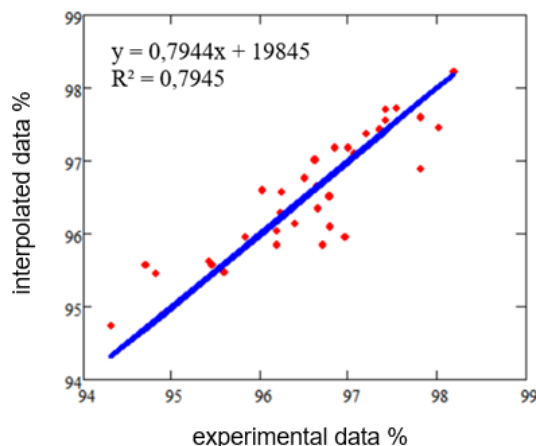
Fig. 6 - Diagram of the correlation of the data obtained experimentally and the data obtained by calculation

CONCLUSIONS

Quality indices are sources of information and criteria for assessing the behaviour of the type of row unit investigated, possibly decision criteria for improving the adopted constructive solutions.

On the basis of the values of the quality indices, conclusions can be drawn on the dominant trends in the operation of row units: a large difference between indices D and M leads to the conclusion of a pronounced tendency to missing seeds (if $M >> D$) or to doubles (overfeeding $D >> M$) , aspects that are inconvenient from the agro-technical point of view, especially since the high values of D and M indices also alter the quality of the feed, expressed by the index A.

From a mathematical point of view, certain constructive requirements must be met to obtain a calculated production on a given area of land, thus, there should be a certain distance between the row units of the planter and between the seeds sown on each row (rows of seeds) the distance should be constant to achieve the norms / densities specific to each crop. Taking into account these specifications, it can be concluded that:

➢ a method of studying the phenomena underlying the distribution process is the development of a mathematical model of distribution;

➢ the achieved mathematical model regards kinematically the seed distribution process, taking into consideration the kinematic factors that interfere in its disturbance;

➢ determining the precision of sowing under simulated conditions in the laboratory led to the elaboration of a mathematical model, the correlation coefficient of the experimental and calculated data being $R = 0.891$.

REFERENCES

[1] Afify M. T., El-Haddad Z. A., Hassan G. E., Shaaban Y., (2009), Mathematical model for predicting vacuum pressure of onion seeds precision seeder, *Misr J. Ag. Eng.*, 26(4), pp. 1776 – 1799, Farm machinery and power;

[2] Cay A., Kocabiyik H., May S., (2018), Development of an electro-mechanic control system for seed-metering unit of single seed corn planters Part I: Design and laboratory simulation, *Computers and Electronics in Agriculture* 144, pp. 71-79;

[3] Cujbescu D., (2019), *Contributions to the study on the working process of seed meters of precision planters, PhD Thesis,* University Politehnica of Bucharest, 2019;

[4]   Daynard T. B., Muldoon J. F., (1983), Plant-to-plant variability of maize plants grown at different densities, *Canadian Journal of Plant Science*, 63(1), pp. 45–59;

[5]   Dobre P., (2010), *Energy base and horticultural machinery*, pp. 69-76, Bucharest;

[6]   Doerge T., Hall T., Gardner D., (2002) New research confirms benefits of improved plant spacing in corn. *Crop Insights* 12(2), pp. 1–5;

[7]   Fanigliulo R., Pochi D., (2011), Air-Flow Distribution Efficiency of a Precision Drill Used in the Sowing of Different Graded Seeds, *Journal of Agricultural Science and Technology* B 1, pp. 655-662;

[8]   Gângu V., Cojocaru I., Marin E., Sorică C., Dobrin I., Prodan M., Jinga V., (2008), Innovative technologies for sowing and fertilizing weeding plants on ridges or directly in stubble field, *INMATEH - Agricultural Engineering*, Vol. 24, No. 1, pp. 13–22;

[9]   Glenn F.B., Daynard T. B., (1947), Effects of genotype, planting pattern, and plant density on plant-to-plant variability and grain yield of corn, *Canadian J. Plant Sci.* 54, pp. 323–330;

[10] Karayel D., Barut Z. B., Ozmerzi A., (2004), Mathematical Modelling of Vacuum Pressure on a Precision Seeder, *Biosystems Engineering,* Volume 87, Issue 4, pp. 437–444;

[11] Karimi H., Navid H., Mahmoudi A., Besharati B. (2018). Estimation of precision planting indexes using an acoustic system, *Research in Mechanics of Agricultural Machineries*. 7(2), pp. 1-12;

[12] Kocher M. F., Coleman J. M., Smith J. A., Kachman S. D., (2011), Corn seed spacing uniformity as affected by seed tube condition, *Applied Eng. in Agric.* 27(2), pp. 177–183;

[13] Kornienko S., Pashenko V., Melnik V., Kharchenko S., Khramov N., (2016), Developing the method of constructing mathematical models of soil condition under the action of a wedge, *Eastern-European Journal of Enterprise Technologies,* Vol. 5, Issue 7, pp. 34–43;

[14] Lauer J. G., Rankin M., (2004), Corn Response to Within Row Plant Spacing Variation, *Agron. Journal*, 96, pp. 1464–1468;

[15] Li D., Geng D., Ma B., Li Q., Wang Zh., (2013), Study on Performance Monitoring System of Corn Precision Seeder, *Journal of Agricultural Mechanization Research*, vol 11, pp. 71–74;

[16] Liu W., Tollenaar M., Stewart G., Deen W., (2004), Impact of planter type, planting speed, and tillage on stand uniformity and yield of corn, *Agron. J.* 96, pp. 1668–1672;

[17] Marin E., Bolintineanu Gh., Sorică C., Manea D., Herak D., Croitoru Ş., Grigore I., (2014), Scientific researches on the qualitative working indexes of the sowing body of a modern technical equipment for sowing weeding plants, *INMATEH - Agricultural Engineering*, vol. 42 (1), pp. 19–26;

[18] Miller E. A., Rascon J., Koller A., Porter W. M., Taylor R. K., Raun W. R., Kochenower R., (2012), Evaluation of Corn Seed Vacuum Metering Systems, Written for presentation at the 2012 *ASABE Annual International Meeting,* Dallas, Texas, July 29 – August 1, Paper Number: 12–1337167;

[19] Mogilnay O., Paschenko V., Kharchenko S., Domashenko V., Siedykh K., (2018), Mathematical modelling of operational stability of sowing machines' mechanical systems, *Eastern-European Journal of Enterprise Technologies* ISSN 1729-3774 4/1 (94), pp. 37–46;

[20] Nielsen R. L., Effect of Plant Spacing Variability on Corn Grain Yield. West Lafayette, *Ind.: Purdue University Department of Agronomy* (2004),
       http://www.agry.purdue.edu/ext/corn/research/psv/Update2004.pdf.;

[21] Singh R. C., Singh G., Saraswat D. C., (2005), Optimisation of Design and Operational Parameters of a Pneumatic Seed Metering Device for Planting Cottonseeds, *Biosystems Engineering*, 92 (4), pp. 429–438;

[22] Şerbu L., (1998), *Research on establishing the disturbing factors of the precision of sowing mechanized plants and their degree of influence*, *PhD Thesis*, University Politehnica of Bucharest, 1998;

[23] Xiaoyan D., Xu L., Caixia S., Haidong H., Qingxi L., (2010), Mathematical model and optimization of structure and operating parameters of pneumatic precision metering device for rapeseed, Journal of Food, *Agriculture & Environment* Vol.8 (3&4), pp. 318–322;

[24] Yazgi A., Degirmencioglu A., Bayram E., (2010) Optimisation of the Seed Spacing Uniformity Performance of a Precision Seeder Using Spherical Materials and Response Surface Methodology, An *ASABE Meeting Presentation*, Paper Number: 1008560.

IMPROVING THE EFFICIENCY OF WOOD CHIPPING OPERATIONS
/
ПОВЫШЕНИЕ ЭФФЕКТИВНОСТИ ПРОЦЕССОВ ПРОИЗДВОДСТВА ДРЕВЕСНОЙ ЩЕПЫ

Igor Grigorev *[1)]*, *Anatoly* Shadrin [2)], *Anna* Voronova [3)], *Nikolay* Kostyukevich [2)],
Dmitry Levushkin [2)], *Vyacheslav* Borisov [2)], *Roman* Diev [2)] [1]
[1)] Yakut State Agricultural Academy, Russian Federation;
[2)] Moscow State Technical University. N. E. Bauman (Mytishchi branch), Russian Federation;
[3)] Petrozavodsk State University, Russian Federation
Tel: 89217513866; E-mail: grigorev.igor@yahoo.com
DOI: https://doi.org/10.35633/inmateh-61-24

ABSTRACT
The paper presents a novel approach to the problem of utilizing wood chips as a valuable raw material. It shows how advances in machine vision can enable the conversion of wood chips from waste to a valuable resource. Empirical dependencies that are used to calculate the slip velocity of wood chips on the walls of the tank have been obtained. The problems of particle–fluid and particle–particle interactions within the flow are solved. Findings may be applied not only in countries with traditionally developed wood industries but also in many others.

АННОТАЦИЯ
В работе представлен новый подход к проблеме использования древесной щепы как ценного сырья. Показано, как на базе достигнутых успехов в деле машинного зрения можно из древесной щепы – отхода сделать древесную щепу – ценное сырьё. Получены эмпирические зависимости, которые были использованы для расчета скорости скольжения древесной щепы на стенках резервуара. Решена задача коллективного взаимодействия потока щепы между собой и с несущим флюидом. Результаты работы могут быть использованы не только в странах с традиционно развитой древесной промышленностью, но и во многих других.

INTRODUCTION

In recent years, approaches to the problem of sorting wood chips have been increasingly gravitating towards solutions based on machine vision *(Verheyen et al., 2016, Kuchin et al., 2020)*. Sorting becomes especially important if production involves substandard wood waste, as this process has a strong and positive environmental effect. Secondary wood that has no defects can serve a good source of wood chips for the chipboard production *(Merrild and Christensen, 2009)*. Finding application for this type of material reduces CO2 emissions during the creation of construction supplies. Secondary wood is usually very dry as compared to primary wood, and the chipboard industry uses 15% less energy when using secondary wood chips.

Designing mathematical models for the movement of wood chips will help find the optimal conditions for better productivity. For comparison, other authors *(Rößler et al., 2018)* presented a simulation of moving wood chips and resin droplets within a resin blending mixer. In particleboard production, the mixing of wood chips and resin droplets is a sub-process called gluing or resin metering (*Papadopoulos, 2006*). *Rudak et al. (2018)* modelled the movement of wood chips with the aim of ensuring production safety. *Polyanin et al. (2019)* partially solved our problem while laying emphasis on the problem of wood chips sorting. *Prosvirnikov*

---

[1]
*Grigorev Igor, Ph.D. Techn. Sci.; Shadrin Anatoly, Ph.D. Techn. Sci.; Voronova Anna, Cand. Techn. Sci.; Kostyukevich Nikolay;
Levushkin Dmitry, Cand. Techn. Sci.; Borisov Vyacheslav, Cand. Techn. Sci.; Diev Roman, Cand. Techn. Sci.*

et al. (2017) discussed mechanical changes that occur in wood when chipping. The geometry of resultant wood chips has been modelled too *(Fomin, 2017)*.

The wood chip-fluid interaction was considered by *Scherer et al. (2016)*, but the present study takes the behaviour of wood chips inside the unit into account in greater detail, i.e., we investigated the collective effect of chip-chip interaction in a semi-empirical way. The importance of mathematical modelling of timber processing operations is emphasized by *Rahman et al. (2018)*. The mentioned research demonstrated the increment of the product cost and the overall improvement in economic efficiency after mathematical optimization of the production process. *Agu et al. (2019)* contributed undertakings associated with the wood chip-fluid interaction modeling.

Wood chip products are usually transported by pneumatic conveyors *(Kaplan and Celik, 2018)*. However, these systems also have a number of drawbacks, among them is the formation of dead zones, especially in wood chip storage tanks *(Alakoski et al., 2016)*. Eliminating these shortcomings is essential to improve the efficiency of production lines, since the occurrence of dead zones may negatively affect the flow behaviour of wood chips, resulting in a blockage. The accumulation of wood chips in a tank together with wood dust and the overheating of electric air pumps significantly increase the fire risk. Theoretical studies relate mainly to the movement of elements of a regular shape and are based on the mathematical models for granular media that have neither analytical solutions, nor calculation methods, nor closing relations *(Rahman et al. 2018)*. Experimental studies of the gravity-driven movement are qualitative and relate mainly to the model elements, which does not allow for the application of results in the practical context. The aim of this paper is to introduce a new approach to the problem of utilizing wood chips as a valuable raw material. Specifically, the paper presents an algorithm for deciding on an optimal travel mode of wood chips in tanks with axial symmetry, which may be of use when designing tanks with only one discharge hole.

MATERIALS AND METHODS

In terms of potential and viscous movement of chipped wood that is dependent on the structural and physico-mechanical properties of material being pushed, the model based on Navier-Stokes equations is of main interest. The movement of falling material in the gravitational field of the tank is considered a non-Newtonian fluid with a viscosity corresponding to the apparent viscosity of the granular medium. The system of equations for the symmetric movement relative to the vertical axis of the tank, with the stream function ψ and the vortex function ω, in the coordinate system ($z;r$) is as follows (*Bedrossian*, *2016*):

$$\rho + r^2 \left[\frac{\partial}{\partial z}\left(\frac{\omega}{r}\frac{\partial \psi}{\partial r}\right) - \frac{\partial}{\partial r}\left(\frac{\omega}{r}\frac{\partial \psi}{\partial z}\right) \right] = \frac{\partial}{\partial z}\left[r^3 \frac{\partial}{\partial z}\left(\frac{\mu+\omega}{r}\right) \right] + \frac{\partial}{\partial r}\left[r^3 \frac{\partial}{\partial r}\left(\frac{\mu+\omega}{r}\right) \right] \tag{1}$$

$$\omega = -\frac{1}{r}\left(\frac{\partial^2 \psi}{\partial r^2} + \frac{\partial^2 \psi}{\partial z^2} - \frac{1}{r}\frac{\partial \psi}{\partial r} \right) \tag{2}$$

where:

ρ is the apparent density of the granular medium, [kg/m^3];

μ is the apparent viscosity of the granular medium, [Pa·s].

Equations (1) and (2) are related and non-linear. They were solved numerically using the finite-difference methods (FDM). In contrast to a viscous fluid with a velocity between the fluid and the solid wall assumed to be zero, a granular medium does not meet this condition. Depending on the value of the wall surface roughness, which is taken into account by the external friction coefficient f, the slip velocity of particles in the vertical and inclined channel of the conical tank can vary from zero to the final value. On the solid boundary (vertical and inclined walls), the value of the vortex function was set as follows.

For the impermeable wall, the stream function was ψ = const, which corresponded to the total pass on the region under consideration. The vortex function ω for the inclined wall corresponded to the conical bottom of the vertical cylindrical tank. To solve the mathematical model, a program was developed for calculating the movement of chipped wood with axial symmetry in a tank with a central discharge hole. The boundary condition for the corresponding vortex function was set as follows:

$$\omega_N = \frac{2}{r \, tg\,(\delta_\_)}\left(\frac{\partial^2 \psi}{\partial r \partial z} \right) - 2\left(\frac{1}{r}\frac{\partial^2 \psi}{\partial r^2} - \frac{1}{r^2}\frac{\partial \psi}{\partial r} \right) \tag{3}$$

where:

δ is external friction angle.

Experimental studies to find the coefficients of external and internal friction were carried out using a shearing apparatus consisting of a shear box, dynamometer and a drive (Fig.1).
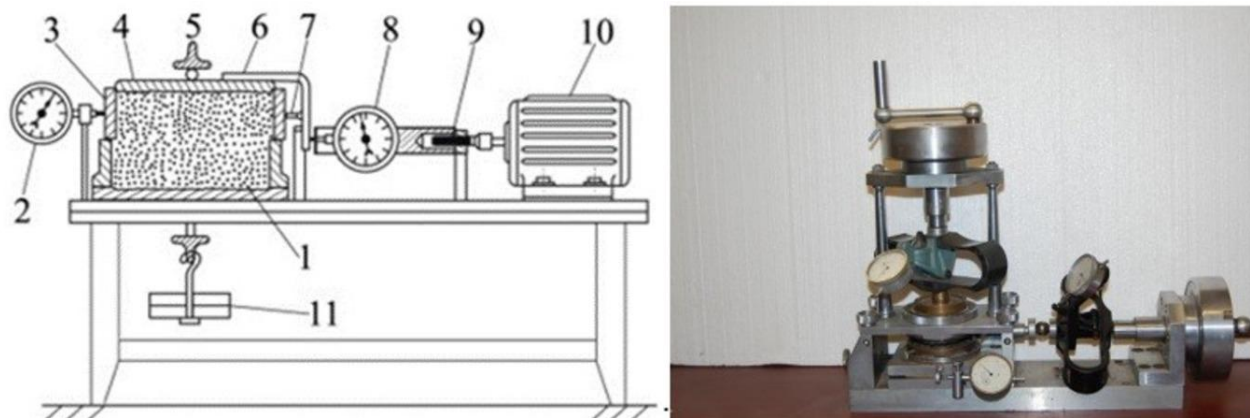
Fig. 1 - A shearing apparatus (schematic view)

1- fixed bottom platen; 2- a dial indicator ;3- a movable side platen, 4 -movable upper platen, 5 - a bent arm; 6,7,8 - a 0.05 N dynamometer,9- a drive, 10 - shear box; 11- weights.

The shearing apparatus allows for measuring the coefficient of internal friction and the shear resistance of the fluid. To find the coefficient of external friction, the stationary half of the shear box was replaced with a wall material model.

The movement of wood chips was experimentally studied on two units, industrial and pilot. The industrial unit was a cylindrical tank feeding wood chips into the pneumatic conveying system. The pilot unit was a physical simulator (Figure 2). The design of the simulator showing a cross-sectional view of a cylinder-conical tank made it possible to capture photos and video of the wood chips and model objects (i.e. coloured balls of varying sizes) moving through the tank.
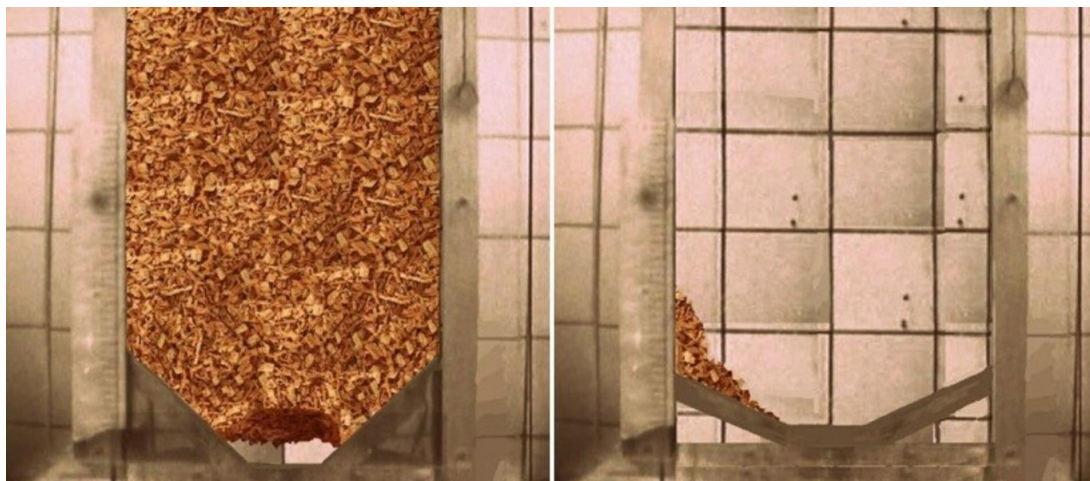
Fig. 2 - A cylinder-conical tank simulator

The bulking factor F_b was investigated on a physical simulator using the method of polynomial least squares. The results are presented in Figure 3. The dependence of the bulking factor on the coordinate was expressed as follows:

$$F_{b/axos} = 0.19 \cdot \bar{z}^3 - 0.44 \cdot \bar{z}^2 + 0.265 \cdot \bar{z} + 0.31 \tag{4}$$

$$F_{b/wall} = 0.0023 \cdot \bar{z}^3 + 0.061 \cdot \bar{z}^2 - 0.132 \cdot z + 0.39 \tag{5}$$

To identify the effect of specific factors on the physico-mechanical characteristics of the fluid passing through the tank, the following parameters of wood chips were measured: particle size, water content, and temperature. As it turned out, the bulking factor and the friction coefficients were bound in a positive correlation. The higher the bulking factor, the higher the friction coefficients.
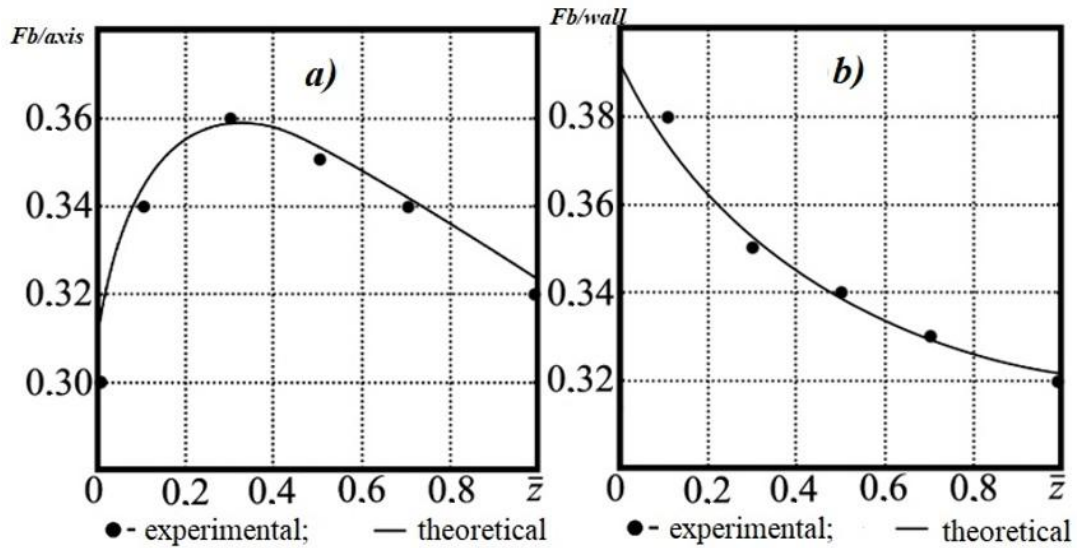
Fig. 3 - The bulking factor distribution (a) along the axis of the tank; b) along the tank wall

The shear resistance K value also increases with the bulking factor F_b and the compaction load P. The coefficients of internal and external friction, however, were not dependent on the compaction load. The theoretical angles of internal δ_+ and external δ_- friction were determined by the following formula:

$$\delta_{+(-)} = Arc \sin\left(F_b \left| \frac{a}{\frac{\partial F_b}{\partial z}} - \frac{b}{\frac{\partial F_b}{\partial r} + B} \right| \right)$$
(6)

where: $a = 5.2897$; $A = 3.2058$; $b = 0.00019$; $B = -0.00033$ are constants.

RESULTS

Experimental measurement of the coefficients of internal and external friction (Figure 4) were carried out using a shearing apparatus.
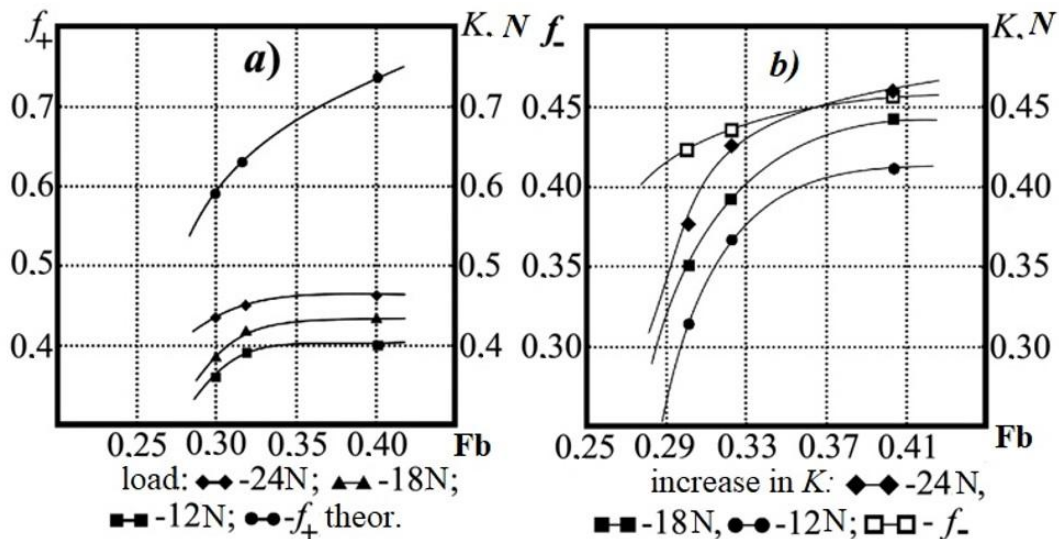
Fig. 4 - Dependence between friction coefficients and bulking factor
(a) internal friction coefficient; b) external friction coefficient)

The physico-mechanical properties of chipped wood demonstrated dependence not only on its structure but also on the fractional size distribution of wood chips, their water content, and temperature (Fig.5).
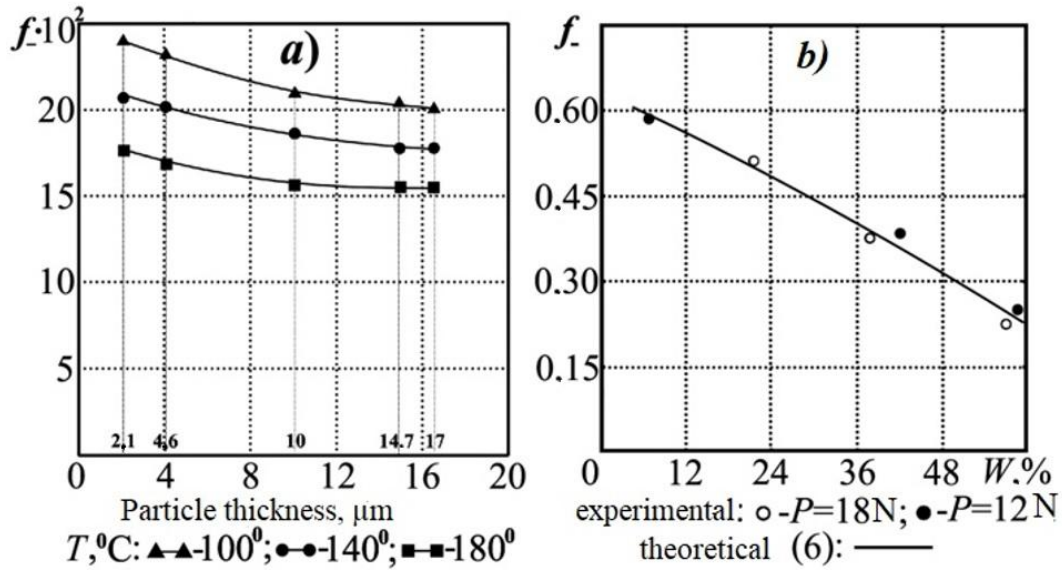
**Fig. 5 - The dependence of external friction coefficient on the following parameters of wood chips:
temperature (a) and water content (b)**

In addition to the experimental dependence of the external friction coefficient *f*, Figure 5b shows a polynomial dependence (7):

$$f_W = 0.634 - 0.622 \cdot W - 0.092 \cdot W^2 \qquad (7)$$

Experimentally, the study revealed dependence between the movement of wood chips and the following parameters:
– *transportation parameters:* discharge intensity; the number of discharge holes; and the way in which wood chips are fed into the tank;
– *tank geometry:* the angle of inclination of walls in the conical bottom; transition radius defining the transition of the cylindrical wall to the conical bottom; transition radius defining the transition of the conical bottom to the cylindrical channel of a discharge hole; the presence/absence of reinforcement on the inner walls of the cylindrical section (grooves, protrusions, etc.);
– the ratio of cylindrical section diameter to the equivalent diameter of a chip, D/d_e;
– the ratio of cylindrical section diameter to the discharge hole diameter, D/D_d;
– the ratio of the discharge hole diameter to the equivalent diameter of a chip, D_d/d_e;
– the relative fill height, H/D;
– *physico-mechanical parameters of wood chips*: particle density; bulking factor; coefficients of internal and external friction.

To eliminate the formation of a dead zone with wood chips accumulating before the hole in a mound arrangement, the D_d / d_e ratio was calculated by the following formula:

$$\frac{D_d}{d_e} = \frac{\sigma \cdot f_+ f_-}{p \cdot g \cdot (1 - F_b) \cdot \delta} \qquad (8)$$

The graphical data in Figure 5b showed that the minimum relative diameter of a discharge hole depended on the maximum length of the particle passing through it *l*.
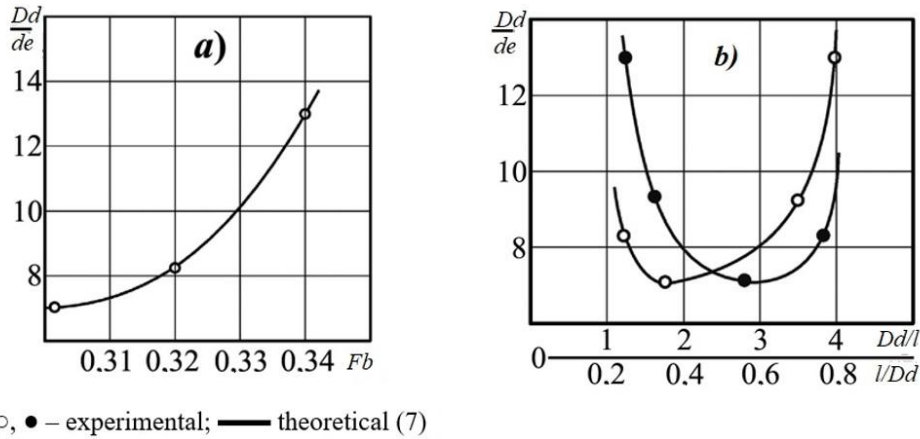
**Fig. 6 - The dependence of a relative discharge hole diameter on the bulking factor (a)
and the relative particle size (b)**

With l/D_d of 0.56, the minimum value of the D_d/d_e ratio will be 6.99. There is a negative correlation between these two dependences. With larger particles, the likelihood of a dead zone was higher. With smaller particles, the bulking factor increased and thus caused the growth of the internal friction coefficient f_+. The implication was a dead zone.

Note that the equation (7) does not take into account the effect of the fill height H and the cross-sectional diameter of the cylindrical section of the tank D_c. After substituting these two parameters into the equation (7), the resultant dependence for the active flow channel diameter D_f can be expressed as follows:

$$D_f = D_{d\,min} + k_1 \cdot \left(\frac{H - k_2 \cdot D_c}{1 + k_3 \cdot tg\theta}\right) \cdot tg(\theta) \tag{9}$$

where: $D_{d\,min}$ is the minimum discharge hole diameter acceptable to ensure a discharge of wood chips without the formation of a dead zone; k_1, k_2, k_3, θ – experimental coefficients.

As it can be seen from formulas (7) and (8), the active flow channel diameter can be increased by adding to the fill height H and to the value of the H/D_c ratio.

The simulation and experimental results of the fluid movement analysis are presented in Figure 6. It turned out that theoretical and experimental trajectories of a wood chip mass almost match. As per the results of theoretical calculation and physical simulation (Figure 7), modifications to the industrial tank were introduced (Figure 8). It was decided to install a fill height control device because changing the discharge hole diameter would require a cost-intensive modification of various metal parts. The final solution is cheap and efficient.

a) without dead zone;   b) with dead zone (blank space)
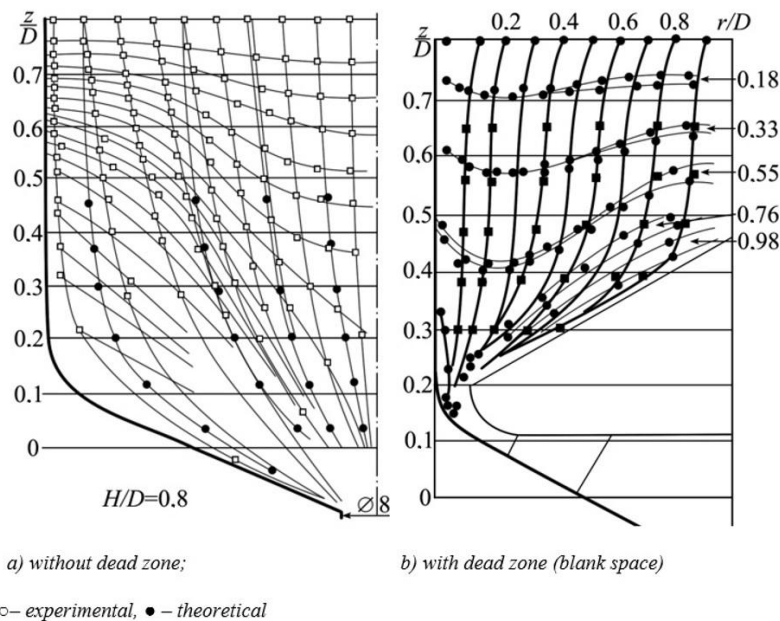
○– experimental, ● – theoretical

**Fig. 7 - A comparative presentation of theoretical and experimental trajectories of chipped wood masses
passing through the slope section of the cylinder-conical tank**

Fig. 8 - A modified industrial tank assembly

CONCLUSIONS

The study offers a novel approach to the problem of efficient and reliable pneumatic conveyance of wood chips. Empirical dependencies have been obtained that were used to calculate the slip velocity of wood chips on the walls of the tank. Tanks are recommended to have a conical bottom with an angle of inclination between 25° and 30° to avoid the formation of dead zones. Additionally, a ratio of tank diameter to discharge hole diameter is recommended to be ≤ 60, that is, a tank shall have a diameter that does not exceed 60 diameters of the discharge hole. The paper builds a semi-empirical simulation of the wood chips flow that was monitored throughout the entire production process from the sorting phase. The problems of particle-fluid and particle-particle interactions within the flow are solved. Using the proposed approach will improve the reliability of pneumatic conveyance with resultant savings in downtime.

ACKNOWLEDGEMENT

REFERENCES

[1] Agu, C. E., Tokheim, L. A., Pfeifer, C., & Moldestad, B. M., (2019), Behaviour of biomass particles in a bubbling fluidized bed: A comparison between wood pellets and wood chips. *Chemical Engineering Journal*, 363, 84-98.

[2] Alakoski, E., Jämsén, M., Agar, D., Tampio, E., & Wihersaari, M., (2016), From wood pellets to wood chips, risks of degradation and emissions from the storage of woody biomass–A short review. *Renewable and Sustainable Energy Reviews*, 54, 376-383.

[3] Bedrossian, J., Masmoudi, N., & Vicol, V., (2016), Enhanced dissipation and inviscid damping in the inviscid limit of the Navier–Stokes equations near the two-dimensional Couette flow. *Archive for Rational Mechanics and Analysis,* 219(3), 1087-1159.

[4] Fomin, A. A., (2017), Determining undeformed chip thickness models in milling and its verification during wood processing. In *Solid State Phenomena,* Vol. 265, pp. 598-605, Trans Tech Publications Ltd.

[5] Kaplan, O., & Celik, C., (2018), An experimental research on woodchip drying using a screw conveyor dryer. *Fuel*, 215, 468-473.

[6]   Kuchin, V., Dvoynikov, M., & Nutskova, M., (2020), Isolation through a viscoelastic surfactant of a fracable hydrocarbon-containing formation. In *Journal of Physics: Conference Series*, Vol.1478, p.012022.

[7]   Merrild, H., & Christensen, T. H., (2009), Recycling of wood for particle board production: accounting of greenhouse gases and global warming contributions. *Waste Management & Research*, 27(8), 781-788.

[8]   Papadopoulos, A. N., (2006), Experimental particleboard made from wood-bark mixtures and bonded with EMDI resin. *Journal of the Institute of Wood Science*, 17(4), 223-224.

[9]   Polyanin, I. A., Makarov, V. E., Egorov, A. V., Lysyannikov, A. V., Kaizer, Y. F., Voldaev, M. N., & Stepanova, K. S., (2019), Improving the technology of sorting wood chips obtained from stump and substandard wood by resin content. In *Journal of Physics: Conference Series*, Vol.1399, No.4, p.044076, IOP Publishing.

[10]   Prosvirnikov, D. B., Baigildeeva, E. I., Sadrtdinov, A. R., & Fomin, A. A., (2017), Modelling heat and mass transfer processes in capillary-porous materials at their grinding by pressure release. In *2017 International Conference on Industrial Engineering, Applications and Manufacturing (ICIEAM),* pp. 1-7, IEEE.

[11]   Rahman, M., Avelin, A., Kyprianidis, K., Jansson, J., & Dahlquist, E., (2018), Model based Control and Diagnostics strategies for a Continuous Pulp Digester. *Proceedings of the TAPPI PaperCon, Charlotte, NC, USA*, pp.15-18.

[12]   Rößler, C., Riegler, M., & Breitenecker, F., (2018), Modeling and simulation of moving wood chips and resin droplets within a resinating mixer using lattice gas cellular automata. *IFAC-PapersOnLine*, 51(2), 55-60.

[13]   Rudak, P., Barcik, S., Ekevad, M., Rudak, O., Vanco, M., & Stefkova, J., (2018), Motion of chips when leaving the cutting zone during chipboard plane milling. *BioResources,* 13(1), 647-661.

[14]   Scherer, V., Mönnigmann, M., Berner, M. O., & Sudbrock, F., (2016), Coupled DEM–CFD simulation of drying wood chips in a rotary drum–Baffle design and model reduction. *Fuel*, 184, 896-904.

[15]   Verheyen, M., Beckers, W., Claesen, E., Moonen, G., & Demeester, E., (2016). Vision-based sorting of medium density fibreboard and grade A wood waste. In *2016 IEEE 21st International Conference on Emerging Technologies and Factory Automation (ETFA),* pp. 1-6, IEEE.

DEFECTS DETECTION METHOD BASED ON K-MEANS WITH PRIOR KNOWLEDGE FOR BIOMASS PARTICLES
/
基于先验知识的 *Kmeans* 聚类生物质颗粒缺陷检测方法

Wei Wang, YuanJuan Gong[*1) 1]
[1)] Shenyang Agricultural University, College of Engineering, Shenyang / China;
Tel: +86-024-88487057; E-mail: gongyjSYND@126.com
DOI: *https://doi.org/10.35633/inmateh-61-25*

ABSTRACT

Biomass particle is one of the most important solid briquette fuels for agricultural and forestry biomass energy. Temperature, pressure, moisture and discharge holes are important factors to control biomass particle forming. The inappropriate setting of the parameters or blocking of the discharge hole will lead to the defects of the biomass particles, such as too short or poor roundness or pits or cracks. In order to detect these defects automatically, this paper proposes a method based on K-Means with prior knowledge. Firstly, the inner boundary tracking region detection algorithm and filling algorithm are combined to extract the regions in the backlight image. The regions are divided into debris, independent biomass particle regions and adhesive biomass particle regions. Secondly, K-Means with prior knowledge is used to segment the adhesive regions to get the independent biomass particle regions. Finally, the features of the biomass particles are extracted to judge the type of defects. The proposed method has been tested on images acquired from the vision system of the ring roller pellet mill. Experimental results show the efficiency of the proposed method in high detection accuracy and short detection time.

摘要

生物质颗粒是农林生物质能源的一种重要的农林生物质能源固体成型燃料。温度、压力、水分和模孔是控制生物质颗粒成型的重要因素。如果参数设置不合适或者模孔堵塞，会造成生物质颗粒长度过短、圆度欠佳、凹坑、裂缝等缺陷。为了自动检测这些缺陷，本文提出一种基于先验知识的 Kmeans 聚类方法。首先，采用基于行扫描的内边界跟踪区域检测和填充算法提取生物质颗粒图像各独立区域。根据区域面积将各独立区域划分为秸秆碎屑、单独的秸秆颗粒区域和粘连的秸秆颗粒区域。其次，使用基于先验知识的 KMeans 算法将粘连的秸秆颗粒区域分割，得到独立的秸秆颗粒区域。最后，对各独立秸秆颗粒提取特征，并据此判断是否存在缺陷。算法在从秸秆颗粒生产线上采集的图片集合中进行验证。实验结果证明本文算法具有较快的检测速度和较快的检测正确率.

INTRODUCTION

It is recommended that farming and forestry resources be reformed into solid briquette fuels to become clean energy *(Zhang and Guo, 2016)*. The biomass particles, which are made of loose biomass by the ring roller pellet mill, are typical solid briquette fuels. The shape and density of them are set by the users according to the specific applications (*Ullah et al, 2019; Rudolfsson et al, 2017*). The production process needs to control the appropriate temperature, pressure, water and the discharge hole should be normal (*Shen L.L., 2016*). If there is something wrong with the parameters and the discharge hole, the defects such as short length, poor roundness, pits, cracks will appear. The traditional method to judge the problems rely on human eyes. As the ring roller pellet mill needs to be installed on the harvester, it is difficult for the users to repeatedly get on and off to check the status of the biomass particles *(Jackson et al, 2016)*. In addition, the users cannot analyse the status of every biomass particle intuitively. Machine vision is an effective way to detect defects, especially biomass particles which are not easy to observe directly *(Sabzi et al, 2020; Bhargava and Bansal, 2020)*. The vision system acquires the images of the biomass particles and judges whether the biomass particles are normal or defective. Because there is a lot of dust in the working condition,

---

[1] *Wei Wang, Ph.D. Stud.; YuanJuan Gong, Prof. Ph.D.*

the lens in the vision system are easy to be polluted, and the images will have a lot of noise, the vision system is put in a black box.

The vision system acquires images with backlight and front light. The images obtained by backlight and front light are used to extract independent biomass particles and features of them respectively. The proposed method is based on the imaging characteristics of biomass particles. Firstly, extract each region with the combination of inner boundary tracking region detection algorithm and filling algorithm. Secondly, get independent biomass particles by K-Means with prior knowledge. Finally, extract the features of the biomass particles and judge the status of biomass particles.

MATERIALS AND METHODS
Diagram

The diagram of the proposed method is shown in Fig. 1. As there is more than one region in the images, the inner boundary tracking algorithm *(Latson et al, 2001)* and filling algorithm are combined to improve the detection speed. The area of debris is much smaller than that of the biomass particle, so the debris can be abandoned if its area is smaller than a set threshold. For the adhesion regions, the segmentation is performed by K-Means *(Soua et al, 2017; Song et al, 2017)* with prior knowledge to get the independent biomass particles. The standardization and feature extraction are performed to the biomass particles in the images obtained under front light to judge their status. The ratio of different defects is computed to speculate the problem with the parameters and discharge hole. The parameters used in the method, such as the range of the permitted length and roundness, the parameters of convolutional neural network *(Moeskops et al, 2016)*, and so on, are obtained offline.
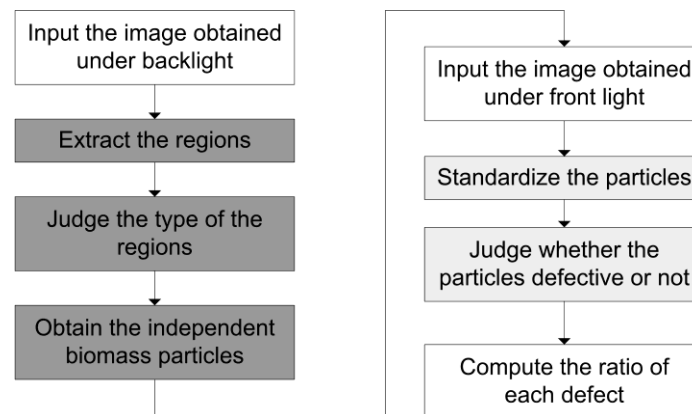
Fig. 1 - Outline of the proposed method

Image acquisition

The images are acquired with the vision system which is shown in Fig.2. There is a controller which can gather the biomass particles and put them on the backlight panel. The camera captures two times with backlight and front light respectively. The image captured under backlight gives clear boundaries which are suitable for region segmentation of the biomass particles. The image captured under front light provides detail textures that help extract the features of the biomass particles.
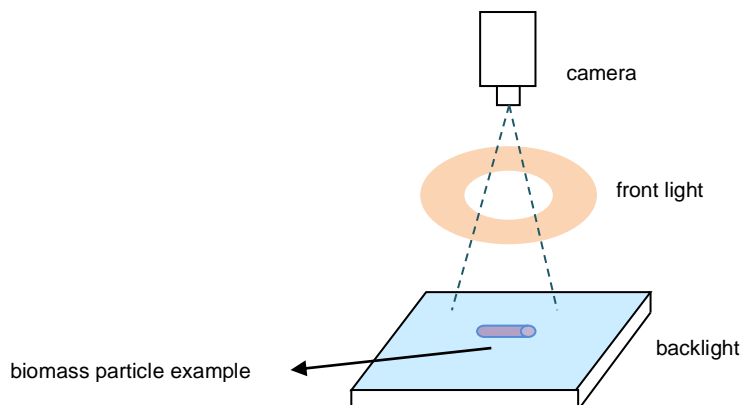
Fig. 2 – The vision system

Extraction of independent biomass particles

The contours of the regions are clear in the image acquired under backlight which is shown in Fig. 3. There are two problems: The first one is that the region should be filled once it was found to avoid being searched again as there are several regions in the image; The second one is that the biomass particles may stick together, so the segmentation should be done to get the independent ones.

For the former problem, the combination of the region extraction algorithm and filling algorithm is proposed. For the latter one, the K-Means with prior knowledge is used.

Fig. 3 - Image under the backlight

Region extraction

The combination of the region extraction algorithm and filling algorithm is as follows:

Step1: denote the number of the point of the inner boundary as n, set n = 0; denote the area of the region as a, set a = 0.

Step2: searching from the top and left of the image until a seed point, which is smaller than the threshold, is found; denote the seed point as P_n, n = n + 1; denote the moving direction from the former inner boundary point to the current one as d_{n-1}, set d_{n-1} = 7;

Step3: searching the eight neighbour of P_{n-1} from i until a point smaller than the threshold is found, otherwise, go to Step 8, in which, the starting number i is computed as Eq. (1):

$$i = \begin{cases} (d_{n-1}+7)\bmod 8 & \text{when } d_{n-1} \text{ is odd} \\ (d_{n-1}+6)\bmod 8 & \text{when } d_{n-1} \text{ is even} \end{cases} \tag{1}$$

where, d_n represents the moving direction from P_{n-1} to P_n.

Step4: judge whether Pn-1 is left inner boundary point or right inner boundary point: P_{n-1} is left inner boundary point when (d_{n-1} = 5) or (d_{n-1} = 6 and d_n ≠ 1) or (d_{n-1} = 7 and d_n ≠ 1and d_n ≠ 2); P_{n-1} is right inner boundary point when (d_{n-1} = 1 and d_n ≠ 7) or (d_{n-1} = 2 and d_n ≠ 5) or (d_{n-1} = 3 and d_n ≠ 1 and d_n ≠ 6);

Step5: fill to the right if P_{n-1} is left inner boundary point and to the left if P_{n-1} is right boundary point, otherwise, go to Step6; During the filling process, set a value larger than the threshold for the points smaller than the threshold and update a = a + 1 in turn until the last point is smaller than the threshold, set it as a boundary point and press it in stack;

Step6: set n = n + 1;

Step7: repeat Step2 – Step5;

Step8: take the boundary point in the stack as the seed point P_n in turn, repeat Step2 – Step7;

As the boundary points in the stack are used as the seed points, the inner boundary points are P_0 - P_{n-1}. These points are reordered in adjacent order to get the sequence of the inner boundary points. The area of the region is a + n. The regions with areas smaller than a threshold are abandoned as debris. The regions with areas larger than a threshold are considered as the adhesion biomass particles. The regions of the independent and adhesion biomass particles are shown in Fig.4.

Fig. 4 - Region of the independent and adhesion biomass particles

Extraction of independent biomass particles

Adhesion is inevitable as the biomass particles are cylindrical and they are free to move arbitrarily. The regions are segmented based on the K-Means with prior knowledge. The segmentation will use the gradient direction of the inner boundary points. So, the gradient lookup table shown in Fig.5 is used to save time. Fig.5a is the direction diagram and Fig.5b is the lookup table in which the abscissa and ordinate represent the horizontal and vertical gradient respectively. The detailed procedure is as follows:

a. gradient direction diagram　　　　　　*b. lookup table*
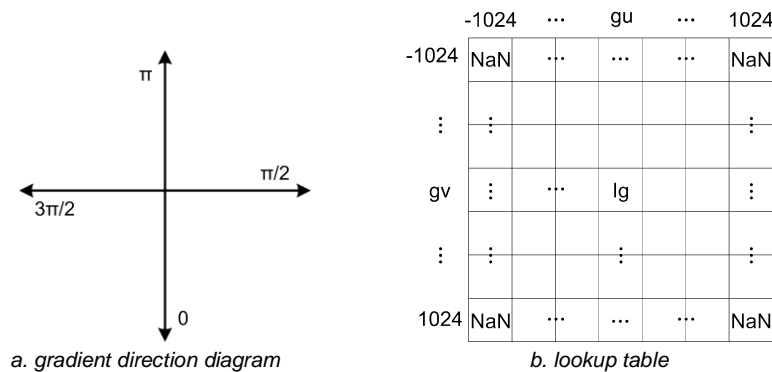
Fig. 5 - Gradient direction look up table

Step1: calculate the horizontal and vertical gradients of inner boundary points, and obtain the gradient direction of them according to the gradient direction lookup table;

Step2: calculate the number of clustering centres according to the area of the region, and select K clustering centres; initialize K sets to store the points of each class.

Step3: The inner boundary points are divided into each set corresponding to the nearest clustering centre points according to the gradient direction;

Step4: calculate the average gradient direction of each class and use them as new clustering centres;

Step5: repeat Step3-Step4 until the error is less than the set value;

Step6: the boundary points in each class are fitted with straight line; use the least square to eliminate the error points; the fitted straight segments with right length are saved;

Step7: select the straight line segment with parallel direction; calculate the distance of the straight line segment with parallel direction respectively; classify the straight line segments, that are closest and the distance of them is about the integral multiple of the average distance, into a group.

Step8: segment the region into several sub-regions according to the distance and length of straight line segments in each group.

Due to that, there are two straight line segments of each biomass particle, the number of clustering centre is calculated as (A / avrA + m) * 2, in which, A and avrA denote the area of current region and the average area of the regions, m denotes the surplus. As Step 6 does not consider the position of the points, the least square is used to eliminate the points that are not on the same line. Different cases should be considered in Step 8 according to the length and distance as follows and the examples in each step are shown in Fig. 5 in which the blue lines are the line segments L1, L2 in each group in Step 8 and the black lines are the supplemental lines and the dotted lines are the other line segments of the region:

Step1: calculate the distance of the two lines in the same group; if the distance meets the allowable distance of an independent biomass particle, go to Step 2, otherwise, go to Step 5;

Step2: if the length of the two lines meets the allowable length of an independent biomass particle, then connect the end points of the lines near each other to get an independent biomass particle region. The example is shown in Fig. 6a. Otherwise, go to Step 3;

Step3: if there is one line L1 which meets the allowable length, then extend another line so that the lines obtained by connecting its two end points with the end points of L1 be perpendicular to L1 to get independent sub-regions; The example is shown in Fig. 6b; otherwise go to Step 4;

Step4: if there are other lines intersected with the two lines, then connect their closer endpoints separately, otherwise, extend the line segment to the boundary of the region to obtain the independent sub-region; The example is shown in Fig. 6c;

Step5: supply line segments which are parallel to the lines of the group and the distance is multiple of average distance between the two line segments of the biomass particle to obtain the independent sub-region; The example is shown in Fig. 6d;

Step6: Search the boundary points around the sub regions; if there are boundary points, the supplied segments of the sub regions are replaced by them, otherwise, the supplied segments are saved.
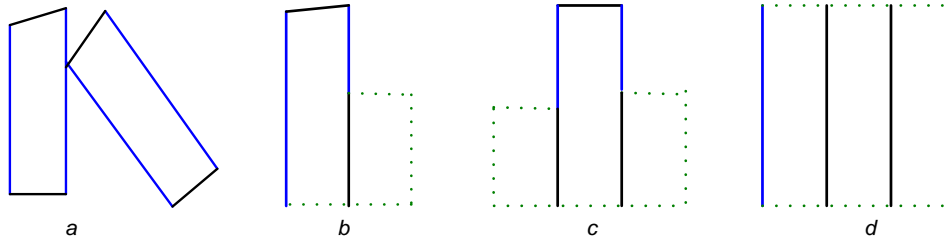
Fig. 6 - Examples of the different cases

The regions obtained with the steps above correspond to the independent biomass particles in the image acquired under front light. They are shown in Fig. 7 with different colour.
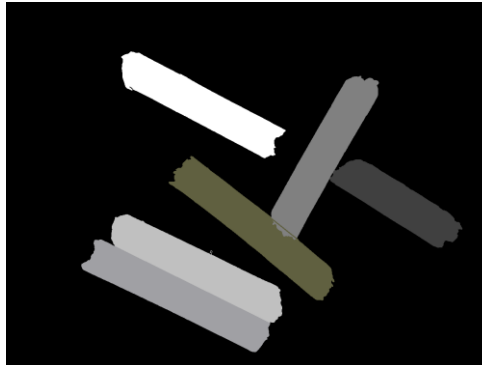
Fig. 7 - Regions of independent biomass particles

Defect detection

The defects are manifested in length, roundness, pits, cracks. The detection of the defects uses the image acquired under front light that is shown in Fig. 8 with boundary points drawn on. Firstly, judge whether the length and roundness meet the requirement; secondly, standardize biomass particles; finally, use convolutional neural network to extract the feature of the biomass particles and estimate the status of them. The detailed steps are as following:
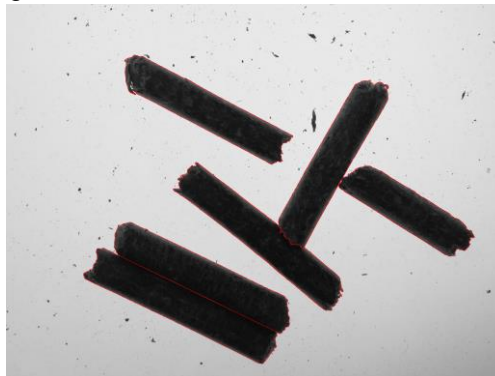
Fig. 8 - Image acquired under front light with boundary points drawn

Firstly, judge whether the length and roundness meet the requirement. The requirement is that the length and roundness of the biomass particle is within the allowable error range around the average length and average roundness. Average length refers to the average length of the two line segments of a single biomass particle. Roundness refers to the ratio of points on one line segment whose distance from another line segment meets the threshold. Average roundness refers to the average roundness of the independent biomass particle.

Secondly, biomass particles meeting the requirements of length and roundness are standardized. The biomass particle is rotated to the vertical state. The rotation angle is the angle between the straight line and the line segments of the biomass particle, as shown in Fig. 9. The rotated biomass particle is scaled according to the average distance of the line segments of the biomass particles offline.
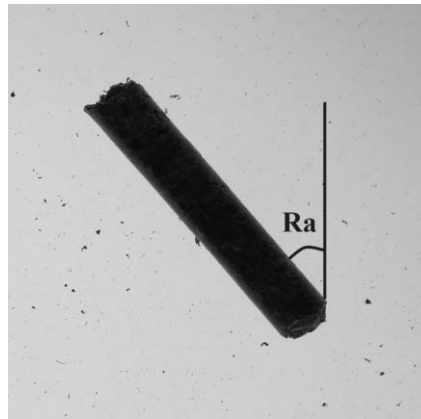
Fig. 9 - Rotation angle diagram

Finally, use the convolution neural network to extract the features of the single biomass particle and classify them. As the position and length are indefinite, overlap block is adopted to avoid the pits and cracks being divided into multiple blocks. The convolutional neural network is adopted to extract feature of each block. As long as one of the blocks is defective, the biomass particle is considered to have the same defects. The ratio of each defect of the image is computed after all biomass particles are detected. And the ratios will be sent to the controller to infer the problem.

RESULTS
Experimental results and discussion
Experimental setup

To verify the performance of the proposed method, the controller is equipped with 2.5 GHz CPU and 8.00GB RAM. The biomass used in this experiment is corn stalk. The images were acquired under different conditions by the vision system installed in the ring roller pellet mill of Liaoning Ningyue Agricultural Machinery Equipment Co., Ltd.. The number and type of different images are shown in Table 1. The pits are caused by the blocking of the discharge hole.

Number and type of images   **Table 1**

Type	Num	Main defect
a	5010	Length
b	5000	Roundness
c	5100	Crack
d	5000	pit
e	5000	No defect

"Type", "Num", represent "image type", "number of defective images"

Performance of proposed method

For the images in Table 1, the four defects were detected with the proposed method, namely, an image may have several defects. The image is considered to have length defect, roundness defect, crack defect, and pit defect when the ratio of biomass particles with length defect, crack defect, and pit defect exceed 3%, 2%, 5%, 3%, respectively. Different defects are shown in Fig. 10.

a. length   *b. roundness*   *c. crack*   *d. pit*   *e. normal*
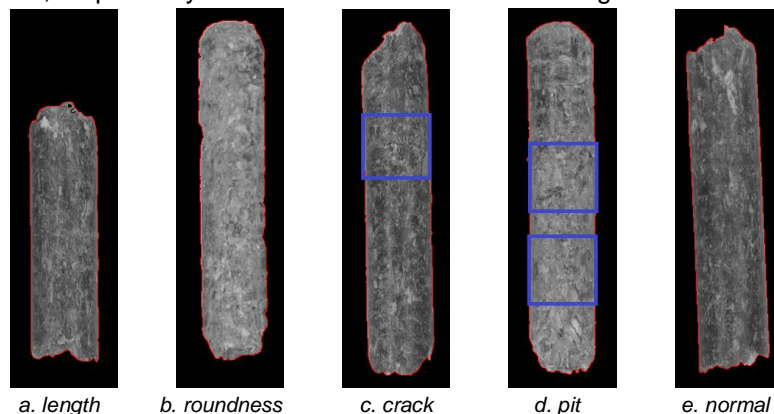
Fig. 10 – Examples of different defects

The experimental results are shown in Table 2, in which, "Type", "Num", "Ra" represent "image type", "number of defective images", "ratio of defective images". For the images whose main defect is length, the length defect detection accuracy is 100 percent and the roundness defect detection accuracy is 24.35% and there are some cracked images, which indicates that the main problem may be too much water and this can cause the collapse of the biomass particles to make the roundness unsatisfactory. For the images whose main defect is roundness, the roundness defect detection accuracy is 100 percent, and there are a few images that have length defect and crack defect, which indicates that the pressure may be unsuitable. For the images whose main defect is crack, the crack defect detection accuracy is 99.35 percent, and the problem may be too little water. As the crack can make the surface rough, the roundness defect accuracy reached 31 percent. The main reason for pit defect is the wear and blocking of the discharge hole. The surface of biomass particle may be rough when it has pit defect, so accuracy of the roundness defect reached 36 percent. The biomass particle may be detected as crack defect when the pit is too long. And the biomass particle will increase its length to meet the free-falling condition when the pit defect is serious. Hence, pit defect is also accompanied by length, roundness, and crack defect. It can be seen from table 2 that the detection accuracy does not reach 100 percent. Through the analysis of the wrongly detected images, the pit and crack defects are relatively few and in the other side of the camera so these defects cannot be detected. For the normal images, no defects are detected by the proposed method. In addition, the average time to detect an image is about 50.43 milliseconds which can meet the real time detection as to the ring roller pellet mill. It shows that the proposed method has a high accuracy and fast detection speed. The proposed method is suitable for the defect detection of the biomass particles made by different biomass. It can avoid the complicate manual operations and help the user improve work efficiency.

Results of the experiment   **Table 2**

Type	Length		Roundness		Crack		Pit		Avr. time (ms)
	Num	Ra (%)	Num	Ra (%)	Num	Ra (%)	Num	Ra (%)	
a	5010	100.00	1220	24.35	122	2.44	0	0.00	50.35
b	100	2.00	5000	100.00	150	3.00	0	0.00	50.89
c	66	1.29	1581	31.00	5067	99.35	15	0.29	50.38
d	9	0.18	1800	36.00	21	0.42	4992	99.84	50.23
e	0	0.00	0	0.00	0	0.00	0	0.00	50.33

CONCLUSIONS

An effective method is proposed to detect the defects of the biomass particles. It can assist the user to judge the problem of the ring roller pellet mill. The proposed method has three unique features:

(1) The first one is the combination of boundary tracking algorithm and filling algorithm which can run simultaneously to improve the detection speed.

(2) The second one is that the features of the biomass particles are used as prior knowledge of K-Means to divide to adhesive biomass particles.

(3) Finally, the process of the images under the backlight and front light is separate to extract the independent biomass particles' regions and detect defects. This benefit comes from the clear contour and texture of the images acquired under the backlight and front light respectively.

Experimental results reveal that the proposed method is effective for the defect detection of the biomass particles. The first one can also be used in other cases similar to the images of the biomass particle.

ACKNOWLEDGEMENT

REFERENCES

[1] Bhargava A., Bansal A., (2020), Quality evaluation of Mono & bi-Coloured Apples with computer vision and multispectral imaging, *Multimedia tools and applications*, online, Dordrecht/Netherlands (DOI: 10.1007/s11042-019-08564-3);

[2] Jackson J., Turner A., Mark T. et al., (2016), Densification of biomass using a pilot scale flat ring roller pellet mill, *Fuel Processing Technology*, vol.148, pp. 43-49, Ed. Elsevier, London/U.K.;

[3] Latson L.A., Powell K.A., Sturm B., et al., (2001), Clinical validation of an automated boundary tracking algorithm on cardiac MR images, *The International Journal of Cardiovascular Imaging*. vol.17(4), pp. 279-286, Dordrecht/Netherlands;

[4] Rudolfsson M., Larsson S.H., Lestander T.A., (2017), New tool for improved control of sub-process interactions in rotating ring die pelletizing of torrefied biomass, *Applied Energy*, vol.190, pp. 835-840, Ed. Elsevier, Oxford/England;

[5] Sabzi S., Javadikia H., Arribas J.I., et al., (2020), A three-variety automatic and non-intrusive computer vision system for the estimation of orange fruit pH value, *Measurement*, vol. 152, pp. 107298, Ed. Elsevier, Oxford/England;

[6] Shen L.L., (2016), *Forming Mechanism and extrusion pressure experiment study on rice straw briquetting machine with vertical ring die (*水稻秸秆压块立式环模成型机理及挤压力试验研究*)*, MSc dissertation, Jiangsu University, Jiangsu/China;

[7] Soua M., Kachouri R., Akil M., (2017), GPU parallel implementation of the new hybrid binarization based on K-means method (HBK)., *Journal of Real-Time Image Processing*, 2018, vol.14, no. 2, pp. 363-377, Berlin/Germany;

[8] Song T., Li J., Han X., et al., (2017), A quick Otsu – K-means algorithm for the internal pipeline detection, *ICM 2017: IEEE International Conference on Mechatronics & Automation*, Gippsland/Australia;

[9] Ullah A., Hong K., Gao Y., et al., (2019), An overview of Eulerian CFD modeling and simulation of non-spherical biomass particles, *Renewable Energy*, vol.141, pp. 1054-1066, Elsevier Science Publishers BV, Oxford/England;

[10] Moeskops P., Viergever M.A., Mendrik A.M., et al., (2016), Automatic segmentation of MR brain images with a convolutional neural network, *IEEE transactions on medical imaging*, vol.35(5), pp. 1252-1261, Institute of Electrical and Electronics Engineers Inc, Piscataway/U.S.A.;

[11] Zhang J., Guo Y., (2016), Physical properties of solid fuel briquettes made from Caragana korshinskii Kom, *Powder Technology*, vol. 256, pp. 293-299, Lausanne/Switzerland.

STRUCTURAL ANALYSIS WITH FINITE ELEMENTS OF A SUBSOILER WORKING PART
/
ANALIZA STRUCTURALĂ CU ELEMENTE FINITE A ORGANULUI DE LUCRU AL UNUI SUBSOLIER

Constantin G.A. [1)], Voicu Gh. *[1)], Olac B.[1)], Ilie F.[1)], Paraschiv G.[1)], Stefan V.[2)], Musuroi G. [1)] [1]
[1)] University Politehnica of Bucharest, Faculty of Biotechnical Systems Engineering / Romania
[2)] INMA Bucharest / Romania
Tel: 0724715585; E-mail: ghvoicu_2005@yahoo.com

Keywords: finite element analysis, subsoiler working part, stress concentrators, equivalent stress

ABSTRACT

The paper presents the way to perform a static analysis with finite elements for the working part of a subsoiler, together with its results. The analysis was made for two different working regimes: a regime in which the working depth of the subsoiler is 0.3 m, and the speed of advance of the aggregate during the work is 2.777 m/s and one in which the working depth is 0.4 m, and the speed of advance is 2.222 m/s. The results of this paper are addressed first of all to the designers of agricultural machines for soil tillage, but not only.

REZUMAT

În lucrare este prezentat modul de realizare a unei analize statice cu elemente finite pentru organul de lucru al unui subsolier, împreună cu rezultatele acesteia. Analiza a fost realizată pentru două regimuri de lucru diferite: un regim în care adâncimea de lucru a subsolierului este de 0,3 m iar viteza de înaintare a agregatului în timpul lucrului este de 2,777 m/s și unul în care adâncimea de lucru este de 0,4 m iar viteza de înaintare este de 2,222 m/s. Rezultatele din această lucrare se adresează în primul rând proiectanților de mașini agricole de lucrat solul, dar nu numai.

INTRODUCTION

Manufacture of working parts of soil tillage machines (and not only) in optimal conditions, assumes that the model made by the design engineers will go through some defined processes. This are: modeling, simulation and analysis processes with the help of CAD software (Computer Aided Design). All of this before sending them to the actual execution. Researchers at home and abroad have contributed to the database of these types of analyses by making it possible, lately, obtaining results as close to reality as possible (*Cardei and Konstandinov, 2012, Gheorghe et al., 2016; Kadam and Chhapkane, 2017; Gheorghe et al., 2018; Biris et al, 2016; Gheorghita et al., 2018, Petru and Konstandinov, 2012, Nagy et al, 2011, Mollazade and Jafari, 2010, Xin et. al, 2013*). The finite element method is a numerical method that can be used to accurately determine solutions to complex engineering problems. Currently, the finite element method is considered to be one of the best methods for efficiently solving a wide variety of practical problems, involving partial differential equations, (*Biris, 2005*). The essence of the finite element method is the discretization of a domain or a region in sub-domains or sub-regions (finite elements). In fig.1 are presented the stages of the analysis using the finite element method.

Input (Pre-processing)	Processing	Output (Post-processing)
- Nodal coordinates; - Types of supports; - Blockages (boundary conditions); - Loads (mechanical, thermal, etc.); - Material properties; - The shape, type and dimensions of the finite elements.		- Stress; - Displacements; - Temperatures; - Current function; - Electric / magnetic flux.
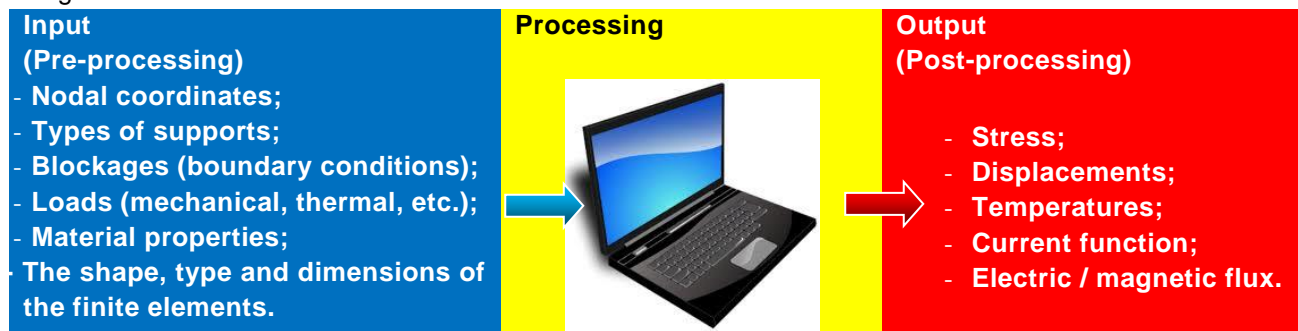
Fig. 1 - Analysis stages using the finite element method, adapted after *Lates (2008)*

---

[1] *Constantin G.A., Lect. Ph.D. Eng.; Voicu Gh., Prof. Ph.D. Eng.; Olac B., PhD.Stud.; Ilie F., Prof. Ph.D. Eng.;*

Paraschiv G., Prof. Ph.D. Eng.; Stefan V, Phd.Stud. Eng; Musuroi G., Lect. Ph.D. Eng.

The purpose of this 3D numerical simulation study with finite elements was to simulate the behaviour of the working part structure of a subsoiler. The structure being subjected to stresses that arise during operation for two different working regimes.

MATERIALS AND METHODS

The role of the working part of a subsoiler is well known. It has to work at slightly greater depths to loosen the soil in depth and to break that layer of hardpan that prevents water from infiltrating the soil. Due to the working regime in the working parts, quite high stresses appear.

In the first stage of this study, the three-dimensional geometric model of the working part for a Maschio Gaspardo subsoiler, Artiglio 250/5 model, was realized. For this purpose, 3D modelling was performed with the Solid Works Premium 2016 S.P. 0.0 parameterized design program.

The three-dimensional modelling of the working part was performed in the "Parts" module of the design program, in fig. 2 different views of the obtained model are presented, as well as the Solid Works program interface.
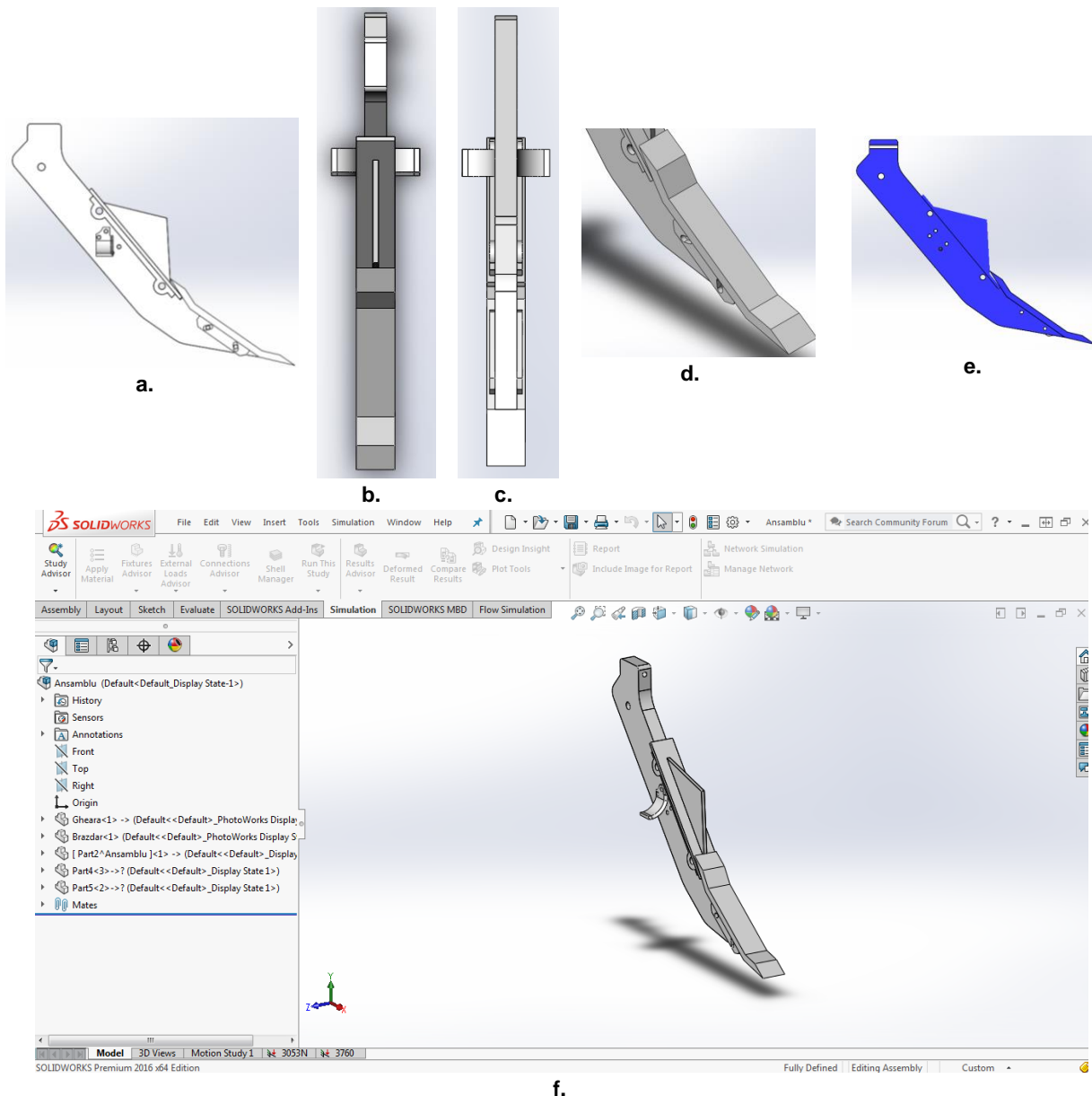
Fig. 2 - Views of the working part from the subsoiler Artiglio

a. Side view, b. top view, c. bottom view, d. detail on the coulter, e. longitudinal section, f. isometric view of the working part, as well as the interface of the software used

After completing this step, we proceeded to the next step which was to introduce the 3D geometric model of the working part in the "Simulation" module of the design program. According to *Gheorghe et al., (2019),* the material most commonly used in the fabrication of the working part of the subsoilers is the 16MnCr5 alloy. In table 1 the characteristics of the material used in the manufacture of the working part are presented, and in fig. 3 the fatigue resistance curve of this material is presented.

S-N Curve

4669.07, 3.34644e+008
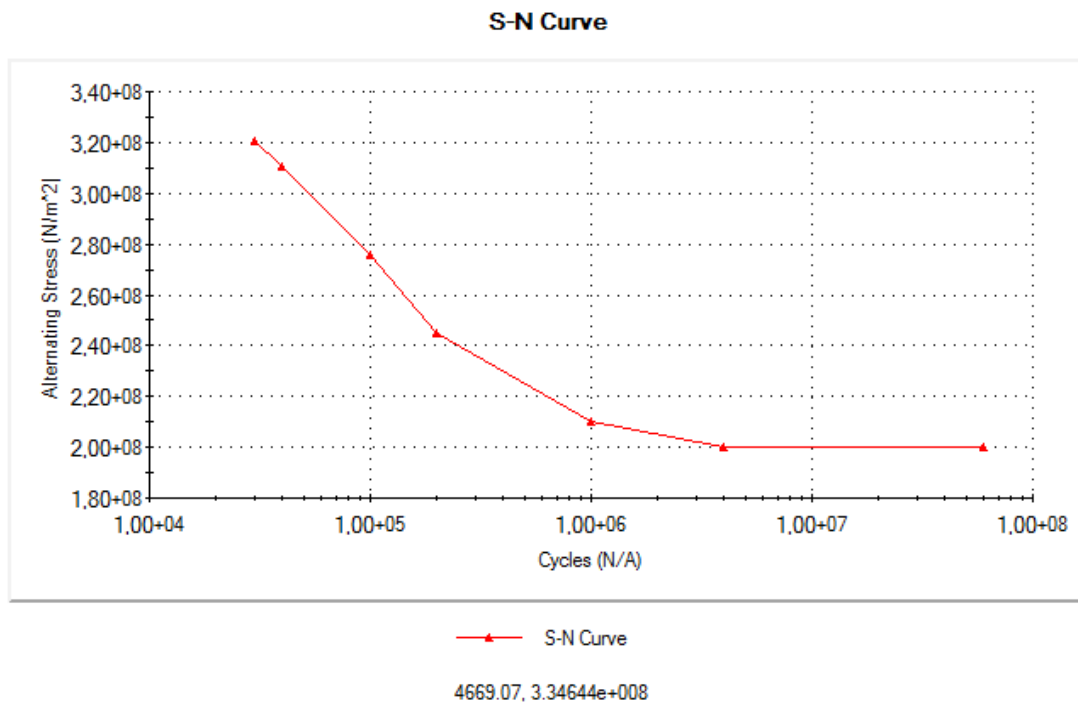
Fig. 3 - Fatigue curve of the 16MnCr5 alloy used to make the subsoiler working part,
(Santosh et. al., 2013)

Table 1

Properties of 16MnCr5 alloy steel

Mechanical property	Value	Unit of measurement
Elastic Modulus	2.100000031e+011	N/m^2
Poisson's Ratio	0.28	-
Shear Modulus	7.9e+010	N/m^2
Mass Density	7800	kg/m^3
Tensile Strength	800000000	N/m^2
Yield Strength	590593984	N/m^2
Thermal Expansion Coefficient	1.1e-005	1/K
Thermal Conductivity	14	W/(m·K)
Specific Heat	440	J/(kg·K)

After choosing the material and introducing the characteristics of the material, the faces on which the forces act were selected and then the advancement resistance on the main working part of the subsoiler was calculated. The total force was calculated using the relations from *Letosnev (1959), Krasnicenko (1964), Sandru et. al (1983), Scripnic and Babiciu (1979)*. It should be noted that two simulations were performed for two different working regimes. First regime is described by 0.3 m working depth of the subsoiler and 2.777 m/s aggregate speed of advance and the second one with 0.4 m working depth and 2.222 m/s advance speed. Thus, the resistance to advancement, in the general case, can be determined by the relation:

$$R = R_1 + R_2 + R_3 \qquad (1)$$

in which: R_1 is the resistance to the subsoil's own movement; R_2 is the opposite resistance to cutting and deforming the soil; R_3 is the opposite resistance to overturning and lateral displacement of the soil.

Resistance R_1 is given by the relation:

$$R_1 = f \cdot G_{org.} \qquad (2)$$

where *f* is the friction coefficient between the soil and the working part of the subsoiler (according to *Scripnic and Babiciu, 1979*, f = 0.15 − 0.5); for this study it was considered that f = 0.3, *G* is the gravity force of the

working part together with the weight of the frame which is the sole of the working part (in the study it was considered G = 2825 N).

Resistance R_2 opposite to cutting, loosening and deformation of the soil is given by the relation:

$$R_2 = k \cdot a \cdot b \cdot n_{org.} \tag{3}$$

where k is the resistance of the soil to cutting, loosening and deformation, a is the working depth, b is the working width of the part, and $n_{org.}$ is the number of parts.

According to *Scripnic and Babiciu (1979)*, depending on the type of soil, k has the following values: 250-350 Pa for light soils; 350-550 Pa for medium soils; 600-800 Pa for heavy soils and 800-1400 Pa for very heavy soils. The value of 1000 Pa was chosen for this study. As mentioned above, the working depth has two values 0.3 m and 0.4 m, for the same working width b = 0.07 m. Because the study is done on a single working part and not on the entire subsoiler, it will be considered $n_{org.}$ = 1.

Resistance R$_3$ opposite to the displacement of the soil is calculated with the relation:

$$R_3 = \varepsilon \cdot a \cdot b \cdot v^2 \tag{4}$$

According to *Scripnic and Babiciu* (1979), ε takes values between 150 and 200 daNs^2/m^4. For this study it was considered ε = 180 daNs^2/m^4, a and b have the same values as above as for v the two values were considered: one of 2.777 m/s for a = 0.3 m and one of 2.222 m/s for a = 0.4. Thus, the two resistances for advancement corresponding to the two working regimes are: R_1 = 3053 N and R_2 = 3760 N. The values of these forces were applied in the two static studies on the top of the ploughshare (see fig. 4).
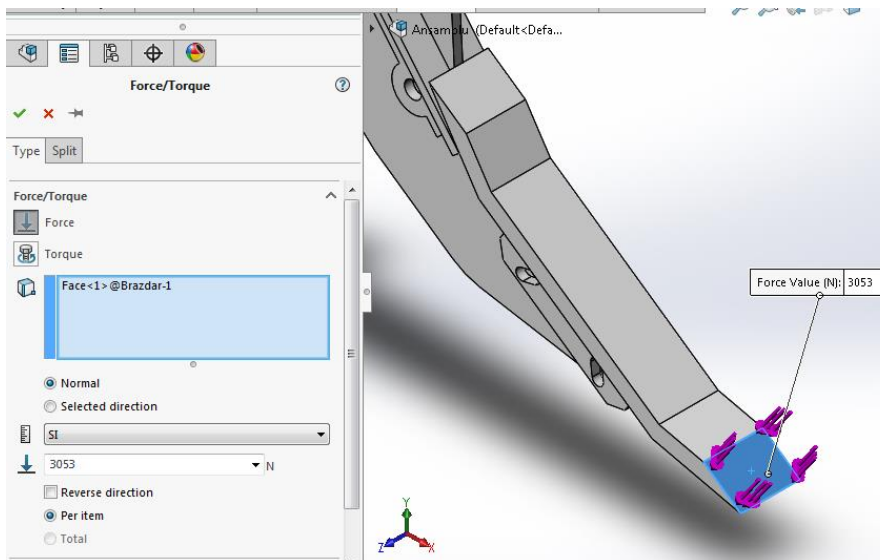
Fig. 4 - The place where the maximum resistance to advancement was applied
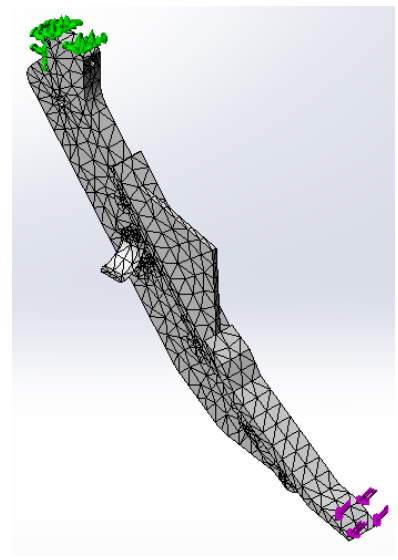
Fig. 5 - Finite element discretization of the geometric model

The finite element discretized model of the working part is presented in fig. 5. After the discretization of the finite element network the simulation was run, its results being presented below.

Following the simulation, the design program provided the results obtained in graphical form. The geometric pattern is divided into areas of a certain colour. Each area comprising the region of the geometric model in which the analysed size has the value specified in the chromatic legend on the right side of the screen.

RESULTS

For the working part model for the modelled and analysed subsoiler, the results obtained from the simulation in Solid Works are presented below. Thus, in figure 6 the values of the displacements that appear in the working body are presented during the defined stresses.

Analysing this data, it can be observed that the largest displacements of the nodes in the structure of the subsoiler working part appear on the peak of the ploughshare in both working regimes (as expected, otherwise). Its maximum value being 1.034 mm in the case of the first working regime and 1.302 mm in the case of the second working regime.
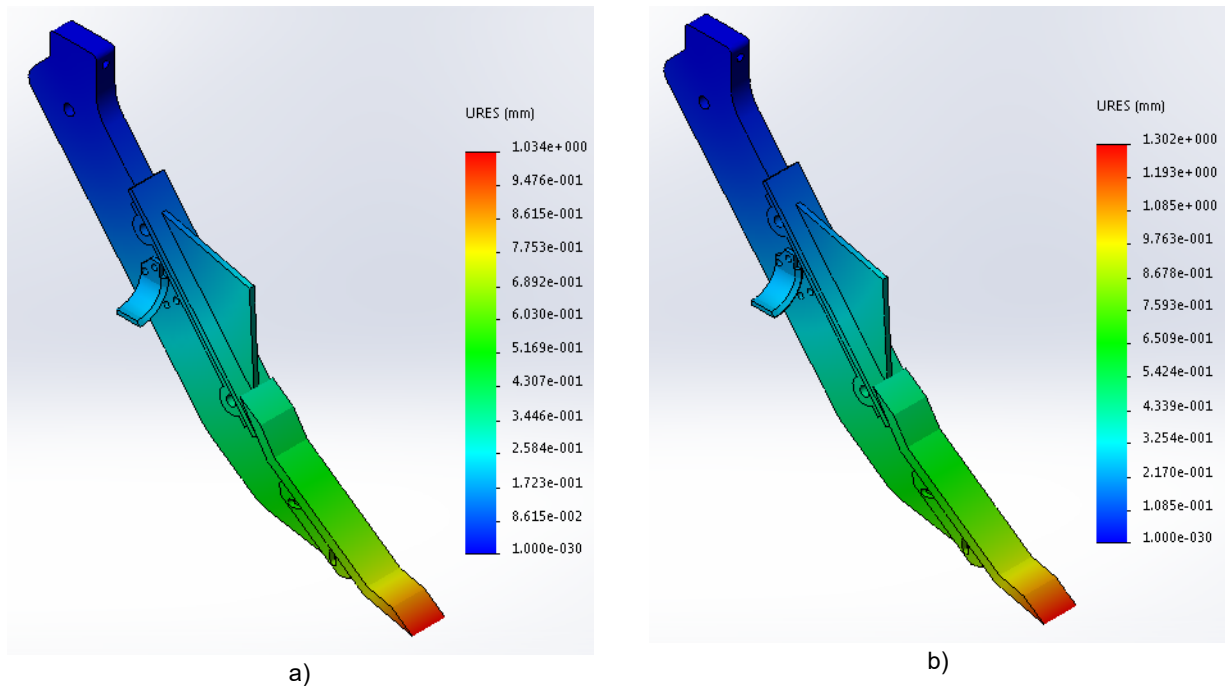
Fig. 6 - The values of the displacements that appeared in the working part during the two working regimes:
a) a = 0.3 m and v = 2.777 m/s; b) a = 0.4 m and v = 2.222 m/s

In figure 7 the values of the equivalent tensions in the working part are presented for the two analysed cases, stresses calculated according to von Mises criterion.
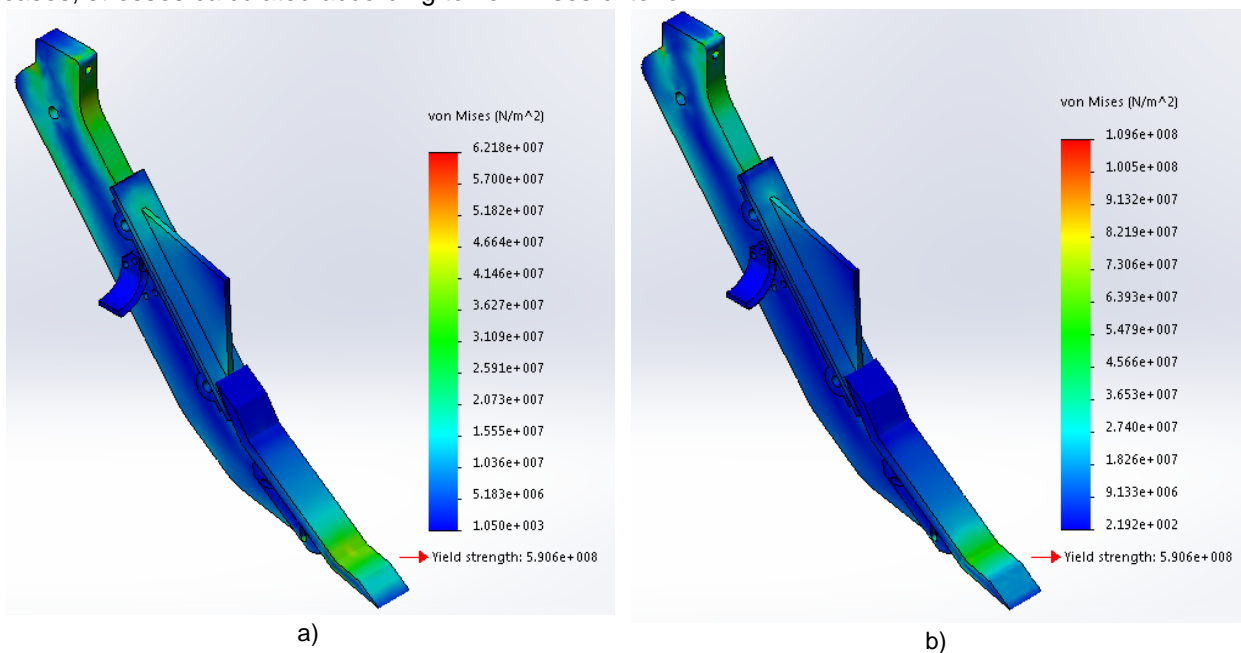
Fig. 7 - The values of the equivalent stresses of the working part during the two working regimes, according to the von Mises criterion
a) a = 0.3 m and v = 2.777 m/s; b) a = 0.4 m and v = 2.222 m/s

Analysing the figure, it can be observed that tension concentrating points appear in the structure of the working part. They are located in the area in which the shear bolt is mounted for the first working mode or behind the holding area of the working part for the second working mode (see fig. 8). The values of the von Mises equivalent stresses created at these points are $6.218 \cdot 10^7$ Pa for working regime 1 and $1.096 \cdot 10^8$ Pa for the working regime 2. Ignoring these points, it can be seen that the maximum stress in the working part for the two working regimes is around $3 \cdot 10^7$ Pa.

a)

b)
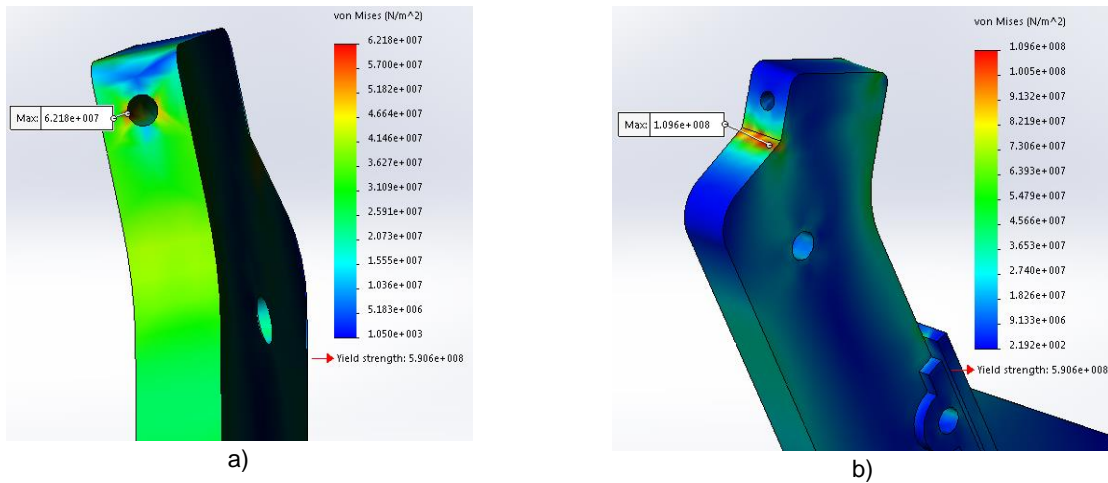
Fig. 8 - The stress concentration points in the working part during the two working regimes
a) a = 0.3 m and v = 2.777 m/s; b) a = 0.4 m and v = 2.222 m/s

a)

b)
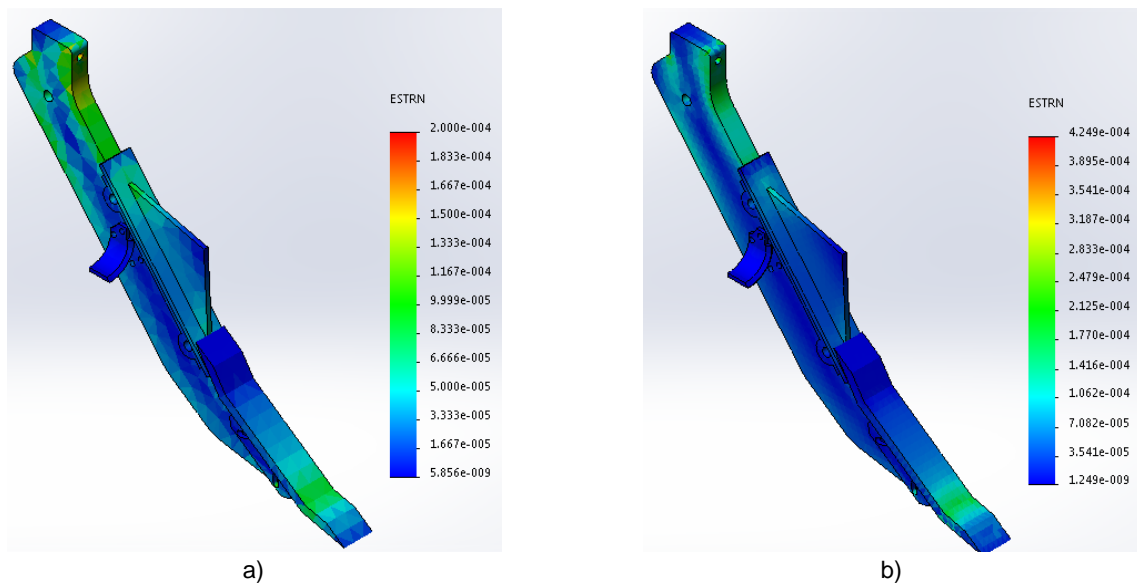
**Fig. 9 - The values of the equivalent deformations that appeared in the working part
during the two working regimes**
a) a = 0.3 m and v = 2.777 m/s; b) a = 0.4 m and v = 2.222 m/s

Analysing figure 9, we can observe the values of equivalent deformations that appear in the working part following the stress to which it is subjected.

a.

b.
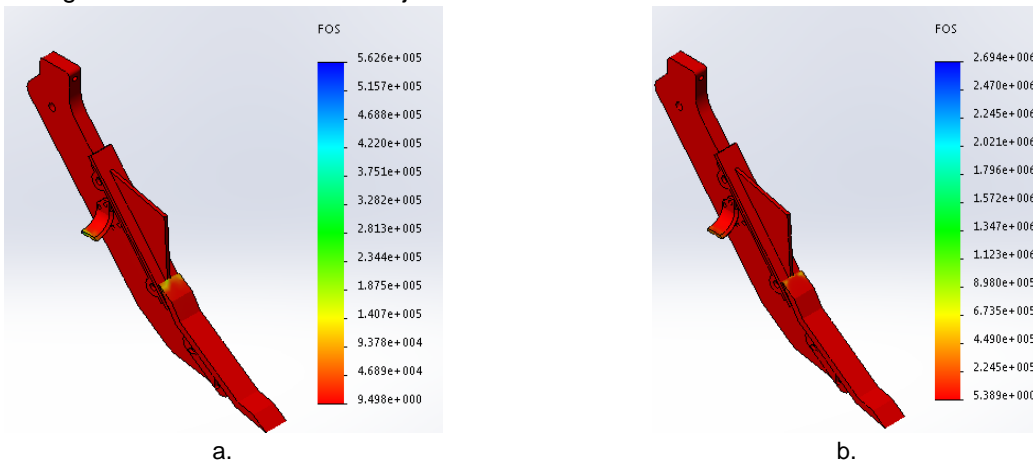
Fig. 10 - Variation of the safety coefficient in the working part during the two working regimes
a) a = 0.3 m and v = 2.777 m/s; b) a = 0.4 m and v = 2.222 m/s

So, the maximum equivalent deformation arises at the same stress concentration points, the deformation value being $2 \cdot 10^{-4}$ for the first working regime 1 and $4.25 \cdot 10^{-4}$ for the second working regime, while the minimum equivalent deformations have values below $5 \cdot 10^{-9}$.

In fig. 10 the oscillation of the safety coefficient in the working part for the two working regimes is presented. The safety factor is calculated relatively to the yield strength stress and varies on the structure border in the two simulations. Between the minimum values of the safety factor in the two variants of simulations is transmitted approximately the same difference, as between the maximum values of the equivalent specific deformation and the equivalent stress.

CONCLUSIONS

The minimum value of the safety coefficient is 9.498, respectively 5.389. For agricultural machines intended for ploughing, the coefficient of safety takes values between 1.8 and 2.2. Thus, it can be said that this subsoil is either oversized or it is made to work in much heavier conditions than those provided by this study, or to withstand even at overload (impact with tree roots, stones etc.).

From the analysis it also resulted that in the structure of the working part there appear stress concentration points, located in the area in which the shear bolt is mounted for the first working regime or behind the holding area of the working part for the second working regime. The values of the equivalent stresses calculated with the von Mises criterion at these points are $6.218 \cdot 10^7$ Pa for working regime 1 and of $1.096 \cdot 10^8$ Pa for working regime 2, values quite close to the breaking limit of the chosen material.

The results presented in the paper can be useful to designers and manufacturers in the agricultural machinery industry, but not only.

ACKNOWLEDGEMENT

REFERENCES

[1] Biris S.St., (2005), *Finite elements method. Fundamental concepts (Metoda elementelor finite. Concepte fundamentale),* 201 p., "PRINTECH" Printing house, Bucharest / Romania;

[2] Biris S.-St., Maican E., Vladut V., Sorin B., Ungureanu N., Vlăduț D.I., (2016), Stress and strains distribution in the frame of agricultural cultivators using the finite element method, *Proceedings of the 44th International symposium on agricultural engineering "Actual Tasks on Agricultural Engineering"*, pp. 111-117, Opatija / Croatia;

[3] Cardei P., Kostadinov G., (2012), Working regimes of the agricultural machines designed to soil tillage: From optimization to fundamentals (2*), INMATEH Agricultural Engineering*, vol. 37, No. 2, pp. 21 – 28;

[4] Gheorghe G., Persu C., Gageanu I., Cujbescu D., (2018), Structural and modal analysis in Solidworks of basic structure of equipment to prepare germinative bed in strips, *Proceedings Engineering for rural development*, pp. 818- 826, Jelgava / Latvia;

[5] Gheorghe G., Persu C., Gageanu I., Cujbescu D., (2019), Structural and modal analysis of the subsoiler equipment to prepare the germinative bed, *Proceedings of the 47th International Symposium "Actual Tasks on Agricultural Engineering"*, pp.79-87, ISSN 1848-4425, Opatija / Croatia;

[6] Gheorghe G., Persu C., Matache M., Mateescu, M., Cujbescu D., (2016), Finite element method use in the calculation and optimization of the active parts of mulch films applying equipment, *Proceedings of the International Symposium of ISB-INMATEH 2016 - Agricultural and mechanical engineering*, pp.629-634, Bucharest / Romania;

[7] Gheorghiță N., Biris S.-St., Ungureanu N., (2018), Contributions to the analysis of the vibratory working tools by FEM, Conference: *International Symposium ISB-INMATEH – Agricultural and Mechanical Engineering*, pp. 579-582, Bucharest/Romania;

[8] Kadam A., Chhapkhane N., (2017), Design and analysis of subsoiler, *International Journal of Modern Trends in Engineering and Science*, ISSN: 2348-3121, pp. 11-14, India;

[9] Krasnicenko A.V., (1964), *Agricultural machinery manufacturer manual*, volume 2, 830 p., Technical Publishing House, Bucharest/Romania;

[10] Lateș M.T., (2008), *Finite elements method, application (Metoda elementelor finite, aplicații),* 164 p., Transilvania University Publishing House, Brașov/Romania ;

[11] Letosnev M.N., (1959), *Agricultural Machines,* 840p., Agrosilvica State Publishing House, Bucharest / Romania;

[12] Mollazade K., Jafari A., (2010), Application of Dynamical Analysis to Choose Best Subsoiler's Shape using ANSYS, *New York Science Journal*, vol.3 (3), pp.93-100, NY/USA;

[13] Nagy M., Cardei P., Cota C., Fechete L., (2011), Method of estimating the soil resistance force to soil working machine parts with applications to the optimization of working regimes of machines used in horticulture, *INMATEH Agricultural Engineering*, vol. 35, No.3, pp.27–32, Bucharest/Romania;

[14] Petru C., Kostadinov G., (2012), Working regimes of the agricultural machines designed to soil tillage: From optimization to fundamentals (1), *INMATEH Agricultural Engineering*, vol. 37, No. 2, pp.13–20, Bucharest/Romania;

[15] Sandru A., Popescu S., Cristea I., Neculaiasa V., (1983), *Agricultural machinery exploitation*, Didactic and Pedagogical Publishing House, Bucharest/Romania;

[16] Santosh Patila, S. F. Patilb and Saravanan Karuppanana (2013), Modal and Fatigue Analysis of a Camshaft using FEA, *International Journal of Applied Engineering Research,* Vol. 8, No. 14, pp. 1685-1694

[17] Scripnic V., Babiciu P., (1979), Agricultural Machines (Masini agricole), 508 p., Ed. Ceres, Bucharest/Romania;

[18] Xin L., Liang J., Qiu L., (2013), Dynamic Analysis and Experimental Research of Vibratory Subsoiler System, *Journal of Theoretical and Applied Information Technology,* Vol. 48, No.2, Pakistan.

CFD NUMERICAL SIMULATION OF TEMPERATURE AND AIRFLOW DISTRIBUTION IN PIGSTY BASED ON GRID INDEPENDENCE VERIFICATION
/
基于网格独立性验证的猪舍温度和气流分布的 *CFD* 数值模拟

Min Jin, Chunguang Wang*, Pengpeng Wang [1]

College of Mechanical and Electrical Engineering, Inner Mongolia Agricultural University, Hohhot, China
Tel: +86 18848110474; E-mail: imauwcg@126.com

ABSTRACT

Grid independence verification was implemented to improve the reliability of CFD numerical simulation in pigsty. The effects of four different grid numbers on airflow and temperature simulation of 0.4m, 1.0m and 1.6m heights were compared. The results showed that the third method of mesh generation and the grid numbers about 2.09 million were more suitable for this pigsty model. The average relative error of airflow velocity and temperature between the simulated and the measured alues were 7.1% and 3.8% respectively, the average NMSE were 0.0012 and 0.0066 respectively. Therefore, grid independence verification is of great significance for CFD numerical simulation.

摘要

为了提高猪舍 CFD 数值模拟的可靠性，对猪舍网格独立性进行了验证。比较了四种不同网格数对 0.4m、1.0m 和 1.6m 高度的气流和温度场模拟的影响。结果表明,第三种网格生成的方法和大约 209 万的网格数量更适合该猪舍模型。气流速度、温度的模拟值和实测值的平均相对误差分别为 7.1%和 3.8%,均方误差分别为 0.0012 和 0.0066。可见，网格独立性验证对提高 CFD 数值模拟的可靠性具有重要的意义。

INTRODUCTION

With the rapid development of large-scale and intensive pig husbandry, higher requirements have been put forward for the environment in pigsty. Temperature and airflow velocity are two of the most important environmental factors in pig farming which are directly related to the economic benefits and pigs' welfare. So, it is necessary to evaluate the environmental indexes efficiently and provide a comfortable environment for the pigs.

There are three main methods to study the airflow and temperature distributions in livestock buildings: field test, laboratory test (or wind tunnel test) and Computational Fluid Dynamics (CFD) numerical simulation *(Hong et al., 2013; Nielsen., 2015; Ntinas., 2017)*. Although the field test should be closer to the real conditions in the pigsty, it is easily affected by the external environment and the accuracy of the sensors. As for the laboratory test (wind tunnel test), under stable conditions, it can work better while requiring a lot of time and cost to repeat the different structural configurations and different weather conditions. CFD offers a feasible way to overcome the shortcomings of these two methods mentioned above; it has been widely used to study airflow and temperature distribution within livestock buildings *(Nielsen et al., 2015; Rojano et al., 2016; Sejun et al., 2014; Sapounas et al., 2013;)*. However, due to the heavy workload of mesh generation, the accuracy and efficiency of the simulation are all greatly affected by the gird numbers and the mesh quality (*Yao et al., 2016; Li et al., 2018)*. The impact of three mesh types (hexahedral, tetrahedral, and hybrid) and five grid numbers on the accuracy and computing costs of air distribution simulations has been conducted in a first-class aircraft cabin; the results showed that the hexahedral meshes can get the best result but also the highest computing costs (*Duan et al., 2015)*. Yu et al. investigated the computational accuracies and convergence rates of triangular and quadrilateral meshes, they concluded that the number of triangular meshes needs to be 4/3 times that of quadrilateral to obtain similar accuracy *(Yu et al., 2012)*.

---

[1] *Min Jin, Ph.D. Stud. Eng.; Chunguang Wang*, Prof. Ph.D. Eng.;　Pengpeng Wang , Ms. Stud. Eng.*

The effect of airflow velocity on heat exchange between cows' standing and tilting was also studied by CFD numerical simulation; the results indicated that CFD can be used as a useful way to get ideal results based on optimal parameters and reasonable mesh model *(Wang et al., 2018)*.

Therefore, prior to conduct the numerical simulation of the pigsty, grid independence verification must be done to minimize the workload of the mesh generation while not affecting the reliability and the accuracy of the results. In this study, field test and CFD numerical simulation are combined to verify the importance of grid independence test for improving the reliability of CFD numerical simulation in pigsty.

MATERIALS AND METHODS

● Data source

The experiment was carried out on a pig farm in Hohhot, Inner Mongolia, China (40°40 '26 "N, 111°21' 46"E). The dimensions of the pigsty are 9.2m (length) × 9.0m (width) × 3.6m (height), with negative pressure ventilation. There are 14 adjustable air inlets (265mm×655mm) at the top of the pigsty, many conveying pipes in the upper space, 2 automatic feeding equipment on the left side, 4 cylindrical finned heating pipes, 2 variable speed fans on the side walls and a 2m deep manure pit beneath the floor. Meanwhile, each pen is surrounded by solid wall and partially slatted concrete floor. The internal structure of the experimental pigsty is demonstrated in Fig.1.

The field test was conducted on January 9, 2018. The environmental temperature was measured and recorded by temperature sensors (HSTL-102WS, China) every 2s. In addition, an intelligent hot wire anemometer (9565-P, TSI, USA) was used to measure the air velocity every 0.2 s and averaged per second for a measurement period of 60s at each measuring point. As shown in Fig.2, the sensors were located in the centre of each pig pen as well as middle of the aisle at 3 different heights: 0.4m (height of lying pig), 1m (height of standing pig) and 1.6m (height of breeder). The 14 adjustable air inlets were set as the velocity inlets and the four outlets set as pressure outlets in GAMBIT. The heating was regarded as a constant heat source in the pigsty and its averaged surface temperature was measured by the infrared thermometer (MT4, Raytek, American) every 5min. Pigs' model was regarded as non-slip wall with constant temperature. In addition, the density of the pigs was 1100 kg.m^3, the specific heat was 3500 J.(kg.K)$^{-1}$ and the thermal conductivity as 0.464 W (m.K)$^{-1}$.

Fig. 1 - Internal structure of the pigsty
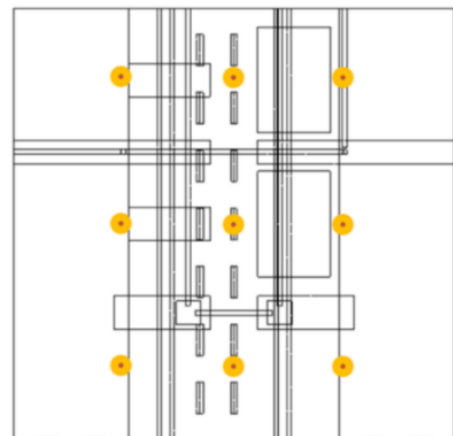
Fig. 2 - Sensor layout scheme in the pigsty

● Numerical simulation

➢ Selection of governing equation

No matter complex or simple the fluid flow is governed by the law of conservation. The basic conservation law mainly includes the mass conservation law, the momentum conservation law, energy conservation law, collectively known as the governing equation. In terms of the control equation of CFD, the continuity equation, the momentum equation and the energy equation are mainly applied (*Osorio Saraz et al., 2013*):

(1) Continuity equation:

$$\frac{\partial(\rho u)}{\partial x} + \frac{\partial(\rho v)}{\partial y} + \frac{\partial(\rho w)}{\partial z} = 0 \tag{1}$$

where:

ρ is density. u, v and w are the components of the velocity vector in the direction of x, y and z.

(2) Momentum equation:

$$\frac{\partial(\rho\phi)}{\partial t} + div(\rho u\phi) = div(\Gamma grad\phi) + S \tag{2}$$

where:

ϕ is general variable, which can represent u, v and w.

Γ is the diffusion coefficient. S is the source item.

(3) Energy equation

$$\frac{\partial(\rho T)}{\partial t} + div(\rho u T) = div\left(\frac{k}{c_p} grad T\right) + S_T \tag{3}$$

where:

c_p is specific heat capacity, T is temperature [°C],

k is the heat transfer coefficient of the fluid and S_T is viscous dissipation term.

➢ **Selection of boundary condition**

The boundary condition is the prerequisites for the solution of the governing equation. Setting boundary condition includes selecting the simulation state, turbulence model and initial conditions.

The steady-state simulation based on pressure is employed in this study since the external climate of the pigsty is stable and the fan is running normally. Then, the renormalization group model (RNG $k - \varepsilon$ Model) is adopted as the turbulence model, which is a basic method that has been commonly used in current turbulence simulation studies with high accuracy and applicability. Besides, air is simplified as the stable and incompressible ideal air because of the fluctuations in airflow velocity and temperature are small. Meanwhile, considering the impact of gravity, the acceleration in the direction of gravity was set as -9.8m·s⁻² and the material parameters of wall and the actual measured initial condition values are shown in Table 1 and Table 2, respectively. Moreover, in order to reduce the mesh numbers, the slatted floor is treated as a porous medium with 2cm width of the slot and 12 cm width of the slat. The inertial drag coefficient in X, Y and Z directions is 80m⁻¹, 1.2×10⁴ m⁻¹ and 1.5×10² m⁻¹, respectively and the viscous drag coefficient is 1.0×10⁵ m⁻², 1.6×10⁷m⁻², 1.2×10⁵ m⁻², respectively. Then, the porosity of the slatted floor is calculated to be 0.14 by formula (4):

$$\frac{\Delta P}{l} = 0.5 \cdot R_1 \cdot \rho_{air} \cdot v_2 + \mu_{air} \cdot R_2 \tag{4}$$

where:

$\frac{\Delta P}{l}$ is the pressure drop per unit length of porous medium [$Pa.m^{-1}$]. R_1 is the inertial drag coefficient [m^{-1}],

R_2 is the viscous drag coefficient [m^{-2}], ρ_{air} is the air density [$kg \cdot m^{-3}$], v is the velocity of air passing through in the porous medium [$m.s^{-1}$], μ_{air} is the velocity coefficient [$kg \cdot (m \cdot s^{-1})$].

Table 1

Wall material parameters

Parameter	Density $[kg \cdot m^{-3}]$	Specific heat capacity $[J \cdot (kg \cdot K)^{-1}]$	Heat conductivity coefficient $[W \cdot (m \cdot K)^{-1}]$
Brick wall	2000	920	0.81
Floor	1800	900	1.9
Roof	1050	1300	0.08

<div align="right">**Table 2**</div>

Initial condition values

Parameter	Object	Measured values
Surface temperature [°C]	Front wall	7.4
	Back wall	8.0
	Left wall	6.4
	Right wall	5.8
	Roof	15.0
	Floor	5.0
Temperature [°C]	Pig	25.0
	Heating	30.0
	Outdoor temperature	-6.0
Velocity [m/s]	Air inlet	0.5

Additionally, to ensure the accuracy of CFD numerical simulation, the actual structure and configuration of the pigsty are kept as much as possible. The railings diameters are small with spacing of 0.1m, which have little effect on the simulation results, so they are not included in the CFD modelling while the shared feeders, the feeding equipment and the pipes in the upper space of the pigsty cannot be ignored because of their larger volumes.

As for pigs, they not only influence the air diffusion but also the temperature distribution. As shown in Fig.3, due to the low temperature in winter, the pigs were huddled together most of the time. Therefore, a cuboid with similar volume of the actual size of the space occupied by the pigs is used instead of multiple cuboids models, which greatly reduce the complexity of mesh partition and the computation cost.

Fig. 3 - Actual status of the pigs

RESULTS

● **Grid independence verification**

Gambit 2.4.6 is employed to establish the pigsty model (Fig.4). The effects of grid numbers are studied by adopting different meshing strategies in different computing domains with hybrid grids under four different densities. The numbers of mesh are 273,423 (represented by letter "A"), 1,648,998 ("B"), 2,090,991 "C"), 3,149,854 ("D") and the worst mesh quality is less than 0.97, which means that the meshing is reasonable and available. Fig.5 is one of the mesh models.
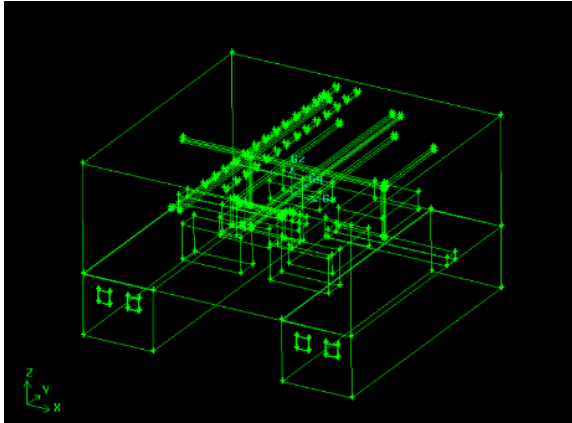
Fig. 4 – 3D model of the Pigsty
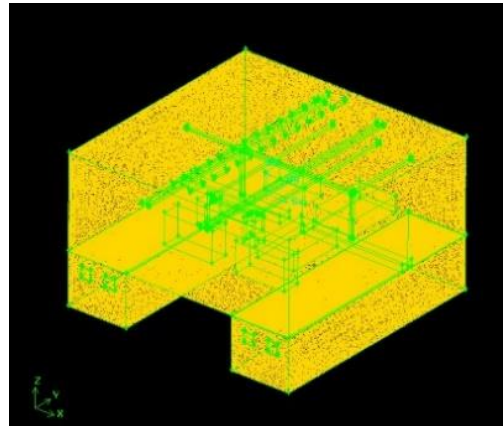
Fig. 5 - Mesh model of the Pigsty

The comparisons of the simulated values of the four different grid numbers A, B, C and D with the actual measured values at different height in the pigsty are presented in Fig.6-11.
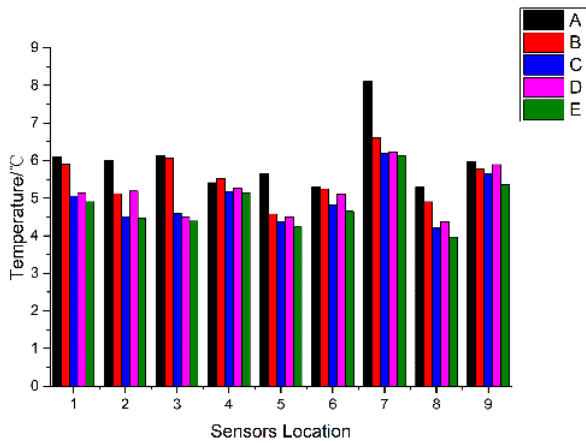
Fig. 6 - Airflow velocity values at height of 0.4m in pigsty
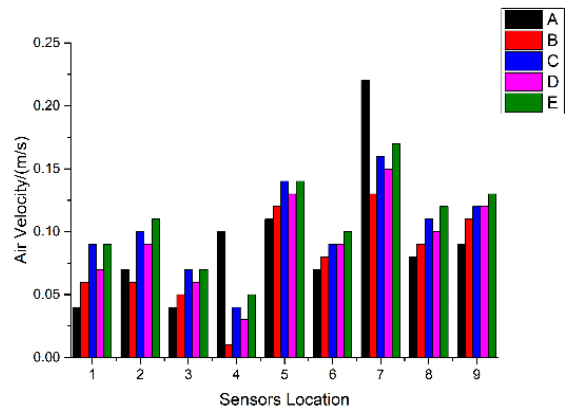
Fig. 7 - Temperature values at height of 0.4m in pigsty
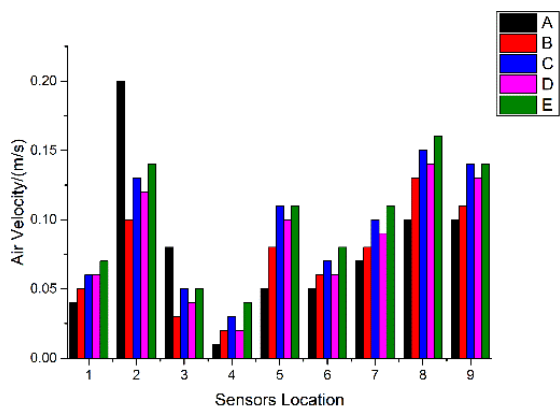
Fig. 8 - Airflow velocity values at height of 1m in pigsty
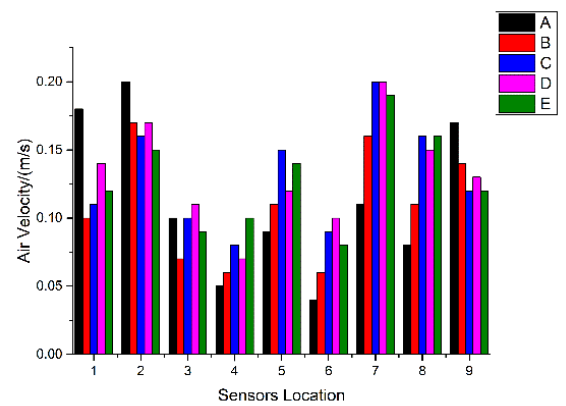
Fig. 9 - Temperature values at height of 1m in pigsty

245
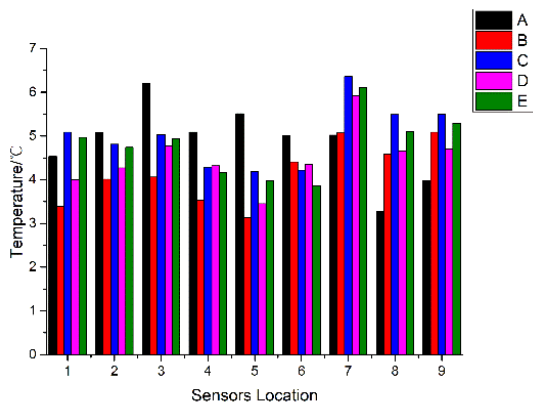
Fig. 10 - Airflow velocity values at height of 1.6m in pigsty (left)
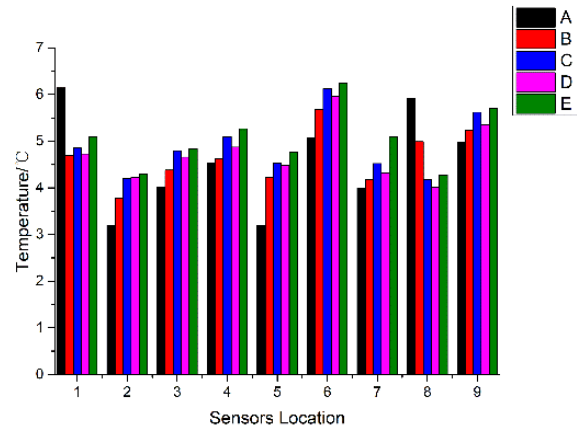
Fig. 11 - Temperature values at height of 1.6m in pigsty (right)

It can be found that grid numbers have great impacts on the accuracy of the simulation results. When the grid numbers are less than 1.64 million, there are large deviations between the simulation results and the measured values. When the grid numbers reached about 2.09 million and 3.14 million, the simulation results are all close to the measured values, but the former is more accurate. Meanwhile, the average relative error of airflow velocity of the four different grid numbers at different heights are presented in Table 3. The average relative error of temperature of the four different grid numbers at the 3 heights are 23.7%, 14.5%, 3.8% and 7.6%, respectively. When the grid numbers reached about 2.09 million, the simulated values are fit well with the actual measured values, and the relative errors of airflow velocity and temperature are the lowest. Then, continuing dividing the grids to 3.15 million, the results indicated that the relative error of airflow velocity and temperature increased by 9.9% and 3.8% compared to the 2.09 million grid number and the time cost is also obviously longer than the previous one. This is because with the mesh encryption, the discrete error decreases while the number of discrete points increase, which leads to the increase of rounding error of the simulation.

Table 3

Relative error at different heights with different grid numbers (%)

	A		B		C		D	
	V	T	V	T	V	T	V	T
0.4 m	48.1	22.3	31.7	11.6	6.8	3.8	16.4	6.4
1.0 m	50.7	25.4	32.0	15.7	6.6	3.3	18.8	7.0
1.6 m	40.4	23.4	22.5	16.3	7.9	4.3	15.7	9.4
Average	46.4	23.7	28.7	14.5	7.1	3.8	17.0	7.6

In order to further analyse the accuracy and reliability of the four mesh schemes, Normalized Mean Square Error (NMSE) is applied to judge the model performance (*Ntinas et al., 2017*). NMSE is defined as follows:

$$NMSE = \frac{\overline{\left(c_s - c_m\right)}^2}{c_{sm} \cdot c_{om}} \tag{4}$$

$$\overline{\left(c_s - c_m\right)}^2 = \frac{\sum_n \left(c_{si} - c_{mi}\right)^2}{c_{sm} \cdot c_{om}} \tag{5}$$

$$E_v = \frac{\left|c_s - c_m\right|}{c_m} \times 100\% \tag{6}$$

where:

c_s is simulated data, c_m is the measured data, c_{sm} is the average of the simulated data, c_{om} is the average of the measured data and E_v is relative error between the simulated data and the measured data.

The comparisons of the NMSE of C-type mesh model is the lowest in the four schemes and the three heights which show its higher reliability in simulating the airflow velocity and temperature (Table 4). Therefore, the C-type mesh model is considered adequate for this pigsty.

Table 4

NMSE values in different planes with different grid numbers

	Airflow velocity				Temperature			
	A	**B**	**C**	**D**	**A**	**B**	**C**	**D**
0.4 m	0.32395	0.11771	0.00599	0.02624	0.05646	0.01511	0.00034	0.00586
1.0 m	0.24143	0.09546	0.00714	0.02368	0.05938	0.02576	0.00126	0.00597
1.6 m	0.21560	0.06061	0.00669	0.02104	0.06052	0.03678	0.00214	0.01182
Average	0.26033	0.09126	0.00661	0.02366	0.05879	0.02588	0.00125	0.00788

● **Temperature numerical simulation in pigsty**

As discovered in Fig.12, the temperature on the plane of Z = 0.81m in the pigsty is not distributed evenly. On the right side (the side with more pigs), the temperature is between 6.45°C and 7.72°C and the average temperature is 6.79 °C, higher than the left side (the side with fewer pigs) since pigs are one of the main heat sources. Meanwhile, the air inlets at the top of the pigsty are near the left side, so, the temperature in this side is lower and the temperatures in the most areas are between 2.64 °C and 5.18 °C, with an average temperature of 4.15 °C. In addition, there are 6 pens in the pigsty, the overall temperature on the right side is close to the outlet and discharged through the negative pressure of the fan, so the temperature in the right pens is higher than the average temperature in the left pens.
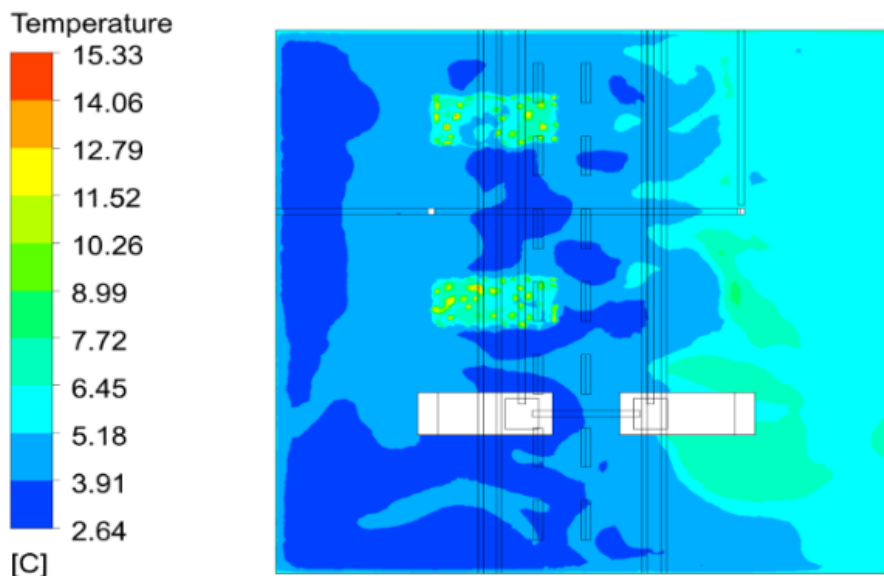
Fig. 12 - Temperature distribution at Z = 0.81m

Fig.13 shows the temperature distribution at Y = 0m, the middle of the longitudinal section of the pigsty. The heat sources in the pigsty mainly come from the heating and the pigs' temperature. The air inlets are located on the upper part of the pigsty, from which the cold air enters. The cold air is heated by the heating in the downward process, then it flows to the pigs. As the other main heat source in the pigsty, the air temperature around the pigs is also improved. With the cold air that continues to move in, most of the heat on the left side enters the manure pit through the slatted floor and is removed by the fans, and the rest of the heat is retained on the upper part of the pigsty due to the turbulence, the temperature is between 6 °C and 9 °C with an average temperature of 6.89 °C. On the right side with fewer pigs, the overall temperature is lower than on the left, except for a small portion of the warmer area around the heating, the temperature is between 3 °C and 6 °C; the average temperature is 4.25 °C.
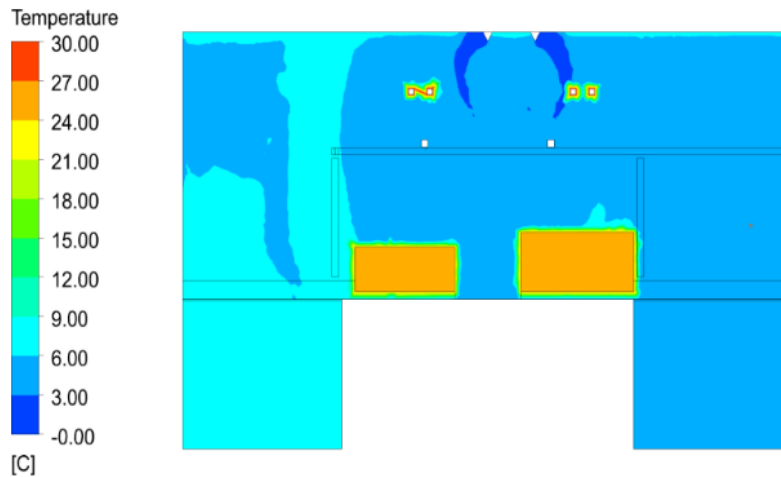
Fig. 13 - Temperature distribution at Y = 0m

● **Airflow numerical simulation in pigsty**

Fig.14 shows the velocity of the airflow distribution at Z = 0.81m. As the figure illustrates, areas with higher airflow velocity are concentrated near the pigs with the maximum value of 0.29 m/s and the other areas is below 0.25 m/s. In addition, the closer the airflow to the outlets, the higher the velocity is, and the uniformity of the airflow gradually increases. The average airflow velocity in this plane is 0.11 m/s. However, the overall airflow uniformity performs poor, which is related to the opening angle of the air inlets and the number of pigs in the pens.
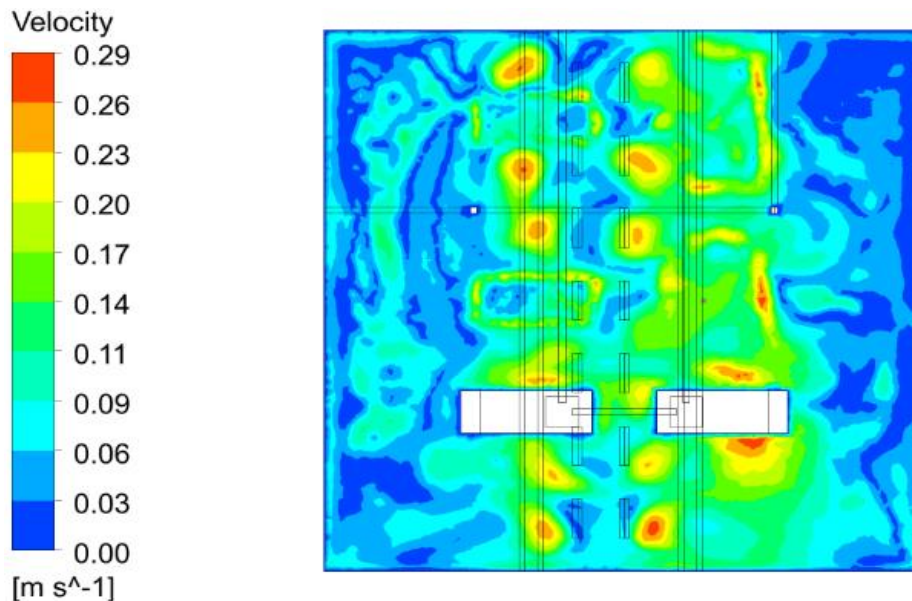
Fig. 14 - Velocity distribution at Z = 0.81m

It can also be seen from Fig.15 that the airflow velocity in the middle of the pigsty at Y= 0 m is between 0.1 m/s and 0.35 m/s, but the airflow velocity around the heating and the large feeding station is between 0m/s and 0.05 m/s due to their obstruction of the airflow. Meanwhile, the airflow velocities both on the left and right sides of the pigsty are all lower, and the airflow is sucked away by the fans in the manure pit through the slatted floor. Although the cold air can remove some harmful gases and toxic particles in the pigsty, it also takes away a lot of heat. As a result, pigs are mainly lying and huddling together on the concrete floor when they are exposed to low temperature which has a great negative impact on pigs' growth since most of the consumed feed is used to maintain body temperature rather than to grow.
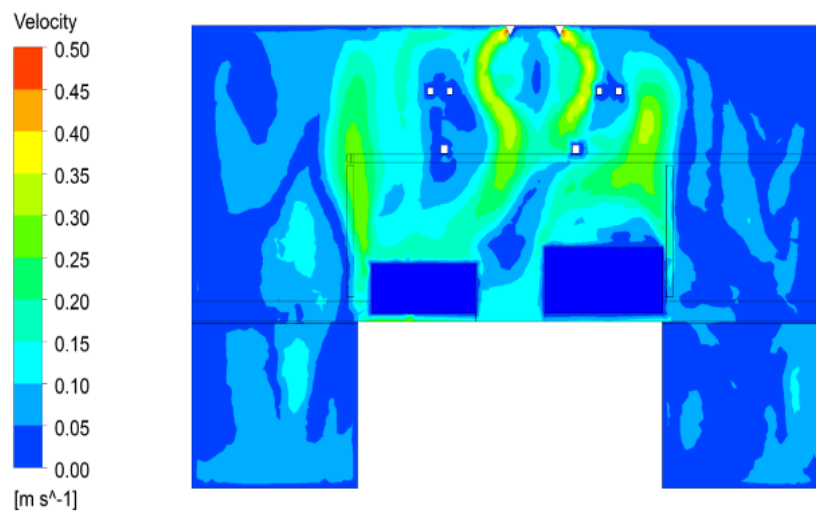
Fig. 15 - Velocity distribution of Y = 0m

CONCLUSIONS

Grid numbers is of great significance to the accuracy of CFD simulation. The average relative error based on C-type mesh model on three different heights of airflow velocity and temperature are 7.1% and 3.8% respectively, the NMSE values are 0.00126 and 0.00669 respectively, which are the best results in all schemes, indicating good agreements between the simulation and the field test results. Moreover, it can be found that if the mesh generation is too sparse (0.27 million), the relative error of airflow velocity and temperature simulation values would be larger, reaching 46.4 and 23.7%. However, the grid numbers are not the more the better, when the mesh generation is too dense (3.14 million), due to the increase of discrete points, the rounding error increases, which leads to the simulation accuracy reduction by 9.9% and 3.8% (compared with 2.09 million). As such, grid independence verification should be carried out before applying the simulation and calculation. Then, the best model with optimal parameters can be used for the CFD simulation in the experimental pigsty. From the distribution diagrams of temperature and airflow velocity, it is easier to see the whole condition inside the pigsty, some suggestions being obtained to improve the welfare of pigs as well as the economic benefit of the pig farm in cold winter. The first is that the overall ventilation of the pigsty can be improved by adjusting the opening angle of the air inlets to avoid cold air flowing directly into pigs' lying areas when the ventilation is needed to remove the harmful gases which is also important for pigs' health. Meanwhile, increasing the number of pigs in the left pens also makes sense since pigs are the other heat source in the pigsty. Furthermore, while decreasing the airflow velocity around the pigs, the airflow velocity on both left and right sides should also be strengthened to create a more balanced and healthier breeding environment.

ACKNOWLEDGEMENT

RERERENCES

[1]   Duan, R., Liu, W., Xu, L., Huang, Y., Shen, X., Lin, C.H., Liu, J., Chen, Q., & Sasanapuri, B. (2015). Mesh type and number for the CFD simulations of air distribution in an aircraft cabin. *Numerical Heat Transfer, Part B: Fundamentals*, *United Kingdom*, 67, 489–506. https://doi.org/10.1080/10407790.2014.985991
[2]   Hong, S.W., Lee, I.B., Seo, I.H., Bitog, J.P., & Kwon, K.S. (2013). Prediction of livestock odour dispersion over complex terrain using CFD technology: Review and simulation study. *Acta Horticulturae, Belgium, 1008,* 29–36. https://doi.org/10.17660/ActaHortic.2013.1008.2

[3]   Li, H., Rong, L., Zhang, G. (2018). Numerical study on the convective heat transfer of fattening pig in groups in a mechanical ventilated pig house. *Computers and Electronics in Agriculture, Netherlands, 149*, 90–100. https://doi.org/10.1016/j.compag.2017.08.013

[4]   Nielsen, P. V. (2015). Fifty years of CFD for room air distribution. *Building and Environment*, *United Kingdom, 91*, 78–90. https://doi.org/10.1016/j.buildenv.2015.02.035

[5]   Ntinas, G.K., Shen, X., Wang, Y., & Zhang, G. (2018). Evaluation of CFD turbulence models for simulating external airflow around varied building roof with wind tunnel experiment. *Building Simulation*, *China, 11,* 115–123. https://doi.org/10.1007/s12273-017-0369-9

[6]   Osorio Saraz, J.A., Arêdes Martins, M., Oliveira Rocha, K.S., Silva Machado, N., & Ciro Velasques, H.J. (2013). Use of computational fluid dynamics to simulate temperature distribution in broiler houses with negative and positive tunnel type ventilation systems. *Revista U.D.C.A Actualidad & Divulgación Científica, Brazil,16,* 159-166. https://doi.org/10.31910/rudca.v16.n1.2013.871

[7]   Rojano, F., Bournet, P.E., Hassouna, M., Robin, P., Kacira, M., & Choi, C.Y. (2016). Computational modelling of thermal and humidity gradients for a naturally ventilated poultry house. *Biosystems Engineering*, *United States,151,* 273–285. https://doi.org/10.1016/j.biosystemseng.2016.09.012

[8]   SeJun Park, Inbok Lee, Sewoon Hong. (2014). New Development of a Straightforward Method of Estimating Age-of-Air Using CFD. *Acta Horticulturae, Belgium, 1037,* 963–969. https://doi.org/10.17660/actahortic.2014.1037.128

[9]   Sapounas, A., Dooren, H. J. C., & Smits, M. C. J. (2013). Natural Ventilation of Commercial Dairy Cow Houses: Simulating the Effect of Roof Shape Using CFD, *Acta Horticulturae, Belgium,1008*, 221-228. https://doi.org/10.17660/ActaHortic.2013.1008.29

[10]   Wang, X., Zhang, G., & Choi, C.Y. (2018). Effect of airflow speed and direction on convective heat transfer of standing and reclining cows. *Biosystems Engineering, United States, 167*, 87–98. https://doi.org/10.1016/j.biosystemseng.2017.12.011

[11]   Yao, J J., Guo, B B., & Ding, W M. (2017). Structural optimization and verification of ventilation system based on CFD simulation of goose house airflow field (基于鹅舍气流场 CFD 模拟的通风系统结构优化 与验证). *Transactions of the Chinese Society of Agricultural Engineering, China, 33*(7), 214-220. https://doi.org/10.11975/j.issn.1002-6819.2017.03.029

[12]   Yu, G. B., Sun, S., & Tao, W. Q. (2012). Comparative Study on Triangular and Quadrilateral Meshes by a Finite-Volume Method with a Central Difference Scheme, *Numerical Heat Transfer, Part B: Fundamentals, United Kingdom, 62* (4), 243-263. https://doi.org/10.1080/10407790.2012.709416

NONDESTRUCTIVE TESTING OF SOLUBLE SOLIDS CONTENT IN CERASUS HUMILIS USING VISIBLE / NEAR-INFRARED SPECTROSCOPY COUPLED WITH WAVELENGTH SELECTION ALGORITHM

/

可见/近红外光谱技术结合波长选择算法欧李可溶性固形物含量的无损检测

Bin Wang[1)], **Junlin** He*[1)], **Shujuan** Zhang*[1)], **Lili** Li[2)] [1]
[1)] College of Engineering, Shanxi Agricultural University, Taigu/China
[2)] College of Information Science and Engineering, Shanxi Agricultural University, Taigu/China
Tel: +86-0354-6288400; E-mail: hejunlin26@126.com and zsujuan1@163.com

Keywords: VIS-NIR spectroscopy, cerasus humilis, soluble solid, partial least square regression, nondestructive testing

ABSTRACT

Soluble solids content (SSC) is one of the most important quality attributes affecting the taste and maturity of fresh fruit. In this study, with the cerasus humilis fruit as the research object, a prediction model of soluble solid content (SSC) in cerasus humilis (CH) is established based on visible / near-infrared spectroscopy to explore a nondestructive testing method of the interior quality of CH. The visible / near-infrared spectral info (350-2500nm) of 160 CHs was collected to extract the reflection spectrum, establishing the linear model (PLSR) and non-linear model (LS-SVM) of CH's spectral info and SSC. The prediction performance and stability of the model were justified using several statistical indicators namely correlation coefficient of the prediction set (Rp), the root mean square error of the prediction set (RMSEP), and the residual predictive deviation (RPD) index. Results showed that multiplicative scatter correction (MSC) was proved to be the best preprocessing method, UVE-CARS was the optimal method of dimension reduction, the quantities of characteristic wavelengths was 10 and the optimal model was UVE-CARS-PLSR, in which Rc is 0.8995, Rp is 0.8579, RMSEC is 0.8897, RMSEP is 0.9059, and RPD is 1.8766, indicating that the redundant data of the original spectrum can be reduced, the wavelength dimensions can be reduced, valid info can be retained and data processing can be simplified as UVE-CARS extracts characteristic wavelengths. Reference and theoretical basis are provided in this research for future research and development of portable detector and online sorting detection of CH internal quality.

摘要

可溶性固形物含量(SSC)是评价鲜果口感和成熟度的重要品质指标之一。本研究以欧李果实为研究对象，基于可见/近红外光谱技术结合化学计量学方法建立欧李果中 SSC 含量的预测模型，探究欧李果内部品质的快速无损伤检测方法。采集 160 个欧李果的可见/近红外光谱信息（350~2500nm），建立欧李果光谱信息和 SSC 的线性模型(偏最小二乘回归算法)和非线性模型(最小二乘支持向量机)预测模型，通过预测集相关系数(Rp)、预测集均方根误差(RMSEP)和剩余预测偏差(RPD)等指标来评价模型的预测性能及稳定性。结果表明，多元散射校正为最佳预处理方法，最佳降维方法为 UVE-CARS，特征波长个数为 10，最优模型为 UVE-CARS-PLS，其中 Rp 为 0.8579，RMSEP 为 0.9059，RPD 为 1.8766。说明 UVE-CARS 提取特征波长可减少原始光谱的冗长数据，降低波长维数，保留有效信息，简化数据处理。本研究为欧李果内部品质后续便携式检测仪和在线分选检测研究提供了参考和理论基础。

INTRODUCTION

Cerasus humilis (Bge.) Sok. (CH) is a kind of rosaceae cherry. It is usually grown in sun-slope sandy land and mountain shrubs, or cultivated in gardens. The fruit ripens around August 20 every year. CH is usually found in the northern regions of Yellow River. CH has a strong reticular root system and is drought-resistant, making it not only fixate soil but also regulate ecosystem, and it is also known as the "fruit rich in calcium" for its high calcium content, and is the third generation exclusive in China. CH's seed kernels are the main source of Yu Li Ren (Semen Pruni), an herb known for the idea of "homology of medicine and

---

[1] *Bin Wang, As. Ph.D. Stud. Eng.; Junlin He, Prof. Ph.D. Eng.; Shujuan Zhang, Prof. Ph.D. Eng.; [2] Lili Li, As. Ph.D. Stud. Eng.*

food". CH pulp can be consumed or made into juice, fruit wine, vinegar and preserved dried fruits, and it is good for health. The CH products have a unique taste and rich aroma and of high nutritional value, so it is known as a "super fruit", and honoured as one of the three high-end fruits with American blueberry and Russian sea-buckthorn.

The internal qualities of CH are abundant. Soluble solid content (*SSC*) and titratable acidity (*TA*) will affect its taste and nutrition when it comes to its quality assessment, and they serve as the measurement standards and important indicators of CH's maturity. Regular testing of CH's internal qualities is destructive, complicated and time-consuming, and its tissues are often damaged, affecting its sales and edibility and lowering its values *(Guo et al., 2010)*.

Near-internal spectroscopy has been successfully applied by domestic and overseas researchers to the fruit internal quality determination in recent years. There are in-depth studies on apples, mangos, tomatoes, kiwis, peaches, pears, strawberries and fresh dates. *Ar et al., (2019)* used near-infrared spectroscopy to predict the possibilities of internal qualities of persimmons such as *SSC, Vc,* total acid and hardness. The results showed that *MSC* is the optimal preprocessing method. With the establishment of a *PLS* calibration model, the optimal factor quantity of the *SSC, Vc,* total acid and hardness of persimmons is 17, 16, 12 and 12, respectively. *Parpinello et al., (2013)* studied a detection method, which combines near-infrared ray (*NIR*) measurement and glucose analysis, and the partial least squares (*PLS*) model based on cross-validation serves as the main statistical parameter where the prediction set determination coefficient is 0.82 and the standard error of prediction is 0.83%°Brix. *Purwanto et al., (2015)* used near-infrared spectroscopy to predict the *SSC* and acidity of the mango species known as "*Gedong Gincu*". The results showed that different preprocessing methods play critical roles in terms of establishing accurate models of mango internal quality prediction. *Maniwara et al., (2014)* used visible light and short-wave near-infrared spectroscopy to establish a *PLSR* prediction model for the indicators of soluble solids content, titratable acid content, ascorbic acid content, ethanol concentration, and peel hardness of passion fruit. Studies showed that *PLSR* prediction model proves to have the best prediction performance on the *SSC* in passion fruit, and the prediction correlation coefficient is 0.923. *Escribano et al., (2017)* collected the *NI* spectra of sweet cherries within the wavelength of 729 to 975 nm, and established a *PLS* prediction model of *SSC* for sweet cherries under two temperature conditions. The results showed that the determination coefficient (R2) of *SSC* calibration set is 0.922 and 0.946 and the standard error is 0.612% and 0.792% when the temperature is 0°C and 23°C, respectively. *Yu et al., (2017)* tested the *SSC* in grapes based on *NIR* and *RC*, *RMSEP* and *RMSEC* of *PLS* are 0.83, 0.76 and 0.84 by using the orthogonal test. *Sun et al., (2018)* used visible / near-infrared semi-transmission spectroscopy to explore the influence of being unpeeled (complete) and peeled on the *SSC* detection accuracy of navel oranges. Studies showed that peel imposes significant impact on the *SSC* detection accuracy under the 5% confidence level. The correlation coefficient and root mean square error of the prediction set of the optimal *PLS* of the *SSC* in unpeeled and peeled navel oranges are 0.888 and 0.456% / 0.944 and 0.324%, respectively. *Zhang et al., (2011)* established the relations among visible light, near-infrared diffuse reflection spectrum (*Vis/NIR*) and the soluble tannin content in persimmons. The results showed that first derivative and detrending algorithms are the optimal preprocessing method, and the modified partial least squares (*MPLS*) demonstrated better prediction performance of the soluble tannin content in astringent persimmon, of which the *RCV, RP2, RMSECV* and *RMSEP* are 0.7227, 0.6785, 0.148 and 0.1763, respectively. The studies above show that it is feasible to use *NIR* to detect the internal qualities of fruits, but there is no research on the internal quality detection of CHs based on *Vis/NIR* spectroscopy.

With cerasus humilis "Nongda 5" as the research object, a prediction model of the SSC in Cerasus Humilis (CH) is established based on visible / near-infrared spectroscopy to explore a nondestructive testing method of the internal quality of CH, hoping to achieve a CH *SSC* prediction model of good stability and high prediction accuracy. ASD Field Spee3 spectrometer has been employed to collect *DRS* data, and a spectral preprocessing method has been selected optimally. Four dimension-reducing methods, which are *PLSR* regression coefficients (*RC*), competitive adaptive reweighted sampling (*CARS*), and successive projections algorithm (*SPA*) and uninformative variable elimination (*UVE*), are used to extract the characteristic wavelengths, and different prediction models are built combined with *PLSR* and *LS-SVM*.

They provide technical support for rapid, nondestructive, low-cost, and large-scale grading detection research of CH qualities.

MATERIALS AND METHODS
Cerasus humilis samples

Sampling was conducted on August 15, 2019. The sampling site was the Jinzhong Agricultural High-Tech Industrial Demonstration Zone Base in Taigu County, Shanxi Province, China (112°29'E, 37°23'N), and the variety was "Nongda 5", sample growth state as shown in Fig. 1. Samples are of consistent maturity, shape and have no damage in order to minimize the influence of individual differences on experiment results. They were placed in a low-temperature fresh-keeping box which was transported to the laboratory the same day. The surface was wiped. Before the data acquisition, all samples were individually numbered and they were placed in an environment where temperature is 25℃ and relative humidity is 20% for 6 hours to prevent the temperature from affecting the spectra and qualities.

Fig. 1 - Growth state of cerasus humilis

A high-precision electronic balance (FA1004N, Shanghai) and a Vernier Caliper (Mitutoyo, Japan) were used to weigh and measure the weight and diameters of each sample.

Table 1 shows the statistics of 160 samples.

Table 1

Statistics of 160 samples

Sample parameters	Min.	Max.	Mean	Standard deviation	Variable coefficient (%)
Diameter [mm]	15.48	28.66	24.72	3.62	14.64
Weight [g]	7.47	16.18	11.39	1.76	15.45

Vis/NIR collection

A FieldSpec3 analytical spectral device (*ASD*, USA) was used to collect the *VIS/NIR* data of samples. The interval of spectral data is 1 nm, the number of scans is 30 times, the resolution is 3.5 nm, and the wavelength range is 350-2500 nm. Diffuse reflection was employed to sample the spectra. Each sample was scanned 3 times at an interval of 120 degrees above the equator, and its average value was taken as the final spectral data. The spectral experiment platform is shown in Fig. 2. The diffuse reflectance spectral data of a total of 160 CH samples were collected.
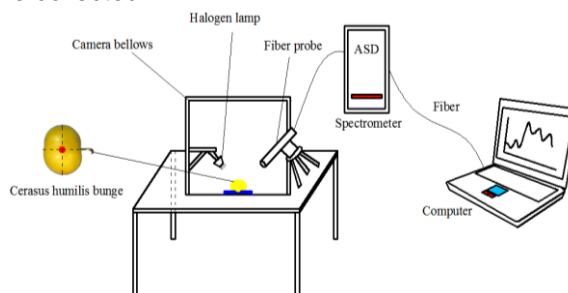
Fig. 2 - Spectral experiment platform

Determination of soluble solids

Refractive digital sugar content PR-101a (Atago, Japan) was employed to determine the *SSC* in CHs in accordance with GB/12295-1990. The scanned part of CHs was immediately sliced off after the spectra were collected for manual juicing, and the juice was filtered. Filtered juice was dripped onto the measurement window of the saccharimeter for *SSC* reading. Three measurements were taken and the mean value was used as the experimental value. The measurement window needs to be cleaned with distilled water and wiped clean after each measurement to avoid impact on experimental values.

Spectrum modeling
Spectral data preprocessing
Employing a feasible spectral preprocessing method can not only eliminate noise, but also minimize or reduce the impact of environmental factors such as lighting and instrumental factors such as random errors, ensuring the precision and validity of extracted spectral data *(Zhang et al., 2012)*. Multiplicative scatter correction (*MSC*), Savitzky-Golay polynomial convolution smoothing (SG smoothing), de-trending, moving average (*MA*), median filtering (*MF*) and *MSC + SG* smoothing (5-point) were employed in this research, and *PLSR* model was used to assess the performance of different spectral preprocessed data.

Extraction of characteristic wavelengths
Four dimension-reducing methods, namely successive projections algorithm (*SPA*) *(Jiang et al., 2016)*, competitive adaptive reweighed sampling (*CARS*) *(Maniwara et al., 2014)*, PLSR regression coefficients (*RC*) *(Liu et al., 2015)* and uninformative variable elimination (*UVE*), were employed to extract characteristic wavelengths. The pros and cons of the prediction stability of the models built based on the aforementioned four methods were analysed, and they were put through secondary dimension reduction in combination with *SPA* and *CARS* for comparison of their pros and cons.

Modeling and prediction
Partial least squares regression (*PLSR*) is a multivariate linear modeling method that conducts linear fitting for curves with least square error sum, and it combines the advantages of correlation analysis, multivariate linear regression and principal components, and is widely applied in spectral modeling *(Gao et al., 2019)*. It may comprehensively measure the sample spectral information and physical-chemical indicators at the same time to obtain the optimal model of calibration.

Least squares support vector machine (*LS-SVM*) is a modified and improved algorithm based on the principle of support vector machine (SVM). It is able to deal with the linear and non-linear problems in multivariate calibration modeling and resolving these relationships in a relatively fast way *(Bao et al., 2015)*. Details of LS-SVM algorithm could be found in the literatures *(Coen et al., 2006)*. . LSSVM regression model was given as follows:

$$y_{(x)} = \sum_{k=1}^{N} a_k K(x, x_k) + b \tag{1}$$

Where:

$K(x, x_k)$ is the kernel function, x_k is the input vector, a_k is the Lagrange multiplier called support value, and b is the bias.

PLSR was established based on different preprocessing methods, and the best preprocessing method was selected in combination with a variety of characteristic wavelength extraction algorithms, establishing a full-spectrum (*FS*) and characteristic wavelength *PLSR* and LS-SVM models, respectively. To verify the prediction performance of different models, the prediction set samples were seen as input variables, and the prediction results of different models were compared and analysed to obtain the optimal prediction model.

Assessment of models
The following five indicators are usually selected to assess the precision and stability of models: the correlation coefficient of the calibration set (*Rc*), the correlation coefficient of the prediction set (*Rp*), the root mean square error of the calibration set (*RMSEC*), the root mean square error of the prediction set (*RMSEP*), and the residual predictive deviation (*RPD*); *RPD* is the ratio of standard deviation (*SD*) to *RMSEP (Tamaki et al., 2015)*. The closer *Rc* and *Rp* are to 1, the smaller and closer the *RMSEC* and *RMSEP* are, the better the prediction performance and stability of the model, and the higher the precision. These assessment parameters were calculated as follows:

$$R_C = \sqrt{\sum_{i=1}^{n_c} \left(\hat{y}_i - y_i \right)^2} \bigg/ \sqrt{\sum_{i=1}^{n_c} \left(\hat{y}_i - y_c \right)^2} \tag{2}$$

$$R_P = \sqrt{\sum_{i=1}^{n_p} \left(\hat{y}_i - y_i \right)^2} \bigg/ \sqrt{\sum_{i=1}^{n_p} \left(\hat{y}_i - y_p \right)^2} \tag{3}$$

$$RMSEC = \sqrt{\frac{1}{n_c}\sum_{i=1}^{n_c}\left(\hat{y}_i - y_i\right)^2} \qquad (4)$$

$$RMSEP = \sqrt{\frac{1}{n_P}\sum_{i=1}^{n_P}\left(\hat{y}_i - y_i\right)^2} \qquad (5)$$

$$RPD = \frac{SD}{RMSEP} \qquad (6)$$

where:

$\hat{y}_i$ and y_i are the predicted and measured value of the ith sample, and y_p are the averaged values of testing samples in the calibration set and prediction set, n_c and n_p are the number of testing samples in the calibration and prediction set, respectively.

The spectral data preprocessing, sample set classification, characteristic wavelengths screening and modeling in this research were conducted in software platforms including The Unscrambler X 10.4 (CAMO ASA, Trondheim, Norway), and Matlab R2010b (The MathWorks, Natick, USA). Diagrams were made in Origin8.5 (Origin Lab, USA).

RESULTS
Classification of sample sets

T2 ellipsometry *(Galvão et al., 2015)* was first used for abnormal sample detection before the classification, and no abnormal sample was detected. A total of 160 samples were classified into calibration set (120 samples) and prediction set (40 samples) randomly by 3:1 according to K-S. Table 2 shows the measurement statistics of the internal qualities of CH samples of both calibration and prediction sets.

Table 2

Statistics of sample set classification based on K-S

Sample quantity	Indicators	Min.	Max.	Mean ± Standard deviation
Calibration set (120)	SSC[°Brix[	7.26	17.28	12.64±1.71
Prediction set (40)	SSC[°Brix]	9.42	15.44	12.56±1.70
Total (160)	SSC[°Brix]	7.26	17.28	12.62±1.69

Table 2 shows that the ranges of SSC values of calibration sets and prediction sets are 7.26～17.28°Brix and 9.42～15.44°Brix, and the SSC distribution of all samples is 7.26~17.28°Brix, and the SSC values of calibration sets and prediction sets are mean values of 12.64 and 12.56°Brix with standard deviation (S.D.) of 1.71 and 1.70°Brix, respectively. Moreover, the SSC range of calibration set is bigger than that of prediction set, which is beneficial for the development of accurate and robust calibration models.

Analysis of spectral characteristics

Figure 3 shows the original near-infrared spectral curves of 160 CH samples, and it can be known that the trends of the curves of all samples have few differences and there is no significant abnormal sample.
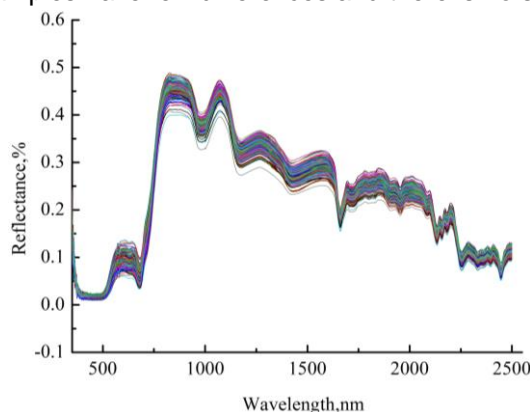
Fig. 3 - The original spectral diagrams of 160 CH samples

Fig. 3 shows that the spectral curve is smooth in the range of 350~500nm where the reflectance value hardly changes. The reflectance of the sample rises rapidly after 690nm, and there are peaks at 610, 875, 1070, 1265, and 1570nm, and troughs at 680, 980, 1174, 1420, and 1660nm.

A significant absorption peak appeared at 680nm which was mainly the result of the fact that the chlorophyll on CH surface was absorbing spectra. Absorption peaks at 980, 1174, 1420, and 1660nm are the result of the strong absorption of water molecules, reflecting the MC of CHs within the waveband. 400-2450nm was chosen for experiment data processing since there are certain signal-to-noise ratio and low noise in the range of 350-399nm and 2451-2500nm.

Comparison of PLSR modeling results of different preprocessing methods

To eliminate the impact of exterior environmental factors as well as instrument noises on the DRS so that the collected spectra could have higher *SNR* and the stability of prediction models could be improved, we have to look for the most effective preprocessing method, offering the best data for following modeling analysis. The spectral data obtained by different preprocessing methods are used as input variables of *PLSR* to establish corresponding prediction models. The comparison of PLSR modeling based on different preprocessing methods is shown in Table 3.

Table 3

Impact of Different Preprocessing Methods on *CH PLSR*

Pretreatment method	Calibration set		Validation set		Prediction set		Factor quantity
	Rc	*RMSEC*	*Rcv*	*RMSECV*	*Rp*	*RMSEP*	
Original spectrum	0.7302	0.9276	0.7223	1.3799	0.7406	1.3398	7
MSC	0.8511	0.8607	0.7587	1.3015	0.7939	1.2125	9
S-G(5-point)	0.8302	0.9021	0.7231	1.3779	0.7406	1.3399	9
De-trending	0.7979	1.1161	0.7217	1.3806	0.7304	1.3622	11
MA	0.8312	0.9176	0.7243	1.3754	0.7406	1.3401	9
MF	0.8351	0.9046	0.7305	1.3624	0.7464	1.3271	7
MSC+S-G(5-point)	0.8302	0.9177	0.7158	1.3928	0.7282	1.3668	9

Based on how to assess a model, Table 3 shows that the *Rc* is 0.8511, *R*p is 0.7939, and *RMSEC* of the model is 0.8607 when original spectra were processed with *MSC*, and the difference with *RMSEP*=1.2125 is minimal, which is 0.3158. Therefore, the model prediction performance is good, and *MSC* is proved to be the optimal preprocessing method. Fig. 4 shows the spectral curves processed with the *MSC* preprocessing method.
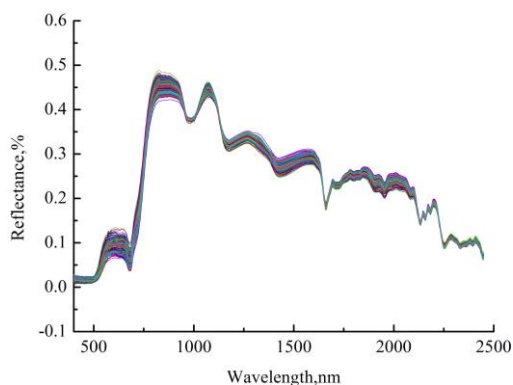
Fig. 4 - CH NIR spectral diagrams after *MSC*

Extraction of characteristic wavelengths
Successive projections algorithm (SPA)

SPA was employed to select the characteristic wavelengths and a conclusion was drawn that the smaller the *RMSE* values, the better the model's stability. Fig. 5 (a) shows the *RMSE* distribution when different number of variables was selected by SPA. When the number of selected wavelength variables is 4, *RMSE* is minimized, which is 1.0323; and Fig. 5 (b) shows the distribution of the number of characteristic wavelengths preferably selected by SPA. The four characteristic wavelengths selected are 1764, 615, 1259, and 2035nm, and their wavelength importance decreases in order.
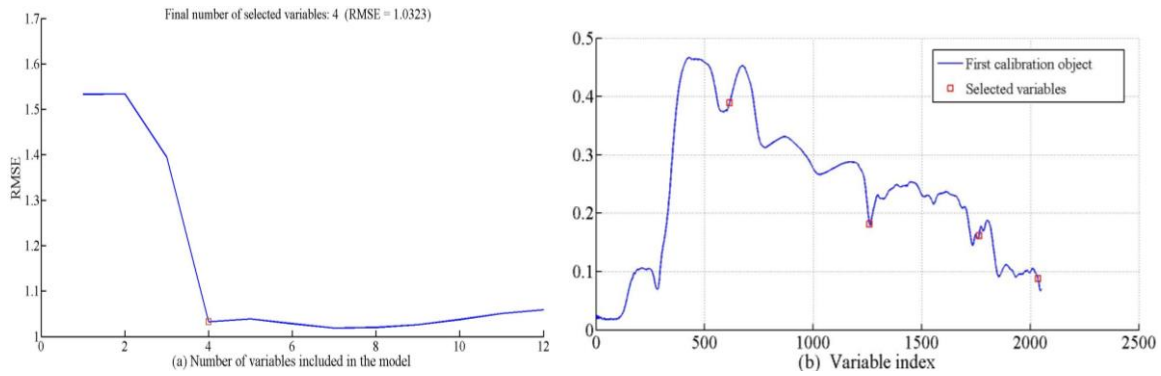
Fig. 5 - Changes of RMSE (a) and the optimal characteristic wavelength selected by SPA (b)

Regression coefficient (RC)

Local extreme values of PLSR regression coefficients (RC) were used to select the number of characteristic wavebands. As shown in Fig. 6, 12 characteristic wavelengths were selected, which are 655, 695, 724, 777, 833, 931, 964, 993, 1102, 1187, 1334 and 1907nm.
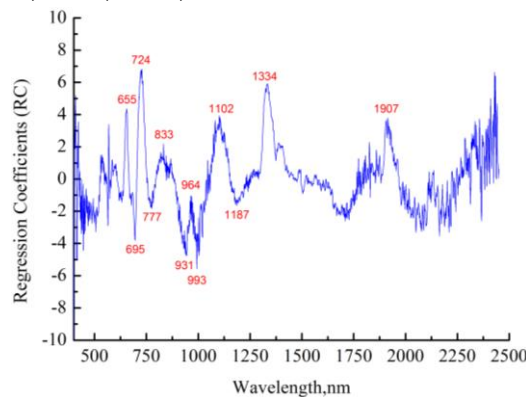
Fig. 6 - Selecting characteristic wavelengths with PLSR RCs

Competitive adaptive reweighted sampling (CARS)

The process of CARS screening characteristic wavelengths is shown in Fig. 7. Monte Carlo Sampling was set 50 times and the number of cross-validation groups is 10. According to Fig. 7 (a), the wavelength number gradually decreased and stabilized at last as the number of sampling runs increased, which verified the rough and fine selection during wavelength screening. As Fig. 7 (b) shows, cross-validation $RMSECV$ decreased gradually before it showed an increasing trend when the sampling runs increased to 34; when $RMSECV$ decreased, it means that the null info among spectral info were eliminated; and when $RMSECV$ increased, it means that valid info among spectral info were eliminated. Fig. 7 (c) shows that when the position of the line of "*" indicated the runs were 34, $RMSECV$ was minimized, which is 0.9553. 19 characteristic wavelengths selected by CARS at this moment were 408, 531, 533, 652, 657, 728, 747, 940, 942, 943, 998, 1003, 1014, 1338, 2328, 2403, 2404, 2423, and 2435nm; these effective variables could be observed in Fig. 8.
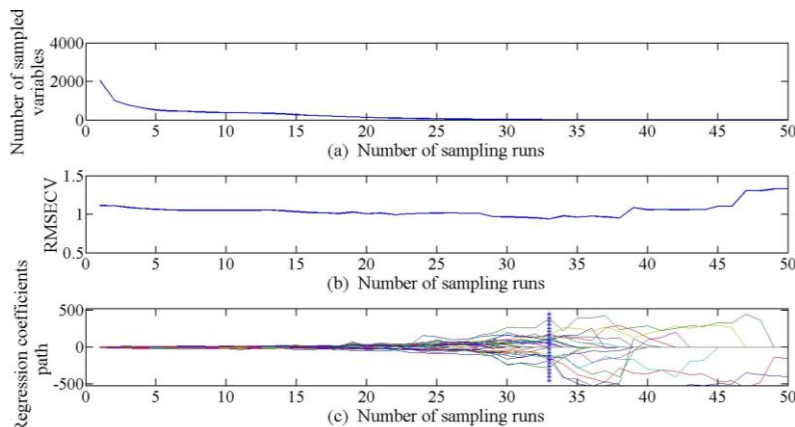
Fig. 7 - Selection of wavelength variables via CARS
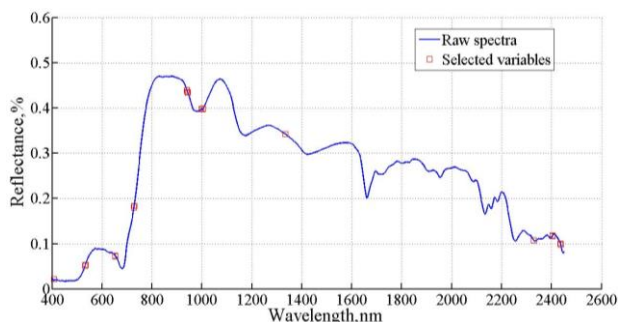
Fig. 8 - Distribution of the optimal characteristic wavelength selected by CARS

Uninformative variable elimination (UVE)

UVE was employed to extract the characteristic wavelengths of CHs, and it was set as five interactive operation where different principal component quantities (6-17) were selected. *RMSECV* was minimized when the principal component quantity was 10, which was 1.0376, as shown in Fig. 9 (a). Fig. 9 (b) shows the stability distribution curve of UVE-PLSR when the principal component quantity was 10. There are the curves of 2,051 wavelength variable on the left of the vertical continuous line, and the curves of 2,051 randomly introduced variables on the right. The two horizontal dotted lines show the selection threshold of random variables (±26.03) where the threshold equals 99% of the maximized stability of random variables. Information bigger than the absolute threshold value is considered informative, namely the information in between the dotted lines are informative while the rest were uninformative. Therefore, 94 variables were determined to be effective variables that were shown in Fig. 9 (c) for SSC detection of cerasus humilis.
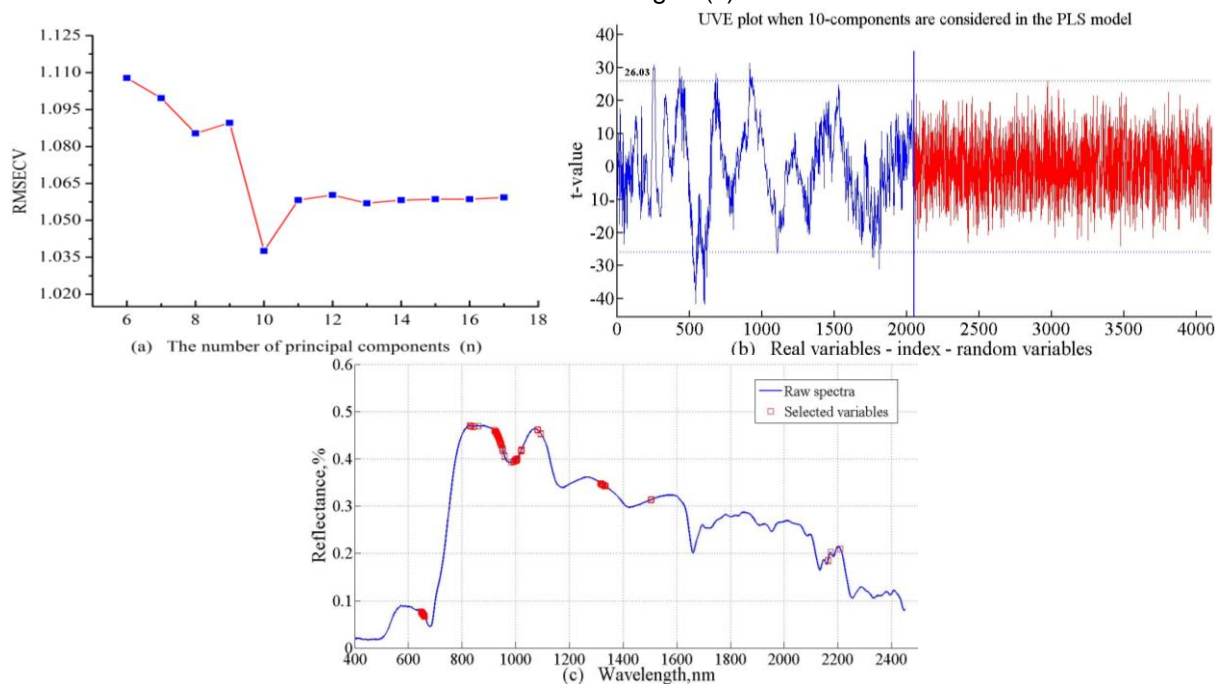
Fig. 9 - RMSECV distribution of different principal components (a), stability distribution curve of UVE-PLSR (b) and distribution of the effective variables in the raw spectral curve (c) Distribution of the optimal characteristic wavelength selected by CARS

Extraction of characteristic wavelengths with secondary dimension-reduction

The dimensions of wavelengths were reduced and null info was eliminated after the use of the aforementioned 4 dimension-reducing methods to extract characteristic wavelengths, thus improving the stability and precision of models. The characteristic wavelengths extracted by *UVE* tend to have more variables, but there may be possible null info. *SPA* and *CARS* were combined, 5 and 10 characteristic wavelengths were selected respectively, which were 937, 1504, 992, 959 and 2163nm as well as 647, 652, 654, 660, 845, 923, 933, 940, 953 and 1082nm, these effective variables could be observed in Fig. 10 and Fig. 11, respectively.
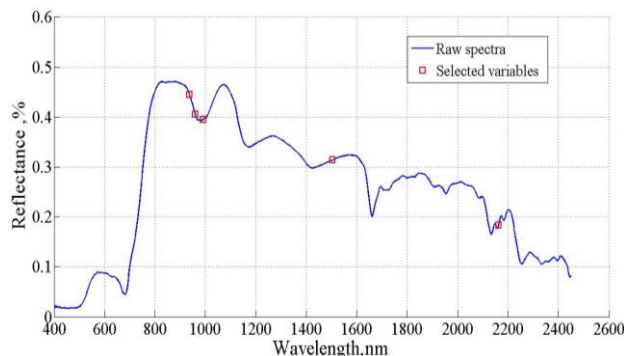
Fig. 10 - Distribution of the optimal characteristic wavelength selected by UVE-SPA
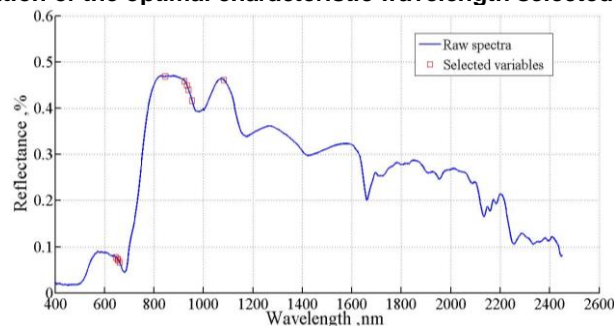
Fig. 11 - Distribution of the optimal characteristic wavelength selected by UVE-CARS

Establishment of PLSR and LS-SVM models based on different variables

In order to compare the linear model *(PLSR)* and non-linear model (*LS-SVM*) for SSC prediction of CH. The characteristic wavelengths extracted by using full spectra by and 6 dimension-reducing methods (*UVE, CARS, RC, SPA, UVE-SPA, UVE-CARS*) were used as input to establish different *PLSR* and *LS-SVM* models, as shown in Table 4 and Table 5.

Table 4

CH SSC PLSR models under full spectra and different characteristic wavelengths

Modeling method	Extraction method	Variable number	Calibration set		Validation set		Prediction set		RPD
			Rc	RMSEC	Rcv	RMSECV	Rp	RMSEP	
PLSR	FS	2051	0.7406	0.9276	0.7223	1.3799	0.7302	1.3398	1.2688
	UVE	94	0.8363	0.9184	0.8806	0.9486	0.8057	0.9577	1.7751
	CARS	19	0.8925	0.9074	0.8362	0.9808	0.8554	0.9259	1.8361
	RC	12	0.7961	0.8973	0.7509	1.3178	0.7711	1.2701	1.3385
	SPA	4	0.8357	0.9236	0.8166	1.0323	0.7415	0.9815	1.7320
	UVE-SPA	5	0.8116	0.9198	0.7962	1.0818	0.7526	1.0443	1.6279
	UVE-CARS	10	0.8995	0.8897	0.8345	0.9859	0.8579	0.9059	1.8766

As shown in Table 4, in accordance with the modeling assessment principles, the comparison between PLSR models, which were built with the characteristic wavelengths extracted by 6 dimension-reducing methods as the input, and *FS-PLSR* (*Full-spectrum-PLS*), the quantity of wavelength variables showed significant reduction, and improvement of model stability and precision to different extents. In addition, *Rc, RMSEC, Rp* and *RMSEP* are all better than those of *FS-PLSR*. By comparing models of *UVE-PLSR, CARS-PLSR, RC-PLSR, SPA-PLSR, UVE-SPA-PLSR*, and *UVE-CARS-PLSR*, *RC-PLSR* retained 12 variables and showed poorer precision; *CARS-PLSR* and *UVE-CARS-PLSR* outperformed the rest, and the comparison between them two showed that their *Rc, RMSEC, Rp* and *RMSEP* are very close. When the variable quantity of *UVE-CARS-PLSR* is 10, *Rc* of *UVE-CARS-PLSR* is 0.8995, and *Rp* is 0.8579, both values are closer to 1; while *RMSEC* is 0.8897, *RMSEP* is 0.9059 and *RPD* is 1.8766, indicating that the models have good calibration and prediction performance, and the preferably selected 10 characteristic wavelengths may effectively reduce the dimensions of original spectral data.

Table 5

CH SSC LS-SVM models under full spectra and different characteristic wavelengths

Modeling method	Extraction method	Variable number	[γ, σ²]		Calibration set		Prediction set		RPD
					Rc	RMSEC	Rp	RMSEP	
LS-SVM	FS	2051	$1.78×10^2$	$1.88×10^3$	0.8558	0.8464	0.8014	0.9625	1.7662
	UVE	94	$1.32×10^2$	$1.87×10^3$	0.8762	0.8914	0.8521	0.9276	1.8327
	CARS	19	$6.68×10^2$	$2.19×10^3$	0.9025	0.8614	0.8743	0.9225	1.8428
	RC	12	$2.43×10^3$	$1.87×10^3$	0.8644	0.8999	0.7961	0.9380	1.8124
	SPA	4	$6.66×10^2$	$2.17×10^3$	0.8352	0.9828	0.7632	0.9883	1.7201
	UVE-SPA	5	$8.28×10^2$	$1.95×10^3$	0.8211	0.9576	0.7825	0.9812	1.7326
	UVE-CARS	10	$4.86×10^3$	$8.45×10^2$	0.9097	0.8528	0.8766	0.9116	1.8649

Table 5 illustrates the performance of the *LS-SVM* models in calibration and prediction. Compared with the establishment *PLSR* model, the established *LS-SVM* model also showed more satisfactory results. and *FS-LS-SVM* model coefficients of calibration set, prediction set and root mean square errors are: Rc = 0.8558, Rp = 0.8014, *RMSEC* = 0.8464, *RMSEP* = 0.9625, *RPD*=1.7662. In *SPA-LS-SVM* model, the Rp of 0.7632 was the lowest and *RMSEP* of 0.9883 was the highest may be because variables with important information were eliminated by *SPA*, and *UVE-SPA-LS-SVM* model did so too. Although *RC-LS-SVM* model the number of variables was reduced to 12, that showed poorer precision. In addition, as shown in Table 5, *UVE-CARS-LS-SVM* model had better prediction performance with higher *RP* of 0.8766, lower *RMSEP* of 0.9116 and higher *RPD* of 1.8648 than *UVE-LS-SVM* model (with Rp=0.8521, *RMSEP*=0.9276, *RPD*=1.8327). For *CARS-LS-SVM* model and *UVE-CARS-LS-SVM* model, that comparison between them two showed that their *Rc, RMSEC, Rp* and *RMSEP* are very close. However, fewer variables (only 10 variables) were used in *UVE-CARS-LS-SVM* model. *Rc* of *UVE-CARS-LS-SVM* is 0.9097, and *Rp* is 0.8766, both values are closer to 1; while *RMSEC* is 0.8528 and *RMSEP* is 0.9116. Therefore, in accordance with the modeling assessment principles, among all *LS-SVM* models, *UVE-CARS-LS-SVM* model was the best for effectively predicting.

RESULTS

As shown in Table 4 and Table 5, *PLSR* and *LS-SVM* models of CH *SSC* content based on full spectra and different wavelengths, all models can achieve the effective prediction. It can be observed that the optimal linear *PLSR* models (*UVE-CARS-PLSR*) has slightly similar prediction ability compared with the optimal *LS-SVM* models (*UVE-CARS-LSSVM*), that their *Rc, RMSEC, Rp* and *RMSEP* are very close. The results indicated that *UVE-CARS* has the potential to select *Vis/NIR* spectroscopy effective wavelengths. However, *UVE-CARS-PLSR* model had better prediction performance with higher *RPD* of 1.8766 than *UVE-CARS-LS-SVM* model (with RPD=1.8649).

Fig.12 shows the scatter plots of measured and predicted *SSC* results of *UVE-CARS-PLSR* built with the preferred characteristic wavelengths with the use of *UVE-CARS* dimension-reducing algorithm.
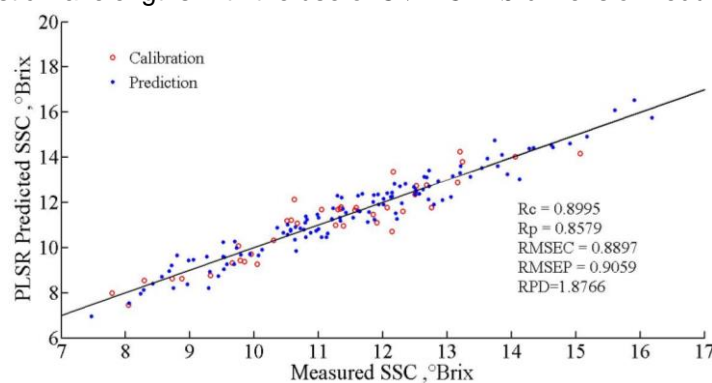
Fig. 12 - SSC indicators predicted by UVE-CARS-PLSR

CH SSC prediction models were established with *MSC-UVE-CARS* and *PLSR* in the research, and 10 characteristic wavelengths were extracted, obtaining *Rc, Rp, RMSEC*, and *RMSEP*, which are 0.8995, 0.8579, 0.8897, and 0.9059, and *RPD* is 1.8766. As for the *PLSR* model on *FS*, its *Rc, Rp, RMSEC*, and *RMSEP* are 0.7406, 0.7302, 0.9276 and 1.3398, and *RPD* is 1.2688. It means that *MSC-UVE-CARS-PLSR* reflects the characteristic spectra absorption of CH SSC more directly than *FS-PLSR* does. For example, the *Ar et al., (2019)* used *MSC* and *PLS* to establish a prediction model for the *SSC* in persimmons. According to the analysis, *Rc* and *RMSEC* are 0.86 and 1.4866; *RMSEP* is 1.4663, *RPD* is 1.79 and CV is 9.84 when the calibration model factor quantity is 17. By comparison, the prediction models established by the author have better stability and precision, which means that different dimension-reducing methods used for original spectra to extract valid variables would improve the stability and prediction precision of models.

CONCLUSIONS

In this study, with cerasus humilis "Nongda 5" as the research object, the spectral info in between 400-2450nm were collected and reflection spectra were extracted to establish the *PLSR* and *LS-SVM* of CH spectral info and SSC, achieving the prediction of CH *SSC*. The main conclusion has been drawn as follows:

(1) The original spectra of CH samples were preprocessed with 6 methods and *MSC* was proved to be the best preprocessing method which improved the *PLSR* modeling performance. *Rc* is 0.8511, *Rp* is 0.7939, *RMSEC* is 0.8607 and *RMSEP* is 1.2125;

(2) Based on the *MSC* preprocessing method, *UVE, CARS, RC, SPA, UVE-SPA* and *UVE-CARS* methods were adopted to extract the characteristic wavelengths, and the numbers of preferred characteristic wavelengths were 94, 19, 12, 4, 5, and 10;

(3) Based on the full spectrum data, *FS, UVE, CARS, RC, SPA, UVE-SPA* and *UVE-CARS* were respectively adopted to extract the characteristic wavelengths to establish the linear model (*PLSR*) and non-linear model (LS-SVM). By comparison, the optimal model is proved to be *UVE-CARS-PLSR*, and its coefficients of calibration set, prediction set and root mean square errors are: *Rc* = 0.8995, *Rp* = 0.8579, *RMSEC* = 0.8897, *RMSEP* = 0.9059, *RPD*=1.8766. Extracting characteristic wavelengths with *UVE-CARS* may cut down the redundant data of the original spectra, reduce the wavelength dimensions, and retain valid info, which can provide references and theoretical basis for subsequent portable detectors and online sorting detection research.

However, it should be noted that samples with consistent size, shape and have no damage were used in this study. In practice, however, size, shape and damage degree of samples is different. Thus, size, shape and damage degree parameter should be considered for establishment of models in future studies. In addition, establishment of various models based on different growing sites, more cultivars and storage days for developing the more accurate and robust prediction models, to improve the universality of the model are necessary.

ACKNOWLEDGEMENT

REFERENCES

[1] Ar N. H., Purwanto Y. A., Budiastra I. W., (2019), Prediction of soluble solid content, vitamin C, total acid and firmness in astringent persimmon (Diospyros kaki L.) cv. Rendeu using NIR spectroscopy, *Materials Science and Enginee*ring, Vol.2019, Issue 557, pp.12-18, Amsterdam/Netherlands;

[2] Bao Y., Liu F., Kong W., et al., (2014), Measurement of soluble solid contents and pH of white vinegars using VIS/NIR spectroscopy and least squares support vector machine, *Food and Bioprocess Technology,* Vol.7, Issue 1, pp.54-61, New York/United States;

[3] Coen T., Saeys W., Ramon H., et al., (2006), Optimizing the tuning parameters of least squares support vector machines regression for NIR spectra, *Journal of Chemometrics,* Vol.20, Issue 5, pp.184-192, London/U.K.;

[4]   Escribano S., BiasiW. V., LerudR., et al., (2017), Non-destructive prediction of soluble solids and dry matter content using NIR spectroscopy and its relationship with sensory quality in sweet cherries, *Postharvest Biology and Technology*, Vol.2017, Issue 128, pp.112-120, Amsterdam/Netherlands;

[5]   Galvão R. K. H., Araujo M. C. U., José G. E., et al., (2005), A method for calibration and validation subset partitioning, *Talanta*, Vol.2005, Issue 67, pp.736-740, Amsterdam/Netherlands;

[6]   Guo Zhiming, Huang Wenqian, Peng Yankun., et al., (2016), Colour compensation and comparison of shortwave near infrared and long wave near infrared spectroscopy for determination of soluble solids content of Fuji apple, *Postharvest Biology and Technology,* Vol.2016, Issue 115, pp.81-90, Amsterdam/Netherlands;

[7]   Gao S., Wang Q., Li Q., et al., (2019), Non-destructive detection of vitamin c, sugar content and total acidity of red globe grape based on near infrared spectroscopy, *Chinese Journal of Analytical Chemistry,* Vol.47, Issue 6, pp.941-949, Beijing/China;

[8]   Jiang S., Sun J., Xin Z., et al., (2016), Visualizing distribution of pesticide residues in mulberry leaves using NIR hyperspectral imaging, *Journal of Food Process Engineering*, Vol.40, Issue 4, pp.1-6, New York/United States;

[9]   Liu D., Zhang S., Wang B., et al., (2015), Detection of hawthorn fruit defects using hyperspectral imaging, *Spectroscopy and Spectral Analysis*, Vol.35, Issue 11, pp.3167-3171, Beijing/China;

[10]   Maniwara P., Nakano K., Boonyakiat D., et al., (2014), The use of visible and near infrared spectroscopy for evaluating passion fruit postharvest quality, *Journal of Food Engineering*, Vol.143, Issue 2, pp.33-43, Los Angeles/California;

[11]   Maniwara P., Nakano K., Boonyakiat D., et al., (2014), The use of visible and near infrared spectroscopy for evaluating passion fruit postharvest quality, *Journal of Food Engineering*, Vol.2014, Issue 143, pp.33-43, Los Angeles/California;

[12]   Parpinello G. P., Nunziatini G., Rombolà A. D., et al., (2013), Relationship between sensory and NIR spectroscopy in consumer preference of table grape (cv Italia), *Postharvest biology and technology*, Vol.2013, Issue 83, pp.47-53, Amsterdam/Netherlands;

[13]   Purwanto Y. A., Sari H. P., Budiastra I. W., (2015), Effects of preprocessing techniques in developing a calibration model for soluble solid and acidity in 'Gedong Gincu' mango using NIR spectroscopy, *International Journal of Engineering and Technology*, Vol.2015, Issue 7, pp.1921-1927, Singapore/Singapore;

[14]   Sun T., Mo X., Liu M., (2018), Effect of pericarp on prediction accuracy of soluble solid content in navel oranges by visible/near infrared spectroscopy, *Spectroscopy and Spectral Analysis*, Vol.38, Issue 5, pp.1406-1411, Beijing/China;

[15]   Tamaki Y., Mazza G., (2011), Rapid determination of carbohydrates, ash, and extractives contents of straw using attenuated total reflectance Fourier transform mid-infrared spectroscopy, *Journal of agricultural and food chemistry,* Vol.59, Issue 12, pp.6346-6352, Washington/United States;

[16]   Yu J., Wang H., Sun X., et al., (2017), Parameter optimization in soluble solid content prediction of entire bunches of grape based on near infrared spectroscopic technique, *Journal of Food Measurement and Characterization*, Vol.11, Issue 4, pp.1676-1680, New York/United States;

[17]   Zhang P., Li J., Meng X., et al., (2011), Research on nondestructive measurement of soluble tannin content of astringent persimmon using visible and near infrared diffuse reflection spectroscopy, *Spectroscopy and Spectral Analysis*, Vol.31, Issue 4, pp.951-954, Beijing/China;

[18]   Zhang S., Zhang H., Zhao Y., et al., (2012), C*omparison of modeling methods of fresh jujube soluble solids measurement by NIR spectroscopy, Transactions of the Chinese Society for Agricultural Machinery*, Vol.43, Issue 3, pp.108-112, Beijing/China.

RAPID DESIGN OF MAIZE EAR HARVESTER HEADER BASED
ON KNOWLEDGE ENGINEERING
/
基于知识工程的玉米果穗收获机割台快速设计

Tai Jianjian[1)], *Li* Haitao[1)], *Du* Yuefeng[1)], *Mao* Enrong[1)], *Zhang* Junnan[1)], *Long* Xinjiani[1)]   [1]
[1)]China Agricultural University, College of Engineering, Beijing/China;
Tel: +86-18612925066; E-mail: jjtai_sdau@163.com
DOI: https://doi.org/10.35633/inmateh-61-29

ABSTRACT

In the design process of maize combine harvester in China, there are characteristics of customization and high demand for diversification. Aiming at the problems of long design and development cycle, the structural design method of maize combine harvester header based on knowledge engineering is put forward, and the header of maize combine harvester is designed rapidly. Firstly, based on the design standards and specifications of agricultural machinery, the general design process of maize ear harvester header is determined. Secondly, according to the design knowledge and experience, the design method of the core parts of the header is determined, and an example model is established. Finally, based on the platform of MFC and Creo, integrating the design knowledge base, inference engine and parametric model, a rapid design system of maize ear harvester header is constructed. The rapid design of maize ear harvester header is realized, and the design and development efficiency of maize ear harvester header is improved so as to provide technical reference and support for improving the intelligent level of typical complex agricultural machinery equipment in China.

摘要

我国玉米联合收获机在设计过程中，存在定制化、多样化需求高的特点，针对其设计及开发周期长等问题，提出基于知识工程的玉米果穗收获机割台的结构设计方法，对玉米果穗收获机割台进行快速化设计。首先，在基于农业机械设计标准与规范的基础上，确定了玉米果穗收获机割台的一般设计流程；其次，根据设计知识和经验，确定了割台核心部件的设计方法，并建立了实例模型；最后，在基于 MFC、Creo 的平台上，融设计知识库、推理机和参数化模型为一体，构建了玉米果穗收获机割台的快速化设计系统。实现了玉米果穗收获机割台的快速化设计，提高了玉米果穗收获机割台的设计和开发效率。以期为提高我国典型复杂农机装备智能化水平提供技术参考与支持。

INTRODUCTION

With the development of manufacturing technology, the period of agricultural equipment upgrading is becoming shorter and shorter. In the face of fast changing market, it is necessary to improve the efficiency of product design, speed up the overall process of products, and meet the increasingly diversified and personalized needs of users to improve the competitiveness of China's agricultural equipment production enterprises (*Liu Hongxin et al, 2019*). Rapid product design is the development and extension of computer aided design and manufacturing technology. In the current market environment of increasingly diversified and personalized user needs, and a product life cycle gradually shortened, rapid design technology emerges as the times require, which is the urgent demand of many manufacturers (*Wagner P.W., 2017)*. Rapid design means rapid response design and agile design. Its main purpose is to shorten product design cycle, improve product quality and the rapid response ability of enterprises to the market (*Li Changlin et al, 2012*).

As one of the most important crops in China, maize has high labour intensity in the harvesting process, accounting for 55% of the total input labour (*Geng Aijun et al, 2016*). China's Maize Mechanized Harvesting started late, and because of the diversity of maize planting mode, the development speed of maize mechanization is slow, which still lags behind the level of wheat and rice mechanized harvesting.

---

[1]   *Tai Jianjian, Ph.D.Eng.; Li Haitao, Prof. Ph.D. Eng.; Mao Enrong, Ph.D. Eng.; Zhang Junnan, Long Xinjiani*

The header of maize ear harvester is the core part of maize ear harvester, and its performance directly affects the whole harvesting performance of maize ear harvester *(Gianfranco La Rocca, 2012)*. During the operation, the maize plants first glide down to the ear picking opening under the function of the divider, the straw feeding device transports the maize plants to the ear picking device, and the ear conveying device transports the maize ear picked to the ear elevator (*Chen Zhi et al, 2014*).

The researches of enterprises and scholars at home and abroad on the maize harvester header often focus on the improvement design of part of the original structure. Such research is often unsystematic and scattered with great limitations (*Cui Tao et al, 2019*). At present, there are still some problems such as the lack of intelligent design ability, design knowledge system and long product development cycle. If the knowledge is collected to build an intelligent rapid design system, it will greatly promote the development speed of products.

In view of this, taking the forward design of maize ear harvester header as the starting point, this paper puts forward the structural design method of maize ear harvester header based on knowledge engineering. The header of maize ear harvester is designed rapidly, and the design process of the maize ear harvester header is established. The classification, expression and storage methods of header design knowledge are studied. A rapid header design system of maize ear harvester is constructed, which integrates the design knowledge base, inference engine and parametric model. The rapid design of maize ear harvester header has been realized, and the design and development efficiency of it has been improved, which is in line with the national medium and long term scientific and technological development planning outline and the "made in China 2025" strategic layout.

FORWARD DESIGN FLOW OF MAIZE EAR HARVESTER HEADER
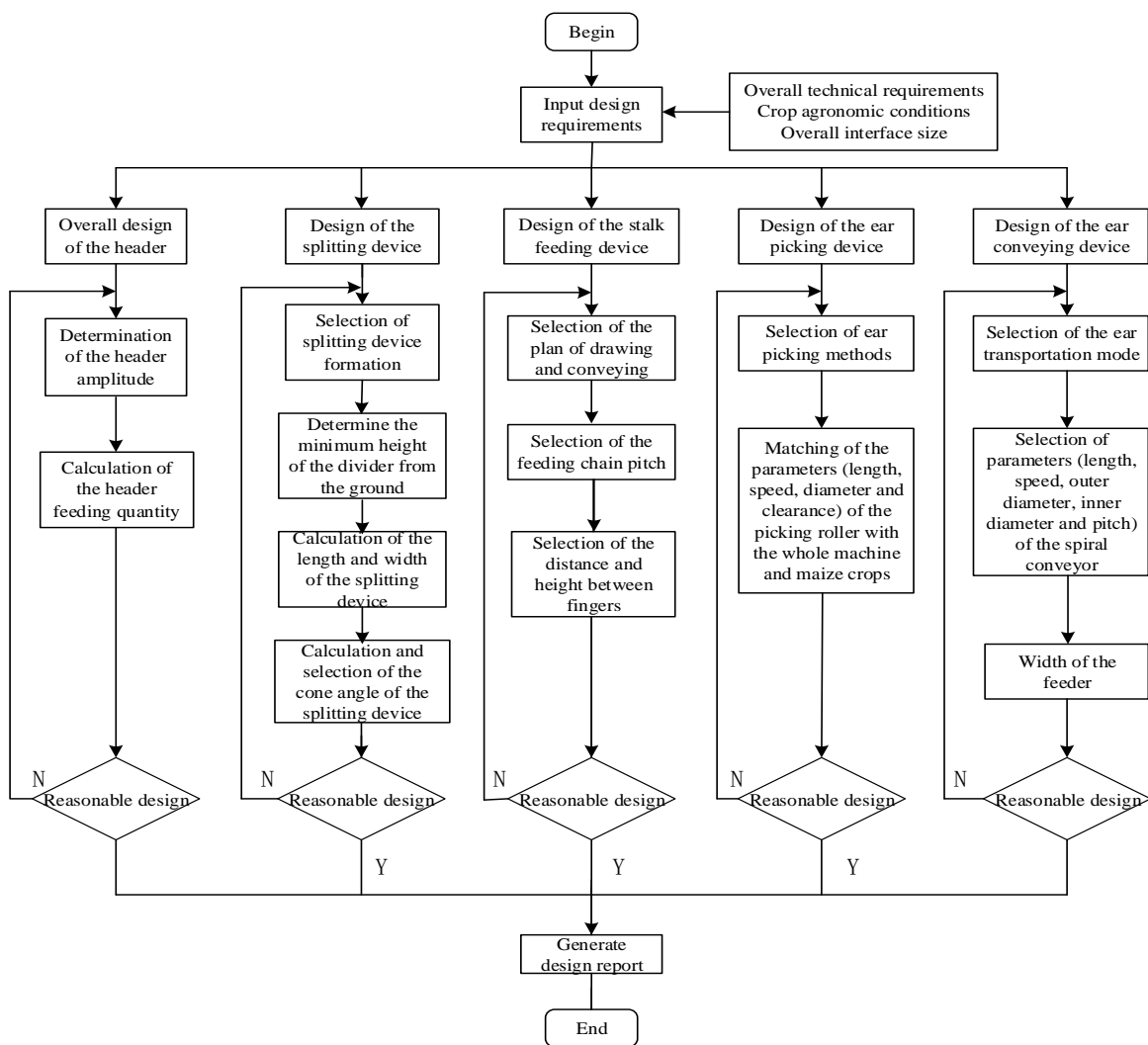
Fig. 1 - General design process of the maize ear harvester header

Before the design of agricultural machinery, it is necessary to plan its general design process based on design standards and specifications, theoretical analysis and reasoning. General design process is a design method with good generality in a design field (*Qiaosheng Liu et, 2011*). For the design of maize ear harvesting header, the general design process should be carried out under the guidance of maize ear harvesting machine design. Header is the core part of maize ear harvester. Design of the header system is bound to be restricted by the whole machine. Therefore, in the design process, the principle of overall design before subsystem design should be followed; that is, on the basis of determining the whole machine, the core parts can be designed. Combined with the theoretical analysis and design manual of agricultural machinery, agricultural policies and regulations and other relevant design standards and specifications, the general design process of the header is determined (*Tong Jin et al, 2007*) .

Firstly, according to the functional requirements of the header, the design requirements are put forward, including the technical requirements of the whole machine, the agricultural conditions of crops and the interface dimensions of the whole machine. Among them, the technical requirements of the whole machine include line number, line spacing, working width, working speed, sales area, function and performance. Crop agronomic conditions mainly include crop varieties, maturity at harvest, planting methods, row spacing, plant spacing, plant height, ear height, stalk diameter, large end diameter of ear and ear length. The interface dimensions of the whole machine mainly include: the minimum height of ear picking, the maximum height of ear picking, the interface dimensions of ear elevator and power transmission mode.

Based on the modular method, according to the specific header design requirements, combined with the structural characteristics of the header, the header assembly design is divided into the overall design of the header, design of the ear picking device, design of the reel conveying device, design of the splitting device and design of the ear conveying device. The specific design process relationship is summarized as shown in Figure 1. The design of each module is independent when the input design requirements are unchanged. If the scheme is reasonable, the design parameters of the header will be output. If not, the header will be redesigned according to the requirements of the process until the scheme outputs reasonably. When each module meets the design requirements, the design report is generated and presented in the form of Excel. Based on the report, a 3D model is established and saved to the model base.

CALCULATION OF THE CORE COMPONENT PARAMETERS OF MAIZE EAR HARVESTER HEADER
Overall design of the header

(1) Calculation of the header cutting width. The cutting width of the harvester header is closely related to the number of rows harvested and the planting row spacing of maize, as shown in Figure 2. The header cutting width meets the following requirements:

$$nB_0 \leq B \leq (n+1)B_0 - 2 \times 90mm \tag{1}$$

Where: B—the cutting width of header, mm; n—the harvest number of maize header;

B_0—the row spacing of maize harvest, mm.
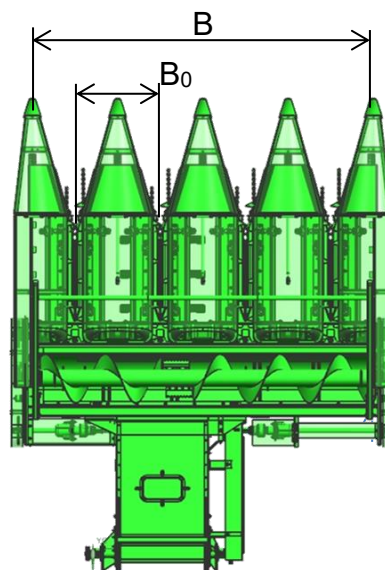
Fig. 2 - Relationship between the overall width of header and planting row spacing

(2) Calculation of the header feeding quantity. The feed quantity of the header is an important index to measure the harvesting efficiency of maize harvester, and its calculation is shown in formula (2).

$$Q = (\frac{v}{\Delta l} + 1) \times n \times \Delta m \tag{2}$$

Where: Q—the feeding quantity of maize ear harvesting header, kg/s; v—the forward speed of combine harvester, m/s; Δl—the plant spacing of maize, m; n—the maize header harvest, row; Δm—the average quality of harvested maize, kg.

Design of the splitting device

During the operation, the maize plant is subdivided at the top of the divider. The maize plants slide along the lower edge of the divider to the middle of it. The reel conveyor feeds the maize plants into the ear picking device. The design of the divider should ensure that the maize plants will not be pushed or broken in the backward sliding process.

(1) Calculation of the cone angle of the divider. In the process of maize harvest, the taper of the divider has a great impact on the quality of it. If the taper design is not reasonable, it is easy to push down the plants and affect the harvest quality.
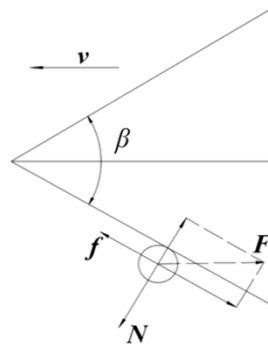
Fig. 3 - Stress analysis of maize under the action of crop dividing device

Take the plant as the research object, and the stress analysis is shown in Figure 3. Neglecting the effect of machine speed v on plants, assuming that there is a force F on plants along the opposite direction of speed v, in order to keep maize plants from being pushed down, the stress relationship of plants should meet the following relationship:

$$F \sin \frac{\beta}{2} = N \tag{3}$$

$$F \cos \frac{\beta}{2} \geq f \tag{4}$$

$$f = f_s N \tag{5}$$

Where: F - the force of maize plant, N; β - the cone angle of the divider; N—the elasticity of the divider to the maize plant, N; f - the maximum static friction of the divider to the maize plant; f_s—the friction coefficient between the divider and maize plant. It can be obtained from (3), (4) and (5),

$$f_s \leq \cot \frac{\beta}{2} \tag{6}$$

According to the range of friction coefficient between maize plant and steel material is 0.2-0.6, it is obtained that 30°≤β≤60°. In order to make the maize plant not be pushed down at any position of the divider, the cone angle of the divider should be designed to be less than 30°.

(2) Calculation of the width of the divider. As shown in Figure 4, maize plants move along the outer surface of the divider from point A at the front tip of it to point B. At point B, the maximum bending angle of corn stalk is α. OA and OB are the two limit positions of maize harvest. When the angle between OA and OB is set as γ, maize plants can just enter the ear plucking device without being broken. At this time, it meets the following requirements:

$$b = 2h \tan \gamma \tag{7}$$

where: *b*—the maximum width of the divider, mm; h—height of the bottom of the divider from the ground, mm.

In order to reduce the ear and grain loss rate of maize, point B is generally lower than the lowest ear point of maize; that is, the height *h* from the bottom of the divider to the ground is smaller than the lowest ear point of the harvested maize. The breaking critical angle of plants should be measured according to the actual situation of local maize harvest. Thus, the allowable value range of the divider *b* can be obtained.
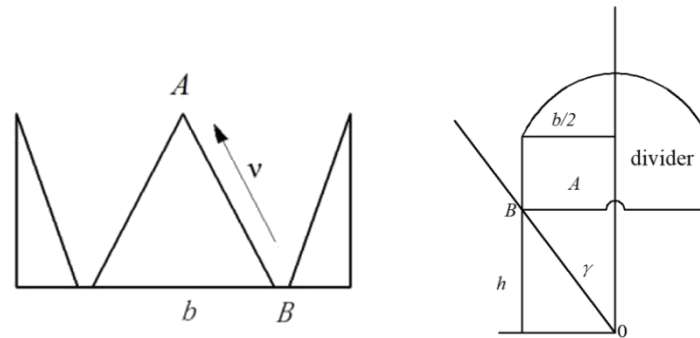
Fig. 4 - Width and height of the divider

Design of maize ear plucking device
    (1) Diameter of the picking roller.
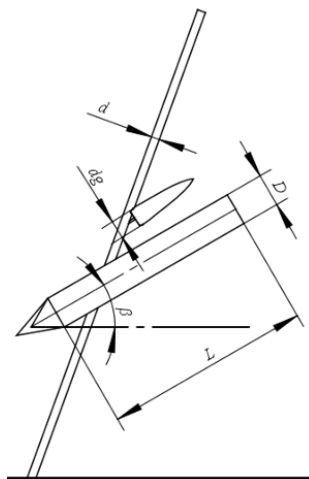
Fig. 5 - Structure diagram of ear picking device

The diameter of ear picking roller should meet the two conditions of grasping the maize stalk but not the maize ear (*Geng Duanyang et al, 2017*). According to the above conditions, the structure of the designed ear picking device is shown in Figure 5, and the diameter of ear picking roller shall meet the following formula:

$$\frac{d_g - \delta}{1 - \dfrac{1}{\sqrt{1+\mu_g^2}}} \geq D \geq \frac{d - \delta}{1 - \dfrac{1}{\sqrt{1+\mu_j^2}}} \tag{8}$$

$$h = (0.3 \sim 0.5)d \tag{9}$$

Where: d_g—the large end diameter of maize ear, mm; d—diameter of maize stalk, mm; δ—horizontal clearance between two picking rollers, mm; μ_g—grabbing coefficient of the picking roller to ear; μ_j—grabbing coefficient of the picking roller to ear; D—diameter of picking roller, mm.

Generally, $\mu_j \approx \mu_g = (1.6 \sim 2.3)f = 0.7 \sim 1.1$, where, f is the friction coefficient of the picking roller to the stalk, and the cast iron f = 0.4~0.5.

    (2) Length determination of the picking roller.

The minimum length *Lmin* of the horizontal ear picking roller should be able to ensure the highest and lowest ear of maize at the position of ear picking. L_{min} can be calculated by the following formula:

$$L_{\min} = L_g \sin \beta \tag{10}$$

Where: β is the horizontal inclination of the picking roller; L_g is the height difference between the highest and

the lowest ear of harvested maize.

(3) Linear speed of the picking roller

The linear speed of the picking roller is one of the important factors that affect the picking performance of the device. In the process of operation, if the linear speed of the picking roller is too low, the relative slippage between the stalk and the picking roller is easy to occur, resulting in blockage; on the contrary, the loss rate will increase. Through a large number of experiments, it is found that, when the vertical and horizontal ear picking rollers are working, the ratio K of the forward speed v_m of the harvester to the picking roller $v \sin\beta$ of the horizontal speed v is in the range of 0.7 -1, and the grain loss is relatively low, that is:

$$K = \frac{v_m}{v \sin \beta} = 0.7 \sim 1 \qquad (11)$$

Where: K is the proportionality coefficient; v_m is the forward speed of harvester, m/s; v is the linear speed of picking roller; m/s; β is the inclination between the picking roller and horizon.

DEVELOPMENT OF KNOWLEDGE-BASED DESIGN SYSTEM FOR MAIZE EAR HARVESTER HEADER

The header rapid design system is to display the header of maize ear harvester in the form of computer application software. In this paper, 64-bit Windows 8 operating system is selected as the development platform, and visual studio 2012 is selected as the environment. MFC based on VC + + has great advantages in code writing, interface design, database connection and secondary development of drawing software. MFC is selected as the development tool of rapid design system.

The header rapid design system of maize harvester mainly includes header parameter forward design calculation module, model base module and knowledge base module. The working process of header parameter forward design calculation module is as follows: According to the prompts of the design wizard, users determine their own design requirements and convert them into specific parameters to input the design system; The design system starts design reasoning and completes design calculation; after calculation, the results are saved and displayed in the form of design report. The model base module can directly retrieve the corresponding 3D models and instances from the model base according to the input parameters of the personnel, thus greatly simplifying the design process. The knowledge base mainly includes header knowledge involved in the design and calculation process.

Forward design and calculation module of the parameters of maize ear harvester header

The calculation module of the header includes two parts: the overall design of header and the design of core components of header. The design of the core components of the header includes the design of the splitting device, the design of the straw feeding device, the design of the ear picking device and the design of ear conveying device.
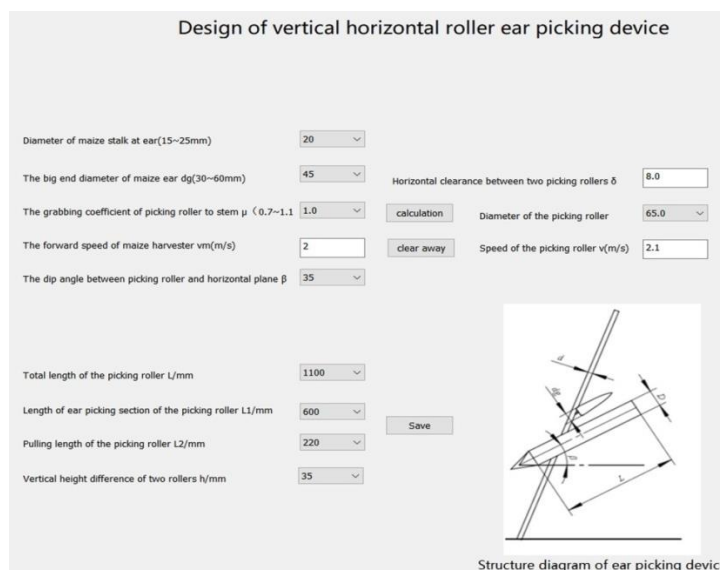
Fig. 6 - Parameter calculation interface of vertical horizontal roller ear picking device

Taking the rapid design of the vertical horizontal roller type ear picking device as an example, Fig 6 shows the rapid design interface of the vertical horizontal roller ear picking device. In the interactive interface, the diameter of maize stalk at the end of maize ear, the diameter of big end of maize ear, the grabbing coefficient of picking roller to the stalk, the inclination angle between the picking roller and the horizontal plane, and the forward speed of the harvester are input. According to the diameter of the maize stalk at the maize ear, the diameter of the big end of the maize ear and the grabbing coefficient of the stripping roller to the stalk, the diameter of the stripping roller and the horizontal gap between the two rollers are determined. The rotation speed of the picking roller is determined according to the inclination of the picking roller and the horizontal plane and the forward speed of the harvester. According to the design experience, the length of each section of the stripping roller and the vertical height difference between the two rollers are selected, and then saved for the next step.

After the forward design calculation, the system can store all the parameters in the design process and directly export the header design parameter report from the rapid design system. The input and output data in the generated parameter report are shown in Tables 1 and 2.

Table 1

Main input data parameter Report

Main input parameters	Numerical value	Unit
Diameter of ear region of maize stem d	20	mm
Big end diameter of maize ear d_g	45	mm
Row spacing of maize planting B_0	400	mm
Plant spacing of the maize Δl	300	mm
The bending angle of maize plant γ	22	°
Average quality of maize ear Δm	0.15	kg
Row number of harvest n	4	row
Forward speed of harvester v	2	m/s
Height of the divider from the ground h	400	mm

Table 2

Main output data parameter Report

Main output parameters	Numerical value	Unit
Feed rate of the header Q	4.6	kg/s
Width of the header B	1420	mm
Cone angle of the divider β	30	°
Maximum width of the divider b	323	mm
Bottom length of the divider l	603	mm
Feed chain pitch of reel t	40	mm
Finger spacing L1	320	mm
Finger height H	50	mm
Horizontal clearance between two picking rollers δ	8	mm
Diameter of the picking roller D	60	mm
Thickness of ear picking plate h0	6	mm
Edge bend angle α	20	°
Spiral conveyor pitch p	370	mm
Spiral conveyor speed n_l	140	r/min

Model base module and knowledge base module

According to the characteristics of the header design knowledge of maize ear harvester, the design knowledge is divided into formula knowledge, parameter knowledge and selection knowledge as shown in Tables 3, 4 and 5. Knowledge is stored in SQL Server in a certain format. Its main storage tables include serial number, number, parameter, formula content, unit, description and knowledge source. Users can view the required knowledge in the design process.

Table 3

Parameter knowledge base

Serial number	No.	Parameter	Minimum value	Maximum value	Explanation	Knowledge sources
1	GC_F_01	Cone angle of the divider β/°	0	25	general take 15-20	Agricultural Machinery Design Manual
2	GC_Z_01	Angle between the picking roller and horizontal line θ/°	25	40	general take 30-35	Agricultural Machinery Design Manual
3	GC_Z_02	Length of ear picking section of picking roller l2/mm	500	700	/	Agricultural Machinery Design Manual
4	GC_Z_03	Length of tension section of picking roller l3/mm	120	320	/	Agricultural Machinery Design Manual
5	GC_Z_04	Length of the picking roller L/mm	740	1300	/	Agricultural Machinery Design Manual
6	GC_Z_05	Horizontal clearance of the picking roller δ/mm	5	17	general take 11-13	Agricultural Machinery Design Manual
7	GC_L_01	Outer diameter of the spiral conveyor D/mm	350	400	/	Agricultural Machinery Design Manual
8	GC_L_02	Pitch of the spiral conveyor p/mm	340	400	/	Agricultural Machinery Design Manual
9	GC_L_03	Rotational speed of the spiral conveyor n/r/min	150	200	/	Agricultural Machinery Design Manual

Table 4

Type selection knowledge base

Project type	China 4YW-2	Yugoslavia ZMAJ-2KM	Yugoslavia ZMAJ-211	CLAAS KGaA mbH	France Bourgoin
No.	GX_G_01	GX_G_02	GX_Z_01	GX_Z_02	GX_Z_03
Type of picking roller or stalk pulling roller	Vertical and horizontal ear picking roller	Vertical and horizontal ear picking roller	maize header (stalk pulling roller)	maize header (stalk pulling roller)	maize header (stalk pulling roller)
dip angle of the picking roller β/(°)	35	35	30	30	33
roller diameter(outer diameter/inner diameter)/mm	94/74	72/52	94	100	100
Roll length /mm	1335	1115	750	480	1100
rotational speed of the roller/(r/min)	750	820	920	1022	850
forward speed of the machine/(m/s)	1.85~2.2	1.1~1.4	1.94	2.2	2.2
Peripheral speed of roller/(m/s)	3.7	3.1	4.5	4.8	4.45
Horizontal speed of roller /(m/s)	2.1	1.76	2.25	2.4	2.4
$K=v_m/v\sin\beta$	0.87~1.04	0.65~0.8	0.87	0.92	0.92

Table 5

Formula knowledge base

Serial No.	No.	Formula	Explanation
1	GG_Z_01	$(d_g-h)/[1-1/(1+\mu_g2)^{\wedge}(1/2)]\geq D\geq(d-h)/[1-1/(1+\mu j2)^{\wedge}(1/2)]$	It is used to calculate the diameter of picking roller, with unit mm.
2	GG_Z_02	$h=(0.3\sim0.5)d$	It is used to determine the horizontal clearance of two picking rollers, with unit mm.
3	GG_Z_03	$L_{min}=L_g\sin\beta$	It is used to determine the minimum working length of the picking section of the horizontal picking roller, with unit mm.
4	GG_Z_04	$K=v_m/v\sin\beta=0.7\sim1$	It is used to determine the matching relationship between the linear speed of the picking roller and the forward speed of the machine.
5	GG_F_01	$f_s\leq\cot(\beta/2)$	It is used to determine the range of the divider cone angle.
6	GG_S_01	$v_t/v_m=\sin\beta/\sin(\beta-\alpha)=K$	It is used to determine the matching relationship between the forward speed of the machine and the speed of the clamping conveyor chain.

The header model base includes header assembly model base, ear picking device model base, splitting device model base and ear conveying device model base. The designer can input the search condition parameters and directly retrieve the corresponding 3D model instances from the model base, and each model base enters the search conditions as shown in the Table 6. For example, if you need to browse the header assembly model base, you can respectively enter the number of lines and ear picking type, browse and call the model. As shown in Figure 7, it is a three-row roller maize ear harvesting header model called according to the search conditions browsing.

Table 6

Search criteria table of model base calls

Serial No.	Model base of each component of the header	Condition 1	Condition 2
1	Header assembly model base	Harvest row number(3-6)	ear picking type of the header(roller type ear picking/ stalk pulling roller type of picking plate)
2	Model base of the ear picking device	Ear picking type(ear picking roller/ stalk pulling roller)	/
3	Model base of the splitting device	Divider position(Middle/Both sides of the header)	/
4	Model base of ear conveyor	Harvest row number(3-6)	Conveying type (to the middle / to one side)
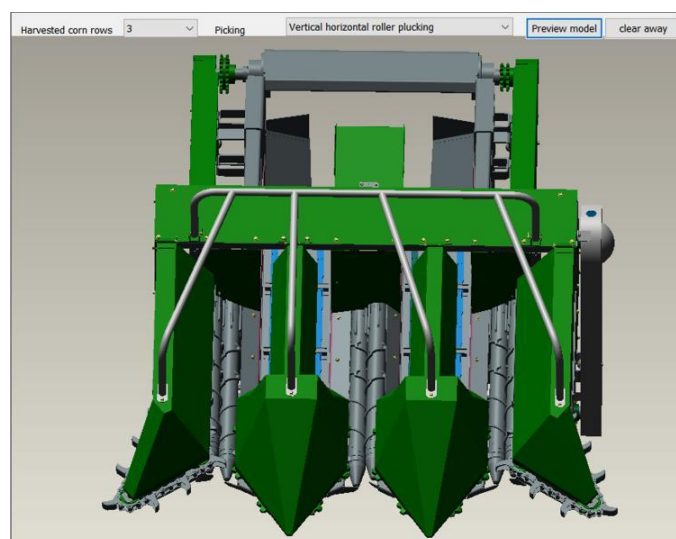
Fig. 7 - Three-row roller maize ear harvesting header model

CONCLUSIONS

1. Based on the modular design method of maize ear harvester header, a rapid design system of maize ear harvester header is established. Based on this system, the rapid design process of maize ear harvester header can be organized reasonably.

2. Through the collection and arrangement of a large number of header design data, design standards and specifications as well as the case data of the whole harvester, the header design knowledge is classified and summarized. The calculation method of the core components of the header is established, and the three-dimensional model of the components is established.

3. Based on MFC, a set of knowledge-based rapid design system for maize ear harvester header is established. The system includes header parameter design calculation module, model base module and knowledge base module. The header parameter design and calculation module include the overall parameter design and calculation of the header and the core components. It can quickly realize the calculation of the header forward design parameters, and generate the design report at the same time. The model base module includes the header assembly model base and the core components model base based on the generated design report, which can be accessed quickly. The knowledge base module includes the design knowledge in the design process.

4. The developed knowledge-based rapid design system of corn ear harvester header will play a positive role in shortening the design cycle of corn ear combine harvester, reducing the design cost, improving the product quality and enhancing the market competitiveness in China.

ACKNOWLEDGEMENT

REFERENCES

[1] Chen Zhi, (2014), Key technology and equipment of corn full value harvest. *China social sciences press*, Beijing/China.

[2] Cui Tao, Fan Chenlong, Zhang Dongxing et al, (2019), Analysis on the research progress of corn mechanized harvesting technology. *Transactions of the Chinese Society of Agricultural Machinery*, Vol.50, Issue12, pp.1-13, Beijing/China.

[3] Geng Aijun, Yang Jianning, Zhang Ji et al, (2016), Analysis of Influencing Factors of Maize Ear Harvesting Machinery Damage. *Transactions of the Chinese Society of Agricultural Engineering*, Vol.32, Issue 22, pp.56-62, Taian/China.

[4] Geng Duanyang, Li Yuhuan, He Ke et al, (2017), Design and experiment of the gap clamping and conveying device for the header of vertical roller corn harvester. *Journal of Agricultural Machinery*, Vol.48, Issue 11, pp.130-136, Zibo/China.

[5] Gianfranco La Rocca, (2012), Knowledge based engineering: Between AI and CAD. Review of a language-based technology to support engineering design. *Advanced Engineering Informatics*, Vol.26, pp.159–179, England/Britain.

[6] Li Changlin, Wang Xueliang, Jin Xiaoping et al, (2012), Expert System Design of Chassis Rapid Design for High-speed Transplanter, *Transactions of the Chinese Society of Agricultural Machinery*, Vol.43, Issue S1, pp.323-328, Beijing/China.

[7] Liu Hongxin, Zhou Xingyu, Jia Ru et al, (2019), Design and Reuse Technology of Mechanical Soybean Seed-metering Device Based on CBR. *Transactions of The Chinese Society of Agricultural Machinery*, Vol.50, Issue 7, pp.39-50, Harbin/China.

[8] Qiaosheng Liu, Juntong Xi, (2011), Case-based parametric design system for test turntable. *Expert Systems with Applications*, Vol.38, pp.6508–6516, United States.

[9] Tong Jin, He Junlin, Chen Zhi et al, (2007), Design and experiment of corn ear picking roller test stand. *Transactions of the Chinese Society of Agricultural Machinery*, Issue 11, pp.48-51, Changchun/China.

[10] Wagner P. William, (2017),Trends in expert system development: A longitudinal content analysis of over thirty years of expert system case studies. *Expert Systems with Applications*, Vol.76, pp.85–96, United States.

ADAPTABILITY TEST OF DRY FARMING TILLAGE TECHNIQUE IN NORTHERN CHINA AND STUDY OF KEY TECHNIQUES
/
中国北方旱作农业耕作技术适应性试验与关键技术研究

Yubing Guo [1)*], Xiaogang Zhang[2)], Chong Zhang [1)] [1]
[1)]School of Economics and Management, Taiyuan University of Science and Technology, Taiyuan 030024, China,
[2)]Shanxi Agricultural Machinery Research Institute Taiyuan 030006, China,
[*] *Tel: 13834683093; E-mail: icesnow80@163.com*

Keywords: dry land, northern dry farming, surface tillage, sustainable technique

ABSTRACT

Based on the problem of insufficient coordination of integrated machinery and technique configuration in the exploration of dry farming regions, a method of two-period comparative test was carried out in Shanxi Province, China. Zones of the effects of different treatments on straw coverage, soil moisture, emergence rate, seedling condition, yield, and benefit were monitored and analysed. The result was that the coverage before sowing decreased to below 55% after surface harrowing or rotary tillage in autumn by using dry farming technology in Northern China. The average number of emerging seedlings through surface tillage was larger than that without surface tillage by 1.7 plants/5 m; emergency rate was increased by 8.37%, and the increase in amplitude of grain yield reached 28% compared with that of traditional farming. Moreover, the input–output ratio reached 1:4.41. The experiments showed that the net income could reach RMB 1,251–1,401/hm², and compared with traditional farming, operating cost was lowered by 23.1%–28.8%, and benefit was elevated by 48.8% with prominent cost saving and benefit increase. The study results will facilitate the improvement of water-saving and production-increasing technologies in Northern China and play a critical role in the development of agricultural cultivation and steady growth of agricultural output in this region.

摘要

基于旱作区域的探索目前存在机艺融合配置不够协调的问题，本文在中国山西省进行了两期对比试验，在每种处理方法中监测和分析了不同的处理对秸秆覆盖率、土壤水分、出苗率、苗情和产量及效益的影响。试验结果是：利用北方旱作农机耕作技术，秋季浅耙或浅旋作业后使播前覆盖率降到 55%以下；经表土耕作的出苗数比无表土耕作的平均数多 1.7 株/5m，出苗率提高 8.37%，粮食产量相比传统耕作增幅达 28%；投入产出比达到 1:4.41；试验表明纯收入可达 1251~1401 元/hm²，和传统作业比较，作业成本降低 23.1%~28.8%，效益提高 48.8%，节本增效尤为显著。本文研究结果将有力推动中国北方地区旱地节水增产技术的改进，进而对这一区域农业耕种发展和农产品产量稳定增长起到关键作用。

INTRODUCTION

Optimal development of dry land potential, scientific utilization of rain and heat resources, nutrient conversion of biological resources, and combined action on ecological environment are always the research focus of agricultural sustainable development worldwide. Since the 1930s, various countries have been exploring advanced technologies and effective patterns of agricultural production on dry lands and seeking for critical technologies, which improve the ecological environment and strengthen land productivity. The north of Kunlun Mountains, Qinling Mountains, and Huaihe River in China are mostly arid, semiarid, semi-humid, and drought-prone regions, including 966 counties and prefecture-level cities in 17 provinces, cities, and districts such as Inner Mongolia, Shanxi, and Shaanxi (*Shangyu et al., 2019*). Most of these regions have annual precipitation of 300–500 mm, where the gross amount of water resources accounts for less than 20% across China, and cultivated lands are averagely 5,580 m3/hm2 in area. The land area in dry farming regions in Northern China occupies 56.0% throughout China, and the cultivated area is approximately 50,451,000 hm2, accounting for 55.4% of the total cultivated land area in China (*Yanqing and Bo, 2019*). In recent years, the agricultural research focus in Northern China has always been on expansion and extension

---

of irrigation techniques, whereas the improvement of agricultural production-increasing techniques in dry farming is relatively ignored. In comparison with irrigation farming, the water-use efficiency and yield of dry farming can be more easily affected by climate changes (*Yi et al., 2010, Shuang et al., 2015*). In arid and semi-arid regions, such as America and Australia, extensive attention has been paid to the improvement of dry farming tillage techniques (*Andrew et al., 2016*). Therefore, this problem should become a focus in Northern China.

The key to dry farming tillage technique lies in "surface mulching, minimum and no-tillage, and combined operation" (*Tiago et al., 2018*), where water storage, preservation of soil moisture, and soil fertilization are achieved by centring on "surface mulching, minimal tillage, and no-tillage" and using "combined operation" as the means (*Neal et al., 2017*). The key technique of minimal tillage is sub-soiling while the soil layer is not ploughed (*Yinzhu et al., 2017*). Hence, this technique has good water storage and moisture preservation effects. No-tillage (hard stubble) sowing is a straw stubble mulched ground and stubble sowing technique (*Yan et al., 2018*). Under the technical requirements, tillage adaptability problems still exist in dry farming regions of Northern China (*Meng et al., 2011*), which are manifested by the following: emergence and preservation of seedlings are difficult because of thick soil mulch; applying farmyard manures is difficult because soil is not ploughed in tillage, and irrigation is not good for water-saving and high crop yield. In recent years, our research group implemented adaptability test and key techniques for dry farming tillage in Pingding County and Tunliu County in Northern China in two periods. The study results show that increasing surface tillage and reducing surface mulching rate can remarkably solve the above-mentioned critical problems.

The theory of integrated machinery and technique configuration are combined, and Pingding County and Tunliu County test sites in China were used as examples. A direct injection-type rainfall simulator was used to perform five different tillage treatments in the test plots and investigate their effects on runoff and infiltration. Through two-period tests, the causes for low production-increasing amplitude in dry farming are found out, and the paths to increase crop yield and economic benefits are sought through dry farming tillage test and studying of key techniques in the second period.

MATERIALS AND METHODS
Profile of the study area

The first-period test was implemented in Pingding County, Shanxi Province, China, which was located at northern latitude of 37°39′30″–38°07′30″ with altitude of 800–1,000 m, low temperature (annual average temperature, 10.9°C), annual frost-free season of 210 days, annual average precipitation of 508.6 mm, annual evaporation capacity of 1,202 mm and 7–15 days with above grade 6 wind in spring, and severe spring drought. The cropping system was one-season corn plantation each year. The main test site for dry farming corn tillage was 3.3 hm^2 in area. Corn was planted in successive years, and the demonstration area was 200 hm^2.

The second-period dry farming tillage test was set in Tunliu County, Shanxi Province, China. As a semi-arid region, Tunliu County had annual frost-free season of 160 days, annual precipitation of 540 mm, annual evaporation capacity of 1,710.9 mm, annual average air temperature of 10°C, and annual sunshine duration of 2,504.1 h. The plantation system was one-season corn plantation each year, and this county had the same natural climatic characteristics as Pingding County.

Test materials

A 4JQ-150-type straw shredding and returning machine produced in Zhaoxian County in Hebei Province, 1S-3-type subsoiler produced by Shanxi rotary tiller plant (Fig. 1a), 2BMF-4-type no-tillage fertilizer-seeder (disk opener; Fig. 1b) produced in Xinjiang County, Shanxi Province, and Dongfanghong SK600G tractor (power machine) were used in the first-period test.

a) 1S-3-type subsoiler   b) 2BMF-4-type no-tillage fertilizer-seeder
Fig. 1 - Materials of the first-period test

The 4JQ-150-type straw shredding and returning machine produced in Shijiazhuang, Hebei Province, was used in the second-period test. A 1GQN-200-type rotary tiller produced by Shanxi rotary tiller plant was used for surface rotary tillage (Fig.2a). A 2BJY-3-type hard stubble planter produced in Xinjiang County, Shanxi Province, was used for seed sowing (Fig.2b), and the Dongfanghong SK600G tractor was used as the power machine.

a) 1GQN-200-type rotary tiller   b) 2BJY-3-type hard stubble planter
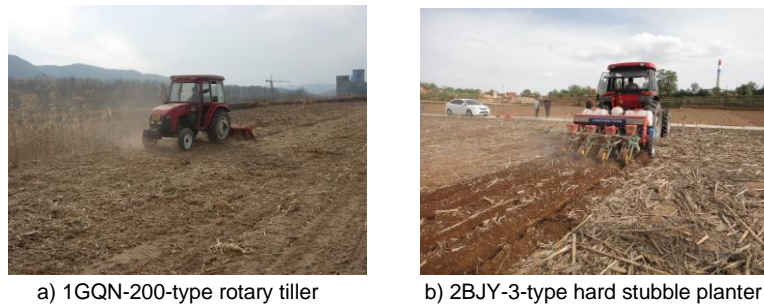
Fig. 2 - Materials of the second-period test

Test design

Five treatments were designed in the first-period test; each treatment was repeated three times. Fifteen plots were planned, and the area of each plot was 0.22 hm^2. The treatments were as follows: no-tillage with straw shredding mulch, no-tillage with complete straw overwhelming mulch, no-tillage with whole maize straw cover, sub-soiling with straw crushing mulch, and traditional mouldboard plough.

The process of this test was as follows: straw treatment after harvest in autumn no-tillage or sub-soiling fallow in winter no-tillage plus fertilization and seed sowing-field management (thinning, topdressing, and weeding) (*Changmin et al., 2013*).

The second-period test site for dry farming corn tillage in Northern China was 3.3 hm^2 in area. Corn was planted in successive years, and the demonstration area was 33.3 hm^2. On the basis of the real cropping pattern in Tunliu County, nine tests were designed, where five treatments were used (each treatment was repeated three times) to explore key technical problems in dry farming tillage in Northern China, each treatment area was 0.33 hm^2. The treatments were as follows: deep ploughing after straws were taken out of field (abbreviated as traditional tillage); crushing and returning to field, no-tillage, and direct sowing in the following year (abbreviated as straw crushing plus no-tillage); surface harrowing after crushing and returning to field (abbreviated as straw crushing plus surface harrowing); surface rotary tillage after crushing and returning to field (abbreviated as straw crushing plus surface rotary tillage); and surface harrowing after crushing and returning to field and surface rotary tillage and sowing in the following year (abbreviated as straw crushing plus harrowing and rotary tillage). The preceding crop of the test plot was corn, and the average yield in the first 3 years was 6,075 kg/hm^2. The seeds were all Tunliu No. 1 corn in the tests, and manures were uniformly phosphorus nitrate and fertilizers for corn. The application amount of seed manure was 360 kg/hm^2. Nitrogen phosphorus potassium mixed fertilizer was used for topdressing with an application amount of 330 kg/hm^2. Seed sowing was implemented on April 15, and plant number per hm^2 was 65,250.

The process of this test was as follows: corn harvesting → straw crushing → no-tillage or sub-soiling for above 30 cm/surface rotary tillage or surface harrowing for 5–10 cm → fallow in winter → surface rotary tillage (when necessary) → fertilizer application and sowing → field management (thinning, weeding, and topdressing).

RESULTS

The first-period test results indicated that northern dry farming tillage had comprehensive benefits of soil and water conservation, soil fertilization, production and income increase, and Eco-environmental improvement, but the production-increasing amplitude was low because of the following reasons: poor sowing quality, straws covered on the surface were swept by wind into piles in the wintering period, which affected the operation of planters. As the latitude was partially northern, after the surface was covered by straws, ground temperature was low before sowing. Consequently, seed germination was slow, and seedlings emerged late. Furthermore, the probability of soil bacteria invasion could be easily increased.

Water and soil conservation test

The direct injection-type rainfall simulator was used to perform five different tillage treatments in the test plot and investigate their effects on runoff and infiltration. The results showed that under artificial rainfall simulation (Fig.3) with intensity of 80 mm/h, runoff started appearing at 39 min in sub-soiling no-tillage treatment with coverage (percentage of straw mulching part in unit cultivated area) of 70%, and runoff started appearing at 33 min in the no-tillage treatment with coverage of 80%, lagging behind bare tillage by 29 min and 23 min, respectively. In 15 min since runoff started appearing in the no-tillage and sub-soiling plug tillage treatment of dry farming, the average runoff intensity was 0.11 mm/min, being 61% of runoff intensity (0.18 mm/min) in traditional tillage. In 30 min since runoff started appearing, the average runoff intensity was 0.21 mm/min, being 51.2% of runoff intensity (0.41 mm/min) in traditional tillage. At 21 h of rainfall simulation, soil moisture content and volume weight within 0–100 cm soil layer were measured. Rainfall infiltration amount and soil water retention capacity in traditional tillage treatment were 38.9 and 270.9 mm, respectively, whereas those in dry farming tillage were 57.2 and 301.20 mm, respectively, which were higher by 47% and 11.1%, respectively.

Fig. 3 - Pictures of direct injection-type rainfall simulator

Soil moisture content test before sowing

The water and soil conservation test was carried out to investigate the protective effect of dry farming tillage technique on water and soil in Northern China, and the soil moisture content test before sowing aimed to study water storage capacity of the technique. Soil samples were sampled from the test plots once in April every year with sampling depth of 0–20 cm. Five sampling points were collected from diagonal cross in each plot of 1 m² to achieve positioned sampling and dynamic study. First, 15 soil samples of the same mass in the same plot were blended as one analytical soil sample, and then five analytical soil samples were obtained from 15 test plots.

As shown in Fig.4, in comparison with traditional tillage, soil moisture contents under different forms of northern dry farming tillage were elevated to different degrees, where the increased amplitude under straw crushing plus sub-soiling was the maximum (by 1.51 percentages), indicating that moisture storage capacity of soil was strengthened.
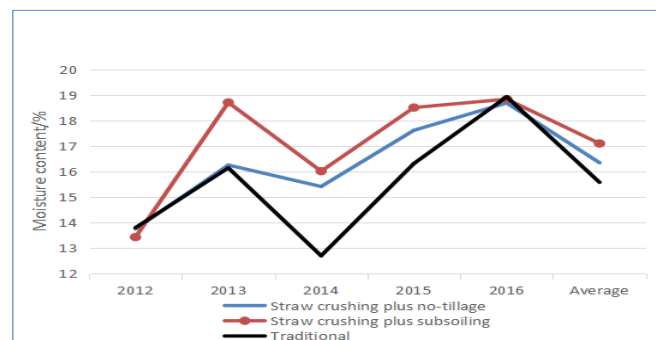
**Fig. 4 - Comparison chart of soil moisture contents at 0–20 cm plough layer
before sowing under different corn treatments**

Soil fertility test

According to the treatments of soil samples, the annual average increase rate of organic content in soil under northern dry farming tillage was 0.046%, which was higher than that (0.0295) under traditional tillage by 35.74%, and the increase rates of hydrolysis nitrogen, rapidly available phosphorus, and rapidly available potassium were 6.55%, 16.4%, and 10.17%, respectively.

Crop yield test

Crop yield test was performed in the form of single threshing and single harvesting in the same plot. Five-year yields under different tillage patterns were shown in Table 1. In comparison with traditional tillage, northern dry farming tillage showed a certain production-increasing ability, where the yields under straw crushing plus no-tillage and straw crushing plus sub-soiling were increased by 14.94% and 13.90%, respectively.

Table 1

Yields under different corn treatments

Item	Treatment mode	Year					
		2012	2013	2014	2015	2016	Average
Yield/t·hm²	Straw crushing plus no-tillage	3.091	8.032	5.090	5.753	4.416	5.2764
	Straw crushing plus sub-soiling	3.202	8.801	4.812	4.782	4.545	5.2284
	No-tillage with complete straw overwhelming mulch	3.188	8.032	5.419	4.354	4.851	5.1688
	Whole maize straw plus no-tillage	2.970	7.260	4.320	3.530		4.5200
	Traditional	2.602	6.665	4.416	4.903	4.366	4.5904

According to the analysis of the first-period dry farming tillage test, the second-period dry farming tillage test started with improving sowing quality. Improvements were made for the no-tillage planter, and combination-type depth-limiting round cutter plus inter-row weed pressing wheel-coordinated anti-blocking device was designed to improve the passing ability of the machine under high straw mulching rate. Different from the traditional tillage technique, northern dry farming tillage was demonstrated by two aspects (*Teodor, 2014*): crop straw stubble mulched the ground surface; no-tillage. These aspects were the primary factors influencing sowing quality and lowering ground temperature, and straw mulching was the main factor. This idea provided a path for the second-period dry farming tillage test.

Straw mulching rate

Steel tape was used to measure surface straw mulching rate. Within 10 m, every 10 cm was obtained as a measuring point (a total of 100 measuring points). The measuring tape was straightened to form 45° angle with the planting direction and randomly placed on the ground. The number of measuring points with straws beneath was counted, and the value was divided by 100 to obtain the mulching rate. The test was performed five times at left and right 45° angles, and the average value was obtained. The change results of the surface straw mulching rate before and after mechanical operation, such as surface rotary tillage and surface harrowing sowing, were presented in Table 2.

As shown in Table 2, the straw mulching rate decreased after different operations, and the declining process was divided into three phases: the straw mulching rate could be reduced by 23%–27% after surface harrowing or surface rotary tillage in autumn; during the fallow period in winter, the straw mulching rate could be lowered by 15%–20% because of air drying and decomposition of straws by natural environment; the straw mulching rate could be lowered by 22% or so before or after sowing. The test indicated that the before-sowing mulching rate decreased to below 55% by increasing surface harrowing or surface rotary tillage in autumn with natural treatment in winter. Consequently, no-tillage sowing and other planters could achieve smooth operation. After sowing, above 30% mulching rate could be kept, and water and soil conservation requirements could be achieved. Moreover, conditions were created for accelerating the recovery of ground temperature. Notably, rotary tillage in straw crushing, autumn harrowing, and spring rotary tillage was an operation designed to elevate ground temperature and guarantee sowing at the right time under special circumstances of low temperature and good soil moisture status in spring (*Ling and* Lixue*, 2013*).

Table 2

Surface straw mulching rates before and after different operations

Treatment	After harvesting (October)	Surface harrowing or surface rotary tillage (October)	Surface rotary tillage (April)	Before or after sowing (April)	
Straw crushing plus no-tillage	95.8	Winter fallow		79.3	45.6
Straw crushing plus surface harrowing	95.2	71.8	Winter fallow	55.8	32.3
Straw crushing plus surface rotary tillage	95.8	68.5	Winter fallow	53.5	30.9
Straw crushing, autumn harrowing plus spring rotary tillage	96.1	74.2	53.6	52.9	30.2
Traditional tillage	0			0	0

Soil moisture

The sampling and treatment methods in the soil moisture test were the same as that in the "soil moisture content test before sowing." The soil moisture test suggested that the smaller the soil treated, the higher the mulching rate and the better the water storage and conservation effect of soil. The treatment results were shown in Table 3.

Table 3

Comparison table of soil moisture content tests

Treatment	2017-02-23				2018-03-20			
Soil depth/cm	5	10	20	30	5	10	20	30
Straw crushing plus no-tillage	13.6	18.3	20.5	17.9	12.1	19.8	21.7	21.3
Straw crushing plus surface tillage	12.4	18.1	20.2	19.2	13.3	22.0	22.2	21.5
Straw crushing plus surface rotary tillage	10.3	19.7	19.1	17.3	13.8	23.2	22.6	21.3
Straw crushing, autumn harrowing plus spring rotary tillage	5.2	18.2	20.1	19.1	3.1	15.6	19.2	19.7
Traditional tillage	6.8	13.3	19.6	19.4	5.3	14.3	16.7	17.3

Emergence rate and seedling conditions

Emergence rate and seedling conditions were determined at 34 days after sowing. Seedlings within 5 m in one row of each segment were treated. A total of five segments were found, and the average emergence rate was obtained. A spot test of leaf number, plant height, and rootlet number of three seedlings was conducted. The average values of the above-mentioned factors in five segments were obtained to confirm seedling conditions, and the results were shown in Table 4. Averagely 22.0 plants/5 m were treated through the three treatment patterns with surface tillage. The number was higher than that without surface tillage by 1.7 plants/5 m. The seedling emergence rate was elevated by 8.37%. The growth conditions of seedlings were identical, and the seedling conditions under straw crushing plus surface rotary tillage were the best, indicating that surface tillage could not only improve sowing quality but also increase emergence rate and ensure complete and strong seedlings.

Determination results of seedling conditions   **Table 4**

Treatment	Seedling number	Leaf number	Elevation/cm	Rootlet number
Straw crushing plus no-tillage	20.3	7	33.1	10
Straw crushing plus surface harrowing	21.9	7	32.8	10
Straw crushing plus surface rotary tillage	22.3	7	35.1	10
Straw crushing, autumn harrowing plus spring rotary tillage	21.7	7	31.8	10
Traditional tillage	16.6	5	31.4	10

Yield and benefit

The test method of yield and benefit was identical with the "test of crop yield". Taking the year of 2018 as an example, the yield and benefit were calculated when the market price of corn was 2 yuan/kg, the test results were shown in Table 5.

Table 5

Input–output test results under different treatments

Treatment	Input/yuan·hm2					Output		Input–output ratio	Net income /t·hm²
	Total	Seed	Fertilizer	Pesticide	Operation	Yield/t·hm²	Output value/yuan·hm²		
Straw crushing plus no-tillage	4,020	360	1,800	300	1,560	8.871	17,742	1:4.41	13,722
Straw crushing plus surface harrowing	4,320	360	1,800	300	1,860	8.8695	17,739	1:4.11	13,419
Straw crushing plus surface rotary tillage	4,320	360	1,800	300	1,860	9.185	18,370	1:4.25	14,050
Straw crushing, autumn harrowing plus spring rotary tillage	4,470	360	1,800	300	2,010	9.684	19,368	1:4.33	14,898
Traditional tillage	4,770	360	1,800		2,610	7.5705	15,141	1:3.17	10,671

In the northern dry farming tillage plus surface tillage, crop yield was additionally elevated, where the yield under straw crushing and spring harrowing plus autumn rotary tillage pattern was the highest, reaching 9.684 t/hm^2, which was higher than that (7.5705 t/hm^2) under the traditional tillage by 2.1135 t; therefore, the increase in amplitude reached 28%, exceeding 14.94% of that in Pingding test plot (Table 5). The yield under straw crushing plus surface harrowing pattern was the lowest, being 8.8695 t/hm^2, which was higher than that (7.5705 t/hm^2) under traditional tillage pattern by 1.299 t; therefore, the increase amplitude was 17.1%, exceeding 13.9% of that in the Pingding test plot. The input–output ratio reached 1:4.41, which was increased by a large margin in comparison with that (1:3.17) under traditional tillage pattern. Through agricultural process improvement in dry farming tillage, mechanized operation techniques were matched, thereby achieving full machine-technique integration (10). Although the mechanized operation cost was enlarged by 150–300 yuan, as the yield was increased by 0.7755 t/hm^2, being equivalent to income increase by 1,551 yuan/hm^2, after the added operating cost was deducted, the net income was 1,251–1,401 yuan/hm^2. In comparison with the traditional operation, the operating cost was lowered by 23.1%–28.8%, and the benefit was increased by 48.8% with remarkable cost-saving and benefit increase effects (Fig.5).
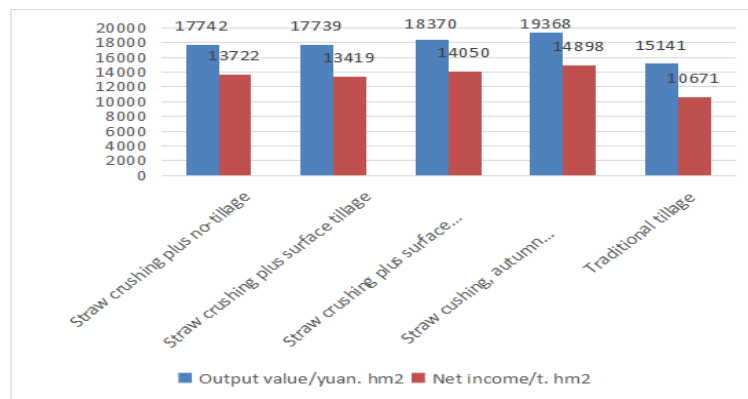
Fig. 5 - Income increase under different treatments

CONCLUSIONS

The technique was verified through two-period comparative tests in Shanxi Province, China, to confirm that northern dry farming tillage technique could boost efficient agricultural development in dry farming regions. Moreover, the two-period test data suggested that keeping a certain straw mulching, the northern dry farming tillage technique appropriately added surface tillage, which could elevate crop yield and increase farmer's income. The concrete conclusions were as follows:

1. Without soil tilling, the northern dry farming tillage technique uses crop straw stubble mulching to strengthen water-retaining and holding capacity of soil. Thus, the full advantages of autumn rains are obtained in spring. Spring drought is resisted in advance in winter, and the economic efficiency is evident.

2. The northern dry farming tillage technique can be popularized only after the adaptability test when applied to different regions. Under years of accumulation of straws and maximum straw quantity in good harvest year in northern latitude regions, surface harrowing or surface rotary tillage and other surface soil operations can be conducted to reduce straw mulching rate, accelerate straw decomposition in the fallow period, elevate before-sowing ground temperature, and strengthen dry farming technique. Although a certain operating cost will be added, in comparison with substantial production increase, the economic input–output ratio is continuously feasible.

3. The northern dry farming tillage technique, which consists of three elements—straw mulching, surface tillage and minimal tillage, and hard stubble sowing—creates good vegetation for bare field in the fallow period using organic resources of crops, and this technique can protect farmland surface soil from frequent erosion of dry and hot wind in winter and spring and radically solve straw burning problem with prominent ecological benefits.

4. The northern dry farming tillage technique has a positive promoting effect on elevating crop yield and increasing farmer's income. The popularization of this technique has three advantages: high reliability, high economic benefit, adaptable conditions. Therefore, active popularization and transformation of this technique have become a key technical measure used to lower cost, improve efficiency, and increase both yield and income in dry farming regions in Northern China.

REFERENCES

[1]   Andrew F., Roger L., Cameron W., (2016), Crop area increases drive earlier and dry sowing in Western Australia: implications for farming systems, *Crop & Pasture Science,* vol.67, issue 12, Csiro, pp.1268-1280;

[2]   Changmin S., Zicheng Q., Min D., Xiying W., Guoqiang L., (2013), Study on the agricultural conservation tillage demonstration pattern of wheat/corn double-crop annually rotated in Rencheng District, Jining City (济宁市任城区小麦/玉米两熟区万亩保护性耕作研究示范模式研究), *Journal of Anhui Agricultural Sciences,* vol.41, issue 19, Anhui Academy of Agricultural Sciences, pp.8121-8125,8123;

[3]   Ling S., Lixue W., (2013), The influence of straw stubble mulch on soil effect of water and temperature and wind erosion(秸秆残茬覆盖对土壤水热效应及风蚀的影响), *Agricultural Science &Technology and Equipment,* issue 12, Liaoning Research Institute for Agricultural Mechanization, pp.24-27;

[4]   Yi L., Shiqing L., Fang C., Shejiao Y., & Xinping C., (2010), Soil water dynamics and water use efficiency in spring maize (Zea mays L.) fields subjected to different water management practices on the Loess Plateau, China, *Agricultural Water Management*, vol.97, issue 5, Elsevier, pp.769-775;

[5]   Neal R.H., Katarina H., Louise E.J., (2017), How does tillage intensity affect soil organic carbon? A systematic review, *Environmental Evidence,* vol.6, issue 1, pp.1-48;

[6]   Shangyu S., Fei W., Kai J., Wenbin D., (2019), Temporal and spatial characteristics of drought based on SPEI in northern China from 1981 to 2017 (基于SPEI的1981-2017年中国北方地区干旱时空分布特征), *Agricultural Research in the Arid Areas*, vol.37, issue 4, Northwest A&F University, pp.215-222;

[7]   Shuang L., Changrong Y., Wenqing H. et al., (2015), Effects of different tillage practices on soil water-stable aggregation and organic carbon distribution in dryland farming in Northern China, *Acta Ecologica Sinica,* vol.35, issue 4, Ecological Society of China, pp.65-69;

[8]   Teodor R., (2014), Energy efficiency and soil conservation in conventional, minimum tillage and no-tillage, *International Soil and Water Conservation Research,* vol.2, issue 4, China Water & Power Press, pp.42-49.

[9]   Tiago S.T., Bastiaan P.R., Alexandre G.M., (2018), Effects of no-tillage on agricultural land values in Brazil, *Land Use Policy,* vol.76, issue 76, Elsevier, pp.124-129;

[10]   Meng W., Yinpeng L., Wei Y., Janet F B., Xiaodong Y., (2011), Effects of climate change on maize production, and potential adaptation measures: a case study in Jilin Province, China, *Climate Research,* vol.46, issue 3, Inter-Research, pp.223-242;

[11]   Yanqing J., Bo Z., (2019), Spatio-temporal changes of the extreme drought and wet events in Northern China from 1960 to 2016 (1960-2016年中国北方地区极端干湿事件演变特征), *Journal of Natural Resources*, vol.34, issue 7, China Society of Natural Resources, pp.1543-1554;

[12]   Yan Z., Xiujun L., Edward G.G. et al.,(2018), No-tillage with continuous maize cropping enhances soil aggregation and organic carbon storage in Northeast China, Geoderma, vol.330, issue 15, Elsevier, pp.204-211.

[13]   Yinzhu J., Yanli Y., Liangshan F., (2017), Effects of subsoiling on maize yield and water-use efficiency in a semiarid area, *Open Life Sciences*, vol.12, issue 1, Walter de Gruyter GmbH, pp.386-392.

ROAD RECOGNITION TECHNOLOGY OF AGRICULTURAL NAVIGATION ROBOT BASED ON ROAD EDGE MOVEMENT OBSTACLE DETECTION ALGORITHM
/
基于道路边缘运动障碍物检测算法的农业导航机器人道路识别技术

Na Yu[1)*], Qing Wang[1)], Shichao Cao[1)] [1]
[1)]Xingtai Polytechnic College, Xingtai, 054000 / China
Tel: 15884277397; E-mail: Yuna@163.com
DOI: https://doi.org/10.35633/inmateh-61-31

ABSTRACT

In order to recognize the road effectively, agricultural robots mainly rely on the tracking and detection data of road obstacles. Traditional obstacle detection mainly studies how to use multiple fusion methods such as vision and laser to analyse structured and simplified indoor scenes. The working environment of agricultural robots is a typical unstructured outdoor environment. Therefore, based on the environmental characteristics of agricultural robot navigation, the mean displacement algorithm is introduced to detect and study the obstacles aiming at the road edge. After explaining the advantages and principle flow of the mean displacement algorithm to effectively realize motion capture, the feasibility of target location and tracking research is discussed. After that, the bottom data acquisition and analysis model is constructed based on the road navigation data of agricultural robots. To capture the movement obstacles of road edge and build the foundation of road recognition technology. In order to improve the effectiveness of motion obstacle capture and detection, a moving target detection algorithm is proposed to optimize and update the mean displacement algorithm, and constructs a feature-oriented hybrid algorithm motion capture model. The simulation results indicate that the proposed optimization model can effectively improve the tracking efficiency of non-rigid targets in outdoor environment, and the number of evaluation iterations can reach 3.5621 times per frame, which shows that the research has good theoretical and practical value.

摘要

    为了有效地识别道路，农业机器人主要依靠道路障碍物的跟踪检测数据。传统的障碍物检测主要研究如何利用视觉、激光等多种融合方法对结构化、简化的室内场景进行分析。农业机器人的工作环境是典型的非结构化户外环境。因此，根据农业机器人导航的环境特点，引入了平均位移算法来检测和研究针对道路边缘的障碍物。在阐述了平均位移算法有效实现运动捕获的优点和原理流程后，讨论了目标定位跟踪研究的可行性。然后，基于农业机器人的道路导航数据，建立了底层数据采集与分析模型。捕捉道路边缘的运动障碍，为道路识别技术奠定基础。为了提高运动障碍物捕获和检测的有效性，提出了一种运动目标检测算法，对平均位移算法进行优化和更新，并构建了一种面向特征的混合算法运动捕获模型。仿真结果表明，该优化模型能有效提高室外环境下非刚性目标的跟踪效率，每帧评估迭代次数可达 3.5621 次，具有良好的理论和实用价值。

INTRODUCTION

In the navigation system of mobile robot, road recognition and obstacle detection are the key technologies of the system. In the past, research on mobile robots focused on indoor and relatively simple environments. Obstacle detection is realized by fusion of sensors, radar, laser and other data sources. Since this method of reduction, the technology is relatively simple and the cost investment is small, but it can obtain relatively abundant technical data. In recent years, the birth of agricultural robots has made up for the gap of theoretical mobile robots. The working environment of this kind of robot is unstructured and the working scene is complex. At this time, the traditional indoor mobile robot cannot effectively complete the task. Therefore, in the research of agricultural robots, it is necessary to attach great importance to the detection and recognition of obstacles in motion, so as to better support the efficient identification of roads in robot navigation.

---

[1] *Na Yu, As.Lec.; Qing Wang, Lec.; Shichao Cao, Lec.*

Tracking and locating detection of moving targets is a new research field born with the development of computer technology intelligence and informatization. Computer vision has achieved a lot of applied results in replacing human visual function, such as face matching, face recognition in detection field, and real-time tracking and detection of moving objects in video surveillance. The main principle that can achieve such a wide range of application results is that machine vision system has more accurate and advanced memory function than human eye recognition. Machine vision can simulate and surpass the human eye's effective capture of moving objects. Based on a large number of data collected in the whole process, it can construct the control of the omni-directional change of motion. Motion target detection and tracking technology, which use computer technology to collect video image information of road edge motion obstacles, have changed the qualitative method of analysing motion and technical skills based on traditional experience and manual observation in the past.

Scholars have achieved many valuable academic achievements in obstacle detection technology. Giannì C mainly studied the obstacle detection technology in mission drones and proposed a multi-sensor obstacle detection method that could overcome the problem of typical targets being difficult to detect *(Giannì C., Balsi M and Esposito S., 2017)*. *Gharani P*. built a visual impairment detection method for people with visual impairment, and proposed an image frame based on two connections to achieve effective detection of indoor obstacle points, which can be implemented on a smartphone and has good performance. *(Gharani P. and Karimi H.A., 2017)*. In order to improve obstacle detection and classification of complex terrain such as farmland and orchard, *Kragh M*. combined appearance and geometric probability fusion detection methods, and used multi-mode fusion algorithm to realize obstacle detection in agricultural scenes *(Kragh M. and Underwood J., 2019)*. Starting from the application needs of augmented reality technology in many fields, *Dawid P*. explored how to achieve real-time assessment of the real environment, using computer systems to provide you with early warning of possible obstacles *(Dawid P., Karolina K. and Kamil K., 2019)*. Hoang V.N. believed that a hybrid structure model can be used to detect obstacles that were needed for people with tactile disabilities, especially in the detection and collection analysis of security factors in unfamiliar environments *(Hoang V.N., Nguyen T.H. and Le T.L., 2017)*. Focusing on providing a safe environment for the elderly, Tzung-Han L proposed a line-laser barrier detection system based on imaging technology that can alert the elderly when an obstacle was detected *(Tzung-Han L., Chi-Yun Y. and Wen-Pin S., 2017)*. Fernando C considered that reliable obstacle detection can only be achieved by using data collected by lidar sensors effectively. Based on the need of obstacle detection in the future Internet of Things, a scheme to improve the reliability of obstacle detection technology was proposed *(Fernando C., Gerardo B. and Alberto V., 2018)*.

In order to achieve accurate tracking and detection and capture of motion trajectory, scholars have done a lot of research on tracking and detection algorithm of mean displacement algorithm. *Xue Ming* is a research on mean displacement algorithm in meteorology field. In order to detect and locate air particles effectively, the meridional and latitudinal data of displacement synthesis vectors were organically combined to improve the computational errors of non-uniformity and singularity MRDM in high latitudes *(Xue Ming. 2017)*. In the study of proteins, based on the generalized Langevin theory, *Hirata F*. proposed an average squared displacement model for analysing incoherent aqueous data, focusing on the effects of physical mutations on temperature gradients *(Hirata F., 2018)*. And *Kim A*. discussed how to use current-limited electronic-design-automation (EDA) tools in the study to track secondary power routing. By tracking the approximate voltage, designers can find problems in current limiting early in the design process (*Ball D, Upcroft B and Wyeth G., 2016)*. In the case of graphic signal processing, Wang X proposed to construct a distributed least squares (DLSR) reconstruction algorithm to realize the iteration of unknown signals, which effectively improved the convergence of the algorithm and controlled the error range of the algorithm *(Wang X., Wang M. and Gu Y., 2015)*. *Yuzhu C*. paid attention to how to effectively solve the problem of line-of-sight occlusion in image rotation processing and proposed a filter tracking algorithm. Based on the analysis of the reasons for the failure of target tracking, a classifier constructed by online support vector machine was proposed to improve the accuracy of tracking model. Experiments showed that the recognition rate of the optimized tracking model had been improved *(Yuzhu C., Dedong Y. and Ning M., 2017)*. In the study of cardiovascular magnetic resonance myocardial function tracking technology, *Morais P.* explored the use of non-rigid elastic registration algorithm and its feasibility and effectiveness. Simulation experiments showed that the algorithm can provide better data support for myocardial function tracking *(Morais P. and Alberto Marchi. 2017)*.

Based on the principle of dynamics, *Li J* proposed an extended Kalman tracking algorithm to predict the target position and optimize the measurement for the performance degradation of the attitude tracking algorithm. The reliability and efficiency of the method were demonstrated in the simulation of the algorithm *(Li J, Wei X and Zhang G., 2017)*. Peng L studied how to improve the tracking algorithm for sunlight in photovoltaic systems. After analyzing the principle of distinguishing the variation of oscillation power and irradiance and the principle of disturbance, the cutting error method and the dynamic disturbance calculation step were used. Simulation experiments showed that the optimization scheme not only improved the tracking speed, but also improved the tracking accuracy *(Peng L, Zheng S and Chai X. 2018)*.

Through the analysis and study of the obstacle detection by scholars, it can be seen that many good results have been achieved in the location of the obstacle, improving the efficiency, speed, robustness and reliability of the obstacle detection. In order to meet the need of road recognition application of agricultural navigation robot, the mean displacement algorithm is improved and optimized to improve the safety, reliability and efficiency of road edge obstacle detection and analysis.

The mean displacement algorithm is studied. Firstly, the theory of the mean displacement algorithm is summarized. Mean displacement algorithm, a typical data detection algorithm, is analysed in terms of its advantages. Then, the flow and model of the mean displacement algorithm are optimized and updated according to the needs and advantages of the agricultural navigation robot in using road recognition to detect motion obstacles. In order to achieve the reliability and validity of motion obstacle detection, a hybrid algorithm model is constructed by introducing tracking and location algorithm.

The study is mainly carried out in three parts. The first part is to analyse the advantages of the mean displacement algorithm in the application of agricultural navigation robot to the recognition of road edge motion obstacles, and to explore the feasibility of the mean displacement algorithm to enhance the detection effect. The analysis of the principle, theoretical basis and implementation process of the mean displacement algorithm are elaborated in the second part. In the third part, the optimization and improvement strategies are put forward to improve the reliability and efficiency of the mean shift algorithm. The main contents are as follows: in the second section, the principle and advantages of the mean shift algorithm are expounded, and the original intention is put forward. The design flow of the mean displacement algorithm is given in the third section. In the fourth section, the optimization strategy of the mean shift algorithm is proposed, and the performance characteristics of the optimization algorithm are introduced. In the fifth section, the research contents of mean displacement algorithm are summarized, and the direction of improving the detection effect of road edge motion obstacles is analysed.

MATERIALS AND METHODS
Mean shift algorithms

In the mean shift algorithm, there is no need to use specific parameters, and it has the characteristics of high efficiency in matching the mathematical algorithm of the target. The theoretical basis is a non-parametric kernel density estimation, which is a mathematical model for calculating the extreme points of probability density function iteratively by gradient method. In the pattern recognition of moving targets, the root of many problems is to use the probability density function of class conditions to estimate. Probability density estimation methods are divided into parametric method and non-parametric method. After a given function, the collected samples can be classified by algorithm. Nonparametric methods do not require prior knowledge, but only rely on training data to achieve estimation, which can be applied to any shape and density estimation, therefore are most widely used. Histogram density estimation is a classical algorithm model in nonparametric estimation. The principle of the algorithm is to construct a probability density with a set of samples. In the one-dimensional state, the real axis can be divided into many cells of equal size, and the density formula for the x point is expressed by the formula (1), where n_j is the number of samples in a cell that spans a point x that express width of dx. N is the number of cells and dx is the size of the cell. The unit existing in the multidimensional observation space can be expressed by the formula (2), where dV is the volume of the jth unit box.

$$\hat{p}(x) = \frac{n_j}{\sum_{L}^{N} n_j dx}$$

(1)

$$\hat{p}(x) = \frac{n_j}{\sum_j n_j dV} \tag{2}$$

The size selection of cell dx has a direct impact on the shape and size of the estimation. Histogram estimation varies with cell size. Under normal conditions, the width of histogram cells represents the density effect, and the larger the density, the smoother it will be. The smaller the cell size, the more significant the details will be. Fig. 1 is the histogram estimation under three cell sizes, and the lowest right corner is the kernel density estimation graph, from which it can be seen that the estimation effect of the kernel function method is closest to the real density situation. This method is simple and easy to use, because it does not need to retain sampling points, the basic histogram will lack continuity of density estimation, and the effectiveness of high-dimensional space is not strong. With the exponential growth of cells, the number of data increases significantly when the density of spatial estimation is high.
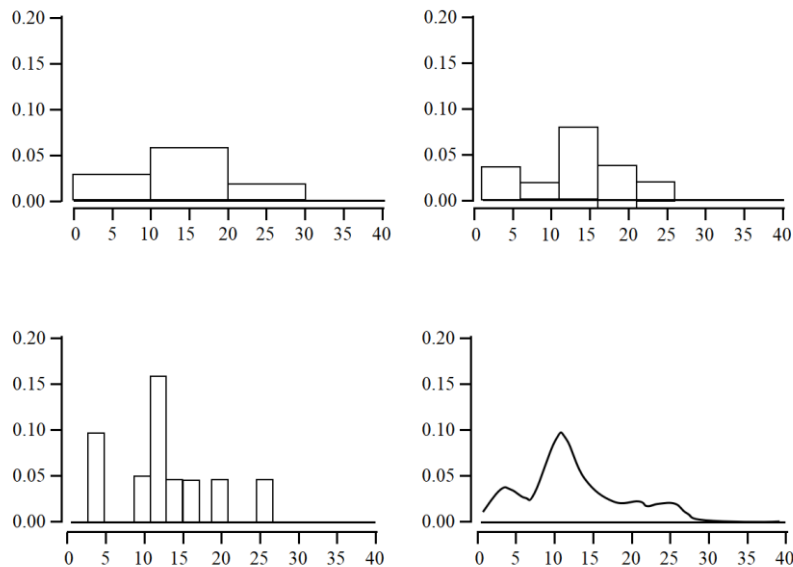
Fig. 1 - Histogram estimation under three cell sizes

In the derivation of the kernel function density estimation method, the first consideration is the one-dimensional condition. Assuming that $\{x_1, L, x_n\}$ is a set of observation data samples used to estimate the density. Formula (3) is the expression of probability density function, from which the relative frequency estimation equation of the sample can be obtained as shown in equation (4), where $\{x_1, L, x_n\}$ is the observation value and w is the rectangular weight function. The definition is shown in the formula (5), it can be estimated from the formula that $\hat{p}(x)$ is a property that accords with the probability density.

$$P(x - h < X < x + h) = \int_{x-h}^{x+h} p(t) dt \approx 2hp(x) \tag{3}$$

$$\hat{p}(x) = \frac{1}{n} \sum_{i=1}^{n} w(x - x_i, h) \tag{4}$$

$$w(t, h) = \begin{cases} \dfrac{1}{2h} & |t| < h \\ 0 & other \end{cases} \tag{5}$$

$\hat{p}(x) \geq 0$ and $\int_{-\infty}^{+\infty} p(t) dt = 0$ are applicable to all x. It can be accepted that this nuclear density estimation uses a rectangular window to observe nearby observation points. The probability density estimate of the fixed observation point is 1/n of the sum of the heights of all the rectangles covering this observation point. When h is increased, the width of the rectangle is also increased correspondingly, which increases the smooth state of the probability density function.

At this time, a trigonometric function and a Gaussian function can be used instead of the rectangular weight function. As shown in Fig. 2, based on the Gaussian function, the density estimates at h = 0.5 and h = 1, the function has been jagged.
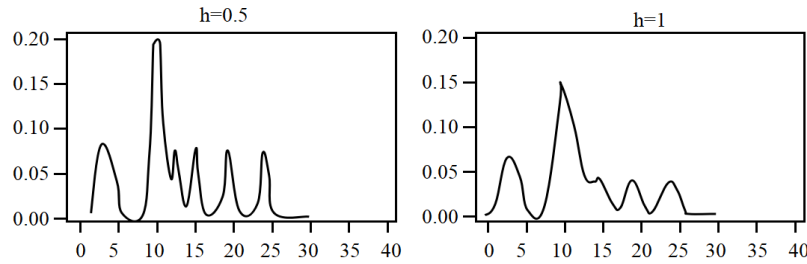
Fig. 2 - Density estimation based on Gauss's function (h=0.5,1)

Figure 3 shows the density estimation based on Gauss function at h = 2 and H = 4, and the shape of the function begins to become smoother.
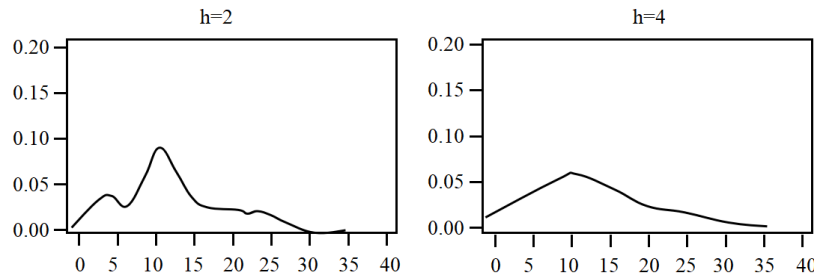
Fig. 3 - Density estimation based on Gauss's function (h=2,4)

Kernel is a standardized weight function, which plays a decisive role in the shape of the weight function. H in weight function $w\ (t,\ h)$ is also called smoothness parameter because it represents bandwidth. Bandwidth determines the smoothness of $p(x)$ estimation. Normal density function, a radially symmetric probability density function, can be used as a kernel function. However, some support kernels themselves do not have the characteristics of density, and can be expressed by negative values at some points, which will lead to negative estimates. When the kernel function and smoothing function are set, the kernel density estimation formula of $P(x)$ is expressed as formula (6), where elements K and H determine the properties of $\hat{p}(x)$. When the value of H is larger, the density display is smoother, but the details are blurred. When the value of H is small, the density estimation can reflect the detail structure more. When h is close to 0, there will be a spike. How to choose K and h to improve the performance of $\hat{p}(x)$ is the direction of algorithm optimization.

$$\hat{p}(x) = \frac{1}{n}\sum_{i=1}^{n} K\left(\frac{x-x_i}{h}\right)$$

(6)

Mean displacement optimization strategy

In the current computer tracking technology, the use of mathematical algorithms has a large amount of computation and a large number of processes, which leads to the need for computers equipped with high-performance computing capabilities, increasing costs and computing cycles, and other issues, which are the main factors affecting its application and promotion. Mean displacement arithmetic originates from statistical theory. The non-parametric technique can effectively improve the simplicity of statistics and probability respectively. The weighted kernel density method can reduce the influence of noise interference on the edge data points of the target, and can effectively improve the overall adaptability and reliability when the weight of the central region of the target is increased accordingly. When the mean moving vector is used to search the direction of density gradient rapidly, the efficiency and speed of the tracking algorithm can be improved effectively. So, the target tracking based on mean displacement algorithm has a good model foundation. To achieve target tracking is to make the search strategy and matching criteria of the target reliable in both moving and stationary background.

To achieve this goal, it is necessary to do in-depth research from three parts: generating target matching template, updating target motion position, and predicting target matching criteria.

$$P(error) = P(x \in R_2, w_1) + P(x \in R_1, w_2)$$
$$= P(x \in R_2, |w_1) P(w_1) + P(x \in R_1, |w_2) P(w_2)$$
$$= \int_{R_2} p(x|w_1) P(w_1) dx + \int_{R_2} p(x|w_2) P(w_2) dx$$

(7)

To locate the detection target that needs to be tracked, it is necessary to collect the corresponding feature identifier, so that the candidate target expression library of the target model can be established according to the feature. The problem of positioning detection in the frame image is converted into a mathematical problem in which the position y is selected in the current frame so that the corresponding density distribution $\hat{p}(y)$ is similar to the density $\hat{p}_u$ distribution of the target model. Here, the mode reality measure is first defined and the degree of similarity of the pattern features is characterized. Starting from the similarity between the error probability and the two probability density distributions, the target location problem is transformed into the similarity estimate between the target model and the candidate model, and the Bayesian error is used to calculate. In pattern recognition theory, two situations are generally considered. First, it is assumed that the binary classifier uses a non-optimal way to divide the space into two parts, *R1* and *R2*. The error classification occurs in the form that the real category is *W1*, and the observed value x is in the region *R2*. Or the real category is *W2* and the observed value x is in region *R1*. These conditions are mutually exclusive and cover the entire space, and thus the error probability calculation formula is as shown in equation (7). The result in one-dimensional space is shown in Fig. 4. The two integrals in equation (7) represent the range covered by the density curve of the function $p(x|w_1) p(w_1)$ on the left and right sides of the decision point x, respectively. When the decision margin moves to x_B, the smallest area of the two regions is the state with the smallest error probability, which is the Bayesian error probability brought by Bayesian decision.
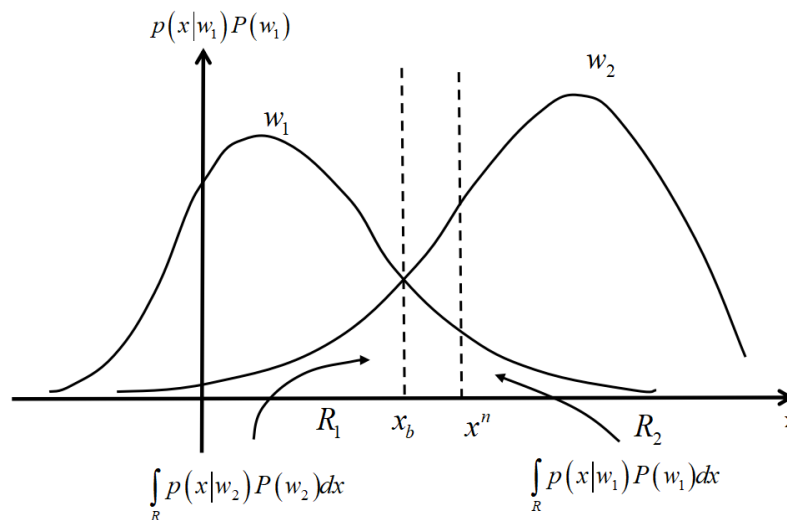
Fig. 4 - Bayesian error probability schematic of one-dimensional model

In the target similarity measure, it is necessary to select an appropriate target similarity measure function, which is processed by means of Bhattacharyya coefficient. The main thing is to confirm the similarity between the two vectors. The process of this confirmation is the process of solving the cosine value of the unit vector represented by the coefficient according to the geometric mathematical principle, as shown in Fig. 5. The measured value of the cosine function value here is to solve the similarity between the image model of the measurement target and the candidate target model.
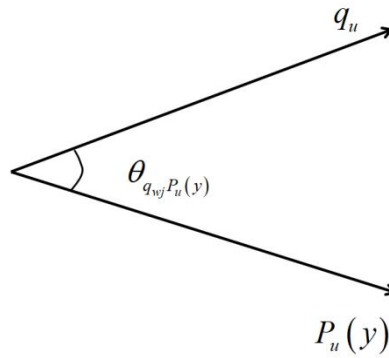
Fig. 5 - The geometric meaning of the coefficient

The Mean Shift tracking algorithm is used in the target positioning, which is welcomed because the moving target can be positioned in a short time and the search time has a great advantage. The principle of implementation is that the algorithm calculates the similarity probability density between the candidate target and the target template, and then uses the direction of the probability density gradient to search for the matching path. The characteristics of this tracking algorithm are that it can calculate the quantity and can track and process in real time. The weighted colour histogram reality is not sensitive to the deformation and occlusion of the target. The principle of using Mean shift algorithm to achieve target tracking is to analyse the RGB colour space in the target region based on statistics. The R.G.B subspace in RGB colour space is divided into k intervals of the same size, which is called bin feature space. The number of Bin represents the dimension of the feature space. The colour histogram here represents the area to be searched in the target model. Searching all the pixels and classifying them by RGB can get the corresponding histogram. These histograms are candidates for comparison in subsequent video image search. Figure 6 is the flow chart of Mean Shift tracking algorithm.
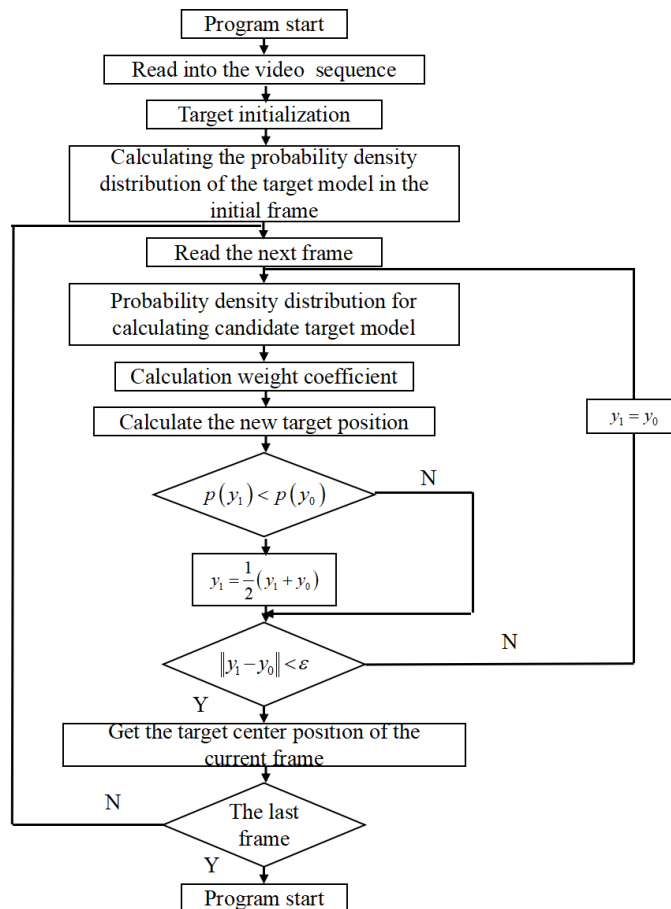
Fig. 6 - Mean Shift tracking algorithm flow chart

RESULTS

Experimental conditions and parameters

On the basis of the robot recognition algorithm, this study designed the agricultural robot. Figure 7 shows the photos of the robot in the field experiment. The main function of the robot is to collect and analyse the common diseases and insect pests and growth information of crops. The robot is a wheel type robot driven by four wheels. The distance between the front and rear wheels is short, which can adapt to the ups and downs of the terrain during field operation. In addition to the walking mechanism, the whole robot includes three modules: vision system, information storage system and energy system. The vision system mainly includes two cameras which are distributed up and down and can rotate freely. The camera is mainly used to collect crop information and road information. The information storage system is mainly used to store crop information. The energy system is responsible for providing energy for robot walking and information.

Fig. 7 - Field work of robot

Simulation experiments are used to verify the optimized mean displacement algorithm. In the navigation of agricultural robots, road edge images often occur, which results in inaccurate capturing and difficult locating of targets by computers. The experiment is aimed at this phenomenon, using the algorithm model which is a mixture of the mean shift algorithm and the colour histogram algorithm proposed in this paper to compare the location and capture efficiency. On the one hand, the stability and accuracy of mean shift algorithm for moving objects are tested. On the other hand, the adaptability of colour histogram is verified to dynamic video, rotating images and different observation perspectives according to the distribution of target colour. In the first frame, the target area is selected manually. In order to verify the performance of mean shift algorithm in different scenarios, video is selected for testing, and the results are marked with yellow box in the tracking process. The target trajectory is displayed by red lines. The experimental video is a game video of basketball players. The size of the video image is 352*240 pixels, the frame rate is 15 frames per second, and the total frame number is 80 frames. The main purpose of the video is to track the track of the road edge obstacles. In this video, the road edge and background are quite different, and the road edge is not occluded by other objects during the whole detection process.

Experiment on tracking effect of motion obstacle optimization algorithms

After tracking the movement of road edge obstacles, the tracking effect is shown in Figure 8. During the whole tracking process, the tracking display frame can lock the edge of obstacle and locate the target correctly. It keeps good similarity with the trajectory, and the tracking algorithm keeps good tracking effect. This is because the proposed optimal mean shift algorithm uses RGB colour to construct feature space, so as to ensure that the tracking process will not be affected by the target deformation, and can also achieve real-time tracking of this non-rigid object.
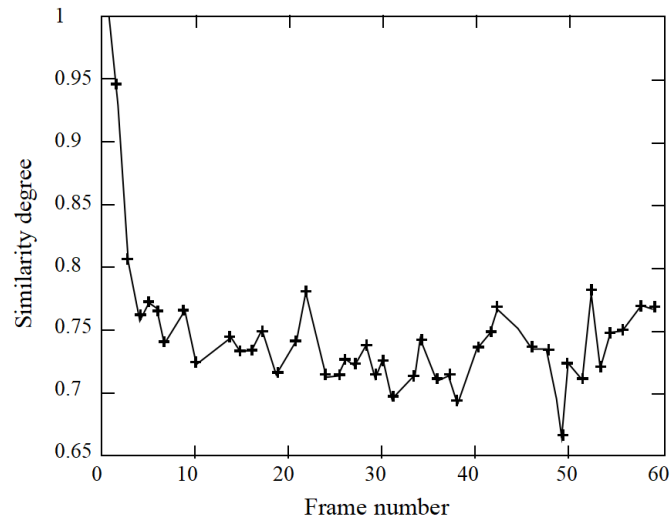
Fig. 8 - Study on similarity of road edge dynamic obstacle tracking process

Tracking performance experiments of motion obstacle optimization algorithms

In practical applications, the scene colour of agricultural robots will be more complex, especially in different lighting conditions, tracking target and site colour are similar, it is easy to appear that the target cannot be located. Therefore, it is necessary to establish tracking feature space based on multiple colours to ensure the stability and reliability of tracking. The statistical results show that the number of iterations for evaluating the video of road edge motion disorder can reach 3.5621 times per frame. Therefore, it can be concluded that the optimized mean displacement algorithm is a simple and efficient tracking algorithm, which has good real-time tracking effect and function. After applying the results of this tracking algorithm to the road recognition of agricultural navigation robot, the road can be accurately positioned and compared, which provides a reference for subsequent scientific decision-making. Figure 9 shows the tracking statistics after tracking the movement of road edge obstacles.
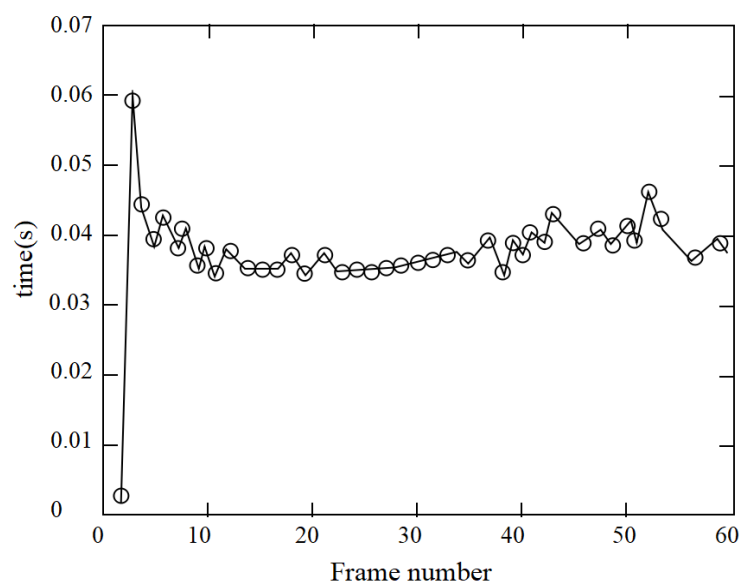
Fig. 9 - Study on tracking speed of road edge motion disorder

Figure 10 shows the performance comparison results of the design algorithm, eNet algorithm and segnet algorithm in parameter amount, calculation amount and different resolution. From the size of the parameters, the parameters of the algorithm designed in this paper are 0.357m, 1.45M for segnet algorithm and 0.993m for eNet algorithm.

From the size of the parameters, the parameters of the algorithm designed in this paper are the smallest. In terms of the amount of calculation, the parameters of the algorithm designed in this paper are 1.36mb, 5.34mb and 3.79mb, respectively. From the result of calculation, the calculation amount of the algorithm designed in this paper is also the smallest. For the image with 360 × 480 resolution, the recognition time of this algorithm is 10ms, the recognition time of eNet algorithm is 13ms, and the recognition time of segnet algorithm is 24ms. For large 512 × 1024 images, the recognition time of the three algorithms is further increased. The algorithm in this study is 26 ms, eNet algorithm is 31 ms, segnet algorithm is 44 ms. From the above results, the algorithm designed in this study is the best in terms of parameters, calculation amount and even key image recognition efficiency.
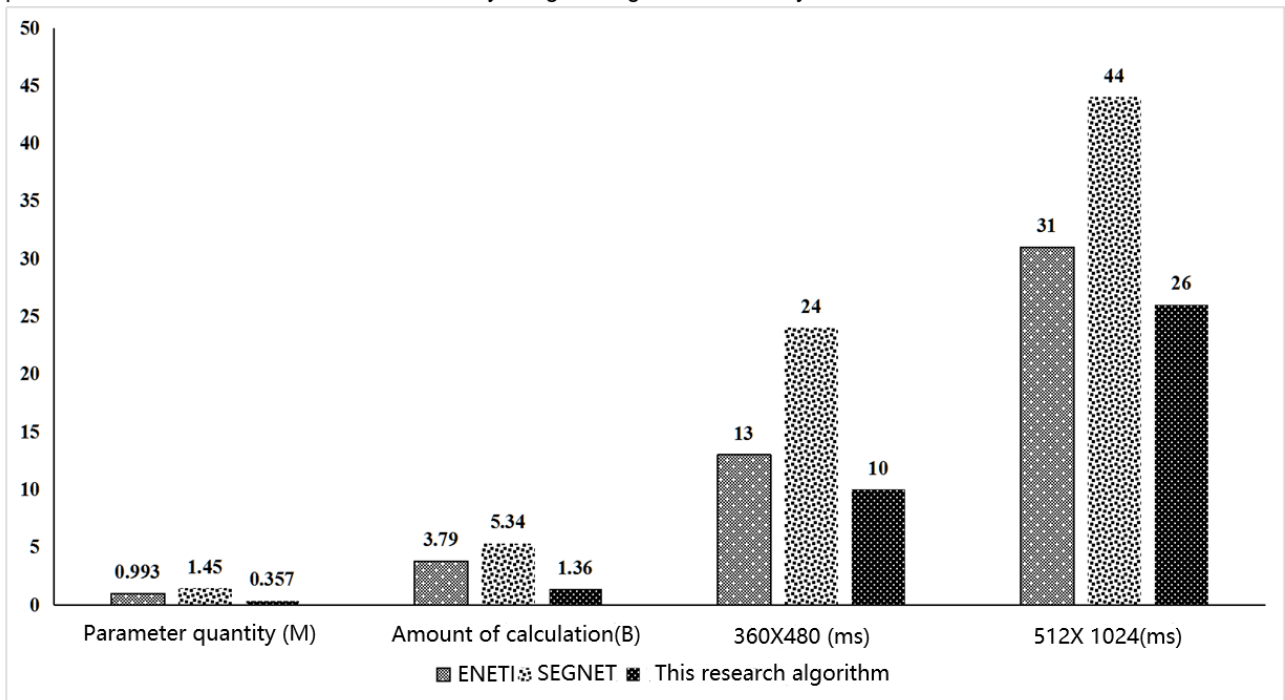
Fig. 10 - Study on tracking speed of road edge motion disorder
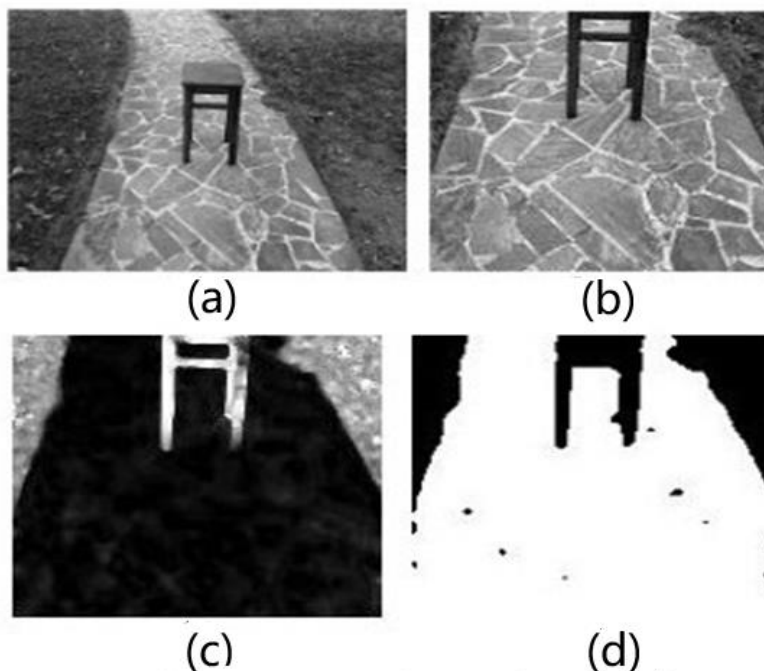
Fig. 11 - Application of agricultural robot road obstacle detection

Figure 11 shows the application results of agricultural robot road obstacle detection. As can be seen from the figure, the agricultural robot can accurately identify the chair in the road through the vision technology, which can effectively avoid the obstacles in the road in the process of agricultural robot moving.

CONCLUSIONS

Mean displacement algorithm is mainly used in the field of target acquisition and positioning. It is widely used in various safety object detection, trajectory capture and evaluation of moving objects. It is more advanced than the accuracy and memory of human eye observation, and also has good application effect in road edge obstacle motion recognition. Therefore, based on the mean displacement algorithm, the road edge motion obstacles in agricultural robot navigation road recognition are studied, which provides a scientific basis for road recognition system. Firstly, the principle and structure of the mean shift algorithm are analysed, and then the target capture technology based on the mean shift algorithm is studied according to the need of moving target tracking on the road edge, and a hybrid optimization algorithm model is proposed. By optimizing the similarity measure function of the target, the fast location of the moving obstacle target can be realized and the searching time of the target can be reduced. The tracking location algorithm is introduced to optimize the mean displacement algorithm, and a hybrid algorithm optimization model is established. Finally, the trajectory of road edge obstacles is selected for simulation test. Experiments show that the proposed optimization algorithm model can effectively improve the speed and accuracy of the algorithm, and make the tracking results be of higher quality. Moreover, the number of iterations for evaluating the video of road edge motion obstacles can reach 3.5621 times per frame, which can effectively improve the shortcomings of the traditional mean displacement algorithm that has a longer period after the increase of computation. It shows that the optimized mean displacement algorithm is a simple and efficient tracking algorithm with better real-time detection effect and function. However, from the results, there are still some improvements in this study. The next step is to improve the algorithm structure of moving target detection model.

REFERENCES

[1] Ball D, Upcroft B, Wyeth G., (2016), Vision-based obstacle detection and navigation for an agricultural robot. *Journal of field robotics*, Vol. 33, Issue 8, pp.1107-1130, USA;

[2] Dawid P, Karolina K, Kamil K., (2019), Obstacle Detection as a Safety Alert in Augmented Reality Models by the Use of Deep Learning Techniques. *Sensors*, Vol.17, Issue 12, pp.2803, Switzerland;

[3] Fernando C, Gerardo B, Alberto V., (2018), Self-Tuning Method for Increased Obstacle Detection Reliability Based on Internet of Things LiDAR Sensor Models. *Sensors*, Vol.18, Issue 5, pp.1508, Switzerland;

[4] Gharani P, Karimi H A., (2017), Context-aware obstacle detection for navigation by visually impaired. *Image and Vision Computing*, Vol.64, pp.103-115, Netherlands;

[5] Giannì C, Balsi M, Esposito S., (2017), Obstacle Detection System Involving Fusion of Multiple Sensor Technologies. *The International Archives of Photogrammetry, Remote Sensing and Spatial Information Sciences*, Vol.42, pp.127, Iran, Islamic Republic;

[6] Hirata F., (2018), On the interpretation of the temperature dependence of the mean square displacement (MSD) of protein, obtained from the inelastic neutron scattering. *Journal of Molecular Liquids*, Issue 8, pp.143-145, Netherlands;

[7] Hoang V N, Nguyen T H, Le T L., (2017), Obstacle detection and warning system for visually impaired people based on electrode matrix and mobile Kinect. *Vietnam Journal of Computer Science*, Vol.4, Issue 2, pp.71-83, Vietnam;

[8] Kragh M, Underwood J., (2019), Multi-Modal Obstacle Detection in Unstructured Environments with Conditional Random Fields. *IEEE Communications Surveys & Tutorials*, Vol.P4, Issue 99, pp.1-12, USA;

[9] Li J, Wei X, Zhang G., (2017), An Extended Kalman Filter-Based Attitude Tracking Algorithm for Star Sensors. *Sensors*, Vol.17, Issue 8, pp.1921, Switzerland;

[10] Morais P, Alberto Marchi., (2017), Cardiovascular magnetic resonance myocardial feature tracking using a non-rigid, elastic image registration algorithm: assessment of variability in a real-life clinical setting. *Journal of Cardiovascular Magnetic Resonance*, Vol.19, Issue 1, pp. 24, USA;

[11]   Peng L, Zheng S, Chai X., (2018), A novel tangent error maximum power point tracking algorithm for photovoltaic system under fast multi-changing solar irradiances. *Applied Energy*, Vol.210, pp.303-316, England;

[12]   Tzung-Han L, Chi-Yun Y, Wen-Pin S., (2017), Fall Prevention Shoes Using Camera-Based Line-Laser Obstacle Detection System. *Journal of Healthcare Engineering*, Issue 2017, pp.1-11, England;

[13]   Wang X, Wang M, Gu Y., (2015), A Distributed Tracking Algorithm for Reconstruction of Graph Signals. *IEEE Journal of Selected Topics in Signal Processing*, Vol.9, Issue 4, pp.728-740, USA;

[14]   Xue Ming., (2017), Error Inhomogeneity in the Computation of Spherical Mean Displacement. *Journal of meteorological: English version*, Issue 2, pp.31, China;

[15]   Yuzhu C, Dedong Y, Ning M., (2017), Visual Tracking Algorithm Based on Adaptive Convolutional Features. *Acta Optica Sinica*, Vol.37, Issue 7, China.

ATOMIZATION CHARACTERISTICS OF FLAT FAN NOZZLES FOR PRECISION PESTICIDE APPLICATION AT LOW PRESSURES
/
针对精准施药的平扇形喷嘴低压雾化特性

Shougen Li, Yaxiong Wang, Chongchong Chen, Feng Kang*), Wenbin Li [1]
School of Technology, Beijing Forestry University, Key Lab of State Forestry Administration
for Forestry Equipment and Automation, Beijing, 10083, China;
*Tel: 13002515042; E-mail: kangfeng98@bjfu.edu.cn

ABSTRACT

At present, the theory of precision pesticide application in agriculture and forestry has some shortcomings. Therefore, the Phase Doppler Interferometer (PDI) was used to establish the atomization model of three common brands (Lechler, Teejet and Feizhuo) flat fan nozzles in near fog field (0.3-0.5m) at low pressure (0.20-0.30mPa). The results show that the average absolute errors of droplet velocity of three brands of nozzles are 0.629, 0.521 and 0.684 m/s respectively, and the relative errors are 9.22, 9.60 and 11.89%, respectively. The average absolute errors of theoretical data of droplet size are 17.821, 13.801 and 22.140 µ m, and the relative errors are 8.40, 5.82 and 11.67%, respectively. The experimental theoretical model has high reliability. In addition, the results show that the droplet velocity and particle size increase with the increase of the equivalent diameter of the nozzle outlet. With the increase of spray angle, droplet velocity and particle size decrease gradually, and the rate of velocity decrease gradually. The research results are of great significance to further analyse the atomization characteristics of flat fan nozzle and guide the precise application of pesticide.

摘要

目前，农林精准施药理论理论存在不足。因此，本研究利用相位多普勒干涉仪（PDI）建立了低压（0.20-0.30mpa）下近雾场（0.30-0.50m）三种常用品牌（Lechler、Teejet 和 Feizhuo）平扇形喷嘴的雾化模型。结果表明，三种品牌喷嘴液滴速度理论数据的平均绝对误差分别为 0.629、0.521 和 0.684 m/s，相对误差分别为 9.22、9.60 和 11.89%。液滴粒径理论数据的平均绝对误差分别为 17.821、13.801 和 22.140µm，相对误差分别为 8.40、5.82 和 11.67%。理论模型非常可信。此外，结果表明，液滴速度和粒径随喷嘴出口等效直径的增大而增大。随着喷雾角度的增大，液滴速度和粒径逐渐减小，且速度降低率逐渐减小。研究结果对进一步分析平风扇喷嘴的雾化特性、指导精准施药具有重要意义。

Nomenclature

a_m	Constant		n	Constant
a_v	Constant		N	Quantity of droplets
b_m	Constant		P	Pressure difference of nozzle and outlet (Pa)
b_v	Constant		r_{in}	Radius of nozzle inlet (mm)
C	Constant		r_{out}	Radius of nozzle outlet (mm)
C_D	Constant		u	Liquid velocity (m/s)
c_m	Constant		u_m	Spray axis droplet velocity (m/s)
C_m	Constant		u_{max}	Maximum droplet velocity (m/s)
c_v	Constant		u_{min}	Minimum droplet velocity (m/s)
C_V	Constant		u_{in}	Velocity of nozzle inlet (m/s)
d_m	Constant		u_{out}	Velocity of nozzle outlet (m/s)
d	Equivalent orifice diameter (mm)		U	Average droplet velocity (m/s)
D	Droplet size (µm)		z	Coordinate value (m)
D_{max}	Maximum droplet size (µm)		α	Spray angle (°)
D_{min}	Minimum droplet size (µm)		σ_l	Droplet surface tension coefficient
Dv	Volume median diameter (µm)		ρ_l	Water density (kg/m^3)
g	Gravity acceleration (m/s^2)		ρ_g	Gas density (kg/m^3)
K	Constant			

---

[1] *Shougen Li, As. PhD. Eng.; Yaxiong Wang, As. PhD. Eng.; Chongchong Chen, As. PhD. Eng.; Feng Kang, As. PhD. Eng.; Wenbin Li, As. PhD. Eng.*

INTRODUCTION

Spraying is an important method for pest control in agriculture and forest. For killing the pests with the habit of up and down migration along the trunk, Kang developed an automatic targeted application system using a barrier treatment and then improved the spray system (Fig. 1). Additionally, spray characteristics, the addition of adjuvants, pulse width modulation technology, and electrostatic spray have also attracted much attention. Spray characteristics mainly include two factors: droplet velocity and size. Droplets with appropriate velocities and size are not easy to drift and rebound, and have good deposition and coverage effects (*Wang S. et al., 2018; Patel M K et al., 2017; Preftakes C J et al., 2019*).

Fig. 1 - The spray system of forest barrier treatment

Current research on the distributions of droplet velocity and size has mostly focused on the industrial field. For example, Cui developed the microhole-measuring system based on a twin fibre Bragg grating (FBG) probe and obtained that small geometric differences had a significant effect on cavitating flow. Ghate studied the effect of orifice divergence on the spray characteristics of hollow cone nozzles. Results revealed that liquid film thickness and the axial and radial velocities at the orifice exit were drastically affected by divergence angle (*Ghate K., Sundararajan T. 2019*). Additionally, Geng found that the length-diameter ratio (L/D) of the nozzle inner structure's parameters had less of an impact than spray pressure or fuel temperature on the spray characteristics (*Geng L et al., 2020*). Moreover, studies on the spray characteristics have also been reported in the dust reduction (*Wang J et al., 2019*), food (*Chen G et al., 2018*), and cleaning industries. In agriculture and forestry, spray characteristic studies are less reported. Based on the assumption that the spray field is a 2D plane, Kang established the droplet velocity and size model by simulation and actual experiments (*Kang F et al., 2011*). A computational fluid dynamics (CFD) model was developed by Musiu to evaluate the distribution of droplet velocity and size at different settings for a greenhouse air blast sprayer, which predicted the actual measuring droplet size value.

Flat fan nozzles are the main nozzle in agriculture and forest. The atomization field of a flat fan nozzle is as shown in Fig. 2. In order to clearly describe it, a rectangular coordinate system in space was established with a nozzle exit centre as the coordinate origin. The X, Y, and Z axes were the long and short axes of the spray cross-section and spray axis, respectively. The shape of the 3D spray cross-section of the fan nozzle is approximately elliptical, which is basically symmetrical along the long and short axes. The spray characteristics of atomization field could be reflected by the distribution of droplet velocity and size along one spray line starting from the nozzle outlet.
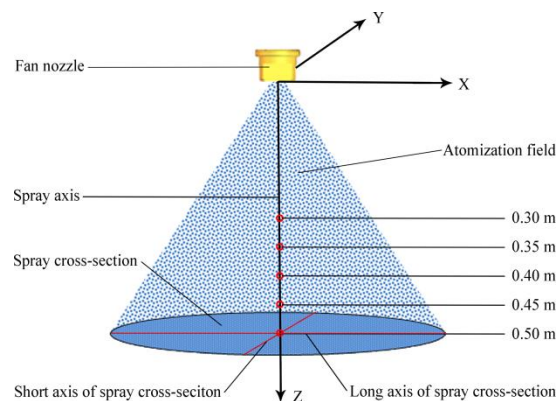
Fig. 2 - The atomization field of a flat fan nozzle. Red circles represent the measurement points

In this context, this study was to analyse the atomization characteristics of flat fan nozzles for agriculture and forest. The main relevant parameters were analysed at low pressures (0.20–0.30 MPa). A Phase Doppler Interferometer (PDI) was used for measuring all data at spray distances ranging from 0.30 to 0.50 m. Based the jet theory, this research improved and established the droplet velocity and size models, and provided guidance for agriculture and forest.

MATERIALS AND METHODS
Selection of nozzle type

Currently, the mainstream brands of flat fan nozzles in the market include Teejet (USA), Lechler (Germany), and Feizhuo (China), which are widely used in surface treatments, the food industry, agricultural and forestry pesticide application, and other fields. To identify similarities between these three brands, the Teejet TP, Lechler 632, and Feizhuo H/U flat fan nozzle series were selected for experimental measurements. In this study, the spray angles of 25°, 40°, 65°, and 80° for the Teejet and Feizhuo nozzles and 30°, 45°, 60°, and 90° for the Lechler nozzle were utilized as test objects (Table 1).

Table 1

The types of nozzles used in this study

α	Manufacturer	d			
		0.70	1.00	1.35	1.65
30	Lechler	632.302.30	632.362.30 [a]	632.442.30 [b]	632.512.30
45		632.303.30 [a]	632.363.30 [a]	632.443.30 [a]	632.513.30 [a]
60		632.304.30 [b]	632.364.30 [a]	632.444.30 [b]	632.514.30 [b]
90		632.306.30	632.366.30 [a]	632.446.30 [b]	632.516.30

α	Manufacturer	d			
		0.80	1.00	1.20	1.40
25	Teejet	2502	2503 [a]	2504 [b]	2505
40		4002 [a]	4003 [a]	4004 [a]	4005 [a]
65		6502 [b]	6503 [a]	6504 [b]	6505 [b]
80		8002	8003 [a]	8004 [b]	8005

α	Manufacturer	d			
		0.91	1.10	1.30	1.40
25	Feizhuo	2502	2503 [a]	2504 [b]	2505
40		4002 [a]	4003 [a]	4004 [a]	4005 [a]
65		6502 [b]	6503 [a]	6504 [b]	6505 [b]
80		8002	8003 [a]	8004 [b]	8005

[a] Nozzles used to establish the model.

[b] Nozzles used to verify the established model.

Abbreviated forms were used as type names in the following text, for example, 632.302.30-302, where 30 and 2 represent the flow rate and spray angle in the abbreviated Lechler, respectively, and 25 and 02 represent the spray angle and flow rate for Teejet and Feizhuo, respectively. Flow rate was determined by the equivalent orifice diameter. The Lechler, Teejet, and Feizhuo nozzles are hereafter referred to as LN, TN, and FN, respectively.

Theoretical basis

The findings of this study will serve the agricultural and forestry pesticide application. Droplet velocity and size are expressed by the average velocity and volume mean diameter (VMD), respectively.

The formulas are as follows:

$$U = (\int_{u_{\min}}^{u_{\max}} u_d \, dN) / (\int_{u_{\min}}^{u_{\max}} dN) \tag{1}$$

$$D_v = ((\int_{D_{\min}}^{D_{\max}} D^3 \, dN) / (\int_{D_{\min}}^{D_{\max}} dN))^{1/3} \tag{2}$$

The pressure (P), spray distance (z), spray angle (α), and equivalent orifice diameter (d) are the main factors that affect axial velocity and size *(Kooij S. et al., 2018)*. Therefore, this study analysed and discussed these factors to establish an axial atomization model for flat fan nozzles.

Assuming that these factors are independent, the function of the axial atomization model was established as follows:

$$u_m, D_v = f(z)f(P)f(d)f(\alpha) \tag{3}$$

For the incompressible flow in the nozzles, pressure and velocity satisfied the Bernoulli formula, as follows:

$$(P / \rho_l) + gz + (u^2 / 2) = K \tag{4}$$

For a given nozzle, the internal flow velocity was inversely proportional to the square of the inner diameter.

The formula is as follows:

$$u_{in} / u_{out} = r_{out}^2 / r_{in}^2 \tag{5}$$

After ejection, liquid film was mainly affected by liquid flow characteristics, gas-liquid two-phase physical properties, and flow conditions. Due to disturbances in the external gas, droplet groups were finally formed after breakage. Sforza proposed that the 3D spray axial velocity is negatively and exponentially decremented by spray distance (*Sforza P M et al., 1966*).

The formula is as follows:

$$u_m = x^{-n} \tag{6}$$

For the flat fan nozzles used in this study, velocity changes caused by gravity and nozzle inlet velocity were negligible. The spray axial velocity was obtained from formulas (3–5):

$$u_m = (2P / \rho)^{0.5} z^{-a_m} \tag{7}$$

Thus far, only a few theoretical studies on the droplet size distribution of flat fan nozzles using 2D and 3D sprays have been reported. Hinze (*Hinze J. O. 1955*) validated the relationship between droplet velocity and size in a steady state using experimental and theoretical approaches.

The formula is as follows:

$$D_{\max} = (8\sigma_l) / (C_D \rho_g u^2) \tag{8}$$

For a given nozzle, the VMD of the droplets was related to the spray pressure and flowrate of the liquid (*Jiang Y. et al., 2019*). Based on this information, Kang obtained the relationship between the average VMD of the atomization field and spray pressure (*Kang F et al., 2018*).

The formula is as follows:

$$D_v = C\Delta P^{-1/3} \tag{9}$$

Therefore, the functional form of axial droplet size would be similar to the functional form of axial droplet velocity.

Experimental design

Tests were conducted in the Laboratory of Agricultural Aviation Aerodynamics, Beijing Academy of Agriculture and Forestry Sciences, China. A laser PIII-X00MD PDI was used to collect data on droplet velocity and size of the atomization field. A 1WZB-25Z PRODN pressure pump was utilized to supply stable pressure for the measuring system, and a 3DOF mobile platform was used to precisely control the PDI position.

The system also included flow meters, pressure gauges, nozzle holders, and a liquid circulatory system (Fig. 3).
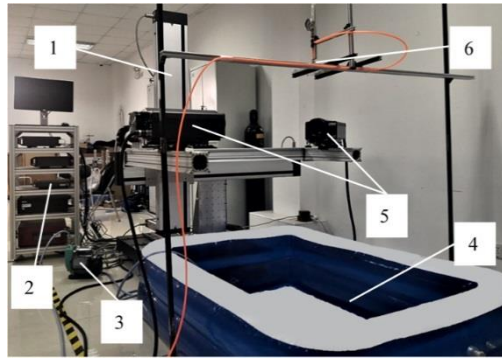
Fig.3 - The system used for velocity and size measurements
(1) 3DOF mobile platform; (2) Control centre; (3) Pump; (4) Liquid circulatory system; (5) PDI; (6) Flat fan nozzle

This study investigated a basic drop velocity and size model. Tests were conducted indoors with no wind at a stable temperature (18°C–22°C) and humidity (40%–60% RH) so that droplet evaporation could be ignored. In order to minimize the influence of gravity, nozzles were directed vertically downward. Five measuring points were selected along the Z-axis ranging from 0.30 to 0.50 m at 0.05 m intervals (Fig. 2). The preset pressures were 0.20, 0.25, and 0.30 MPa. Three replicates were conducted at each measurement point, and at least 5000 droplets were measured per replicate to ensure the accuracy of measurement data. Droplet velocities and sizes at the measurement points were thereby obtained.

Axial droplet velocity and size data were acquired using an Automated Instrument Management System (AIMS) software. Origin 2018 was used to draw the best-fit curves for droplet velocity and size of different factors.

RESULTS
Establishment of the droplet velocity model

The spray axial velocities at different distances of 18 selected nozzles were investigated (Fig. 4). The spray axial velocity at three spray pressures gradually decreased as spray axial distance increased, which was due to the kinetic energy gradually being reduced and the droplet velocity, thereby being reduced due to air resistance. Additionally, the velocity reduction rate gradually decreased as spray axial distance increased. This phenomenon was a result of the air resistance of droplets being inversely proportional to the square of its velocity; the lower the droplet velocity, the smaller the resistance. The mathematical functions of the best fit curve of axial velocity and spray distance for the three brands of nozzles were obtained as follows:

$$u_m = z^{a_m} \tag{10}$$

Where a_m was -0.58 for LN and -0.55 for TN and FN. Fitting degrees of the spray axial velocity and spray axial distance are provided (Table 2).

Table 2

Fitting degrees of spray axial velocity and distance

Parameter	LN 362	LN 363	LN 443	LN 513	LN 364	LN 366
R^2	0.996	0.997	0.998	0.946	0.981	0.997
Parameter	TN 2503	TN 4003	TN 4004	TN 4005	TN 6503	TN 8003
R^2	0.997	0.981	0.993	0.998	0.908	0.980
Parameter	FN 2503	FN 4003	FN 4004	FN 4005	FN 6503	FN 8003
R^2	0.996	0.999	0.997	0.993	0.951	0.986
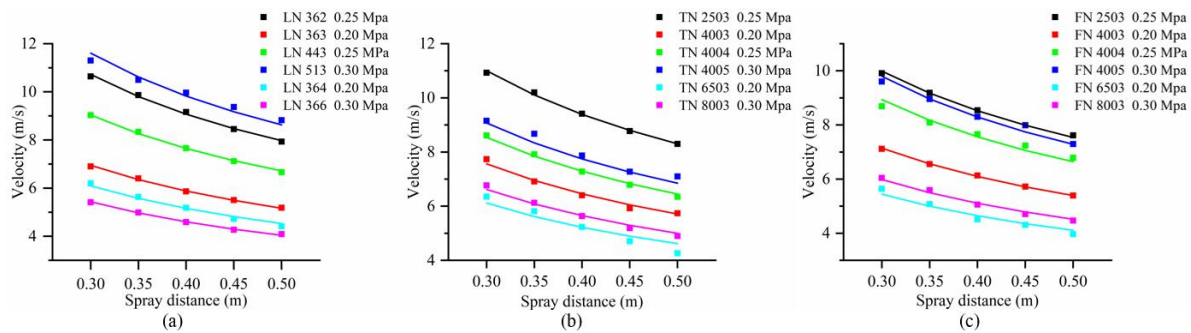
Fig. 4 - The relationship between axial velocity and spray distance

Results revealed that the spray axial velocities decreased as spray angle increased among the 15 nozzles from the three brands (Fig. 5). That was because droplets were more affected by air resistance at the same flow rate, as spray width increased with the increase of the spray angle. The relationship between the spray angle and axial velocity by fitting satisfied the following function:

$$u_m = \exp(b_m + c_m / \alpha) \tag{11}$$

Where b_m and c_m were 1.14 and 32.16 for LN, and 1.34 and 21.41 for TN and FN, respectively. Fitting degrees of the spray axial velocity and angle are provided (Table 3).

Table 3

Fitting degrees of spray axial velocity and spray angle

Parameter	LN 0.30 m	LN 0.35 m	LN 0.40 m	LN 0.45 m	LN 0.50 m
R^2	0.988	0.994	0.996	0.995	0.998
Parameter	TN 0.30 m	TN 0.35 m	TN 0.40 m	TN 0.45 m	TN 0.50 m
R^2	0.985	0.980	0.998	0.993	0.989
Parameter	FN 0.30 m	FN 0.35 m	FN 0.40 m	FN 0.45 m	FN 0.50 m
R^2	0.987	0.993	0.989	0.988	0.991
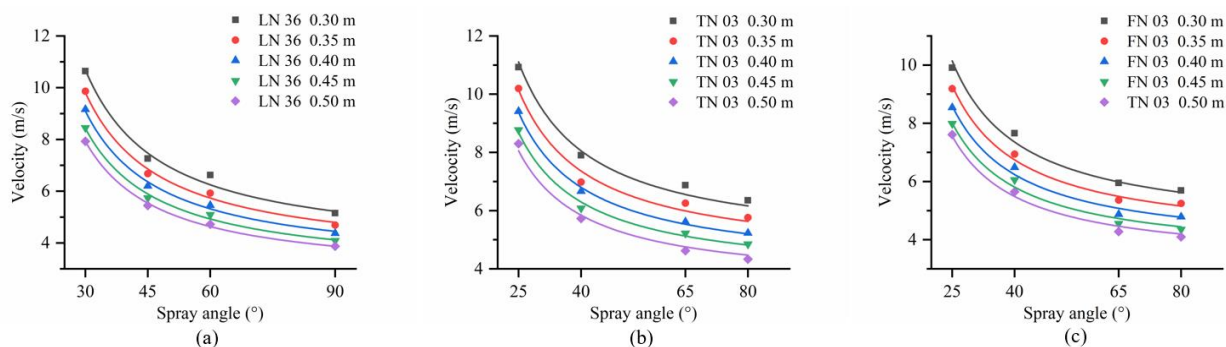
Fig. 5 - The relationship between axial velocity and spray angle

Axial velocity increased as the equivalent orifice diameter increased at a spray angle of 45° for LN and 40° for TN and FN (Fig. 6).

The relationship between the equivalent orifice diameter and spray axial velocity by fitting satisfied the following function:

$$u_m = d^{d_m} \tag{12}$$

Where d_m was 0.66 for LN, 0.60 for TN and 0.80 for FN. Fitting degrees of the spray axial velocity and equivalent orifice diameter are provided (Table 4).

Fitting degrees of spray axial velocity and equivalent orifice diameter

Parameter	LN 0.30 m	LN 0.35 m	LN 0.40 m	LN 0.45 m	LN 0.50 m
R^2	0.980	0.949	0.966	0.964	0.957
Parameter	TN 0.30 m	TN 0.35 m	TN 0.40 m	TN 0.45 m	TN 0.50 m
R^2	0.946	0.979	0.956	0.972	0.983
Parameter	FN 0.30 m	FN 0.35 m	FN 0.40 m	FN 0.45 m	FN 0.50 m
R^2	0.988	0.990	0.983	0.970	0.981
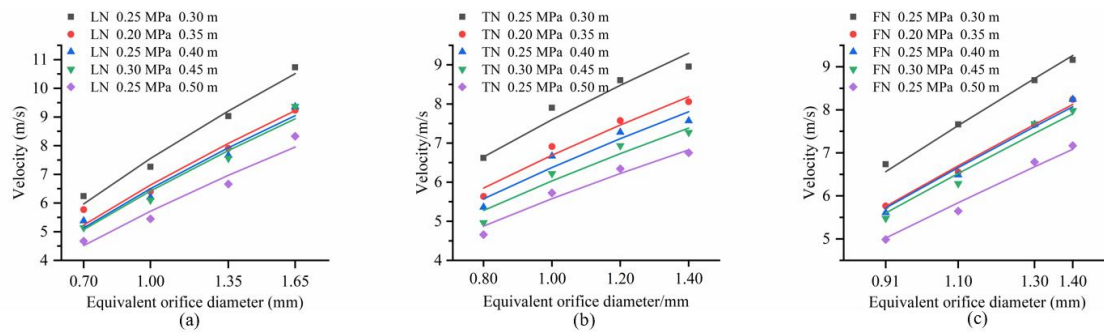
Fig. 6 - The relationship between droplet size and equivalent orifice diameter

By combining formulas (10)–(12), the spray axis velocity formula was established as follows:

$$u_m = \left(2P/\rho\right)^{0.5} z^{a_m} \exp(b_m + c_m/\alpha) d^{d_m} \qquad (13)$$

The parameter values of the three different nozzle brands in the formula are provided (Table 5).

Parameter values of the droplet velocity formula

Parameter	LN	TN	FN
a_m	-0.58	-0.55	-0.55
b_m	1.14	1.34	1.34
c_m	32.16	21.41	21.41
d_m	0.66	0.60	0.80

Establishment of the droplet size model

No noticeable changes were observed in the droplet size between the six nozzles of each brand at five measuring spray axial distances (Fig. 7).

This result was due to the fact that droplets were blended and ran along the original motion trajectory after the liquid film was broken twice, thereby forming stable droplet groups. Evaporation of the droplets could be ignored through the measurement ranges. As a result, droplet size hardly changed along the spray axial distance and was independent of spray axial distance. Therefore, the average droplet size at the five measuring positions under the same conditions can be considered the droplet size in subsequent research.
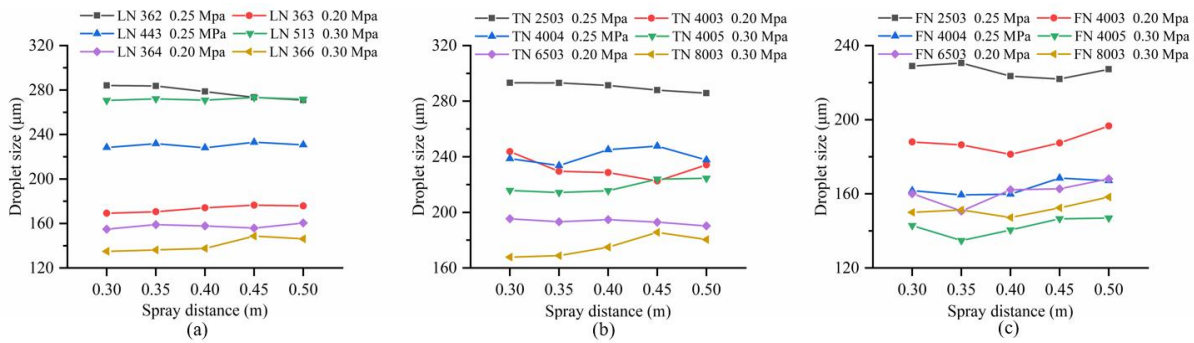
Fig. 7 - The relationship between droplet size and spray distance

Spray axial droplet size decreased as spray angle increased (Fig. 8). This phenomenon was due to the widening range of the fan liquid film as spray angle increased, forming more droplets that were smaller in size at the same flow rate and pressure. The fitting function of spray angle and axial droplet size was as follows:

$$D_v = (1 + a_v * \exp(-\alpha / 10)) \tag{14}$$

Where a_v was 18.00 for LN and 7.5 for TN and FN. Fitting degrees of the axial droplet size and spray angle are provided (Table 6).

Table 6

Fitting degrees of axial droplet size and spray angle

Parameter	LN 0.20 MPa	LN 0.25 MPa	LN 0.30 MPa
R^2	0.959	0.985	0.965
Parameter	TN 0.20 MPa	TN 0.25 MPa	TN 0.30 MPa
R^2	0.935	0.962	0.931
Parameter	FN 0.20 MPa	FN 0.25 MPa	FN 0.30 MPa
R^2	0.966	0.993	0.969
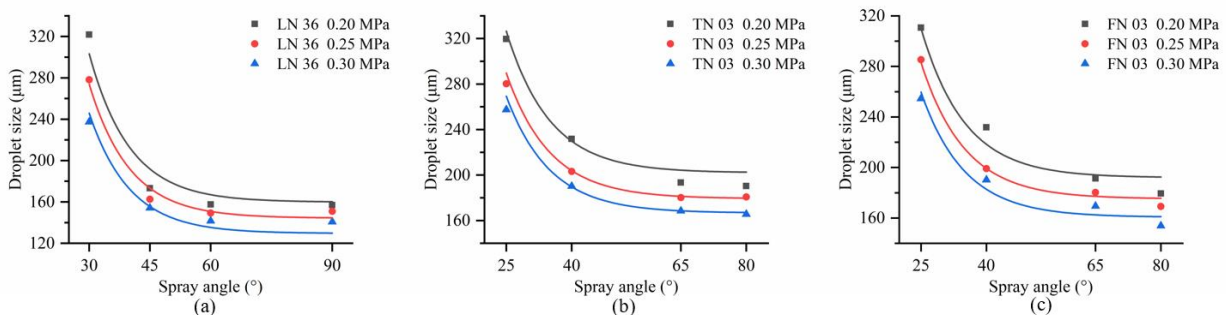
Fig. 8 - Fitting curves of droplet size and spray angle

Axial droplet size gradually decreased as pressure increased (Fig. 9). According to formulas (8) and (9), nozzle outlet velocity increased as nozzle inlet pressure increased, and the liquid film subsequently broke to produce smaller droplets. The fitting function of spray axial droplet size and pressure by fitting was as follows:

$$D_v = P^{b_v} \tag{15}$$

Where b_v was -0.30 for LN and TN and -0.40 for FN. Fitting degrees of axial droplet size and spray pressure are provided (Table 7).

Table 7

Fitting degrees of axial droplet size and spray pressure

Parameter	LN 362	LN 363	LN 443	LN 513	LN 364	LN 366
R^2	0.795	0.998	0.979	0.989	0.938	0.935
Parameter	TN 2503	TN 4003	TN 4004	TN 4005	TN 6503	TN 8003
R^2	0.930	0.946	0.998	0.987	0.964	0.921
Parameter	FN 2503	FN 4003	FN 4004	FN 4005	FN 6503	FN 8003
R^2	0.953	0.905	0.984	0.958	0.876	0.957
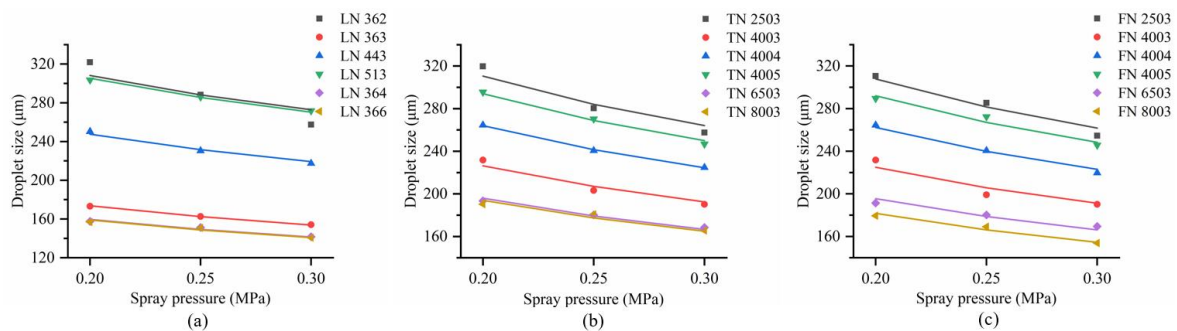
Fig. 9 - Fitting curves of droplet size and spray pressure

The relationship between the equivalent orifice diameter and spray axial droplet size at three pressures in the 16 nozzles was investigated at a spray angle of 40° for LN and 45° for TN and FN. Spray axial droplet size was positively correlated with the equivalent orifice diameter (Fig. 10). The fitting function of the spray axial droplet size and equivalent orifice diameter by fitting was as follows:

$$D_v = d^{c_v} \tag{16}$$

Where c_v was 0.95 for LN, 0.82 for TN and 1.10 for FN. Fitting degrees of axial droplet size and the equivalent orifice diameter are provided (Table 8).

Table 8

Fitting degrees of axial droplet size and the equivalent orifice diameter

Parameter	LN 0.20 MPa	LN 0.25 MPa	LN 0.30 MPa
R^2	0.970	0.985	0.987
Parameter	TN 0.20 MPa	TN 0.25 MPa	TN 0.30 MPa
R^2	0.985	0.983	0.994
Parameter	FN 0.20 MPa	FN 0.25 MPa	FN 0.30 MPa
R^2	0.967	0.964	0.969
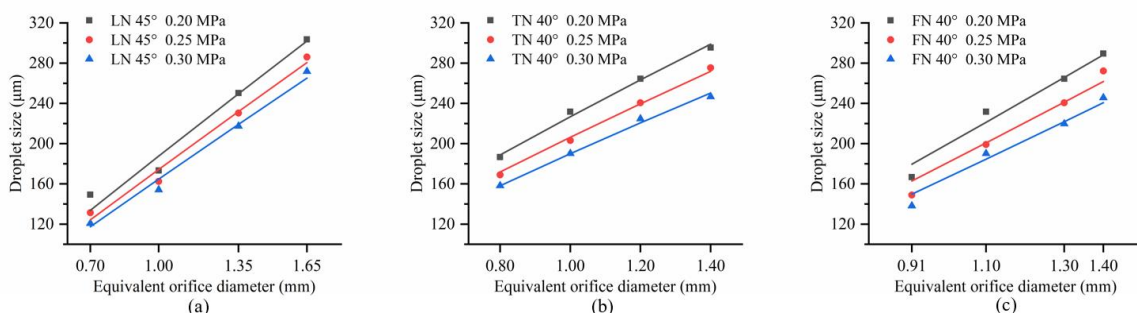
Fig. 10 - Fitting curves of axial droplet size and the equivalent orifice diameter

The following formula for spray axis droplet size was obtained from formulas (14)–(16):

$$D_v = (1 + a_v \exp(-\alpha/10)) P^{b_v} d^{c_v} \qquad (17)$$

The parameter values of different nozzle brands in the formula are provided (Table 9).

Table 9

Parameter values of the droplet size formula

Parameter	LN	TN	FN
a_v	18.00	7.50	7.50
b_v	-0.30	-0.40	-0.40
c_v	0.95	0.82	1.10

Validation

In order to ensure the accuracy of the axial droplet velocity and size model, the aforementioned parameters were calculated using formulas (13) and (17); the axial droplet velocity and size distribution curves of the three brands of nozzles were subsequently obtained (Fig. 11 and 12): (T) represents the theoretical data, and (A) represents the actual measured data. The results showed that the actual measured data were generally smaller than the theoretical data for velocity, and were two orders of magnitude larger for droplet size. The average absolute and relative errors for droplet velocity and size of the three brands are provided (Table 10). Although the theoretical data were larger or smaller than the actual measured data, the trends of the measured and theoretical data were roughly the same. This phenomenon was due to the liquid characteristics, design and processing of the nozzles, as well as air resistance and entrainment effects of the droplets during flight. Additionally, droplet velocity and size could be enlarged or reduced when multiplying the obtained formulas by fitting different parameters. For axial droplet size, the most important explanatory factor for theoretical droplet size was much smaller than the actual data because the direct relationship between axial droplet size and the liquid characteristics of the nozzle outlets was not established. Therefore, formulas (13) and (17) should be appropriately compensated to ensure that the theoretical values are closer to the actual values.
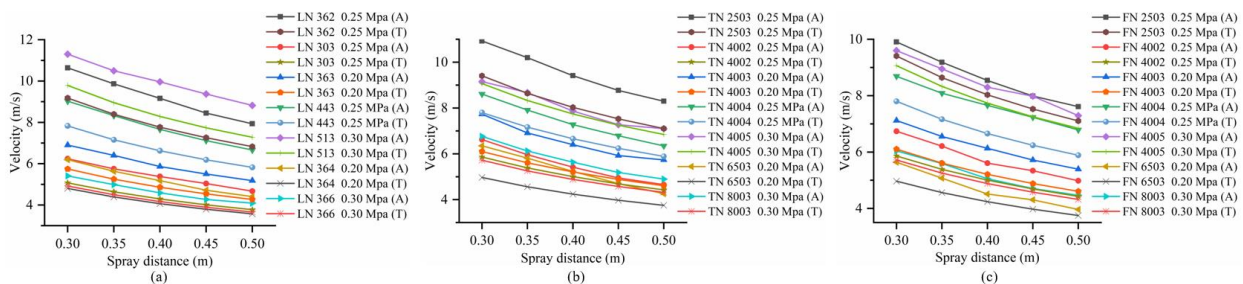
Fig. 11 - Comparison between the actual and theoretical axial velocities before compensation
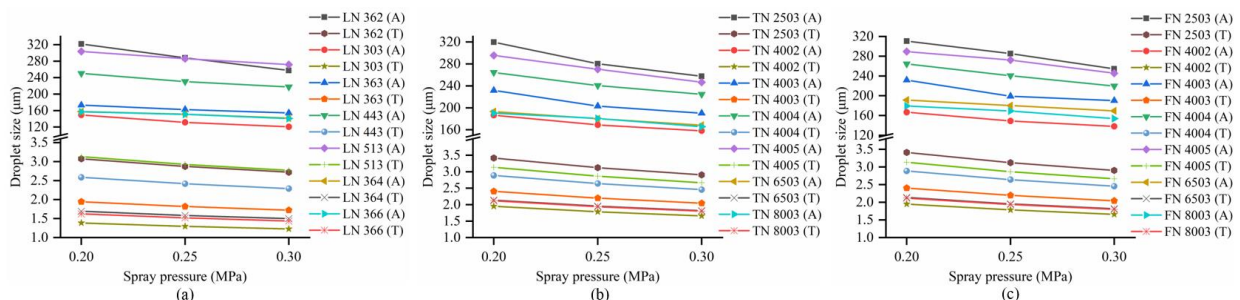
Fig. 12 - Comparison between the actual and theoretical axial droplet sizes before compensation

Table 10

The absolute and relative errors of droplet velocities and sizes before compensation

Manufacturer	Droplet velocity		Droplet size	
	Absolute error (m/s)	Relative error	Absolute error (μm)	Relative error
LN	1.071	14.49%	331.188	99.43%
TN	0.954	13.74%	339.385	99.49%
FN	1.151	17.24%	327.975	99.53%

By comparing the actual and theoretical data, the compensation values of the axial droplet velocities and sizes (i.e., C_m and C_v, respectively) of the three brands of nozzles based on spray angle were obtained (Table 11). Five nozzles of each brand were selected to validate the axial droplet velocity and size model. The comparison between the compensated and measured data is presented (Fig. 13 and 14), of which (TO) represents the compensated theoretical data. After compensation, the average absolute and relative errors for droplet velocity and size of the three brands are provided (Table 12). Therefore, the compensation values were reasonable and effective. The axial droplet velocity and size formulas are as follows:

$$u_m = C_m \left(2P / \rho\right)^{0.5} z^{a_m} \exp(b_m + c_m / \alpha) d^{d_m} \tag{18}$$

$$D_v = C_v (1 + a_v \exp(-\alpha / 10)) P^{b_v} d^{c_v} \tag{19}$$

Table 11

Compensation coefficients of the theoretical formulas for the three nozzle brands

Parameter	LN				TN				FN			
	30°	45°	60°	90°	25°	40°	65°	80°	25°	40°	65°	80°
C_m	0.86	0.83	0.80	0.90	0.86	0.91	0.82	0.86	0.94	0.88	0.91	0.95
C_v	100	96	94	97	90	94	91	90	89	90	91	84

The average absolute and relative errors of the axial droplet velocity and size of the three brands of nozzles after compensation are provided (Table 12).
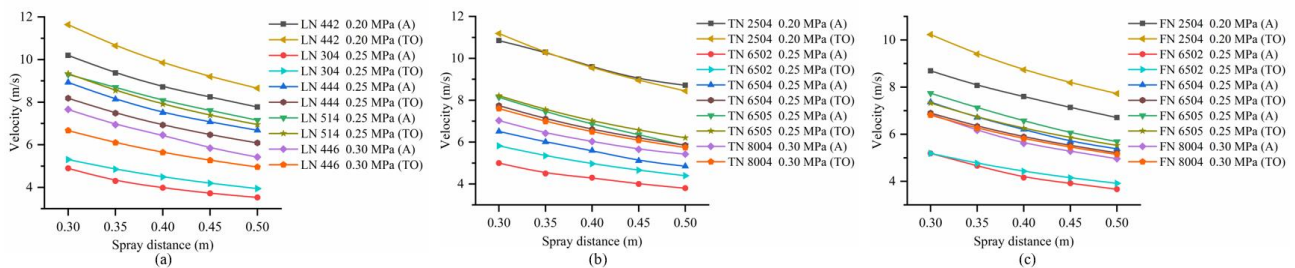
Fig. 13 - Comparison between the actual and theoretical axial droplet velocities after compensation
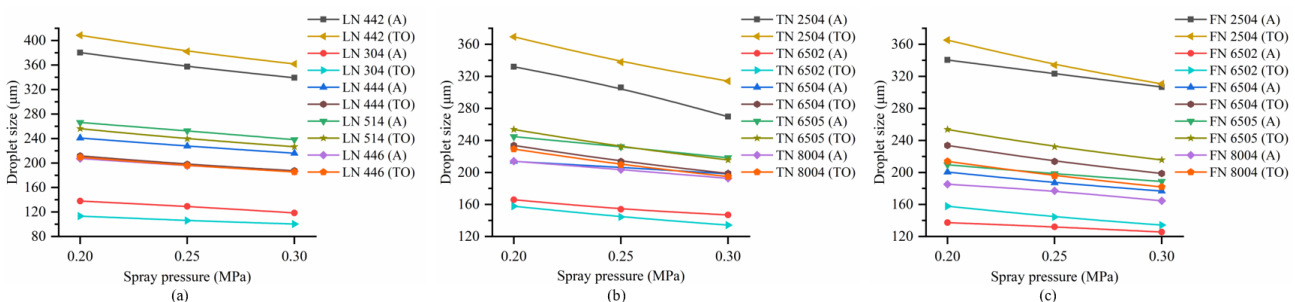
Fig. 14 - Comparison between the actual and theoretical axial droplet sizes after compensation

Table 12

The average absolute and relative errors for droplet velocities and sizes after compensation

Manufacturer	Droplet velocity		Droplet size	
	Absolute error (m/s)	Relative error	Absolute error (μm)	Relative error
LN	0.629	9.22%	17.821	8.40%
TN	0.521	9.60%	13.801	5.82%
FN	0.684	11.89%	22.140	11.67%

CONCLUSIONS

Based on the theoretical derivations and actual tests, this study established an axial droplet velocity and size model of the flat fan nozzle for agriculture and forest. Results revealed that the maximum average absolute and relative errors of the droplet velocity model were 0.684 m/s and 11.89%, respectively. The maximum average absolute and relative errors of the droplet size model were 22.140 μm and 11.67%, respectively. Thus, the theoretical atomization model was suitable and matched the actual test results.

Additionally, this study indicated that spray distance and spray angle were negatively correlated with axial velocity. There was a negative correlation detected between spray angle, pressure, and the axial droplet size. Axial droplet size was positively correlated with the equivalent orifice diameter. Moreover, the axial droplet size remained unchanged as spray distance increased within the spray range of 0.30–0.50 m. Thus, larger spray distances and spray angle should be selected at the same pressure. Although the axial droplet velocity and size models for the three brands of nozzles had the same functional form, the parameters were different, which may be due to the machining error and the different design standards.

REFERENCES

[1] Chen G., Gu Y., Tsang H., (2018), The effect of droplet sizes on overspray in aerosol-jet printing. *Advanced Engineering Materials*, Vol.20, Issue 8, pp. 1701084, Germany;

[2] Geng L., Wang Y., Wang J., (2020), Numerical simulation of the influence of fuel temperature and injection parameters on biodiesel spray characteristics. *Energy Science & Engineering*, Vol.8, Issue 2, pp.312-326, USA;

[3] Ghate K., Sundararajan T., (2019), Effects of orifice divergence on hollow cone spray at low injection pressures. Proceedings of the Institution of Mechanical Engineers, Part G: *Journal of Aerospace Engineering*, Vol.233, Issue 11, pp.4091-4105, USA;

[4] Hinze J.O., (1955), Fundamentals of the hydrodynamic mechanism of splitting in dispersion processes, *Aiche Journal.*, Vol.1, Issue 3, pp.289-295, USA;

[5] Jiang Y., Li H., Hua L., (2019), Experimental study on jet breakup morphologies and jet characteristic parameters of non-circular nozzles under low-intermediate pressures. *Applied Engineering in Agriculture*, Vol.35, Issue 4, pp.617-632, USA;

[6] Kang F., Pierce F. J., Walsh & D.B., (2011), An automated trailer sprayer system for targeted control of cutworm in vineyards. Trans. *ASABE*, Vol.55, Issue 5, pp.2007-2014, USA;

[7] Kang F., Wang Y., Li S., (2018), Establishment of a static nozzle atomization model for forest barrier treatment. *Crop Protection*, Vol.112, pp.201-208, England;

[8] Kooij S., Sijs R., Morton M.D., (2018), What determines the drop size in sprays? Physical Review X. Vol.8, Issue 3, pp. 031019, USA;

[9] Patel M.K., Praveen B., Sahoo H. K., (2017), An advance air-induced air-assisted electrostatic nozzle with enhanced performance. *Computers and Electronics in Agriculture*, Vol.135, pp.280-288, England;

[10] Preftakes C. J., Schleier J., Kruger G. R., Weaver, D. K., Peterson, R. K., (2019), Effect of insecticide formulation and adjuvant combination on agricultural spray drift. PeerJ, Vol. 7, pp. e7136, England;

[11] Sforza P. M., Steiger M. H., Trentacoste N., (1966), Studies on three-dimensional viscous jets. *AIAA JOURNAL*. Vol.4, Issue 5, pp.800-806, USA;

[12] Wang J., Zhou G., Wei X., (2019), Experimental characterization of multi-nozzle atomization interference for dust reduction between hydraulic supports at a fully mechanized coal mining face. *Environmental Science and Pollution Research*, Vol.26, Issue 10, pp.10023-10036, Germany;

[13] Wang S., He X., Song J., et al., (2018), Effects of xanthan gum on atomization and deposition characteristics in water and Silwet 408 aqueous solution. *International Journal of Agricultural and Biological Engineering*, Vol.11, Issue. 3, pp. 29-34, China.

DEVELOPMENT AND TEST OF SPEED CONTROL SYSTEM FOR COMBINE HARVESTER THRESHING AND CLEANING DEVICE
/
联合收获机脱粒滚筒与清选风机速度调控系统设计与试验

Zhuohuai Guan [1)], **Zhou Zhang** [2)], **Tao Jiang** [1)], **Ying Li** [1)], **Chongyou Wu** [1)], **Senlin Mu** [1*)]   [1]

[1)] Nanjing Research Institute for Agricultural Mechanization, Ministry of Agriculture and Rural Affairs, Nanjing, China
[2)] School of Management & Engineering, Nanjing University, Nanjing, China
*Tel: 02584346274; *E-mail: 675290487@qq.com*

ABSTRACT

Aiming at real time rotation speed control of threshing drum and cleaning fan for combine harvester, a stepless speed regulation mechanism was developed. Test show that the adjustable range of fan was 600∼1150 r/min, average adjustment speed was 9.2 r/s, the absolute error of stable speed was less than 0.72 r/min. The average speed response time was 1.33s, the overshoot was less than 8 r/s. The adjustable range of the drum was 700∼1100 r/min and the average adjustment speed was 2.1 r/s. The absolute error of stable speed did not exceed 0.62 r/min, and the maximum relative deviation was 0.38%.

摘要

针对联合收割机脱粒滚筒和清选风机转速实时控制问题,研制了一种无级调速系统.试验表明,风机的调速范围为 600∼1150 r/min,平均调节速度 9.2 r/s,稳定转速的绝对误差小于 0.72 r/min.平均转速响应时间为 1.33s,超调量小于 8 r/s.风机转速的可调范围为 700∼1100 r/min,平均调节速度为 2.1 r/s,稳定转速绝对误差不超过 0.62 r/min,最大相对误差为 0.38%.

INTRODUCTION

Combine harvester is mainly used for harvesting rice, wheat, corn, millet and other grain crops as well as some cash crops such as rape and soybean. It can complete several procedures such as cutting, threshing, separating, cleaning, bagging or unloading grain in one go in the field. The technical development level of the combine harvester is an important symbol of the degree of agricultural modernization *(Liang Z. et.al, 2018; Ryszard M. and Ewelina J., 2016; Ma Z. et al, 2015)*. The harvesting capacity of the combine harvester is mainly determined by the threshing and separating capacity, which determines the level and performance of the combine harvester and is the core working part of the combine *(Guan Z. et al, 2016; Li Y. et al, 2015; Lenaerts B. et al, 2014)*. As the "digestion system" of the combine harvester, the performance of the cleaning device affects the working performance and efficiency of the whole machine directly. Cleaning device remove the residual impurities such as glume, broken spikes, short stalks from the separated mixture after threshing so as to obtain clean grains. The impurity content and loss rate of the cleaned grains are also the main indexes for measuring the product quality of the combine harvester *(Wang L. et al, 2016; Guan Z. et al, 2019; Xu L. et al, 2019)*.

The loss rate of combine harvester is mainly related to the structural parameters and working parameters of threshing and cleaning device *(Wan X. et al, 2018)*. Among which the rotational speed of threshing cylinder and cleaning fan greatly affect the loss rate *(Badretdinov I. et al, 2019)*. For the threshing cylinder, its speed generally no longer changes after setting according to experience. But the feeding amount, crop moisture content, etc. will affect the power of the threshing system. Affected by these random factors, the drum speed would deviate from the set value, resulting in the increase of harvest loss *(Li Y. et al, 2013 and Tang Z. et al, 2012)*. The speed of cleaning fan affects the impurity content and cleaning loss. If the wind speed is too small, the increase of impurity content is high, and if the wind speed is too large, the loss rate is high.

---

[1] Zhuohuai Guan, Assist. Prof. Ph.D.; Zhou Zhang, Grad. Stud; Tao Jiang, Assist. Prof.; Ying Li, Assist. Prof. Ph.D.; Chongyou Wu, Prof. Ph.D.; Senlin Mu, Asst. Prof.

Harvest loss, grain damage and impurities are complex multiple input multiple output relationship with threshing cylinder speed and cleaning fan speed *(Liang Z. et al, 2019)*. In order to obtain the best correspondence among them, comparative experiments under different parameters need to be carried out. At the same time, the operating parameters need to be adjusted by the intelligent control system according to the working conditions. *(Myhan R. and Jachimczyk E., 2016)*.

The optimal model and intelligent regulation system both depend on the regulation of the cylinder speed and cleaning fan speed (*Toshikazu M., and Tatsuro S., 2017*). The power of combine harvester cylinder and cleaning fan are too high to be driven directly by motors. The hydraulic system has enough power, but adding a hydraulic system on combine harvester is very complex. The transmission system of the original harvester can't be changed with complex structure due to the production cost. Facing the above-mentioned problems, a mechanical stepless speed regulation mechanism for combine threshing cylinder and cleaning fan was designed. The working performance was tested in an experiment. It provided a reference for efficient and low-loss operations of combine harvesters.

MATERIALS AND METHODS
Test Platform

The speed control system for combine harvester threshing and cleaning device was developed based on 4YZ-6T combine harvester. The main parameters of combine harvester are shown in table.1.

Table 1

Main parameters of combine harvester

Items	Parameters	Items	Parameters
Rated power [kw]	118	**Cleaning fan form**	Centrifugal
Machine quality [kg]	6 450	**Number of fans**	1
Header width [mm]	2 750	**Fan dimensions [mm]**	450
Feed rate [kg·s⁻¹]	≤6	**Operating speed [km·h⁻¹]**	1.6 ~ 7.2
Cylinder dimensions (diametre×length) [mm]	550×3230	**Cylinder type**	Longitudinal axial with nail
Concave clearance [mm]	15 ~ 40	**Productivity [hm²·h⁻¹]**	0.7 ~ 1.5

Structure and Working Principle

Parts are as shown in figure 1a. The fan speed stepless regulation system includes a pair of stepless speed regulation pulleys, a transmission pulley, a stepper motor and a turbine worm reducer. The stepless speed regulation pulley includes a driving wheel and a passive wheel. The system works as follows: The power output pulley transmits the speed to the drive pulley. The driving wheel and driven wheel of stepless speed-adjusting pulley move coaxially with the same speed. The driving wheel transmits power to the driven wheel through a belt, which drives the cleaning fan to rotate. When speed adjustment is needed, the stepper motor drives the sprocket through the reducer, rotates the speed adjustment mechanism on the driving wheel, and adjusts the belt pulley spacing of the driving wheel. The inside of the pulley is inclined, and the belt width is constant. The actual transmission diameter of the pulley can be changed with the opening and closing of the pulley. Rotating the stepless speed governor of the drive pulley can change the distance between the drive pulley belts. Because the transmission centre distance is constant, when the drive pulley belt distance decreases, the drive diameter of the drive pulley increases and the belt tension increases. As the belt tension increases, the force of the belt compressing the inner wall of the driven pulley increases, the distance between the driven pulleys increases, and the actual transmission diameter decreases. The transmission diameter of the driving wheel increases and the diameter of the passive transmission decreases, while the transmission ratio increases. Similarly, when the distance between the belt pulleys of the driving wheels increases, the driving diameter of the driving wheels decreases, the diameter of the passive driving increases, and the transmission ratio decreases. The change of the transmission ratio is continuously adjustable, which realizes the continuously variable transmission. The principle of the threshing cylinder speed regulating device is the same as the one of the cleaning fan, which is shown in figure 1b.

a)   b)
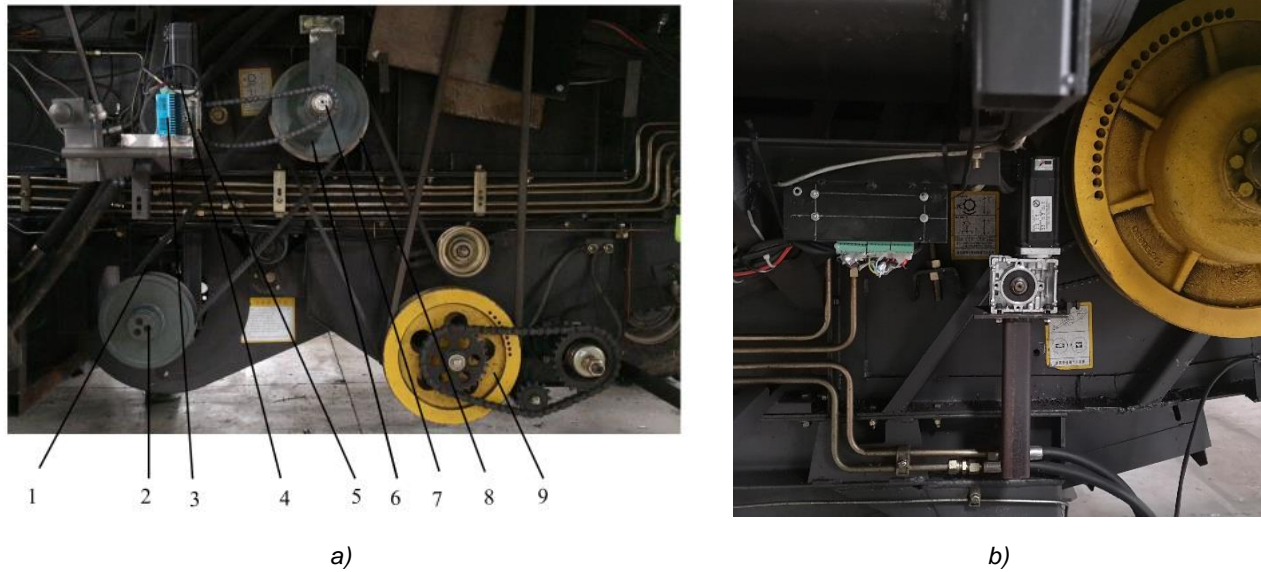
Fig. 1 - Stepless speed regulating mechanism
1 – cleaning fan; 2 – stepless speed regulation pulleys passive wheel; 3 – driver; 4 – stepper motor; 5 – reducer;
6 stepless speed regulation pulleys driving wheel; 7 – sprocket; 8 – drive pulley; 9 – power output pulley

Control model

Firstly, the kinetic model of the threshing drum rotary motion needs to be established. The threshing drum is a variable mass system, and the dynamic model of the drum is established from the angle of energy conservation.

$$\frac{d\omega}{dt} = \frac{N}{J\omega} - \frac{1}{J}\left(A + B\omega^2\right) - \frac{q\omega R}{2(1-f)J} \cdot \frac{\gamma + \lambda}{1+\gamma} \tag{1}$$

$$q = H\rho v \tag{2}$$

Where:

ω is angular velocity of thresh drum, r/min; J、R、f are rotary inertia of the drum, equivalent radius and rubbing coefficient; v is the combine harvester speed, m/s; H is cutting width, m; N is power provided by the engine to the drum, J; ρ is crop density, kg/m³; γ is ratio of grain to grass; A is friction coefficient of motion; B is air resistance coefficient; λ is ratio of grain export velocity; q is feed quantity, kg/s.

The efficiency and effect of cleaning fan are determined by the air flow and the size of the fan outlet. Under the excitation force of the fluid, the centrifugal fan:

$$[M]\left\{\ddot{X}(t)\right\} + [C]\left\{\dot{X}(t)\right\} + [K]\left\{X(t)\right\} = \left\{F(t)\right\} + \left\{Q(t)\right\} \tag{3}$$

Where:

$[M]$, $[C]$, $[K]$ are mass matrix, damping matrix and stiffness matrix of the system respectively; $\{F(t)\}$ is the fluid excitation force; $\{Q(t)\}$ is the centrifugal force generated when the impeller rotates; $\{X(t)\}$ is the system displacement vector.

The threshing drum and cleaning fan are controlled by PID control algorithm. PID control technology is more mature in control engineering, has formed a whole set of PID control methods. It can be applied not only to control systems whose mathematical models are known, but also to nonlinear system processes that are difficult to determine for most mathematical models. PID control has merit of simple structure, easily adjusting parameters, as well as good controlling effect. Since the roller motion equation is a nonlinear differential equation, the system has time delay and inertia, crop density is a random variable, and some parameters of the system are also uncertain, so the system is an uncertain nonlinear random system, and PID control is more suitable.

The control law is:

$$u(t) = K_p\left[e(t) + \frac{1}{T_i}\int_0^t e(t)dt + T_d\frac{de(t)}{dt}\right] = K_p e(t) + K_i\int_0^t e(t)dt + K_d\frac{de(t)}{dt} \tag{4}$$

where:

K_p is proportional coefficient; T_i is integral time constant; T_d is differential time constant; K_i is integral coefficient; K_d is differential coefficient.

The transfer function is

$$G(s) = K_p \left(1 + \frac{1}{T_i s} + T_d s \right) \tag{5}$$

The differential proportional time constant T_N is introduced

$$G(s) = K_p \left(1 + \frac{1}{T_i s} + \frac{T_d s}{1 + T_d s / T_N} \right) \tag{6}$$

Since the actual signal is discretized, discrete PID control is adopted *(Jumiyatun J. and Mustofa M., 2018)*, so the actual control model of the system is

$$u_k = K_p e_k + K_i \sum_{j=0}^{k} e_j + K_d \left(e_k - e_{k-1} \right) \tag{7}$$

where:

k is sampling serial number; u_k is computer output; e_k is input deviation; T is sampling period.

Control System

The control system includes speed detection and motor control. The control system is mainly composed of STM32 processor, core circuit, power circuit, and motor drive circuit, speed monitoring circuit, CAN communication circuit and reserved interface. The STM32 processor is the information processing and computing centre of the entire speed regulation system. On the one hand, it is responsible for analysing the instructions issued by the main controller and controlling the speed-adjusting drive motor; on the other hand, it reports the current drum fan speed information regularly. The core circuit is the most basic circuit required for the normal operation of the STM32 processor. The power supply circuit provides power for the entire single driver operation. The motor drive circuit is mainly used to transfer the control signal of the cylinder and fan speed control motor as shown in Figure 2a. The speed monitoring circuit supplies the Hall sensor and reads the Hall sensor signal as shown in Figure 2b. Data exchange between stepper motor driver and main controller is made through CAN bus. The reserved interface is the basic IO port on the STM32 processor, which is mainly for the convenience of later function expansion. During the harvesting operation, the main controller sends the speed signals of threshing drum and cleaning fan to the CAN bus. The Hall sensors collect the speed signals of the drum and the fan. Each motor driver filters out the speed instructions for the CAN message and analyses the speed after the signal, configuring the timer to output a specific control signal to drive the motor to rotate.

a. Stepper motor drive   b. Speed monitoring
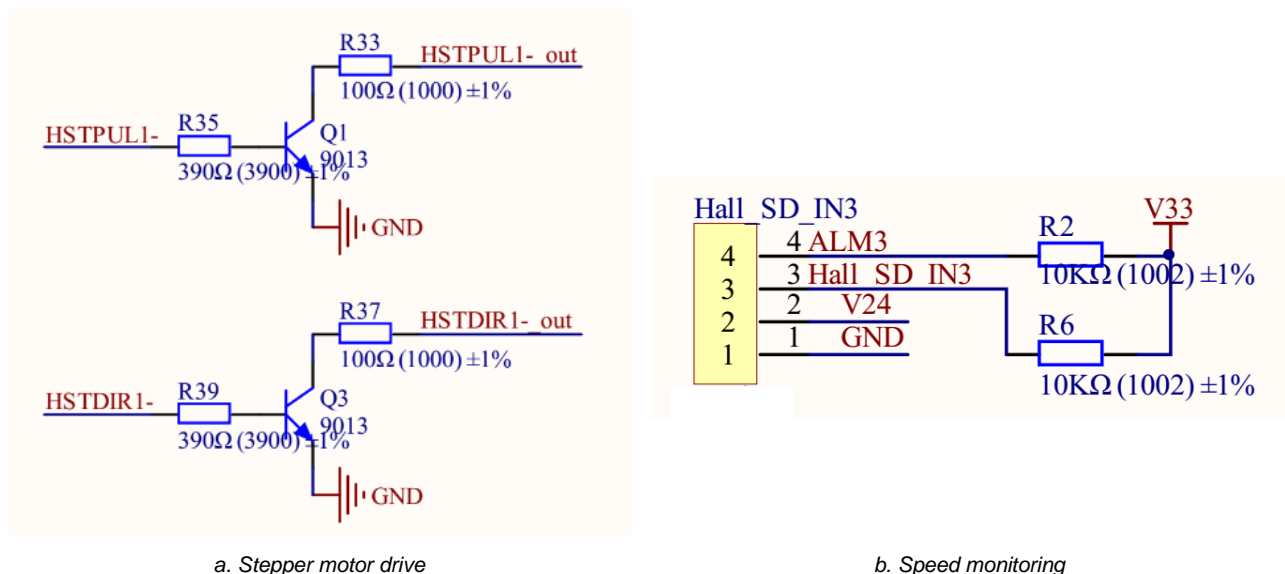
Fig. 2 - Key circuit

RESULTS
Speed regulation test

The adjustable range of the fan speed is tested as shown in figure 3. The adjustable range of fan speed is 600~1150 r/min, the time from the lowest speed to the highest speed is 59.7s, and the average adjustment speed is 9.2 r/s. The acceleration curve of the fan can be fitted as $y=0.1153x-64.691$, $R^2=99.17\%$, and the deceleration curve of the fan can be fitted as $y=-0.1138x+122.82$, $R^2=99.15\%$.
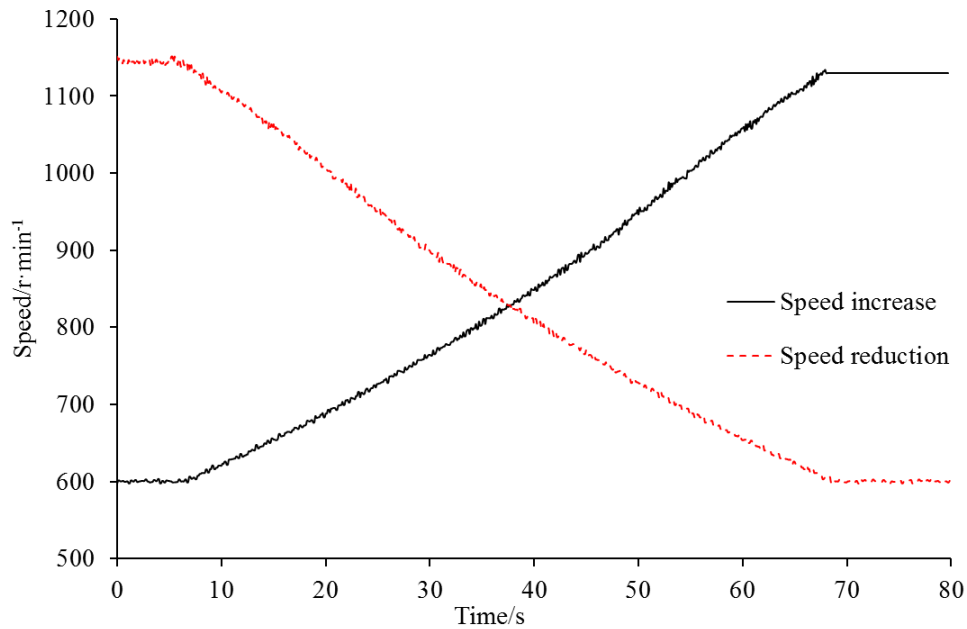
Fig. 3 - Fan speed regulation curve

The adjustable range of the fan speed is tested as shown in figure 4. The adjustable range of the rotating speed of cylinder is 700-1100r/min, the time from the lowest speed to the highest speed is 190.5s, and the average adjusting speed is 2.1r/s. The acceleration curve of the cylinder can be fitted as $y=2.06x+683.32$, $R^2=99.51\%$, and the deceleration curve of the cylinder can be fitted as $y=-2.0823x+1079.8$, $R^2=99.47\%$. Compared with the fan speed regulation, the roller speed regulation is slower, mainly because the roller speed regulation belt pulley needs a larger torque. In order to generate enough torque, the chain drive selects a larger transmission ratio, so the regulation speed is slower.
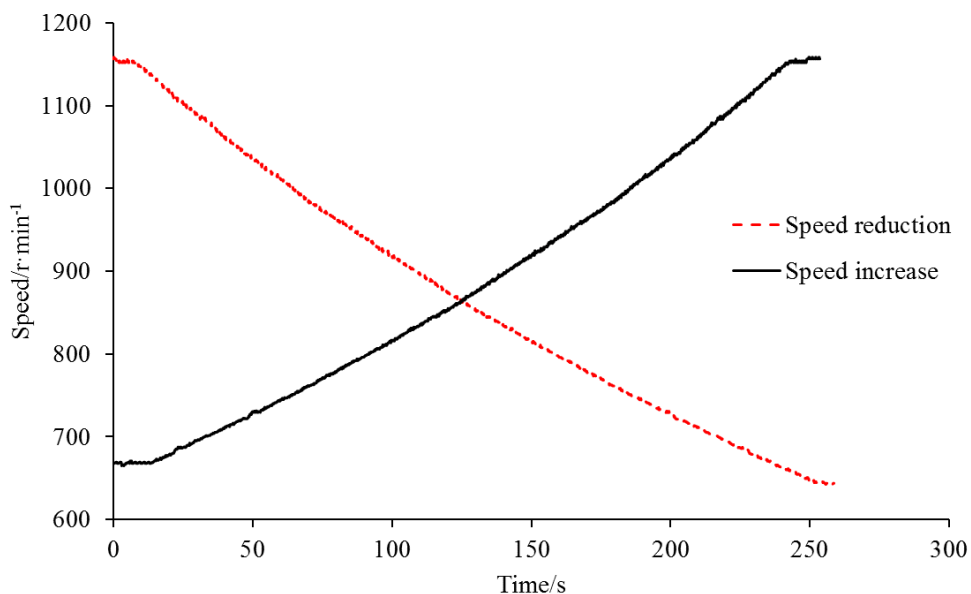
Fig. 4 - Threshing cylinder speed regulation curve

Speed Response Test

During the operation of the fan, the set value of the fan speed is changed, and the speed response curve of the fan is shown in Figure 5. It can be known from the test results that the set value of the fan speed is 745-900-950-850-900r/min. Under the function of speed control system, the actual fan speed changes as follows.
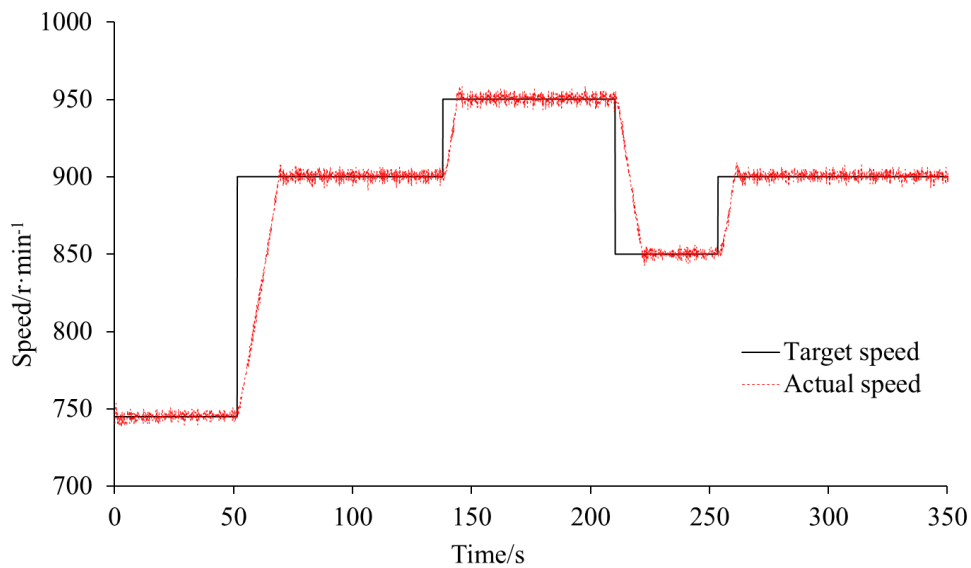
Fig. 5 - Fan speed tracking

When the system is in stable operation, the actual fan speed is shown in Table 2. The average absolute error between the actual speed of the fan and the set speed does not exceed 0.72 r/min, the relative error does not exceed 0.07%, the mean square error does not exceed 2.77 r/min, and the maximum relative deviation is 0.95%.

Table 2

Stabilization phase of cleaning fan

Items	value					Average
Time period [s]	0～51	69～138	144～210	222～253	261～350	\
Target speed [r/min]	745	900	950	850	900	\
Actual speed [r/min]	745.5	900.8	950.8	850.5	901	\
Absolute error [r/min]	0.5	0.8	0.8	0.5	1	0.72
Relative error [%]	0.06%	0.08	0.08	0.06	0.11	0.07
Mean square deviation [r/min]	2.64	2.97	3.01	2.48	2.73	2.77
Deviation range [r/min]	-6.1～8.8	-8.47～7.7	-8.1～8.5	-7.3～5.9	-7.1～9.1	\
Maximum phase relative deviation [%]	1.2	0.9	0.9	0.7	1.0	0.95

The changes in actual speed during the speed regulation phase are shown in Table 3. The average response time of the fan speed is 1.33 s, the average adjustment time is 6.58 s, the adjustment speed is 11.25 r/s, the overshoot is less than 8 r/s, and the overshoot percentage is less than 0.85%. The fan speed can be adjusted quickly according to the set value.

Table 3

Speed regulation stage of cleaning fan

Items	value				Average
Current speed [r/min]	745	900	950	850	\
Target speed [r/min]	900	950	850	900	\
Response delay [s]	0.9	1.6	1.1	1.7	1.33
Adjustment time [s]	12.2	4	5.2	4.9	6.58
Adjusting speed [r/s]	12.7	12.5	9.6	10.2	11.25
Overshoot [r/min]	7	8.5	7.3	9.1	8.00
Overshoot percentage [%]	0.7	0.8	0.9	1	0.85

During the operation of threshing cylinder, the set value of the threshing cylinder is changed, and the speed response curve of threshing cylinder is shown in Figure 6. It can be known from the test results that the set value of the fan speed is 1000-1050-950-1000 r/min. Under the function of speed control system, the actual fan speed changes as follow.
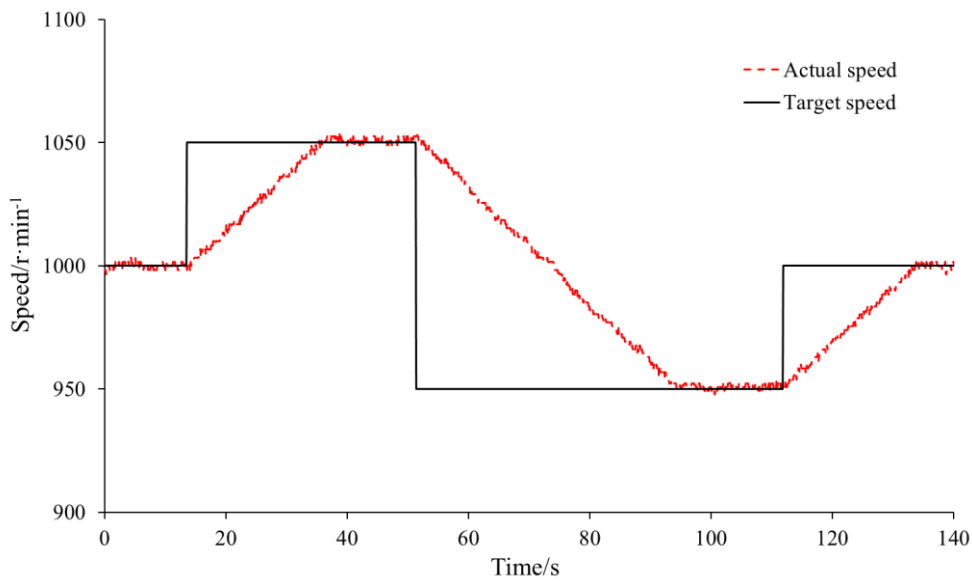
Fig. 6 - Threshing cylinder speed tracking

When the system is in stable operation, the actual threshing cylinder speed is shown in Table 4.The average absolute error between the actual speed of the fan and the set speed does not exceed 0.62 r/min, the relative error does not exceed 0.06%, the mean square error does not exceed 1.15 r/min, and the maximum relative deviation is 0.38%.

Table 4

Stabilization Phase of threshing cylinder

Items	value				Average
Time period [s]	0～13	37～51	95～111	134～160	\
Target speed [r/min]	1000	1050	950	1000	\
Actual speed [r/min]	1000.07	1051.2	951.2	1000	\

Items	value				Average
Absolute error [r/min]	0.07	1.2	1.2	0	0.62
Relative error [%]	0	0.11	0.13	0	0.06
Mean square deviation [r/min]	1.20	1.20	1.05	1.14	1.15
Deviation range [r/min]	-3.2～3.3	-1.1～5.5	-2.2～3.9	-3.3～1.67	\
Maximum phase relative deviation [%]	0.3	0.5	0.4	0.3	0.38

The changes in actual speed during the speed regulation phase are shown in Table 5. The average response time of the fan speed is 1.5 s, the average adjustment time is 27.37 s, the adjustment speed is 12.43 r/s, the overshoot is less than 1.5 r/s, and the overshoot percentage is less than 0.17%.

Table 5

Speed Regulation Stage of threshing cylinder

Items	value			Average
Current speed [r/min]	1000	1050	950	\
Target speed [r/min]	1050	950	1000	\
Response delay [s]	1.2	1.6	1.7	1.50
Adjustment time [s]	21.3	41.3	19.5	27.37
Adjusting speed [r/s]	2.3	2.4	2.6	2.43
Overshoot [r/min]	4.5	\	\	1.50
Overshoot percentage [%]	0.5	\	\	0.17

Variable load test

Set the fan speed to a fixed value and change the engine speed through the throttle to simulate the effect of the load on the speed of the working parts under actual conditions. Set the fan speed to 800r / min; the fan speed when the engine speed is changed is shown in figure 7.
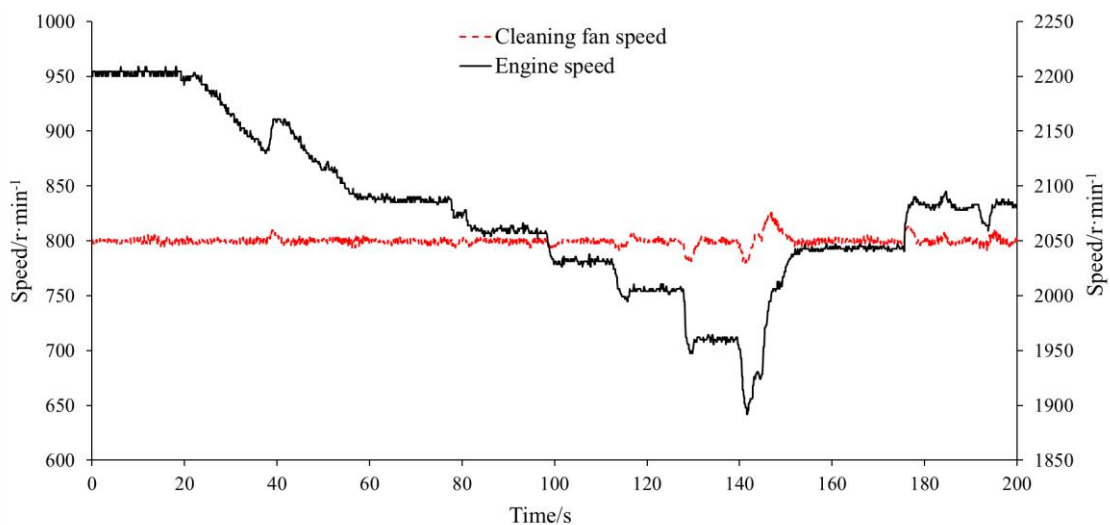
Fig. 7 - Fan speed during sudden load changes

At the initial state, the engine speed is 2200 r/min and the fan speed is 800 r/min. When the engine speed varies from 1890 to 2200 r/min, the average speed of the fan is 800.1 r/min and the mean square deviation is 4.5 r/min. When the engine speed increases suddenly (1890-2040 r/min), the maximum fan speed is 826.1, with a change of no more than 3.3%.When the engine speed drops suddenly (2010-1950 r/min), the minimum fan speed is 787.4 r/min, with a change of no more than 1.6%.The test shows that after adding the engine speed control system, the fan can be stably maintained at the set speed when the input speed changes.

CONCLUSIONS

Aiming at the problem that the rotation speed of the threshing drum and the cleaning fan of the combine harvester cannot be controlled in real time, a stepless speed regulation mechanism for the threshing drum and the cleaning fan speed of the combine harvester is designed and controlled by a stepper motor. The test shows that the adjustable range of the fan speed is 600～1150 r/min, the average adjustment speed is 9.2 r/s, the absolute error of stable speed does not exceed 0.72 r/min, and the maximum relative deviation is 0.95%. The average speed response time is 1.33 s, the overshoot is less than 8 r/s, and the speed change when the engine speed suddenly changes does not exceed 3.3%. The test shows that the adjustable range of the rotation speed of the drum is around 700～1100 r/min, the time from the lowest speed to the highest speed is 190.5 s, and the average adjustment speed is 2.1 r/s. The absolute error of stable speed does not exceed 0.62 r/min, and the maximum relative deviation is 0.38%. The average speed response time is 1.50 s, and the overshoot is less than 1.5 r/s.

ACKNOWLEDGEMENT

REFERENCES

[1]   Badretdinov I., Mudarisov S., Lukmanov R., et al, (2019), Mathematical modelling and research of the work of the grain combine harvester cleaning system, *Computers and Electronics in Agriculture*, vol.165, pp.104966;

[2]   Guan Z., Wu C., Tang Q., et al., (2016), Finite element mode analysis and experiment of combine harvester threshing cylinder, 联合收获机脱粒滚筒有限元模态分析与试验, *Journal of Agricultural Mechanization Research*, vol.38, Issue 8, pp.136-140;

[3]   Guan Z., Wu C., Wang G., et al, (2019), Design of bidirectional electric driven side vertical cutter for rape combine harvester, 油菜联合收割机双向电驱动分行竖割刀设计, *Transactions of the Chinese Society of Agricultural Engineering*, vol.35, Issue 3, pp.1-8;

[4]   Lenaerts B., Aertsen T., Tijskens, et al, (2014), Simulation of grain-straw separation by discrete element modelling with bendable straw particles, *Computers and Electronics in Agriculture*, vol.101, pp.24-33.

[5]   Li Y., Sun T., Xu L., (2013), Performance test and analysis of rape multi cylinder threshing and separating device, 油菜多滚筒脱粒分离装置的性能试验与分析, *Transactions of the Chinese Society of Agricultural Engineering*, vol.29, Issue 8, pp.36-43;

[6]   Li Y., Zhou W., Xu L., et al, (2015), Parameter test and optimization of tangential-horizontal-horizontal threshing and separating device, 单切双横流脱粒分离装置参数试验与优化, *Transactions of the Chinese Society of Agricultural Machinery*, vol.46, Issue 5, pp.62-67;

[7]   Liang Z., LI Y., Josse D., et al, (2019), Development and testing of a multi-duct cleaning device for tangential longitudinal flow rice combine harvesters, *Biosystems Engineering*, vol.182, pp.95-106;

[8]   Liang Z., Li Y., Xu L., (2018). Grain sieve loss fuzzy control system in rice combine harvesters, *Applied Science*s, vol.9, Issue 1, pp.114-126.

[9]   Jumiyatun J., Mustofa M., (2018), Controlling dc-dc buck converter using fuzzy-PID with DC motor load, *IOP Conference Series Earth and Environmental Science*, vol.156, Issue 1, pp.012013;

[10] Ma Z., Li Y., Xu L., (2015), Discrete-element method simulation of agricultural particles' motion in variable-amplitude screen box, *Computers and Electronics in Agriculture*, vol.118, pp.92-99;

[11] Myhan R., Jachimczyk E., (2016), Grain separation in a straw walker unit of a combine harvester: process model, *Biosystems Engineering*, vol.145, pp.93-107;

[12] Ryszard M., Ewelina J., (2016), Grain separation in a straw walker unit of a combine harvester: Process model, *Biosystems Engineering*, vol.145, pp.93-107;

[13] Tang Z., LI Y., Xu L., et al, (2012), Experiment and evaluating indicators of wheat threshing and separating on testbed of longitudinal axial-threshing unit, *切纵流联合收获机小麦脱粒分离性能评价与试验*, *Transactions of the Chinese Society of Agricultural Engineering*, vol.28, Issue 3, pp.14-19;

[14] Toshikazu M., Tatsuro S., (2017), The evaluation of harvest loss occurring in the ripening period using a combine harvester in a shattering-resistant line of common buckwheat, *Japanese Journal of Crop Science*, vol.86, Issue 1, pp.62-69;

[15] Wan X., Liao Q., Xu Y., et al, (2018), Design and evaluation of cyclone separation cleaning devices using a conical sieve for rape combine harvesters, *Applied Engineering in Agriculture*, vol.34, Issue 4, pp.677-686;

[16] Wang L., Zhang C., Ding Z., (2016), Structure optimization of cleaning screen for maize harvester, *玉米收获机清选筛体结构优化*, *Transactions of the Chinese Society for Agricultural Machinery*, vol.47, Issue 9, pp.108-114;

[17] Xu L., Wei C., Liang Z., et al., (2019). Development of rapeseed cleaning loss monitoring system and experiments in a combine harvester, *Biosystems Engineering*, vol.178, pp.118-130.

DESIGN AND EXPERIMENTAL OPTIMIZATION OF AIRFOIL-TRIANGLE
SIEVE FOR HAMMER MILL
/
锤片式粉碎机翼型三角形筛片设计与试验优化

Di Wang [1)], Changbin He [1)], Haiqing Wang [1)], Fei Liu [1)], Haiqing Tian*[1)], Liang Ma [2)] [1]
[1)] Inner Mongolia Agricultural University, College of Mechanical and Electrical Engineering, Hohhot/China;
[2)] Tuoketuo Senior Vocational Middle School, Hohhot/China
Tel: +86-0471-4309215; E-mail: hqtian@126.com
DOI: https://doi.org/10.35633/inmateh-61-34

ABSTRACT

The performance of a hammer mill is affected by the formation of a circulation layer. In this paper, an airfoil-triangle sieve was designed to destroy the circulation layer and improve the performance of the hammer mill. To determine the optimal design parameters of the airfoil-triangle sieve, three-factor and three-level tests were carried out by using the productivity and output per kW·h as the evaluation indexes and the airfoil camber, angle of attack and isosceles angle as the influencing factors. The order of the influences on the productivity was airfoil camber>angle of attack>isosceles angle. The order of the influences on the output per kW·h was angle of attack>airfoil camber>isosceles angle. The optimum combination after parameter optimization was determined to be as follows: airfoil camber of 0.15, angle of attack of 10° and isosceles angle of 113°. A test was carried out with to the optimum parameter combination. The results showed that the productivity and output per kW·h were 1101.56 kg/h and 188.97 kg/kW·h, respectively, which were consistent with the predicted results. The regression model was reliable.

摘要

针对锤片式粉碎机工作时物料环流层影响机器性能（生产率、功率消耗）的问题，本文以 CPS-420 型锤片式粉碎机为研究样机，设计了翼型三角形筛片，以破坏物料环流层，提高粉碎机性能。为确定筛片最佳设计参数，以翼型三角形筛片的弯度、冲角、等边角度数为试验因素，以生产率和度电产量为评价指标，利用 Box-Benhken 试验方法进行了三因素三水平响应面试验分析。结果表明：对生产率影响的主次因素为：弯度>冲角>等边角度数；对度电产量影响的主次因素为：冲角>弯度>等边角度数。基于响应面法进行参数优化，确定筛片设计最佳参数组合为弯度 0.15，冲角 10°，等腰角度数 113°。以优化后的参数组合进行试验验证，试验结果为：生产率和度电产量分别为 1101.56kg/h、188.97kg/kW·h，与模型预测结果基本吻合，回归模型可靠。

INTRODUCTION

Hammer mill is widely used in feed production because of their simple structure, good generality and convenient maintenance (*Zhang et al., 2019; Bochat et al., 2015; Nakamura et al., 2015; Polari et al., 2019*). However, in the working process of a hammer mill, a circulation layer easily forms in the grinding chamber. The existence of a circulation layer can lead to the problems of high energy consumption and excessive grinding of materials (*Cao, 2010; Wang et al., 2013; Wang et al., 2017; Qian et al., 2020*).

To solve this problem, many methods have been used to destroy the circulation layer and improve the performance of hammer mill. Changing the shape of the grinding chamber is a common method. Drip type grinding chambers are most commonly used in production because this type of chamber can constantly change the gap between the hammer and sieve to destroy the circulation layer and improve the performance of the hammer mill (*Cui et al., 2018*). In addition, some researchers have designed hexagonal and elliptical grinding chambers (*Qin, 2009*). A jet nozzle was added to the grinding chamber, and high-pressure gas was used to spray the circulation layer to destroy it. Research has shown that this method can improve the productivity and service life of hammer mill (*Kong et al., 2018*). Some researchers have also used vibrating sieves to destroy the circulation layer (*Chen et al., 2008*). Cao Liying (*Cao, 2010*) designed a new type of hammer mill, replacing the sieve in the grinding chamber with a truss plate and installing the sieve at the

---

[1] *Di Wang, Ph.D. Stud. Eng.; Changbin He, Lec. Ph.D. Eng.; Haiqing Wang, M.S. Eng.; Fei Liu, As. Prof. Ph.D. Eng.;*
  Haiqing Tian, Prof. Ph.D. Eng.; Liang Ma, Eng.

outlet, to eliminate the circulation layer in the grinding chamber. Although the above methods can improve the performance of hammer mill to a certain extent, these methods are difficult to realize.

Considering that it is easy to change the shape of the sieve, this paper aimed to destroy the circulation layer by designing a new type of sieve, and then improve the performance of the hammer mill. The structural parameters of a CPS-420-type hammer mill were referred, and an airfoil-triangle sieve was designed. The Box-Benhken test method was used to obtain the optimal parameter combination for the airfoil-triangle sieve. The research results provide a theoretical basis and reference for the optimal design of the hammer mill sieve.

MATERIALS AND METHODS

- **Test materials and equipment**

Corn grain was selected as the test material. The variety of corn used was JINSHAN-126, with a moisture content of 12.54% and bulk density of 723 kg/m^3. The test equipment included a TCS-150 type electronic scale (accuracy of 0.01 kg), a BT223S type electronic balance (accuracy of 0.001 g), an electric energy meter, a stopwatch and a drying box, etc.

- **Overall structure and working principle**

CPS-420 type hammer mill is mainly composed of a feeding hopper, a sieve, a hammer, an outlet, a frame, and a motor. The structure of the hammer is shown in Fig. 1, and the main specifications are given in Table 1.
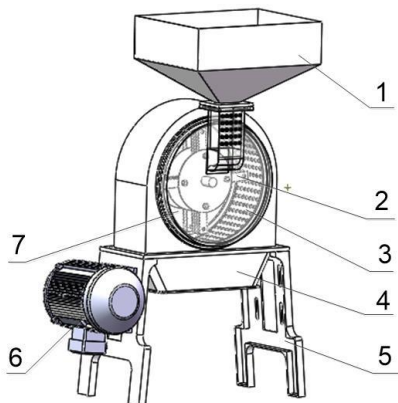
Fig. 1 – **Overall structure of hammer mill**

1 – Feeding hopper; 2 – Hammer; 3 – Sieve frame and sieve; 4 – Outlet; 5 – Frame; 6 – Motor; 7 – Grinding chamber

Table 1

Specification of hammer mill

Specification	Value
Motor power	3 kW
Rotational speed of rotor	4400 r/min
Number of hammers	24
Sieve width	180 mm
Size of the sieve holes	3 mm
Size (length × width × height)	850×800×1300 mm

When the hammer mill is working, the corn materials enter the grinding chamber through the feed hopper and are broken down by the high-speed rotating hammer. After that, the materials collide with the sieve at a higher speed and are further broken down. The particles that are small enough enter the outlet through the sieve holes, and the large particles continue to be ground until the particle size is smaller than the sieve hole diameter.

- **Design of the airfoil-triangle sieve**

The design requirements of the airfoil-triangle sieve should meet the installation size of the sieve frame and support a simple manufacturing process. Additionally, the airfoil-triangle sieve should be able to destroy the circulation layer and improve the performance of the hammer mill.

The design principle of the airfoil-triangle sieve is shown in Fig. 2. Considering the uniform stress on the sieve, the sieve was evenly divided into four equal parts along the circumference, each of which was composed of the airfoil arc, arc and isosceles angle. The circumference line (D=400 mm) is formed by connecting the vertices of each isosceles angle in each equal part and is concentric with the arc (d=380 mm). Additionally, the diameters D and d are the installation size of the sieve on the sieve frame and represent the inner diameter and outer diameter of the groove of the sieve frame, respectively. The airfoil arc is composed of arcs with radii of R_1 and R_2. The centres of the two arcs are determined by points a, b and c. Points a and b are the contact points between the airfoil arc and arc of diameter d and depend on the central angle δ of the airfoil arc. Point c is the highest chord point of the airfoil arc according to the airfoil design theory (*Du., 2015*), which is located at 1/4 of the chord length of the airfoil arc (from point a to b). The value of the isosceles angle is θ, which is located in the middle of each equal part. The equations for R_1 and R_2 can be obtained from Fig. 2.
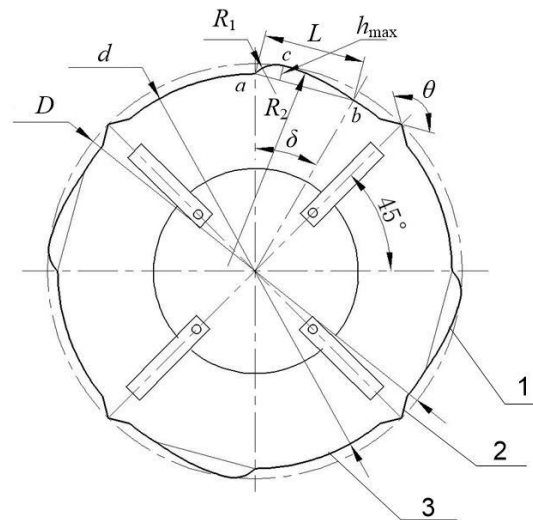
Fig. 2 – Design principle diagram of airfoil-triangle sieve
1 – Airfoil arc 2 – Isosceles angle 3 – Arc

$$R_1 = \frac{h_{max}^2 + (\frac{L}{4})^2}{2h_{max}} \tag{1}$$

$$R_2 = kf \tag{2}$$

$$f = \frac{h_{max}}{L} \tag{3}$$

$$L = d\sin\frac{\delta}{2} \tag{4}$$

Where:

h_{max} is maximum chord height of the airfoil arc, [mm];

L is chord length of the airfoil arc, [mm];

f is the airfoil camber, which is determined by the installation size of the sieve.

In this paper, the range of f is 0.1-0.15; k is the radius coefficient, which is derived from the geometric relationship between radius R_2 and chord ab; and the range is 1000-2000.

In the area of the airfoil arc, the air flow has a great influence on the material sieving efficiency, and the air flow is related to the angle of attack.

As shown in Fig. 3 (n is the rotor speed, r/min, and v_s is the air flow velocity, m/s), the angle of attack τ is the angle between the chord of the airfoil arc and the air flow direction, and the geometric relationship shows that $\delta=2\tau$; previous research showed that when the angle of attack was in the range of 3-15° (*Du., 2015*), the sieving efficiency of the material was the best.
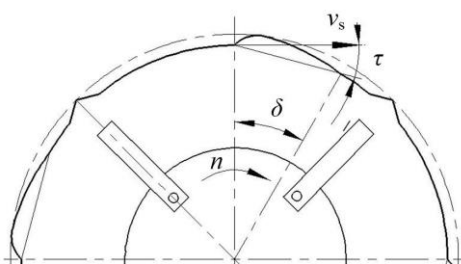
Fig. 3 – Schematic diagram of the angle of attack

A physical picture of the airfoil-triangle sieve is shown in Fig. 4.

Fig. 4 – Airfoil-triangle sieve

- **Theoretical analysis of the installation of an airfoil-triangle sieve in a hammer mill**

As shown in Fig. 5, when the hammer moves to the nearest distance from the sieve, the gap between the hammer and sieve is very small, and the circulation layer forms a reduced air flow jet through this area. Additionally, the high-speed rotation of the rotor produces a radial centrifugal force, which produces radial air flow. The reduced air flow jet collides with the radial air flow to form vortices. This vertical motion destroys the circulation layer and increases the probability that the hammer hits the material. In addition, the movement of multiple vortices continue to consume energy, thus reducing the speed of materials, resulting in a larger relative speed between materials and hammers and improving the grinding efficiency.
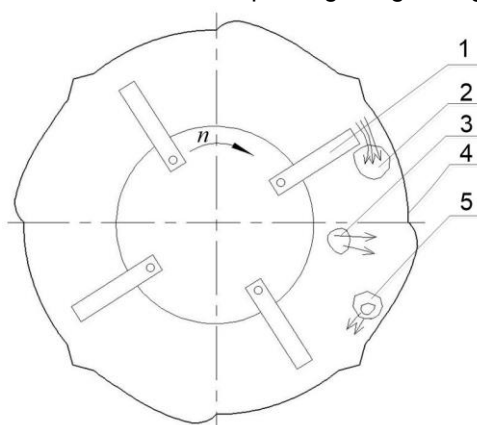
Fig. 5 – Schematic diagram of flow field motion analysis in an airfoil-triangle sieve
1-Hammer; 2-Reduced air flow jet; 3-Radial air flow; 4-Airfoil-triangle sieve; 5-Vortex

- **Experimental design**

Previous research has shown that the airfoil camber, angle of attack and isosceles angle of the airfoil-triangle sieve have a great influence on the performance of hammer mill. According to the structural parameters of the sieve frame and the above analysis data, the range of the airfoil camber is 0.1-0.15, the range of the angle of attack is 9-15°, and the range of the isosceles angle is 90-150°. The Box-Benhken test scheme was used to investigate three factors and three levels of test research. Each group of tests was repeated three times, and the average value of the test results was taken. The test factors and levels are shown in Table 2.

Experimental factors and levels

Levels	Airfoil camber A	Angle of attack B	Isosceles angle C
	/	[°]	[°]
-1	0.1	9	90
0	0.125	12	120
1	0.15	15	150

- **Performance evaluation of hammer mill**

According to the Chinese national standard GB/T 6971-2007, the productivity and output per kW·h were taken as the performance evaluation indexes of the hammer mill. The calculation formulas are given by formulas (5) and (6) (*China National Standardization Committee, 2007*).

$$E_c = \frac{Q_c}{T_c} \tag{5}$$

where E_c is the productivity of the hammer mill, kg/h; Q_c is the mass of the fragmented test sample, kg; and T_c is the duration of grinding of a single test sample, h.

$$G = \frac{Q_c}{G_n} \tag{6}$$

where G is the output per kW·h of the hammer mill, kg/kW·h; and G_n is the power consumption during grinding of a single test sample, kW·h.

RESULTS

- **Test results and analysis**

According to the test scheme, 17 groups of tests were performed, and each group of tests was repeated three times. The average values were taken as the test results, and the indexes were calculated according to formulas (5) and (6). The test results are shown in Table 3.

The test results

Test number	Airfoil camber A	Angle of attack B	Isosceles angle C	Productivity	Output per kW·h
	/	[°]	[°]	[kg/h]	[kg/kW·h]
1	-1	1	0	1059.24	178.49
2	0	-1	1	1054.92	183.47
3	0	1	1	1048.66	177.23
4	-1	-1	0	1058.52	184.31
5	0	-1	-1	1062.26	187.91
6	1	0	1	1086.34	187.62
7	0	0	0	1081.46	185.16
8	1	0	-1	1103.16	186.12
9	0	1	-1	1045.4	179.14
10	1	1	0	1082.52	185.28
11	0	0	0	1084.12	185.63
12	-1	0	1	1068.28	178.25
13	-1	0	-1	1061.24	183.37
14	1	-1	0	1100.86	194.57
15	0	0	0	1085.9	186.91
16	0	0	0	1086.42	184.35
17	0	0	0	1082.76	185.29

Analysis of variance and the regression model

The test results were analysed by Design-Export 10 software, and the results are presented in Table 4. The regression models of E_c and G were obtained as formulas (7) and (8). From the analysis of variance, we can see that the two models were extremely significant (P<0.01), and the lack of fit was not significant (P>0.05). The fitting coefficients R^2 of model 1 and model 2 were 0.9941 and 0.9745, respectively, which

showed that the correlation between the predicted and actual values was high, and the test error was small. Through the analysis of variance, it can be concluded that the order of the influences on the productivity was airfoil camber A>angle of attack B>isosceles angle C, and there was extreme significance between each factor. From Table 4, the order of the influences on the output per kW·h was angle of attack B>airfoil camber A>isosceles angle C, and the AC interaction item had a significant influence on the output per kW·h.

$$E_c = 1084.13 + 15.70A - 5.09B - 1.73C - 4.77AB - 5.97AC + 2.65BC + 9.05A^2 - 17.90B^2 - 13.43C^2 \tag{7}$$

$$G = 185.47 + 13.65 - 3.76B - 1.25C - 0.87AB + 1.66AC + 0.63BC + 1.05A^2 - 0.85B^2 - 2.68C^2 \tag{8}$$

where A is the airfoil camber; B is the angle of attack, °; and C is the isosceles angle, °.

Table 4

The results of variance analysis

Source	DF	MS	F Value	P Value	Source	DF	MS	F Value	P Value
Model 1	9	545.67	130.80	< 0.0001 **	**Model 2**	9	31.69	29.76	< 0.0001 **
A	1	1971.92	472.69	< 0.0001 **	**A**	1	106.36	99.90	< 0.0001 **
B	1	207.47	49.73	0.0002 **	**B**	1	113.40	106.51	< 0.0001 **
C	1	24.01	5.76	0.0475 *	**C**	1	12.43	11.67	0.0112 *
AB	1	90.82	21.77	0.0023 **	**AB**	1	3.01	2.83	0.1366
AC	1	142.32	34.12	0.0006 **	**AC**	1	10.96	10.29	0.0149 *
BC	1	28.09	6.73	0.0357 *	**BC**	1	1.60	1.50	0.2599
A²	1	344.78	82.65	< 0.0001 **	**A²**	1	4.63	4.35	0.0755
B²	1	1348.49	323.25	< 0.0001 **	**B²**	1	3.07	2.88	0.1333
C²	1	758.98	181.94	< 0.0001 **	**C²**	1	30.16	28.33	0.0011 **
Lack of Fit	3	3.94	0.91	0.5126	**Lack of Fit**	3	1.32	1.52	0.3385
Pure Error	4	4.35			**Pure Error**	4	0.87		
Cor Total	16				**Cor Total**	16			

*Note: P < 0.01 (extremely significant, **), P < 0.05 (significant, *);*
Model 1 is variance analysis of productivity.
Model 2 is variance analysis of output per kW·h.

a) E$_C$ (A, B) *b) E$_C$ (A, C)*

c) E$_C$ (B, C) *d) G (A, C)*
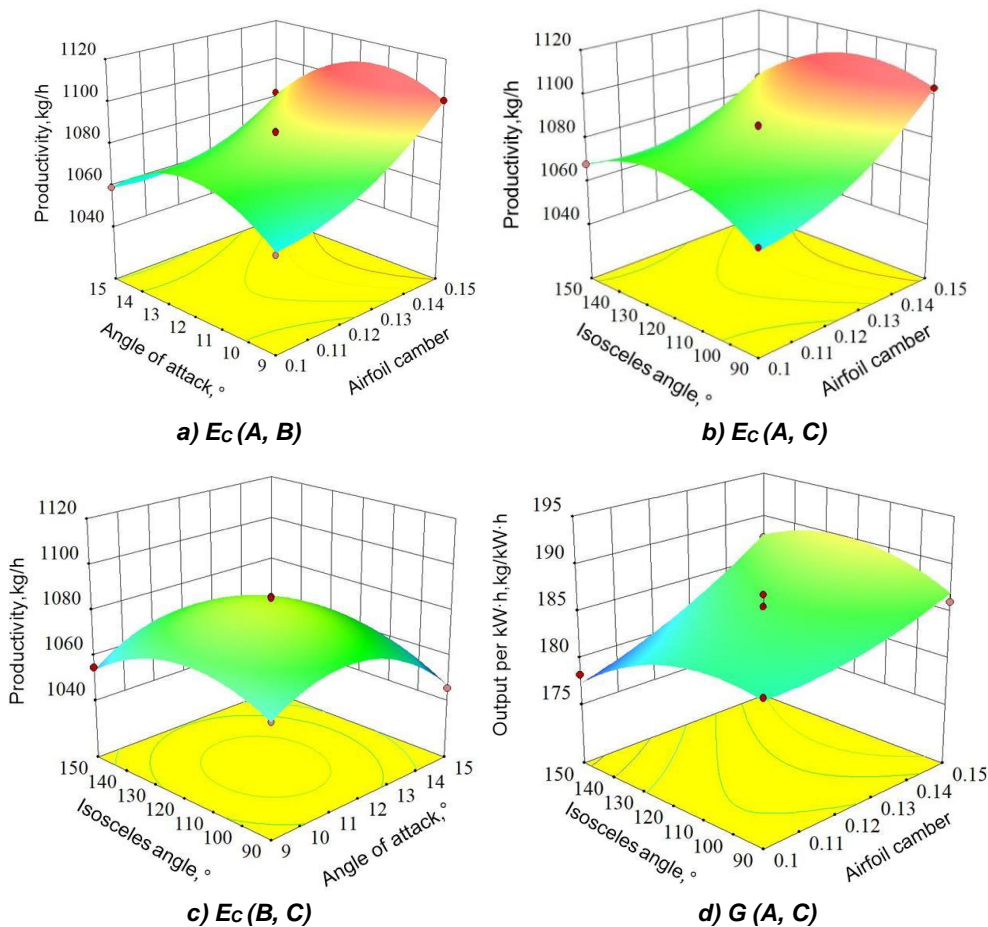
Fig. 6 – Response surface results

- **Analysis of the influences of the interaction factors on productivity**

The response surfaces of the airfoil camber, angle of attack and isosceles angle with productivity are shown in Fig. 6a-6c. When the isosceles angle was 120°, the productivity increased with increasing airfoil camber. With increasing impact angle, the productivity first increased and then decreased (Fig. 6a). When the angle of attack was 12°, the productivity increased slowly with increasing isosceles angle (Fig. 6b). When the airfoil camber was 0.125, with increasing isosceles angle and impact angle, the production first increased and then decreased (Fig. 6c).

The overall influence trend was that the productivity was high when the angle of attack and isosceles angle were moderate and the airfoil camber was large. The main reasons for these results are as follows: When the airfoil camber increases, the intensity of the vortices in the area of the airfoil arc increases. These vortices continuously turn the material over, and the probability of the material being hit by the hammer is increased, improving the grinding efficiency of the material and improving the productivity of the hammer mill. The isosceles angle affects the angle of the material impacting the sieve. When the isosceles angle is very large or small, the material and sieve do not have an ideal impact angle, thus reducing the efficiency of the material sieving and further reducing the productivity of the hammer. When the angle of attack is small, the air flow has less effect on the material. When the impact angle is large, the air flow resistance coefficient becomes larger, which hinders the material sieving and reduces the productivity of the hammer.

- **Analysis of the influence of the interaction factors on the output per kW·h**

The response surface of the isosceles angle and airfoil camber with the output per kW·h is shown in Fig. 6d. When the angle of attack was 12°, the output per kW·h first increased slowly and then decreased with increasing isosceles angle. The change in the output per kW·h was very small with increasing airfoil camber.

The overall influence trend was that the output per kW·h was high when the isosceles angle was moderate. This occurs because when the isosceles angle is large or small, the impact angle between the material and sieve is not ideal. The sieving efficiency is reduced, material particles are excessively ground, and the electric energy consumption of hammer increases.

- **Parameter optimization and validation**

To obtain the optimal design parameters of the airfoil-triangle sieve, the regression equation was further solved by using Design-Export 10 software (*Wang et al., 2019*; *Du et al., 2019*). The objective function and constraints are as follows:

$$\begin{cases} \max E_C \\ \max G \\ A \in [0.1 - 0.15] \\ B \in [9° - 15°] \\ C \in [90° - 150°] \end{cases} \tag{7}$$

From the optimization, the optimum parameter combination of the airfoil-triangle sieve was obtained as follows: airfoil camber of 0.15, angle of attack of 10° and isosceles angle of 113°. The predicted values of the productivity and output per kW·h were 1109.62 kg/h and 192.54 kg/kW·h, respectively.

To verify the reliability of the predicted values, a validation test was carried out, and the test results were as follows: the productivity was 1101.56 kg/h, and the output per kW·h was 188.97 kg/kW·h. The prediction error was less than 2%, which showed that the prediction model of this study was reliable.

CONCLUSIONS

1. In this paper, an airfoil-triangle sieve was innovatively designed. It was verified that the airfoil-triangle sieve could destroy the circulation layer and improve the performance of the hammer mill.

2. The regression models of the productivity and output per kW·h were established, and the primary and secondary factors affecting the performance indexes of the hammer mill were obtained. The results showed that the order of the influences on the productivity was airfoil camber>angle of attack>isosceles angle, and the order of the influences on the output per kW·h was angle of attack>airfoil camber>isosceles angle.

3. The optimum combination after parameter optimization was determined to be as follows: airfoil camber of 0.15, angle of attack of 10° and isosceles angle of 113°. A test was carried out according to the optimum parameter combination. The results showed that the productivity and output per kW·h were 1101.56 kg/h and 188.97 kg/kW·h, respectively. This was consistent with the optimization results, and thus, the regression model was reliable.

REFERENCES

[1] Bochat A, Wesolowski L, Zastempowski M, (2015), A Comparative Study of New and Traditional Designs of a Hammer Mill, *Transactions of the ASABE*, Vol. 58, Issue 3, pp.585-596, MI/USA;

[2] Cao Liying, (2010), *Measuring and Simulating Analysis on Material-Sieving Properties for a New Hammer Mill* (新型锤片式粉碎机分离特性的模拟与测试分析), PhD dissertation, Inner Mongolia Agricultural University, Hohhot/China;

[3] Chen Weixu, Ma Jun, Shen Chengjun, (2008), Experimental research on the SZF-11 pulveriser (SZFS-11 粉碎机的试验研究), *Journal of Agricultural Mechanization Research*, Vol.30, Issue 12, pp. 134-135, Harbin/China;

[4] Du Jianan, (2015), *The design and experimental study on airfoil sieve crushing chamber of hammer mill* (锤片式粉碎机翼形筛片的设计与试验研究), MSc dissertation, Inner Mongolia Agricultural University, Hohhot/China;

[5] Kong Tenghua, Gong Guifen, (2018), Optimization design of the crushing chamber of the hammer mill (锤片式粉碎机粉碎室的优化设计), *Feed Research*, Vol.41, Issue 1, pp.47-52, Beijing/China;

[6] Nakamura H, Kan H, Takeuchi H, et al, (2015), Effect of stator geometry of impact pulveriser on its grinding performance, *Chemical Engineering Science*, Vol.122, pp.565-572, England/UK;

[7] Polari J. J., Wang S. C., (2019). Hammer mill sieve design impacts olive oil minor component composition, *European Journal of Lipid Science and Technology*, Vol. 121, Issue 10, DOI:10.1002/ejlt.201900168, Weinheim/GERMANY;

[8] Qian Yi, Wang Di, Zhang Jue, et al, (2020), Numerical simulation and experimental research on gas flow field of special-shaped sieve sheet of crusher (粉碎机异形筛片气流场数值模拟及试验研究), *Journal of China Agricultural University*, Vol.25, Issue 3, pp. 79-87, Beijing/China;

[9] Qin Yonglin, (2009), *Studies on the Effects of Hammer Mill Performance on the Grinding Results of Normal Feedstuffs* (锤片式粉碎机性能对常规饲料粉碎效果影响), MSc dissertation, Jiangnan University, Wuxi/China;

[10] Cui Xiangquan, Li Hansong, He Xiaodong, et al, (2018), The designing of the pulveriser with the water drop-shaped teeth-claw model No.FSSP8020 (FSSP8020 型水滴形齿爪粉碎机的设计), *Feed Industry*, Vol.39, Issue 15, pp. 11–13, Shenyang/China;

[11] Wang Weiguo, Yu Xinguo, Yu Zheng, (2017), Latest advancement in technology innovation of fine grinding hammer mill (锤片式微粉碎机技术创新的最新进展), *Feed Industry*, Vol.38, Issue 13, pp.1-4, Shenyang/China;

[12] Wang Jianxin, Zhang Guangyi, Cao Liying, (2013), Research of materials motion law in separation flow of new type hammer feed grinder (新型锤片式饲料粉碎机分离流道内物料运动规律). *Transactions of the Chinese Society of Agricultural Engineering*, Vol.29, Issue 9, pp. 18-23, Beijing/China;

[13] Wang Shengsheng, Ji Jiangtao, Jin Xin, et al, (2019), Design and experimental optimization of cleaning system for peanut harvester, *INMATEH-Agricultural Engineering*, Vol. 57, Issue 1, pp.243-252, Bucharest/Romania;

[14] Xiaobin Du, Junlin He, Yongqiang He, et al, (2019), Parameter Optimisation and Experiment on the Combing of Cerasus Humilis, *INMATEH-Agricultural Engineering*, Vol. 57, Issue 1, pp.103-114, Bucharest/Romania;

[15] Zhang Yongjie, Xu Hongmei, Liu Shuang, et al, (2019), Finite element analysis and topology optimization of hammer feed grinder frame plate (锤片式饲料粉碎机架板的有限元分析及拓扑优化), *Journal of Huazhong Agricultural University*, Vol.38, Issue 4, pp.1-5, Wuhan/China;

[16] ***China Agricultural Machinery Standardization Technical Committee, (2007), Test method for feed mill, *GB/T6971-2007*, Standards Press of China, Beijing/China.

THE EFFECT OF CONSERVATIVE AGRICULTURAL WORKS ON SOIL AND FIELD PLANTS AND OPTIMIZED MECHANIZATION TECHNOLOGIES
/
EFECTUL LUCRĂRILOR AGRICOLE CONSERVATIVE ASUPRA SOLULUI ŞI PLANTELOR DE CÂMP ŞI TEHNOLOGII DE MECANIZARE OPTIMIZATE

Bularda M.[1,2], Vişinescu I.[1], Ghiorghe A.[1], Vlăduţ V.[3], Cujbescu D.*[3]
[1]SCDA Brăila / Romania; [2]Univ. Dunărea de Jos Galaţi / Romania; [3]INMA Bucharest / Romania
Tel: +40.770.967.180; Corresponding author E-mail: dancujbescu@gmail.com
DOI: https://doi.org/10.35633/inmateh-61-35

ABSTRACT
In this paper was performed a thorough analysis of the effects of the conservative system of mechanized works, minimum-till (hard disc and scarifier) and no till (direct sowing), compared to the classic system (ploughing), highlighting the influences on soil and plants, the ways to reduce the technological costs, the improvement of soil quality indices, by accumulating organic matter and increasing humus supply, the need to reduce the traffic of mechanical equipment and opportunities to reduce fuel consumption, the improvement of conditions for retaining and capitalizing water reserves in the soil, the reduction of working hours and labour requirements.

REZUMat
În lucrarea de fata s-a realizat o analiză aprofundată a efectelor sistemului conservativ de lucrări mecanizate, minimum-till (disc greu şi scarificat) şi no till (semănatul direct), raportat la sistemul clasic (arat), evidenţiindu-se influentele asupra solului si plantelor, modalitatile de reducere a costurilor tehnologice, ameliorarea indicilor calitativi ai solului, prin acumularea materiei organice şi creşterea aprovizionării cu humus, necesitatea reducerii traficului utilajelor mecanice şi posibilitatile de reducere a consumului de carburanţi, îmbunătăţirea condiţiilor de reţinere şi valorificare a rezervelor de apă din sol, reducerea timpilor de lucru şi a necesarului de forţă de muncă.

INTRODUCTION
It can be considered that at present humanity is facing great difficulties that profoundly affect the food supply of agriculture, climatic conditions that undergo brutal changes, with sharp increases in air temperature, reduced rainfall with natural implications on plants. The current climate changes are taking place in the sense of expanding the aridisation of large agricultural areas. All these unfavourable impacts occur in the conditions of an emphasized demographic explosion *(Baltag G., 2020)*.

In this context, in addition to expanding the irrigation areas, in order to ensure food security, efforts must also focus on combating the effects of drought and desertification by other means *(Dabney et al, 2001)*.

Working systems for soil conservation are considered the main components of the agricultural technology for soil water conservation and soil carbon sequestration strategies and are part of Sustainable Agriculture *(Li and Chen, 1999)*. Working systems for soil conservation involve reducing the number of mechanical works to direct sowing and keeping plant debris at the soil surface in a proportion of at least 30 % (*Crismaru I., 2006; Stelian et al, 1983*). The working systems for water conservation in the soil have as objective the assurance of an aerohydric regime corresponding to the intensification of the biological activity and the balance in the solubilization of the nutrients *(Vlăduţ et al, 2014)*. Thus, it is necessary to mention the initiation of afforestation and reforestation actions in many states of the world, the use of agroforestry practices adopted by farmers in some countries, in order to protect their crops and pastures, the construction of drainage networks for reduction of excess moisture and salinization *(Cooper et al, 2017)*.

Even when irrigation is applied on large areas, it is and will be necessary to store and retain all the water from rainfall *(Toma et al, 1981; Scripnic and Babiciu, 1979)*. Storing and retaining a single millimetre of rainfall in the soil means a saving per hectare of 10 m^3 (10 tons) of irrigation water *(Deng et al, 2005)*. Conservation and management of soil water is done through specific techniques among which the proper working of soil plays an important role *(Farcas N., 2019)*. Rising temperatures, melting of glaciers, increased droughts and floods are signs that climate change is intensifying over time, due to human activities, which lead to an increase in the concentration of greenhouse gases in the atmosphere *(Chen et al, 2008)*. Drought and its associated phenomena, namely aridification and desertification, are, after pollution, the second biggest problem that humanity is facing in the last half century *(Shi et al, 2006)*. The global expansion of

these destructive phenomena is highlighted by climatic data that reveal a progressive warming of the atmosphere and a reduction in rainfall, which lead to the occurrence of drought *(Croitoru et al, 2015; Dobre et al, 2017)*. In addition to global climate change, increased drought and desertification are also due to anthropogenic pressure. Excessive logging, expanding agricultural areas and poor land management, rapid population growth and, last but not least, poverty are being considered *(Bronick and Lal, 2005; et al, 2010)*.

In our country, the climatic changes are manifested by the decrease of the annual rainfall level, by an uneven distribution of them both in time and in space and especially by an outphasing of the water supply compared to the critical periods of the plants, by an increase of daytime temperatures and an intensification of spring winds. Climate change taking place in the North Bărăgan area manifests by expanding of the aridisation of large agricultural areas. Climate analyses carried out by SCDA Brăila predict an unfavourable evolution in the perspective of 2025 and 2050. It is estimated a decrease in the average multiannual rainfall from 445 mm currently to 440 mm in 2025 and 435 mm in 2050, an increase in the multiannual average temperature from 11°C currently to 11.3°C in 2025 and 11.5°C in 2050, an increase in the potential multiannual average evapotranspiration from 715 mm currently to 730 mm in 2025 and to 750 mm in 2050.

There is an increasing pressure on agriculture to find remediation solutions to ensure, through soil works, the increase of capacity to access and store water, preservation and increase of soil quality indices, finding and applying the technologies to ensure these requirements, establishing of crop structures with increased drought resistance and with the best agricultural yields (*Vlăduţ et al, 2015; Wang et al, 2003*).

Starting with the combination of different working methods, conservative tillage works include a wide range of methods, with and without furrow turning (chisel, paraplough, "goose foot" tools, disc harrows, etc.), which ends with the formation of the layer of mulch at soil surface, until the cessation of soil mechanical works according to the No-till type (zero tillage, direct sowing). (*Şandru et al, 1983; Dragan G., 1969)*.

Farmers must be prepared for lifelong learning and have information on all achievements in the field. Sources of knowledge can be very diverse, starting with European farmers which apply this system and ending with the most advanced scientific papers *(Garnett et al., 2013)*. Today, it is difficult to convince that one can change the concept of farmers to switch to new unknown technologies if there are no calculations regarding the yield of sales that they will be able to argue their economic reasoning. High costs, the need for knowledge of farmers and the uncertainty of yield (green bridge effect and oscillation of crops) have led to indecision among farmers *(Toma et al., 1981)*.

Innovative approaches for soil maintenance are constantly being analysed and improved. The limitation of conventional tillage works may include soil aggressive mechanical reversal, which leads to high losses of organic carbon (C), disturbance of soil biology and erosion caused by wind and water *(Reicosky D., 2015)*. Many agrotechnical works were unjustly considered conservative *(Gumovschi A., 2019)*. In recent years, the importance of sustainability in intensive agriculture has grown in prominence *(Crotty et al, 2017)*.

Conservation techniques can preserve a limited amount of organic residue on soil surface and can create a good environment for the growth and development of agricultural crops. Conservative agriculture is beneficial as it can stop soil degradation, expand soil fertility and ensure the efficient application of natural resources, increase the productivity and help ensure food security *(Derpsch R., 2008; Ceretto C., 2007)*.

Soil structure has a direct impact on several aspects of soil functioning, including: the transfer of water, solutes, fine particles and gas within the soil; the development and activity of root systems; the biological activity (*Bronick and Lal, 2005)*. Stability of soil structure, often assessed by the degree of soil aggregation, strongly determines a soil's ability to resist and recover from disturbances (e.g., tillage, erosion).

MATERIALS AND METHODS

The research works were carried out to preserve soil fertility and to increase yield quantity and quality to the main species of cultivated plants, between 2014-2018. The research was carried out in Brăila area (Brăila county) and Dăbuleni area (Dolj county) and aimed at establishing the technological elements with impact on plant cultivation and on growth of agricultural yields in dry areas and quantifying the influence of new mechanized agricultural works systems on crops as well as for preserving and conserving soil fertility. To achieve a complete picture of the approached problem, the experiments were performed in both irrigated and non-irrigated dry areas. Also, the researches aimed to highlight the influence of different technological elements (soil works, sowing, fertilization, irrigation) performed with the classic and modern working techniques, for different crops, on agricultural yields in order to highlight and promote the works with favourable technical and economic impact on drought-affected soils. It was aimed to specify the influence of microclimate modifying solutions by creating forest curtains for agricultural protection.

The synthesis of the results of the paper can contribute to the influence of the production costs in the sense of their decrease, to the promotion of the conservative systems for soil works, to the completion of the range of agricultural equipment and to the production reorientation in the construction of agricultural machines. The need to model the agricultural perimeters in order to improve the microzonal climate framework with the help of forest curtains is also aimed. The element of novelty is the promotion of the necessity concept of summing up the effects of the two groups of measures (agricultural and forestry) that are likely to improve the results of agricultural production to a greater extent and on long term.

The complex experiments took place in two ameliorating situations, both non-irrigated and irrigated and in four points of work located in two dry areas, with representative pedoclimatic conditions, respectively: field experiments at CE Chiscani in irrigated regime and in non-irrigated regime, on plain and chernozemic soils, at CE IMB in irrigated and non-irrigated regime, on meadow and clay soils, at CE Dăbuleni for plain and sandy soils. Seven experimental crops were used: wheat, corn, sunflower, soybeans in Brăila and rye, beans, sorghum for grains in Dăbuleni. A complex experimental system was applied, with experiences aiming crops structure, basic soil works, densities and sowing times and also experiments regarding crops structure, fertilization system with assortments, doses and times of application of mineral and organic fertilizers. In the planning phase of the activities included in the study, actions were performed regarding the choice of representative experimental points, conception and design of the experimental plan, by establishing the experimental scheme (Figure 1).

Fig. 1 - Scheme of the complex experimental field in the Chiscani - Brăila Experimental Centre

By sizing and arranging the plots in correlation with the flow of technological and experimental works, experimental sheets were prepared, the structure of crops and crop rotation in the experimental perimeters were established, designing of agricultural technologies for experimental crops and drawing up the calendar of technical and technological works for mounting and conducting field experiments were made.

During the research, 4 types of mechanized works were studied:

1. classic system (A1) – application of basic soil works with the plough;
2. no-tillage system (A2) – performing the sowing works directly in the stubble;
3. minimum-tillage system 1 (A3) – application of basic soil works with heavy disc;
4. minimum-tillage system 2 (A4) - application of the basic soil works with scarifier.

Table 1 presents the aggregates used to perform the basic soil works both in the plain and in the meadow, respectively: Belarus 820 tractor + M 3 reversible plough for ploughing work, Belarus 820 tractor + Gaspardo Nina 300 seeder, equipped with disc coulters for no-tillage work with direct sowing in the stubble, the John Deere 8200 tractor + Kuhn Discover XM2 heavy disc in the plain and the Horsch Joker 8 RT heavy disc in the meadow, for the minimum-tillage work 1 and the John Deere 8200 tractor + the Strom Terraland 3000 scarifier in the plain and the Alpego Super Craker scarifier in the meadow, at the minimum-tillage work 2.

Table 1

The systems of mechanized works researched at experimental fields in Chiscani and Great Island of Brăila

Systems of mechanized works	Aggregates used for the execution of basic soil works in CE Chiscani	Aggregates used for the execution of basic soil works in CE Great Island of Brăila
A1 – Classic system – application of basic soil works with the plough	Belarus-820 tractor + reversible plough M-3	Belarus-820 tractor + reversible plough M-3
A2 – No-tillage system – performing the sowing works directly in the stubble	Belarus-820 tractor + Gaspardo Nina 300 seeder equipped with disc coulters	Belarus-820 tractor + Gaspardo Nina 300 seeder equipped with disc coulters
A3 – Minimum-tillage system (1) – application of basic soil works with heavy disc	John Deere-8200 tractor + Kuhn Discover XM2 heavy disc	John Deere-8200 tractor + Horsch Joker 8 RT heavy disc
A4 – Minimum-tillage system (2) - application of basic soil works with scarifier	John Deere-8200 tractor + Strom Terraland 3000 scarifier	John Deere-8200 tractor + Alpego Super Craker scarifier

RESULTS

The effect of systems of mechanized works on soils

➢ *The effect of systems of mechanized works on soil physical and hydrophysical indices*

The researched systems of mechanized works, ploughing (classic system), the two types of minimum tillage (heavy disc and scarification), by mobilizing the soil in optimal conditions had a beneficial effect on some physical and hydrophysical indices of the soil, ensuring their positive evolution.

Thus, the apparent density in the 0 - 50 cm layer was slightly reduced both in the plain from 1.15 g/cm^3 to 1.12 g/cm^3, and in the meadow from 1.24 g/cm^3 to 1.21 g/cm^3 for all basic soil works, excepting the no-till work. The hydrophysical indices in the 0 - 50 cm layer underwent a slight improvement, the field capacity increasing from 24.5 to 24.7 % in the plain and from 33.5 % to 33.8 % in the meadow. Also, soil fertility indices remained within the same quality categories.

➢ *The effect of systems of mechanized works on soil compaction*

To establish the compaction effect achieved on each hectare, by passing with tractors and agricultural equipment to perform all technological works, basic soil works including seedbed preparation, soil herbicide, sowing, basic and phase fertilizer, herbicide in vegetation, phytosanitary treatments, harvesting, determinations were performed on each experimental crop. Important differences were highlighted on the sum of passes with tractors and agricultural equipment, expressed by the trampled area (in ha) per cultivated hectare, for the 4 types of researched systems of mechanized works.

The strong impact on soil compaction is achieved by the ploughing work on the classic mechanization system, the minimum-till and especially no-till systems determining an essential diminished impact compared to the classic system. Thus, in the plain for wheat ROP, the total surface of the passes that compact the soil, compared to the control ploughed plot, through the works performed on 1 ha, represented 54 % for no-till, 66 % for heavy disc and 73 % for scarifier, as presented in Table 2.

In the maize crop, compared to the ploughed control plot, the total surface of the passes that compacts the soil, made by works on 1 ha represented 57% for no-till, 69% for heavy disc and 75% for scarifier. In the sunflower crop, compared to the ploughed control plot, the total surface of the passes that compacts the soil made on 1 ha represented 57% for no-till, 69% for heavy disc and 75% for scarifier. In the soybean crop, compared to the ploughed control plot, the total surface of the passes that compacts the soil made on 1 ha represented 58% for no-till, 69% for heavy disc and 75% for scarifier.In the meadow, for the same crops (wheat, maize, sunflower and soybeans), the passes with tractors and agricultural equipment on total technology applied to crops showed diminished values compared to the classic mechanization system (with ploughing), at a level of 53-56% (depending on crop type) at no-till, 62-65% at minimum till 1 (heavy disc) and 70-72% at minimum till 2 (scarified), as presented in Table 3. The differentiated and lower values of the compacted soil surfaces through the passes with the equipment in the meadow compared to the plain with approx. 4 % is due to the types of equipment used for minimum till, heavy disc and scarification works.

Table 2

The effect of the system of mechanized works on soil compaction through the passes of agricultural equipment in the experimental field Chiscani

Specification	Achieved technology; Inputs quantity; M.U	Wheat Exp.1 Comp. surface [ha]	W A1	W A2	W A3	W A4	Maize Exp.1 Comp. surface [ha]	M A1	M A2	M A3	M A4	Sunflower Exp.1 Comp. surface [ha]	S A1	S A2	S A3	S A4	Soybean Exp.1 Comp. surface [ha]	Sb A1	Sb A2	Sb A3	Sb A4
Work - Basic fertilization	-Fertilization, Belarus 820 tractor + MA-3,5	0.06	3	5	4	4	0,06	3	4	4	3	0.06	3	4	4	3	0.06	3	4	4	3
	Chopping of vegetable debris	0	0	0	0	0	0	0	0	0	0	0	0.44	0	0	0	0	0	0	0	0
Soil works	Types of soil works: A1- ploughing 25 cm: Belarus 820 tractor + reversible plough, 22.10.2016	0.88	41	0	0	0	0.88	38	0	0	0	0.88	38	0	0	0	0.88	38	0	0	0
	A2-no till: direct sowing in meadow	0	0	0	0	0	0	0	0	0	0	0	0	0	0	0	0	0	0	0	0
	A3-heavy disc: John Deere 8200 (220 HP) tractor + KUHN Discover XM2 heavy disc, 2.10.2016	0.23	0	0	15	0	0.23	0	0	14	0	0.23	0	0	14	0	0.23	0	0	14	0
	A4-scarification: John Deere 8200 (220 HP) tractor + Strom Terraland 3000 scarifier (t=3.0 m, H=0,6 m, 5 knives), 24.10.2016	0.36	0	0	0	22	0.36	0	0	0	20	0.36	0	0	0	20	0.36	0	0	0	20
Seedbed preparation	-discing + harrowing: Belarus 820 tractor + GD 3,2 + GCR 1,7	0	0	0	0	0	0.25	11	17	15	14	0.25	11	17	15	14	0.25	11	17	15	14
	-combiner: Belarus 820 tractor + CTT 30.03.2017 combiner	0	0	0	0	0	0.20	9	14	12	11	0.2	9	14	12	11	0.2	9	14	12	11
	- cutting: Belarus 820 tractor + Maschio Gaspardo cutter	0.26	12	21	17	16	0	0	0	0	0	0	0	0	0	0	0	0	0	0	0
Work - Soil herbicide	- Soil herbicidation, Belarus 820 tractor + MET-1200	0.06	3	5	4	4	0.06	3	4	4	3	0.06	3	4	4	3	0.06	3	4	4	3
Work - Sowing	-Sowing, Belarus 820 tractor + Gaspardo Nina 300 seeder	0.26	12	21	17	16	0	0	0	0	0	0	0	0	0	0	0.26	11	18	15	14
	-Sowing, Belarus 820 tractor + SPC-6	0	0	0	0	0	0.22	9	15	13	12	0.22	9	15	13	12	0	0	0	0	0
Work – Phase fertilization	- Phase fertilization, Belarus 820 tractor + MA-3,2	0.06	3	5	4	4	0.06	3	4	4	3	0.06	3	4	4	3	0.06	3	4	4	3
Work - Herbicide in vegetation	- Herbicidation in vegetation, Belarus 820 tractor + MET-1200	0.05	2	4	3	3	0.05	2	3	3	3	0.05	2	3	3	3	0.05	2	3	3	3
Work - Treatments	-Treatments, Belarus 820 tractor + MET-1200	0.05	2	4	3	3	0.05	2	3	3	3	0.05	2	3	3	3	0.05	2	3	3	3
Other works	Block 1 – non-irrigated	0	0	0	0	0	0	0	0	0	0	0	0	0	0	0	0	0	0	0	0
Irrigation	Block 2 – irrigated: watering I-600 m³/ha, 21-23.07.2017	0	0	0	0	0	0	0	0	0	0	0	0	0	0	0	0	0	0	0	0
Harvesting	Harvesting: 19-20.09.2017	0.24	11	19	16	15	0.24	10	17	14	13	0.24	10	17	14	13	0.24	10	17	14	13
TOTAL	A1-ploughing (ha; %) Mt.	1.92 / 100%	100	-	-	-	2.07 / 100%	100	-	-	-	2.07 / 100%	100	-	-	-	2.12 / 100%	100	-	-	-
	A2-no-till (ha; %)	1.04 / 53%	-	100	-	-	1.19 / 57%	-	100	-	-	1.19 / 57%	-	100	-	-	1.24 / 57%	-	100	-	-
	A3-heavy disc (ha; %)	1.27 / 62%	-	-	100	-	1.42 / 69%	-	-	100	-	1.42 / 69%	-	-	100	-	1.47 / 69%	-	-	100	-
	A4-scarified (ha; %)	1.40 / 70%	-	-	-	100	1.55 / 75%	-	-	-	100	1.55 / 75%	-	-	-	100	1.60 / 75%	-	-	-	100

Exp. 1 – System of soil works, crop structure, densities and seeding times; Compacted surface by working a ha of soil [ha]; Share of compaction in the total crop technology / work system and crop technology (%), columns A1, A2, A3, A4.

Table 3

The effect of the system of mechanized works on soil compaction through the passes with the agricultural equipment on the experimental field IMB

All crop sections headed: *Exp. 1 – System of soil works, crop structure, densities and seeding times.* Sub-columns A1–A4 represent the "Share of compaction in the total crop technology (%)" (Wheat) / "Share of compaction in the total work system and crop technology (%)" (Maize, Sunflower, Soybean). "Compacted" = Compacted surface by working a ha of soil [ha].

Specification	Achieved technology; Inputs quantity; M.U	Wheat Compacted [ha]	W A1	W A2	W A3	W A4	Maize Compacted [ha]	M A1	M A2	M A3	M A4	Sunflower Compacted [ha]	S A1	S A2	S A3	S A4	Soybean Compacted [ha]	Sb A1	Sb A2	Sb A3	Sb A4
Work - Basic fertilization	-Fertilization, Belarus 820 tractor + MA-3,5	0.06	4	8	7	6	0.06	6	5	4	4	0.06	6	5	4	4	0.06	3	5	4	4
Chopping of vegetable debris		0	0	0	0	0	0	0	0	0	0	0	0	0	0	0	0	0	0	0	0
Soil works	Types of soil works: A1-ploughing 25 cm: Belarus 820 tractor + reversible plough, 22.10.2016	0.88	55	0	0	0	0.88	38	0	0	0	0.88	38	0	0	0	0.88	44	0	0	0
	A2-no-till: direct sowing in meadow	0	0	0	0	0	0	0	0	0	0	0	0	0	0	0	0	0	0	0	0
	A3-heavy disc: John Deere 8200 (220 HP) tractor + KUHN Discover XM2 heavy disc, 2.10.2016	0.18	0	0	20	0	0.18	0	0	14	0	0.18	0	0	14	0	0.8	0	0	14	0
	A4-scacification: John Deere 8200 (220 HP) tractor + Strom Terraland 3000 scarifier (l=3.0 m, H=0.6 m, 5 knives), 24.10.2016	0.32	0	0	0	31	0.32	0	0	0	20	0.32	0	0	0	20	0.32	0	0	0	22
Seedbed preparation	discing + harrowing: Belarus 820 + GD 3,2 + GCR 1,7 tractor	0	0	0	0	0	0.25	13	23	20	17	0.25	13	23	20	17	0.25	12	22	19	17
	combiner: Belarus 820 tractor + CTT 30.03.2017 combiner	0	0	0	0	0	0.20	10	18	16	14	0.20	10	18	16	14	0.20	9	17	15	14
	discing: Belarus 820 tractor + Maschio Gaspardo disc	0.26	12	21	17	16	0	0	0	0	0	0	0	0	0	0	0	0	0	0	0
Work - Soil herbicide	- Soil herbicide, Belarus 820 + MET-1200 tractor	0	0	0	0	0	0	0	0	0	0	0	0	0	0	0	0	0	0	0	0
Work - Sowing	-Sowing, Belarus 820 tractor + Gaspardo Nina 300 seeder	0.26	16	36	29	25	0	0	0	0	0	0	0	0	0	0	0	0	0	0	0
	-Sowing, Belarus 820 + SPC-6 tractor	0	0	0	0	0	0.19	9	15	13	12	0.19	9	15	13	12	0	0	0	0	0
Work – Phase fertilization	- Phase fertilization, Belarus 820 + MA-3,2 tractor	0	0	0	0	0	0	0	0	0	0	0	0	0	0	0	0.22	11	19	17	15
Work - Herbicide in vegetation	- Herbicide in vegetation, Belarus 820 + MET-1200 tractor	0.06	4	8	7	6	0.06	6	5	4	4	0.06	6	5	4	4	0.06	3	5	4	4
Work - Treatments	-Treatments, Belarus 820 + MET-1200 tractor	0.05	3	7	6	5	0.05	2	4	3	3	0.05	2	4	3	3	0.05	2	4	2	3
Other works	-	0.05	3	7	6	5	0.05	2	4	3	3	0.05	2	4	3	3	0.05	2	4	2	3
Irrigation	Block 1 – non-irrigated	0	0	0	0	0	0	0	0	0	0	0	0	0	0	0	0	0	0	0	0
	Block 2 – irrigated: wetting I-600 m³/ha, 21-23.07.2017	0	0	0	0	0	0	0	0	0	0	0	0	0	0	0	0	0	0	0	0
Harvesting	Harvesting: 19-20.09.2017	0.24	15	33	26	23	0.24	12	22	19	17	0.24	12	22	19	17	0.24	12	21	18	16
	A1-ploughing (ha; %) Mt.	1.86 100%	100	-	-	-	1.98 100%	100	-	-	-	1.98 100%	100	-	-	-	2.01 100%	100	-	-	-
	A2-no-till (ha; %)	0.98 53%	-	100	-	-	1.10 56%	-	100	-	-	1.10 56%	-	100	-	-	1.13 56%	-	100	-	-
	A3- heavy disc (ha; %)	1.16 62%	-	-	100	-	1.28 65%	-	-	100	-	1.28 65%	-	-	100	-	1.31 65%	-	-	100	-
	A4-scarifier (ha; %)	1.30 70%	-	-	-	100	1.42 71%	-	-	-	100	1.42 71%	-	-	-	100	1.45 72%	-	-	-	100

➤ *The effect of systems of mechanized works on agricultural yields*

As it results from the situation of yields made in experimental crops (Table 4-6) in conventional (classic) and unconventional mechanization systems, conservative (no-till and minimum till), crop yields responded to environmental conditions (climate, soil), technological conditions and improving conditions (application of irrigation).

Table 4

The impact of mechanization systems on agricultural yields to autumn crops, in Brăila, kg/ha

Specification	Locations	Classic system types	No-till system types	Minimum-till system types (with disc)	Minimum-till system types (with scarifier)
Wheat yield	Non-irrigated, Chiscani	5.950	6.645	5.391	5731
	Irrigated, Chiscani	7.153	7.518	7.455	8.019
	Average Chiscani	**6.522**	**7.081**	**6.418**	**6.845**
		100 %	**108 %**	**98 %**	**105 %**
	Non-irrigated, IMB	5.628	5.881	5.518	6.333
	Irrigated, IMB	6.538	6.772	7.313	7.246
	Average IMB	**6.083**	**6.327**	**6.415**	**6.789**
		100 %	**104 %**	**105 %**	**112 %**
Average		**6.317**	**6.704**	**6.416**	**6.817**
		100 %	**106 %**	**102 %**	**108 %**

Table 5

The impact of mechanization systems on agricultural yields to spring crops, in Brăila, kg/ha

Specification	Locations	Classic system types (ploughing)	No-till system types	Minimum-till system types (with disc)	Minimum-till system types (with scarifier)
Maize yield	Non-irrigated, Chiscani	8.318	7.439	6.930	6.715
	Irrigated, Chiscani	13.540	13.642	14.115	12.860
	Average Chiscani	**10.929**	**10.540**	**10.522**	**9.787**
		100 %	**96 %**	**96 %**	**89 %**
	Non-irrigated, IMB	9.891	8.865	9.475	8.962
	Irrigated, IMB	10.014	9.648	11.368	12.346
	Average IMB	**9.952**	**9.256**	**10.556**	**10.654**
		100 %	**93 %**	**106 %**	**107 %**
Average		**10.441**	**9.898**	**10.539**	**10.221**
		100 %	**95 %**	**101 %**	**98 %**
Sunflower yield	Non-irrigated, Chiscani	3.868	2.864	2.933	3.139
	Irrigated, Chiscani	4.196	3.617	3.378	3.761
	Average Chiscani	**4.032**	**3.240**	**3.155**	**3.450**
		100 %	**80 %**	**78 %**	**85 %**
	Non-irrigated, IMB	3.947	3.998	4.139	3.975
	Irrigated, IMB	4.327	4.023	4.223	4.444
	Average IMB	**4137**	**4010**	**4181**	**4209**
		100 %	**97 %**	**101 %**	**102 %**
Average		**4.084**	**3.625**	**3.668**	**3.830**
		100 %	**89 %**	**90 %**	**95 %**
Soybean yield	Non-irrigated, Chiscani	1.546	1.707	1.630	1.630
	Irrigated, Chiscani	4.083	3.913	3.770	3.711
	Average Chiscani	**2814**	**2810**	**2700**	**2670**
		100 %	**100 %**	**96 %**	**95 %**
	Non-irrigated, IMB	2.614	2.669	2.632	3.600
	Irrigated, IMB	3.422	3.952	4.310	3.789
	Average IMB	**3018**	**3310**	**3471**	**3694**
		100 %	**109 %**	**115 %**	**122 %**
Average		**2.916**	**3.060**	**3.085**	**3.182**
		100 %	**105 %**	**106 %**	**109 %**

Table 6

The impact of mechanization systems on agricultural yields in Dăbuleni, kg/ha

Specification	Locations	Classic system types (ploughing)	Minimum-till system types (with disc)	Minimum-till system types (with scarifier)
Rye yield	Dăbuleni	3141	2791	2866
		100 %	83 %	86 %
Sorghum yield	Dăbuleni	7384	7196	7321
		100 %	97 %	99 %
Beans yield	Dăbuleni	3499	2175	2197
		100 %	62 %	63 %

The non-conventional (conservative) system of mechanized works was located at yield levels compared to the classic level, in the 4 experimental crops in a percentage of 89-109% in Brăila and 62-99% in Dăbuleni, and the beneficial effect on soil and environment as well as the economic effect prevailed.

Regarding the effect of the mechanization systems applied on the agricultural yields for the conditions from North Bărăgan, Brăila, on plain and meadow and on the sands from Dăbuleni, the following conclusions can be presented:

- for North Bărăgan area in the plain (SCDA Brăila), for wheat cultivation, the average yields showed values at classic system (ploughing) of 6522 kg/ha (100%), at no-till 7081 kg/ha (108 %), at minimum-till system (heavy disc) 6418 kg/ha (98%), respectively at minimum-till system (scarification) 6845 kg/ha (105%);
- in the meadow (SCDA Brăila), for wheat cultivation, the average yields had the following values: for classic work (ploughing) 6083 kg/ha (100%), for no-till 6327 kg/ha (104%), for minimum-till system (heavy disc) 6415 kg/ha, (105%), respectively for minimum-till system (scarification) 6789 kg/ha (112%);
- average plain-meadow, for wheat cultivation, the yield for classic work (ploughing) was 6317 kg/ha (100%), for no-till 6704 kg/ha (106%), for minimum-till system (heavy disc) 6416 kg/ha (102%), respectively for minimum-till (scarification) 6817 kg/ha (108%);
- for North Bărăgan area in the plain (SCDA Brăila), for maize cultivation, the yields presented the average values for the classic work (ploughing) of 10929 kg/ha (100%), for no-till 10540 kg/ha (96%), for minimum-till system (heavy disc) 10522 kg/ha (96%), respectively for minimum-till system (scarification) 9787 kg/ha (89%);
- in the meadow (SCDA Brăila), for maize crop, the average yield for the classic work (ploughing) was 9952 kg/ha (100%), for no-till work 9256 kg/ha (93%), for minimum-till system (heavy disc) 10556 kg/ha, (106%), respectively for minimum-till system (scarification) 10654 kg/ha (107%);
- average plain-meadow, for maize cultivation, the average yield for classic work (ploughing) 10441 kg/ha (100%), for no-till works 9898 kg/ha (104%), for minimum-till system (heavy disc) 10539 kg/ha (101%), respectively for minimum-till system (scarification) 10221 kg/ha (98%);
- for North Bărăgan in the plain (SCDA Brăila), for sunflower crop, the yields compared to those for the classic work (ploughing) were 4032 kg/ha (100%), for no-till works 3240 kg/ha (80%), for minimum-till system (heavy disc) 3155 kg/ha (78%), respectively for minimum-till system (scarification) 3450 kg/ha (85%);
- in meadow (SCDA Brăila), for sunflower crop, the average yield for classic work (ploughing) was 4137 kg/ha (100%), for no-till works 4010 kg/ha (97%), for minimum-till system (heavy disc) 4181 kg/ha (101%), respectively for minimum-till system (scarification) 4209 kg/ha (102%);
- average meadow-plain for sunflower crop, the yield on classic work (ploughing) was 4084 kg/ha (100%), for no-till works 3625 kg/ha (89%), for minimum-till system (heavy disc) 3668 kg/ha (90%), respectively for minimum-till system (scarification) 3830 kg/ha (95%);
- for North Bărăgan area in the plain (SCDA Brăila), for soybean crop the yield for the classic work (ploughing) was 2814 kg/ha (100%), for no-till 2810 kg/ha (100%), for minimum-till system (heavy disc) 2700 kg/ha (96%), respectively for minimum-till system (scarification) 2670 kg/ha (95%);
- in the meadow (SCDA Brăila), for soybean crop, the average yield for the classic work (ploughing) was 3018 kg/ha (100%), for no-till works 3310 kg/ha (109%), for minimum-till system (heavy disc) 3471 kg/ha (115%), respectively for minimum-till system (scarification) 3694 kg/ha (122%);
- average plain-meadow for soybean crop, the average yield for classic work (ploughing) was 2916 kg/ha (100%), for no-till works 3060 kg/ha (105%), for minimum-till system (heavy disc) 3085 kg/ha (106%), respectively for minimum-till system (scarification) 3182 kg/ha (109%);
- in the sands from Dăbuleni for the rye crop, the average yield at the classic work (ploughing) was 3.141 kg/ha (100%), for minimum-till system (heavy disc) 2.791 kg/ha (83%), respectively for minimum-till system (scarification) 2866 kg/ha (86%);
- for sorghum crop, the average yield for the classic work (ploughing) was 7384 kg/ha (100%), for minimum-till system (heavy disc) 7196 kg/ha (97%), respectively for minimum-till system (scarification) 7321 kg/ha (99%);

- for bean crop, the average yield for the classic work (ploughing) was 3499 kg/ha (100%), for minimum-till system (heavy disc) 2175 kg/ha (62%), respectively for minimum-till system (scarification) 2197 kg/ha (63%);

➢ ***The effect of irrigation on agricultural yields, within the conservative systems of mechanized works***

In the agricultural year 2017-2018, spring crops have faced an acute water deficit as they entered the warm period of the year, especially in the conditions of the accentuated lack of water from rainfall and the manifestation of the pedological drought. Under these conditions, irrigation had a particularly beneficial role, the watering applied during July and August ensuring special yields related to the conditions of non-application of irrigation. The yields for irrigated maize crop with values of 12860-14115 kg/ha in the plain and 9648-12346 kg/ha in the meadow obviously exceeded the non-irrigated yields for all systems of soil works, which reached 6715-8318 kg/ha in the plain and 8865-9991 kg/ha in the meadow (Table 7).

Table 7

The effect of irrigation on agricultural yields for maize and soybean crops in the plains and meadows

Crop		Meadow				Plain			
		Ploughing	No-till	Heavy disc	Scarification	Ploughing	No-till	Heavy disc	Scarification
Maize	**Non-irrigated**	8.318 100 %	7.439 100 %	6.930 100 %	6.715 100 %	9.991 100%	8.865 100 %	9.475 100 %	8.962 100 %
	Irrigated	13.540 162 %	13.642 183 %	14.115 204 %	12.860 191 %	10.172 102%	9.648 109 %	11.638 123 %	12.346 138 %
Soybean	**Non-irrigated**	1.546 100 %	1.707 100 %	1.630 100 %	1.630 100 %	2.614 100%	2.669 100 %	2.632 100 %	3.600 100 %
	Irrigated	4.083 264 %	3.913 229 %	3.770 231 %	3.711 228 %	3.422 132%	3.952 130 %	4.310 164 %	3.789 105 %

The ratio between the irrigated and non-irrigated work systems has values of 1.83-2.04 in the plain and 1.02-1.38 in the meadow. It should be noted that for non-irrigated maize, the yields reported were higher in the meadow by approx. 1200-2100 kg/ha compared to the plain, attesting the beneficial effect of the groundwater intake on the meadow soils. Similarly, in the irrigated soybean crop with values in the irrigated regime of 3711-4083 kg/ha in the plains and 3422-4310 kg/ha in the meadow, the non-irrigated yields were obviously exceeded in all soil works systems, which reached 1546-1707 kg/ha in the plain and 2614-3600 kg/ha in the meadow. The irrigated - non-irrigated ratio has values of 2.28-2.64 in the plain and 1.05-1.64 in the meadow, but the yields for non-irrigated in the meadow exceed those in the plain by 1000-2000 kg/ha, attesting also the beneficial effect of groundwater intake for this crop.

The effect of systems of mechanized works on productivity and fuel consumption of agricultural equipment

➢ ***The effect of systems of mechanized works on agricultural equipment productivity***

In order to emphasize the productivity of the agricultural equipment, a parameter was used that represents the time necessary to carry out a work on one ha (in hours/ha), as it is presented in Table 8. The time required for the application of the experimental technology to the agricultural crops on 1 ha resulted by summing and comparing the cumulated times for all the applied works. It differs greatly depending on the intensity of the mechanical intervention performed on the soil, varying from the control plough (on average for wheat, maize and soybean crops), as follows: at no-till 61% with the highest productivity, followed by lower productivities at minimum-till (heavy disc) 67% and at minimum-till (scarifier) 72%.

Table 8

Productivity of agricultural equipment within the researched systems of mechanized works

Time required (hours) for the application of the technology experimental crops, on 1 ha								
Crop	Location	Types of applied systems of works						
		A1 ploughing		A2 no-till		A3 minimum-till (heavy disc)		A4 minimum-till (scarifier)	
		hours/ha	%	hours/ha	%	hours/ha	%	hours/ha	%
Wheat	CE Chiscani	7.69	100	5.34	69	5.62	73	6.14	80
	CE IMB	7.69	100	5.34	69	5.66	74	5.87	76
Maize	CE Chiscani	6.62	100	4.27	65	4.65	70	5.07	77
	CE IMB	4.89	100	2.54	52	2.86	58	3.07	63
Sunflower	CE Chiscani	5.51	100	3.16	57	3.44	62	3.96	72
	CE IMB	4.32	100	1.97	46	2.29	53	2.50	58
Soybeans	CE Chiscani	6.16	100	3.81	62	4.09	66	4.61	75
	CE IMB	5.91	100	3.56	60	4.13	70	4.09	69
Media		**6.10**	**100**	**3.75**	**61**	**4.09**	**67**	**4.41**	**72**

➤ *The effect of mechanized works systems on fuel consumption*

The fuel consumption on total crop technology for the types of mechanized works attests obvious differences of the conservative works (no till and minimum-till), compared to the classic ploughing work. Thus, the fuel consumption per hectare, average on the 4 experimental crops for the control work (ploughing) totalled 61.3 l/ha, at the no-till work 35.8 l/ha, representing 57% of the control, for the minimum-till (heavy disc) 46.5 l/ha, representing 75% of the control and for the minimum-till work (scarifier) 55.3 l/ha representing 90% of the control, according to the data in Table 9.

Table 9

Fuel consumption on total technology of experimental crops

Crop	Location	Types of applied systems of works							
		A1 - ploughing		A2 – no-till		A3 – minimum-till (heavy disc)		A3 – Minimum-till (scarifier)	
		l/ha	%	l/ha	%	l/ha	%	l/ha	%
Wheat	CE Chiscani	62.6	100	37.1	59	47.6	76	57.1	91
	CE IMB	75.1	100	49.6	66	60.6	81	68.6	91
Maize	CE Chiscani	69.2	100	43.7	63	54.2	78	63.7	92
	CE IMB	56.6	100	30.9	55	41.9	74	49.9	88
Sunflower	CE Chiscani	49.9	100	24.5	49	34.9	70	44.5	89
	CE IMB	39.7	100	14.2	36	25.2	64	33.2	84
Soybeans	CE Chiscani	68.6	100	43.1	63	53.6	78	63.1	92
	CE IMB	68.9	100	43.4	63	54.4	79	62.4	91
Average		61.3	100	35.8	57	46.5	75	55.3	90

Characterization of basic soil works in terms of water conservation in soil, plains and meadows (CE Chiscani, CE IMB). Regarding the effect of the system for basic soil works on the moisture regime under the wheat crop in the plain, as well as in the meadow, the small differences of moisture determined on the 4 types of the soil works system (no-till, minimum-till 1 (heavy disc), minimum-till 2 (scarifier) and ploughing) can be highlighted. In the plain, in the soil layer between 0-25 cm, the ascending order of the basic works of the soil regarding the degree of water retention accessed from the initial reserves of the soil and from rainfall is as follows: scarified, ploughed, heavy disc, no-till, according to the data in Table 10.

Table10

Characterization of basic soil works in terms of soil water conservation in the plains and meadows (CE Chiscani, CE IMB)

Location	Systems of mechanized work	A1 (plough)	A2 (no-till)	A3 (heavy disc)	A4 (scarifier)
CE Chiscani	Average soil moisture during vegetation (% gravitational)	18.1	18.9	18.5	18.1
	Degree of water conservation in the soil (%)	100	104	102	100
CE IMB	Average soil moisture during vegetation (% gravitational)	31.9	33.0	32.7	31.5
	Degree of water conservation in the soil (%)	100	103	102	99
Dăbuleni	Average soil moisture during vegetation (% gravitational)	15.6	-	13.4	14.5
	Degree of water conservation in the soil (%)	100	-	86	93

The same distribution of water reserves specified for soil layer between 0-25 cm deep, depending on the basic soil works, is kept for layer 0-50 cm and largely in layer 0-100 cm. Analysis of moisture reserves in the meadow on all the basic works of the soil on the soil layer between 0-25 cm for wheat cultivation, as well as on the other deeper layers 0-50 cm and 0-100 cm, for the periods after sowing, during the vegetation period and at harvest, attests small differences between the basic soil works in terms of water retention capacity, attesting the rich water regime of the meadow soil ensured by a substantial groundwater intake, together with the climatic water intake, and the ranking order of accessed water retention degree is the same as in the plain: scarified, ploughed, heavy disc, no-till.

➤ *The effect of systems of mechanized works on the economic result of agricultural crops*

The economic effect is a result of the achieved yield, correlated with the natural, ameliorative and technological framework in which the systems of mechanized works have a significant share. Regarding the economic effect, the financial result on the types of soil works, resulted in the following:

❖ for wheat crop, on plain, the financial result is: 1911 RON/ha (100 %) for the classic system, for no-till 2500 RON/ha (130%), for heavy disc 1912 RON/ha (100%) and for scarification 1988 RON/ha (104%), according to Table 11.

Table 11

The effect of systems of mechanized works on the economic result in wheat crop

Economic effect (financial result), RON/ha					
Specification	Location	A1 Plough	A2 No-till	A3 Minimum-till (heavy disc)	A3 Minimum-till (scarifier)
Wheat	Non-irrigated Chiscani	1.502	2.203	1.210	1.178
	Irrigated Chiscani	2.320	2.797	2.614	2.798
	Average Chiscani	**1.911**	**2.500**	**1.912**	**1.988**
		100 %	130 %	100 %	104 %
	Non-irrigated IMB	1.469	1.854	1.467	1.898
	Irrigated IMB	2.011	2.460	2.688	2.864
	Average IMB	**1.740**	**2.157**	**2.077**	**2.381**
		100 %	124 %	119 %	137 %
Average		**1.825**	**2.328**	**1.994**	**2.184**
		100 %	127 %	109 %	120 %

- for wheat crop, in the meadow, the financial result is: 1740 RON/ha (100%) for the classic system, for no-till 2157 RON/ha (124%), for heavy disc 2077 RON/ha (119%), respectively for scarification 2381 RON/ha (137%);

- average plain - meadow wheat crop presents financial results of: 1825 RON/ha (100%) for the classic system, for no-till 2328 RON/ha (127%), for heavy disc 1994 RON/ha (109%), respectively for scarification 2184 RON/ha (120%);

- for maize crop in the plain, the financial result is: 3820 RON/ha (100%) for the classic system, for no-till 4339 RON/ha (114%), for heavy disc 3208 RON/ha (84%), respectively for scarification 3090 RON/ha (81%), as presented in Table 12;

- for maize crop in the meadow, the financial result is: 3923 RON/ha (100%) for the classic system, for no-till 4026 RON/ha (103%), for heavy disc 3730 RON/ha (95%), respectively for scarification 3615 RON/ha (93%);

- average plain - meadow maize crop presents the following financial results: 3871 RON/ha (100%) for the classic system, for no-till 4182 RON/ha (107%), for heavy disc 3469 RON/ha (90%), respectively for scarification 3352 RON/ha (87%);

Table 12

The effect of systems of mechanized works on the economic result in maize, sunflower and soy crops

Economic effect (financial result), RON/ha					
Specification	Location	A1 - Plough	A2 – No-till	A3 – Minimum-till (heavy disc)	A3 – Minimum-till (scarifier)
Maize	Non-irrigated Chiscani	1.773	2.746	2.531	2.274
	Irrigated Chiscani	5.867	5.933	3.885	3.906
	Average Chiscani	**3.820**	**4.339**	**3.208**	**3.090**
		100 %	114 %	84 %	81 %
	Non-irrigated IMB	2.150	2.172	2.837	2.261
	Irrigated IMB	4.295	5.881	4.624	4.969
	Average IMB	**3.923**	**4.026**	**3.730**	**3.615**
		100 %	103 %	95 %	93 %
Average		**3.871**	**4.128**	**3.469**	**3.352**
		100 %	107 %	90 %	87 %
Sunflower	Non-irrigated Chiscani	2.468	1.586	1.028	2.147
	Irrigated Chiscani	2.674	2.180	1.907	2.002
	Average Chiscani	**2.572**	**1.883**	**1.468**	**2.074**
		100 %	73 %	57 %	81 %
	Non-irrigated IMB	2.758	2.612	3.199	2.275
	Irrigated IMB	1.904	2.362	2.689	3.213
	Average IMB	**2.331**	**2.487**	**2.944**	**2.744**
		100 %	107 %	126 %	117 %
Average		**2.451**	**2.185**	**2.206**	**2.409**
		100 %	89 %	90 %	98 %
Soybeans	Non-irrigated Chiscani	-38	701	-205	-636
	Irrigated Chiscani	2.485	3.657	2.387	3.589
	Average Chiscani	**1.223**	**2.180**	**1.091**	**1.476**
		100 %	178 %	90 %	121 %
	Non-irrigated IMB	1.170	1.060	1.131	3.070
	Irrigated IMB	2.791	4.480	4.280	3.703
	Average IMB	**1.980**	**2.770**	**2.706**	**3.386**
		100 %	140 %	136 %	171 %
Average		**1.602**	**2.474**	**1.898**	**2.431**
		100 %	154 %	118 %	152 %

- for sunflower crop in plain, the financial results are: 2571 RON/ha (100%) for the classic system, for no-till 1883 RON/ha (73%), for heavy disc 1468 RON/ha (57%), respectively for scarification 2075 RON/ha (81%);

- for sunflower crop in meadow, the financial results are: 2330 RON/ha (100%) for the classic system, for no-till 2487 RON/ha (107%), for the heavy disc 2,944 RON/ha (126%), respectively for scarification 2744 RON/ha (117%);

- average plain - meadow for sunflower crop presents the following financial results: 2451 RON/ha (100 %) for the classic system, for no-till 2185 RON/ha (89%), for heavy disc 2206 RON/ha (90%), respectively for scarification 2409 RON/ha (98%);

- for soybean crop in the plain, the financial results are: 1223 RON/ha (100%) for the classic system, for no-till 2180 RON/ha (178%), for heavy disc 1091 RON/ha (90%), respectively for scarification 1476 RON/ha (121%);

- for soybean crop in meadow, the financial results are: 1980 RON/ha (100%) for the classic system, for no-till 2769 RON/ha (140%), for heavy disc 2705 RON/ha (136%), respectively for scarification 3386 RON/ha (171%);

- average plain-meadow for soybean crop presents the following financial results: 1602 RON/ha (100%) for the classic system, for no-till 2474 RON/ha (154%), for heavy disc 1898 RON/ha (118%), respectively for scarification 2431 RON/ha (152%).

> **The effect of existing agroforestry curtains on agricultural crops**

In order to obtain information on the effect of agroforestry curtains on protected crops, observations were made in some perimeters equipped with agroforestry arrangements for the protection of agricultural crops (Figure 2).

Fig. 2 - Satellite view of the agroforestry curtain from the Albina location, researched in the project

The observations on the effect of an agroforestry curtain from the location of Albina village, Brăila county, regarding the preservation of the protective layer of snow on the field attested the specific conditions of low intensity of solid rainfall in the winter of 2015-2016, which determined the deposition of a reduced snow layer of 5-7 cm in the shelter of the curtain. Analysing the values of penetration resistance with the portable penetrometer, it can be seen that these values are higher in the snow accumulation area with increased moisture values during the cold period, the field works contributing to a more accentuated soil compaction.

> *Designing of agroforestry curtains on the SCDA land in the Big Island of Brăila*

In order to improve the much more unfavourable climatic environment in the meadow compared to the plain in the very dry years, in the Big Island of Brăila, on the territory of the research resort was designed a network of curtains for agroforestry protection of agricultural crops (Figure 3).
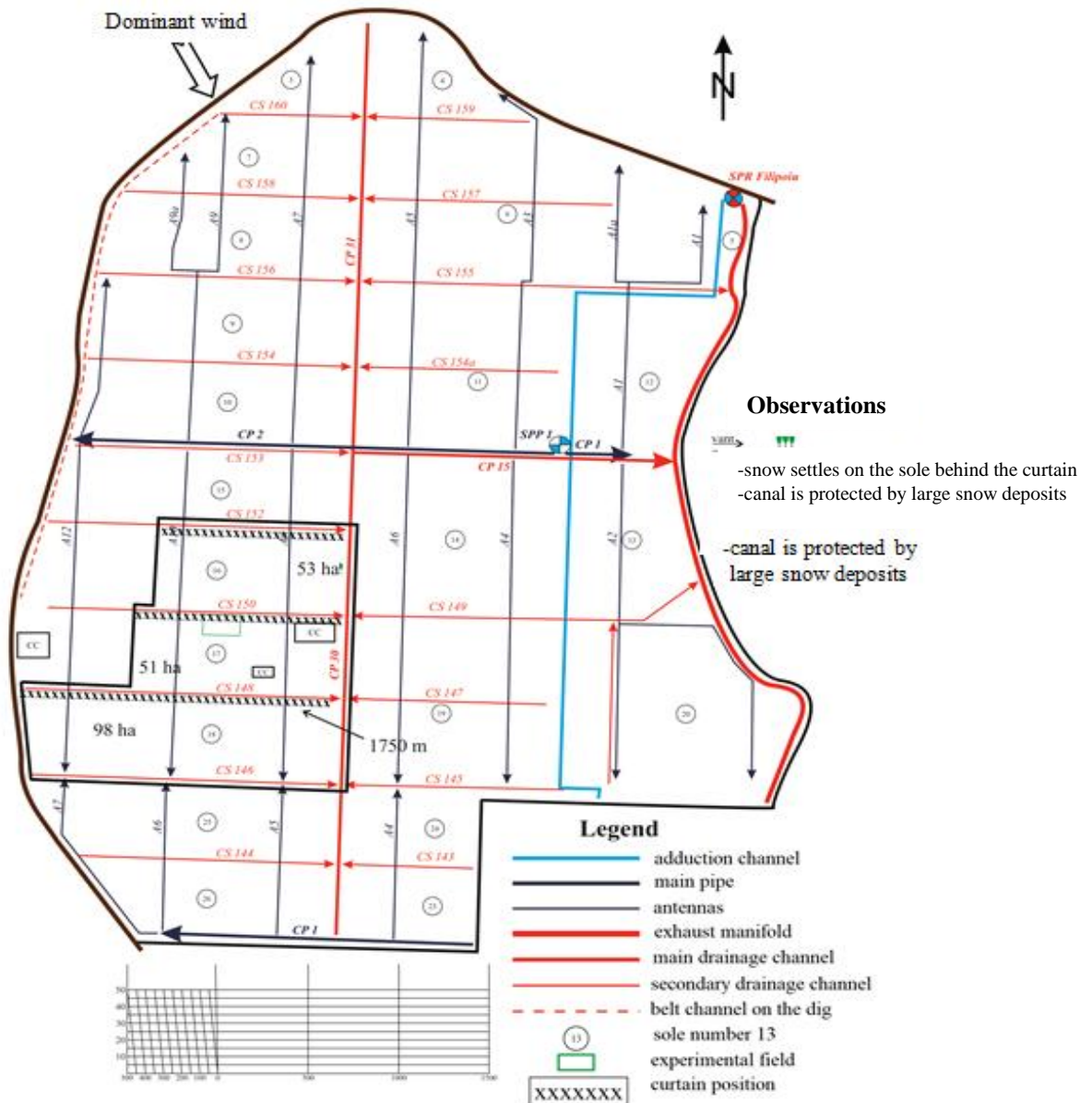
Fig. 3 - Network of agroforestry curtains designed in the Big Island of Brăila

Among the technical parameters of the curtain network, there are: east-west direction, perpendicular to the direction of the prevailing wind, the composition of 3 curtain lines totalling a length of 3950 m, spaced at 500 m, with a width of 8 m and with acacia forest species.

Elaboration of optimal technologies to combat the effects of drought on experimental crops

Based on the performed research, it was possible to develop optimal technologies to combat the effects of drought on experienced crops with elements argued by increased agricultural yields and superior economic results (Tables 13 and 14).

➢ *Optimal technological elements for wheat crop argued by increased yield (p) and superior economic effects (e)*

    1) Fertilization:
- Basic fertilization with complex fertilizers in full dose of 40 kg/ha s.a. (arg. P + e);
- Phase fertilization with urea at a dose of 100 kg/ha s.a. applied fractionally (1/2 autumn and 1/2 spring) (arg. p + e);
- Organic fertilization with manure 10 t/ha (arg. p+e).

    2) Soil works:
- Ploughing (arg. p);
- Direct sowing in the field -no-till (arg. e);
- Scarification (arg. p);

Table 13

Optimal technology to combat the effects of drought on straw crops

Specification	Optimal technology for combating the effects of drought on experimental autumn crops with variants argued by yield and economic results - *Wheat*		
	Achieved technology; Amount of inputs; M.U	Yield arguments	Economic arguments
Basic fertilization with complex fertilizers 18.46.0	Fractional doses of phosphorus; Variant F1f: 20 kg/ha s.a, (*43.4 kg/ha r.s.*), autumn 20 kg/ha s.a, (*43.4 kg/ha r.s.*), spring	xx	xx
	Variant G: Manure autumn; G1 – *10 t/ha*	xx	xx
Soil works	-*ploughing 25 cm*: Belarus 820 tractor + reversible plough	xx	-
	-no-till: direct sowing	-	xx
	-*scarification*: John Deere 8200 (220 HP) tractor + Strom Terraland 3000 scarifier (l=3.00 m. H=0.60 m, 5 knives)	xx	-
Sowing	-Equipment: Belarus 820 tractor + Gaspardo Nina 300 seeder -Sowing densities: 500 bg/m^2 (*280 kg/ha*)	x	x
Phase fertilization with urea	-Variant E 2: *100 kg/ha a.s.* (*217.3 kg/ha* r.s.)	xx	xx
Herbicide in vegetation	Primstar *1.5 g/ha;* Hudson *0.5 l/ha*	x	x
Treatment for diseases	Artea *0.4 l/ha*	x	x
Pest treatment	-	x	x
Irrigation	-	x	x
Harvesting	*Harvesting* with self-propelled combine	x	x

xx - experimentally argued technological element

x - current technological element

Optimal technological elements for spring crops

1) Basic fertilization with complex fertilizers:
- *Maize,* dose 40 kg/ha, integral + fractionated (arg. p+e);
- Organic fertilization with manure 10 t/ha (arg. p+e);
- *Sunflower* and *soybeans*, dose 80 kg/ha integral, 40 kg/ha fractionated (arg. e);

2) Phase fertilization with urea:
- *Maize,* dose 150 kg/ha s.a., integral (arg. p.);
- *Sunflower*, dose 50 kg/ha, integral + fractionated (arg. p), 100 kg/ha fractionated (arg. p+e);
- *Soya*, dose 100 kg/ha, integral + fractionated (arg. p+e);

3) Soil works:
- *Maize* - ploughing (arg. p+e); direct sowing (arg. e); heavy disc (arg. e);
- *Sunflower* – ploughing and scarification (arg. e);
- *Soybeans* – ploughing + heavy disc (arg. p+e); direct sowing (arg. e**)**.

Table 14

Optimal technology to combat the effects of drought on maize, sunflower and soybean crops

Technological elements	Maize			Sunflower			Soybeans		
	Achieved technology; Amount of inputs; M.U	Yield arguments	Economic arguments	Achieved technology; Amount of inputs; M.U	Yield arguments	Economic arguments	Achieved technology; Amount of inputs; M.U	Yield arguments	Economic arguments
Basic fertilization with complex fertilizers 18.46.0	Variant F 1: 40 kg/ha s.a. (*86.9 kg/ha r.s.)*, autumn	xx	xx	Variant F 1: 40 kg/ha a.s. (*86.9 kg/ha r.s.)*, autumn	-	-	Variant F 1: 40 kg/ha a.s. (*86.9 kg/ha r.s.)*, autumn	-	-
	Variant F 2: 80 kg/ha a.s. (*173.9 kg/ha r.s.)*, autumn	-	-	Variant F 2: 80 kg/ha a.s. (*173.9 kg/ha r.s.)*, autumn	xx	-	Variant F 2: 80 kg/ha a.s.(*173.9 kg/ha r.s.)*, autumn	xx	xx
	Variant F1f: *20 kg/ha* a.s. autumn *20 kg/ha* a.s. spring	xx	xx	Variant F1f: *20 kg/ha* autumn *20 kg/ha* a.s. spring	xx	-	Variant F1f: *20 kg/ha* a.s. autumn *20 kg/ha* a.s. spring	xx	xx
	Variant F2f: *40 kg/ha a.s. autumn 40 kg/ha* a.s. spring	-	-	Variant F2f: *40 kg/ha* a.s. autumn *40 kg/ha* a.s. spring	-	-	Variant F2f: *40 kg/ha* a.s. autumn *40 kg/ha* a.s. spring	-	-
	Manure – *10 t/ha*	xx	xx	Manure – *10 t/ha*	-	-	Manure – *10 t/ha*	-	-
	Manure – *20 t/ha*	-	-	Manure – *20 t/ha*	-	-	Manure – *20 t/ha*	-	-
Soil works	-*ploughing 25 cm*, Belarus 820 tractor + reversible plough	xx	xx	-*ploughing 25 cm*, Belarus 820 tractor + reversible plough	xx	-	-*ploughing 25 cm*, Belarus 820 tractor + reversible plough	xx	xx
	-*no-till* - direct sowing in unprocessed soil	-	xx	-*no-till* – direct sowing in unprocessed soil	-	-	-*no-till*– direct sowing in unprocessed soil	-	xx
	- *heavy disc* – John Deere tractor (220 HP) + KHUN Discover XM2 heavy disc	xx	-	- *heavy disc* – John Deere tractor (220 HP) + KHUN Discover XM2 heavy disc	-	-	- *heavy disc* – John Deere tractor (220 HP) + KHUN Discover XM2 heavy disc	xx	xx
	-*scarification* - John Deere 8800 tractor (220 HP) with Storm Terraland 3000 scarifier (l=3.00	-	-	-*scarification* - John Deere 8800 tractor (220 HP) with Storm Terraland 3000 scarifier (l=3.00	xx	-	-*scarification* - John Deere 8800 tractor (220 HP) with Storm Terraland 3000 scarifier (l=3.00	-	-

Technological elements	Maize			Sunflower			Soybeans		
	Achieved technology; Amount of inputs; M.U	Yield arguments	Economic arguments	Achieved technology; Amount of inputs; M.U	Yield arguments	Economic arguments	Achieved technology; Amount of inputs; M.U	Yield arguments	Economic arguments
	m, H=0.60 m, 5 knives)			m, H=0.60 m, 5 knives)			m, H=0.60 m, 5 knives)		
	Seedbed preparation: -*discing+ harrowing*, Belarus 820 tractor + GD 3.2 + GCR 1.7	x	-	Seedbed preparation: -*discing+ harrowing*, Belarus 820 tractor + GD 3.2 + GCR 1.7	-	-	Seedbed preparation: -*discing+ harrowing*, Belarus 820 tractor + GD 3.2 + GCR 1.7	-	-
	-*combiner*, Belarus 820 tractor + CCT	x	-	-*combiner*, Belarus 820 tractor + CCT	-	-	-*combiner*, Belarus 820 tractor + CCT	-	-
Soil herbicide	-	-	-	Clinic *2.5 l/ha*	-	-	-	-	-
Sowing	-Equipment –Belarus 820 tractor + SPC-6 -Sowing distance: 70 cm -Sowing depth: 5 cm -Sowing densities: 65 thousand bg/ha (*20 kg/ha*)	x	x	-Equipment –Belarus 820 tractor + Haldrup SP 35 - Sowing distance: 70 cm - Sowing depth: 4 cm - Sowing densities: 60 thousand bg/ha (*4 kg/ha*)	x	x	-Equipment –Belarus 820 tractor + Haldrup SP 35 - Sowing distance: 70 cm - Sowing depth: 4 cm - Sowing densities: 60 bg/ha (*90 kg/ha*)	-	-
Phase fertilization with urea	-Variant E 1 – 50 kg/ha a.s. (*108.6 kg/ha*)	-	-	-Variant E 1 – 50 kg/ha a.s. (*108.6 kg/ha*)	xx	-	-Variant E 1 – 50 kg/ha a.s. (*108.6 kg/ha*)	-	-
	-Variant E 2 – 100 kg/ha a.s. (*217.3 kg/ha*)	-	-	-Variant E 2 – 100 kg/ha a.s. (*217.3 kg/ha*)	-	-	-Variant E 2 – 100 kg/ha a.s. (*217.3 kg/ha*)	xx	xx
	-Variant E 3 – 150 kg/ha s.a (*326 kg/ha*)	xx	-	-Variant E 3 – 150 kg/ha s.a (*326 kg/ha*)	-	xx	-Variant E 3 – 150 kg/ha s.a (*326 kg/ha*)	-	-
	Variant E 1f – 25 kg/ha a.s. (*54.3 kg/ha*)	-	-	Variant E 1f – 25 kg/ha a.s. (*54.3 kg/ha*)	xx	-	Variant E 1f – 25 kg/ha a.s. (*54.3 kg/ha*)	-	xx
	-Variant E 2f – 50 kg/ha a.s. (*108.6 kg/ha*)	-	-	-Variant E 2f – 50 kg/ha a.s. (*108.6 kg/ha*)	-	xx	-Variant E 2f – 50 kg/ha a.s. (*108.6 kg/ha*)	xx	-
	-Variant E 3f – 75 kg/ha a.s. (*163 kg/ha*)	-	-	-Variant E 3f – 75 kg/ha a.s. (*163 kg/ha*)	-	-	-Variant E 3f – 75 kg/ha a.s. (*163 kg/ha*)	-	-
Herbicide in vegetation	Mistral *0.25 l/ha* Casper *1.4 kg/ha* Eucarol *0.5 l/ha*	x	x	Pulsar *1.2 l/ha* (Listego) Fusilade *1 l/ha*	x	x	Pulsar *1.2 l/ha* Fusilade Forte *1.5 l/ha* Dash *1.5 l/ha*	x	x
Irrigation	-1 wetting of 600 m³/ha	x	x	-1 wetting of 600 m³/ha	x	x	-1 wetting of 600 m³/ha	x	x
Harvesting	*Harvesting*	x	x	*Harvesting*	x	x	*Harvesting*	x	x

xx - experimentally argued technological element

x - current technological element

CONCLUSIONS

1. The climate change taking place in the North Bărăgan area manifests by increased aridisation of large agricultural areas, so that through performed studies, SCDA Brăila predicts that these soil and climatic conditions will have an unfavourable evolution in the perspective of 2025 and 2050. An average decrease in multiannual rainfall is currently estimated from 445 mm to 440 mm in 2025 and 435 mm in 2050; an increase in the multiannual average temperature from 11°C at present to 11.3^{o}C in 2025 and to 11.5^{o}C in 2050; an increase in the potential multiannual average evapotranspiration from 715 mm at present to 730 mm in 2025 and to 750 mm in 2050.

2. In drought conditions, the actions to counteract the negative effects are subscribed to some anthropic interventions of general character, which include the whole range of agropedoameliorative and agrophytotechnical measures necessary for the achievement of production cycle in the agricultural system.

3. The high variability of climatic parameters that take place during a year creates different conditions for plant growth and development in correlation with these situations, which is why separating the influence of mechanical works on agricultural crops is quite difficult to achieve over a short period of time for several years.

4. In terms of the effect of the system of basic soil works on moisture regime under crops in plain, as well as in meadow, the small differences of moisture determined on the 4 variants of soil works system (no-till, minimum-till 1 (heavy disc), minimum-till 2 (scarifier) and ploughing) can be highlighted. The main advantage of conservative works is mainly soil protection and increasing its fertility, which are factors of profitability.

5. In terms of the effect of fertilization on soil water conservation, it is recommended to apply integral norms in the case of low working width management machines and fractional norms in the case of long working width management machines, simultaneously with the same route, and to achieve increased productions, it is recommended to combine the administration variants depending on the sole crop.

REFERENCES

[1] Baltag G., (2020), Comparative analysis of the economic efficiency of nutrient use in conventional and conservative soil work systems, *Publishing House Economica*, No. 1 (111), pp. 22-33;

[2] Barilli E, Jeuffroy M.H., Gall J. et al, (2017), Weed response and crop growth in winter wheat-lucerne intercropping: a comparison of conventional and reduced soil-tillage conditions in northern France, *Crop Pasture Sci*, Vol. 68 (10–11), pp. 1070–1079;

[3] Boincean B., (2011), Tillage - Trends and Perspectives, *Journal of Science, Innovation, Culture and Art "Akademos"*, No. 3 (22), pp. 61-67;

[4] Bronick C.J., Lal R., (2005), Soil structure and management: a review. *Geoderma*, Vol. 124, Issues 1–2, pp. 3-22, https://doi.org/10.1016/j.geoderma.2004.03.005;

[5] Ceretto C.K., (2007), No-Till. Relationship between No-till, plant debris, plant nutrition and soil. *Dnepropetrovsk*, 236 c;

[6]   Chen H., Li H., Gao H., Wang X., He J., Li W., Wang Q., (2008), Effect of long-term controlled traffic conservation tillage on soil structure, *Transactions of the Chinese Society of Agricultural Engineering*;

[7]   Cooper R.J., Ham-Aziz Z., Hiscock K.M., Lovett A.A., Dugdale S.J., Sünnenberg G., Noble L., Beamish J., Hovesen P., (2017). Assessing the farm-scale impacts of cover crops and non-inversion tillage regimes on nutrient losses from an arable catchment. *Agriculture, Ecosystems & Environment*, Vol. 237, pp. 181–193;

[8]   Creamer R. E., Brennan F., Fenton O., Healy M. G., Lalor S. T. J., Lanigan G. J., Regan J. T., Griffiths B. S., (2010), Implications of the proposed Soil Framework Directive on agricultural systems in Atlantic Europe – A review. *Soil Use and Management*, Vol. 26(3), pp. 198–211;

[9]   Crîșmaru I. (2006), Agricultural machinery and installations / Mașini și instalații agricole, *Online course;*

[10]   Croitoru S., Bădescu M., Ungureanu N., Boruz S., Vlăduţ V., Usenko M., Marin E., Manea D., Caba I., Cujbescu D., (2014), Research on the application of agricultural conservative technologies with deep loosening works in Romania and worldwide, *Annals Of The University of Craiova - Agriculture, Montanology, Cadastre,* Series, Vol. 44, No. 2, pp. 61-71;

[11]   Crotty V.F., Stoat C., (2019), The legacy of cover crops on the soil habitat and ecosystem services in a heavy clay, minimum tillage rotation, *Food and Energy Security*, pp. 1-16;

[12]   Dabney S. M., Delgado J. A., Reeves D. W., (2001), Using winter cover crops to improve soil and water quality. *Communications in Soil Science and Plant Analysis*, Vol. 32 (7–8), pp. 1221–1250;

[13]   Deng Z., Huang G., Zhao C., Xin P., (2005), Effects of controlled traffic tillage irrigation on soil water and yield of film-mulched spring wheat. *Journal of Gansu Agricultural University*;

[14]   Derpsch R., (2008), Critical Steps to No-till Adoption, *No-till Farming Systems*, *Eds., WASWC*. pp. 479-495;

[15]   Dobre P., et al., (2017), Energy base and machinery / Baza energetică și mașini, *Ex. Terra Aurum Publishing House,* Bucharest;

[16]   Drăgan Gh., (1969), Agricultural machinery / Mașini agricole, *Didactic and Pedagogical Publishing House,* Bucharest;

[17]   Farcaș N., et al., (2019), *Mechanization of agriculture / Mecanizarea agriculturii, Ex. Terra Aurum Publishing House, Bucharest*;

[18]   Gao H. W., Li H., Chen J., (1999), Research on Sustainable Mechanized Dryland Farming. *Agricultural Reseach In the Arid Areas*;

[19]   Garnett et al., (2013), Sustainable intensification in agriculture: Premises and policies, *Science*, Vol. 341 (6141), pp. 33–34. https://doi.org/10.1126/science.1234485;

[20]   Gumovschi A., (2019), Increasing soil fertility and reducing drought effects by applying conservative agriculture, *EcoSoEn*, No. 1-2, JEL: O13, Q15, pp. 192-198;

[21]   Reicosky D.C., (2015), Conservation tillage is not conservation agriculture, *Journal of Soil and water conservation*, Vol. 70, No. 5. http://www.jswconline.org/content/70/5/103A.extract;

[22]   Scripnic V., Babiciu P., (1979), Agricultural machinery / Mașini agricole, *Ceres Publishing House,* Bucharest;

[23]   Shi J.-l., Liu J.-Z., Wu F.-Q., (2006), Research advances and comments on conservation tillage; *Agricultural Research in the Arid Areas*;

[24]   Stelian N., et al., (1983), Tractors / Tractoare*, Didactic and Pedagogical Publishing House, Bucharest*;

[25]   Șandru A, et al., (1983), Operation of agricultural equipment / Exploatarea utilajelor agricole, *Didactic and Pedagogical Publishing House,* Bucharest;

[26]   Toma D., et al., (1981), Tractors and agricultural machinery, Part I and II / Tractoare şi maşini agricole, partea I şi II. *Didactic and Pedagogical Publishing House,* Bucharest;

[27]   Vlăduţ I.D., Biriş S.Şt., Boruz S., Matei Gh., Vlăduţ V., Bungescu S., Marin E., Ungureanu N., Sorică C., Duţu I., Croitoru Şt., Voicea I., Matache M., Cujbescu D., Covaliu C., Danciu A., Brăcăcescu C., (2014), State of the art regarding conservative tillage technologies, *Annals of the University of Craiova - Agriculture, Montanology, Cadastre*, Series, Vol. 44, No. 2, pp. 256-264;

[28]   Vlăduţ I.D., David L., Marin E., Biriş S.Şt., Voiculescu I., Maican E., Vlăduţ V., Ungureanu N., Vlăduţoiu L., Fechete L., Croitoru Şt., Boruz S., Voicea I., Matache M., Bungescu S., (2015), Research on the development of a conservative technology, using optimized active bodies for soil tillage, *Annals Of The University Of Craiova - Agriculture, Montanology, Cadastre*, Series, Vol. 45, No. 2, pp. 247-252;

[29]   Wang X. Y., Gao H. W., Li H. W., (2003), A model of runoff and soil water balance under mechanized conservation tillage. *Agricultural Research in the Arid Areas*.

TECHNICAL AND ECONOMIC ASPECTS OF BIOGAS PRODUCTION AT A SMALL AGRICULTURAL ENTERPRISE WITH MODELING OF THE OPTIMAL DISTRIBUTION OF ENERGY RESOURCES FOR PROFITS MAXIMIZATION

/

ТЕХНІЧНІ ТА ЕКОНОМІЧНІ АСПЕКТИ ВИРОБНИЦТВА БІОГАЗУ НА МАЛОМУ СІЛЬСЬКОГОСПОДАРСЬКОМУ ПІДПРИЄМСТВІ З МОДЕЛЮВАННЯМ ОПТИМАЛЬНОГО РОЗПОДІЛУ ЕНЕРГЕТИЧНИХ РЕСУРСІВ ДЛЯ МАКСИМІЗАЦІЇ ПРИБУТКУ

Tokarchuk D.M., Pryshliak N.V., Tokarchuk O.A., Mazur K.V. [1]
Vinnitsa National Agrarian University / Ukraine
Tel: +380970447755; E-mail: pryshliak.vnau@gmail.com
DOI: https://doi.org/10.35633/inmateh-61-36

ABSTRACT

The use of biogas is one of the ways to supplement and partially replace traditional fuels in rural areas. The feasibility of farms' energy supply from their own energy source and the need to reduce harmful emissions into the environment make the biogas plant an indispensable element of modern livestock complexes. The article considers the possibility of using biogas for energy supply of an agricultural enterprise. The schemes and design capabilities of biogas plant for small and medium size farms are considered. The list and volume of products that can be obtained from the operation of the biogas plant have been determined. Economic indicators of the use of animal manure for biogas production have been determined. A comparison of the cost-effectiveness of using biogas energy products has been conducted.

РЕЗЮМЕ

Одним із шляхів доповнення і часткової заміни традиційних видів палива в сільській місцевості є використання біогазу. Доцільність автономного енергозабезпечення ферм з власного джерела енергії та необхідність зменшення шкідливих викидів у навколишнє середовище роблять блок з виробництва біогазу обов'язковим елементом сучасних тваринницьких комплексів. У статті розглянуто можливість використання біогазового палива для енергозабезпечення сільськогосподарського підприємства. Розглянуто схеми і конструктивні можливості фермерської біогазової установки для малих і середніх ферм. Обраховано перелік та обсяг продукції, яку даватиме біогазова установка підприємству. Визначено економічні показники використання гною тварин на виробництво біогазу. Проведено порівняння економічної ефективності використання енергетичних продуктів біогазового виробництва.

INTRODUCTION

The processing and disposal of organic waste by decomposing it under anaerobic conditions to produce combustible gas and its energy use has been utilised by people since ancient times. At the same time, the process of biological decomposition of organic substances with the formation of methane has not changed over the past millennia. The issue of waste accumulation and recycling combines environmental, resource and energy aspects, since waste is not only polluting the environment, but it is also a carrier of useful components (*Berezyuk S. et al 2019).* The increasing interest of utilizing biogas as substitute to natural gas or its exploitation as transport fuel opened new paths in the development of biogas upgrading techniques (*Angelidaki I. et al*, 2018).

---

[1] *Tokarchuk D.M., Ph.D. Econ.; Pryshliak N.V., Ph.D. Econ.; Tokarchuk O.A., Ph.D. Eng.*

Countries that lack energy reserves, as well as those that are concerned about the negative impacts of the production and use of fossil fuels, actively stimulate the development, production and consumption of alternative energy in general and bioenergy, in particular, at the state level (*Kaletnik H. et al, 2019*).

In Ukraine, one of the promising areas is the processing of livestock biomass by anaerobic digestion with the formation of biogas, which is then used to produce bioenergy. An important argument in favour of this energy source is the need to solve environmental problems arising from the disposal of agricultural waste.

The energy and climate policies in the EU and the introduction of various support schemes for promoting the utilization of renewable resources have encouraged the development of biogas plants for energy production. Anaerobic digestion provides opportunities for biogas to be used for generating energy, such as electricity, heat and fuel with additional economic, environmental and climate benefits. (*Scarlat N. et al, 2018*).

The environmental impacts and high long-term costs of poor waste disposal have pushed the industry to realize the potential of turning this problem into an economic and sustainable initiative. Anaerobic digestion and the production of biogas can provide an efficient means of meeting several objectives concerning energy, environmental, and waste management policy (*Adnan A. et al, 2019.*)

Ukraine has identified development of its agriculture as a strategic goal (*Zulauf C. et al, 2018*). At the same time 115 million tons of agricultural plant waste and about 97 million tons of animal waste are generated annually in Ukraine (*Pryshliak N., Tokarchuk D., 2020*).

An important aspect in the introduction of sustainable crop production and livestock production is the development of integrated technologies using methane digestion processes in the utilization of biomass, which produces biogas. Fermentation from agricultural waste produces not only biogas, but also concentrated organic fertilizers, which are a valuable product for use in modern technologies for growing crops. At the same time, biogas production requires considerable financial investment to implement innovative projects, however, the expected benefit from using biogas products outweighs what has to become an influential factor in stimulating production (*Tokarchuk, D., 2016*).

A number of works by foreign and domestic scientists have been devoted to the study of the current state and prospects of development of biogas technologies. As noted by *Holm-Nielsen J. et al, (2009)*, anaerobic digestion of animal manure and slurries offers several benefits by improving their fertilizer qualities, reducing odours and pathogens and producing a renewable fuel – the biogas. *Rasi S. et al, (2007)*, studied biogas composition and variation in three different biogas production plants to provide information pertaining to its potential use as biofuel. *Achinas S. et al, (2017)*, noted that biogas economy is related to factors such as waste availability and logistics, process efficiency, and end-product properties.

Manure is a livestock residue that causes high environmental burdens in different categories. Its usage in biogas production is an environmentally beneficial way not only to reduce these impacts, but also to produce energy and biofertilizers (*Esteves E. et al, 2019*). The use of biomethane lowers water, soil and air pollution not only because it eliminates fossil fuel related pollution but the risk of potentially devastating accidents is also remarkably reduced (*Bharathiraja B. et al, 2018*).

Korznikova M. et al, (2008), explored the possibilities of using biotechnology to process livestock and poultry waste into biogas to produce clean energy and prevent environmental pollution. Taking into account microbiological and biochemical bases of conversion of organic matter waste, the authors determined the optimal technological parameters of the process.

Suslov D., (2014), considered the use of biogas for agricultural gas supply. The author has developed a gas supply system for a pig farm, which includes a gas supply source – a biogas plant. *Blades. L. et al, (2017),* investigates the application of a circular economy in a rural agricultural setting in Northern Ireland, centred around a typical anaerobic digestion (AD) plant, showing its potential to provide renewable energy for the electricity and transport fuel needs of an average dairy farm and associated milk processing facilities.

Kurbatova T., (2018), analyses energy potential of agricultural biomass in Ukraine, economic tools, aimed at stimulating electricity generation from biogas based on animal waste, the results of their impact on biogas plants deployment.

Based on the EU experience and features of farm functioning, *Yevdokimov Y. et al, (2018),* approved that the biogas installation has not only the economic effect (profit and additional profit) for company, but also ecological and social effects for rural area, where this farm was located.

Therefore, to ensure efficient utilization of agricultural waste while ensuring energy generation, it is expedient to study more deeply the technical and economic aspects of biogas production. The aim of this study is to investigate technical and economic aspects of biogas production at a small agricultural enterprise and to model the optimal distribution of energy resources for profits maximization.

MATERIALS AND METHODS

Livestock waste is considered to be the most appropriate substrates for biogas production (as a separate substrate or in combination with other substrates). Unlike other types of biomass, such as energy crops, manure is produced as by-products of animal husbandry, which require disposal in an environmentally sustainable manner. In addition, manure is a good substrate for biogas production, as it is easily mixed with other feedstock, such as corn silage, plant residues and others.

The biogas plant operates on the principle of anaerobic digestion (without oxygen access). Liquid biowaste is delivered via a self-alloyed manure removal system to a receiving tank or pumped by faecal pumps through a pipeline. The primary preparation of raw materials takes place in a receiving tank (homogenization tank), biowaste is brought to a certain moisture consistency by mixing. After this, the primary fermentation of excrement occurs and biofeedstock is loaded into the reactors (bioreactor, fermenter). The bioreactor is a completely sealed tank, treated with anti-acid and anti-corrosion coating from the outside. Also, bioreactors are insulated, for each biogas plant the layer of insulation is calculated individually. It depends on the climatic conditions of the region where the biogas plant will be built. In conditions of Ukraine, insulation is necessary as winter temperatures are low enough.

The bioreactor can be made of both monolithic reinforced concrete and steel tanks. The biogas reactor operates on a continuous cycle basis. The prepared substrate is loaded into bioreactors daily, and the fermented feed is discharged from the reactor. The operation of the entire biogas station is controlled by commands from the central software module in the program-time mode and by limit value sensors. In biogas plants, a modular principle is applied, which enables the installation to operate in a complex, involving all reactors. In the case if there is a need to replace or shut down individual reactors, it is possible to regulate the technological process. It allows in case of an emergency to repair the unit without completely stopping the entire technological module. The application of the modular principle with increasing power can easily increase the number of bioreactors in a modular complex.

Mixing is carried out mechanically by means of mixers installed in the reactor or hydraulically (by pumps or by the pressure of the produced gas).

After fermentation of biowaste, two products are obtained - biogas and mineralized nitrogen fertilizers. The biogas reactor can be used for more than 25-30 years.

There are many different designs of biogas plants. They are distinguished by:
- way of loading raw materials;
- appearance;
- constituent parts of the structure;
- the materials from which they are constructed (*Kaletnik, G. 2018*).

By the method of loading feedstock, the digestors are divided into batch and continuous loading. Such installations differ in the time of fermentation and the regularity of loading feedstock. The most efficient in terms of biogas production and fertilizer production are continuous loading installations.

By design, the plants vary depending on the method of accumulation and storage of biogas. Gas can be collected in the upper solid part of the reactor, under a flexible dome, or in a special gas tank, floating or standing separately from the reactor.

We consider the possibility of producing biogas at a small agricultural enterprise in our study. This enterprise has the following annual livestock population: cattle - 30 heads, pigs - 15 heads, dairy cows - 15 heads, sheep - 30 heads.

Since the number of animals is small, the enterprise needs a low-power biogas plant. Its advantages are a high level of equipment standardization.

For small and medium-sized farms we offer the biogas production plant (fig. 1) with the possibility of processing from 0.3 to 1.5 tons of feedstock per day. The volume of the reactor ranges from 5 to 25 m^3.

Loading and mixing of raw materials are mechanized and carried out using a pneumatic system. With the help of mechanical mixers, the fermentation process in the reactor is distributed evenly throughout the volume.

Raw materials are heated in the biogas plant reactor using a heat exchanger with a biogas-fired boiler. The fermentation mixture remains in the reactor for as long as it is biologically necessary for the decomposition of biological substances by bacteria. The pipeline for unloading raw materials has branches for collecting biofertilizers in storage and for loading them into vehicles for transportation to the field.

The device of this biogas plant (see Fig. 1.) provides manual preparation and pneumatic loading of raw materials into the reactor, part of the produced biogas is used to heat the raw materials in the reactor. Mixing is done by biogas.
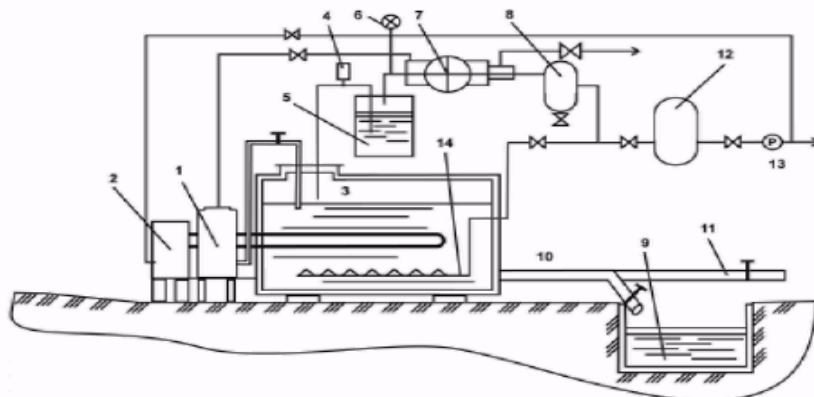

Fig. 1 - Scheme of a farm biogas plant with a gas tank, manual preparation and pneumatic loading and mixing of raw materials, with heating of the raw materials in the reactor

1 - feed hopper; 2 - water heating boiler, 3 - reactor; 4 - safety valve; 5 - a water lock; 6 - pressure gauge;
7 - compressor; 8 - receiver; 9 - biofertilizer storage; 10 - unloading of raw materials;
11 - pipe removal for loading into transport; 12 - gas tank; 13 - gas gear; 14 - mixing device.

Biogas plant for medium and large farms is proposed (Fig. 2). Its distinctive feature is the presence of a special tank for the preparation of raw materials, from which they are supplied with a compressor to the loading hopper, and then, using compressed biogas, to the installation reactor.
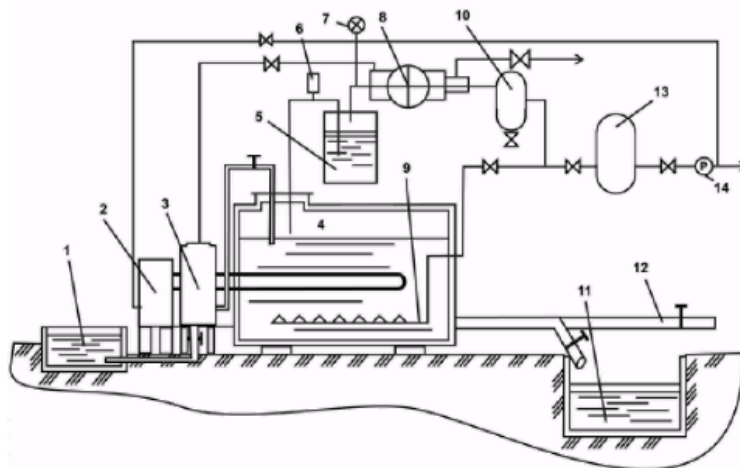
Fig. 2 - Scheme of a farm biogas plant with a gas tank, mechanical preparation and pneumatic loading and mixing of raw materials with heating of raw materials in the reactor

1 - manure receiver; 2 - water boiler; 3 - loading hopper; 4 - reactor; 5 - a water lock; 6 - safety valve;
7 - pressure gauge; 8 - compressor; 9 -gas mixer; 10 - receiver; 11 – biofertilizer storage;
12 - pipe removal for loading into vehicles; 13 - gas tank; 14 - gas gear.

Part of the biogas products is used for the operation of the heating system. The plant is equipped with automatic biogas extraction and a gas tank for its storage. The presence of a heating system allows you to operate a biogas plant in all modes of fermentation. Biogas is selected automatically and is stored in the gas tank. The installation can operate in any temperature regime of fermentation of raw materials.

To perform the task of improving the technical characteristics of a simple biogas plant that can be used in a conventional small enterprise, it is proposed to improve the design of the biogas reactor. The proposed design is based on the task of improving the biogas reactor by increasing the efficiency of maintaining the substrate heating temperature for biogas separation.

To solve the problem of optimal distribution of energy resources (based on biogas from waste) in order to maximize the profit of the enterprise mathematical methods were used. For this, the adapted technique of *Gavrisha V.I.* and *Perebinis I.* (*2014*) was used.

In the calculations, we take the indices for the use of biogas:

1 - for cogeneration unit.

2 - in a gas engine generator,

3 - in a gas boiler,

4 - for refuelling agricultural machinery.

Biogas consumption in the ith direction will be denoted by x_i (m^3).

It is proposed to consider the annual economic effect of the use of biogas in a conditional enterprise as a criterion of an economic-mathematical model. It makes the difference between the cost of energy resources (motor fuel, electric and thermal energy) obtained with the help of biogas, and the costs of acquiring and operating the corresponding energy equipment (cogeneration unit, heat-generating equipment, automobile gas-filling compressor station).

RESULTS

The results achieved in the development of rural technical support for the use of biogas plants are only a small step in solving the general complex problem. Technologies for processing organics using biomass of plant origin in biogas plants are spreading due to the reduction in the number of cattle and the increase in the cost of traditional energy sources.

The cost of a biogas plant (Fig 1) that meets the needs of a notional enterprise in Ukraine is 12.7 thousand Euros. In addition to the biogas plant itself, the enterprise will need a cogeneration plant, which will turn biogas into electric and heat energy. Its cost in Ukraine is 3.8 thousand Euros. Thus, the total cost of the equipment will be 16.5 thousand Euros. It is relatively low, since the capacity of the installation is small and amounts to 40.5 thousand m^3 of biogas per year.

The amount of produced biogas depends on the physicochemical properties of the feed, loaded into a fermenter. The level of biogas production is calculated per kilogram of dry mass contained in raw materials.

The biogas output from animal waste is significantly affected by the animal feeding ration, their age, and other factors that appear during the experimental study of fermentation processes.

The amount of generated waste depends on the age and type of keeping animals, as well as on the time of year. The average amount of biogas that can be obtained from 1 m^3 of animal excretion is estimated at 20-25 m^3, although the volume of 30-35 m^3 is considered to be a cost-effective amount in the technical and technological plan. It is also possible to add plant wastes having a high dry matter content to animal manure. According to the proposal of the equipment manufacturer (biogas plant Fig. 1), biogas is usually processed into heat and electric energy by a cogeneration unit. In addition, the biogas plant will give ready to use biofertilizer, which can be implemented on the market or used on the farm. The amount of biogas production products per day and per year is shown in Table 1.

Table 1

The list and quantity of products that the biogas plant will provide to the enterprise

List of products received	Quantity per day	Quantity per year
Biogas output		
Biogas output from cattle manure, (m^3)	63.8	23287.0
Biogas output from pig manure, (m^3)	3.2	1170.0
Biogas output from sheep manure, (m^3)	7.1	2592.0
Biogas output from dairy cow manure, (m^3)	37.1	13530.0
Total biogas output, (m^3)	111.2	40579.0
Biofertilizer output		
Biofertilizer output from cattle manure, (t)	5.6	2027.0
Biofertilizer output from pig manure, (t)	0.3	102.0
Biofertilizer output from sheep manure, (t)	0.6	226.0
Biofertilizer output from dairy cow manure, (t)	3.2	1178.0
Total biofertilizer output, (t)	**9.7**	**3532.0**
Electric and heat energy production		
Electric energy based on biogas, (kW · h)	225.0	82132.0
Heat energy based on biogas, (kW · h)	244.6	89274.0

The obtained heat and electric energy will be partially used to support the operation of the biogas plant, and the rest will be replaced by the purchase of similar products.

We analyse the economic efficiency of introducing biogas production based on the use of animal waste in a notional enterprise in Ukraine in the Table 2. To calculate the annual economic effect, we add the cost of electric and heat energy based on biogas and biofertilizers and subtract the reduced costs of a biogas plant. We calculate the payback period of investments as the quotient of dividing the investments by the annual economic effect (see Table 2).

Table 2

Economic indicators of the use of animal manure for biogas production

Indicator	Value
The cost of electricity based on biogas, (thousand Euro)	4.51
The cost of heat energy based on biogas, (thousand Euro)	4.80
The cost of biofertilizers, (thousand Euro)	5.53
Capital investments, (thousand Euro)	19.77
Depreciation of equipment, (thousand Euro)	1.65
Costs of servicing a biogas plant (salaries, payroll, electricity, repairs and maintenance), (thousand Euro)	2.68
Presented costs for a biogas plant, (thousand Euro)	7.30
Annual economic effect, (thousand Euro)	7.55
Payback period, (years)	2.62

The calculations showed that the annual economic effect will be 7.55 thousand Euro, the payback period for a biogas and cogeneration plant is relatively small - 2.6 years.

So, we calculated **the list and quantity of products that the biogas plant will provide to the enterprise** and the economic efficiency of the biogas plant (Fig.1) according to the parameters proposed by the equipment manufacturer.

To improve the natural and economic indicators of biogas production and products based on it, it is necessary to technically improve the biogas plant. Low productivity is the disadvantage of most small biogas plants due to uneven heating of the substrate and the technical complexity of the design.

The problem is solved by equipping the heating element with a cleaning device, that periodically moves to different sides of the rotating screw, at the ends of which there are reversing switches, and cleans the surface of the elements from sticking particles of the biomass substrate *(Liubin M.V., Tokarchuk O.A. et al, 2018)*. A scheme of an improved biogas reactor and A-A section are shown in Fig. 3, 4.
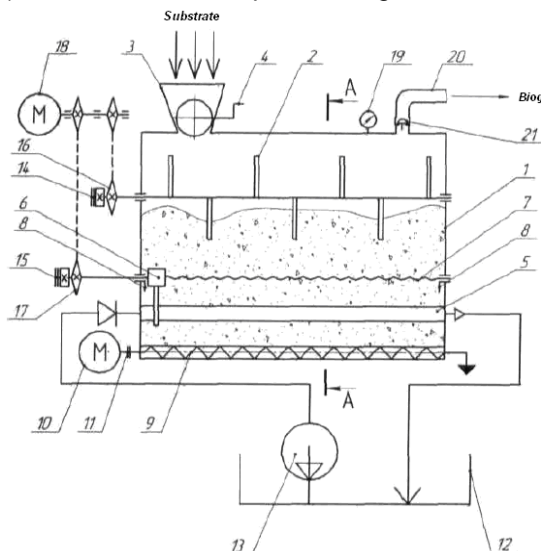
Fig. 3 - Scheme of biogas reactor   **Fig. 4 - A-A section**
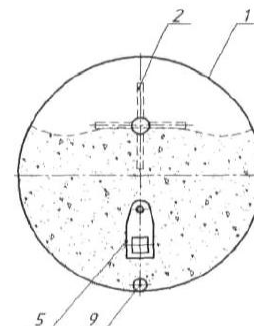
Biogas reactor contains a tank *1* with a stirrer *2* located inside it, a loading hopper *3* with an integrated slide gate valve *4*, a heating element *5*, equipped with a cleaning device *6*, that periodically moves along a rotary screw *7*, at the ends of which there are reversing switches *8*, an unloading screw *9*, which transfers the torque from the gear motor *10* using the clutch *11* to the tank *12*, the pump *13*, the electromagnetic

clutches *14* and *15*, located on the corresponding sprockets *16* and *17*, the electric motor *18*, electric contact pressure gauge *19* and a consumer pipe *20* equipped by mechanical valve *21*.

Biogas reactor operates as follows. With the open gate valve *4* through the hopper *3*, the substrate is fed into the tank *1*, which is filled in 2/3 of the volume. For an effective fermentation process, an electric motor *18* is turned on, followed by an electromagnetic clutch *14* located on the sprocket *16*, which drives the stirrer *2*. To increase the efficiency of fermentation in biogas reactor, a thermophilic mode is used, in which the temperature inside the biogas reactor must be maintained within the range of 50...55°C, therefore, from the tank *12*, the coolant (hot water) is supplied through the pump *13* to the heating element *5*, which heats the substrate.

In the process of heating the substrate, its particles stick to the surface of the heating element *5* over a period of time, which leads to a decrease in heat transfer. Therefore, to ensure efficient heat transfer of the heating element *5* during operation of the motor *18* by activating the electromagnetic clutch *15* located on the sprocket *17*, the cleaning device 6 is actuated, which moves along the heating element *5* by means of rotating screw *7*, at the ends of which switches *8* are arranged, that provide a change in the direction of movement of the treatment device *6*. Biogas resulting from the fermentation of the substrate, accumulates in the upper part of the tank *1*. At that time electric contact pressure gauge *19* controls pressure. If the pressure increases, the mechanical valve *21* is opening and biogas is released from the tank *1* through the consumer pipe *20* and the pressure is reduced.

By reducing the intensity of biogas production, the biomass substrate is discharged from the tank *1*. To do this, gear motor *10* is turned on, which transmits torque through the clutch *11* to the discharge screw *9*. Particular attention should be paid to the homogeneity of the fermentation mixture. The bacteria must be constantly supplied with organic matter in the reactor. This requires a constant flow of homogeneous organic mixture into the reactor.

Biogas has a small amount of sulphur in its composition, which affects the durability of biogas plants. To extract sulphur from biogas, fresh air is blown onto the surface of the fermentation mixture in the reactor by a small compressor. This leads to the fact that special microorganisms convert gaseous sulphur into a solid state, which becomes a valuable component of organic fertilizers.

Thus, the application of proposed cleaning device for heating element of the biogas reactor *15* makes it possible to significantly improve the efficiency of heat transfer and to ensure the continuous release of biogas for a certain period of time.

It is expected that after the proposed improvement of the reactor, the economic indicators of biogas production will improve: the annual economic effect will be 7.87 thousand Euro, the return period - 2.58 years.

Not only the efficient process of biogas production, but also its rational use is important for agricultural enterprise. There are different ways of using the obtained biogas within the agrarian formation; it is necessary to choose the option that will be most effective in the enterprise. The electricity generated from biogas is partly used to support the operation of the plant, and most of it is used for the enterprise's own needs. Excess energy can be sold to the state at a "green tariff". In addition to electricity, it also generates thermal energy that is used for the needs of the enterprise. It is also possible to use biogas as a motor fuel. Our task is to develop an economic and mathematical model of optimal distribution of biogas for energy purposes.

The purpose of mathematical modelling is to determine which energy needs and in what volumes it is advisable to use the resulting biogas to replace traditional energy resources at the maximum possible cost.

Thus, the objective function, which represents the annual economic effect, has the following form:

$$W = Ee + Eh + Ef - \sum_{i=1}^{n} (E_{H_i} \cdot K_i + OC_i) - W \cdot Pe - Q \cdot Pe \rightarrow max \qquad (1)$$

where *Ee, Eh, Ef* – gross income from the production of electric energy, heat energy and diesel substitution, respectively, (Euro);

E_{H_i} – normative coefficient of economic efficiency of capital investments in the ith direction of the use of biogas;

K_i – capital investments buried in the ith direction of biogas use, (Euro);

n – number of directions of biogas use;

OC_i – operating costs for the maintenance of energy equipment for the ith direction of biogas use, (Euro/year);

Pe – the price of electricity purchased by the enterprise, (Euro/(kWh));

W, Q – shortage, respectively, of the electrical and thermal energy required to ensure the operation of the biogas plant, (kWh).

The components of the gross income from the replacement of energy resources are the following.

1. Electricity:

$$Ee = \begin{cases} \left(\dfrac{x_1 + x_2}{be_e} - We_0\right) \cdot Pe & with \quad \dfrac{x_1 + x_2}{be_e} \leq We_0 + We_f \\[4mm] We_f \cdot Pe + \left[\dfrac{x_1 + x_2}{be_e} - We_0 - We_f\right] \cdot Pe_0 & with \quad \dfrac{x_1 + x_2}{be_e} \geq We_0 + We_f \end{cases} \tag{2}$$

where be_e – specific biogas consumption for electric energy production, (m³/(kWh));

We_0, We_f – annual electricity demand for biogas plant and enterprise, (kWh);

Pe_0 - wholesale price for electricity, (Euro / (kWh)).

2. Gross income from the use of thermal energy:

$$Eh = \begin{cases} 0 & with \quad \dfrac{x_1}{be_h} + \dfrac{x_3}{be_b} \leq Qe_0 \\[4mm] \left[\left(\dfrac{x_1}{be_h} - Qe_0\right) \cdot \dfrac{T_0}{365} - \dfrac{x_3}{be_b}\right] \cdot P_f & with \quad \dfrac{x_1}{be_h} + \dfrac{x_3}{be_b} < Qe_0 + Qe_f \end{cases} \tag{3}$$

where T_o – annual duration of the enterprise's need for heat energy, (days); be_h, be_b – specific consumption of biogas for heat energy production in cogeneration and boiler plants, (m³/kWh);

Qe_0, Qe_f – annual heat demand for biogas plant and enterprise, (kWh);

P_f – the price of heat energy, (Euro/kWh).

3. Gross revenue from diesel replacement by biogas:

$$Ef = \frac{x_4 \cdot Q_b}{\rho \cdot Q_d} \cdot P_f \tag{4}$$

where: ρ – diesel density, ρ = 0,83 kg/l; Q_b, Q_d – lower calorific value of biogas and diesel fuel, respectively, (MJ/m³ (MJ/kg)); P_f – the price of diesel fuel, (Euro/l).

The deficit of electric and thermal energy to ensure the operation of a biogas plant is determined by the formulas:

$$W = \begin{cases} 0 & with \quad \dfrac{x_1}{be} + \dfrac{x_2}{be} \geq Ne_0 \\[4mm] We_0 - \left(\dfrac{x_1}{be} + \dfrac{x_2}{be}\right) & with \quad \dfrac{x_1}{be} + \dfrac{x_2}{be} < Ne_0 \end{cases} \tag{5}$$

and

$$Q = \begin{cases} 0 & with \quad \dfrac{x_1}{be_h} + \dfrac{x_3}{be_b} \geq Qe_0 \\[4mm] Qe_0 - \left(\dfrac{x_1}{be} + \dfrac{x_2}{be}\right) & with \quad \dfrac{x_1}{be_h} + \dfrac{x_3}{be_b} < Qe_0 \end{cases} \tag{6}$$

We consider the limitations of the parameters of the objective function. Limitations on annual biogas use will be as follows:

$$\sum_{i=1}^{n} x_i \leq V, \tag{7}$$

where V - annual production of biogas, m³.

The amount of thermal energy that can be produced is limited by two components. The first is the restrictions on its use for the needs of a biogas plant and the enterprise:

$$\left(\frac{x_1 \cdot T_0}{365 \cdot be_h} + \frac{x_2}{be_b}\right) < Qe_0 + Qe_f \tag{8}$$

The second limitation is due to the fact that the daily use of biogas by heat generating capacities should not exceed the productivity of a biogas plant. This condition has the following mathematical notation:

$$V \geq x_1 + x_2 + x_3 \cdot \frac{365}{T_0}$$
(9)

Here we do not take into account the simultaneous use of biogas to provide the enterprise with thermal energy and the replacement of biogas of diesel fuel, because they do not coincide in time.

Limitations on the replacement of diesel fuel, which uses agrarian formations, also has two components, the first one is the maximum need for gaseous fuel:

$$x_4 \leq (1 - \lambda) \cdot Md \cdot \frac{Q_6}{Q_\partial}$$
(10)

where: λ – the proportion of inflammatory dose of diesel fuel when the diesel engine is operating on the gas-diesel cycle; Md – annual requirement of the enterprise in diesel fuel, (kg).

The second one takes into account the duration and simultaneity of the work of agricultural machinery with other biogas consumers and is limited by the daily output of a biogas plant:

$$V \geq x_1 + x_2 + x_4 \cdot \frac{365}{T_{am}}$$
(11)

where: T_{am} - annual duration of use of agricultural machinery, (days).

Thus, the objective function (1) and the restrictions on the use of biogas in various directions are formulated. To solve this problem, a program was developed in the Excel environment using the built-in "Solution Search" function.

It is necessary to determine the optimal use of biogas from agricultural waste for a notional enterprise. The productivity of biogas plant is 40.5 thousand m³ per year. The company buys natural gas in the amount of 4 thousand m³ per year, as well as diesel fuel, part of which can be replaced by biogas.

The efficiency of using energy products of biogas production offered by the manufacturer of equipment for biogas plants, after the proposed improvement of the reactor and optimized variants for the conditions of the notional enterprise are shown in table 3.

Table 3

Comparison of the economic efficiency of the use of energy products of biogas production

Indicator	Option offered by equipment manufacturer	Optimized option 1	Option after the proposed improvement of the reactor	Optimized option 2
Biogas costs in different directions, (thousand m³):				
• cogeneration plant	40.5	25.5	41.5	26.1
• gas boiler	0	6.9	0	7.1
• motor fuel	0	8.1	0	8.3
Power of cogeneration plant, (kW)				
• electric	10.0	6.5	10.2	6.6
• heat	12.0	7.7	12.3	7.9
Boiler plant power, (kW)	0	8.5	0	8.7
Annual production, (thousand kWh)				
• electric energy	82.1	55.5	84.1	56.9
• energy	89.3	45	91.5	46.1
Substituted diesel fuel, (m³)	0.00	4.7	0	4.8
Additional investments, (thousand Euro)	19.80	24.5	20.3	25.1
Annual economic effect (value of the objective function), (thousand Euro)	7.55	9.78	7.87	10.19
Payback period, (years)	2.62	2.51	2.58	2.46

It is advisable for the enterprise to convert only part of the biogas into electric and heat energy. It is economically viable to use part of biogas as a substitute for natural gas.

It is necessary to take into account in the calculations that biogas is equal to natural gas at a coefficient of 0.6, therefore, 6.9 thousand m^3 of biogas will meet 4.1 thousand m^3 of natural gas, that is, the notional enterprise will be able to completely refuse to purchase natural gas. The cost of purchasing diesel fuel is growing annually, so it is advisable to partially replace it by biogas.

CONCLUSIONS

Biogas production is an important area of providing agricultural enterprises with energy resources. Simple biogas plants are recommended to be installed for small farms, which, on the one hand, are easy to operate, and on the other, have problems with the uniformity of substrate heating. In the proposed design of a biogas reactor, the problem is solved by the retrofitting of the heating element with a treatment device.

The economic indicators of using a simple biogas plant and a plant with an advanced reactor are calculated. Using economic and mathematical modelling, the optimal distribution of the energy resource based on biogas from waste was carried out. The calculations performed show that for a conditional enterprise with 30 head of cattle, 15 head of pigs, 15 head of dairy cows and 30 head of sheep, the best option is to use biogas to ensure the operation of the cogeneration plant, boiler and diesel fuel replacement, that differ from the option that the manufacturer of equipment for biogas plants offers.

REFERENCES

[1] Achinas S., Achinas V., Euverink G. J. W. (2017). A technological overview of biogas production from biowaste. *Engineering*, 3(3), 299-307. DOI: https://doi.org/10.1016/J.ENG.2017.03.002;

[2] Adnan A. I., Ong M. Y., Nomanbhay S., Chew K. W., Show P. L. (2019). Technologies for biogas upgrading to biomethane: a review. *Bioengineering*, 6(4), 92. DOI: https://doi.org/10.3390/bioengineering6040092;

[3] Angelidaki I., Treu L., Tsapekos P. Luo, G., Campanaro S., Wenzel H., Kougias, P. G. (2018), Biogas upgrading and utilization: Current status and perspectives. *Biotechnology advances*, 36(2), 452-466. DOI: https://doi.org/10.1016/j.biotechadv.2018.01.011;

[4] Berezyuk S., Tokarchuk D., Pryhliak N., (2019), Resource Potential of Waste Usage as a Component of Environmental and Energy Safety of the Sate. *Journal of Environmental Management and Tourism*, (Volume X, Fall), 5(37): 1157 - 1167. DOI:10.14505/jemt.v10.5(37).23, Craiova/Romania;

[5] Bharathiraja B., Sudharsana T., Jayamuthunagai J., Praveenkumar R., Chozhavendhan S., Iyyappan, J. (2018). Biogas production–A review on composition, fuel properties, feed stock and principles of anaerobic digestion. *Renewable and sustainable Energy reviews*, 90(C), 570-582. DOI: https://doi.org/10.1016/j.rser.2018.03.093;

[6] Blades L., Morgan K., Douglas R., Glover S., De Rosa M., Cromie, T., Smyth, B. (2017), Circular biogas-based economy in a rural agricultural setting. *Energy Procedia*, 123, 89-96. DOI: https://doi.org/10.1016/j.egypro.2017.07.255;

[7] Esteves E. M. M., Herrera A.M.N., Esteves V.P.P., Morgado C.D.R.V. (2019), Life cycle assessment of manure biogas production: a review. *Journal of Cleaner Production*, 219, 411-423. DOI: https://doi.org/10.1016/j.jclepro.2019.02.091;

[8] Gavrish V.I., Perebinis I., (2014), Economic Efficiency of Bioconversion of Vegetable Raw Materials to Biogas (Економічна ефективність біоконверсії рослинної сировини в біогаз). *Scientific Papers of the National University of Food Technology (Наукові праці Національного університету харчових технологій),* Vol.20, 6, 68-75, Kiev/Ukraine;

[9] Holm-Nielsen J.B., Al Seadi T., Oleskowicz-Popiel P., (2009), The future of anaerobic digestion and biogas utilization. *Bioresource technology*, 100(22), 5478-5484, Netherlands;

[10] Kaletnik G., (2018), *Production and use of biofuels*: Second edition, supplemented: textbook. Vinnytsia: LLC "Nilan-Ltd", 336, Kiev/Ukraine;

[11] Kaletnik H., Pryshliak V., Pryshliak N., (2019), Public Policy and Biofuels: Energy, Environment and Food Trilemma. *Journal of Environmental Management and Tourism*, (Volume X, Summer), 3(35): 479-487. DOI:10.14505/jemt.v10.3(35).01, Craiova/Romania;

[12] Korznikova M.V., Blokhin A. Yu., Kozlov Yu.P., (2008), Assessment of the degree of conversion of organic matter from livestock and poultry waste into biogas (taking as an example the Russian Federation) (Оценка степени превращения органических веществ из отходов животноводства и птицеводства в биогаз (на примере Российской Федерации). *Bulletin of Voronezh State University.*

Series: Chemistry. Biology. Pharmacy (Вестник Воронежского государственного университета. Серия: Химия. Биология. Фармация), (2), 108-111, Voronezh/Russia;

[13] Kurbatova T., (2018), Economic benefits from production of biogas based on animal waste within energy co-operatives in Ukraine. *International Journal of Sustainable Energy Planning and Management,* 18, 69-80, Aalborg University, Aalborg/Denmark.

[14] Lubin M.V., Tokarchuk O.A., Yaropud V.M., Tokarchuk D.M., (2018), *Biogas reactor*. Utility Model Patent, Ukraine, (Біогазовий реактор. Патент на корисну модель, Україна). UA 127444, Owner: Vinnytsia National Agrarian University (Власник: Вінницький національний аграрний університет), bul. 14 of 25.07.18, Vinnytsia/Ukraine;

[15] Pryshliak N., Tokarchuk D., (2020), Socio-economic and environmental benefits of biofuel production development from agricultural waste in Ukraine. *Environmental & Socio-economic Studies*, 8(1), 18-27. DOI:10.2478/environ-2020-0003;

[16] Rasi S., Veijanen A., Rintala J., (2007), Trace compounds of biogas from different biogas production plants. *Energy*, 32(8), 1375-1380, United Kingdom;

[17] Scarlat N., Dallemand J.F., Fahl F., (2018), Biogas: Developments and perspectives in Europe. *Renewable energy*, *129*, 457-472. DOI: https://doi.org/10.1016/j.renene.2018.03.006;

[18] Suslov D. Yu., (2014), Development of a gas supply system for an agricultural enterprise using biogas (Разработка системы газоснабжения сельскохозяйственного предприятия с использованием биогаза). *Bulletin of the Bryansk State Technical University named after V.G. Shukhov* (*Вестник Белгородского государственного технологического университета им. В.Г. Шухова*), 4, 183-186, Bryansk/Russia;

[19] Tokarchuk D.M., (2016), Investment support for biogas production by Ukrainian agricultural enterprises (Інвестиційна підтримка виробництва біогазу українськими сільськогосподарськими підприємствами). *Economy. Finances. Management: Topical Issues in Science and Practice (Економіка. Фінанси. Менеджмент: актуальні питання науки та практики)*, 12, 26-35, Vinnytsia/Ukraine;

[20] Yevdokimov Y., Chygryn, O., Pimonenko T., Lyulyov O., (2018), Biogas as an alternative energy resource for Ukrainian companies: EU experience (Біогаз як альтернативний енергетичний ресурс для українських компаній: досвід ЄС). *Innovative Marketing (Інноваційний маркетинг)*, 14, 7-15, Sumy/Ukraine;

[21] Zulauf C., Prutska O., Kirieieva E., Pryshliak N., (2018), Assessment of the potential for a biofuels industry in Ukraine. *Problems and Perspectives in Management*, 16(4): 83-90. DOI:http://dx.doi.org/10.21511/ppm.16(4).2018.08, Sumy/Ukraine.

WRITING INSTRUCTIONS

Article Types

Three types of manuscripts may be submitted:

1. **Regular articles:** These should describe new and carefully confirmed findings, and experimental procedures should be given in sufficient detail for others to verify the work. The length of a full paper should be the minimum required to describe and interpret the work clearly (max.10 pages, <u>even number</u>);

2. **Reviews:** Submissions of reviews and perspectives covering topics of current interest are welcome and encouraged (max.12 pages, <u>even number</u>).

Manuscripts should be written in English (American or British usage is accepted, but not a mixture of these) and submitted **electronically** at the following e-mail addresses: *inmatehjournal@gmail.com*
Please be sure to include your full affiliation and e-mail address (see Sample manuscript)
The authors are responsible for the accuracy of the whole paper and references.
There are allowed 2 papers by each first author.
The text layout should be in single-column format. To avoid unnecessary errors it is strongly advised to use the "spell-check" and "grammar check" functions of your word processor.

Review Process

All manuscripts are reviewed by 2 members of the Scientifically Review Office. Decisions will be made as rapidly as possible and the journal strives to return reviewers' comments to authors in approx.3 weeks.
The editorial board will re-review manuscripts that are accepted pending revision.

NOTE:

Submission of a manuscript implies: that the work described has not been published before (excepting as an abstract or as part of a published lecture or thesis) that it is not under consideration for publication elsewhere.

1. REGULAR ARTICLES

- Manuscripts should be concise, in *1.15 line spacing*, and should have 2 cm all over margins. The font should be *Arial 10 pt.* Ensure that each new paragraph is clearly indicated, using **TAB at 1 cm**.
- Title will be *Arial 12 pt.* and explicit figures will be *Arial 9 pt*.
- Text will be written in English.
- Chapters' titles are written by *Arial 10 pt, Bold, Uppercase* (e.g. **INTRODUCTION, MATERIALS AND METHODS**), between chapters is left a space for 10 pt. At the beginning of each paragraph, TAB of 1 cm.
- The paper body will be written in *Arial 10 pt., Justify alignment*.

TITLE *Arial 12 pt., Uppercase, Bold, Center* (in English language) and *Bold Italic (in native language).*
Should be a brief phrase describing the contents of the paper. Avoid long titles; a running title of no more than 100 characters is encouraged (without spaces).

AUTHORS *ARIAL 9, Bold, Centre alignment*
Under the paper's title, after a space (enter) 9 pt., write *authors' names* and *affiliations (Arial 8 pt.-Regular)*
When the paper has more than one author, their name will be followed by a mark (Arabic numeral) as superscript if their affiliation is different. Less than 6 authors.
Corresponding author's name (next row), *(Arial 8 pt.)*. Should be added also: phone, fax and e-mail information, for the paper corresponding author (*font: 8 pt., Italic*).

KEYWORDS *(In English)* about 4 to 7 words that will provide indexing references should be listed (<u>title</u>: *Arial 10pt, bold italic,* text *Arial 10 pt., italic*).

A list of non-standard *Abbreviations* should be added. In general, non-standard abbreviations should be used only when the full term is very long and used often. Each abbreviation should be spelled out and introduced in parentheses the first time it is used in the text. Standard abbreviations (such as ATP and DNA) need not to be defined.
ABSTRACT *(in English and Native language, Arial 10 pt.)*, the title *bold*; the text of abstract: *italic*) should be informative and completely self-explanatory, briefly present the topic, state the scope of the experiments, indicate significant data, and point out major findings and conclusions. The Abstract should be max.250 words. Complete sentences, active verbs, and the third person should be used, and the abstract should be written in the past tense. Standard nomenclature should be used and abbreviations should be avoided. No literature should be cited.
INTRODUCTION (*Arial 10 pt.)* should provide a clear statement of the problem, the relevant literature on the subject, and the proposed approach or solution. It should be understandable to colleagues from a broad range of scientific subjects. We should refer to the current stage of researches performed in the field of the paper to be published, by quoting up-to-date specialty studies, preferably published after 2006, excepting certain referential specialty

books/studies, especially papers issued in magazines/journals/conferences/ISI quoted symposia or in other international data bases, which are well known and available.

MATERIALS AND METHODS (*Arial 10 pt.)* should be complete enough to allow experiments to be reproduced. However, only truly new procedures should be described in detail; previously published procedures should be cited, and important modifications of published procedures should be mentioned briefly. Methods in general use need not be described in detail.

RESULTS (*Arial 10 pt.)* should be clarity presented. The results should be written in the past tense when describing findings in the authors' experiments. Results should be explained, but largely, without referring to the literature. Discussion, speculation and detailed interpretation of data should not be included in the Results, but should be put into the Conclusions section.

CONCLUSIONS (*Arial 10 pt.)* The main conclusions drawn from results should be presented in a short Conclusions section. Do not include citations in this section.

Formulae, symbols and abbreviations: Formulae will be typeset in Italics (preferable with the Equation Editor of Microsoft Office 2003) and should be written or marked as such in the manuscript, unless they require a different styling. They should be referred to in the text as Equation (4) or e.g. (4). The formulae should be numbered on the right side, between brackets *(Arial 10 pt.)*:

$$P = F \cdot v \tag{1}$$

Terms of the equation and the unit measure should be explained, e.g.

     P is the power, [W];
     F – force, [N];
     v – speed, [m/s]

SI units must be used throughout.

Tables should be self-explanatory without reference to the text. The details of the methods used in the experiments should preferably be described in the legend instead of in the text. The same data should not be presented both in table and graph form or repeated in the text.

Table's title will be typed *Arial 9 pt, Bold, Centered*

In the table, each row will be written Arial 9 pt, single-spaced throughout, including headings and footnotes.

The table should be numbered on the right side, *Arial 10 pt.*

Figures (Arial 9 pt., Bold, Center) should be typed in numerical order (Arabic numerals). Graphics should be high resolution (e.g.JPEG). Figure number is followed by what represent the figure or graph e.g.:

Fig. 1 – Test stand

Legend: Arial 8 pt, Italic, Center, e.g.:

     1 - plansifter compartments; 2- break rolls; 3 – semolina machines; 4 – reduction rolls; 5 – flour

ACKNOWLEDGMENTS (*Arial 10 pt.)* of people, grants, funds etc should be brief (*if necessarily*).

REFERENCES (*Arial 10 pt.)*

     (In alphabetical order, in English and in the original publication language).
     Minimum 10 references, last 10 years, minimum 3 references from the last 2 years

It can be used "*References*" tool from the *Word Editor*. **APA Style (American Psychological Association)**
https://apastyle.apa.org/style-grammar-guidelines/references/examples

All references must be provided in English
Authors are fully responsible for the accuracy of the references.

References should be **alphabetically**, with complete details, as follows:

Examples:

Books: https://apastyle.apa.org/style-grammar-guidelines/references/examples/book-references

Jackson, L. M. (2019). *The psychology of prejudice: From attitudes to social action* (2nd ed.). American Psychological Association. https://doi.org/10.1037/0000168-000

Kesharwani, P. (2020). *Nanotechnology based approaches for tuberculosis treatment*. Academic Press.

Sapolsky, R. M. (2017). *Behave: The biology of humans at our best and worst*. Penguin Books.

Torino, G. C., Rivera, D. P., Capodilupo, C. M., Nadal, K. L., & Sue, D. W. (2019). *Microaggression theory: Influence and implications*. John Wiley & Sons. https://doi.org/10.1002/9781119466642

In text:
- ***Parenthetical citations***: (Jackson, 2019; Sapolsky, 2017)
- ***Narrative citations***: Jackson (2019) and Sapolsky (2017)

Journal Article:

https://apastyle.apa.org/style-grammar-guidelines/references/examples/journal-article-references

Grady, J. S., Her, M., Moreno, G., Perez, C., & Yelinek, J. (2019). Emotions in storybooks: A comparison of storybooks that represent ethnic and racial groups in the United States. *Psychology of Popular Media Culture*, *8*(3), 207–217. https://doi.org/10.1037/ppm0000185

In text:
- ***Parenthetical citation***: (Grady et al., 2019)
- ***Narrative citation***: Grady et al. (2019)

Conference or Symposium:

https://apastyle.apa.org/style-grammar-guidelines/references/examples/conference-proceeding-references

Duckworth, A. L., Quirk, A., Gallop, R., Hoyle, R. H., Kelly, D. R., & Matthews, M. D. (2019). Cognitive and noncognitive predictors of success. *Proceedings of the National Academy of Sciences*, *USA*, *116*(47), 23499–23504. https://doi.org/10.1073/pnas.1910510116

In text:
- ***Parenthetical citation***: (Duckworth et al., 2019)
- ***Narrative citation***: Duckworth et al. (2019)

Dissertation / Thesis:

https://apastyle.apa.org/style-grammar-guidelines/references/examples/published-dissertation-references

Zambrano-Vazquez, L. (2016). *The interaction of state and trait worry on response monitoring in those with worry and obsessive-compulsive symptoms* [Doctoral dissertation, University of Arizona]. UA Campus Repository. https://repository.arizona.edu/handle/10150/620615

In text:
- ***Parenthetical citations***: (Kabir, 2016; Miranda, 2019; Zambrano-Vazquez, 2016)
- ***Narrative citations***: Kabir (2016), Miranda (2019), and Zambrano-Vazquez (2016)

https://apastyle.apa.org/style-grammar-guidelines/references/examples/unpublished-dissertation-references

Harris, L. (2014). *Instructional leadership perceptions and practices of elementary school leaders* [Unpublished doctoral dissertation]. University of Virginia.

In text:
- ***Parenthetical citation***: (Harris, 2014)
- ***Narrative citation***: Harris (2014)

Patents: Names and initials of authors, year (between brackets), patent title (Italic), patent number,country:

Grant, P. (1989). *Device for Elementary Analyses*. Patent. No.123456. USA.

Legal regulations and laws, organizations:

https://apastyle.apa.org/style-grammar-guidelines/references/examples/iso-standard-references

International Organization for Standardization. (2018). *Occupational health and safety management systems— Requirements with guidance for use* (ISO Standard No. 45001:2018). https://www.iso.org/standard/63787.html

Occupational Safety and Health Administration. (1970). *Occupational safety and health standards: Occupational health and environmental control: Occupational noise exposure* (OSHA Standard No. 1910.95). United States Department of Labor.

https://www.osha.gov/laws-regs/regulations/standardnumber/1910/1910.95

In text:
- ***Parenthetical citations***: (International Organization for Standardization, 2018; Occupational Safety and Health Administration, 1970)
- ***Narrative citations***: International Organization for Standardization (2018) and Occupational Safety and Health Administration (1970)

Web references: The full URL should be given in text as a citation, if no other data are known. If the authors, year, and title of the documents are known and the reference is taken from a website, the URL address has to be mentioned after these data.

Citation in text

Please ensure that every reference cited in the text is also present in the reference list (and vice versa). **Do not cite references in the Abstract and Conclusions !**.

Unpublished results, personal communications as well as URL addresses are not recommended in the references list.

Making personal quotations (one, at most) should not be allowed, unless the paper proposed to be published is a sequel of the cited paper. Articles in preparation or articles submitted for publication, unpublished, personal communications etc. should not be included in the references list.

Citations style

Text: All citations in the text may be made directly (or parenthetically) as bellow.

- *single author*: the author's name (without initials, unless there is ambiguity) and the year of publication:
     "as previously demonstrated *(Brown, 2010)*".

- *two authors*: both authors' names and the year of publication: *(Adam and Brown, 2008; Smith and Hansel, 2006; Stern and Lars, 2009)*

- *three or more authors*: first author's name followed by "et al." and the year of publication: "As has recently been shown *(Werner et al., 2005; Kramer et al., 2000)* have recently shown ...."

Citations of groups of references should be listed first alphabetically, then chronologically.

Units, Abbreviations, Acronyms
- Units should be metric, generally SI, and expressed in standard abbreviated form.
- Acronyms may be acceptable, but must be defined at first usage.

2. REVIEWS

Summaries, reviews and perspectives covering topics of current interest in the field, are encouraged and accepted for publication. Reviews do not have the requirements for regular articles. However, should include: (*) an introductory chapter, (**) a careful and critical presentation of the relevant aspects of the topic approached and (***) emphasis of the aspects that aren't known and require further research to progress. Reviews should be concise (max. 12 pages).